

NASA-CP-2376-VOL-4  
19850026416

NASA CP-2376  
V 4

# 19TH INTERNATIONAL COSMIC RAY CONFERENCE

LA JOLLA, USA AUGUST 11-23, 1985

## CONFERENCE PAPERS



11

12



# 19TH INTERNATIONAL COSMIC RAY CONFERENCE

LA JOLLA, USA AUGUST 11-23, 1985

## CONFERENCE PAPERS



**SH**  
SESSIONS  
VOL. 4

## PUBLICATION COMMITTEE

F C Jones, Chm  
J Adams  
G.M Mason

NASA Conference Publication 2376

Published by  
Scientific and Technical Information Branch  
National Aeronautics and Space Administration  
Washington, D.C. 20546

August 1985

For sale by the National Technical Information Service, Springfield, VA 22151

## PREFACE

The 19th International Cosmic Ray Conference, under the auspices of the Cosmic Ray Commission of the International Union of Pure and Applied Physics, is being held on the campus of the University of California, San Diego, on 11 through 23 August 1985. In keeping with the tradition begun in 1971 by the Australian organizers of the 12th ICRC, the Proceedings of this conference are appearing in two sets of volumes. The first set, consisting of volumes 1 through 8, is being distributed to all participants at the beginning of the conference. This set contains the contributed papers. The second set, distributed after the conference, contains invited, rapporteur, and highlight papers. The papers are reproduced here exactly as they were received from the authors, without refereeing.

For the 19th ICRC, the scientific program was organized according to three major divisions-- OG (cosmic rays and gamma rays of Galactic Origin), SH (Solar and Heliosphere), and HE (High Energy). Technical papers are included in each of the three divisions.

This conference depended on funds from several agencies of the United States government, including major financial support from the National Aeronautics and Space Administration and support from the National Science Foundation, the Department of Energy, and the Air Force Geophysics Laboratory. Important financial support also came from the Center for Astrophysics and Space Sciences of the University of California, San Diego, from the California Space Institute of the University of California, from the Department of Physics and Astronomy of the University of Maryland, College park, from the International Union for Pure and Applied Physics, and from several corporate sponsors who will be acknowledged by name in the post-conference volumes.

We appreciate the confidence placed in the conference organizers by the Cosmic Ray Commission, and acknowledge with thanks the role of the Commission members in setting up the rules for the conference and in advising the organizers during its planning.

We are grateful to all of the members of the various organizing committees listed at the front of this volume. The three Program Committees went to great effort to organize a coherent scientific program and to schedule four parallel sessions with a minimum of conflicts. The Local Organizing Committee has worked long and hard to ensure efficient and hospitable accommodations for all the participants, both in the scientific sessions and outside them. The Publications Committee not only took great pains to assemble these volumes but also maintained an orderly data base of papers and authors which was extremely helpful to the program committees. The General Organizing Committee made important contributions of ideas and efforts to make the conference possible; this committee included international representation from all of North America, thus the departure from the traditional name of National Organizing Committee. And the entire effort was coordinated by the dedicated members of the Steering Committee.

Martin H. Israel, Chairman  
General Organizing Committee

August, 1985

## LETTER FROM THE EDITORS

This conference marks a departure from previous conferences in this series in that the publication of the Conference Papers was carried out an entire continent away from the activities of Local Organizing Committee. This posed some problems but, to the considerable surprise of the Publications Committee members, the one that was expected to be the most trouble turned out not to be significant. The overwhelming majority of those submitting papers and abstracts sent them to the correct address, not to La Jolla as was feared. We wish to thank our many authors for their alertness and commend them for handling a complicated situation so well.

There are eight volumes to be distributed to the conference participants in addition to the Conference Program and Author Index: three volumes for OG, two for SH and three for HE. the detailed makeup of these volumes is described in the prefaces written by the Scientific Program chairmen for their respective volumes. Out of some 1100 abstracts that were accepted by the Scientific Program Committees for inclusion in the conference some 929 papers were finally received in time for inclusion in the Conference Papers. This represents a response of approximately 84 percent, a modest improvement. Even if one excludes the 42 one page papers that should be considered as "confirming abstracts", even though there was no such formal category, the response was somewhat higher than that of recent years. We attribute this to the carrot of a later deadline than before coupled with the stick of there being no printing of post deadline contributed papers. We believe that this decision of the General Organizing Committee was a wise one. Of course invited, rapporteur, and highlight talks will be printed in volumes to be distributed to the participants after the conference as usual.

The Publications Committee had much generous help in performing its duties: from Goddard Space Flight Center we had the help of B. Glasser, L. Harris, E. Schronce, N. Smith, J. Esposito and T. Smith. From the Naval Research Laboratory we were helped by T. Mazzotta, and at the University of Maryland M. L. Snidow and J. Mucha gave much needed assistance. Special thanks are due to Caryl Short, the lone staff member of the Publications Committee. She maintained the computer data base, organized the abstracts as they arrived, and kept track of the papers themselves to see that the finally arrived in the right place at the right time. Without her help the job would have been far more difficult than it was.

PUBLICATIONS COMMITTEE

August, 1985

Frank C. Jones, Chm.  
Jim Adams  
Glen M. Mason

# SH SESSIONS VOLUME IV

**10th INTERNATIONAL COSMIC RAY CONFERENCE  
LA JOLLA, USA  
AUGUST 11-23, 1985**

**INTERNATIONAL UNION OF PURE AND APPLIED PHYSICS  
MEMBERS OF THE COMMISSION ON COSMIC RAYS OF IUPAP**

AE Chudakov, Chm	PH Fowler	TO Montmerle	BV Sreekantan
FB McDonald	D Hovestadt	H Moraal	K Suga
GC Castagnoli	J Kota	JR Prescott	J Wdowczyk

**STEERING COMMITTEE**

F McDonald, Chm	T Gaisser	F Jones	R Mewaldt
G Burbage	M Israel	R Lingenfelter	L Peterson
M Forman			

**GENERAL ORGANIZING COMMITTEE**

M Israel, Chm	V Jones	B Price	J Simpson
M Bercovitch	S Krimigis	R Ramaty	B Stone
P Freier	J Kurfess	F Reines	D Venkatesan
R Gall	J Lockwood	M Shapiro	J Waddington
R Jokipii	P Meyer	M Shea	S White
L Jones			

**PROGRAM COMMITTEES**

<b>OG SESSIONS</b>	<b>SH SESSIONS</b>	<b>HE SESSIONS</b>	<b>PUBLICATIONS</b>
R Mewaldt, Chm	M Forman, Chm	T Gaisser, Chm	F Jones, Chm
G Cassidy	H Hudson	K Lande	J Adams
C Fichtel	G Mason	J Linsley	G Mason
A Harding	B McKibben	E Loh	
J Matteson	M Pomerantz	G Yodh	
D Muller			
W Webber			

**LOCAL ORGANIZING COMMITTEE**

L Peterson, Chm	A Buffington	J Linsley	O Piccioni
G Burbidge	M Burbidge	K Marti	M Thieme
R Lingenfelter	W Fillius	G Masek	W Thompson
R Rothschild	R Gall	J Matteson	H Ticho
J Arnold	R Gould	C McIlwain	R White
W Baity	H Hudson	R Mewaldt	

**Sponsored by**

National Aeronautics and Space Administration  
National Science Foundation  
Department of Energy  
Center for Astrophysics and Space Science, University of California, San Diego  
California Space Institute, University of California  
Department of Physics and Astronomy, University of Maryland, College Park

## PREFACE TO THE VOLUMES 4 AND 5 (SH)

The category SH includes all papers on solar and heliospheric energetic particle phenomena. SH combines the MG (modulation of galactic) and SP (solar particles) categories used in previous conferences, with papers on particles accelerated in the solar wind. Papers about techniques and instrumentation for science in the SH category are now included in SH. Cosmogenic nuclide studies, formerly in OG (origin and galactic) are also in the new SH category. Papers on particles of strictly magnetospheric origin were not included in this conference.

The SH heading numbers are :

- SH1. Particle Acceleration on the Sun and in the Heliosphere
- SH2. Composition, Spectra and Anisotropy
- SH3. Propagation of Solar and Interplanetary Energetic Particles
- SH4. Solar-Cycle Modulation and Propagation of Galactic Particles in the Heliosphere
- SH5. Transient Modulations
- SH6. Geomagnetic and Atomospheric Effects and Response Functions
- SH7. Cosmogenic Nuclides
- SH8. Solar Neutrinos
- SH9. Techniques
- SH10. Others

Papers appear in this volume in a numerical sequence determined primarily by this numbering system. For example, paper number SH2.1-8 is the eighth paper in the first session formed of papers in category SH2.

We thank the SH program committee for devising this numbering system, for reading every abstract submitted and for organizing on the basis of their content coherent sessions with reasonable length for presentation. We thank them also for selecting the rapporteurs and for advice in the selection of invited and highlight speakers. The committee members are: Hugh Hudson (UCSD), Bruce McKibben (U. of Chicago), Glenn Mason (U. of Maryland), Martin Pomerantz (Bartol Res. Foundation, U. of Delaware) and alternate Walker Fillius (UCSD).

These contributed papers are reviewed in plenary session by a team of expert rapporteurs at the end of the Conference. These extremely useful reports can only be prepared during the Conference, and so their written versions will be included in a later volume. We thank the rapporteurs in advance for their willing service.

Miriam A. Forman, Chairman  
Solar - Heliospheric Program Committee

This conference is the 19th in a series. Previous conferences in this series were held at:

Cracow, Poland	-	1947
Como, Italy	-	1949
Bagnères-de-Bigorre, France	-	1953
Guanajuato, Mexico	-	1955
Varenna, Italy	-	1957
Moscow, USSR	-	1959
Kyoto, Japan	-	1961
Jaipur, India	-	1963
London, UK	-	1965
Calgary, Canada	-	1967
Budapest, Hungary	-	1969
Hobart, Australia	-	1971
Denver, USA	-	1973
München, FRG	-	1975
Plovdiv, Bulgaria	-	1977
Kyoto, Japan	-	1979
Paris, France	-	1981
Bangalore, India	-	1983



---

SH 1.1  
SOLAR FLARE ACCELERATION

---

PAPER CODE		PAGE
SH 1.1-3	PROPAGATION OF SOLAR FLARE PARTICLES IN A TURBULENT CORONAL LOOP  JM RYAN	1
SH 1.1-4	STOCHASTIC PARTICLE ACCELERATION IN SOLAR FLARES  W DROGE,R SCHLICKEISER	2
SH 1.1-5	FIRST-ORDER FERMI SHOCK ACCELERATION IN SOLAR FLARES  DC ELLISON,R RAMATY	6
SH 1.1-6	PROMPT ACCELERATION OF IONS BY OBLIQUE TURBULENT SHOCKS IN SOLAR FLARES  RB DECKER,L VLAHOS	10
SH 1.1-7	FAST DRIFT KILOMETRIC RADIO BURSTS AND SOLAR PROTON EVENTS  EW CLIVER,SW KAHLER,HV CANE,RE MCGUIRE TT VON ROSENVINGE,RG STONE	14
SH 1.1-8	STUDY OF PHOTON EMISSION BY ELECTRON CAPTURE DURING SOLAR NUCLEI ACCELERATION I. TEMPERATURE-DEPENDENT CROSS SECTION FOR CHARGE CHANGING PROCESSES  J PEREZ-PERAZA,M ALVAREZ,A LAVILLE A GALLEGOS	18
SH 1.1-9	STUDY OF PHOTON EMISSION BY ELECTRON CAPTURE DURING SOLAR NUCLEI ACCELERATION II. DELIMITATION OF CONDITION FOR CHARGE TRANSFER ESTABLISHMENT  J PEREZ-PERAZA,M ALVAREZ,A GALLEGOS	22

SH 1.1-10	STUDY OF PHOTON EMISSION BY ELECTRON CAPTURE DURING SOLAR NUCLEI ACCELERATION: III. PHOTON PRODUCTION EVALUATIONS	26
	J PEREZ-PERAZA, M ALVAREZ, A GALLEGOS	

---

SH 1.2  
FLARE X-RAYS AND ELECTRONS

---

PAPER CODE		PAGE
SH 1.2-2	STUDY OF NON-THERMAL PHOTON PRODUCTION UNDER DIFFERENT SCENARIOS IN SOLAR FLARES: I. SCENARIOS AND FORMULATIONS  J PEREZ-PERAZA,M ALVAREZ,A GALLEGOS	30
SH 1.2-3	STUDY OF NON-THERMAL PHOTON PRODUCTION UNDER DIFFERENT SCENARIOS IN SOLAR FLARES: II. THE COMPTON INVERSE AND BREMSSTRAHLUNG MODELS AND FITTINGS  J PEREZ-PERAZA,M ALVAREZ,A LAVILLE A GALLEGOS	34
SH 1.2-4	SPECTRAL AND SPATIAL PROPERTIES OF SOLAR MICROFLARES  GM SIMNETT,BR DENNIS	38
SH 1.2-6	TEMPORAL EVOLUTION OF AN ENERGETIC ELECTRON POPULATION IN AN INHOMOGENEOUS MEDIUM. APPLICATION TO SOLAR HARD X-RAY BURSTS  N VILMER,AL MACKINNON,G TROTTET	42
SH 1.2-7	QUANTITATIVE ANALYSIS OF FLARE ACCELERATED ELECTRONS THROUGH THEIR HARD X-RAY AND MICROWAVE RADIATION  KL KLEIN,G TROTTET	46
SH 1.2-8	AN EXTENDED "SUPERHOT" SOLAR FLARE X-RAY SOURCE  HS HUDSON,KI OHKI,S TSUNETA	50
SH 1.2-9	OBSERVATIONS OF SOLAR FLARE PHOTON ENERGY SPECTRA FROM 20 KEV TO 7 MEV  M YOSHIMORI,H WATANABE,N NITTA	54
SH 1.2-10	ION ENERGY STORAGE FOR POST-FLARE LOOPS  HS HUDSON	58

xii  
VOLUME 4

SH 1.2-11	TWO TYPES OF ELECTRON EVENTS IN SOLAR FLARES	62
	EI DAIBOG,VG KURT,YI LOGACHEV VG STOLPOVSKY	
SH 1.2-12	TWO CLASSES OF SOLAR ENERGETIC PARTICLE EVENTS ASSOCIATED WITH IMPULSIVE AND LONG DURATION SOFT X-RAY FLARES	66
	HV CANE,RE MCGUIRE,TT VON ROSENVINGE	
SH 1.2-13	A DOMINANT ROLE FOR PROTONS AT THE ONSET OF SOLAR FLARES	70
	GM SIMNETT	
SH 1.2-14	THE ENERGY SPECTRA OF SOLAR FLARE ELECTRONS	74
	P EVENSON,D HOVESTADT,P MEYER,D MOSES	

---

SH 1.3  
GAMMA-RAY FLARES AND INTERPLANETARY  
PROTONS

---

PAPER CODE		PAGE
SH 1.3-1	ONSET OF SOLAR FLARES AS PREDICTED BY TWO-DIMENSIONAL MPD-MODELS OF QUIESCENT PROMINENCES  J GALINDO TREJO	78
SH 1.3-2	THE STARTING CONDITIONS FOR AN OPTICALLY SMALL SOLAR GAMMA RAY FLARE  GM SIMNETT, JM RYAN	82
SH 1.3-5	ON THE DETECTABILITY OF KEV-MEV SOLAR PROTONS THROUGH THEIR NONTHERMAL LYMAN-ALPHA EMISSION  RC CANFIELD, CR CHANG	86
SH 1.3-6	OBSERVATIONS OF SOLAR FLARE GAMMA-RAYS AND PROTONS  M YOSHIMORI, H WATANABE	90
SH 1.3-7	ENERGETIC PROTONS FROM A DISAPPEARING SOLAR FILAMENT  SW KAHLER, EW CLIVER, HV CANE, RE MCGUIRE RG STONE, NR SHEELEY	94
SH 1.3-8	HELIOS 1 ENERGETIC PARTICLE OBSERVATIONS OF SOLAR GAMMA RAY/NEUTRON FLARE EVENTS OF 7, 21 JUNE 1980 AND 3 JUNE 1982  FB MCDONALD, MAI VAN HOLLEBEKE JH TRAINOR	98
SH 1.3-9	INJECTION OF ENERGETIC PARTICLES FOLLOWING THE GAMMA-RAY FLARES ON JUNE 7, 1980, AS OBSERVED ON HELIOS-1  HH NEUSTOCK, G WIBBERENZ, B IWERS	102

xiv  
VOLUME 4

SH 1.3-11	ULTRARELATIVISTIC ELECTRONS AND SOLAR FLARE GAMMA-RADIATION	106
	PE SEMUKHIN,GA KOVALTSOV	
SH 1.3-13	SOURCE ENERGY SPECTRA FROM DEMODULATION OF SOLAR PARTICLE DATA BY INTERPLANETARY AND CORONAL TRANSPORT	110
	J PEREZ-PERAZA,M ALVAREZ,F RIVERO	
SH 1.3-14	SPECTRA OF SOLAR PROTON GROUND LEVEL EVENTS USING NEUTRON MONITOR AND NEUTRON MODERATED DETECTOR RECORDINGS	114
	PH STOKER	
SH 1.3-15	GROUND INCREASE OF COSMIC RAY INTENSITY ON FEBRUARY 16, 1984	118
	AV BELOV,YAL BLOKH,EA EROSHENKO VN ISHKOV,VG YANKE	
SH 1.3-17	THE SCR FLARE OF 16 FEBRUARY 1984 AS RECORDED BY THE SAYAN SPECTROGRAPH	122
	SA KOZLOV,NI PAKHOMOV,LA SHAPOVALOVA AL YANCHUKOVSKY	

---

SH 1.4  
SOLAR FLARE NEUTRONS

---

PAPER CODE		PAGE
SH 1.4-1	THE EXTENDED PRODUCTION OF NEUTRONS DURING A SLAR FLARE  EL CHUPP,DJ FORREST,WT VESTRAND H DEBRUNNER,E FLUCKIGER,JF COOPER G KANBACH,C REPPIN,GH SHARE	126
SH 1.4-2	FURTHER OBSERVATIONS OF PROTONS RESUTING FROM THE DECAY OF NEUTRONS EJECTED BY SOLAR FLARES  P EVENSON,R KROEGER,P MEYER	130
SH 1.4-3	SUGGESTIONS FOR IMPROVING THE EFFICIENCY OF GROUND-BASED NEUTRON MONITORS FOR DETECTING SOLAR NEUTRONS  N IUCCI,M PARISI,C SIGNORINI,M STORINI G VILLORESI	134
SH 1.4-5	SEARCH FOR SOLAR NEUTRONS USING NM-64 EQUIPMENT  NJ MARTINIC,A REGUERIN,E PALENQUE MA TAQUICHIRI,M WADA,A INOUE,K TAKAHASHI	138
SH 1.4-6	A SEARCH FOR SOLAR NEUTRINOS ON A LONG DURATION BALLOON FLIGHT  R KOGA,GM FRYE,A OWENS,BV DENEHY,O MACE J THOMAS	142
SH 1.4-7	NEUTRAL PION PRODUCTION IN SOLAR FLARES  DJ FORREST,WT VESTRAND,EL CHUPP E RIEGER,JF COOPER,GH SHARE	146
SH 1.4-8	HIGH ENERGY NEUTRON AND GAMMA RADIATION GENERATED DURING THE SOLAR FLARES  GE KOCHAROV,NZ MANDZHAVIDZE	150

xvi  
VOLUME 4

SH 1.4-9	ON THE ANGULAR AND ENERGY DISTRIBUTION OF SOLAR NEUTRONS GENERATED IN P-P REACTIONS	154
	YUE EFIMOV,GE KOCHAROV	
SH 1.4-10	POSSIBLE DETECTION OF FLARE-GENERATED POSITRONS BY HELIOS 1 ON 3 JUNE 1982	158
	E KIRSCH,E KEPPLER,K RICHTER	



---

SH 1.5  
INTERPLANETARY ACCELERATION

---

PAPER CODE		PAGE
SH 1.5-1	SHOCK AND STATISTICAL ACCELERATION OF ENERGETIC PARTICLES IN THE INTERPLANETARY MEDIUM  JF VALDES-GALICIA,X MOUSSAS,JJ OUNBY FM NEUBAUER,R SCHWENN	162
SH 1.5-3	ENERGETIC ION ACCELERATION AT COLLISIONLESS SHOCKS  RB DECKER,L VLAHOS	166
SH 1.5-4	ACCELERATION OF IONS AND ELECTRONS NEAR-COSMIC RAY ENERGIES IN A PERPENDICULAR SHOCK: THE JANUARY 6, 1978 EVENT  SM KRIMIGIS,ET SARRIS	170
SH 1.5-5	PARTICLE ACCELERATION DUE TO SHOCKS IN THE INTERPLANETARY FIELD: HIGH TIME RESOLUTION DATA AND SIMULATION RESULTS  RL KESSEL,TP ARMSTRONG,R NUBER,J BANDLE	174
SH 1.5-6	PITCH ANGLE DISTRIBUTIONS OF 35-1000 KEV PROTONS AT QUASI-PERPENDICULAR INTERPLANETARY SHOCKS  A BALOGH,G ERDOS	178
SH 1.5-12	SPATIAL DEPENDENCE OF THE LOCAL DIFFUSION COEFFICIENT UPSTREAM OF THE NOVEMBER 12, 1978 INTERPLANETARY TRAVELING SHOCK  G GLOECKLER,FM IPAVICH,B KLECKER D HOVESTADT,M SCHOLER	182
SH 1.5-14	LATITUDE DEPENDENCE OF CO-ROTATING SHOCK ACCELERATION  RE GOLD,LJ LANZEROTTI,CG MACLENNAN SM KRIMIGIS	186

xviii  
VOLUME 4

SH 1.5-15	ELEMENTAL ABUNDANCES IN COROTATING EVENTS	190
	TT VON ROSENVINGE, RE MCGUIRE	
SH 1.5-16	SOLAR AND INTERPLANETARY PARTICLES AT 2 TO 4 MEV DURING SOLAR CYCLES 21: SOLAR CYCLE VARIATIONS OF EVENT SIZES, AND COMPOSITIONS	192
	TP ARMSTRONG, JC SHIELDS, PR BRIGGS S ECKES	
SH 1.5-17	COSMIC RAY ACCELERATION BY STELLAR WIND. SIMULATION FOR HELIOSPHERE	196
	SI PETUKHOV, AA TURPANDV, VS NIKOLAEV	
SH 1.5-18	THE ENERGY SPECTRUM OF JOVIAN ELECTRONS IN INTERPLANETARY SPACE	200
	SP CHRISTON, AC CUMMINGS, EC STONE WR WEBBER	
SH 1.5-19	THE JOVIAN ELECTRON SPECTRUM: 1978 - 1984	201
	P EVENSON, P MEYER, D MOSES	

---

SH 2.1  
SOLAR PARTICLES,  $Z > 1$

---

PAPER CODE		PAGE
SH 2.1-1	OBSERVATION OF THE FLUXES OF NUCLEI WITH ENERGIES OF 10-20 MEV PER NUCLEON DURING THE SOLAR FLARE OF APRIL 26, 1984  VV BOBROVSKAYA,NL GRIGOROV,DA ZHURAVLEV MMA KONDRATYEVA,RA NYMMIK,CHA TRETYAKOVA NV ALEKSEEV,PV VAKULOV,PV VAKULOV VP SECHINOV	205
SH 2.1-3	ENERGETIC PARTICLE OBSERVATIONS OF SOLAR GAMMA RAY/NEUTRON FLARE EVENTS OF 3 JUNE 1982 AND 21 JUNE 1980 ISOTOPIC AND CHEMICAL COMPOSITION  MAI VAN HOLLEBEKE,FB MCDONALD JH TRAINOR	209
SH 2.1-4	PRECISION MEASUREMENTS OF SOLAR ENERGETIC PARTICLE ELEMENTAL COMPOSITION  HH BRENEMAN,EC STONE	213
SH 2.1-5	SOLAR CORONAL AND PHOTOSPHERIC ABUNDANCES FROM SOLAR ENERGETIC PARTICLE MEASUREMENTS  HH BRENEMAN,EC STONE	217
SH 2.1-6	SILICON TO IRON ABUNDANCES IN SOLAR COSMIC RAYS AND IN THE SUN  MN VAHIA,S BISWAS,N DURGAPRASAD	221
SH 2.1-7	VARIATION IN ELEMENTAL COMPOSITION OF SEVERAL MEV/NUCLEON IONS OBSERVED IN INTERPLANETARY SPACE  RE MCGUIRE,TT VON ROSENVINGE,DV REAMES	225

xx  
VOLUME 4

SH 2.1-8	ON THE RETENTION OF HIGH-ENERGY PROTONS AND NUCLEI WITH CHARGES $Z \geq 2$ IN LARGE SOLAR FLARES AFTER THE PROCESS OF THEIR ACCELERATION	229
	NN VOLODICHEV, BM KUZHEVSKY, OYU NECHAEV IA SAVENKO	
SH 2.1-9	DIFFUSION IN THE CHROMOSPHERE, AND THE COMPOSITION OF THE SOLAR CORONA AND ENERGETIC PARTICLES	233
	S VAUCLAIR, JP MEYER	
SH 2.1-10	ANOMALOUS ABUNDANCES OF SOLAR ENERGETIC PARTICLES AND CORONAL GAS: COULOMB EFFECTS AND FIRST IONIZATION POTENTIAL (FIP) ORDERING	237
	DJ MULLAN	
SH 2.1-11	MEAN CHARGE STATES OF N, NE, MG, SI, AND S DURING SOLAR ENERGETIC PARTICLE EVENTS	241
	A LUHN, D HOVESTADT, B KLECKER, M SCHOLER G GLOECKLER, FM IPAVICH, AB GALVIN, CY FAN LA FISK	
SH 2.1-12	CALCULATIONS OF HEAVY ION CHARGE STATE DISTRIBUTIONS FOR NONEQUILIBRIUM CONDITIONS	245
	A LUHN, D HOVESTADT	
SH 2.1-13	ABUNDANCES FROM SOLAR FLARE GAMMA RAY LINE SPECTROSCOPY	249
	RJ MURPHY, B KOZLOVSKY, R RAMATY DJ FORREST	
SH 2.1-14	SOLAR FLARE GAMMA RAY LINE SPECTROSCOPY	253
	B KOZLOVSKY, RJ MURPHY, R RAMATY	

---

SH 2.2  
HELEUM-3 RICH SOLAR EVENTS

---

PAPER CODE		PAGE
SH 2.2-1	ISOTOPIC OVERABUNDANCES AND THE ENERGETIC PARTICLE MODEL OF SOLAR FLARES  R PEREZ-ENRIQUEZ,S BRAVO	257
SH 2.2-2	NUCLEOSYNTHESIS IN THE TERRASTIAL AND SOLAR ATMOSPHERES  C YU,R ZHOU,S ZHAN	261
SH 2.2-3	TYPE III SOLAR RADIO BURSTS AND **3HE-RICH EVENTS  DV REAMES,RG STONE	265
SH 2.2-4	SOLAR SOURCE REGIONS OF 3**HE-RICH PARTICLE EVENTS  SW KAHLER,RP LIN,DV REAMES,RG STONE M LIGGETT	269
SH 2.2-5	**3HE IN SOLAR NON-RELATIVISTIC ELECTRON EVENTS  DV REAMES,RP LIN,DV REAMES	273
SH 2.2-6	ELEMENTAL ABUNDANCE DIFFERENCES BETWEEN NUCLEI ACCELERATED IN CIR SHOCKS AND SOLAR FLARES3HE-RICH SOLAR FLARES  WF DIETRICH,JA SIMPSON	277
SH 2.2-7	THE HEAVY ION COMPOSITION IN **3HE-RICH SOLAR FLARES  GM MASON,DV REAMES,D HOVESTADT TT VON ROSENVINGE	281
SH 2.2-8	MEAN CHARGE OF SILICON IN 3**HE-RICH SOLAR FLARES  A LUHN,B KLECKER,D HOVESTADT,E MOBIUS	285

xxii  
VOLUME 4

SH 2.2-9	ON THE CONNECTION BETWEEN THE **3HE-ENRICHMENT AND SPECTRAL INDEX OF SOLAR ENERGETIC PARTICLES	289
	LG KOCHAROV,YAV DVORYANCHIKOV	
SH 2.2-10	THE PLASMA MECHANISM FOR PREFERENTIAL ACCELERATION OF HEAVY IONS	293
	LG KOCHAROV,AV DRISHCHENKO	

---

SH 3.1  
CORONAL PROPAGATION AND ANISOTROPY

---

PAPER CODE		PAGE
SH 3.1-1	OBSERVATIONS OF SOLAR ENERGETIC PARTICLES AT A SYNCHRONOUS ORBIT  T TAKENAKA,T YANAGIMACHI,K ITO,Y OHI T KOHNO,K SAKURAI	297
SH 3.1-2	CORONAL PROPAGATION OF SOLAR FLARE PARTICLES OBSERVED BY GEOSTATIONARY SATELLITE  T KOHNO,N NITTA,M WADA,T SUDA	301
SH 3.1-3	CORONAL PROPAGATION OF FLARE ASSOCIATED ELECTRONS AND PROTONS  G SCHELLERT,G WIBBERENZ,H KUNOW	305
SH 3.1-5	GEOMETRY OF THE DIFFUSIVE PROPAGATION REGION IN THE AUGUST 14, 1982 SOLAR ELECTRON EVENT  P EVENSON	309
SH 3.1-6	PECULIARITIES OF PROAGATION OF CHARGED PARTICLES IN SOLAR CORONA  EI MOROZOVA,NF PISARENKO,NA MIKRYUKOVA VV KLIMENKO,VE TIMOFEEV,YUG SHAFER	313
SH 3.1-7	SOME CHARACTERISTICS OF THE SOLAR FLARE EVENT OF FEBRUARY 16, 1984  H DEBRUNNER,E FLUCKIGER,JA LOCKWOOD RE MCGUIRE	317
SH 3.1-8	CONSTRAINTS ON SOLAR FLARE PARTICLE TRANSPORT MODELS FROM ANISOTROPY OBSERVATIONS AT VOYAGER 1  DC HAMILTON,GM MASON,G GLOECKLER	321

xxiv  
VOLUME 4

SH 3.1-9	LOW ENERGY PROTON BIDIRECTIONAL ANISOTROPIES AND THEIR RELATION TO TRANSIENT INTERPLANETARY MAGNETIC STRUCTURES: ISEE-3 OBSERVATIONS	322
	RG MARSDEN, TR SANDERSON, KP WENZEL EJ SMITH	
SH 3.1-10	SECOND-ORDER COMPTON-GETTING EFFECT ON ARBITRARY INTENSITY DISTRIBUTION	326
	CK NG	
SH 3.1-11	DETERMINATION OF THE PITCH-ANGLE DISTRIBUTION AND TRANSVERSE ANISOTROPY OF INTERPLANETARY PARTICLES	330
	CK NG	
SH 3.1-13	PITCH ANGLE DISTRIBUTIONS OF SOLAR ENERGETIC PARTICLES AND THE LOCAL SCATTERING PROPERTIES OF THE INTERPLANETARY MAGNETIC FIELD	334
	J BEECK, G WIBBERENZ	



SH 3.2  
SOLAR PARTICLE PROPAGATION

PAPER CODE		PAGE
SH 3.2-1	EXPONENTIAL ANISOTROPY OF SOLAR COSMIC RAYS JW BIEBER, PA EVENSON, MA POMERANTZ	335
SH 3.2-2	ENERGETIC SOLAR PARTICLE EVENTS KB FENTON, AG FENTON, JE HUMBLE	339
SH 3.2-3	CHANNELED PROPAGATION OF SOLAR PARTICLES KA ANDERSON, WM DOUGHERTY	342
SH 3.2-4	THE PROPAGATION OF SOLAR ENERGETIC PARTICLES IN MAGNETIC CHANNELS FB MCDONALD, LF BURLAGA	346
SH 3.2-5	RADIAL TRANSPORT OF $\sim 1$ MEV/NUCLEON IONS DURING THE 22 NOVEMBER 1977 SOLAR PARTICLE EVENT GM MASON, DC HAMILTON, G GLOECKLER B KLECKER	347
SH 3.2-6	ENERGETIC SOLAR FLUXES OUT TO 3 AU DURING THE MAY 7, 1978 FLARE EVENT JA LOCKWOOD, H DEBRUNNER	351
SH 3.2-8	THE LOCAL CHARACTERISTIC FUNCTION OF INTERPLANETARY PARTICLE PROPAGATION G GREEN, W SCHLUTER	355
SH 3.2-9	INVESTIGATION OF COSMIC RAY PROPAGATION IN INTERPLANETARY SPACE EA CHEBAKOVA, EV KOLOMEETS VN SEVAST'YANOV	356
SH 3.2-10	DIFFUSION-CONVECTION FUNCTION OF COSMIC RAYS GL YANG, GL ZHANG	360

xxv1  
VOLUME 4

- SH 3.2-11 MONTE CARLO CALCULATIONS OF RELATIVISTIC SOLAR PROTON PROPAGATION IN INTERPLANETARY SPACE 364  
M LUMME,JJ TORSTI,E VAINIKKA,J PELTONEN  
M NIEMINEN,E VALTONEN,H ARVELA
- SH 3.2-13 ON REFLECTING BOUNDARY BEHIND THE EARTH'S ORBIT AT PROPAGATION OF FAST PARTICLES FROM SOLAR FLARES 368  
AS NISKOVSIIKH,AT FILIPPOV

---

SH 4.1  
EPISODIC MODULATION

---

PAPER CODE		PAGE
SH 4.1-2	THE DISPERSIVE EVOLUTION OF CHARGED-PARTICLE BUNCHES IN RANDOM MAGNETIC FIELDS  VK BABAYAN, MB BAGDASARIAN	372
SH 4.1-3	NUMERICAL DESCRIPTIONS OF COSMIC-RAY TRANSPORT  JA EARL, JR JOKIPII	376
SH 4.1-4	NUMERICAL AND ANALYTIC DESCRIPTIONS OF COSMIC-RAY TRANSPORT  JA EARL	380
SH 4.1-7	THE ROLE OF SHOCK WAVES IN MODULATION OF GALACTIC COSMIC RAYS  R GALL, H DURAND	384
SH 4.1-9	THE INTENSITY RECOVERY OF FORBUSH-TYPE DECREASES AS A FUNCTION OF HELIOCENTRIC DISTANCE AND ITS RELATIONSHIP TO THE 11-YEAR VARIATION  JA LOCKWOOD, WR WEBBER, JR JOKIPII	388
SH 4.1-10	CUMULATIVE EFFECT OF FORBUSH DECREASES IN THE HELIOSPHERE MODULATION DURING THE PRESENT SOLAR CYCLE  SP AGRAWAL, BL MISHRA, AK JAIN D VENKATESAN	392
SH 4.1-11	COSMIC RAY MODULATION AND MERGED INTERACTION REGIONS  LF BURLAGA, FB MCDONALD, ML GOLDSTEIN	396
SH 4.1-12	PROPAGATION OF THE PHASE OF COSMIC-RAY MODULATION  MA FORMAN, FC JONES	400

SH 4.1-13	LATITUDE VARIATION OF RECURRENT FLUXES IN THE OUTER SOLAR SYSTEM	404
	SP CHRISTON, EC STONE	
SH 4.1-14	LONGITUDINAL DISTRIBUTION OF COSMIC RAYS IN THE HELIOSPHERE	405
	RE GOLD, D VENKATESAN	
SH 4.1-16	THE 1973-1984 SOLAR MODULATION OF COSMIC RAY NUCLEI	409
	M GARCIA-MUNOZ, KR PYLE, JA SIMPSON M GARCIA-MUNOZ	
SH 4.1-20	COSMIC RAY MODULATION IN A RANDOM ANISOTROPIC MAGNETIC FIELD	413
	LI DORMAN, YUI FEDOROV, MI KATZ, SF NOSOV BA SHAKHOV	
SH 4.1-21	EVIDENCE FOR REGIONS OF NEGLIGIBLE COSMIC-RAY MODULATION IN THE INNER HELIOSPHERE (<10 AU)	417
	EC ROELOF	

---

SH 4.2  
LONG TERM MODULATION AND NEUTRAL SHEET  
EFFECTS

---

PAPER CODE		PAGE
SH 4.2-3	NOTES ON DRIFT THEORY  RA BURGER,H MORAAL,GM WEBB,H MORAAL	421
SH 4.2-4	DRIFT AND OBSERVATIONS IN COSMIC-RAY MODULATION. I.  MS POTGIETER	425
SH 4.2-5	DRIFT AND OBSERVATIONS IN COSMIC-RAY MODULATION. II  MS POTGIETER	429
SH 4.2-6	COSMIC RAY NORTH-SOUTH ANISOTROPY 1965-1982:  JW BIEBER,MA POMERANTZ	433
SH 4.2-7	NORTH-SOUTH ASYMETRY IN ACTIVITY ON THE SUN AND COSMIC RAY DENSITY GRADIENTS  DB SWINSON,MA SHEA,JE HUMBLE	437
SH 4.2-8	COSMIC RAY INTENSITY AND THE TILT OF THE NEUTRAL SHEET  T SAITO,DB SWINSON	441
SH 4.2-9	DIFFERENTIAL MEASUREMENT OF COSMIC-RAY GRADIENT WITH RESPECT TO INTERPLANETARY CURRENT SHEET  SP CHRISTON,AC CUMMINGS,EC STONE KW BEHANNON,LF BURLAGA	445
SH 4.2-10	SPATIAL VARIATION OF COSMIC RAYS NEAR THE HELIOSPHERIC CURRENT SHEET  JR JOKIPII,J KOTA	449

xxx  
VOLUME 4

SH 4.2-11	EFFECTS OF A WAVY NEUTRAL SHEET ON COSMIC RAY ANISOTROPIES	453
	J KOTA, JR JOKIPII	
SH 4.2-12	EFFECTS OF SOLAR MAGNETIC FIELD ON COSMIC RAYS	457
	GA GONCHAR, EV KOLOMEETS, AKH LYAKHOVA NV SLYUNYAEVA, NV STEKOL'NIKOV	
SH 4.2-13	DETERMINATION OF GALATIC COSMIC RAY LATITUDINAL GRADIENT USING EARTH BASED DETECTORS	461
	BADRUDDIN, RS YADAV	
SH 4.2-14	THE EXPECTED COSMIC RAY DENSITY AND STREAM DISTRIBUTIONS AT THE HELIOLATITUDINAL ASYMMETRY OF SOLAR WIND	465
	MV ALANIA, RG ASLAMAZASHVILI, LI DORMAN K ISKRA	
SH 4.2-16	LATITUDINAL GRADIENTS OF COSMIC RAYS AND THE POLARITY REVERSAL OF THE HELIOSPHERIC MAGNETIC FIELD: A PRELIMINARY EVALUATION	469
	G NEWKIRK, JA LOCKWOOD, M GARCIA-MUNOZ JA SIMPSON	
SH 4.2-17	THE INFLUENCE OF NONSTATIONARITY OF THE SOLAR ACTIVITY AND GENERAL SOLAR FIELD ON MODULATION OF COSMIC RAYS	473
	AG ZUSMANOVICH, ON KRYAKUNOVA LF CHURONOVA, YAE SHVARTSMAN	
SH 4.2-18	THE EFFECT OF THE NEUTRAL SHEET STRUCTURE OF THE INTERPLANETARY MAGNETIC FIELD ON COSMIC RAY DISTRIBUTION IN SPACE	477
	MV ALANIA, RG ASLAMAZASHVILI TB BOCHORISHVILI, TV DJAPIASHVILI VS TKEMALADZE	

SH 4.2-19	ON THE INFLUENCE OF THE HELIOMAGNETOSPHERIC PERIPHERY ON THE GALACTIC COSMIC RAYS	481
	MMB KRAINEV,YUI STOZHKO TN CHARAKHCHYAN	
SH 4.2-20	SPATIAL DISTRIBUTION OF COSMIC RAYS IN MAGNETIC CYCLES OF THE SUN	485
	MV ALANIYA,RT GUSHCHINA,LI DORMAN	
SH 4.2-21	11- AND 22-YEAR VARIATIONS OF THE COSMIC RAY DENSITY AND OF THE SOLAR WIND SPEED	489
	NP CHIRKOV	
SH 4.2-22	DIFFERENCE BETWEEN EVEN AND ODD 11-YEAR CYCLES IN COSMIC RAY INTENSITY	493
	JA OTAOLA,R PEREZ-ENRIQUEZ JF VALDES-GALICIA	
SH 4.2-23	THE DEPENDENCE OF SOLAR MODULATION ON THE SIGN OF THE COSMIC RAY PARTICLE CHARGE	497
	M GARCIA-MUNOZ,P MEYER,KR PYLE JA SIMPSON,P EVENSON	
SH 4.2-24	AN UPDATE ON THE CORRELATION BETWEEN THE COSMIC RADIATION INTENSITY AND THE GEOMAGNETIC AA INDEX	501
	MA SHEA,DF SMART	





## THE PROPOGATION OF SOLAR FLARE PARTICLES IN A TURBULENT CORONAL LOOP

J. M. Ryan  
Space Science Center, University of New Hampshire  
Durham, New Hampshire 03824 USA

ABSTRACT

Energetic solar flare particles, both electrons and protons, must survive the turbulent environment of a flaring loop and propagate to the lower corona or chromosphere in order to produce hard X-ray and  $\gamma$ -ray bursts. This plasma turbulence, often observed in soft x-ray line widths to be in excess of 100 km/s, is presumably capable of efficiently scattering the fast flare particles. This prevents to some degree the free streaming of accelerated particles and depending on the amplitude of the turbulence, restricts the particles to diffusive propagation along the length of the loop to the target chromosphere. In addition this turbulence is capable of performing additional acceleration of the fast particles by the second order Fermi mechanism. For compact flares with rise times  $< 10$ s, the acceleration effect is small and the propagation of the particles is governed by spatial diffusion and energy loss in the ambient medium.

The solution of the time dependent diffusion equation with velocity dependent diffusion and energy loss coefficients yields for the case of non-relativistic protons particle precipitation rates which are necessary for calculating thick target  $\gamma$ -ray emission and also yields the total thin target emissivity. The thick target emission is necessarily delayed with respect to the particle acceleration or injection by more than the mere travel time of the particle over the loop length. Equivalent numbers are calculated for the case of relativistic electrons where in addition the time-dependent electron population at the top of the loop is calculated. This is useful in estimating the resulting  $\mu$ -wave emission. The results show relative timing differences in the different emission processes which are functions of particle species and energy and the point of injection of the particles into the coronal loop.

## STOCHASTIC PARTICLE ACCELERATION IN SOLAR FLARES

W. Dröge, R. Schlickeiser  
 Max-Planck-Institut für Radioastronomie  
 Auf dem Hügel 69, 5300 Bonn 1, FRG

## ABSTRACT

We propose that particles during the second phase of solar flares are accelerated by stochastic resonant scattering off hydromagnetic waves and first-order Fermi acceleration in shock waves generated in the impulsive phase of the flare. Our solutions allow arbitrary power law momentum dependences of the momentum diffusion coefficient as well as the momentum loss time. The acceleration time scale to a characteristic energy  $\sim 100$  keV for protons can be as short as 5 s. The resulting electron spectra show a characteristic double power law with a transition around 200 keV and are correlated to the proton spectra evaluated under equal boundary conditions, indicating that electrons and protons are accelerated by the same mechanism. The correlation between the different spectral indices in the electron double power law and between electron and proton spectra are governed by the ratio of first-to second-order acceleration and therefore allow a determination of the Alfvén Mach number of the shock wave.

1. Introduction. We propose that the combination of first- and second-order Fermi acceleration is the mechanism responsible for second-phase acceleration in solar flares. This model has a number of distinct advantages over previous models, in that it gives a natural explanation for the various observed time delays between first and second phase as well as for the dependence of the particle spectra to the strength of the flare and the correlation between electron and proton spectral indices.

2. Theory. Parker and Tidman (1958) have pointed out that Fermi acceleration is an intrinsic property of any sufficiently agitated plasma of energetic particles. The effects of second-order Fermi acceleration due to irregularly moving magnetized fluid elements, first-order Fermi acceleration off strong shocks as well as loss and escape processes can be incorporated into a transport equation in phase space (Ramaty 1979)

$$\frac{\partial f}{\partial t} - \frac{1}{p^2} \frac{\partial}{\partial p} [p^2 D(p) \frac{\partial f}{\partial p}] - \frac{1}{p^2} \frac{\partial}{\partial p} [p^2 (\dot{p}_G + \dot{p}_L) f] + \frac{f}{T(p)} = Q(p, t) \quad (1),$$

where  $p$  is the particle momentum,  $N(p) = 4\pi p^2 f(p, t)$  the number of particles per unit momentum and unit volume, and  $Q(p, t)$  represents sources and sinks of particles. Using the concept of the age distribution (Schlickeiser and Lerche 1985) the effects of spatial diffusion, convection and catastrophic losses have been combined in a momentum-dependent escape time  $T(p) = T_0 p^{-b}$ .

In a plasma with a strong MHD turbulence both the momentum diffusion coefficient  $D(p)$  and the spatial diffusion coefficient along the mean magnetic field  $K_{\parallel}(p)$  are governed by the turbulence simultaneously. By using quasi-linear theory  $K_{\parallel}(p)$  can be related rigorously to the spectrum

of the magnetic field fluctuations (Jokipii 1977). Assuming a power law spectrum for the magnetic irregularities  $W(k) = W_0 k^{-q}$  we may write

$$K_{||}(p) = \delta v(p) p^{2-q} = \kappa p^\eta \quad (2)$$

( $\delta, \kappa = \text{const.}$ ) and

$$D(p) = \alpha_2 \frac{V_A^2}{K_{||}} p^2 \quad (3)$$

( $V_A$ : Alfvén speed,  $\alpha_2$ : constant). As gain process, we consider quasi-continuous momentum gain by acceleration at a shock wave moving through the plasma with speed  $V_S$ . The momentum gain by first-order Fermi acceleration at a single shock wave has been determined by Drury (1983)

$$\dot{p}_G = \alpha_1 \frac{V_S^2}{K_{||}} p \quad (4)$$

( $\alpha_1$ : constant). Möbius et al. (1982) pointed out that for conditions in the flare site the rate of systematic acceleration exceeds the rate of momentum loss. Thus we assume that  $\dot{p}_G \gg \dot{p}_L$  at least at all momenta of interest. Using (2), (3) and (4) in equation (1) and considering the steady-state case ( $\partial f / \partial t = 0$ ) yields

$$\frac{1}{p^2} \frac{d}{dp} [p^{4-\eta} \frac{df}{dp} - a p^{3-\eta}] - \lambda p^b = Q(p) \quad (5)$$

( $a_1 = \alpha_1 V_S^2 / \kappa$ ,  $a_2 = \alpha_2 V_A^2 / \kappa$ ,  $a = a_1 / a_2$ ,  $\lambda = 1 / a_2 T_0$ ). We assume that the injection takes place at some momentum  $Q(p) = q_0 \delta(p - p_0)$  and we find for the steady-state particle number density  $N(p) = 4\pi p^2 f(p)$  (see Dröge and Schlickeiser (1985) for details):

$$N(p) = \frac{8\pi q_0}{a_2 |\eta+b|} \frac{p^{-a+1}}{p_0^{\frac{\eta-a+1}{2}}} \frac{p^{\eta+a+1}}{p^{\frac{\eta+a+1}{2}}} \begin{cases} K_\nu \left( \frac{2\lambda^{1/2}}{|\eta+b|} p_0^{\frac{\eta+b}{2}} \right) I_\nu \left( \frac{2\lambda^{1/2}}{|\eta+b|} p^{\frac{\eta+b}{2}} \right) & p < p_0 \\ I_\nu \left( \frac{2\lambda^{1/2}}{|\eta+b|} p_0^{\frac{\eta+b}{2}} \right) K_\nu \left( \frac{2\lambda^{1/2}}{|\eta+b|} p^{\frac{\eta+b}{2}} \right) & p > p_0 \end{cases} \quad (6)$$

$\nu = |(3+a-\eta)/(\eta+b)|$ . In the limit  $\eta+b \rightarrow 0$  solution (6) approaches a power law distribution

$$N(p) = \frac{2\pi q_0}{a_2 \sqrt{\frac{(3+a-\eta)^2}{4} + \lambda}} \frac{p^{-a+1}}{p_0^{\frac{\eta-a+1}{2}}} \frac{p^{\eta+a+1}}{p^{\frac{\eta+a+1}{2}}} \begin{cases} (p/p_0)^{\sqrt{\frac{(3+a-\eta)^2}{4} + \lambda}} & p < p_0 \\ (p/p_0)^{-\sqrt{\frac{(3+a-\eta)^2}{4} + \lambda}} & p > p_0 \end{cases} \quad (7)$$

Equations (6) and (7) are generalizations of the solutions of Ramaty (1979;  $b=0$ ,  $a=0$ ,  $\eta=0,1$ ), Barbosa (1979;  $a=0$ ), Pikel'ner and Tsytoich (1976;  $a=0$ ,  $b=0$ ). The solutions (6) and (7) allow arbitrary momentum power law dependences of the spatial diffusion coefficient ( $\eta$ ) and the escape time ( $b$ ). The parameter  $a = (\alpha_1 / \alpha_2) (V_S^2 / V_A^2) = (\alpha_1 / \alpha_2) M_A^2$  is of the order of the square of the shock's Mach number and describes the ratio of first- to second-order Fermi acceleration. In the case of no Fermi ac-

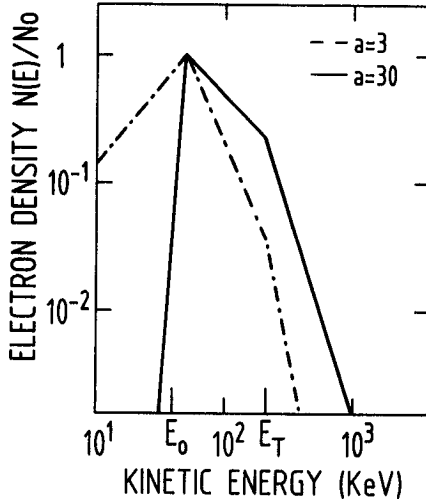


Fig. 1: Normalized steady-state electron number density. Particles are injected at  $E_0 = 50$  keV. At  $E_T = 200$  keV a transition from solution (6) to (7) occurs.

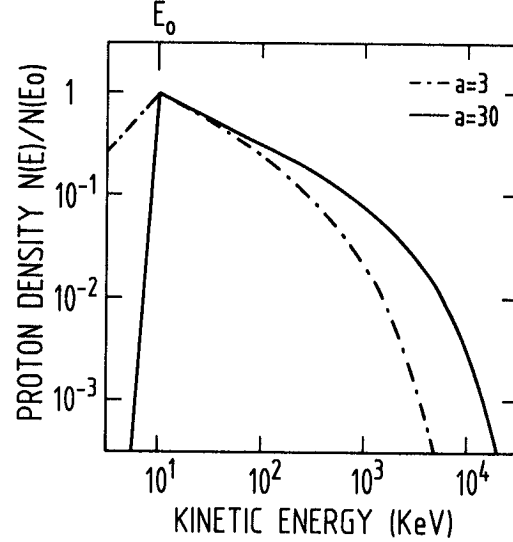


Fig. 2: Normalized steady-state proton number density. Particles are injected at  $E_0 = 10$  keV.

celeration at shock waves ( $a=0$ ) (6) and (7) reduce to the solutions of previous models as quoted above.

**3. Discussion.** The energy spectra of electrons accelerated in large flares exhibit a characteristic double power law with a break around  $E_T \approx 200$  keV (Lin et al. 1982). From this we conclude that for nonrelativistic kinetic energies ( $E < E_T$ ) the Bessel function solution (6) holds, which for small arguments is approximately a power law, whereas for  $E > E_T$  the particles are relativistic ( $p = mc \hat{=} E = 200$  keV for electrons) and the distribution function approaches the power law solution (7) (cf. Fig. 1). We take spatial diffusion along the mean magnetic field as the relevant escape process. The escape time then is  $T(p) = L^2/K_{||} = (L^2/\kappa) p^{-\eta}$ , where  $L$  is the length scale of the system and  $\eta = b = 0$  in the relativistic and  $\eta = b = 1$  in the nonrelativistic case. Thus we may consider the evolution of the particle spectra in the hard-sphere approximation (cf. Möbius et al. 1982), which gives us

$$K_{||}(p) = \frac{1}{3} v(p) \ell \quad (8)$$

$v(p)$  is the velocity and  $\ell$  the momentum independent mean free path of the particles. For comparison with data we transform (6) and (7) into energy space where  $N(E) = N(p) (1/v)$  and  $E = (p^2 c^2 + m^2 c^4)^{1/2} - mc^2$  is the particle kinetic energy. An "effective power law" exponent can be calculated ( $E > E_0$ )

$$\gamma_{\text{eff}}(E) = - \frac{d \lg N(E)}{d \lg E} = \begin{cases} -\frac{a}{4} + \frac{a+2}{4} \sqrt{1 + \frac{4x^2}{(a+2)^2} \frac{2E}{mc^2}} & p < mc \\ -\frac{a+1}{2} + \frac{a+3}{2} \sqrt{1 + \frac{4x^2}{(a+3)^2}} & p > mc \end{cases} \quad (9)$$

$$(10)$$

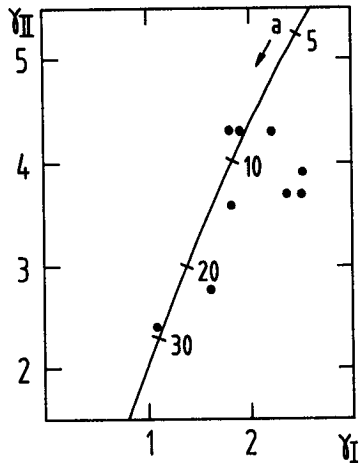


Fig. 3: Correlation between electron spectral exponent below 200 keV  $\gamma_I$  and exponent above 200 keV  $\gamma_{II}$  as a function of  $a$

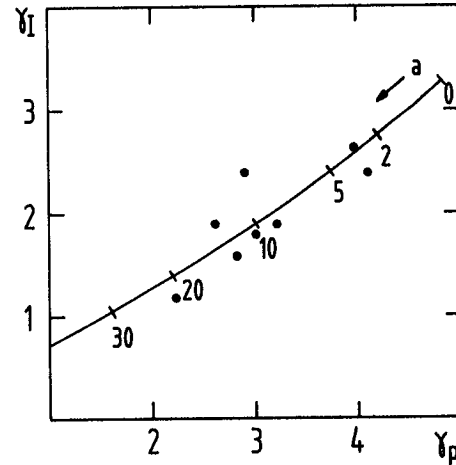


Fig. 4: Correlation between  $\gamma_I$  and proton spectral exponent above 10 MeV as a function of  $a$

$x = \ell_c / L V_A$  is a free parameter which may have different values for electrons and protons and for different flares. Equations (9) and (10) allow us to determine the correlation between the mean spectral index below 200 keV  $\gamma_I$  and above 200 keV  $\gamma_{II}$  for electrons (Fig. 3) as well as the correlation between  $\gamma_I$  and the proton spectral exponent above 10 MeV  $\gamma_p$  (Fig. 4) as a function of  $a$ . The curves obtained from (9) and (10) are in excellent agreement with the measurements of Lin et al. (1982), indicating that the strongest shock waves have an Alfvén Mach number  $M_A \sim 4$ , corresponding to  $a \sim 30$  (see Dröge and Schlickeiser (1985) for details).

**4. Conclusions.** Combining first- and second-order Fermi mechanism in solar flare second-phase acceleration successfully explains the observed ion and electron energy spectra. The model correctly accounts for the sometimes very short delay times, and reproduces quantitatively the correlations of nonrelativistic with relativistic electron spectral indices, and the correlation of nonrelativistic electron with proton indices.

#### References

- Barbosa, D.D., (1979), *Astrophys. J.* **233**, 383  
 Dröge, W., Schlickeiser, R., (1985), in preparation  
 Drury, L.O.C., (1983), *Rept. Progr. Phys.* **46**, 973  
 Jokipii, J.R., (1977), *Proc. 15th Int. Cosmic Ray Conf. (Plovdiv)*, Vol. 2, 429  
 Lin, R.P. et al., (1982), *Astrophys. J.* **253**, 949  
 Möbius, E. et al., (1982), *Astrophys. J.* **259**, 397  
 Parker, E.N., Tidman, D.A., (1958), *Phys. Rev.* **111**, 1206  
 Pikeln'ner, S.B., Tsytoich, V.N., (1976), *Sov. Astron.* **19**, 450  
 Ramaty, R., (1979), *Particle Acceleration Mechanisms in Astrophysics*, eds. J. Arons, C. Max, C. McKee, American Institute of Physics, New York, p. 135  
 Schlickeiser, R., Lerche, I., (1985), this conference, OG 7.2-8

## FIRST-ORDER FERMI SHOCK ACCELERATION IN SOLAR FLARES

Donald C. Ellison

Astronomy Program, University of Maryland, College Park, MD 20742  
and

Reuven Ramaty

LHEA, Code 665, NASA/Goddard Space Flight Center, Greenbelt, MD 20771

**ABSTRACT.** We compare the simultaneous first-order Fermi shock acceleration of electrons, protons, and alpha particles to solar energetic particle events. For each event, a unique shock compression ratio in the range,  $r \sim 1.5$  to 3 produces spectra in good agreement with observation. The range in  $r$  predicts that the wide spread in  $e/p$  ratios observed at MeV energies is considerably reduced at an assumed injection energy of 100 keV. The model predicts that the acceleration time to a given energy will be approximately equal for electrons and protons and can be on the order of 1 second to  $\sim 100$  MeV.

**1. Introduction.** We model the simultaneous acceleration of protons, alpha particles, and relativistic electrons by first-order Fermi shock acceleration (e.g. Axford et al. 1977). Shock acceleration in solar flares has been considered previously (e.g. Achterberg and Norman 1980; Lee and Fisk 1982; Bai et al. 1983; Lee and Ryan 1984). Here, we compare the predictions of Fermi shock acceleration to solar energetic particle events where interplanetary electron, proton and, in some cases, alpha-particle spectra are available (Lin et al. 1982; Evenson et al. 1984; McDonald and Van Hollebeke 1985; R. McGuire private communication) (see also Ellison and Ramaty 1985). In all cases examined, we find that for any given event, a single shock compression ratio in the range  $\sim 1.5$  to 3 simultaneously produces reasonably good fits to the electron, proton, and alpha-particle spectra.

We also determine the effects of the shock strength and injection conditions on the electron to proton ( $e/p$ ) intensity ratio. This ratio is sensitive to the injection conditions and large variations in the  $e/p$  ratio at MeV energies result from variations in shock strength. We find that these results are in good agreement with the observations.

The acceleration time for shock acceleration is estimated for typical solar conditions. We find that for scattering mean free paths that scale as the gyroradius, shocks can produce rapid acceleration with equal acceleration times for electrons and protons. This result is consistent with the gamma-ray observations (Chupp 1984).

**2. Model.** In the test particle limit of shock acceleration with no losses, wherein particles gain energy by scattering freely between the converging upstream and downstream plasmas, the accelerated distribution function (at the shock) is a power law in momentum (Blandford and Ostriker 1978). The spectral index depends only on the compression ratio,  $r = u_1/u_2$ , where  $u_1(u_2)$  is the upstream (downstream) bulk plasma flow velocity. The corresponding differential particle intensity is given by

$$\left(\frac{dJ}{dE}\right)_0 \propto n_{inj} (E_1^2 + 2E_1 m_o c^2)^{3/[2(r-1)]} (E^2 + 2Em_o c^2)^{-1/2(r+2)/(r-1)}, \quad (1)$$

where  $n_{inj}$  is the density of seed particles injected far upstream and

$m_0 c^2$  is the rest mass energy. Equation (1) assumes that the particles are injected at kinetic energy,  $E_i$ , where  $E_i$  is much greater than thermal energy. This expression holds, however, for any injected distribution which is steeper, at a given energy, than the resultant power law. For flatter injected distributions, the shock will boost the intensity of the injected spectrum while maintaining its slope. The limiting non-relativistic and ultra-relativistic spectral indexes are  $\Gamma_{N-R} = 1/2 (r+2)/(r-1)$  and  $\Gamma_{U-R} = (r+2)/(r-1)$ , respectively. The differential intensity steepens in going from the non-relativistic to the ultra-relativistic regime and the spectral index doubles. If, as is normally the case for solar flare events, non-relativistic proton and relativistic electron spectra are observed, acceleration by a single shock of a given  $r$  produces an electron spectrum steeper than the proton spectrum (Achterberg and Norman 1980).

The compression ratio can be determined from the Rankine-Hugoniot conservation relations. We find that for typical solar conditions,  $r$  lies in the range  $\sim 1.5$  to  $3$ . For example, a coronal shock with  $u_1 \approx 1000 \text{ km s}^{-1}$ , temperature  $T_1 \approx 10^6 \text{ K}$ , density  $n_1 \approx 10^9 \text{ cm}^{-3}$ , and magnetic field perpendicular to the shock normal  $B_1 \approx 10 \text{ Gauss}$ , yields  $r \approx 1.54$ . If  $u_1$  is increased to  $2000 \text{ km s}^{-1}$ ,  $r \approx 2.7$ .

To model effects such as adiabatic deceleration (Lee and Fisk 1982; Lee and Ryan 1984), finite shock lifetimes (Forman 1981), and finite shock sizes (e.g. Ellison 1984), we assume the spectra will turnover approximately exponentially such that,  $dJ/dE \propto (dJ/dE)_0 \exp(-E/E_0)$ , where  $E$  and  $E_0$  are energy for electrons and protons and energy per nucleon for ions.

For concreteness, we assume the diffusion coefficient of all energetic particles to be,  $\kappa = \kappa_0 (v/v_0)(R/R_0)$ , where  $R = pc/(Ze)$  is rigidity,  $v$  is velocity measured in the local plasma frame, and  $\kappa_0$ ,  $v_0$ , and  $R_0$  are constant.

We also assume that the high energy turnover is produced by a shock of finite spatial extent. This implies that the electron turnover energy will be twice that of the protons and that the alpha particle turnover energy will be  $1/2$  that of the protons.

If spectra that are power laws in momentum are plotted as a function of energy, the ratio  $e/p$  will decrease with increasing energy as the electrons become relativistic. The decrease in the  $e/p$  ratio will be greater for smaller  $r$ . If shocks of different strengths produce a range of particle spectra, as observed for solar flare accelerated particles, a wide range in  $e/p$  will result at MeV energies even if the injection conditions are similar (see Fig. 3).

Estimates of the acceleration time (Ellison and Ramaty 1985) suggest that the solar environment should allow acceleration of electrons and ions to  $100$ 's of MeV in times on the order of  $1 \text{ sec}$ . These estimates assume, of course, that the background turbulence has sufficient power to scatter both electrons and protons from injection energies to  $100$ 's of MeV.

3. Comparison with Observations. We have compared the model, using a single set of parameters to simultaneously describe electron, proton, and alpha-particle spectra, to spectra observed in space (see Figs. 1 and 2).

In all cases we choose, for each event, a single compression ratio and  $E_0$  that produces the best combined fits to the electron, proton, and alpha-particle spectra. We find that: (1) In all cases, the model

provides an excellent fit to the electron spectra above the assumed injection energy of  $\sim 100$  keV. (2) In all events where multiple species are observed, a single set of parameters (apart from the normalization) provides a fair description of all spectra. (3) The model provides a natural explanation for events with very flat proton spectra such as 3 June 1982 and can be applied over a wide energy range (see Ellison and Ramaty 1985).

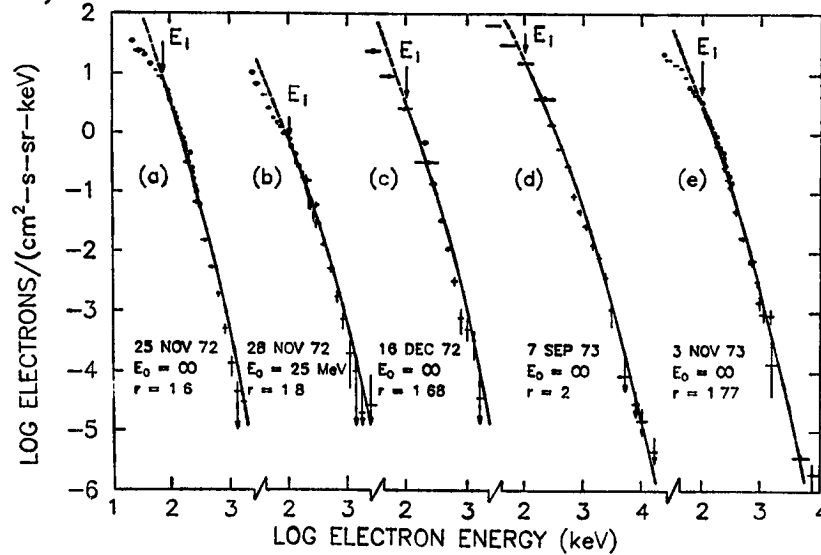


Fig. 1. Electron intensity vs. energy. The line is the spectrum expected from shock acceleration and is calculated for the  $r$  and  $E_0$  shown.  $E_1$  is the injection energy of 100 keV. Data is from Lin et al. (1982).

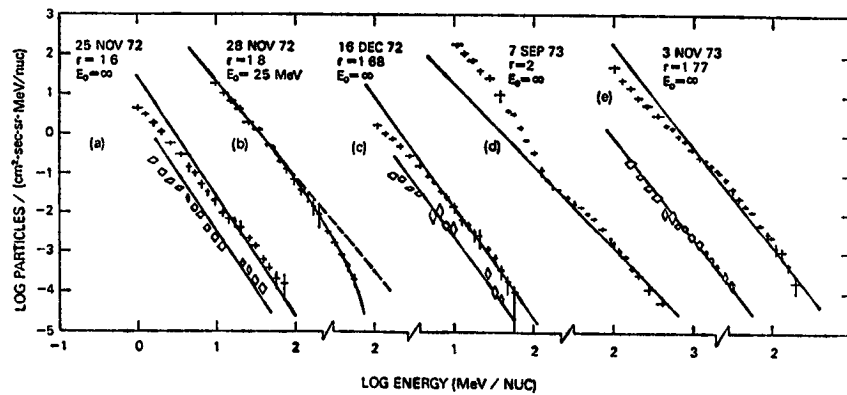


Fig. 2. Proton (crosses) and alpha-particle (diamonds) intensities vs. energy. The data is from IMP 7 and 8 (R. McGuire private communication).

The essential point of the spectral fits is that a single model with a single set of shock parameters produces a reasonable fit to all species. In some cases, in fact, all spectra are fit by a single parameter,  $r$ .

A wide range in e/p ratios is observed at MeV energies (Lin et al. 1982; Evenson et al. 1984). Shock acceleration can produce a spread in e/p in two ways. First, steep spectra produce a smaller e/p ratio at high energies than flat spectra assuming the same injection conditions. Second, the injection conditions may vary for electrons and protons.



Using the data of Evenson et al. (1984), we have plotted in Fig. 3 the e/p ratio measured in the energy interval 25-45 MeV (crosses) versus the relativistic electron spectral index,  $\Gamma_e$ . There is a very clear correlation showing that flatter spectra generally produce higher e/p ratios. We also show with the lower solid lines, the predicted correlation between e/p and spectral index or, equivalently,  $r$ . The two lines indicate a factor of 10 spread in injection conditions.

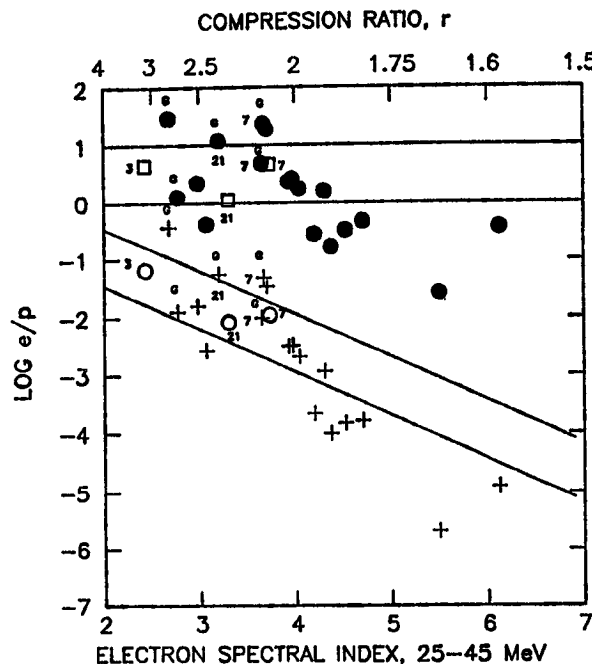


Fig. 3. Crosses are e/p ratios as observed by Evenson et al. (1984). June, 7 and 21 1980 and 3 June 1982 are indicated by open circles and number. These ratios projected to 100 keV are indicated by open squares. Gamma-ray events are indicated by "G". The lower solid lines are the relationship between e/p and  $r$  predicted by shock acceleration.

The solid dots in Fig. 3 show the e/p ratios measured at  $\sim 33$  MeV extrapolated to the assumed injection energy of 100 keV. A strong reduction in the spread of e/p results. Gamma-ray events are identified in Fig. 3 with a "G" and it is clear that they tend to have the largest injection e/p ratios and the largest compression ratios.

**4. Conclusions.** We find that shock acceleration can model many solar flare energetic particle spectra with a single set of parameters for both electrons and protons. The production of power laws in momentum by shocks provides a natural explanation for much of the large spread in the observed e/p ratios at MeV energies. Events that produce gamma rays can be accommodated in this model and do not need to be treated as a distinct class of events. We also find that shocks should allow the acceleration of both electrons and protons to 100's of MeV in seconds.

**5. Acknowledgements.** We are grateful to Bob McGuire for

allowing us to use unpublished data from IMP 7 and 8. This work was supported, in part, by a NASA STTP grant and NSF Grant AST-83-17755.

#### References

- Achterberg, A., and Norman, C.A. 1980, *A. A.*, 89, 353.  
 Axford, W.I. et al. 1977, *15th ICRC (Plovdiv)*, 11, 132.  
 Bai, T. et al. 1983, *Ap.J.*, 267, 433.  
 Blandford, R.D., and Ostriker, J.P. 1978, *Ap.J. Lett.*, 221, L29.  
 Chupp, E. L. 1984, *Ann. Rev. A. A.*, 22, 359.  
 Ellison, D.C. 1984, *J.G.R.*, 90, 29.  
 Ellison, D.C., and Ramaty, R. 1985, *Ap.J.*, in press.  
 Evenson, P. et al. 1984, *Ap.J.*, 283, 439.  
 Forman, M.A. 1981, *Adv. in Space Res.*, 1, 41.  
 Lee, M.A., and Fisk, L.A. 1982, *Sp. Sci. Rev.*, 32, 205.  
 Lee, M.A., and Ryan, J.M. 1984, preprint.  
 Lin, R.P. et al. 1982, *Ap.J.*, 253, 949.  
 McDonald, F.B., and Van Hollebeke, M. 1985, *Ap.J. (Letters)*, 290, L67.

# PROMPT ACCELERATION OF IONS BY OBLIQUE TURBULENT SHOCKS IN SOLAR FLARES

R. B. Decker and L. Vlahos  
The Johns Hopkins University, Applied Physics Laboratory  
Laurel, MD 20707  
USA

1. Introduction. Solar flares often accelerate ions and electrons to relativistic energies. The details of the acceleration process are not well understood, but until recently the main trend was to divide the acceleration process into two phases (1). During the first phase electrons and ions are heated and accelerated up to several hundreds of keV simultaneously with the energy release. These mildly relativistic electrons interact with the ambient plasma and magnetic fields and generate hard X-ray and radio radiation. The second phase, usually delayed from the first by several minutes, is responsible for accelerating ions and electrons to relativistic energies. Relativistic electrons and ions interact with the solar atmosphere or escape from the sun and generate gamma-ray continuum, gamma-ray line emission, neutron emission or are detected in space by spacecraft. In several flares the second phase is coincident with the start of a type II radio burst that is believed to be the signature of a shock wave (2). Observations from the Solar Maximum Mission spacecraft have shown, for the first time, that several flares accelerate particles to all energies nearly simultaneously (3). These results posed a new theoretical problem: How fast are shocks and MHD turbulence formed and how quickly can they accelerate ions to 50 MeV in the lower corona? We address this problem in this brief report.

2. Model. We consider the following model for shock formation during a solar flare. During the flare's impulsive phase, magnetic energy is transferred to plasma particles inside the energy release volume by increasing the random mean square velocity (i.e., heating the bulk plasma) and by accelerating the tail of the velocity distribution. The high plasma pressure inside the energy release expands against the external magnetic field and forms a shock nearly instantaneously (4). The angle  $\theta_{Bn}$  between the mean upstream magnetic field and the mean shock normal  $\hat{n}$  and the level of magnetic fluctuations in the shock vicinity play a crucial role in accelerating particles to high energies. Since the detailed evolution of energetic ions in a generally oblique turbulent shock is a complex process, we have designed a numerical code that integrates along energetic (i.e.,  $\gtrsim 100$  keV) test ion orbits in such an environment (5).

We define  $K[X, Y, Z]$  as a system fixed with the shock, with the unit vector  $\hat{X} = -\hat{n}$ , such that the shock discontinuity coincides with the  $Y$ - $Z$  plane and separates the upstream ( $X < 0$ , subscript 1) from downstream ( $X > 0$ , subscript 2) regions. The quantities  $\vec{U}_1 = U_1 (\cos \delta_1, 0, \sin \delta_1)$  and  $\vec{B}_{01} = B_{01} (\cos \theta_1, 0, \sin \theta_1)$  denote, respectively, the upstream plasma flow velocity and mean magnetic field (where  $\theta_1 = \theta_{Bn}$ ). Then, in  $K$  the mean electric field on either side of the shock is  $-\vec{U}_1 \times \vec{B}_{01}/c$ . Given values of the upstream Alfvén Mach number  $M_{A1}$  and the plasma beta  $\beta_1$ , the mean downstream conditions are

calculated by solving the MHD jump equations (for a ratio of specific heats of 5/3).

We model magnetic fluctuations by superposing upon  $\vec{B}_{0i}$  ( $i = 1$  or  $2$ ) a zero mean, random magnetic field component  $\vec{b}_i(z)$  which, in either the upstream or downstream plasma frame, varies only with the coordinate  $z$  along  $\vec{B}_{0i}$ , is transverse to  $\vec{B}_{0i}$ , and is static, so that scattering is elastic in either plasma frame. We assumed for this study that  $\vec{b}_i(z)$  is a superposition of 4096 circularly polarized, parallel-propagating Alfvén waves, each with a random phase, and with the amplitude of each such Fourier component with wave number  $k$  derived from a power spectrum  $P(k)$  using a technique described by Owens (6). For synthesized realizations of  $\vec{b}_i(z)$ , the Lorentz force equation was solved for a particle orbit using the field  $\vec{B}_i(z) = \vec{B}_{0i} + \vec{b}_i(z)$  in the appropriate plasma frame, and Lorentz transformations were performed between plasma frames at shock crossings. Each particle orbit was followed until a pre-set boundary (spatial or temporal) was crossed.

The source(s) and spectral form of Alfvénic turbulence are, of course, largely unknown in the vicinity of lower coronal shocks. Possible sources upstream include the turbulent pre-flare plasma and Alfvén waves driven by energetic ( $\sim 100$  keV) ion beams streaming upstream from the shock following reflection at the shock and/or leakage from the hot downstream plasma. Possible sources downstream include the upstream MHD turbulence convected through and amplified by the shock as well as turbulence excited by the flare release mechanism. We assumed the spectral form  $P(k)$  of Alfvén waves shown in Figure 1. The spectrum extends from  $k_S$  to  $k_L$ , with correlation length  $z_c = 10^5$  cm, and slope  $-5/3$  for  $k \gg z_c^{-1}$ . The integrated power or variance  $\sigma^2$  assumed was  $\sigma_1^2 = 0.19 B_{01}^2$  upstream and  $\sigma_2^2 = 0.38 B_{02}^2$  downstream. Figure 1 is the upstream spectrum for  $B_0 = B_{01} = 50$  G. This spectral form was chosen because it provides power for resonant scattering (gyro-radius  $\sim k^{-1}$ ) of protons (top scale) with energies spanning the range of flare-associated energies from 100 keV to 10 GeV.

**3. Results.** Figures 2 and 3 show results for  $\delta_1 = 0^\circ$ ,  $U_1 = 3.3 \times 10^8$  cm/s,  $B_{01} = 50$  G,  $M_{A1} = 3$ ,  $\beta_1 = 0.1$ , various values of  $\theta_1$  from  $0^\circ$  to  $75^\circ$ , and protons injected upstream of the shock with energy  $E_0 = 100$  keV. We define the scale time  $\tau_{01} = eB_{01}/m_0c = 1.3 \times 10^{-5}$  sec (nonrelativistic upstream proton gyroperiod). Figure 2 shows the energy  $E$  versus acceleration time  $t/\tau_{01}$  after a total

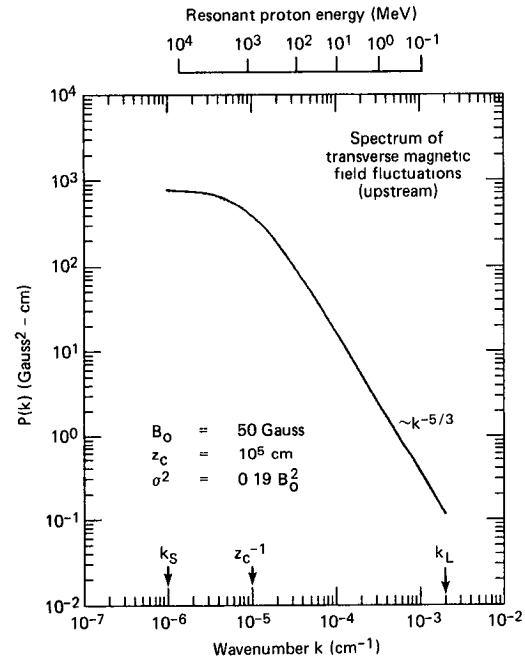


Fig. 1 Power spectrum  $P(k)$

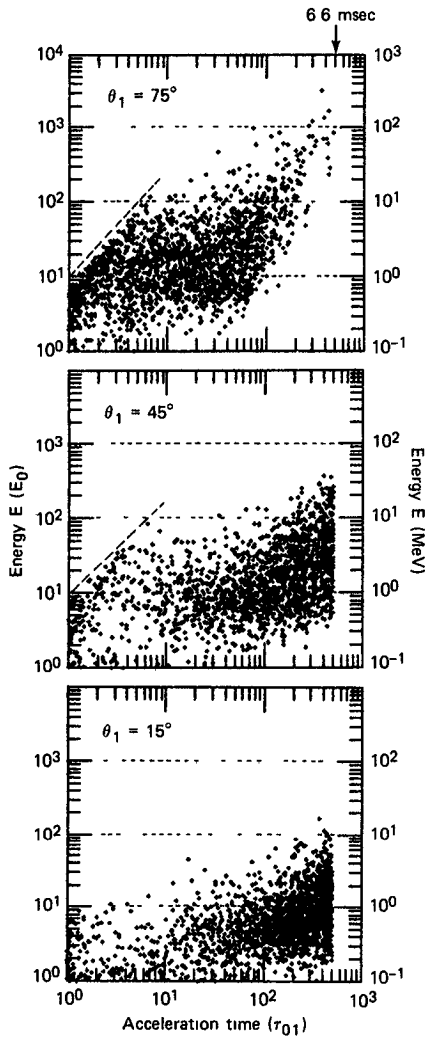


Fig. 2 Energy versus acceleration time

Figure 2 reveals the following. (a) An increase in  $\theta_1$  from  $15^\circ$  to  $75^\circ$  increases the fraction of protons above 10 MeV within 6.6 msec. This results from the increasing contribution from the drift acceleration with increasing  $\theta_1$ . (b) For  $\theta_1 = 15^\circ$  most particles are still available for further acceleration (note the high density of points near the 6.6 msec cutoff), whereas for  $\theta_1 = 75^\circ$  most particles have been convected far downstream and will undergo no further acceleration. (c) For  $\theta_1 = 75^\circ$  and, to some extent, for  $\theta_1 = 45^\circ$  the shock drift process produces a spectrum extending from  $100 \text{ keV}$  to  $\sim 10 \text{ MeV}$  during a super-prompt acceleration phase lasting  $\sim 0.1 \text{ msec}$ , with an apparent upper energy limit indicated by the dashed diagonal lines. Particles in this separate population are those that, through an interplay between pitch angle scattering and drift, remain at the shock and undergo an intensive period of drift acceleration.

SH 1.1-6  
elapsed time of  $500 \tau_{01} = 6.6 \text{ msec}$  for each of 2200 protons injected at shocks with  $\theta_1 = 15^\circ$ ,  $45^\circ$  and  $75^\circ$  (all other parameters held fixed). Plotted is the total energy of each particle against the time taken to reach that energy, or equivalently, the time of the particle's last shock crossing. Points with  $t/\tau_{01} < 500$  imply that these particles spent the time  $500 - t/\tau_{01}$  diffusing without net energy change in the upstream or downstream regions.

Particles injected into our turbulent oblique shock model gain energy through both the shock drift and diffusive acceleration processes. Shock drift acceleration, relatively fast and most effective at quasi-perpendicular ( $45^\circ \lesssim \theta_1 \leq 90^\circ$ ) shocks, results as particles undergo an effective grad-B drift along the  $\vec{U} \times \vec{B}$  electric field during shock encounters (7). Diffusive acceleration, relatively slow and most effective at quasi-parallel ( $0 \leq \theta_1 \lesssim 45^\circ$ ) shocks, results as particles diffuse back and forth across the shock and are compressed between the converging upstream and downstream flows (8). Reference (5) shows a sample orbit.

SH 1.1-6

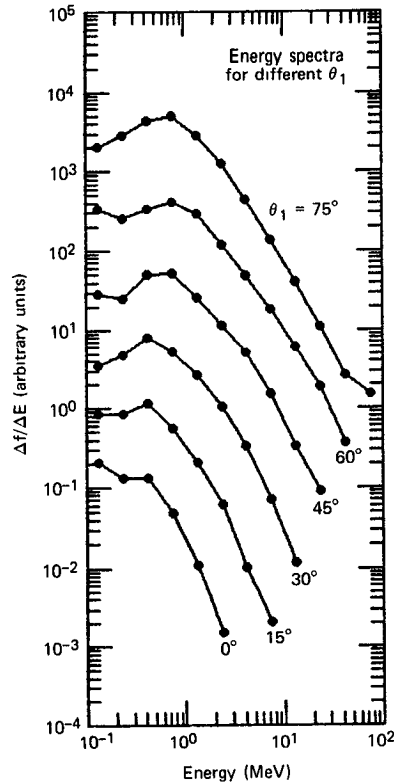


Fig. 3 Energy spectra for various  $\theta_1$

In Figure 3 we show energy spectra for values of  $\theta_1$  from  $0^\circ$  to  $75^\circ$  (all other quantities held fixed), again for a total elapsed time of 6.6 msec. The quantity  $\Delta f(E)/\Delta E$  is the fraction of particles with energy  $E$  within  $\Delta E$  centered at the logarithmically spaced plot points. The spectra are separated for clarity and statistical standard deviations are within twice the size of the plot points. Because the drift process produces relatively large and fast energy gains, quasi-perpendicular shocks are clearly most effective in producing power law spectra above  $\sim 2$  MeV (spectral slope  $\sim 2.1$  for  $75^\circ$  and  $\sim 1.9$  for  $60^\circ$ ) within  $\sim 7$  msec. Because of the decrease in the drift contribution as well as the slowness of the diffusive acceleration process with decreasing  $\theta_1$ , quasi-parallel shocks yield spectra that are steeper and extend to successively lower energies as  $\theta_1$  decreases.

**4. Conclusions.** We have shown that in solar flares oblique turbulent shocks can accelerate an initial population of 100 keV protons to 50 MeV in less than 7 msec (well below the instrumental resolution of existing instruments) through a combination of diffusion and the shock drift acceleration process. The implication of this prompt acceleration for the overall flare problem is beyond the scope of this brief report.

**5. Acknowledgements.** This work was supported in part by the JHU/APL Independent Research and Development Program under Navy Contract N00024-83-C-5301 and in part by NSF Grant ATM 83-05537.

#### References

1. Ramaty, R., et al.: (1980), Solar Flares, (Colorado Press), 117.
2. Frost, K. J. and Dennis, B. R.: (1970), Ap. J., **165**, 655.
3. Chupp, E.: (1985), Ann. Rev. Astron. Astrophys., **22**, 359.
4. Goodrich, C., et. al.: (1985), EOS Trans. AGU, **66**, 331.
5. Decker, R. B., and Vlahos, L.: (1985), Paper SH 1.5-3, these proceedings.
6. Owens, A. J.: (1978), JGR, **83**, 1673.
7. Armstrong, T. P., et al.: (1977), "Study of Travelling Interplanetary Phenomena", (Reidel), 367.
8. Drury, L. O. C.: (1983), Rep. Prog. Phys., **46**, 973.

## FAST DRIFT KILOMETRIC RADIO BURSTS AND SOLAR PROTON EVENTS

E. W. Cliver

Air Force Geophysics Laboratory, Hanscom AFB, Massachusetts 01731 USA

S. W. Kahler

Emmanuel College, Boston, Massachusetts 02115 USA

H. V. Cane\*, R. E. McGuire\*, T. T. von Rosenvinge, and R. G. Stone  
NASA/Goddard Space Flight Center, Greenbelt, Maryland 20771 USA

## ABSTRACT

We present initial results of a comparative study of major fast-drift kilometric bursts and solar proton events from Sep 1978 - Feb 1983. We find that only about half of all intense, long duration ( $> 40$  min above 500 sfu) 1 MHz bursts can be associated with  $E > 20$  MeV proton events. However, for the subset of such fast-drift bursts accompanied by metric Type II and/or IV activity ( $\sim 40\%$  of the total), the degree of association with  $> 20$  MeV events is 80%. For the reverse association, we found that proton events with  $J(> 20 \text{ MeV}) > 10^{-2} \text{ pr cm}^{-2} \text{ s}^{-1} \text{ sr}^{-1} \text{ MeV}^{-1}$  were typically ( $\sim 80\%$  of the time) preceded by intense 1 MHz bursts that exceeded the 500 sfu level for times  $> 20$  min (median duration  $\sim 35$  min).

1. Introduction For both scientific and practical reasons, it is useful to identify solar phenomena that typically accompany energetic proton events. Radio signatures identified thus far include metric Type II and Type IV bursts (cf., Cliver et al., 1985). Cane et al. (1981) drew attention to a class of intense, long duration, fast-drift kilometric bursts observed by the low frequency radio experiment on ISEE-3 that occurred in conjunction with metric Type II emission. They suggested that the electrons exciting the fast-drift kilometric emission were accelerated by a coronal shock; subsequently these events were referred to as "shock associated" or SA events. Cane et al. reported that all of the SA events they identified were associated with solar energetic particle (SEP) events while more than half of the proton events detected at 1 AU during the period of their study were associated with possible SA events. Cliver et al. (1983) and Kahler et al. (1985) have recently used the SA signature and the position angle data from the ISEE-3 low frequency experiment to trace SEP events back to atypical origins -- in one case  $> 500$  MeV protons to a weak impulsive phase flare and in the other prompt  $> 50$  MeV protons to a disappearing filament. Thus there is reason to believe that the SA event may serve as an indicator of energetic proton acceleration/escape in flares. To date, however, no detailed comparison of low frequency ( $< 2$  MHz) radio events and SEP events has been made. Thus we do not know whether all major fast-drift kilometric bursts signal the occurrence of a solar proton event or if, conversely, all significant SEP events are preceded by large low frequency

---

\*Also: University of Maryland, College Park, Maryland 20742 USA

bursts. It is also unclear at present if the so-called SA events can be distinguished from the kilometric extension of long metric Type III bursts (Kundu *et al.*, 1985). In this study, we address such questions.

**2. Data Analysis** A description of the Meudon/GSFC kilometric radio astronomy experiment on ISEE-3 is given in Knoll *et al.* (1978). The  $> 20$  MeV proton data were obtained by the GSFC detectors on IMP-8 and ISEE-3. To do the study, we began with a sample of large kilometric bursts and examined their proton associations and then reversed the procedure.

A computer generated list of 658 candidate SAs occurring from Sep 1978 - Feb 1983 was provided by R. MacDowall. This list consisted of all 1 MHz bursts with durations, defined to be the time interval that the intensity (after background subtraction) remained above 500 solar flux units (sfu), of  $> 20$  min. From this list we selected the subset of 110 events with durations  $> 40$  min. We divided these events into two classes: those associated with metric Type II and/or IV bursts and those unaccompanied by such activity. We made the meter- $\lambda$  associations using data reported only by Ft. Davis, Culgoora, or Weissenau in *Solar Geophysical Data* (data unavailable for two events). Approximately 40 % (46/108) of the candidate SAs were associated with metric Type II and/or Type IV bursts. For 15 of these 46 cases, either no fresh injection of protons was observed during a time that the  $> 20$  MeV background was enhanced ( $> 10^{-4}$  pr cm $^{-2}$  s $^{-1}$  sr $^{-1}$  MeV $^{-1}$ ) due to an event in progress (possibly masked event) or an apparently related proton event is more likely to have originated in another solar flare (ambiguous cases). No proton data were available for one low frequency event. Eighty percent (24/30) of the remaining events, originating anywhere on the sun, were associated with a  $> 20$  MeV event at 1 AU. For the non-Type II/IV-associated events (62/108 cases), approximately 30 % (11 of 35 events with "clean" proton circumstances) could have been associated with a  $> 20$  MeV proton event at Earth. Only three of the eleven flare associations are of high confidence and two of these flares had accompanying continuum (but not Type II or IV) metric emission. The non-II/IV events were associated in most cases with groups of metric Type III bursts. There is no marked difference between the durations of the 1 MHz bursts in our sample that were associated with metric Type II/IV bursts and those unaccompanied by such activity. The II/IV-associated events tend to be slightly longer with a median duration  $\sim 50$  min vs. 46 min for the non-II/IV events. A significant difference does exist between the distributions of the time averages of the logarithm of the 1 MHz flux-densities (sfu) for the two groups of events. Obtaining a mean-flux-density value by this procedure reduces the effect of short but intense peaks in the burst time profile. The median value of this parameter is 4.16 for the II/IV-associated events and 3.85 for the non-II/IV group. Thus, for the big events with durations  $> 40$  min, the mean-flux-densities, as defined here, of the II/IV-associated events are statistically higher by a factor of two.

For the reverse association -- beginning with the proton events -- we examined the ISEE-3 low frequency data at the times of the parent flares of all proton events with  $J(> 20 \text{ MeV}) > 10^{-2}$  pr cm $^{-2}$  s $^{-1}$  sr $^{-1}$  MeV $^{-1}$  occurring during this period that could be reasonably well associated with a solar event. Flare associations were made without reference to the low frequency data. For each of the 48 events with available 1

MHz data, we found associated bursts that had durations above 500 sfu ranging from  $< 10$  min to  $> 60$  min. Approximately 80 % (39/48) of the bursts had durations  $> 20$  min (median duration  $\sim 35$  min). The distribution of durations is given in Fig. 1. Events with lower confidence parent flare associations are cross-hatched. For two higher confidence events the 1 MHz bursts were only  $\sim 10$  min long.

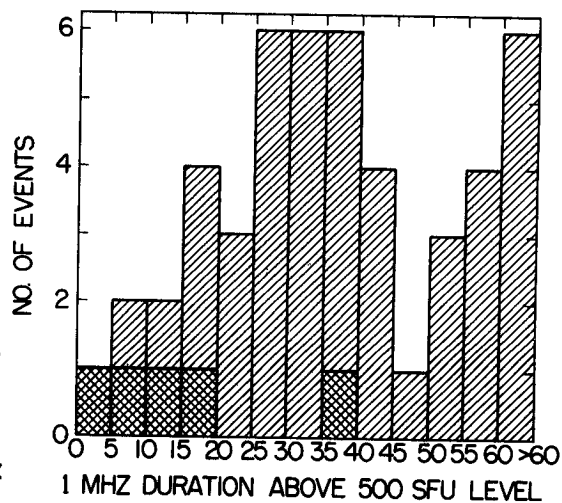


Fig. 1 Histogram of 1 MHz durations (min) for 48 proton events.

In an attempt to gain insight into the question of whether the electrons responsible for the 1 MHz emission in these proton flares were accelerated by shocks or impulsively accelerated in association with metric Type III bursts, we determined the composite fraction of time that the 1 MHz bursts had concomitant metric Type II and Type III emission, respectively. Type II emission covered  $\sim 45$  % of the total combined durations of the 1 MHz bursts while Type III bursts covered anywhere from 32 - 65 %, depending on how weak intermittent activity and storms that may begin well before the kilometric event are treated. An example of good time correspondence between a metric Type II burst and intense 1 MHz emission observed in a major proton flare is given in Fig. 2. Even for this event,

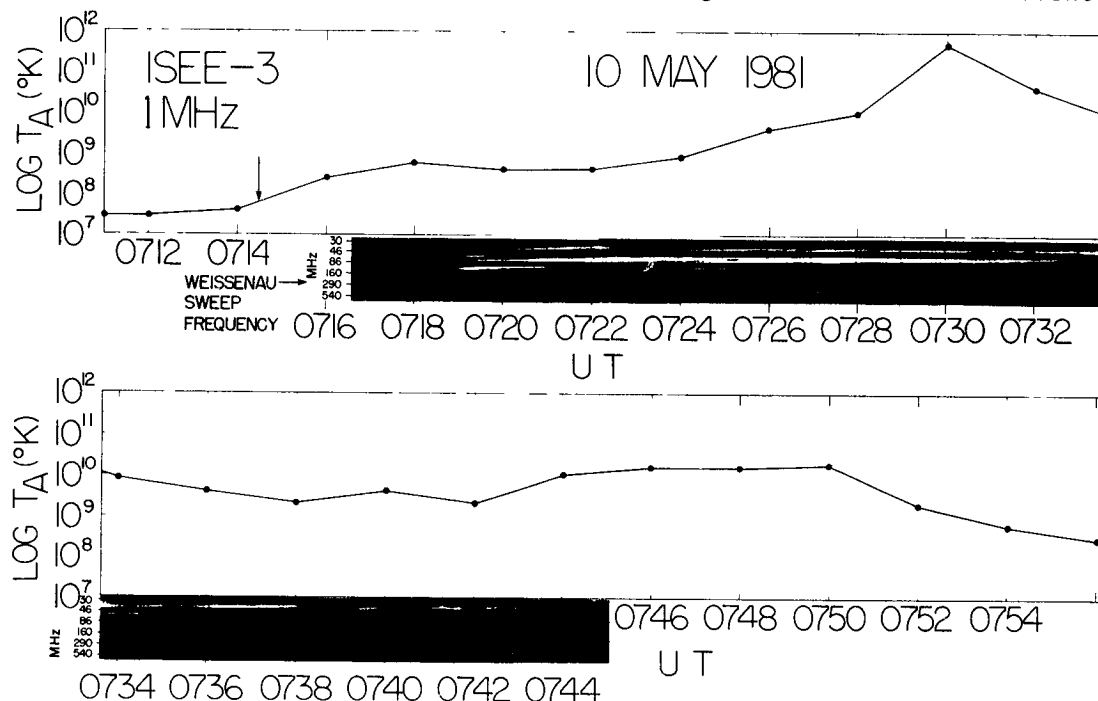


Fig. 2 The ISEE-3 1 MHz time profile and the Weissenau meter- $\lambda$  sweep frequency record for the 10 May 1981 proton flare.



however, for which no Type III emission was observed, the 1 MHz event starts earlier (arrow indicates time at which 500 sfu level crossed) than the metric Type II and the possibility of a Type III burst with starting frequency in the 2 - 20 MHz gap between ground-based and ISEE-3 observations cannot be ruled out.

**3. Discussion** Our preliminary results from this study of the relationship between major fast-drift kilometric bursts and SEP events are as follows: (1) only about half (35 of 65 "clean" cases) of all intense, long duration ( $> 40$  min above 500 sfu) 1 MHz bursts are associated with  $E > 20$  MeV proton events, (2) for the subset of such fast-drift bursts accompanied by metric Type II and/or IV activity ( $\sim 40$  % of the total), the degree of association with  $> 20$  MeV events is 80 %, and (3)  $\sim 80$  % of proton events with  $J(> 20 \text{ MeV}) > 10^{-2} \text{ pr cm}^{-2} \text{ s}^{-1} \text{ sr}^{-1} \text{ MeV}^{-1}$  are associated with 1 MHz bursts with durations of  $> 20$  min above the 500 sfu level (median duration  $\sim 35$  min).

In terms of the well-established impulsive/second phase paradigm for particle acceleration in solar flares (Wild et al., 1963; Lin, 1970; Svestka and Fritzkova-Svestkova, 1974), it seems logical to ascribe at least some of the intense 1 MHz emission that typically accompanies significant proton flares to escaping shock-accelerated electrons. At the same time, it appears that the majority of the long duration kilometric events are simply low frequency extensions of "impulsive phase" Type III bursts (cf., Kundu et al., 1985). The 1 MHz bursts associated with proton events were accompanied by metric Type II bursts for  $\sim 45$  % of their composite durations and by metric Type IIIs for 32 - 65 %. The contribution of impulsively accelerated electrons to the kilometric bursts accompanying proton flares will have to be clarified using actual meter- $\lambda$  sweep frequency records instead of the SGD compilations we have relied on thus far. It remains to be seen if low frequency bursts due to impulsively accelerated electrons can be distinguished from kilometric activity excited by SA electrons on the basis of differences in such parameters as burst time-profiles, spectra, or drift-rates, none of which were addressed herein. We have noted that the Type II/IV-associated events with durations  $> 40$  min had significantly higher (factor of two) mean-flux-densities than non-II/IV-associated events. While this may indicate the presence of an additional acceleration mechanism, i.e., a coronal shock wave, it may also be a Big Flare Syndrome (Kahler, 1982) result in that the larger flares that generate Type IIs and IVs might be expected to have stronger impulsive phases and thus higher mean-flux-densities at 1 MHz.

#### References

- Cane, H. V., et al., 1981, Geophys. Res. Letters **8**, 1285.  
 Cliver, E. W., et al., 1983, Solar Phys. **89**, 181.  
 Cliver, E. W., et al., 1985, J. Geophys. Res. (in press).  
 Kahler, S. W., 1982, J. Geophys. Res. **87**, 3439.  
 Kahler, S. W., et al., 1985, (these proceedings).  
 Knoll, R., et al., 1978, IEEE Trans. Geosci. Electronics **GE-16**, 199.  
 Kundu, M. R., et al., 1985, EOS, **66**, 330.  
 Lin, R. P., 1970, Solar Phys. **12**, 266.  
 Svestka, Z., and Fritzkova-Svestkova, L., 1974, Solar Phys. **36**, 417.  
 Wild, J. P., et al., 1963, Ann. Rev. Astron. Astrophys. **1**, 291.

# STUDY OF PHOTON EMISSION BY ELECTRON CAPTURE DURING SOLAR NUCLEI ACCELERATION: I. TEMPERATURE-DEPENDENT CROSS SECTION FOR CHARGE CHANGING PROCESSES.

J. Pérez-Peraza \* and M. Alvarez \*  
Instituto de Geofísica UNAM, 04510, C. U. México, D.F.

A. Laville  
Instituto Nacional de Astrofísica Óptica y Electrónica, Tonanzintla, 72000 Puebla, México.

A. Gallegos  
UPICSA, 08400 - México, D. F.

1. INTRODUCTION. The study of charge-changing cross-sections of fast ions colliding with matter provides the fundamental basis for the analysis of the charge states produced in such interactions. Given the high degree of complexity of the phenomena, there is no theoretical treatment able to give a comprehensive description. In fact, the involved processes are very dependent on the basic parameters of the projectile, such as velocity  $v$ , charge state  $q$  and atomic number  $Z$ , and on the target parameters  $Z_t$ ,  $q_t$ , the physical state (molecular, atomic or ionized matter) and density. The target velocity,  $v_t$ , may have also incidence on the process, through the temperature  $T$  of the traversed medium. In addition, multiple-electron transfer in single collisions intricates more the phenomena. Though, in simplified cases, such as protons moving through atomic hydrogen, considerable agreement has been obtained between theory and experiments, however, in general the available theoretical approaches have only limited validity in restricted regions of the basic parameters. Since most measurements of charge-changing cross-sections are performed in atomic matter at ambient  $T$ , models are commonly based on the assumption of targets at rest ( $T \approx 0$ ); however at Astrophysical scales,  $T$  displays a wide range in atomic and ionized matter. Therefore, due to the lack of experimental data we attempt here to quantify  $T$ -dependent cross-sections on basis to somewhat arbitrary, but physically reasonable assumptions.

II.- CHARGE TRANSFER IN FINITE-TEMPERATURE MATTER. Let introduce the relative velocity

$$V_R = v + v_t \quad [1]$$

in the kinematics of the collision, where the target velocity,  $v_t$ , is the most probable thermal velocity of free electrons or hydrogen atoms in ionized or atomic matter respectively. If  $v_t$  is fixed in (1), for instance at  $v_t = 0$ , the dependence of charge-changing cross sections on the projectile velocity behaves as is shown in panel-1, for hydrogenic ions in atomic hydrogen, where  $\sigma_{pc}$  = loss cross-section,  $\sigma_{cc}$  = Coulomb capture cross-section and  $\sigma_{cr}$  = radiative capture cross-section. A rough interpretation of that velocity-dependence may be seen in terms of the idealized "free-collision approximation" (though the Born approximation which allows for screening effects gives qualitatively the same description): electrons are preferentially captured into states of orbital velocities  $u < v$  and preferentially lost at  $v > u$ . Since the impact parameter behaves as  $q q_t / M v^2$ , where  $M$  is the reduced mass,  $\sigma_{pc}$  at  $v > u$  decreases with  $v$ , whereas at  $v < u$ ,  $\sigma_{pc}$  increases with  $v$  because the adiabatic nature of the collision. Similarly, since the capture radius  $R_c \propto 1/v^2$ , electron capture declines

\* On leave for the INAOE, Tonanzintla, A.P. 51, 72000-Puebla.

with the projectil velocity. At relatively low  $v$  when  $R_c$  is large, electrons are readily captured far from the nucleus, where the energetic levels are very closed among them, falling much probably in an allowed state. So, there is photon emission because the electron braking in the capture; this is called Coulomb Capture. When  $v$  is relatively high, electron binding takes place at small  $R_c$ , where the energetic states are widely separated: the probability is high for the electron to fall in a forbidden state, such that a photon is emitted for the electron to be placed in an allowed orbit; this is known as Radiative Capture. Obviously,  $\sigma_{cr}$  at low  $v$  and  $\sigma_{cc}$  at high  $v$  are not null. According to [1], at Kinetic Energies  $E \gtrsim 9 \text{ MeV/n}$ ,  $\sigma_{cr}$  becomes predominant over  $\sigma_{cc}$ . It can be seen in (1), from  $V_R$ , that Coulomb capture in plasmas ( $T \gg 0$ ) becomes a rare process, even at low  $v$ , because the electron thermal  $v_t$  is quite significant. Now let fix  $v$  in

(1) to analyze the temperature behavior of cross-sections: for electron capture in atomic gas ( $T < T_i$ , = ionization temperature of the target medium) it is expected that cross-sections increase with the increase of the target  $T$ , because the binding energy of the atomic target electrons decline with  $T$ , so that when the electronic clusters of the projectil and target come close, it is easier to pick-up a target electron. At  $T > T_i$ , when the "free-collision approximation" is near to occur, the  $T$ -dependence of cross-sections is similar to the  $v$ -dependence, because the increase of  $V_R$  with the subsequent decrease in  $R_c$ . In the limit of high energy particles in high- $T$  plasmas only  $\sigma_{cr}$  is significant. The point  $\sigma_{cc} = \sigma_{cr}$  is reached at lower ion energies than  $9 \text{ MeV/n}$  as  $T$  increases ( $E_{\text{impact}} = E_{\text{ion}} + E_t = 9 \text{ MeV/n}$ ).

For electron loss, the effect of  $T$  on  $\sigma_{pc}$  may be seen as a shift in energy, in the sense that, a given value of  $\sigma_{pc}$  is reached at lower ion velocities as  $T$  increases. Although it is not expected a noticeable change in  $\sigma_{pc}$  in ionized with respect to atomic H, because the electronic screening of the target nuclei is negligible relative to the ionization potentials in the projectil ions, however, the increase of the medium- $T$  increase the impact energy, and so  $\sigma_{pc}$  is affected: for a fixed  $v$  in the range  $v > u$ ,  $\sigma_{pc}$  decreases with  $T$  because collisions take place at smaller impact parameters, while in the range of adiabatic collisions ( $v \lesssim u$ ),  $\sigma_{pc}$  at a fixed  $v$  increases with  $T$ . This is rather seen in atomic media, since a relatively high  $T$  the Thermal velocities are high, such that  $V_R \gtrsim u$ , in which case, as we said before the  $T$ -dependence show the same behavior as the  $v$ -dependence.

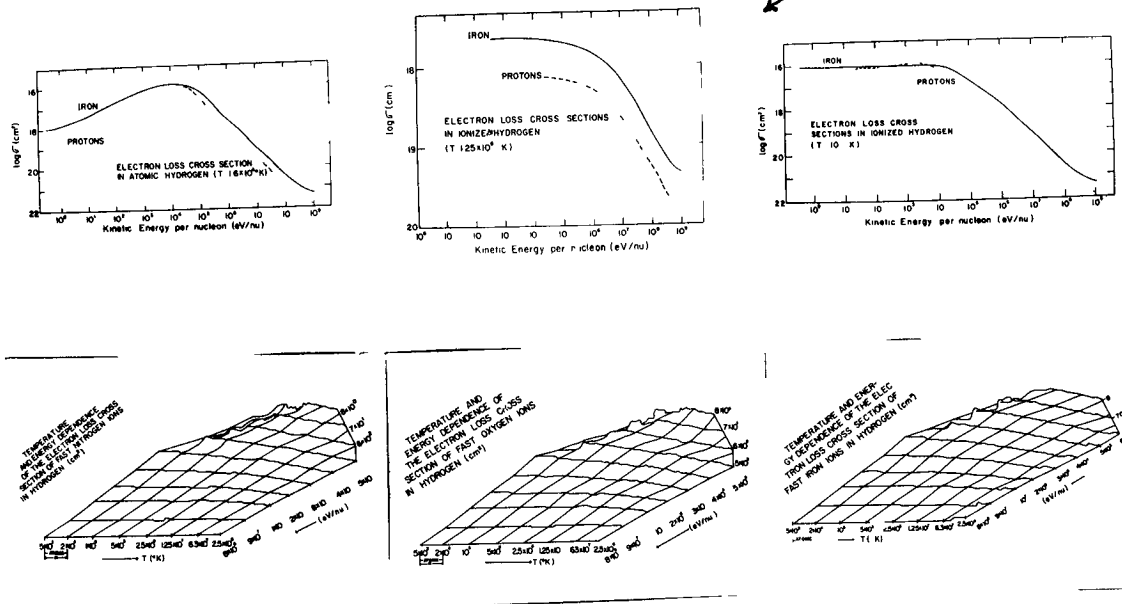
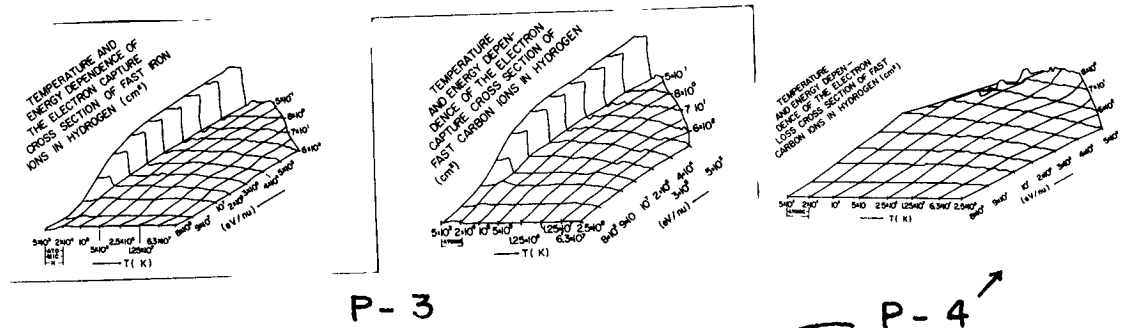
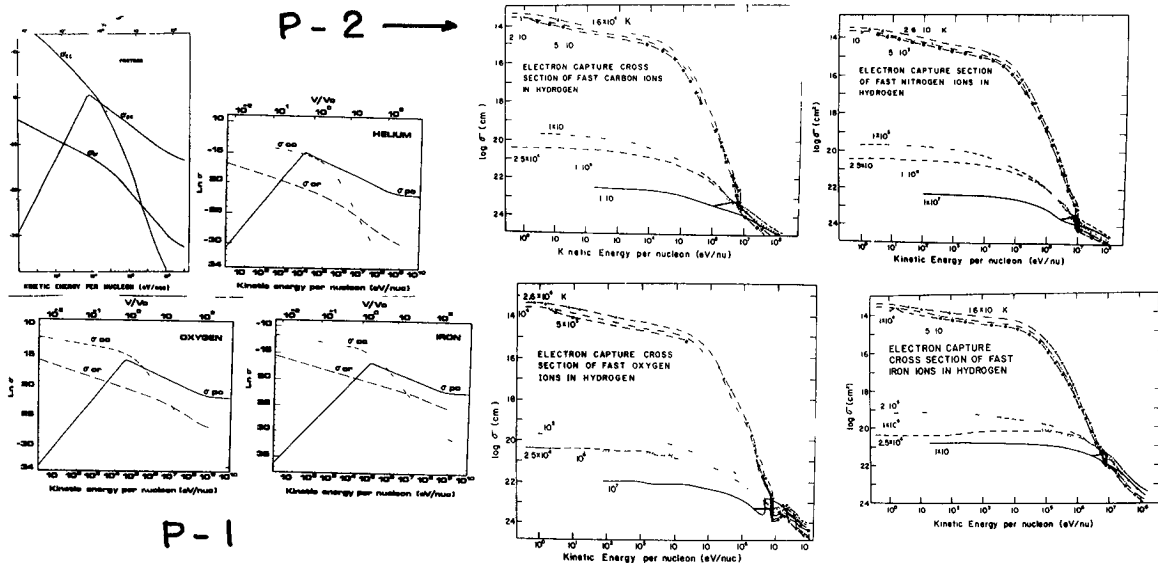
III. METHODS AND RESULTS. Our analysis here is limited to the case for which projectil ions are accelerated from the background thermal matter, so that their initial velocities and initial charge states correspond to thermal temperatures. For the local charge states,  $Q_L$ , we are mainly based on the Solar-System ionization fractions in [2]. We arbitrarily assume that the accelerated ions undergo charge equilibrium in the source (solar flare matter), such that the charge evolves according to the effective charge  $q^* = Z[1 - \xi \exp(-130\beta/Z^{0.66})]$ , with  $\beta = v/c$  and  $\xi = \exp[-130(kT/mc^2)]$   $k$ =Boltzman constant and  $m$  the hydrogen or the electron mass depending on whether  $T \lesssim T_i$  or  $T > T_i$ . Normalization of  $Q_L$  with  $q^*$  is made by means of

$q = [(Z - Q_L)(q^* - q_{th}^*) / (Z - q_{th}^*)] + Q_L$ , where  $q_{th}^*$  is the effective charge of the accelerated ions where they are at thermal velocities. For the electron binding in atomic H we assume that the attractive potential is of the form  $U_C \psi(T)$ , where  $U_C$  is the Coulomb Potential and  $\psi(T) = 1 - \exp(-T_i/T)$ . To account for the increase of capture cross-sections with  $T$  we divided the prevailing cross-sections in atomic media ( $T \approx 0$ ) by  $\psi(T)$ , with  $T_i = 2.5 \times 10^4$  K. At  $T > T_i$  there is an abrupt fall in the capture cross sections because the drastic change in  $v_t$  from atomic to electron thermal velocity. For  $T < T_i$  in panels 2-3 we plotted  $\sigma_{cc}/\psi(T)$  at  $E_{\text{impact}} < 9 \text{ MeV/n}$  and  $\sigma_{cr}/\psi(T)$  at higher energies. Due to the predominance of  $\sigma_{cr}$  in plasmas, for  $T > T_i$  we plotted  $\sigma_{cr}/\psi(T)$  with  $T$  fixed at  $2 \times 10^4$  K. The cross  $\sigma_{cc} = \sigma_{cr}$  is indicated by a transversal solid line. For  $\sigma_{pc}$  we introduced, as in electron capture cross-sections, the normalized charge and  $V_R$  instead of  $v$ , and we ran it for any  $T$  value (panels 4-5). We employed the conventional temperature-independent cross-sections for atomic matter: so, for atomic sources of solar particles we have according to [3] that, for highly charged nuclei ( $q \ll Z-1$ )  $\sigma_{cc1} = \pi a_0^2 q^2 Z_t^* 2^{1/3} (v_0/v)^9 (1 + 4Z_t^{*2} v_0^2/v^2)^{-4}$  and according [4]  $\sigma_{pc1} = \pi a_0 q^{-3} Z^{4/3} Z_t^{2/3} (v/v_0)^2$  if  $v < v_1$ , or according to [5]  $\sigma_{pc2} = \pi a_0^2 q^{1/3} Z_t^2 (v_0/v)^3$  if  $v > v_1$ , where  $v_1$  corresponds to  $\sigma_{pc1} = \sigma_{pc2}$ . For very high velocities, when nuclei become hydrogenics, according to [5] we have  $\sigma_{pc3} = 4 \pi a_0^2 Z^{1/3} Z_t^2 (v_0/v)^3$ , ( $v > Z v_0$ ), and according [3]  $\sigma_{cc2} = \pi a_0^2 Z^5 Z_t^{*5} (2v_0/v)^{12} (1 + 4Z_t^{*2} v_0^2/v^2)^{-4}$ . The case of low velocity hydrogenic heavy ions in atomic media has only a meaning when particles are injected into the acceleration region from a preliminary acceleration stage, so it is excluded within the present context. At high  $T$ , in sources of ionized H, we used  $\sigma_{pc1}$  and  $\sigma_{pc2}$  with  $q$  instead of  $Z$ , and according to [6],  $\sigma_{cr1} = 6.15 q^2 q^4 (v_0/c)^3 (v_0/v)^2 (v_0/v^2 + q^2 v_0^2)$  if  $v \ll 3 q v_0$  and  $\sigma_{cr} = 9.1 \times 10^{-21} (q^2 v_0^2/v^2 + q^2 v_0^2)^2 (q^2 v_0^2/v^2) \exp[-(4 q v_0/v) \arctg(v/2v_0)] / [1 - \exp(-2 \pi q v_0/v)]$  if  $v > 3 q v_0$ ; for hydrogenic ions (very high  $T$  or  $v$ ) we used according to (5)  $\sigma_{pc4} = \pi a_0^2 Z^{-5/3} Z_t^{1/3} (v/v_0)^2$  if  $v < v_2$  and  $\sigma_{pc3}$  if  $v > v_2$ , where  $v_2$  correspond to  $\sigma_{pc3} = \sigma_{pc4}$ . Obviously, at  $E_{\text{impact}} > 9 \text{ MeV/n}$  in sources of atomic H, we used  $\sigma_{cr}$  instead of  $\sigma_{cc1}$  or  $\sigma_{cc2}$ . It can be noted that due to continuous changes of the normalized  $\alpha$ , there are oscillations in the cross-section values, that for reason of scale can not be smoothed at high energies as easy as in low energies.

**IV. CONCLUSIONS.** Under the arbitrary assumption that electronic screening of the target H is not very important compared with the screening of the projectile ions, we extrapolate charge-changing cross sections in atomic matter at  $T \approx 0$  to finite temperature media, by introducing the target velocities. Nevertheless, for atomic media we have considered the effect of the target electronic screening on capture cross-sections, as  $T$  increases. We feel that the obtained results are of more realistic nature, for astrophysical goals, that the mere extrapolation of the conventional  $T$ -independent cross-sections.

#### REFERENCES

- [1] Briggs, J.S. and Detmann, K., *Phy. Rev. Letters* **33**, 1123, 1974.
- [2] Jain, N.K. and Narain, V., *Astron. Astrophys. Suppl.* **31**, 1, 1978.
- [3] Nicolaev, V.S., *Soviet Phys. Uspekhi* **8**, 269, 1965.
- [4] Bohr, N. and Lindhard J., *Dan. Mat. Fys. Medd.* **28**, 1, 1954.
- [5] Bohr, N., *Dan. Mat. Fys. Medd.* **18**, 8, 1948.
- [6] Bethe, H. and Salpeter, E.E., *Quantum Mechanics of 1-2 electron atoms*, Springer Verlag, 1957.



# STUDY OF PHOTON EMISSION BY ELECTRON CAPTURE DURING SOLAR NUCLEI ACCELERATION. II. DELIMITATION OF CONDITIONS FOR CHARGE TRANSFERT ESTABLISHMENT.

J. Pérez-Peraza\* and M. Alvarez \*

Instituto de Geofísica, UNAM, 04510, C.U. México 20, D.F.

A. Gallegos

UPICSA, 08400, México, D.F.

**I. INTRODUCTION.** In preceeding works 1, 2, we have examined the conditions for the establishment of charge transfert of solar particles during their acceleration in the dense medium of their sources: In 1, we restricted our analysis to the case of hydrogenic projectile ions, and in 2 we studied the case of highly charged ions (effective charge =  $q^* < z = \text{atomic number}$ ). But in both cases, we did not take into account the charge transfer cross-section dependence on the target velocity, i.e. we ignored the effect of the finite temperature of matter. A more accurate evaluation of the charge transfer criteria developed in the previous papers needs of the results derived in SH.1.1-8. With this goal in mind let us remind that the conditions for the passage of fast ions through matter at laboratory scale and in astrophysical sources of energetic particles are to some extent of opposed nature. In the first case a monoenergetic flux of high energy particles is injected into the matter, whereby particles lose energy through energy transfert to the electrons and nuclei of the target medium. When the amount of traversed matter is greater than the mean free path for charge changing processes, the charge equilibrium is established; if the particle velocity is higher than the orbital velocities of its electrons the ion is rapidly stripped, however, as the particle velocity is degraded by collisional losses to a lower velocity than the orbital velocity of the first captured electron, the electron capture cross-section gradually dominates over the electron loss cross-section. As particles slow down and electron capture leads them toward the neutralization, they may be stopped by thermalization with a low effective charge, or even in the neutral state. On the other hand, in astrophysical sources instead of that tendency toward thermalization, particles are accelerated from thermal energies up to high energies, beginning with their local charge state  $Q_L$ , which is determined by ionization equilibrium at the peculiar source temperature. In order to elucidate whether particles keep their thermal charge state during that acceleration stage or not, the conditions for the establishment of charge transfert have been investigated. The behavior of particle charge during acceleration is very important due to several implications related to the mass and charge spectra of particles, the acceleration efficiency and secondary electromagnetic radiation.

**II. CRITERIA FOR THE ESTABLISHMENT OF CHARGE CHANGING PROCESSES.** As we explained in 1 the criteria for establishment of charge-changing processes may be seen as an evaluation of the relative importance between the mean free path for charge transfert and the characteristic length of the acceleration step, provided that the later one be shorter than the mean free path for Coulomb inelastic collisions. In order to avoid masking the effects of concurrence between the processes of charge interchange and acceleration, on the behavior of particle charge, it is convenient for the task of simplicity to consider those acceleration mechanisms whose rates are independent of charge: stochastic acceleration (Fermi mechanism) and acceleration by secularly varying magnetic fields (Betatron mechanism),

\* On leave for the INAOE, Tonanzintla, A.P. 51, 72000-Puebla

which rates in the non-relativistic range may be expressed as  $(dE/dt) = \alpha E^n$ , with  $n = 1/2$ ,  $\alpha = \alpha_f(2\mu C^2)^{0.5}$  and  $n = 1$ ,  $\alpha = 2\alpha_b$  for the Fermi and Betatron mechanisms respectively,  $E = \mu v^2/2$ ,  $\mu$  = atomic mass unit and  $\alpha_f$ ,  $\alpha_b$  the hydromagnetic acceleration efficiencies. Using  $(d/dt) = v(d/dx)$  the above rate becomes  $v^{2(1-n)}dv = (\alpha/2)(\mu/2)^{n-1}dx$ . Now let define a cross-velocity  $v_c$  where both cross-sections for electron capture and loss are equated. So, integrating the acceleration rate from  $v$  to  $v_c$  in the domain of electron capture ( $v < v_c$ ) through the thickness  $L$  of the traveled matter, and from  $v_c$  to  $v$  in the domain of electron loss, and introducing the condition of establishment of charge transfert, that the corresponding mean free path ( $\lambda$ ) must be shorter than the amount of traversed matter ( $\lambda = 1/n\sigma < L$ ), where  $n$  and  $\sigma$  are the number density and the corresponding cross-section, we obtain the following expressions  $\alpha < 2(v_c^{3-2n} - v^{3-2n})n\sigma/(3-2n)(\mu/2)^{n-1}$  and  $\alpha < 2(v^{3-2n} - v_c^{3-2n})n\sigma/(3-2n)(\mu/2)^{n-1}$  for the establishment of capture and loss at  $v < v_c$  and  $v > v_c$  respectively, when an acceleration process of efficiency  $\alpha$  is modulating the velocity of the traversing particle through the source matter. However, such an acceleration efficiency must overcome the deceleration efficiency from the rate of inelastic losses in order to produce suprathermal particles. That is, the condition  $\alpha/\alpha_c > 1$  must be satisfied, where  $\alpha_c$  is the threshold value of the acceleration efficiency above the which the acceleration dominates energy losses. Values of  $\alpha_c(n)$  were given in [1] as  $\alpha_c = 3.38 \times 10^{-13} n q^{0.5}/A$  and  $\alpha_c = 4.5 \times 10^9 n q^{0.16}/T^{0.27} A^{0.78}$  for the Fermi and Betatron processes in atomic H, and  $\alpha_c = 3.89 \times 10^{-7} n^{0.98} q^{1.92}/T^{0.96} A^{0.88}$  and  $\alpha_c = 0.28 n^{0.97} q^{1.87}/T^{1.45} A^{0.67}$  in plasmas. So, our criteria are reduced to 4 evaluations of  $(\alpha_f/(2\mu C^2)^{0.5} \alpha_c) > 1$ , two for electron capture (in atomic and ionized H) and two for electron loss, and similarly other 4 evaluations with  $(\alpha_b/2\alpha_c) > 1$ . On the next figures we have omitted the subfixes f and b, but indicated the considered acceleration mechanism. It must be emphasized that these criteria become independent of number density but strongly dependent on cross-sections and the cross-velocity  $v_c$ . Values of  $v_c$  for the particular case of targets at rest ( $T \approx 0$ ) were given in [2]. Here we use the  $\sigma$  values of SH1.1-8 and so the corresponding  $v_c$  values were numerically obtained. For the evolution of the charge  $q$  appearing in the  $\sigma$  and  $v_c$  values, we normalized to the thermal  $Q_L$  values as explained in SH1.1-8, when charge equilibrium was found. In the case that the shortness of the characteristic acceleration step only allows for electron capture but not electron loss, we arbitrarily employed in the normalization  $q_c^* = Q_L \exp\{-130(\beta - \beta_{th})^{0.33}/Z^{0.66}\}$ , whereas in the opposite case we used  $q_c^* = Z\{1 - \xi \exp(-130\beta^{0.33}/Z^{0.66})\}$  where  $\beta$  and  $\beta_{th}$  are the projectil velocity and its thermal velocity respectively and  $\xi$  as given in SH1.1-8. The results discussed below may be considered as a lower limit in the amount of electron capture and loss, because the main considered target is H. If heavier elements are considered, electron capture becomes much more important, because the employed cross-sections scale as  $Z_t Q_L^5$  for Coulomb capture and  $\sim Z_t$  for radiative capture; so in evaluating electron pick-up with heavy targets we multiplied  $\sigma_{cr1}$  and  $\sigma_{cr}$  in SH1.1-8 by  $Z_t$ .

**III. RESULTS AND CONCLUSIONS.** We explored the conditions for establishment of charge transfert during acceleration of nuclei up to Fe, for typical conditions of solar flare regions  $T = 5 \times 10^3 - 2.5 \times 10^8$  K. Our results show that such conditions are widely assorted, depending on the acceleration mechanism, the kind of projectil ions and their velocity, the target elements, the source temperature and consequently on the degree of ionization of matter and the local charge state of the accelerated ions.

Nevertheless, in spite of that assorted behavior, there are some general tendencies that can be summarized as follows. In atomic H electron capture is systematically established from thermal energies up to high energies, whatever the element and for both acceleration process. For a given element and fixed  $T$ , the probability and energy domain of electron capture and loss with Fermi are higher than with Betatron acceleration. For a given acceleration process the heavier the ion the higher the probability and the wider the energy range for electron capture and loss. For a given acceleration mechanism and fixed element the importance and energy domain of capture and loss increase with  $T$ : for those reasons, the energy range of charge equilibrium (illustrated with solid lines on the next figs.) is wider with Fermi and increases with temperature and atomic number of projectiles. For the same reasons, electron loss is smaller while the lighter the element, the lower the temperature and the Betatron process, such that there are conditions for which electron loss is not allowed at low energies, but only electron capture is established. Consequently, the energy domain for pure electron capture (illustrated with crosses) is wider the lighter the element, the lower  $T$  and with the Betatron mechanism. On the other hand, at high energies electron capture is not allowed and only electron loss is established (illustrated with small squares) up to high energies, while the heavier the element and the higher the temperature. These results, illustrated through figures (1)-(4) show higher importance of electron capture than that found in [1], [2], because the increase of the cross-section with  $T$  in atomic matter described in SH1.1-8. Obviously, the employment of the conventional effective charge expression for charge equilibrium is not adequate when only electron capture is established and particles tend to neutralization, or when pure electron loss is established and particles strip faster. In ionized H electron capture is only established with Fermi acceleration for  $T > 2 \times 10^8 \text{ K}$  and  $Z > 10$  provided they are at thermal hydrogenic state ( $Q_L = Z$ ). Under these conditions the heavier the ion the higher the probability and energy domain for electron capture. Electron loss is more important with Fermi than with Betatron and the higher the temperature the higher the probability and the wider the energy domain. At low energies electron loss is more important while the lighter the element and at high energies electron loss becomes more important while the heavier the element as can be understood from the  $q$ -dependence of cross-sections in SH1.1-8. We have illustrated these effects on Figs. (5)-(7). An interesting effect that appears with the consideration of the target temperature, in contraposition of the conventional picture described in panel-1 of SH1.1-8, is that in low- $T$  plasmas ( $T > T_i$ ) and low velocities ( $v < v_c$ ),  $\sigma_{pc}$  may become higher than  $\sigma_{cr1}$  because the shift to low velocities of the  $\sigma_{pc}$ -pick and the decrease of  $\sigma_{cr1}$  with the increase of relative velocity  $v_r$ . On the other hand, although  $\sigma_{cr1}$  decreases with  $T$  roughly as  $v_r^2$ , however the reason for which electron capture is established only at high  $T$  ( $> 2 \times 10^8 \text{ K}$ ) and that electron loss at low velocities increases with  $T$ , is due to the fact that  $v_c$  increases with  $T$ , in such a way that at high  $T$  in our criteria expressions we have, for instance in the Fermi case, that  $(v_c^2 - v^2)$  increases faster with  $T$  than the decrease of  $\sigma_{cr1}$ . Finally, in Fig. 8, we have illustrated the energy domain of charge equilibrium in ionized matter for different ions, when instead of H we consider heavy targets: beyond the end of those curves, at higher energies, only electron loss is established. These cases are very important in evaluating photon emission from electron capture, since our criteria for charge-transfer establishment are density-independent, and so, only  $\sigma$  and  $v_c$  determine the electron capture domain.

#### REFERENCES

- [1] Pérez-Peraza, J., et al., Adv. Space Res. 2, 197, 1983.
- [2] Pérez-Peraza, J., et al., 18th Int. Cosmic Ray Conf. 9, 309, 1983.



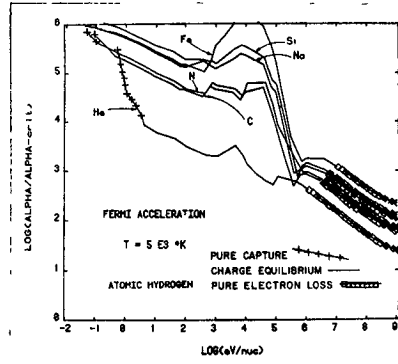


FIG. 1

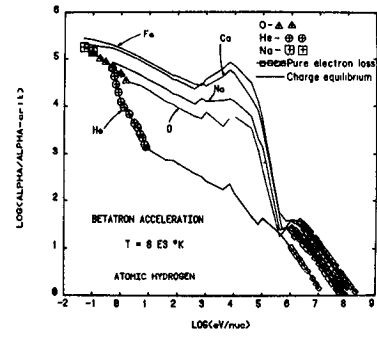


FIG. 2

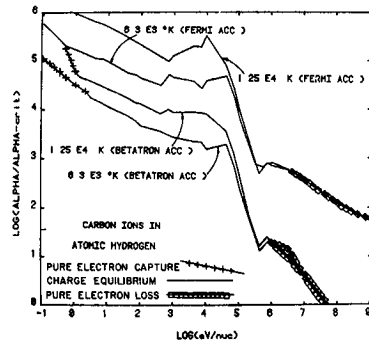


FIG. 3

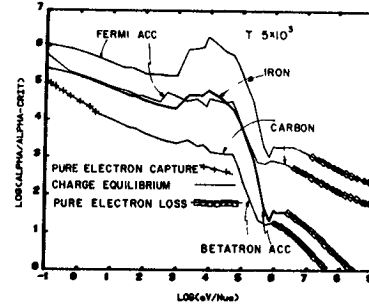


FIG. 4

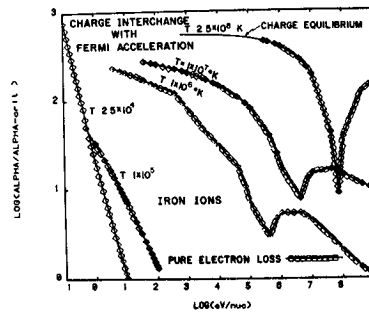


FIG. 5

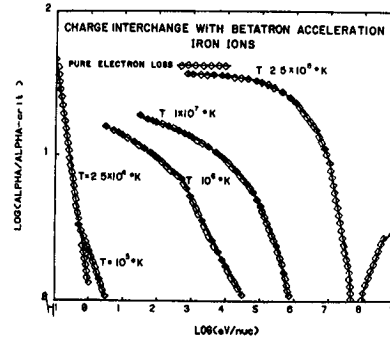


FIG. 6

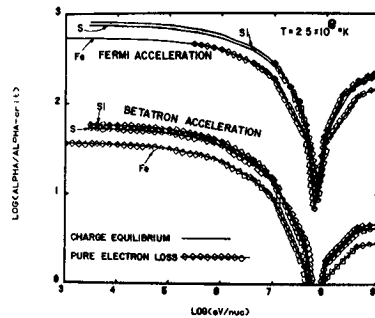


FIG. 7

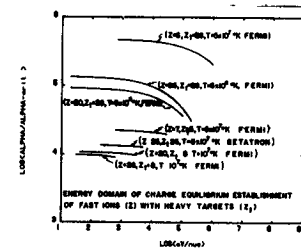


FIG. 8

# STUDY OF PHOTON EMISSION BY ELECTRON CAPTURE DURING SOLAR NUCLEI ACCELERATION: III. PHOTON PRODUCTION EVALUATIONS.

J. Pérez Peraza\* and M. Alvarez\*

Instituto de Geofísica, UNAM, 04510- C. U., México, D. F., MEXICO

A. Gallegos

UPICSA, 08400 - México, D. F., MEXICO

**1. Introduction.** Electromagnetic emission from the interaction of hydrogenic nuclei with atomic media has been widely studied in Laboratory. At astrophysical scale a similar scenario has been studied: high energy Cosmic Rays (bare nuclei) traversing a certain amount of interstellar matter while losing energy by Coulomb interactions. Here we study to some extent the opposite scenario, in the sense that particle interaction and emission takes place as particles are being accelerated from the source thermal energies up to high energies. As particle sources we have chosen the Solar chromosphere and corona, where local ions are generally not bare nuclei, and there are often situations for which the amount of traversed matter is enough for the establishment of electron pick-up during acceleration, as was shown in paper SH 1.1-9. Here we limit our calculations to photon emission following electron capture and do not consider emissions following de-excitations. According to SH 1.1-9 results electron capture is systematically established in atomic H conditions, but in ionized H it is established only at  $T > 2 \times 10^8 \text{ K}$  for nuclei of  $Z > 10$  and  $E < 30 \text{ MeV/n}$ ; however, since  $\sigma_{cr}$  in ionized matter scales as  $Z_t = \text{target}$  atomic number, electron pick-up is established at  $T > 2 \times 10^6 \text{ K}$  when the contribution of heavy targets is considered. Actually, since the criteria for charge transfer establishment (SH 1.1-9) are practically independent of matter density, most of the electromagnetic emission expected here appears in this form. It should be noted that such criteria are limited in validity for the condition that the particle flight time within the acceleration volume be enough long for the amount of traversed matter ( $X$ ) be higher than the corresponding mean free path ( $\lambda$ ) of the charge transfer process ( $\rho v t > H/\sigma$ ): it can be seen that given a density ( $\rho$ ) and particle velocity ( $v$ ), since the cross-section ( $\sigma$ ) decreases with  $T$ , the behavior of the time ( $t$ ) is fundamental in determining whether ( $X > \lambda$ ) or not. This can be tested from the employed acceleration time  $t_f = [2/(2\mu c^2)^{0.5} \alpha_f] (E^2 - E_{th}^2)$  in the Fermi process, and the betatron acceleration time  $t_b = (1/2\alpha_b) \ell_n (E/E_{th})$ , where  $E_{th}$  is the thermal energy per nucleon of the accelerated ions. For the evaluation of the acceleration efficiencies we recurred to the results of the criteria  $(\alpha_f/\alpha_c)$ ,  $(\alpha_b/\alpha_c)$  in SH 1.1-9, such that  $\alpha_f = (\text{criterion value}) \alpha_c(\text{fermi})$ ,  $\alpha_b = (\text{criterion value}) \alpha_c(\text{betatron})$ . The general tendency in ionized matter is the increase of the acceleration time with  $T$  because  $\alpha_c$  decreases with  $T$ , so, the above inequality is satisfied easily while the higher  $T$ . In atomic matter  $t_f$  decreases with  $T$  because  $\alpha_c(\text{Fermi})$  is  $T$ -independent, but the electron capture cross-section increases with  $T$ , as we shown in SH 1.1-8, so the inequality is satisfied. With betatron,  $t_b$  increases slowly with  $T$  as  $\alpha_c(\text{betatron})$  decreases with  $T$ , however, conditions are such that the inequality is systematically conserved. Similarly, though the electron loss cross-section decreases with  $T$ , as  $t_f$  does, much of conditions satisfy that inequality. Therefore, even if the density is very low the inequality is conserved because  $\alpha_c$  decreases with density and the acceleration times becomes proportionally longer.

**2. Method for Photon Production Evaluation.** Once we have determined the energy range where electron capture is established, we know the initial charge state  $q_i^*$  at the corresponding lower energy value according to the normalization described in SH 1.1-8 of the effective charge for charge equilibrium to the thermal charge state, when charge equilibrium was established at that particle energy level, or, the arbitrary expression  $q_i^*$  for pure capture given in SH 1.1-9 (if electron loss does not establish). If electron capture begins from thermal energies  $q_i^* = Q_L$ . Since acceleration is

increasing particle energy, we test at each energy value whether  $q_i^* - q_c^* \geq 1$  if charge equilibrium is established, or,  $Q_L - q_c^* \geq 1$  if only pure electron loss is established; if not, we iterate to the next energy value with the corresponding  $q_i^*$  and  $q_c^*$  values in the former case, or  $Q_L - q_c^*$ , with  $q_c^*$  evaluated at the new energy in the 2nd case. When we find that an electron is captured, we evaluate the number of electrons retained by the ion  $N_e = Z - q_c^*$ . Further, we fit this number to the degeneracy condition  $2n^2$ : if the  $n$ -orbit is not still filled, we begin calculating orbit radius  $r_n = n^2 h^2 / Ze^2 m_e$  [but, if it is filled we begin to evaluate orbit radius from  $(n+1)$ ] in order to compare them with the capture radius ( $r_c = q^* e^2 / m_e V_R^2$ ), and in this way to determine at which energy level the electron will be captured; if  $r_{n+i}^- < r_c < r_{n+i+1}$  we infer that the capture orbit is at  $r_{n+i} = r_f$ . When  $r_c < r_n$  ( $n=1$ ), we recur to the Sommerfeld elliptic orbits  $r_k = \kappa n^2 / m_e Z^2$ , where  $\kappa$  is the quantic number determining the angular moment, and so, we proceed the evaluation from  $\kappa=n-1$  till  $\kappa=1$ . In the cases that  $r_c < r_k$  ( $\kappa=1$ ) we fall in the domain of relativistic mechanics that we have not studied in this preliminar work: this is the case at  $T > 5 \times 10^7$  K, when  $V_R$  becomes extremely high. Therefore, at each energy value we imposed 3 conditions for making possible the evolution of photon emission: (1) electron capture is established, (2) we find  $q_c^* \leq q_i^* - 1$  (3)  $r_c \geq r_k$  ( $\kappa=1$ ). Once these conditions are remplished we evaluate the photon energy  $h\nu = E(r_c) - E(r_f) \sim q^* e^2 / r_f - q^* e^2 / r_c$ , and the photon flux at 1. A.U.,  $F/n_t = N(E) \sigma_c / 4\pi R^2$  (photons/eV st/target atom). For our

calculations we took the energy spectrum of protons demodulated for interplanetary propagation of the 4-VIII-72 event [1],  $N(E) = 8 \times 10^{35} \text{ E}^{-3}$ , and typical solar particle abundances [2], such that under the assumption  $(O/H)_0 = 0.77\%$  we built the heavy ions spectra. For radiative capture we did not evaluate photon emission from electron braking as we have done in the case of Coulomb capture.

3. Results and Discussions. As is shown in the next series of pictures, our results are widely assorted depending on  $T$ ,  $Z_t$ ,  $Z$ ,  $N(E, Z)$  and the acceleration

process. The general tendencies show a frequency drift toward high photon energies as particles increase their energy during acceleration, because  $h\nu \sim 1/r_c$  and  $r_c \sim 1/V_R$ : oscilations are due to charge changes and the separation between  $r_c$

and the quantic level at  $r_f$  which is very sensitive to  $V_R$ . Typical drifts in atomic matter produces continuum radiation from IR to X-ray ( $10^{-3} - 5 \times 10^3$ ) eV in  $\Delta t \sim 1$  s, whereas in ionized matter we obtained emission lines from UV to X-rays (50 eV-6.2 KeV), with a finite width covered in  $\Delta t \leq 0.5$  s. It can be appreciated on the drift figures ( $h\nu - E$ ) that the heavy the projectil the emission drifts to higher energies, because  $h\nu \sim q^* / r_c^2 \sim Z^2$ . The range of energy drift widens with

$T$ , because the particle energy range for electron capture increases with  $T$ . Also the photon energy increase with  $T$  because the increase of  $V_R$  with  $T$ , but with

oscilations due to the  $V_R$ -sensitivity of the separation between  $r_c$  and the nearest orbit  $r_f$ . On the figures of energy spectra (Flux- $h\nu$ ) it can be noted that the

heavier the target and the projectil the higher the intensity of the emission spectrum. This follows from the fact that  $F/n_t \sim \sigma_c N(E, Z)$  and  $\sigma_c$  increases with  $Z$  and  $Z_t$ . However, this tendency may also show oscilations because  $N(E, Z)$  does

not increase always monotonically with  $Z$ . Also, the emission intensity increases with  $T$  in atomic matter and decreases with  $T$  in ionized matter, because the corresponding  $\sigma_c$  increases and decreases with  $T$  respectively. Photon fluxes in atomic and

ionized matter are in the range  $10^{-7} - 10^7 \text{ ph./eVst/target-atom}$  and  $10^{-12} - 10^8 \text{ ph./eVst/target-atom}$ . On the time profiles figures (Flux  $\sim t$ ) the  $t$ -axis refers to  $t_f$  and  $t_b$ ,

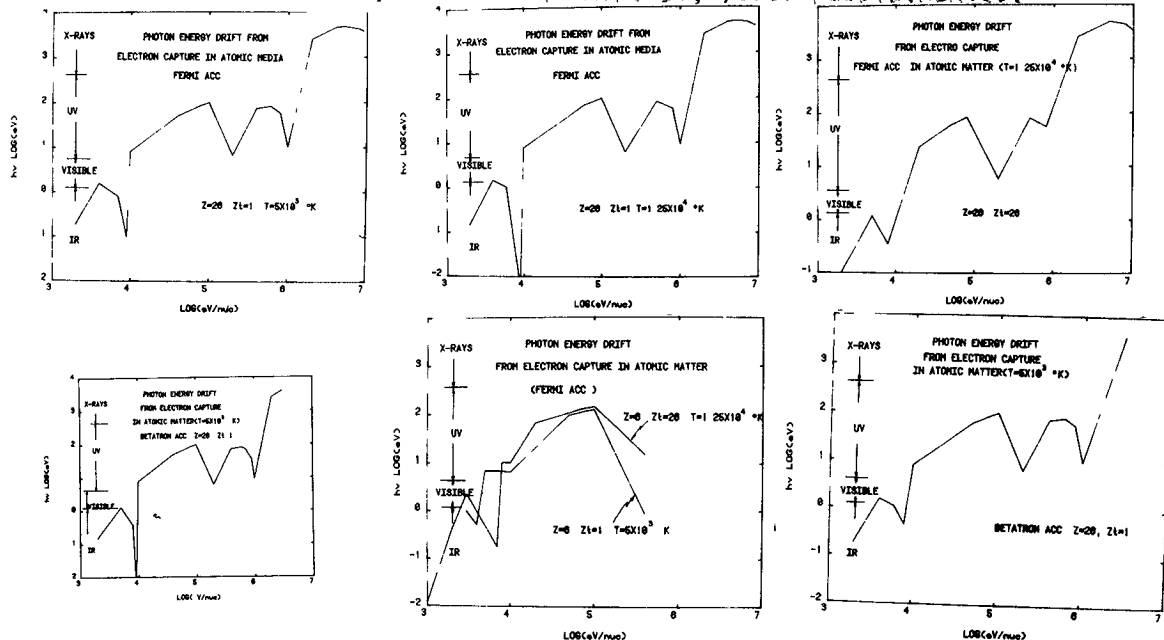
which are increasing functions of particle energy  $E$ . Since  $N(E, z)$  is a decreasing function with  $E$ , therefore, photon fluxes decrease with time during acceleration. Photon emission begins faster after acceleration onset with Fermi than with betatron acceleration, and more faster, in atomic than in ionized media, since acceleration efficiencies are higher in atomic matter: for instance, with Fermi acceleration begins  $(10^{-5}-10^{-3})$ s after acceleration onset, while with betatron begins  $(10^{-3}-10^{-2})$ s after acceleration onset, whereas in ionized matter corresponding time delays are  $(0.5-3.5)$ s and  $\sim 2.3$ s respectively. From the values  $\alpha_f \sim (4 \times 10^{-3}-10^4)s^{-1}$  and  $\alpha_b \sim (3.5 \sim 10^5)s^{-1}$  in atomic matter, it is realized that acceleration from thermal energies in deep chromospheric layers is restricted to extremely constrained conditions of strong turbulence with extremely short length scales and very high magnetic field gradients, that might only occur in association with fast magnetic field annihilation in active neutral current sheets. On the other hand  $\alpha_f \sim (3 \times 10^{-2}-0.2)s^{-1}$ ,  $\alpha_b \sim 2.4s^{-1}$  in coronal ionized matter is quite reasonable.

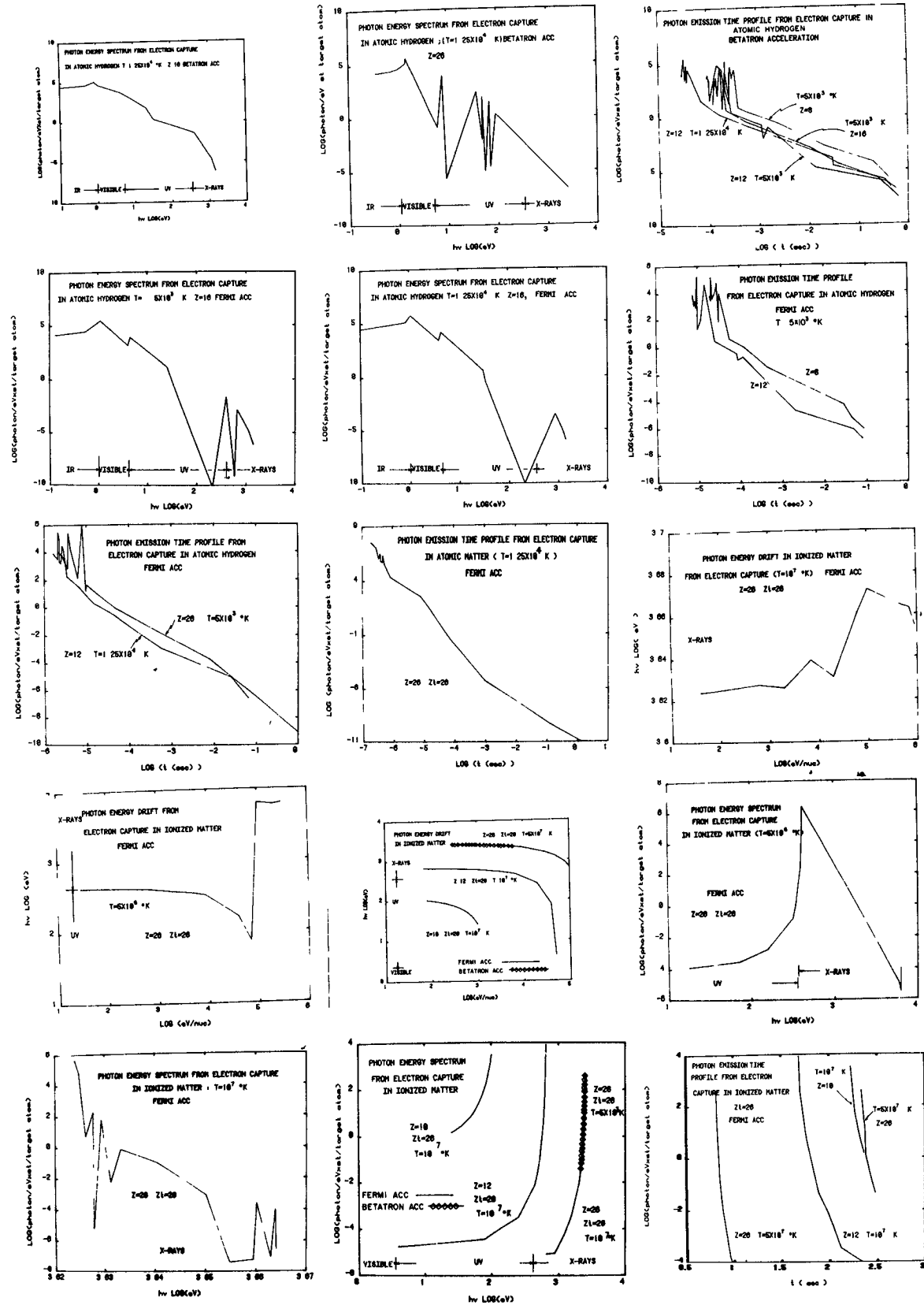
**4. Conclusions.** We have evaluated lower limits of photon fluxes from electron capture during acceleration in solar flares, because the arbitrary  $q^*$  assumed in this work evolves very slow with velocity, probably much more slowly than the physical actual situation: in fact, more emission is expected toward the IR region. Nevertheless, we claim to have shown the factibility of sounding acceleration processes, charge-evolution processes and physical parameters of the source itself, by the observational analysis of this kind of emissions. For instance, it would be interesting to search observationally, for the predicted flux and energy drift of  $F_e$  ions interacting with the atomic O and  $F_e$  of the source matter, or, even more feasible for the X-ray lines at 4.2 KeV and  $2.624 \pm 0.003$  KeV from Fe and S ions in ionized Fe at  $T = 10^7$ °K respectively, the  $418 \pm 2$  eV and  $20 \pm 4$  eV lines of Fe and S in ionized Fe at  $5 \times 10^6$ °K, which are predicted from Fermi acceleration.

#### References

- [1] Miroshnichenko, L. I. and Petrov, V. M., "Dynamics of Radiation Conditions in Space", Energoatomizdat, Moscow, 1985.
- [2] Dietrich, W. F. and Simpson, J. A., Ap. J. **225**, L41, 1978.

\*On leave for the INAOE, Tonanzintla A.P. 51, 72000-Puebla, MEXICO.





# STUDY OF NON-THERMAL PHOTON PRODUCTION UNDER DIFFERENT SCENARIOS IN SOLAR FLARES: I. SCENARIOS AND FORMULATIONS.

J. Pérez Peraza\* and M. Alvarez-M.\*

Instituto de Geofísica, UNAM, 04510, México, D. F. MEXICO

A. Gallegos

Depto. de Física, UPICSA, 08400, México, D. F., MEXICO

I. INTRODUCTION. In order to study the overall phenomenology involved in solar flares, it is necessary to understand their individual manifestation before building a corresponding description of the global phenomenon. Here we are concerned with the production of X and  $\gamma$ -rays in solar flares. Following the model in (1), flares are initiated very often within the closed magnetic field configurations of active centers. According (2) when  $\beta$  = kinetic energy density/magnetic energy density  $\geq 0.2$ , the magnetic trap configuration is destructed within the time scale of the impulsive phase of flares ( $< 100$  s). A first particle acceleration stage occurs during this phase as indicated by impulsive microwave and hard-X-rays bursts. In some flare events, when the field strength  $B$  is very high, the broken field lines may close again, such that later, in the course of the flash and main phases more hot plasma of very high conductivity is created, and so, the field and frozen plasma expand outward, as the kinetic pressure inside the closed loops increases. The magnetically trapped particles excite strong Alfvén wave turbulence of small transverse scale. According to (3), small scale turbulence of linear dimensions  $\sim (1 - 10)$  Km may account for effective stochastic acceleration up to relativistic energies. In addition, according to (4) a high pressure piston which drives a shock within the closed configuration may be formed: magnetized turbulent cells remain bounded in the wake of the "bottle up" shock wave. Since the shock moves faster than the expanding bottle, the stochastic acceleration overcomes the 1st. order Fermi process (adiabatic losses) due to the expansion of the bottle. As discussed in (4) the expanding bottle opens or not depending on whether the duration of the flare induced shock is larger or not than the Raleigh-Taylor instability growth time. Therefore, when the conditions of the opening are satisfied we expect a definite slope change in the energy spectrum, indicating two different particle populations. In the case that the magnetic trap is not destructed during the impulsive phase, because  $\beta < 0.2$ , the population of the 1st. acceleration stage mix within the expanding bottle with that of the second stage, in which case not a noticeable change in the spectrum slope is expected. On the other hand, in the case that the conditions for the opening of the expanding bottle are not remplished, but the magnetic loop of the impulsive phase was broken ( $\beta \geq 0.2$ ), only the component of the first acceleration stage will be observed. Obviously if the closed magnetic structures do not open during the impulsive phase ( $\beta < 0.2$ ) neither during the subsequent expansion in the main phase, no particle event is expected. Finally, if the flare does not occur within a closed magnetic field configuration, only one main acceleration stage is expected.

II. SCENARIOS FOR X AND  $\gamma$ -RAYS PRODUCTION. Within this context, four scenarios have been examined: (a) Production of the radiation in the source of particle acceleration during the impulsive phase, in a tick geometry context (high amount of traversed matter: high density  $n$  and/or long time  $t$ ); (b) Production of the radiation in the source of secondary particle (\*) On leave for the INAOE, Tonanzintla, 72000 Puebla, MEXICO

acceleration (tick geometry); (c) Production of the radiation during secondary acceleration by the superposition, of particles of that stage mixed with the component of the 1st. acceleration stage when  $\beta < 0.2$  (tick geometry), and (d) Production of the radiation out of the source of impulsively accelerated particles in a thin geometry context (low amount of traversed matter in the source), either in coexistence or absence of closed field structures. Though particles do not lose energy in the source, they are decelerated by Coulomb collisional losses during transport to the emission volume (dense chromosphere or coronal condensations).

**III. ENERGY LOSSES OF SOLAR FLARE ELECTRONS.** The main energy losses are: Coulomb-Collisional losses (CC), Bremsstrahlung (BR), Inverse Compton Effect (IC), Synchrotron Losses (SY) and Adiabatic Losses (AD). The later are negligible at low energies, becoming gradually important at high energies, however, since the acceleration rates also increase with energy, the predominance of acceleration is conserved. Therefore we have only considered (AD) losses within the frame of scenario (c), with a rate given as  $(dE/dt)_{AD} = - (2/3)(V_r/R) \beta W (eV/s)$ , where  $\beta = v/c$  is the particle velocity in terms of the light velocity  $c$ ,  $W$  is the total energy,  $V_r = 2000 \text{ Km/s}$  the expansion velocity and  $R = 0.7 R_\odot$  is the expanded distance, with  $R_\odot$  = the solar radius. For (SY) losses we used the next formula  $(dE/dt)_{SY} = -0.98 \times 10^{-3} B^2 (\beta^2 / (1-\beta^2)) (eV/s)$ , however, they are only important at relatively high energies and strong magnetic fields (Fig. 1); since for the field strength prevailing in flares the electromagnetic radiation produced by synchrotron effects falls very far from the X-ray domain, for the task of simplicity we ignore them in a first approximation. Though (CC) effects do not contribute to X-ray production, energy losses are very important at low energies in determining whether or not the acceleration rate is enough high to generate energetic particles from the thermal solar plasma. Therefore the considered prevailing processes are:

$$(dE/dt)_{CC} = - \frac{K_1}{\beta} \ln \Lambda \{ K_2 [0.88 \operatorname{erf}(X_p) - 1.84 \times 10^3 X_p e^{-X_p^2}] + K_3 [0.88 \operatorname{erf}(X_e) - 2X_e e^{-X_e^2}] \} (eV/s) \quad [1]$$

where  $K_1 = 1.57 \times 10^{-35} n$ ,  $\Lambda = 4.47 \times 10^{16} \beta^2 (T/n)^{0.5}$ ,  $K_2 = 5.98 \times 10^{23}$ ,  $K_3 = 1.1 \times 10^{27}$ ,  $X_p = 2.33 \times 10^6 \beta T^{-0.5}$  and  $X_e = 5.44 \times 10^4 \beta T^{-0.5}$ , where  $T$  is the temperature ( $^\circ K$ ). For non-Relativistic (BR) we used

$$(dE/dt)_{BR} = - 4.74 \times 10^{-11} n \beta \quad [2]$$

whereas in the relativistic range we have

$$(dE/dt)_{BR} = - 1.37 \times 10^{-16} n [1n W/m_e c^2 + 0.36] W (eV/s) \quad [3]$$

where  $m_e c^2$  is the electron rest energy. For (IC) we have

$$(dE/dt)_{IC} = - 1.02 \times 10^{-25} \omega_{ph} W^2 (eV/s) \quad [4]$$

where  $\omega_{ph}$  ( $eV/cm^3$ ) is the mean photon energy density; for the photon field we have employed the local field in the flare volume due to the flare phenomenon itself, instead of the back ground photospheric field. In fact, if the photon field is computed from the black body low integrated over

all frequencies for a  $T \sim 6000$  °K, therefore,  $\omega_{ph} = 2.7 a k T^5$   
 $= 5.5 \times 10^{12}$  eV/cm<sup>3</sup> where  $a$  and  $k$  are the Radiation Density and Boltzman constants; however when this photon field reaches a distance of  $\sim 2 \times 10^9$  cm where flares occur, that value falls to  $\omega_{ph} \sim 2 \times 10^{12}$  eV/cm<sup>3</sup> due to absorption, mainly from dispersion by electrons. On the other hand, if we considered observed radiative output at flare maximum as a lower limit of the total photon field generated in flare regions, we have according to (5) that for a typical subflare (5/IX/1973) is  $10^{27}$  erg/s, so that adopting as typical time that of 400s for the rise and fall of X-ray data in that event, the radiative output becomes  $4 \times 10^{29}$  erg. Therefore following (6), volumes of this kind of flares are  $(0.3-2) \times 10^{26}$  cm<sup>3</sup>, so that  $\omega_{ph} \geq 1.2 \times 10^{15}$  eV/cm<sup>3</sup>. On the other extreme, class 3 flares show radiative outputs of  $\sim 10^{32}$  erg, so that for  $V \leq 6 \times 10^{32}$  cm<sup>3</sup> we obtain  $\omega_{ph} \geq 10^{16}$  eV/cm<sup>3</sup>. It can be appreciated from Fig. 1, that the preponderant energy loss process are (CC), at least up to 1 MeV, whereas synchrotron losses for  $B < 100$  gauss are weaker in relation to the other processes. Also it may be noted that if the photospheric photon field is considered the (BR) process is predominant over the (IC) process for  $n \geq 10^{11}$  cm<sup>-3</sup>. If the flare radiation field is considered the (IC) process dominates over the (BR) process for  $n \leq 10^{12}$  cm<sup>-3</sup>, however, in the case of small flares in very high density media  $n \geq 10^{13}$  cm<sup>-3</sup> (BR) may become dominant over (IC), (Fig. 1).

IV. ENERGY SPECTRA OF THE FLARE ELECTRONS. Source energy spectra may be derived from a steady-state continuity equation of the Fokker Planck form,

$$\frac{d}{dE} (N dE/dt) + N/\tau = q(E) \quad [5]$$

for scenarios (a) to (c) we assume that particles are accelerated from the thermal background, so that the injection spectrum  $q(E) = 0$ ; in addition, if  $N$  is the number of particles per unit energy, the solution of [5] may be reduced to the well known relation of the age-energy analogy for the differential flux

$$N(E) = N_0 e^{-t/\tau/\tau} (dE/dt) \quad (\text{particles/energy} \cdot \text{cm}^2 \text{sr s}) \quad [6]$$

where  $\tau$  may be identified with a characteristic remain time in the acceleration volume and  $N_0$  the number of local particles that participate to the acceleration process. For computation of the thermal flux we integrated the Maxwell velocity distribution from the arbitrary value  $V_a = B^2/(4\pi\rho)^{0.5}$  up to  $\infty$ , where  $\rho$  is the mass-density:

$N_0 = 1.63 \times 10^{-7} n T^{-0.5} (4.79 \times 10^{22} B^4/n + 3 \times 10^{11} T) \exp(-1.58 \times 10^{11} B^4/nT)$  (particles/cm<sup>2</sup>sr s). For solving eq. [6] the following equilibrium equations have been employed

$$(dE/dt) = (dE/dt)_{acc} - (dE/dt)_{CC} - (dE/dt)_{IC} \quad [7]$$

$$(dE/dt) = (dE/dt)_{acc} - (dE/dt)_{CC} - (dE/dt)_{BR} \quad [8]$$

with the exception of scenario (b) where (AD) losses have been included. Within the frame of scenario (a) two different acceleration mechanisms have been worked out: impulsive acceleration may be provided by the betatron process  $(dE/dt)_{acc} = \alpha_b \beta^2 W$  (eV/s) and electric field acceleration processes  $(dE/dt)_{acc} = ce\epsilon\beta$  (eV/s), where  $\alpha_b$  is the betatron hydromagne-



tic acceleration efficiency,  $\varepsilon$  the electric field, and  $e$  the electron charge. For scenario (b) we employed the stochastic Fermi-type process  $(dE/dt)_{acc} = \alpha_f \beta (eV/s)$ . In scenario (c) we use the same acceleration rate that in scenario (b), and for  $N_0$  we considered the composition of two components, those of scenario (a) with spectrum  $N(E)$  and the thermal spectrum  $N_0(th)$ , in the site of secondary acceleration. For scenario (d), the general solution of eq.[5], with  $dE/dt = - (dE/dt)_{CC}$  gives

$$N(E) = \frac{e^{-t/\tau}}{(dE/dt)_{CC}} \left\{ \int_{E_{th}}^{E_{max}} q(E) e^{t/\tau} dE + N_0(th) (dE/dt)_{th} \right\} \quad [9]$$

within the frame of this scenario, the 2nd term refers to thermal particles, and so we neglected it because only the impulsively accelerated particles with injection spectrum  $q(E)$  travel to the emission region. For  $q(E)$  we considered the spectrum of neutral current sheet acceleration derived in (7), per interval time  $\tau$ ,  $q(E) = N(E)/\tau$ .

$$N(E) = (9.1 \times 10^{-2} n V_d / E_0) \left( \frac{E}{E_0} \right)^{-\frac{1}{4}} \exp[-1.12 (E/E_0)^{3/4}] \text{ (part./eV cm}^2 \text{sr s)} \quad [10]$$

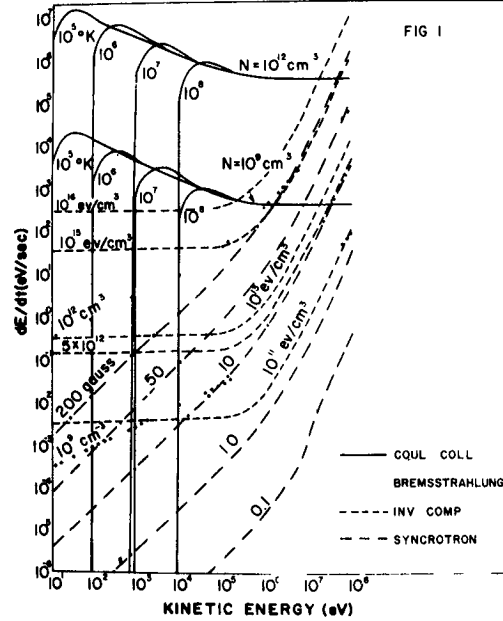
where the characteristic energy value  $E_0$  and the plasma diffusion velocity  $V_d$  depend on the adopted model for neutral current sheet acceleration: for the Priest's model  $V_d = 0.057 V_a$  (cm/s) and  $E_0 = (2.75 \times 10^{18} m_e^{1/2} e L V_d \epsilon)^{2/3}$  (eV), where  $L$  is the scale length of the neutral sheet. The deconvolution of particle spectra in photon spectra and results are discussed in paper SH 1.2-3.

V. CONCLUSIONS. The consideration of the local photonic field of the flare instead of the conventional photospheric field, gives rise the importance of the Inverse Compton effect for the production of electromagnetic radiation by accelerated particles.

#### REFERENCES

- [1] Pérez-Peraza, J., Invited Talk in Proc. of the 9th. European Cosmic Ray Conference, Kosice, 1984.
- [2] Meerson, B. I. and Sasorov, P. V., adv. Space Research 1, 77, 1981.
- [3] Pérez-Peraza, J., J. Geophys. Res. 80, 3535, 1975.
- [4] Mullan, D. J., Ap. J. 269, 765, 1983.
- [5] Canfield et. al., Skylab Workshop on Solar Flares, ed. Sturrock, P., (1979)
- [6] Moore et al., Skylab Workshop on Solar Flares, ed. Sturrock, P., (1979)
- [7] Pérez-Peraza, J. et. al., Space Research 18, 365, 1978.

#### ENERGY LOSSES OF ENERGETIC ELECTRONS



# STUDY OF NON-THERMAL PHOTON PRODUCTION UNDER DIFFERENT SCENARIOS IN SOLAR FLARES. II. THE COMPTON INVERSE AND BREMSSTRAHLUNG MODELS AND FITTINGS.

J. Pérez-Peraza\* and M. Alvarez\*, A. Laville\*\*

Instituto de Geofísica UNAM, 04510-C.U., México, D. F., MEXICO

A. Gallegos

Depto. de Física, UPICSA, 08400 - México, D. F., MEXICO

1. Introduction. Energy spectra of photons emitted from Bremsstrahlung (BR) of energetic electrons with matter, is obtained from the deconvolution of the electron energy spectra derived in SH 1.2.-2. According to Kane and Anderson (1970), the differential photon flux at the earth level is

$$\frac{dJ(h\nu)}{d(h\nu)} = \frac{3.53 \times 10^{-28} E.M.}{n} \int_E^{E_m} \frac{d\sigma(E, h\nu)}{dE} N(E) dE \quad (\text{photons/s KeV cm}^2) \quad [1]$$

where  $d\sigma(E, h\nu)/dE$  is the differential cross-section for electron-proton (BR), given in the non-relativistic range by the Bethe-Heitler formula (Jackson, 1962) and in the relativistic domain by the Koch and Motz formula (Bai and Ramaty, 1976);  $E.M. = n^2V$  is the emission measure, with  $n$  and  $V$  the number density and volume respectively. For Inverse Compton (IC) we followed Sheng (1972), introducing  $\sigma(W, h\nu) = \sigma_T \delta[h\nu - (4/3)\bar{\epsilon} (W/m_e c^2)^2]$  in eq. (1) for  $W < (m_e c^2)^2 / 4\bar{\epsilon} \sim 290$  MeV, where  $W$  = total electron energy,  $\sigma_T = 6.65 \times 10^{-25} \text{ cm}^2$  = Thompson cross-section and  $\bar{\epsilon} = 2.7kT$  = mean thermal photon energy, and we obtained at 1 Astronomical Unit.

$$dJ(h\nu)/d(h\nu) = (4.39 \times 10^{-31} E.M. \omega_{ph}(h\nu)^{1/2} / n^2 T^{3/2}) N(E = m_e c^2 \{(3h\nu/4\bar{\epsilon})^{1/2} - 1\}) \quad (\text{photons/s KeV cm}^2) \quad [2]$$

For the evaluation of the electron energy spectra we have explored different combinations of the source physical parameter in the scenarios displayed in SH 1.2-2:  $n = 10^{10} - 10^{13} \text{ cm}^{-3}$  with  $T = 10^5 - 10^7 \text{ }^\circ\text{K}$  in scenario (a),  $n = 10^{10} - 10^{12} \text{ cm}^{-3}$  with  $T = 10^6 - 10^7 \text{ }^\circ\text{K}$  in scenario (b). For scenario (c) we used the combination of the two previous parameter sets. Values of  $B$  were delimited from the thermal flux  $N_0$  in SH 1.2-2, for every couple  $(n, T)$ , by normalization of  $N_0$  with the point of maximum flux and minimum energy in the observational photon spectra. For the evaluation of the spectrum [10] of scenario (d) we swept  $n = 10^{10} - 10^{13} \text{ cm}^{-3}$ ,  $L = 10^8 - 10^9 \text{ cm}$ ,  $B = 10^2 - 10^3 \text{ gauss}$  and  $\epsilon = 10^{-3} - 10 \text{ V/cm}$ ; in this case two assumptions were worked out for the transport and photon emission regions respectively, first  $n = 10^{10} - 10^{11} \text{ cm}^{-3}$ ,  $T = 10^5 - 10^6 \text{ }^\circ\text{K}$  with  $n = 10^9 - 10^{10} \text{ cm}^{-3}$ ,  $T = 10^6 - 10^8 \text{ }^\circ\text{K}$ , and on the other hand  $n = 10^{10} - 10^{12} \text{ cm}^{-3}$ ,  $T = 10^5 - 10^6 \text{ }^\circ\text{K}$  with  $n = 10^{12} - 10^{13} \text{ cm}^{-3}$ ,  $T = 10^4 - 10^5 \text{ }^\circ\text{K}$ . For the acceleration efficiencies of the Fermi, Betatron and electric field acceleration processes in scenarios (a)-(c) we have required that the net energy change rate  $dE/dt > 0$  in eqs. [7] and [8] of paper SH 1.2-2. The mean acceleration time  $\tau$  in eq. [6] is the free parameter of our analysis, however, we have restricted it to physically reasonable values quoted in the literature. Similarly we have proceeded for the selection of the three characteristic times of scenario (d): the characteristic time  $\tau^i$  of the injection rate in eq. [5] of SH 1.2-2, and the mean remain times  $\tau_1$  and  $\tau_2$  of particles in the trans-

\*\*INAOE

\* On leave for the Instituto Nacional de Astrofísica, Óptica y Electrónica, A.P. 51, Z.P. 7200 - Puebla, México.

port and emission regions respectively. It should be noted that, although electric field acceleration in scenario (a) and neutral sheet acceleration in scenario (d) is basically the same process, in the former case we are adopting a thick geometry, while in the later energy losses in the acceleration volume are neglected (thin geometry), and the spectrum is derived in a quite a different form, by following particle trajectories in the electromagnetic field of the sheet is diffusion region. For the photon field we swepted from  $\omega_{ph} = 10^{12}-10^{18}$  eV/cm<sup>3</sup>.

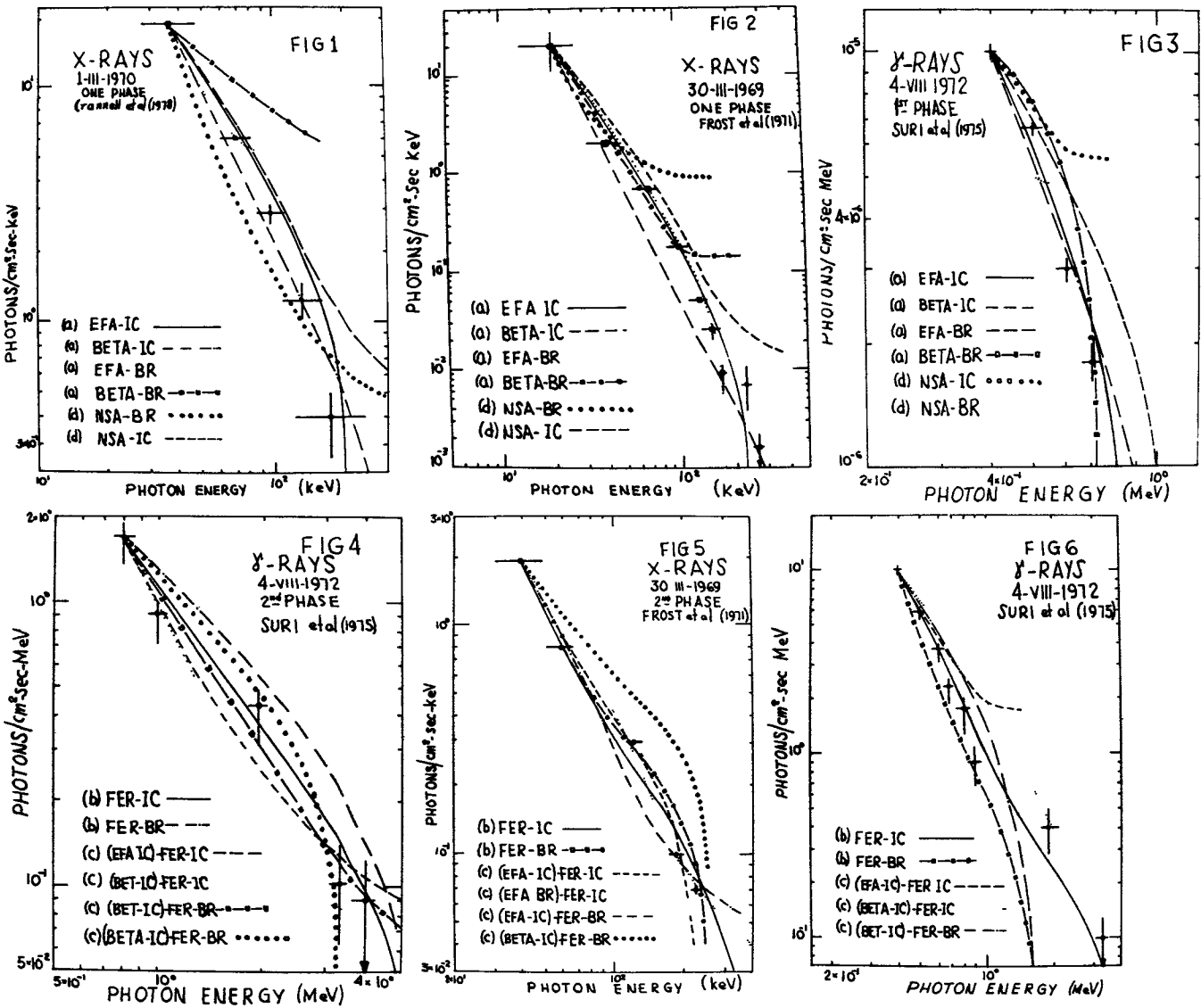
**2. Results.** Low energy events and the impulsive phase of high energy events are better described within the frame of scenario (a) rather than with (d) (Figs.1-3). Acceleration in those events is better described by impulsive electric field acceleration in the context of thick geometries, while the dominant radiation process is the (IC) effect, even within the frame of the thin geometry of scenario (d). The range of accelerating electric fields falls between  $6.5 \times 10^{-3}-10^{-2}$  V/cm, whereas in scenario (d) higher fields are required (1-15) V/cm. Similarly, the adequate magnetic field strengths are 50-100 gauss, whereas in scenario (d) it is needed 400-500 gauss. Typical number densities are  $10^{11}$  cm<sup>-3</sup>, but  $10^{10}$  cm<sup>-3</sup> in the acceleration region with  $10^{13}$  cm<sup>-3</sup> in the emission region in scenario (d). Temperatures of  $10^6$  °K and photon fields  $> 10^{17}$  eV/cm<sup>3</sup> prevail in the source. Characteristic acceleration times are 0.03-0.06 s and much higher (30-50)s in scenario (d), where corresponding emission times are ~80-100 s. Non-impulsive energy spectra of low and high energy events (usually associated to 2nd acceleration stage) are better described by stochastic acceleration from thermal energies, scenario (b), and radiation from (IC) than with injection from a preliminar acceleration phase within the volume of secondary stochastic acceleration scenario (c), in which case radiation appears from (BR). The acceleration efficiency in this kind of events must be very high ( $\alpha=10-20$  s<sup>-1</sup>), while the corresponding acceleration times are quite shorter ~ 0.002 s, but if the contribution of a first acceleration step is considered the acceleration efficiency turns to be lower. Typical parameters involved in these events are  $n=10^{11}$  cm<sup>-3</sup>,  $T \sim 10^6$  °K,  $B \sim 50$  gauss, while  $\omega_{ph}$  values ( $10^{16}-10^{17}$ ) eV/cm<sup>3</sup> are lower than in impulsive events. On the other hand, the global description of energy spectra composed of two different components (usually associated with two acceleration phases) is better assuming scenario (c) than with (b), in which case radiation from (IC) is dominant, with  $\omega_{ph} \geq 10^{17}$  eV/cm<sup>3</sup>,  $\alpha \sim 1$  s<sup>-1</sup>,  $\tau=0.02$ s,  $n=10^{11}$  cm<sup>-3</sup>,  $T=10^6$  °K and  $B=50$  gauss. Optimum fits to the observational spectra are summarized in table 1.

**3. Conclusions.** From this study it can be inferred that the scenario for the production of (X-γ) rays continuum in solar flares may vary from event to event, however, it is possible in many cases to associate low energy events to impulsive acceleration, and the high energy phase of some events to stochastic acceleration. In both cases, flare particles seems to be strongly modulated by local energy losses. Electric field acceleration, associated for instance to neutral current sheets is a suitable candidat for impulsive acceleration. Finally we claim that the predominant radiation process of this radiation is the (IC) effect due to the local flare photon field.

EVENT	BEST SCENARIO	ACCEL. & LOSSES PROCESSES	RAD. PROC.	$\omega_{ph}$ (eV/cm <sup>3</sup> )	ACCEL. PARAMETERS		FLARE PARAMETERS			BEST FITTING (FIGS.1-6)
					$\epsilon$ (V/cm) $\alpha$ (s <sup>-1</sup> )	$\tau$ (s) $\tau', \tau_1, \tau_2$ (s)	$n$ (cm <sup>-3</sup> )	$T$ (°K)	$B$ (gauss)	
1-III- 970	(a)	EFA=electric field acceleration	IC	$5 \times 10^{17}$	$\epsilon=10^{-2}$	$6 \times 10^{-3}$	$10^{11}$	$10^6$	90	EFA-IC
X-RAYS	(a)	BETA= betatron	IC	$3 \times 10^{16}$	$\alpha=1$	0.3	$10^{11}$	$10^7$	100	
35-160 KeV	(d)	NSA=neutral sheet acceleration	BR	-	$\epsilon=10$	50,500,100	$10^{10}-10^{13}$	$10^6$	500	
ONE PHASE										
30-III-1969	(a)	EFA	IC	$10^{17}$	$\epsilon=6 \times 10^{-3}$	$6 \times 10^{-3}$	$10^{11}$	$10^6$	50	EFA-IC
X-RAYS	(a)	EFA	BR	-	$\epsilon=2$	10	$10^{13}$	$2 \times 10^5$	100	
28-254 KeV	(d)	NSA	IC	$3 \times 10^{17}$	$\epsilon=15$	50,2000,100	$10^{10}-10^{13}$	$10^6$	400	
ONE PHASE										
4-III-1972	(a)	EFA	IC	$10^{17}$	$\epsilon=5 \times 10^{-2}$	$3 \times 10^{-2}$	$10^{11}$	$10^6$	50	EFA-IC
γ-RAYS	(a)	BETA	IC	$10^{16}$	$\alpha=1$	0.2	$10^{11}$	$10^7$	120	
0.4-0.7 MeV	(a)	BETA	BR	-	$\alpha=10$	1.	$10^{11}$	$10^6$	50	
1st PHASE	(d)	NSA	IC	$2.5 \times 10^{17}$	$\epsilon=1$	30,400,80	$10^{10}-10^{12}$	$10^6$	400	
4-III-1972	(b)	FERMI	IC	$10^{17}$	$\alpha=20$	$2 \times 10^{-3}$	$10^{11}$	$10^6$	50	FERMI-IC
γ-RAYS	(b)	FERMI	BR	-	$\alpha=1$	1.	$10^{11}$	$10^6$	50	
0.8-7MeV	(c)	(BETA-IC)-FERMI	BR	$10^{16}$	$\alpha=1$	$5 \times 10^{-2}$	$10^{11}$	$10^7$	160	
2nd. PHASE										~
30-III-1969	(b)	FERMI	IC	$10^{16}$	$\alpha=10$	$2 \times 10^{-3}$	$10^{11}$	$10^6$	45	FERMI-IC
X-RAYS	(b)	FERMI	BR	-	$\alpha=0.5$	0.5	$10^{11}$	$10^6$	40	
28-254 KeV	(c)	(EFA-IC)-FERMI	BR	$10^{17}$	$\epsilon=10$	$2 \times 10^{-2}$	$10^{12}$	$10^6$	100	
2nd. PHASE										~
4-VIII-1972	(b)	FERMI	IC	$10^{16}$	$\alpha=10$	$1.5 \times 10^{-3}$	$10^9$	$10^7$	45	~
γ-RAYS	(b)	FERMI	BR	-	$\alpha=1$	0.3	$10^{10}$	$10^6$	50	
0.4-7 MeV	(c)	(EFA-IC)-FER	IC	$10^{17}$	$5 \times 10^{-2}$	$2.5 \times 10^{-2}$	$10^{11}$	$10^6$	50	
1st. & 2nd. PHASE	(c)	(BETA-IC)-FERMI	IC	$2 \times 10^{17}$	1.	0.02	$10^{11}$	$10^6$	50	(BETA-IC)-FERMI-IC
	(c)	(BETA-IC)-FERMI	BR	$3 \times 10^{16}$	$\alpha=10$	$7 \times 10^{-2}$	$10^{11}$	$10^7$	100	

## References

- Bai, T. and Ramaty, R., *Solar Phys.* 49, 343, 1976  
 Chung-Chih-Cheng, *Space Sc. Rev.* 13, 3, 1972  
 Chupp, E. L. et al, *Solar  $\gamma$ -X and EUV Radiation*, IAU 68, 341, 1975  
 Crannel, C. J. et al, *Ap. J.* 223, 1978  
 Frost, K. J. and Dennis, B. R., *Ap. J.* 165, 655, 1971  
 Jackson, W., *Classical Electrodynamics*, John Wiley & Sons, Chap. 15, 1962  
 Kane, S. R. and Anderson, K.A., *Ap. J.* 162, 1003, 1970  
 Suri, A.N. et al, *Solar Phys.* 43, 415, 1975



## SPECTRAL AND SPATIAL PROPERTIES OF SOLAR MICROFLARES

G.M. Simnett  
Department of Space Research  
University of Birmingham  
England

B.R. Dennis  
Goddard Space Flight Center  
Code 684, Greenbelt,  
MD 20771 USA

## ABSTRACT

Solar microflares are studied using both hard ( $> 28$  keV) and soft (3.5-8.0 keV) X-ray observations. The soft X-ray events have durations  $< 3$  m at 0.1x maximum intensity, and typically have similar rise and decay times. The fastest decay observed was  $< 15$  s ( $1/e$ ). Soft and hard X-ray intensities are uncorrelated. The events are very compact, consistent with a projected area  $\leq 8'' \times 8''$ . They are normally not associated with  $H\alpha$  or type III emissions and their time profiles suggest a thermal origin at the top of the chromosphere. If the primary energy release site is in the corona, an energy transfer agent consistent with the observations is a non-thermal proton beam.

1. Introduction Studies of the simplest energetic phenomena which can be identified on the Sun should lead to important boundary conditions on the nature of the primary energy release at the onset of flares, the energy transfer mechanism, and the location of the energy transfer to the X-ray emitting plasma. In simple events the interpretation is not confused by secondary effects which are inevitable in large flares. Short, simple soft X-ray spikes may be close to providing answers to these fundamental points.

2. The Observations

Figure 1 shows three examples of fast, soft X-ray spikes observed by the Hard X-ray Imaging Spectrometer (HXIS) (1) on SMM during 1980. The event on June 27, 19:50 UT was seen only in the HXIS coarse field of view (resolution  $32''$ ) and during the peak was consistent with a source  $< 32''$ , but  $> 8''$ , in dimension. The spectrum was soft, consistent with a two-component thermal source corresponding to  $26 \times 10^6$  K, emission measure  $1.7 \times 10^{46} \text{ cm}^{-3}$ , and  $6.6 \times 10^6$  K, emission measure  $5.7 \times 10^{48} \text{ cm}^{-3}$ . There was no hard X-ray burst observed, no radio emission, and no  $H\alpha$  flare. The rapid decay suggests a chromospheric origin. If we assume a density of  $5 \times 10^{10} \text{ cm}^{-3}$ , consistent with the top of the chromosphere in model F of Vernazza et al. (2), and an area  $10^4 \times 10^4 \text{ km}^2$ , this would correspond to a depth of 230 km below the transition zone.

The event of July 7, 07:08 UT was qualitatively very similar, only slightly weaker. Again, there were no reports of any other coincident activity on the Sun. The event was confined almost totally to two HXIS

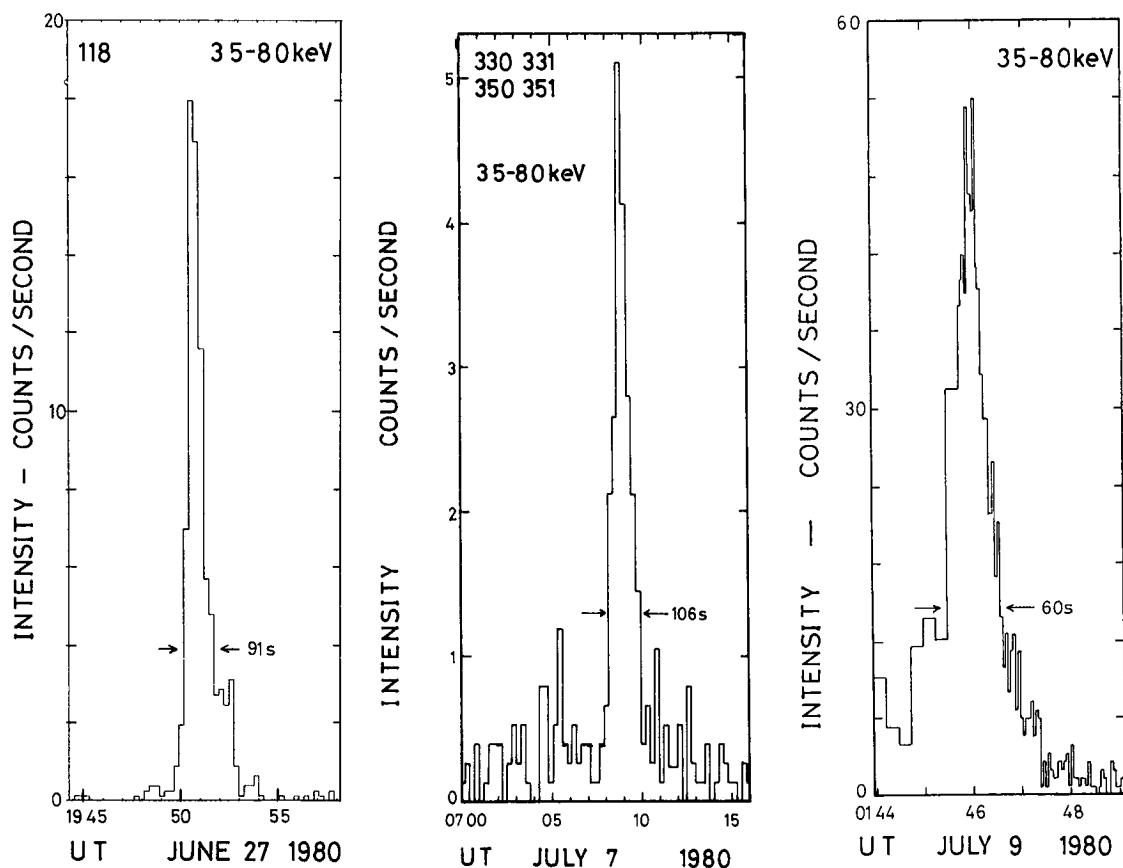


Fig. 1 The 3.5 - 8.0 keV intensity time histories for three events in 1980

fine field of view pixels (resolution 8"), so allowing for the point spread function of the instrument it is deduced that the projected area was  $< 8'' \times 8''$ . The spectrum was even softer than the June 27 event, and both events had an e-folding decay time  $\sim 40$  s.

The third event, on July 9, 01:45 UT was much stronger and started from an already enhanced background associated with a SF flare at 01:40 UT, peak 01:42 UT. The Hard X-ray Burst Spectrometer (HXRBS) (3) on SMM observed an X-ray spike starting at 01:45:35 UT, with a width  $\sim 35$  s. This is simultaneous within the resolution of the data, with the soft X-ray and microwave onsets. However, the hard X-ray and microwave events ceased at  $\sim 01:46$  UT, the time of the soft X-ray maximum. If the event has a thermal origin, it would appear that the extremely high temperature required for the hard X-rays cools a factor of 2 or 3 times faster than that required for the soft X-rays. The event is seen close to the solar limb as a compact,  $< 8'' \times 8''$  bright point. The decay time in soft X-rays is  $\sim 24$  s.

If these events are due to energy deposition from the corona, then

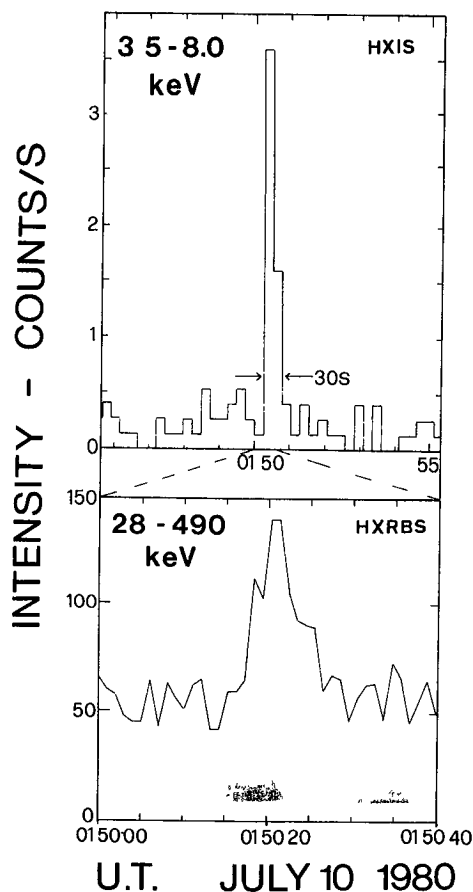


Fig. 2 In the event on July 10, 1980 the hard X-ray intensity is shown expanded.

normal flare event. Examples are on April 27, 02:23 UT and July 7, 10:17 UT; the latter seen by HXRBS. We suspect that there are many other examples of these events, but a systematic data search has not yet been made.

**3. Discussion.** From the lack of any consistent correlation with hard X-rays, microwaves,  $H\alpha$  or type III emissions it seems unlikely that the soft X-ray spikes originate in a simple acceleration and impulsive injection of electrons from the corona. The events are all very compact, consistent with a projected dimension  $\leq 8''$ . The rapid decay of the soft X-rays suggests that the emission is from a high density thermal plasma, at least of chromospheric densities. However, it does not produce an  $H\alpha$  response, so this suggests the events are confined to the top of the chromosphere.

The July 10 event showed that a notable hard X-ray burst could be associated with a very weak soft X-ray burst (Figure 2). It is possible that this arises because the hard X-rays come from a simultaneous event beyond the HXIS field of view. However, there was no substantial event seen by the GOES full-Sun soft X-ray instrument at this time, so we

it might be expected that the more energetic events deposit energy at a higher density, and therefore have a faster decay. This is consistent with the observations, but is only one of a number of possible interpretations.

Not all events are as long as that shown in Figure 1. Figure 2 is an example on July 10, 01:50 UT which lasted  $< 30$  s. HXIS data sampling times are shown in black on the hard X-ray enlargement. The data are consistent with a simultaneous start of the hard and soft X-rays, in which case the soft X-ray peak flux would be enhanced; there is a small residual soft X-ray flux from 01:50:30 - 01:50:38 UT. The event was compact and on the limb; there was a type III burst, but no optical or microwave report.

An almost identical soft X-ray event occurred on June 27, 15:24:20 UT, except without any other radiation signatures. Such events occur in isolation, but others are seen on the decay of a



believe this interpretation is unlikely. It is then significant that events where the soft X-ray intensity is higher by almost an order of magnitude have no observed hard X-rays. This would reinforce the above conclusion that these events did not originate as non-thermal bremsstrahlung from an electron beam accelerated in the corona for the following reason. If the explanation for the lack of hard X-rays is that the accelerated electron spectrum is very soft, it would also mean that the bulk of the energy would be deposited in the corona. The heated coronal plasma would then be expected to have a much longer decay time than that observed (4). Note that the threshold energy for electrons to reach the chromosphere from the corona (e.g. an altitude of  $\sim 10^4$  km) is  $> 30$  keV for any reasonable atmospheric model.

As an electron beam is an unattractive explanation for the spikes, a possible alternative is that the events are multithermal, with the energy transfer by means of a non-thermal proton beam. Such a mechanism has recently been suggested as an important feature of the impulsive phase of flares in general (5). The lack of a long decay for these events indicates that there had been no ablation of hot chromospheric plasma into the corona. This is consistent with a recent theoretical model (6) which argues that for a substantial amount of material to be ablated the deposited energy flux should exceed a threshold value. (6) specifically dealt with electron fluxes, but this conclusion should not be significantly different for protons. If the energy flux is below the threshold, most of the power is radiated away by the dense chromosphere with only a small temperature increase. If the events are due to non-thermal protons, they should be in the energy region  $10^2 - 10^3$  (5). Such protons will produce none of the radio radiation signatures expected from electrons, and not seen in most of our events, but would produce intense heating at the energy deposition site if it were sufficiently compact. If the heating is sufficiently high and rapid, thermal hard X-rays and microwaves will be observed. The occasional type III burst may arise from run-away electrons from the very hot thermal plasma.

4. Acknowledgements. This work has benefitted from discussions with Dr. A.O. Benz. The author thanks the Institute of Astronomy, ETH, Zurich for their kind hospitality while the paper was completed.

#### References

1. Van Beek, H.F. et al., (1980), Solar Phys. 65, 39
2. Vernazza, J.E. et al., (1981), Ap.J.Suppl. 45, 635
3. Orwig, L.E. et al., (1980), Solar Phys. 65, 25
4. Moore, R. et al., (1980), in "Solar Flares", ed. P.A. Sturrock, Colorado University Press
5. Simnett, G.M., (1985), Paper SH 1.2 - 13
6. MacNeice, P. et al., (1984), Solar Phys. 90, 357

TEMPORAL EVOLUTION OF AN ENERGETIC ELECTRON  
POPULATION IN AN INHOMOGENEOUS MEDIUM.  
APPLICATION TO SOLAR HARD X-RAY BURSTS.

N. Vilmer\*, A.L. MacKinnon\*\*, G. Trotter\*

\* UA 324, Observatoire de Paris, Section d'Astrophysique de Meudon,  
DASOP, F 92195 Meudon CEDEX, France.

\*\* Department of Astronomy, The University, Glasgow G128QQ, UK

1. Introduction. Energetic electrons accelerated during solar flares can be studied through the hard X-ray emission they produce when interacting with the solar ambient atmosphere. In the case of the non thermal hard X-ray emission, the instantaneous X-ray flux emitted at one point of the atmosphere is related to the instantaneous fast electron spectrum at that point. A hard X-ray source model then requires the understanding of the evolution in space and time of the fast particle distribution. The physical processes involved here are energy losses due to Coulomb collisions and pitch angle scattering due to both collisions and magnetic field gradients.

The evolution of the distribution is properly described by a Fokker-Planck equation (1) which has been solved numerically for steady state or impulsive ( $\delta$  function) electron injections (2,3). However, its application in cases where the electron collisional lifetime and injection duration are of similar magnitudes has not yet been considered. Such cases are relevant for long-duration events where electrons are injected over a finite period. As a first approximation, a simpler mathematical approach is the use of a first order, non dispersive continuity equation in phase space, taking into account mean rates of change of the phase space variables. Such an equation relates the number of electrons of a specified energy and mean pitch angle at a given point to an arbitrary source function. The angular distribution of the electrons is not correctly described in this treatment, except in a mean sense. However, it includes pitch angle scattering adequately for purposes of hard X-ray spatial distribution calculations and it has the great advantage of giving analytic, time dependant solutions for arbitrary source functions and ambient density structures. In this contribution, the main properties of the analytic solutions are presented for simple situations in order to illustrate the potential use of such calculations in the interpretation of coronal propagation of energetic electrons and of hard X-ray spatial distribution.

2. Basic characteristics. Energetic electrons are injected into an inhomogeneous, plane parallel atmosphere defined by a density  $n(z)$  and a magnetic field  $B(z)$  where  $z$  is the depth from some arbitrary point.  $B(z)$  is assumed to be purely in the  $z$ -direction and the electron pitch-angle  $\theta$  is the angle between the  $z$ -axis and the electron velocity ( $\mu = \cos \theta$  is positive, resp. negative for an electron moving downwards, resp. upwards.) Electrons are injected for  $t > 0$  at a rate  $q(E, t, z, \mu)$  (number of electrons injected per second between  $z$  and  $z + dz$ , with energies between  $E$  and  $E + dE$  and with  $\cos \theta$  between  $\mu$  and  $\mu + d\mu$ ). The electron population evolves in the medium through different processes such as energy losses (mean rate  $dE/dt$ )

and scattering (mean rate  $d\mu/dt$ ). The continuity equation is then given by :

$$\frac{\partial N(E, t, z, \mu)}{\partial t} + \frac{\partial}{\partial E} \left[ N(E, t, z, \mu) \frac{dE}{dt} \right] + \frac{\partial}{\partial z} \left[ N(E, t, z, \mu) \frac{dz}{dt} \right] + \frac{\partial}{\partial \mu} \left[ N(E, t, z, \mu) \frac{d\mu}{dt} \right] = q(E, t, z, \mu) \quad (I)$$

where  $dE/dt$  is the energy loss-rate through electron-electron Coulomb collisions (4) and  $d\mu/dt$  is the sum of pitch angle scattering due to Coulomb collisions (5) and to magnetic field gradient (adiabatic invariance of the magnetic moment). Equation I has been solved analytically. The solutions and their physical interpretation are discussed in (6) and (7). The most critical approximation which consists to omit the velocity dispersion due to Coulomb collisions has also been discussed in (6). It has been shown that for mildly relativistic electrons (initial energy below 200 keV), the mean behaviour of the electrons is fairly well described by the analytic treatment.

3. Evolution of the energetic electron population in some specific cases. We will examine two extreme cases where either pitch angle scattering due to the magnetic field gradient or to Coulomb collisions is negligible. In both cases, a non thermal electron distribution is continuously injected at an arbitrary depth  $z = 0$  in a stratified medium with a density scale height  $H$  [ $n(z) = n_0 e^{z/H}$ ] and a magnetic field  $B(z)$ . We then compute :

$$N(E, t, z) = \int_0^1 d\mu N(E, t, z, \mu) \text{ for } E < 160 \text{ keV} \quad (II)$$

For simplicity,  $q(E, t, z, \mu)$  is chosen as :

$$\left. \begin{aligned} q(E, t, z, \mu) &= S_0 E^{-\gamma} F(t) G(z) H(\mu) \\ \text{where : } F(t) &= t(2t_0 - t) \text{ for } 0 \leq t \leq 2t_0 \\ &= 0 \quad \text{elsewhere} \\ G(z) &= \delta(z) \text{ where } \delta(z) \text{ is the Dirac delta function} \end{aligned} \right\} \quad (III)$$

Two extreme cases are considered for  $H(\mu)$  : a beam distribution [ $\delta(\mu - \mu_0)$ ] and an isotropic one [ $H(\mu) = 1$  for  $\mu > 0$ ].

Figure 1 shows electron spectra as a function of depth at  $t = t_0$  (maximum of the injection) and at  $t = 2t_0$  (end of the injection) for both a beamed injection and an isotropic one, when the magnetic field is assumed to be uniform.

Figure 2 is similar to figure 1, in the case where  $B(z)$  is given by : (e.g. 8) :

$$B(z) = \begin{cases} B_0 \left[ 1 + \frac{z^2}{z_T^2} (R_m - 1) \right] & z < z_T \\ B_0 R_m & z \geq z_T \end{cases}$$

where  $R_m$  is the mirror ratio at  $z = z_T$ .

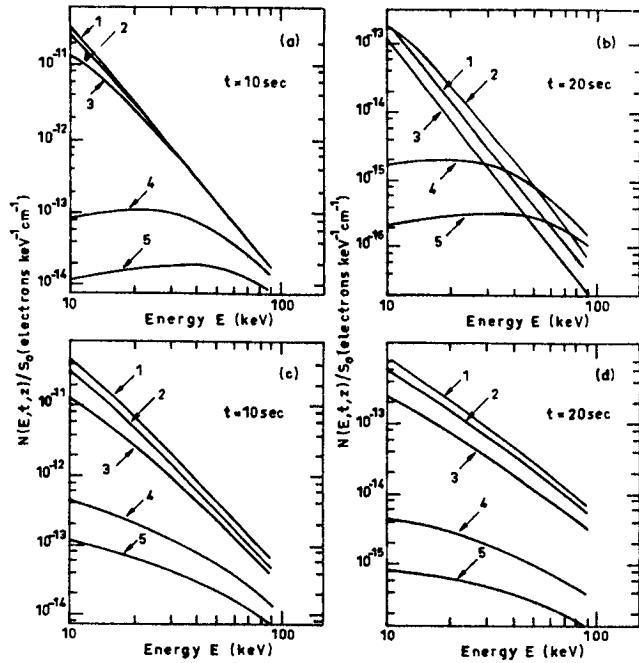


Fig. 1 :

Evolution with depth and time of  $N(E, t, z)/S_0$  when the pitch angle scattering is due to collisions alone. Figures 2a and 2b correspond to a beamed injection ( $\mu_0 = 0.5$ ). Curves 1, 2, 3, 4, 5 correspond respectively to  $z = 5 \cdot 10^7 \text{ cm}$ ,  $10^8 \text{ cm}$ ,  $2 \cdot 10^8 \text{ cm}$ ,  $5 \cdot 10^8 \text{ cm}$  and  $6 \cdot 10^8 \text{ cm}$ .

The chosen parameters are :  $\gamma = 3$ ,  $t_0 = 10 \text{ sec}$ ,  $n_0 = 10^{10} \text{ cm}^{-3}$  at the injection point ( $z = 0$ ).

For both cases,  $H$  is assumed to be  $10^8 \text{ cm}$ . The general behaviour of electron spectra with depth is a progressive hardening. However, there are differences between beamed or isotropic injections or between the different scattering processes.

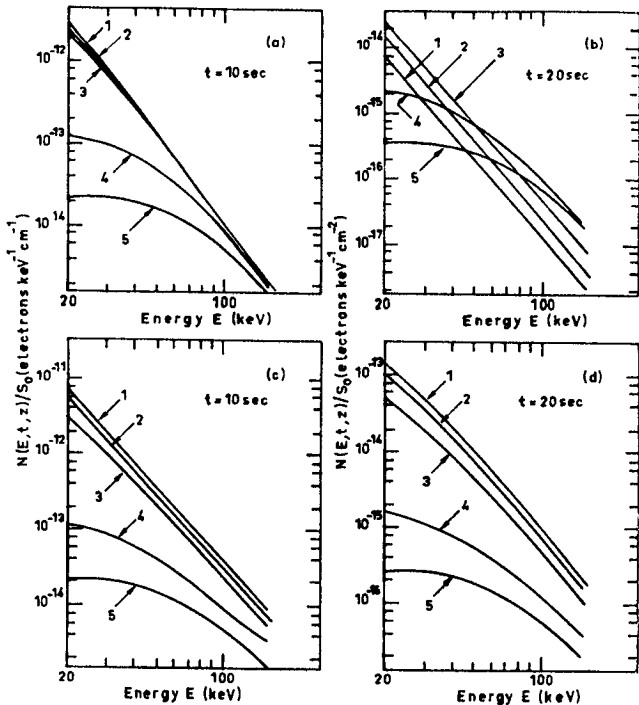


Fig. 2:

Same as figure 1 when scattering is due to a varying magnetic field with  $R_m = 2$  and  $z_T = 3 \cdot 10^9 \text{ cm}$ .

Pitch angle scattering due to collisions : For a beamed injection, there are "humps" in the spectra at large depths, especially at the maximum of the injection. At  $t = 2 t_0$ , spectra are softer and "humps"

are less pronounced because of the combined effects of the temporal behaviour of the injection and of the electron propagation and energy losses. For an isotropic injection, the hardening of the spectrum is less important and "humps" are no longer visible. At  $t = 2t_0$ , contrary to the case of a beam, the spectra are harder than for  $t = t_0$  at each depth. However, "humps" may develop in that case after the end of the injection. These differences are due to the presence here of electrons with large pitch angles. The results presented here are similar to the ones obtained with steady-state treatments which also predict "humps" in the electron spectra at large depths for both a beamed (8) and an isotropic injection (2). The present treatment generalizes then previous results and allows moreover to study the time appearance of "humps" at each depth. Such a behaviour ("humps") indicates the breakdown of the purely collisional treatment of the evolution of the electron population.

Pitch angle scattering due to magnetic field gradients : The hardening of the electron spectra is smaller with depth and "humps" do not develop during the injection, even for a beam. These differences are due to the combined effects of the scattering process and of the magnetic mirroring. An increase in the magnetic field gradient still enhances this effect and harder spectra are generally obtained at least at low depths.

Calculations made for an extended injection region lead to results similar to the ones presented here for large depths as compared to the source extent. Of course, for both cases, at a given depth, the electron spectrum, as well as the hardness difference between different depths, strongly depend on the injection height.

4. Discussion and Conclusions. The model presented here allows to study the temporal, spatial and spectral evolution of non thermal electrons injected continuously in an inhomogeneous medium and to estimate the X-ray flux produced at each depth. This evolution depends on the characteristics of the electron injection and of the ambient medium. In these conditions, various evolutions with depth of electron spectra may be obtained. This is consistent with stereoscopic observations of partially occulted X-ray flares. Indeed, for coronally occulted events with similar occulting heights, different flux ratios and spectral hardness differences between occulted (observed by the instrument detecting the higher part of the flare) and unocculted fluxes are observed (9). Finally, the present calculations can provide a powerful and convenient framework for the interpretation of spatially resolved hard X-ray observations and the understanding of electron coronal propagation towards the interplanetary medium.

#### References

1. Rosenbluth, M.N. et al : 1957, Phys. Rev., 107, 1.
2. Leach, J. and Petrosian, V. : 1981, Astrophys. J., 251, 781.
3. Kovalev, V.A. and Korolev, O.S. : 1981, Sov. Astron., 25, 215.
4. Bai, T. and Ramaty, R. : 1979, Astrophys. J., 227, 1072.
5. Brown, J.C. : 1972, Solar Phys., 26, 441.
6. Vilmer, N. et al : 1985, Astron. Astrophys., submitted.
7. Craig, I.J.D. et al : 1985, M.N.R.A.S., submitted.
8. Emslie, A.G. and Smith D.F. : 1984, Astrophys. J., 279, 882.
9. Kane, S.R. : 1983, Solar Phys., 86, 355.

QUANTITATIVE ANALYSIS OF FLARE ACCELERATED ELECTRONS  
THROUGH THEIR HARD X-RAY AND MICROWAVE RADIATION

K.-L. Klein and G. Trottet

UA 324, Observatoire de Paris, Section d'Astrophysique de Meudon,  
DASOP, F-92195 Meudon Cédex, France

1. Introduction. A key question of particle acceleration during solar flares is whether electrons and ions are accelerated by a single physical process, or whether a second, distinct step of acceleration must be invoked for the high particle energies attained in some flares. Information on the particles can be inferred from an analysis of their electromagnetic radiation by means of model computations. As far as electrons are concerned, the most direct information is furnished by their hard x-ray ( $h\nu > 30$  keV) emission (electron-ion bremsstrahlung), which has been shown /1, 2, 3/ to vary in close temporal correlation with microwaves, although these are produced by a different mechanism (gyrosynchrotron radiation). This correlation is generally interpreted in terms of a common electron distribution /1, 2, 4/ continuously injected into sources at different heights (e.g. /5/). It gives the possibility to test, if the results inferred from hard x-rays are consistent. Gyrosynchrotron radiation does, however, not directly reflect the electron distribution because of various processes of suppression and absorption at low frequencies /6/. Quantitative investigations of the correlation have been carried out by many authors (e.g. /2, 4, 7, 8, 9/). However, on the one hand the radio radiation was often treated in a homogeneous configuration, whereas the gyrosynchrotron mechanism depends strongly on variations of the magnetic field. Furthermore, analytical simplification has often been used, by which the low frequency effects cannot be treated consistently. On the other hand, the analyses were mostly restricted to the instant of peak flux, and no information on the temporal evolution of the injected electrons could be inferred.

Our purpose is to present hard x-ray and microwave modelling that takes into account the temporal evolution of the electron spectrum as well as the inhomogeneity of the magnetic field and the ambient medium in the radio source. We illustrate this method for the June 29 1980 10:41 UT event and discuss briefly the implication on the process of acceleration/injection.

2. Method of analysis. The model of the x-ray source has been described by Trottet and Vilmer (/10/ and references therein). The radiation is assumed to be produced by non thermal electrons injected continuously with an injection function

$$q(E, t) = q_0 E^{-\gamma} f(t) \quad (0 < t \leq t_0, \quad 0 \text{ elsewhere}), \quad (1)$$

with  $\gamma$  being kept constant during each injection. Precipitation is considered in the limits of weak (collisions) and strong (waves) diffusion. Electrons are assumed to lose energy through collisions with ambient electrons. From this model, the injection function, the source density

and the total number of energetic electrons are deduced.

The microwave source is represented by a collection of dipolar field lines in an ambient medium with a hydrostatic density model /11/. The electron distribution is composed of a Maxwellian and a non thermal part resulting from the injection function (1).

3. Analysis of the 29 June 1980 flare. The flare has been observed with several SMM and ground-based instruments /12, 13/. Its temporal evolution is shown for a high-energy x-ray channel and one radio frequency in fig. 1.

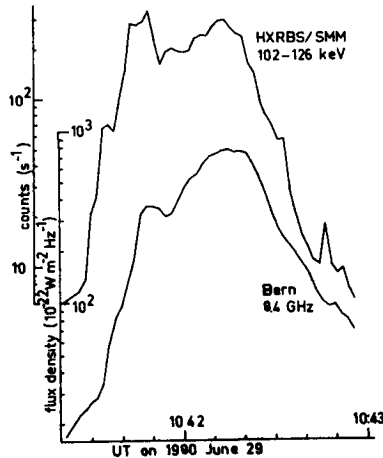


Fig. 1 : Temporal evolution of the observed hard x-ray and microwave fluxes

It has been shown in /10/ that the energetic phase of the event between 104130 UT and 1043 UT can be decomposed into five successive electron injections, whose parameters are listed in table 1 of /10/. The hard x-ray source is found to be a high density medium, from which most of the radio frequencies cannot escape. The microwave and hard x-ray sources are then not cospatial. We assume the structure of the microwave source to be identical with the spatially resolved x-ray source below 30 keV (HXIS observations, /12/). Two magnetic loops of different sizes are observed. The geometric parameters of the loops, the x-ray inferred density /12/ and the assumed magnetic field strengths at the top and in the feet of the loop

are listed in table 1. In the following we assume the temperature to be identical in both loops, although slight

Table 1

	Loop A	Loop B
height (cm)	$6 \cdot 10^8$	$5 \cdot 10^9$
volume (cm <sup>3</sup> )	$1.1 \cdot 10^{27}$	$2.1 \cdot 10^{28}$
temp. (K)	$5 \cdot 10^7$	$5 \cdot 10^7$
dens. (cm <sup>3</sup> )	$7 \cdot 10^{10}$	$2 \cdot 10^9$
B <sub>top</sub> (G)	175	21
B <sub>feet</sub> (G)	240	240

differences are reported in /12/. As the event is a limb flare, we consider in the following magnetic loops in the plane of the sky. They are supposed homogeneous along the line of sight. Following the hypothesis of /12/, we suppose that a quarter of the electron number inferred from hard x-rays is injected into each of the two arches. We compute the microwave spectrum from a simplified form of (1), considering a parabolic  $f(t)$  ( $t = 2 t_{\text{max}}$ ). Further-

more, the electrons are assumed to be perfectly trapped during each injection, but no particles from previous injections are retained.

4. Results. Fig. 2 shows gyrosynchrotron spectra computed at two instants during the injection where the fluxes are greatest, together with microwave observations at four discrete frequencies (5.2 GHz, 8.4 GHz, 11.8 GHz, 19.6 GHz; Bern University, courtesy A.Magun), integrated over 2 s. Because of absorption in the terrestrial atmosphere the measured 19.6 GHz flux represents a lower limit. Both the low and

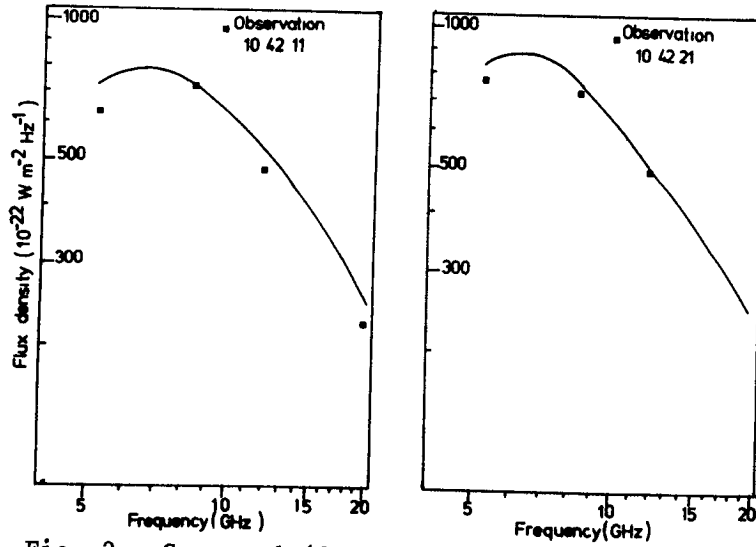


Fig. 2 : Computed (full line) and observed (squares) microwave spectra during injection 4.

the high frequency parts of the spectrum radiated by electrons with the injection function inferred from hard x-rays account for the observations. Emission at the high frequency end is dominated by the small loop A. Its emission is weak at low frequencies because of self absorption by the energetic electrons and a small amount of gyroresonant absorption by the Maxwellian electrons.

This part of the spectrum comes predominantly from loop B.

The temporal evolution of the microwave flux during injection 4 is plotted for two discrete frequencies in fig. 3. Up to the end of

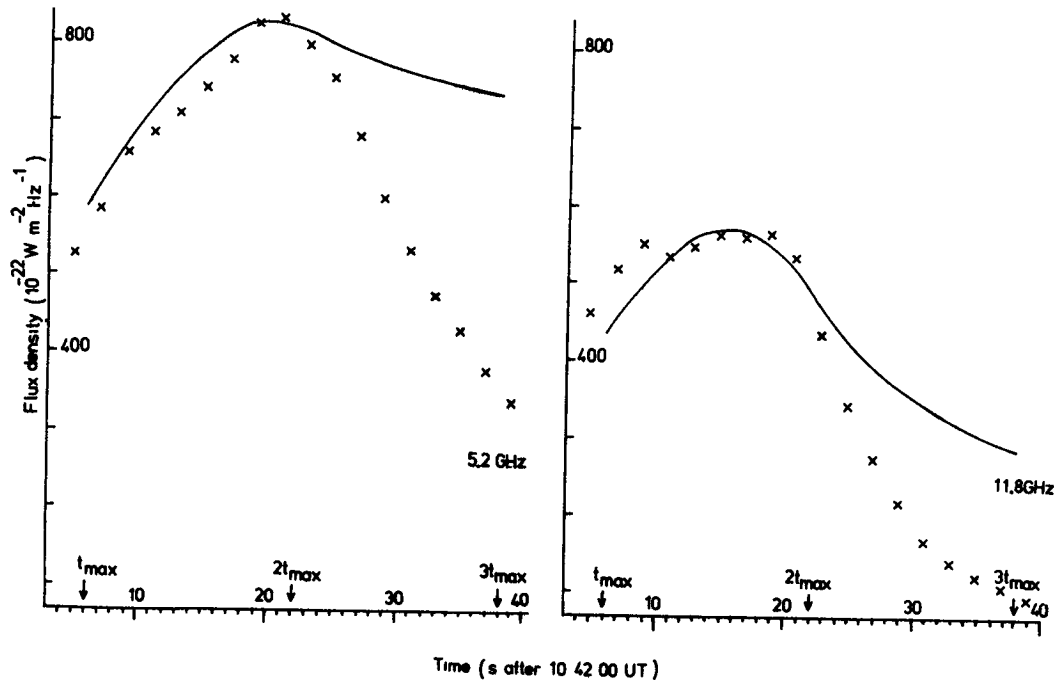


Fig. 3 : Computed (full line) and observed (crosses) evolution of microwave fluxes at a low and a high frequency during injection 4 .



the injection the computed curve fits the observations. Afterwards electron losses through precipitation are revealed by the observed flux decreasing faster than that computed for perfectly trapped particles. The low frequency peak lags that at high frequencies by several seconds both in the model and in observations. This is because growing electron density during the injection increases emission and self absorption. While the latter does not affect high frequencies, it diminishes the low frequency flux, which peaks only in the late phase of the injection, when the instantaneous number density has gone down.

At the very beginning of the event, the computed flux is not compatible with the observed spectrum, which peaks at higher frequencies than afterwards when the flux has grown. This microwave phase might be dominated by thermal electrons, but then a temperature of some  $10^8$  K is required /14/.

5. Discussion. The analysis of the 29 June 1980 flare has shown that in the most energetic part the hard x-ray inferred injection function and total number of electrons are compatible with microwaves. A long lasting controversy existed, because various authors had claimed the number of radio emitting electrons to be up to four orders of magnitude smaller than that producing hard x-rays (review in /2/, recent discussion in /9/). Account for suppression and absorption, source inhomogeneity and for energy losses during a continuous injection of particles solves this discrepancy and explains spectra and temporal evolution of radiations.

The discussed event is compatible with several electron injections, during each of which the spectral index remains constant. This lends strong support to a single step acceleration process.

Acknowledgements. We wish to acknowledge Drs. A. Magun (Bern) and B. Dennis (NASA) for kindly providing microwave and hard x-ray data. K.-L.K. acknowledges support by an ESA fellowship.

#### References

1. Peterson, L.E., and Winckler, J.R.: 1959, J. Geophys. Res. 64, 697
2. Svestka, Z.: 1976, "Solar Flares", D. Reidel Publ., Dordrecht
3. Cornell, M.E., et al.: 1984, Astrophys. J. 279, 875
4. Holt, S.S., and Ramaty, R.: 1969, Solar Phys. 8, 119
5. Klein, L., et al.: 1983, Solar Phys. 84, 295
6. Ramaty, R.: 1969, Astrophys. J. 153, 753
7. Takakura, T.: 1972, Solar Phys. 26, 151
8. Böhme, A., et al.: 1977, Solar Phys. 53, 139
9. Gary, D.E.: 1984, submitted to Astrophys. J.
10. Trotter, G., and Vilmer, N.: 1984, Adv. Space Res. 4, 153
11. Klein, K.-L., and Trotter, G.: 1984, Astron. Astrophys. 141, 67
12. Hernandez, A.M.: 1985, in preparation
13. Kundu, M.R.: 1982, Adv. Space Res. 2, 159
14. Batchelor, D.A.: 1984, PhD thesis, NASA Tech. Memorandum 86102

## AN EXTENDED "SUPERHOT" SOLAR FLARE X-RAY SOURCE

Hugh S. Hudson

Center for Astrophysics and Space Sciences, Univ. of California, San Diego  
La Jolla CA 92093, U.S.A.

K.-I. Ohki

Tokyo Astronomical Observatory, Mitaka-shi, Tokyo, Japan  
and

S. Tsuneta

Institute for Space and Astronautical Science  
Komaba, Meguro-ku, Tokyo, Japan

## ABSTRACT

The *Hinotori* hard X-ray imaging instrument observed a "superhot" ( $T > 3 \times 10^7$  K) source during a solar flare occurring beyond the W limb of the Sun on March 28, 1981. Because of the circumstance of occultation by the limb, we determine a height of  $(3.1 \pm 0.8) \times 10^4$  km. The source extended  $4 \times 10^4$  km along the limb and was smaller than the instrumental resolution perpendicular to the limb. After the disappearance of the X-ray source, weak H $\alpha$  emission occurred at the position of the X-ray sources, suggesting the formation of a loop prominence system. The cooling time estimated for thermal conduction appears to be considerably shorter than the observed time scale of the event, even including a factor of ten to represent suppression of conduction due to possible field-line convergence. We conclude that either stronger forms of suppression, or else extended energy deposition, will be required to explain events of this type.

1. Introduction. The hard X-ray spectrum of a solar flare may give us the key information regarding the basic release of energy. Kane<sup>1</sup> showed that the hard X-rays above about 20 keV<sup>2-3</sup> (the "impulsive" component) have a strikingly different time history from the softer X-rays<sup>4</sup> (the "gradual" component). Recent observations<sup>5</sup> have shown that the spectral evolution exhibits more complexity than had previously been supposed, and that an intermediate spectral component also exists. This new feature, often referred to as the "superhot" component, appears to be thermal but has temperatures considerably above the mean temperature of the bulk of the flare emission measure, typically in the vicinity of  $2 \times 10^7$  K.

The Solar Maximum Mission obtained images of a superhot source in the May 21, 1980 flare; its temperature was initially estimated<sup>6</sup> at  $7 \times 10^7$  K, but later revised downwards to  $4 \times 10^7$  K (for a full discussion, see Duijveman<sup>7</sup>). At the present time there appears to have been no systematic study of the HXIS superhot sources, although Duijveman carried out a complete analysis of the 1980 May 21 event. In the meanwhile the *Hinotori* observed many such events including images of five of them<sup>8</sup>. Of the five, three were compact at the *Hinotori* resolution, but two were extended<sup>8</sup>.

This paper describes a single superhot source imaged by *Hinotori* in special circumstances: occultation by the solar limb. In this configuration we obtain a clear altitude separation and can make definite statements about the source geometry. The characterization of this source as "superhot" is vague, mainly because of the lack of good spectral data, but the analysis here does not depend upon the classification.

2. Flares in Late April, 1981. In late April, 1981, the *Hinotori* spacecraft observed a sequence of energetic solar flares, including a major one on April 27 (onset about 08:00 UT) that produced  $\gamma$ -ray line emission<sup>9</sup>. The flare to be discussed in this paper occurred on April 28, with an onset in the *Hinotori* data at about 21:10 U.T. Although the April 28 event had a smaller soft X-ray flux than the April 27 event, both had the "long duration event" characteristics described by Kahler<sup>10</sup>. Each produced type II, III, and IV meter-wave radio bursts.

At the time of the April 28 event, the active region responsible for this activity (Hale Region 17590, central meridian passage April 21.1) was already well beyond the limb. From a plot of flare longitudes, we extrapolate to a position  $18.8 \pm 2.3$  degrees beyond the limb. This position corresponds to an occultation height of 31000( $\pm 8000$ ) km. An examination of H $\alpha$  data from Big Bear Solar Observatory (S. Martin, private communication) suggests that the faint flare-like brightenings represented late-brightening components of a classical loop prominence system. They initially appeared in the Big Bear films at 21:57 (at disk intensity) and ended at 23:54, with the N component preceding the S component by about ten minutes.

Several other characteristics of these two events are worth mentioning. From the time profiles of hard X-ray emission, little evidence exists for impulsive hard X-ray emission. We believe that the impulsive phase of the April 28 flare occurred while *Hinotori* was in sunlight because of the timing of the meter-wave radio events reported in Solar-Geophysical Data. If so, the April 28 event had a striking deficiency of impulsive hard X-ray emission, consistent with earlier OSO-7<sup>11</sup> and ISEE-3<sup>12</sup> observations of limb-occultation events.

3. The *Hinotori* Hard X-ray Images. A representative hard X-ray image from the SXT instrument on board *Hinotori* appears in Figure 1; many images from different times during the evolution of the event show approximately the same shape and location. The energy range of the the image was nominally 17-40 keV. The smoothness of the time profile and the spectral steepness indicate that this was a "superhot" source, probably with a temperature exceeding  $3 \times 10^7$  K. The great elongation of the source along the limb suggests that we are viewing the topmost structures of the usual arcade of post-flare loops, a conclusion confirmed by the presence of the H $\alpha$  brightening at the same position later on.

4. Analysis. We analyze these data using the simplest approximation of conductive energy transport, assuming a constant flux-tube cross-section. This gives a cooling time

$$\tau = 1.25^{-10} n_e t^2 T^{-2.5}$$

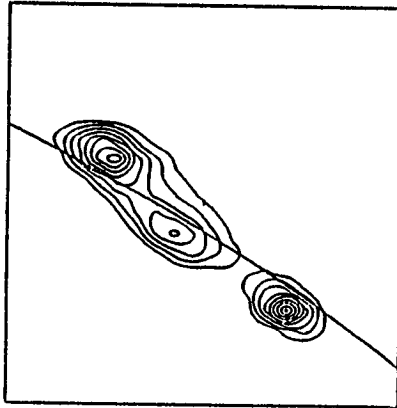


Fig. 1. Image from the *Hinotori* hard X-ray imaging instrument in a nominally 17-40 keV spectral band, taken at 2114 UT, using the ART (algebraic reconstruction technique) method. A smooth time profile, plus the softness of the hard X-ray spectrum, shows that this image comes from a "superhot" source. The appearance of the S component inside the limb may be an artifact.

from the Culhane *et al.*<sup>13</sup> estimate. In the absence of accurate parameters for physical conditions in the source, we can evaluate this time constant for the parameter values that would give the fastest and slowest plausible rates as shown in Table 1. To lengthen the "slow" time maximally, we have included a factor of 10 to account for suppression due to field-line convergence<sup>14</sup>.

The results of these simple estimates range from 6.8 msec (probably unphysically small) to about 100 sec. The long-limit time does not agree well with the observed event lifetime, although the cooling time properly refers to the decay of source temperature, for which we have no good observational limit. We conclude that the extended lifetime of the event probably requires either (a) a more effective mechanism of suppressing thermal conduction through new physics, or (b) a continued supply of energy to the source.

5. Conclusions. We have identified a "superhot" hard X-ray source in a solar flare occulted by the solar limb, and find its hard X-ray image to show great horizontal extent but little vertical extent. An H $\alpha$  brightening at the same limb position about an hour later suggests a multi-component loop prominence system, so that it appears that a superhot source can evolve in the same manner as a normal solar soft X-ray source. The assignment of plausible values to physical parameters in the source suggests (from the simplest form of classical thermal-conduction theory) that either new physics will be required to suppress conduction, or else that gradual energy release well after the impulsive phase of the flare must occur. In this respect too, the superhot source appears to resemble ordinary soft X-ray sources, except of course that its temperature is higher.

6. Acknowledgements. This work was supported by NASA grant NSG-7161 and by the NSF under the U.S.-Japan Cooperative Science Program.

TABLE 1

## Parameters for Conductive Cooling Estimates

	Fast	Slow	
Density	$10^8$	$10^{10}$	$\text{cm}^{-3}$
Temperature	$5 \times 10^7$	$3 \times 10^7$	K
Length scale	$3.1 \times 10^9$	$6.2 \times 10^9$	cm
Convergence suppression	none	10	
Conductive cooling time	$6.8 \times 10^{-3}$	98	sec

References

1. Kane, S.R., 1969, *Astrophys. J. (Lett.)*, **157**, L139.
2. Peterson, L.E., and Winckler, J.R., 1959, *Journ. Geophys. Res.* **64**, 697.
3. Frost, K., 1964, in W.N. Hess (ed.), *The Physics of Solar Flares* (NASA SP-50), p. 139.
4. White, W.A., 1964, in W.N. Hess (ed.), *The Physics of Solar Flares* (NASA SP-50), p. 131.
5. Lin, R.P., Schwartz, R.A., Pelling, R.M., and Hurley, K.C., 1981, *Astrophys. J.* **251**, L109.
6. Hoyng, P., and 11 co-authors, 1981, *Astrophys. J.* **246**, L155.
7. Duijveman, A., 1983, *X-ray Imaging and Interpretation of Impulsive Solar Flare Phenomena*, Thesis (Utrecht), p. 71.
8. Takakura, T., Tanaka, K., and Hiei, E., *Adv. Space Res.* **4**, No. 7, p. 143.
9. Yoshimori, M., 1983, *Solar Phys.* **86**, 375.
10. Kahler, S.W., 1977, *Astrophys. J.* **214**, 891.
11. Hudson, H.S., 1978, *Astrophys. J.* **224**, 235.
12. Kane, S.R., 1983, *Solar Phys.* **86**, 358.
13. Culhane, J.L., Vesecky, J.F., and Phillips, J.H., 1970, *Solar Phys.* **15**, 394.
14. Antiochos, S., and Sturrock, P.A., 1976, *Solar Phys.* **49**, 359.

OBSERVATIONS OF SOLAR FLARE PHOTON ENERGY SPECTRA  
FROM 20 KEV TO 7 MEV

\*

M. YOSHIMORI, H. WATANABE and N. NITTA  
Department of Physics, Rikkyo University, Toshima-ku,  
Tokyo 171, JAPAN.

\* Tokyo Astronomical Observatory, University of Tokyo,  
Mitaka 181, JAPAN.

ABSTRACT

Solar flare photon energy spectra in the 20 keV to 7 MeV range are derived from the Apr. 1, Apr. 4, Apr. 27 and May 13, 1981 flares. The flares were observed with a hard X-ray and a gamma-ray spectrometers on board the Hinotori satellite. The results show that the spectral shape varies from flare to flare and the spectra harden in energies above about 400 keV. Effects of nuclear line emission on the continuum and of higher energy electron bremsstrahlung are considered to explain the spectral hardening.

1. Introduction

The acceleration of electrons and ions during solar flares has been an essential key problem in the study of high energy solar phenomena. Electrons accelerated to the MeV energy range emit radiowaves through synchrotron radiation and hard X-ray and gamma-ray continuum through bremsstrahlung. Solar hard X-rays in the 10 to 200 keV range have been extensively observed, and various problems on the electron acceleration mechanism and the correlation between radiowaves and hard X-rays have been discussed. Most of the hard X-ray spectrum are approximated by a power law spectrum with index of 3.0 to 5.0. However, only a few observations of the photon spectrum extending to gamma-ray energies have been reported. The solar X-rays and gamma-rays were first simultaneously observed from the 4 Aug., 1972 flare (Hoyng et al., 1976; Chupp et al., 1973). The photon spectrum extending to 7 MeV was reported (Suri et al., 1975). The observed spectrum revealed a change in the spectral shape at about 700 keV. Contributions of unresolved gamma-ray lines and new hard component were suggested to explain the spectral change. However, the hard X-ray and gamma-ray spectra were little reported after the observation of the 4 Aug., 1972 flare. It is because of no satellite dedicated to the solar X- and gamma-ray observations. Recently, more data of solar X- and gamma-rays were obtained from SMM and Hinotori observations. These two satellite observations have made it possible to discuss in detail the photon spectrum extending to gamma-ray energies and the hard X- and gamma-ray emission processes. In the present paper, the photon spectra in the 20 keV to 7 MeV range observed from the 1 Apr., 4 Apr., 27 Apr. and 13 May, 1981 flares are presented and the photon spectral shapes are discussed.

2. Observations

The Hinotori satellite is dedicated to solar flare observations and its prime objective is to study high energy flare phenomena in the X- and gamma-ray energies. The hard X-ray spectrometer (8.9 cm dia. x 1 cm thick NaI scintillator) covers the energy range of 17 to 370 keV. The primary data output is a full resolution 7 channel pulse height spectrum every 125 ms (Ohki

et al., 1982). The gamma-ray spectrometer (8.9 cm dia. x 5 cm thick CsI scintillator) covers the energy range of 0.3 - 7 MeV range. The primary data output is a full resolution 128 channel pulse height spectrum every 2 s (Yoshimori et al., 1983a). Some of the Hinotori hard X- and gamma-ray data have been already reported (Ohki et al., 1983; Nitta et al., 1983; Yoshimori et al., 1983b). However, no photon spectrum in the 20 keV to 7 MeV range has been presented. The photon energy spectra from the 1 Apr., 4 Apr., 27 Apr., and 13 May, 1981 flares are presented here. Time histories of these flares were described (Yoshimori, 1985).

The 1 Apr., 1981 flare occurred at 0134 UT and lasted for about 26 min. The flare revealed the gradual time history. The  $H\alpha$  importance and the GOES class were 2B and X2.3, respectively. The photon spectrum observed in the interval of 0144:57 to 0156:40 UT is shown in Fig. 1. The photon spectrum is approximated by a power law spectrum with index of 3.75 in energies below about 300 keV, but the spectrum reveals a hardening in energies above about 400 keV.

The 4 Apr., 1981 flare occurred at 0502 UT and lasted for about 80 s. The flare revealed the impulsive time history. The  $H\alpha$  importance and the GOES class were 2B and X1.9, respectively. The photon spectrum observed in the interval of 0502:17 to 0503:05 UT is shown in Fig. 2. The photon spectrum is approximated by the power law spectrum with index of 3.28 or an exponential thermal spectrum with temperature of  $7.28 \times 10^8$  K in energies above 300 keV. A hard spectral component is apparent in energies above 400 keV.

The 27 Apr., 1981 flare occurred at 0750 UT and lasted for about 30 min. The flare revealed the gradual and multi-peak time history. The  $H\alpha$  importance was not recorded, but the GOES class were 3B. The photon spectrum observed in the interval of 0810:05 to 0814:21 UT is shown in Fig. 3. The photon spectrum is approximated by the power law spectrum with index of 4.00 in energies below 300 keV. The hard spectral component is apparent in energies above 400 keV.

The 13 May, 1981 flare occurred at 0412 UT and lasted for about 18 min. The flare revealed the gradual time history with small increase. The  $H\alpha$  importance and the GOES class were 3B and X1.5, respectively. The photon spectrum observed in the interval of 0419:42 to 0428:13 UT is shown in Fig. 4. The photon spectrum is approximated by the power law spectrum with index of 3.22 in energies below 300 keV. The spectrum reveals the hardening in energies above 400 keV.

### 3. Discussion

The Hinotori satellite hard X- and gamma-ray observations reveal that the photon spectral shapes do not much vary from flare to flare. The power law spectral indices in energies of the 20 to 370 keV range between 3.22 and 4.00, which is consistent with ones observed previously. These power law photon spectra have been interpreted in terms of electron bremsstrahlung. Further, the present results indicate that the spectral hardening occurs at about 400 keV. This spectral hardening seems to be a common characteristics for the gamma-ray flares. It is known that the instrumental effect sometimes cause a spectral bending. However, such instrumental effect is possibly rejected because the spectral analysis in the 20 to 700 keV range has been correctly made for the 7 Oct. and 14 Oct., 1981 flares (Nitta et al., 1983), and the SMM observations also have revealed the similar spectral hardening for the 4 June and 7 June, 1980 flares (Orwig et al., private communication).

Various physical processes which could produce such observed hardening are

considered. Such processes are (1) the effect of observed nuclear gamma-ray line emission on the continuum and (2) the significant contribution of higher energy electron bremsstrahlung. The effect of gamma-ray line emission of positron annihilation at 511 keV, of prompt deexcitation lines of Ne at 1.64 MeV, Mg at 1.36 MeV, Si at 1.78 MeV and Fe at 0.84 and 1.25 MeV and of neutron capture line at 2.22 MeV may be able to explain to some degree the spectral hardening in energies above about 400 keV. The possibility of higher energy electron bremsstrahlung is also considered (Suri et al., 1975). The observed photon spectra probably can not be explained by a population of electrons with a single power law index. Another population of electrons with a harder spectra in energies above a few hundred keV, should be needed to explain the observed spectral hardening. The similar spectral hardening has been reported in large flares such as the 4 Aug., 1972 flare (Suri et al., 1975). The observed spectral hardening represents a characteristics of particle acceleration process in solar flare. The effects of gamma-ray line emission and of higher energy electron bremsstrahlung will be in detail evaluated in near future.

### References

- Chupp, E.L., Forrest, D.J., Higbie, P.R., Suri, A.N., Tsai, C., and Dunphy, P.P.: 1973, *Nature* **241**, 333.
- Hoyng, P., Brown, J.C., and Van Beek, H.F.: 1976, *Solar Phys.* **48**, 197.
- Nitta, N., Takakura, T., Ohki, K., and Yoshimori, M.: 1983, *Solar Phys.* **86**, 241.
- Ohki, K., Nitta, N., Tsuneta, S., Takakura, T., Makishima, K., Murakami, T., Ogawara, Y., and Oda, M.: *Proc. Hinotori Symp. on Solar Flares* (ISAS, 1982, Tokyo). p.246.
- Ohki, K., Takakura, T., Tsuneta, S., and Nitta, N.: 1983, *Solar Phys.* **86**, 301.
- Suri, A.N., Dunphy, P.P., Chupp, E.L., and Forrest, D.J.: 1975, *Solar Phys.* **43**, 415.
- Yoshimori, M., Okudaira, K., Hirasima, Y., and Kondo, I.: 1983, *Nucl. Instr. and Methods* **215**, 255.
- Yoshimori, M., Okudaira, K., Hirasima, Y., and Kondo, I.: 1983, *Solar Phys.* **86**, 375.
- Yoshimori, M.: 1985, *J. Phys. Soc. Jpn.* **54**, 1205

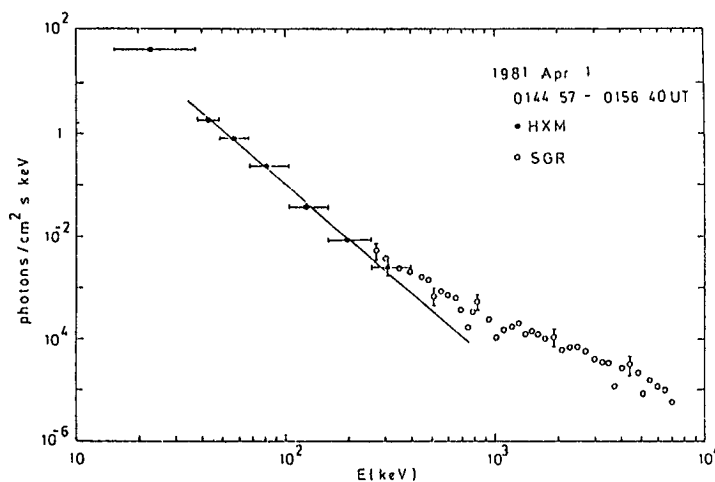


Fig. 1



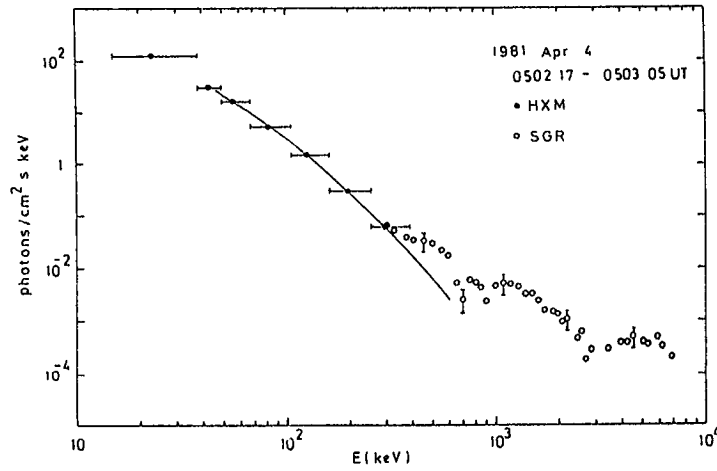


Fig. 2

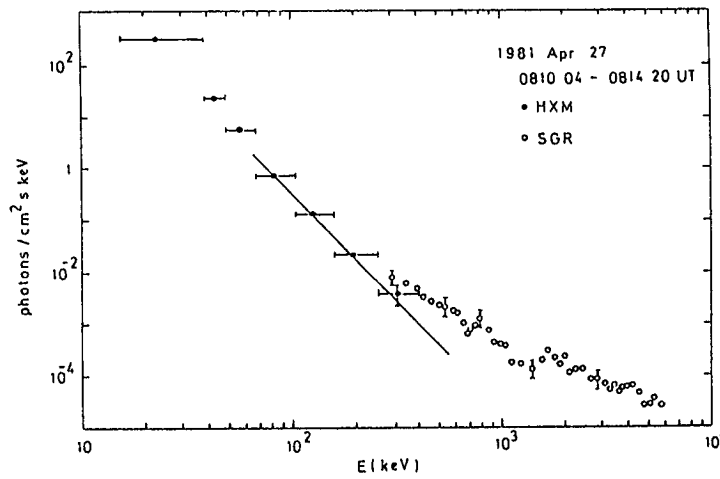


Fig. 3

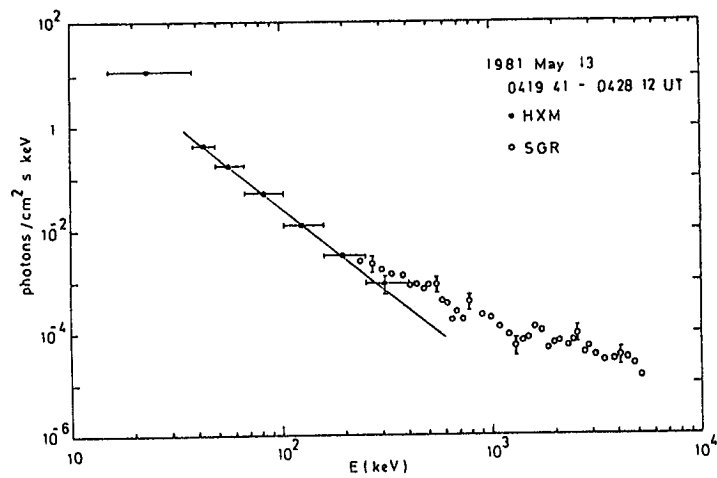


Fig. 4

## ION ENERGY STORAGE FOR POST-FLARE LOOPS

Hugh S. Hudson

Center for Astrophysics and Space Sciences, Univ. of California, San Diego  
La Jolla, CA 92093 USA

## ABSTRACT

Low-energy non-thermal protons may have long lifetimes in coronal loops with low density and high temperature. If energy were stored in such protons in the initial phases of a solar flare, it could be released slowly during the later phases. Within the present observational limits for post-flare loops, this mechanism should be considered in addition to a field-line reconnection theory of the Kopp and Pneuman type. The thin-target  $\gamma$ -ray emission from the trapped protons is below present limits, but more sensitive observations can test the hypothesis.

1. Introduction. Solar flares consist of distinct impulsive and gradual phases<sup>1</sup> plus other associated phenomena. The impulsive phase exhibits powerful energy release and particle acceleration. The gradual phase - the period of main H $\alpha$  and soft X-ray emission - may also require energy release, although on a slower time scale. The need for this energy release is seen in the gradual growth of the soft X-ray loops of the gradual phase<sup>2</sup> interpreted as a sequential excitation of independent flux loops. Although greater uncertainties exist, theoretical estimates of cooling times also suggest gradual energy release<sup>3</sup> within a given loop. The gradual phase also has a strong association with the acceleration of the coronal mass ejections and the copious production of interplanetary particles<sup>4</sup>, so that non-thermal processes must continue during this phase.

The role of energetic protons in solar flares has a long history, stimulated by the observation at Earth and in the interplanetary medium of the "solar cosmic rays." Elliott<sup>5</sup> propounded the idea of energy storage in protons, taking advantage of long Coulomb-scattering lifetimes. The difficult point about understanding the role of protons in the flare proper has remained their essential un-detectability: basically only those particles above thresholds near 10 MeV produce  $\gamma$ -ray spectral line emission, and even this has only generally been diagnostically useful for solar flares since the launch of the Solar Maximum Mission in 1980. Other than theoretical inference from the interplanetary particles and from the high-energy  $\gamma$ -ray-emitting particles, at present we have only the possibility of optical spectroscopy as a means for remotely sensing flare protons at low energies<sup>6-7</sup>.

2. An Ion Energy-Storage Scenario. As indicated by the  $\gamma$ -radiation, the impulsive phase of a solar flare powerfully accelerates energetic ions. This acceleration begins at about the same time as the non-thermal electron production of the impulsive phase, but may take place<sup>8</sup> in a "second step".

The scenario discussed in this paper simply is that bulk acceleration

of energetic ions in flare loops adjacent to those of the impulsive phase may leave a non-thermal ion population in these loops. Coulomb scattering will then extract this energy from the ions and give it to the electrons, as long as the ions can remain stably trapped. The electrons couple the energy strongly into radiation or conduct it into the chromosphere. The main attractive feature of this scenario, aside from its simplicity, is that the excitation of post-flare loops follows a definite pattern of later loops having lower densities<sup>9</sup>, which would have a natural explanation in terms of Coulomb collisions. This scenario of ion energy storage was first proposed by Jefferies and Orrall<sup>10</sup>, but has not received much attention in the light of modern data.

3. Coulomb Scattering: Simple Physics. Coulomb scattering describes the physics of charged-particle interactions. The electrostatic force between two particles, one considered as a test particle and the other as a member of the background plasma, will change the energy and momentum of the test particle relative to the background. To apply the Coulomb collision theory, we must specify the velocity distribution functions of the test particles and field particles. In general, flare energy release should result in non-Maxwellian, anisotropic distributions. To avoid this complication, we assume here that the ion and electron components have separately relaxed to Maxwellian distributions characterized by temperatures  $T_i$  and  $T_e$  respectively. We further assume that the ions are protons. At low proton energies<sup>11</sup>,

$$\tau_{pe} = 12.6 T_e^{3/2} / n_e;$$

note that the equilibration depends solely upon the temperature and density of the electron distribution. For a typical soft X-ray temperature of  $10^7$  K and a density of  $10^{10} \text{ cm}^{-3}$ , we have  $\tau = 39.8 \text{ s}$ .

For proton energies exceeding  $(M/m)kT$  (1.57 MeV at  $T_e = 10^7$  K), the time scale begins to increase approximately as

$$\tau_{pe} = 2.0 \times 10^{11} E_p^{3/2} / n_e,$$

with  $E_p$  in MeV. For example, at 10 MeV in a density  $10^{10} \text{ cm}^{-3}$ , we have  $\tau = 632 \text{ s}$ .

4. Coulomb Scattering: Complications. The discussion above describes the basic minimum physics of the interactions between differentially heated electrons and protons. Beyond this physics, other processes could play roles important to the question of energy storage: (i) Scattering. The trapped protons may escape by pitch-angle scattering into the loss cone. This scattering could occur as a result of Coulomb collisions or "anomalously" from interactions with waves<sup>12-13</sup>. (ii) Drift. Non-adiabatic motion may lead trapped protons into the loss cone or move them to open field lines<sup>13</sup>; this process depends crucially on the geometry of the flux tubes. (iii) Charge exchange. Low-energy protons can neutralize by picking up a free electron, thus permitting them to cross magnetic field lines and escape from a trap. (iv) Filamentation. If the post-flare loops

contain small-scale filaments, undetectable at present resolution, the higher density in the filaments would shorten the proton Coulomb lifetime.

These processes would in each case reduce the storage time of the protons, making their energy less likely as an explanation for the observed late-phase heating in solar flares. It is likely that pitch-angle scattering from ion-cyclotron waves, driven by the anisotropy of the loss-cone distribution of the mirroring trapped particles, would occur on time scales much shorter than the Coulomb energy losses<sup>12</sup>. Nevertheless the instability calculations are model-dependent and it is worthwhile to consider the Coulomb scattering alone, since this mechanism cannot fail to operate.

From the above estimates of time scales, we can draw the immediate conclusion that proton energy storage would not have long enough time scales for post-flare loops (100 - 10000 s) except at low enough densities ( $n < 10^8 \text{ cm}^{-3}$ ) or for high enough proton energies; in the latter case the protons may be energetic enough to exceed the excitation thresholds and produce  $\gamma$ -ray emission.

5. Comparison with Observations. Gamma-ray Production. To compare the theoretical time scales with the observations, we examine the flare of August 21, 1973, for which MacCombie and Rust<sup>14</sup> have given estimates of the physical conditions in the post-flare loops. Density  $5 \times 10^9 \text{ cm}^{-3}$  and temperature decay time of  $1.7 \times 10^4 \text{ s}$  lead to a proton energy of 43 MeV. This energy is high enough to produce  $\gamma$ -ray emission lines from thin-target interactions as the protons bounce between the hypothetical magnetic mirrors.

The total number of trapped protons can be estimated from the total energy of the soft X-ray source. From the emission measure and density quoted by MacCombie and Rust, we find a total energy  $W = 5 \times 10^{29} \text{ ergs}$ . This requires about  $7 \times 10^{33}$  protons at 43 MeV. For the 4.43 MeV  $\gamma$ -ray line of  $^{12}\text{C}$ , Ramaty *et al.*<sup>15</sup> give a cross-section of about 40 mb; assuming a carbon abundance of  $1.6 \times 10^{-4}$  relative to hydrogen, we would have a  $\gamma$ -ray flux of about  $8 \times 10^{-4} (\text{cm}^2\text{sec})^{-1}$ . This is about one order of magnitude below the faintest reported solar fluxes<sup>16</sup>, so that the energy could be stored in protons and not detected via its  $\gamma$ -ray emission.

6. Conclusions. Elliott<sup>5</sup> proposed the pre-flare storage of energy in energetic protons, based upon their long Coulomb time scales. This idea may still not conflict irreconcilably with observations, although the theoretical question regarding the impulsive nature of the primary flare energy release would remain unexplained. This problem may also exist for the post-flare energy storage hypothesis: experienced observers of  $\text{H}\alpha$  line spectra in flares have noted that distinctly unusual  $\text{H}\alpha$  profiles occur predominantly at the outer edges of expanding flare ribbons<sup>17</sup>. This implies fairly directly that non-thermal energy release takes place late in the flare development, and provides some of the best evidence in favor of the magnetic flux reconnection<sup>18</sup> as a cause of post-flare heating. These red-shifted or broadened hydrogen emission-line profiles have no simple

explanation in terms of the proton energy-storage hypothesis, since the energy release should occur gradually, but no detailed calculation of the energy transfer between the particle populations presently exists.

I conclude that the proton energy storage hypothesis could work from an energetics point of view. Sensitive  $\gamma$ -ray observations can test the hypothesis directly by observing the thin-target emission of the trapped protons. In the meanwhile, better knowledge of physical conditions in the flare soft X-ray sources would be helpful. Theoretically, further studies of the limits on stable trapping would form part of the necessary treatment of the complete evolution of a flaring loop. Even if ion energy storage turns out to play no role in post-flare energy release, such studies would be well worth while in view of the likelihood that ions and electrons will have different distribution functions.

7. Acknowledgments. This research was supported by NASA under grant NSG-7161. I enjoyed helpful discussions with the Heliobeeer participants, plus Bob Lin, Richard Lingenfelter, and Dean Smith.

#### References

1. Kane, S.R., *Astrophys. J. (Lett.)* 157, L57.
2. Petrasso, R.D., Nolte, J.T., Gerassimenko, M., Krieger, A.S., Krogstad, R., Seguin, F.H., and Svestka, Z., 1979, *Solar Phys.* 62, 133.
3. Moore, R., and 15 co-authors, in P.A. Sturrock (ed.), *Solar Flares* (Colorado), p. 341.
4. Kahler, S.W., Hildner, E., and van Hollebeke, M.A.I., 1978, *Solar Physics*, 57, 429.
5. Elliott, H., 1973, in R. Ramaty and R.V. Stone (eds.), *High-Energy Phenomena in Solar Flares* (NASA SP-342), p. 12.
6. Orrall, F.B., and Zirker, J., 1976, *Astrophys. J.* 208, 618.
7. Canfield, R.C., and Chang, C.-R., 1985, UCSD preprint SP-84-29.
8. Bai, T., 1982a, in *Gamma Ray Transients and Related Astrophysics*, ed. R.E. Lingenfelter, H.S. Hudson, and D.M. Worrall (New York: AIP), p. 409.
9. Svestka, Z., Martin, S.F., and Kopp, R.A., 1980, in M. Dryer and E. Tandberg-Hanssen (eds.), *Solar and Interplanetary Dynamics* (Reidel), p. 217.
10. Jefferies, J.T., and Orrall, F.Q., 1965, *Astrophys. J.* 141, 519.
11. Spitzer, L. Jr., 1962, *The Physics of Fully Ionized Gases* (Interscience), Ch. 5.
12. Meerson, B.J., and Rogachevskii, I.V., 1983, *Solar Phys.* 87, 337.
13. Zweibel, E.G., and Haber, D.A., 1983, *Astrophys. J.* 264, 648.
14. MacCombie, W.J., and Rust, D.M., 1979, *Solar Physics* 61, 69.
15. Ramaty, R., Kozlovsky, B., and Lingenfelter, R.E., 1979, *Astrophys. J. (Suppl.)* 40, 487.
16. Chupp, E.A., 1984, *Annual Reviews Astron. Astrophys.*, to be published.
17. Svestka, Z., Dodson-Prince, H.W., Martin, S.F., Mohler, O.C., Moore, R.L., Nolte, J.T., and Petrasso, R.D., 1982, *Solar Phys.* 78, 271.
18. Kopp, R.A., and Pneuman, G.W., 1976, *Solar Physics*, 50, 85.

## TWO TYPES OF ELECTRON EVENTS IN SOLAR FLARES

E.I.Daibog, V.G.Kurt, Yu.I.Logachev, V.G.Stolpovsky

Institute of Nuclear Physics, Moscow State University,  
Moscow 119899, USSR

**Abstract.** The fluxes and spectra of the flare electrons measured on board Venera-13 and 14 space probes are compared with the parameters of the hard ( $E_x \geq 55$  keV) and thermal X-ray bursts. The electron flux amplitude has been found to correlate with flare importance in the thermal X-ray range ( $r \sim 0.8$ ). The following two types of flare events have been found in the electron component of SCR. (1) The electron flux increase is accompanied by a hard X-ray burst and the electron spectrum index in the  $\sim 25$ -200 keV energy range is  $\gamma \sim 2$ -3. (2) The electron flux increase is not accompanied by a hard X-ray burst and the electron spectrum is softer ( $\Delta\gamma \sim 0.7$ -1.0).

1. Method and statistics.

The fluxes and spectra of the 25-1500 keV electrons and 55-100 keV hard (Xh-) X-rays were systematically measured in 1981-1983 on board Venera-13 and 14 /1-3/. 300 SCR events were selected which could be considered as flare-induced. Only the SCR events which could be identified, using  $H_\alpha$  and thermal X-rays, with the flares in the Sun's Western hemisphere were selected in order to study the relationships between the flare electron fluxes injected to interplanetary space and the X-rays. The events were only analysed where the  $> 70$  keV electrons were observed, for it is obvious that the  $> 55$  keV X-rays are produced by the electrons with  $E_e > E_x$ . Such events amount to 130; out of them only 67 were accompanied by the Xh-bursts; in 63 cases such an accompaniment was not detected. These sets of events will be henceforth designated  $eXtXh$  and  $eXt\bar{X}h$ .

2. Distribution functions.

We constructed the size distributions of the number of events with given parameter  $Y$ :  $f(Y) = (1/N)(dN/dY)$ , where  $N$  is the number of events in a given set. The highest electron fluxes ( $J_e$ ) and the amplitudes  $J_{Xt}$  and  $J_{Xh}$  of, respectively, the  $Xt$ - and  $Xh$ -bursts are used as  $Y$ . The functions  $f(J_e)$ ,  $f(J_{Xt})$ , and  $f(J_{Xh})$  are shown in Fig. 1a, b, c where the crosses and the dashed lines relate to the  $eXtXh$  set. From Fig. 1 it is seen that, throughout the major part of the interval of the amplitudes  $J_e$ ,  $J_{Xt}$ , and  $J_{Xh}$  the distribution functions may be approximated by a power law with index  $\alpha$ . It is seen that (1) the distribution functions of various parameters within the same set are alike and have similar indices and (2) the distribution functions of the same parameters within different sets are characterized by different  $\alpha$ . We have  $\alpha \sim 1.2$ -1.4 for  $eXtXh$  and  $\alpha \sim 1.7$ -1.8 for  $eXt\bar{X}h$ . Thus, by using the additional indication (the accompanying Xh-burst), we have obtained two sets of events in which the

intensity distributions differ in slopes. This means that two types of electron events are realized in SCR which correspond to different conditions for particles acceleration and leakage in solar flares. We think that the conventional approach (see, for example, /4/) makes it difficult to discriminate the types of flare events in SCR because in this case the distribution function of the events of given parameter is usually constructed, irrespectively of the relationships of these events to other parameters of flare activity.

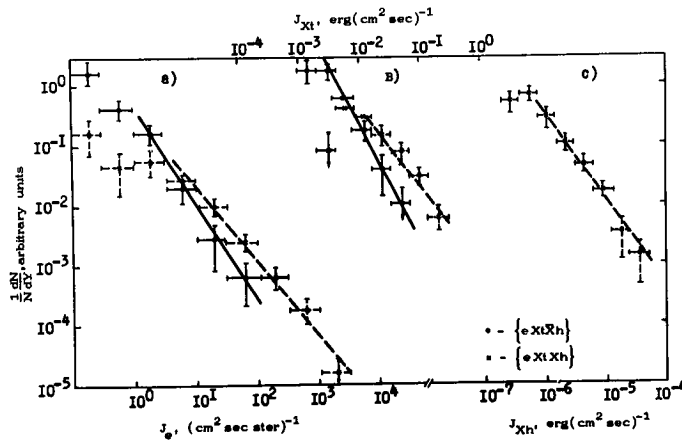


Fig. 1

the probability for the flare to be accompanied by the entire spectrum of flare events rises also. However, two types of the SCR events can hardly be accounted for only by the difference in the power of parent flares. From Fig. 1 it is seen that there exists the interval of the  $J_e$  and  $J_{Xt}$  amplitudes where the SCR events of both types are realized.

#### The electron spectra

Fig. 2 shows the results of comparing between the differential electron energy spectra in the  $eXtXh$  and  $eXtXh$  events. In the energy range  $E_e \sim 25-210$  keV the electron

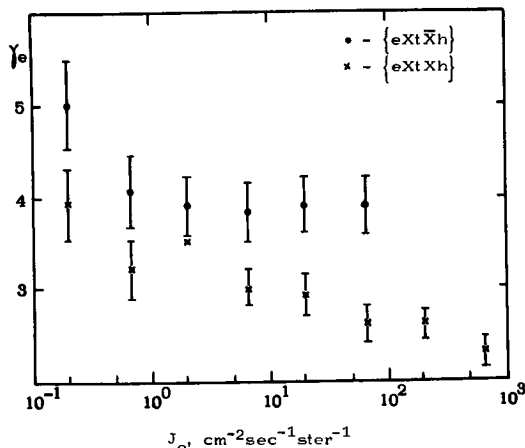


Fig. 2

From Fig. 1 it is seen that the  $eXtXh$  to  $eXtXh$  events number ratio increases with amplitudes  $J_e$  and  $J_{Xt}$  and that, starting from certain values of the amplitudes, only the  $eXtXh$  events occur. This is understandable in terms of the big flare syndrome /5/ according to which, as the power of a flare rises,

spectra were approximated by a power law with exponent  $\gamma_e$ . The values of  $\gamma_e$  presented in Fig. 2 have been obtained by averaging over the number of the events of given type in the intensity interval  $[J_e, J_e + \Delta J_e]$ . The dots relate to the  $eXtXh$  events, and the crosses to the  $eXtXh$  events. According to Fig. 2, the  $eXtXh$  events differ from the  $eXtXh$  events in the electron spectrum slope ( $\Delta \gamma_e \sim 0.7-1.0$ ) and in the dependence of  $\gamma_e$  on  $J_e$ . Nevertheless, the differences in the spec-

tral characteristics of electron fluxes cannot account in all cases for the Xh-burst accompaniment of the SCR events. It is easy to verify that the identical electron fluxes at  $\Delta\gamma_e \approx 2$  produce the quantum fluxes differing by a factor of less than 3. In some cases, therefore, we must have seen both an Xh-burst and a SCR electron event.

The most probable condition for the  $eXtXh$  events to be realized consists in that the plasma density  $n$  in the acceleration region is low and all the accelerated electrons or the majority of them, are ejected to interplanetary medium within a period smaller than the Coulomb loss time. The values of  $J_e$  and  $\gamma_e$  from Figs. 1 and 2 were used to estimate the upper limit of the density for the  $eXtXh$  events:  $< 5 \times 10^9 - 10^{10} \text{ cm}^{-3}$ .

### Correlations

The coincidence of the slopes of the distribution functions of events for the amplitudes of various parameters (see Fig. 1) ensues from the correlation between the electron events and X-ray bursts: This is confirmed by direct calculations of the correlation coefficients between the intensities of X-ray bursts and electron fluxes from the central and western flares.  $r(\lg J_e, \lg J_{Xt}) \sim 0.8 \pm 0.02$  for 147 events with the  $> 25 \text{ keV}$  electrons and 130 events with the  $> 70 \text{ keV}$  electrons. Such value of  $r_{ext}$  means that (1) the energy lost for SCR electron acceleration is approximately proportional to the flare energy because the energy release in the  $Xt$ -range is proportional to the energy realized in the flare /4/ and (2) the  $Xt$ -flux may be also a measure of the power of a SCR event. We have also obtained that  $r(\lg J_e, \lg J_{Xh}) \sim 0.69$ . Partly, this may be relevant to the fact that the electron flux must be compared with the total number of quanta or with energy release in a burst  $\epsilon = \int J_{Xh} dt$  rather than with the  $J_{Xh}$ -burst amplitude, because it is  $\epsilon$  that is proportional to the particle number in the generation region of the Xh-rays in terms of the nonthermal model. Fig. 3 shows the correlation between  $\epsilon$  and  $J_e$ . It

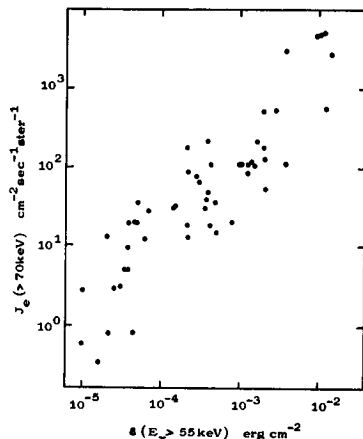


Fig. 3

is seen that the relationship between  $J_e$  and  $\epsilon$  is nearly linear and that the calculated  $r_{exh} \sim 0.79 \pm 0.03$ . From this it follows that the effectiveness of electron leakage to interplanetary medium is approximately constant irrespectively of flare intensity.

Considering the index of the Xh-ray quantum spectrum  $\delta$  is  $\sim 4$  and varies little with flare intensity, we obtain for the energy release  $\epsilon$  and the particle number at the Xh-ray source  $n_s$ :  $n_s = k(\delta) \epsilon$ , where  $k(\delta) \approx 1.3 \times 10^{41}$  at the threshold values  $E_x = 70 \text{ keV}$  and  $E_e = 55 \text{ keV}$  in case of thick target or trap



model /6/. Considering that  $\epsilon = bJ_e$  (see Fig. 3) and turning to the number of particles injected from the source,  $n_{inj}$ , we obtain the following relation between  $n_s$  and  $n_{inj}$  in terms of the diffusion model:  $n_s = A n_{inj}$  and  $A \approx 10^3$ .

#### References

1. Daibog E.I. et al. Kosm issl., 1983, v.21, p.574.
2. Daibog E.I. et al. Izv. Akad. Nauk SSSR, ser.fiz., 1984, v.48, No.II, p.2158.
3. Belyakov S.A. et al. Kosm issl., 1984, v.22, p.906
4. Hudson H.S. Solar Phys. 1978, v.57, p.237.
5. Kahler S.W., J. Geophys.Res., 1982, v.87, p.3439.
6. Merlose D.B., Brown J.C. Mon. Not. R.astr.Soc., 1976, v.176, p.15.

## TWO CLASSES OF SOLAR ENERGETIC PARTICLE EVENTS ASSOCIATED WITH IMPULSIVE AND LONG DURATION SOFT X-RAY FLARES

H. V. Cane, R. E. McGuire and T. T. von Rosenvinge  
Laboratory for High Energy Astrophysics  
Greenbelt, MD 20771  
USA

### ABSTRACT

Solar energetic particle events observed in space have different properties depending on the class of associated flare. Impulsive flares, which occur low in the corona in regions of high energy density, are associated with particle events which are deficient in protons. These events are rarely associated with coronal mass ejections and interplanetary shocks. The vast majority of large, high energy proton events are associated with long duration flares, many of which are also associated with fast coronal mass ejections and strong interplanetary shocks. Such flare events originate relatively high in the corona.

1. Introduction. Recently it has been pointed out from two different viewpoints that there may be more than one class of interplanetary solar energetic particle (SEP) event. In the first study [1] it was found that there were SEP events which showed high abundances of electrons relative to protons at energies near 35 MeV and which were well correlated with gamma ray events. Previously it had been found that there was a poor relationship between particle fluxes inferred from gamma ray observations and fluxes measured in space [2,3]. In another study [4] a few examples of SEP events were found which were not associated with coronal mass ejections (CMEs). In this work it was noted that these rare events were associated with impulsive flares. It had been previously established that the flares associated with CMEs and interplanetary shocks (and by inference SEPs) [5,6,7,8] tend to be predominately of a different class, namely 'long duration'. A study in 1977 [9] showed that impulsive and long duration flares, as observed in soft X-rays, occurred in different regions of the corona. Long duration flares occur higher in the corona than impulsive flares.

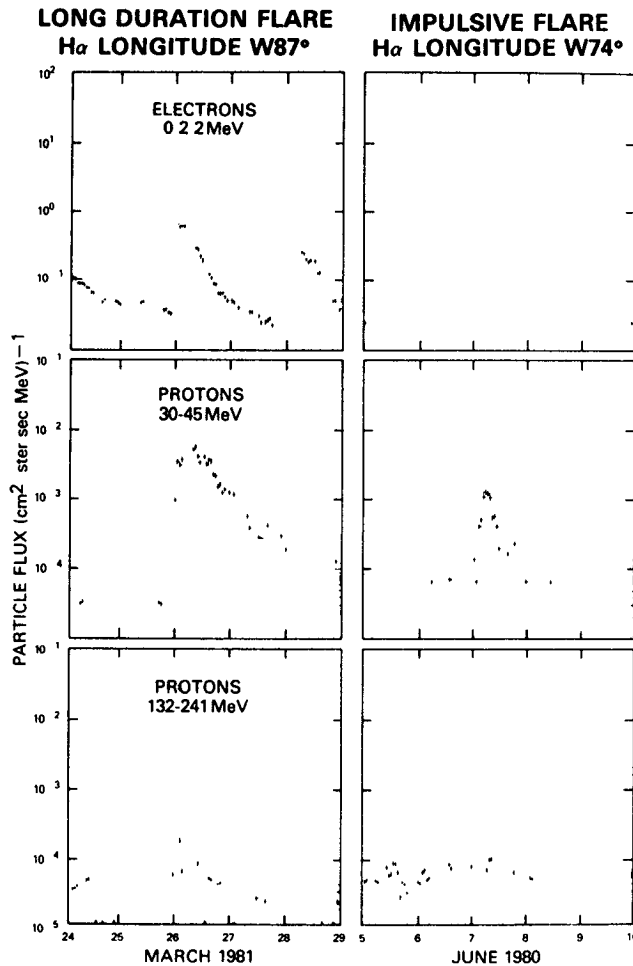
We have made a study of SEP events and find that there are two classes. Although in one class the events tend to be 'proton poor' and are not, in general, associated with CMEs, the important distinguishing feature is their association with impulsive flares.

2. The Data. We have used data from Goddard Space Flight Center detectors on IMP-8 and ISEE-3 to assemble a list of solar flare events which produced relativistic electrons ( $>3$  MeV) above approximately  $5 \times 10^{-4}$  electrons/(cm<sup>2</sup>.ster.sec.MeV) during the interval September 1978 to December 1983. Only events with a confident source association were included. For the majority of the events, this meant that there were H-alpha, soft X-ray and

metric radio phenomena that occurred at the same time. The events were divided into two classes depending on the durations of the associated (1-8 Å) soft X-ray events.

We term "long duration" those particle events associated with soft X-ray flares which lasted for more than 1 hour at greater than 10% of the peak intensity. "Impulsive events" were associated with X-ray flares with a duration of less than 1 hour at greater than 10% of the peak intensity. Four further events without X-ray observations were included in this group on the basis of the short duration of the associated H-alpha activity.

It is important to note that the terminology "impulsive" and "long duration" refers to the soft X-ray profiles and not to the particle time histories. However, the SEP events associated with impulsive flares do tend to have short durations relative to 'normal' proton events as can be seen in Figure 1.



The 73 events of our study are listed elsewhere [10] along with a more detailed description of the selection criteria. There are two lists corresponding to the two classes. The information provided is as follows; a) flare timing and location, soft X-ray intensity and duration; b) timings and intensities of associated metric bursts of Types III, II and IV; c) average speed to earth of any associated interplanetary shock; d) electron onset and peak fluxes in two energy bands (~1 and 10 MeV); e) peak proton fluxes

Fig.1 Proton and electron fluxes as a function of time for three events. There were two events on June 07, 1980 but they are unresolved in these figures.

in two bands (~10 and 60 MeV), f) the ratio of the high energy electron flux to the low energy proton flux; and g) approximate electron and proton spectral indices based on the ratios of the high to low energy fluxes of each specie.

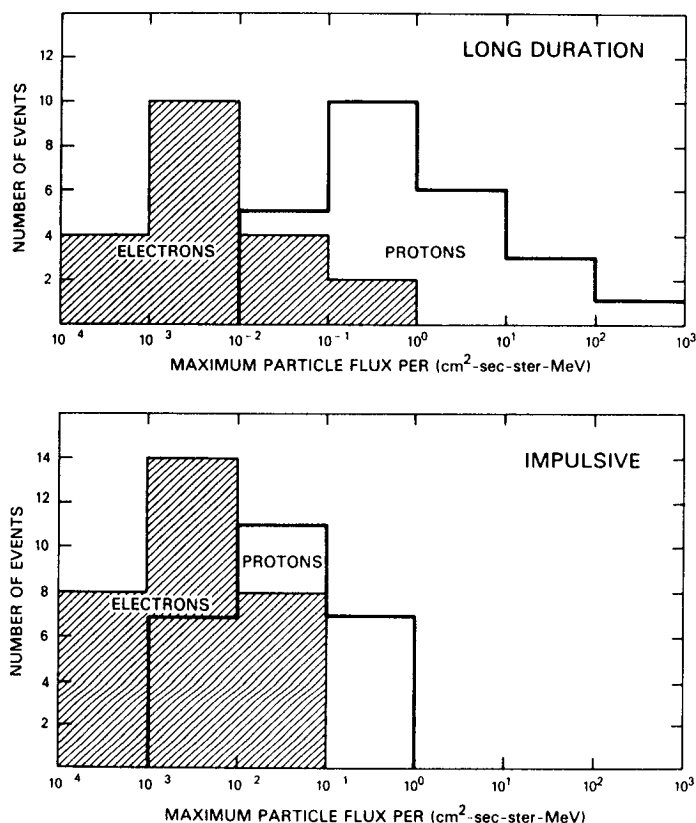


Figure 2 shows event size distributions for electrons (4-19 MeV) and protons (9-23 MeV) for both long duration and impulsive events. Whereas both classes have similar electron events, proton events with peak fluxes above  $1/(\text{cm}^2\text{-sec-ster-MeV})$  occur only with long duration flares. Additionally high energy proton events occur only rarely with impulsive flares. The particle fluxes show that the impulsive events are 'proton poor'.

The key to understanding our results is in the metric radio bursts. We find that the impulsive flare events of our study produced strong Type III bursts, the majority (77%) including Type V continuum. Conversely the Type III/V burst occurred with only 15% of the long duration flares. Type II bursts occurred about equally (~80%) for both classes. Type IV occurred more frequently with long duration flares (72%) than with impulsive flares (23%).

3. Discussion. Our results, and other recent results, require modifications to many long held ideas about particle acceleration in flares, in particular to the ideas about the two phases. It was originally proposed [11] that in the first phase only non-relativistic electrons were accelerated. Observations of gamma-rays and the association of a class of proton and relativistic electron events with strong Type III bursts show that this is incorrect. Acceleration at coronal shocks was assumed necessary for the production of protons and high energy electrons. Since Type II bursts (the signatures of shocks) always follow

associated Type III bursts it was assumed that the first phase was necessary for the generation of shocks and the subsequent second phase acceleration. We find that there is a good correlation between high energy proton events and Type II and Type IV bursts but note that some events are not preceded by Type III bursts. Proton events with weak impulsive phases have been discussed before [12]. We believe that the relationship between the two phases is the following: A shock can form as a consequence of the initial impulsive energy release in energetic solar events. At essentially the same time beams of high energy particles can be created but the probability is greatest low in the corona. When the coronal shock strengthens (relatively high in the corona) it can accelerate high energy particles which escape to the interplanetary medium. In this scenario there is no relationship between the intensity of the first phase and that of the second. However in very 'big' flares both phases will be strong.

4. Conclusions. Our results suggest that energy releases that take place high in the corona are most likely to be associated with a CME and the particles observed in space may include substantial fluxes of both electrons and protons. Energy releases in the low corona occur rapidly and are most likely to produce fluxes of particles that in the interplanetary medium are deficient in protons.

5. Acknowledgements. This work was supported in part by NASA grant NGR 21-002-316.

#### References

1. Evenson, P. et al., (1984), *Astrophys. J.*, 283, 439.
2. von Rosenvinge, T. T. et al., (1981), 17th ICRC, 3, 28.
3. Cliver, E. W. et al., (1983), 18th ICRC, 10, 342.
4. Kahler, S. W. et al., (1984), *J. Geophys. Res.*, 89, 9683.
5. Sheeley, N. R., Jr., et al., (1983), *Solar Wind* 5, 693.
6. Sheeley, N. R., Jr., et al., (1985), *J. Geophys. Res.*, 90, 163.
7. Cane, H. V. and Stone, R. G., (1984), *Astrophys. J.*, 282, 339.
8. Cane, H. V., (1985), *J. Geophys. Res.*, 90, 191.
9. Pallavicini, R., et al., (1977), *Astrophys. J.*, 216, 108.
10. Cane, H. V. et al., (1985) to appear in *Astrophys. J.*
11. Wild, J. P., et al., (1963), *Ann. Rev. Astron. Astrophys.*, 1, 291.
12. Cliver, E. W., et al., (1983), *Astrophys. J.*, 264, 699.

## A DOMINANT ROLE FOR PROTONS AT THE ONSET OF SOLAR FLARES

G.M.Simnett

Department of Space Research, University of Birmingham, U.K.

## ABSTRACT

We suggest that recent observations have cast considerable doubt on the generally accepted explanation that non-thermal electron beams transfer most of the flare energy during the onset of solar flares. In this paper we argue that non-thermal protons in the energy region  $10^2$ - $10^3$  keV are a more probable energy transfer mechanism. An important consequence of this hypothesis is that the hard X-ray burst must be thermal.

1.Introduction It was shown many years ago(1) that the energy released in a solar flare was consistent with the total energy in non-thermal electrons above 20 keV, assumed to be responsible for the hard X-ray burst via non-thermal bremsstrahlung in a thick target. Since that time support for this hypothesis has grown to the extent that many regard it as an established fact. For example, it has recently been stated(2) that to account for many large flares no significant energy input, other than electrons  $> 25$  keV, needs to be invoked. In another recent paper(3) it was argued that over  $10^{36}$  electrons.s<sup>-1</sup> were required during the impulsive phase of the 1981 April 24 flare.

We believe that improved observations made during the last solar maximum have cast doubt over this interpretation of the impulsive phase of flares. Among the more significant observations are the following:

- a) The high plasma turbulence seen in heavy ions, eg Ca<sup>XIX</sup>, prior to the onset of the hard X-ray burst, including in some cases significant mass upflows(2,4).
- b) The presence of high energy protons at the onset of the impulsive phase of some gamma ray flares(5,6).
- c) The complete absence of metric/decimetric radio emissions during many large flares including the impulsive phase of the 1981 April 24 flare(7).

When the energy inputs required for a) and b) are taken into account, together with the energy in the whole electron spectrum, the total flare energy budget becomes heavily oversubscribed. In addition, if the efficiencies of the acceleration processes are also considered, which are quite probably less than 50%, the situation is even worse. Thus another significant point is:

- d) When the energy in the pre-impulsive phase plasma turbulence and upflows is added to the energy in the non-thermal electrons and ions, together with an efficiency factor, the flare energy budget appears to be exceeded.

To overcome these problems an alternative hypothesis is suggested, namely

that the primary energy release results in the coronal acceleration of non-thermal protons which have the bulk of their energy in the  $10^2$ - $10^3$  keV region. We shall show that this offers an attractive alternative to both the non-thermal electron hypothesis discussed above and the alternative thermal models suggested recently(8,9). Our model is essentially a non-thermal proton model which results in excessive heating of the chromospheric plasma to produce the hard X-ray burst by thermal bremsstrahlung.

2.The Non-Thermal Proton Hypothesis We now consider the four points a)-d) mentioned above in more detail.

a) The plasma turbulence and upflows observed before the onset of the hard X-ray burst cannot be caused by the impact of electron beams on the chromosphere without producing X-rays. As soon as an electron beam is accelerated a reverse current will be set up to avoid charge separation. Emslie(10) has shown that when reverse current losses of the beam are taken into account the electron energy must exceed  $\sim 60$  keV to penetrate below the transition zone for any reasonable atmospheric model. Theory has shown(11) that energy must be dumped below the transition zone for significant mass to be ablated.

Protons in the region  $10^2$ - $10^3$  keV can do this readily. Depending on the atmospheric model the threshold energy for penetration to the top of the chromosphere from the corona is  $400 \pm 150$  keV, with the lower limit probably more appropriate to the onset of a flare. Reverse current losses are largely eliminated by having accompanying electrons of the same velocity as the protons. The energy content of such electrons is negligible compared with the protons.

b) Gamma ray production at the flare onset is accounted for by a slightly more efficient acceleration process which raises the high energy tail of the proton energy spectrum. This need only have a minor effect on the total energy of the accelerated protons, which explains in a natural way why many gamma ray flares are optically small, with relatively low total energy. On the conventional model, if the typical flare is dominated energetically by non-thermal electrons then the gamma ray flares must invoke a proton acceleration process which suddenly becomes important. We believe such a scenario is unattractive.

c) Radio emission is an important electron signature. In a magnetic field relativistic electrons emit gyrosynchrotron radiation, which in the flare situation appears in the microwave region. An electron beam with a velocity distribution increasing towards high energies will emit plasma radiation; such beams are frequently observed as type III bursts and only  $\sim 10^{29}$  electrons  $> 20$  keV are required for these to be detectable by modern radio-telescopes. Correlation of microwave bursts with hard X-rays is very high; virtually 100% for bursts  $> 1000$  counts.s $^{-1}$  detected by the Hard X-Ray Burst Spectrometer on SMM. Yet 15% (7) of the same flares have no metric/decimetric radio emission.

It might be argued that the required velocity distribution in the electron

beam builds up too slowly for a type III burst to be produced. However, observations(12) of very fast ( $\ll 1$ s) hard X-ray fluctuations argue just the opposite, namely that the release must be impulsive unless the acceleration site is very close,  $\sim 10^3$  km, to the chromosphere. Hard X-ray imaging observations from SMM suggest that such small distances are unlikely in a typical flare (13).

The impulsive phase of the white-light flare on 1981 April 24 had 35 GHz emission of  $\sim 5000 \cdot 10^4$  Jy(3). Microwave emission at this level occurred in only nine flares during 1979-82, so this is truly a major event. However, it produced no metric/decimetric emission until the onset of the gradual phase some 5m after the impulsive phase maximum. On the non-thermal electron hypothesis over  $10^{36}$  electrons  $\cdot s^{-1}$  are required to produce the X-rays and the impulsive phase lasts for over 100s. It is very surprising that during this time enough electrons to produce a type III burst -  $10^{29}$  - did not escape into the corona.

d) It has been proposed recently(2) that electrons  $> 25$  keV may provide the energy for the entire flare. This, however, neglects the energy in electrons  $< 25$  keV and there is no basis from observations to suggest that these electrons are negligible. In fact, to the contrary. Lin et al(14) made high spectral resolution observations of a flare which showed that the electron spectrum extended to 13 keV (the low energy cut-off of the measurement) without a change in spectral index. As the spectral index was  $-4.5$  this implies an order of magnitude increase in energy content going from 25 keV to 10 keV. We have no way of estimating the proton energy spectrum at the Sun below  $\sim 5$  MeV. However, analysis of the 1972 August 4 flare(15) indicated over two orders of magnitude more protons than electrons at 5 MeV and extrapolation of the spectrum produced equal numbers of protons and electrons at 40 keV. While there is no basis in this flare for such an extrapolation, it shows proton energy should not be disregarded. The accelerator is presumably  $< 100\%$  efficient at producing non-thermal particles. Even if we assume 50% efficiency, it appears that we would have no difficulty in estimating a total energy which is a factor of 20-40 higher than that contained in electrons above 25 keV.

From the above there is no doubt that the arguments for the total flare energy residing in non-thermal electrons  $> 25$  keV are weak and that there is substantial evidence against their existence in any energetically-dominant form at all. It now remains for us to show that non-thermal protons can explain the phenomena better. Protons of a few 100 keV can readily drive the plasma turbulence and ablation without producing hard X-rays. They are necessary for the gamma rays, and they can easily heat the chromospheric plasma to produce the soft X-ray emission. The principal difficulty with a proton beam is in hard X-ray generation. To do this there must be rapid heating in a way that produces electron temperatures significantly above ion temperatures. Such a mechanism has been suggested in the context of Tokomaks(16), which invokes plasma instabilities in fine-scale filamentary structures where electron temperatures



are enhanced by  $10^2$  or more. While this is probably not directly applicable to the flare situation, it indicates that anomalous effects are likely in plasmas with high beam currents and that extremes in temperature might occur.

In terms of energy, thermal hard X-ray production is  $\sim 30$  times more efficient than a non-thermal process (17). In addition our model only requires one acceleration mechanism to be operating to account for all flares. There are other important observations, such as the insensitive way  $O\bar{V}$  emission correlates with hard X-rays and the negative results from polarization studies that also argue against non-thermal electron dominance (18,19).

3. Conclusions. We have shown that there is considerable evidence against non-thermal electron beams as the dominant energy transfer mechanism during the impulsive phase of solar flares. Instead we suggest that non-thermal protons in the energy region  $10^2$ - $10^3$  keV are a more likely energy carrier. The advantages of protons are that they can account for the plasma turbulence and upflows seen before the hard X-ray burst, they can produce gamma ray emission from optically weak flares and they can account for the lack of metric/decimetric emission in many large flares. In addition, only one acceleration process need be advocated to account for all flares provided it is approximately velocity dependent. Such a process is the MHD shock, which certainly has all the right properties when observed in interplanetary space. An important consequence of our model is that the hard X-ray burst must be thermal in the impulsive phase.

#### References

- 1) Lin R.P. and Hudson H.S. (1976) Sol Phys 50, 153
- 2) Antonucci E. et al (1984) Ap J 287, 917
- 3) Kane S.R. et al (1985) Ap J 290, L45
- 4) Antonucci E. et al (1982) Sol Phys 78, 107
- 5) Chupp E.L. et al (1982) Ap J 263, L95
- 6) Forrest D.J. et al (1981) Proc 17th Int Cosmic Ray Conf 10, 5
- 7) Benz A.O. and Simnett G.M. (1985) (in preparation)
- 8) Brown J.C. et al (1979) Ap J 228, 592
- 9) Smith D.F. and Lilliequist C.G. (1979) Ap J 232, 582
- 10) Emslie A.G. (1980) Ap J 235, 1055
- 11) MacNeice P. et al (1984) Sol Phys 90, 357
- 12) Kiplinger A.L. et al (1984) Ap J 287, L105
- 13) Hoyng P. et al (1981) Ap J 246, L155
- 14) Lin R.P. et al (1981) Ap J 251, L109
- 15) Ramaty R. et al (1980) in "Solar Flares" ed P.A. Sturrock, Colorado Univ Press
- 16) Haines M.G. and Marsh F.J. (1982) J Plasma Phys 27, 427
- 17) Smith D.F. and Harmony D.W. (1982) Ap J 252, 800
- 18) Poland A.I. et al (1984) Ap J 280, 457
- 19) Tramiel L.J. et al (1984) Ap J 280, 440

## THE ENERGY SPECTRA OF SOLAR FLARE ELECTRONS\*

Paul Evenson<sup>+</sup>, Dietrich Hovestadt<sup>†</sup>, Peter Meyer<sup>x</sup>, and Dan Moses<sup>x</sup><sup>+</sup>Bartol Research Foundation, University of Delaware  
Newark, DE 19716 USA<sup>†</sup>Max-Planck Institute for Extraterrestrial Physics  
8046 Garching, West Germany<sup>x</sup>Enrico Fermi Institute and Department of Physics  
University of Chicago, Chicago, IL 60637 USA

**ABSTRACT.** A survey of 50 electron energy spectra from .1 to 100 MeV originating from solar flares has been made by the combination of data from two spectrometers onboard the ISEE-3 (ICE) spacecraft. The observed spectral shapes of flare events can be divided into two classes through the criteria of fit to an acceleration model. This "standard" two step acceleration model, which fits the spectral shape of the first class of flares, involves an impulsive step that accelerates particles up to 100 keV and a second step that further accelerates these particles up to 100 MeV by a single shock. This fit fails for the second class of flares that can be characterized as having excessively hard spectra above 1 MeV relative to the predictions of the model. Correlations with soft x-ray and meter radio observations imply that the acceleration of the high energy particles in the second class of flares is dominated by the impulsive phase of the flares.

1. **INTRODUCTION.** Previous surveys of electron flare spectra with energies extending up to 10 MeV have been conducted by Datlowe (1971), Simnett (1974), Lin *et al.* (1982), and Evenson *et al.* (1984). The study presented in this paper has the advantage of nearly continuous coverage over a four year period of high solar activity in the absence of magnetospheric effects due to the orbit of the spacecraft. Two independently well calibrated instruments on the same spacecraft are used to cover two adjacent energy ranges. The total energy range and the resolution are well suited to explore the spectral regime characteristic of the second step of acceleration. The combination of improvements in this study yield results not identified in previous surveys.

2. **METHOD.** Measurements of solar flare electrons in the energy range of .075 to 1.30 MeV were obtained from the ULEWAT spectrometer (Hovestadt *et al.* 1978) and electron spectra in the range of 5 to 100 MeV were measured with the MEH spectrometer (Meyer and Evenson, 1978). No attempt was made at normalization of the two sources of data as each instrument was judged to be adequately calibrated by independent methods. The time interval of the survey extends from launch of ISEE-3 in August 1978 through December 1982.

\*Supported, in part, by NASA contract NAS5-26680 and NASA grant NGL-14-001-005.

Two requirements for inclusion of a flare in the survey were applied: first, all energy bins in the ULEWAT data must have an impulsive ( $\sim 1$  day rise time) enhancement over background and, second, all energy bins in the MEH data through the 10 MeV bin must also have an impulsive enhancement over background. The majority of events observed with ULEWAT has no measurable counterpart in MEH. To relate the interplanetary particle spectrum to the source spectrum, the assumptions were made that the spectrum of particles escaping from a flare is identical to the spectrum of particles accelerated in that flare and that the propagation of particles from the flare is a simple diffusion process which does not change the energy of the particles. With these assumptions the spectrum at the source is obtained by subtracting the pre-flare background flux from the flare maximum flux in each energy bin (Lin *et al.* 1982).

The classification of spectral shape by comparison with the prediction of a single shock acceleration is equivalent to comparison with a spectral shape which is a power law in momentum (Blandford and Ostriker, 1978). Following Ellison and Ramaty (1985), the loss of efficiency in acceleration of the highest energy particles due to effects such as the diffusion length of the particle being greater than the size of the shock is modeled by an exponential roll-off in energy above a characteristic energy,  $E_0$ . A good power law in momentum fit to an energy spectrum is shown in the example of Figure 1, and replotted as a function of rigidity in Figure 2. The case of a spectrum that deviates from a power law in momentum (rigidity) predicted by the single shock model is obvious on a rigidity plot (Figure 3).

3. **RESULTS.** A detailed list of the properties of the individual flares in this study will be presented in a full paper now in preparation. Of the 50 events included in the survey, 31 can be modeled by the single shock mechanism and these will be referred to as class II events. The events which deviate from a power law in momentum will be referred to as class I events. Sixteen of the class I spectra are consistent with a power law shape in kinetic energy while 3 spectra are flatter at high energies. Events with an identified source position on the sun show a selection effect in favor of well connected flares which is more pronounced in the class I events. The average 25-45 MeV proton flux from the class II events is higher than that of the class I events while the average electron to proton ratio at 25-45 MeV of the class II events is lower than that of the class I events.

4. **DISCUSSION.** While the spectra of class II electron flare events are well

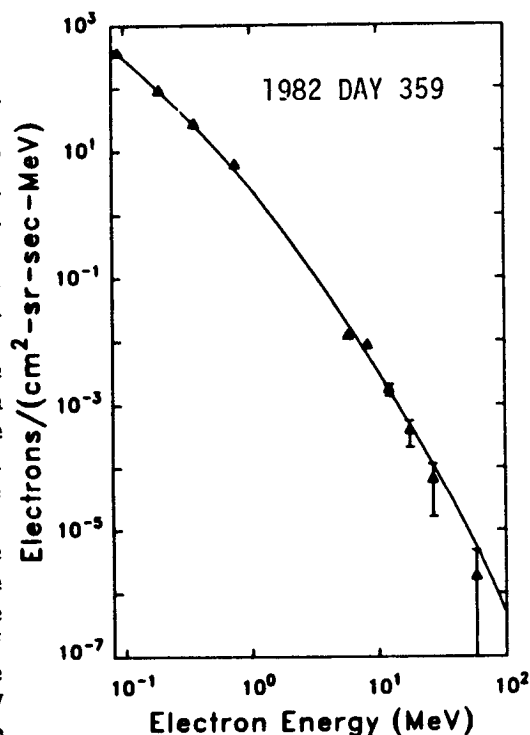


*Fig. 1: Flare energy spectrum fit by single shock model with compression ratio,  $r=2.3$ , and  $e$ -folding energy,  $E_0=60$  MeV.*

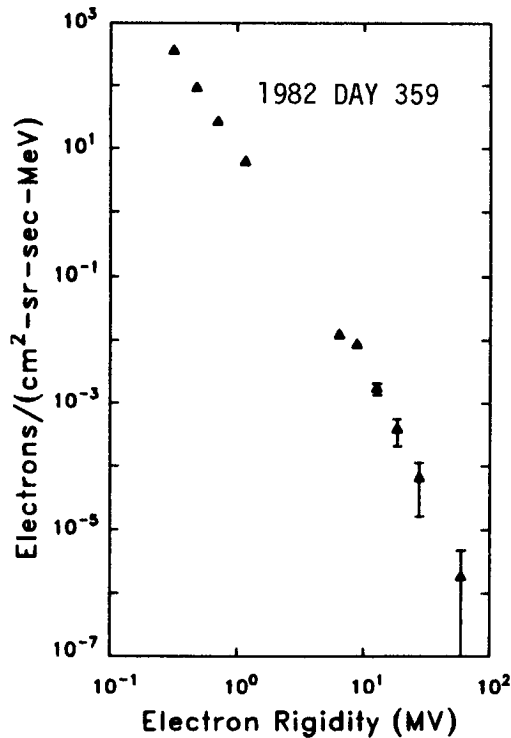


*Fig. 2: Flare rigidity spectrum of a typical class II event.*

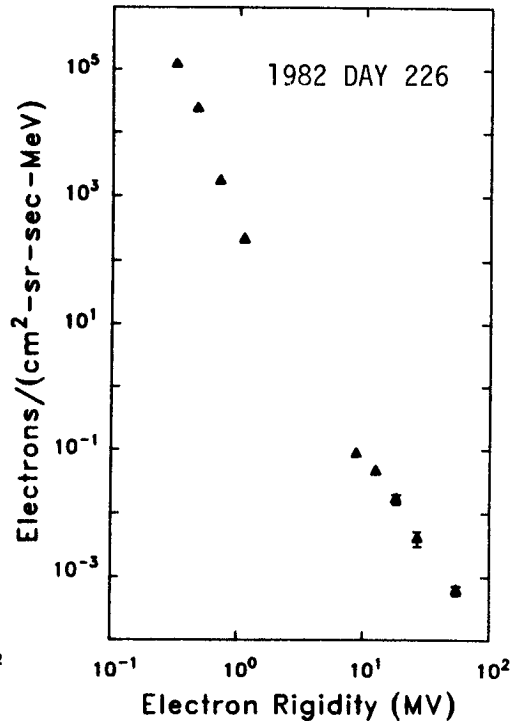


*Fig. 3: Flare rigidity spectrum of a typical class I event.*

modeled by single shock acceleration, the spectra of class I events require more complicated models. Obvious candidates include more than one acceleration site, a single shock with a compression ratio which varies in either space or time, an energy dependent escape mechanism, and an injection spectrum at high energies which is flatter than the spectrum produced by the shock. The electron spectra alone cannot distinguish between these options.

The duration of the soft x-ray thermal emission (1-8 Å) of flares provides a powerful tool in classifying flares associated with energetic interplanetary electrons as was first recognized by Cane *et al.* (1985). For all interplanetary particle events associated with soft x-ray events listed in Solar Geophysical Data, the class I events are associated with the impulsive (< 1 hour duration) soft x-ray events while the class II events are associated with the long duration (> 1 hour duration) soft x-ray events. Pallovicini *et al.* (1977) have demonstrated that the duration of the soft x-ray emission is further associated with the volume and coronal height of a flare: the impulsive flares (class I) are compact and low in the corona while the long duration flares (class II) are diffuse and higher in the corona.

The association of class II events with diffuse events high in the corona is consistent with the single shock acceleration model used to fit the electron spectra. Also, in support of the single shock acceleration model for class II events is the correlation by Cane *et al.* (1985) of the long duration x-ray events with interplanetary shocks and coronal mass ejections. The duration of gamma-ray emission bursts (Chupp, 1984) in

the class II events is also consistent with a shock of velocity  $10^3$  km/s traversing the  $10^{13}$ - $10^{14}$  km<sup>3</sup> volume associated with the long duration soft x-ray events. The relative height in the corona of class II flares results in less coronal diffusion than of class I flares and predicts less sensitivity to the degree of connection with the flare site.

The association of class I events with impulsive, compact events low in the corona is inconsistent with a single shock model with a compression ratio which varies in time or space. Multiple acceleration sites would be expected to produce multiple soft x-ray impulses which are not seen. The spectral shape of the gamma-ray continuum for the impulsive 1972 August 4 flare suggests that the electron spectrum at the acceleration site has a class I spectral shape (Ramaty *et al.* 1975) and thus the escape mechanism is not energy dependent.

A model of class I flare acceleration dominated by the impulsive (magnetic reconnection) phase of the event is consistent with both the observed electron spectral shape and the soft x-ray emission by a compact and impulsively heated volume of plasma. One might expect evidence of beaming along the direction of the electric field resulting from magnetic reconnection and Cane *et al.* (1985) have found a correlation of the impulsive soft x-ray events with strong type III radio bursts which accompany streaming electrons. Tentative association of the directivity of gamma-rays described by Vestrand *et al.* (1984) with class I events provides further evidence for electron beaming. The component of shock accelerated particles appears to be restricted to the lower energies by the size and density of the heated plasma region and the shape of the electron spectrum is consistent with such a component.

5. ACKNOWLEDGEMENTS. We would like to thank Mr. Leo Krawczyk and Ms. Judith Fontana-Kroeger for assistance in preparing this paper. We would also like to thank Mr. Richard Kroeger for helpful discussions.

#### REFERENCES

- Blandford, R. and Ostriker, J. 1978, *Ap.J.* 221, L29.  
 Cane, H., McGuire, R. and von Rosenvinge, T. 1985, submitted to *Ap.J.*  
 Chupp, E. 1984, *Ann. Rev. Astron. Astrophys.*, 22, 359.  
 Datlowe, D. 1971, *Solar Phys.* 17, 436.  
 Ellison, D. and Ramaty, R. 1985, accepted in *Ap.J.*  
 Evenson, P., Meyer, P., Yanagita, S. Forrest, D. 1984, *Ap.J.* 283, 439.  
 Hovestadt, D., Gloeckler, G., Fan, C., Fisk, L., Ipavich, F., Klecker, B., O'Gallagher, J., Scholer, M., Arbing, H., Cane, J., Hofner, H.  
 Kunne, E., Laeveranz, P. and Tums, F. 1978, *IEEE Trans.* GE16, 166.  
 Lin, R., Mewaldt, R. and Van Hollebeke, M. 1982, *Ap.J.* 253, 949.  
 Meyer, P., Evenson, P. 1978, *IEEE Trans.* GE16, 180.  
 Pallavicini, R., Serio, S. and Vaiana, G. 1977, *Ap.J.* 216, 108.  
 Ramaty, R., Kozlovsky, B. and Lingenfelter, R. 1975, *Space Sci. Rev.* 18, 341.  
 Simnet, G.M. 1974, *Space Sci. Rev.* 16, 257.  
 Vestrand, W., Forrest, D., Chupp, E., Rieger, E. and Share, G. 1984, *Bull. of AAS.* 16, 475.

# ONSET OF SOLAR FLARES AS PREDICTED BY TWO-DIMENSIONAL MHD-MODELS OF QUIESCENT PROMINENCES

J. GALINDO TREJO

Instituto de Geofísica, UNAM, 04510 - México, D. F., MEXICO

1. Introduction. It is well known the close connection between the sudden disappearance ("disparition brusque") of the quiescent prominences and the two-ribbon flares (see e.g. [6]). During this dynamic phase the prominence ascends rapidly (typically with a velocity about 100 Km/sec) and disappears. In another later stage is observed material falling back into the chromosphere. The impact of this downfalling matter on the chromosphere produces the  $H\alpha$ -brightening, which shows the symmetric double pattern. The occurrence of the "disparition brusque" is thought to be a consequence of a plasma instability of magnetohydrostatic structures (see e.g. [11]). Two-dimensional MHD-models for quiescent prominences have been worked out since the fifties. They describe the prominence in magnetohydrostatic equilibrium under the action of Lorentz forces, gas pressure gradients and the gravitational force. However, the stability properties of most of these models are not yet determined. We analyze by means of the MHD-energy principle [2] the stability properties of four prominence models. We show that all considered models undergo instabilities for parameters outside of the observed range at quiescent prominences. We consider the possibility that such instabilities in the flare parameter range may indicate just the onset of a flare.

2. Equilibrium and Stability Theory. We define a coordinate system with x-axis along prominence, y-axis perpendicular to the prominence sheet and z-axis vertical (opposed direction of the gravity acceleration). We take into account only plasma structures, which are independent on x. In a two-dimensional theory the magnetic field can be expressed as:

$$\underline{B} = \nabla A(y, z) \times \underline{e}_x + B_x(y, z) \underline{e}_x \quad (1)$$

where A is the x-component of a vector potential. The equilibrium condition, which A must satisfy reads:

$$\Delta A = -4\pi \frac{\partial \Pi(A, \phi)}{\partial \phi}, \quad \Pi(A, \phi) = P(A, \phi) + \frac{1}{8\pi} B_x^2(A) \quad (2)$$

where P is the plasma pressure, the external gravitational field and  $\rho = -\partial \Pi / \partial \phi = -\partial P / \partial \phi$  the mass density. Any two-dimensional prominence model corresponds to a particular choice of the functions  $P(A, \phi)$ ,  $B_x(A)$  and the boundary conditions. In order to analyze the stability properties of

prominence models we use the MHD-energy principle of Bernstein et al. (1958), according to which the stability of an equilibrium configuration is determined by the behaviour of the potential energy functional  $\delta W(\xi, \xi^*)$  resulting from a perturbation  $\xi(\underline{r}, t)$  to the system. For the two-dimensional equilibrium class the functional  $\delta W(\xi, \xi^*)$  may be written in the form:

$$\delta W(\xi, \xi^*) = \frac{1}{2} \int \left\{ \frac{1}{4\pi} |\nabla_\perp a|^2 - \frac{\partial^2 \pi}{\partial A^2} |a|^2 + \frac{1}{4\pi} |B_\perp \nabla_\perp \xi_x - B_x \nabla_\perp \xi_x|^2 + k^2 \left[ \frac{1}{4\pi} |B_x \xi_1 - \xi_x B_1|^2 + \right. \right. \\ \left. \left. + \mathcal{P} |\xi_x|^2 \right] + \frac{1}{4\pi} |B_\perp \nabla_\perp \xi_x - B_x \nabla_\perp \xi_x|^2 + \mathcal{P} |\nabla_\perp \xi_x|^2 - 2 \operatorname{Re} [\varrho (\nabla_\perp \xi_1) \xi_1^* \nabla_\perp \phi] - \frac{\partial \varrho}{\partial \phi} |\xi_1 \nabla_\perp \phi|^2 + 2k \operatorname{Im} \left[ \frac{1}{4\pi} \right. \right. \\ \left. \left. (\nabla_\perp a \cdot \underline{e}_x) \cdot (B_x \xi_1^* - \xi_x^* B_1) - \frac{\Delta A}{4\pi} \xi_x^* \partial^* - \mathcal{P} \xi_x (\nabla_\perp \xi_1^*) + \varrho \xi_x (\xi_1^* \nabla_\perp \phi) - \frac{B_x}{8\pi} \Delta A (\xi_1 \times \xi_1^*) \cdot \underline{e}_x \right] \right\} d^3 \underline{r} \quad (3)$$

where  $\nabla_\perp = \underline{e}_y \frac{\partial}{\partial y} + \underline{e}_z \frac{\partial}{\partial z}$ ,  $a = -\xi_\perp \nabla_\perp A$ ,  $B_\perp = \nabla_\perp A \times \underline{e}_x$ . We have supposed complex three-dimensional displacements of the following generalized form:

$$\xi(\underline{r}, t) = \xi(\underline{r}) e^{i\omega t} = [\xi_x(y, z) \underline{e}_x + \xi_\perp(y, z)] e^{ikx + i\omega t} \quad (4)$$

It is assumed periodic boundary conditions along the prominence axis (x-direction) and  $\xi = 0$  on the edge of the plasma region in the y, z-plane. The x-integration in equation (3) is to be carry out over one period. If  $\delta W$  is positive for all displacements which satisfy the boundary conditions, then the equilibrium is stable. The MHD-energy principle is a necessary and sufficient criterion for stability. The stability problem reduces therefore to analyze the sign of the minimum of  $\delta W$ . It is interesting to note that to the variational problem which implies the minimisation of  $\delta W$ , is associated the Euler-Lagrange equation:

$$-\varrho \omega^2 \xi(\underline{r}) = F(\xi(\underline{r})) \quad (5)$$

where  $F$  is a self-adjoint differential operator with time independent coefficients (see e.g. [1]). We use the normalization constraint:  $\frac{1}{2} \int \varrho |\xi|^2 d^3 \underline{r} = 1$  and obtain the spectrum of eigenvalues further one has  $\omega_{min}^2 = \operatorname{Min} \delta W(\xi, \xi^*)$

3. Stability Results for Prominence Models. We have evaluated the energy principle for four prominence models: Menzel, (M), [10]; Dungey, (D), [3]; Kippenhahn and Schlüter, (KS), [7]; Lerche and Low, (LL), [9]. One obtains generally stability statements by two procedures: (a) analytically, by manipulating the energy functional  $\delta W$  to recognize a definite sign and so to infer about the stability properties, (b) numerically, by carrying out the minimisation of  $\delta W$  with the aid of a computer code. Our analytical results concerning to these models are reported elsewhere [4]. We obtain global stability for the KS-model in case of arbitrary 3D-displacements [5]; for the other models the stability statements are restrictive to special

classes of displacements (2D, long wavelengths, etc.). In order to obtain more general results concerning to broader class of displacements we have developed a numerical code based on the finite element-method. This procedure provides, besides qualitative stability statements, the largest growth rate in case of instability and the frequency of the fundamental oscillations of stable systems. Our code was tested successfully by applying it to simple systems, whose dynamic properties are well known (e.g. Alfvén waves, current sheets and sound waves in a constant gravitational field). We obtain numerically a stable behaviour for the four models in the parameter range of the observations of typical quiescent prominences ( $T=7.10^3$ °K,  $n_e=5.10^{10}$ cm $^{-3}$ ,  $B=5$ G, thickness  $Y=5.10^3$  Km, height  $Z=1.5-5.10^4$  Km). All models describe horizontal large-scale oscillations with periods between 16 and 80 min (see Table 1). Reported data indicate that quiescent prominences undergo actually horizontal oscillations from and towards the perturbation, which is originated in solar flares. The observed periods range from 6 to 80 min. [2], [8], [1].

Table 1. Periods of horizontal oscillations in quiescent prominences.

Model	Period (min)
M	40
D	55-80
KS	16
LL	17-50

Unstable behaviour is found only out of the observed parameter range. When one considers typical parameters of flares (e.g.  $T \sim 10^7$ °K,  $n \sim 10^{11}$ cm $^{-3}$ ,  $B \sim 50$  G) one obtains  $\beta = \frac{8\pi n_e k T}{B^2} \gtrsim 1$ . Just for

these parameters we get instability only in case of

LL model. The other models continue stable around these parameters. Figure 1 shows function of  $\alpha \equiv \beta/2$  (we use dimensionless variables, so that  $\omega_{\min}^2$  is normalized by  $g/h$ , where  $g=2.74 \times 10^4$ cm/sec $^2$ ,  $h=kT/mg$  is the density scale height and  $m$  is the proton mass). We have separated the different physical effects (electromagnetic, compressional and gravitational parts) in the energy functional  $\delta W(\xi_{\min}, \xi_{\min}^*)$ , so that it is possible to infer about the nature of the instability. For the situation illustrated on Fig. 1 we find that the instability is driven mainly by electromagnetic forces. Gravitation provides also an instabilizing effect. In opposition to this, the compression has continually a stabilizing effect. Such a gravitational-electromagnetic mixed instability has a typical growth rate  $\Gamma = \sqrt{g/h} |\omega_{\min}| / 2\pi \sim 4.77 \cdot 10^{-5}$ sec $^{-1}$ , i. e. a growth time  $\tau \sim 5.8$  h. On the other hand, the impulsive phase of a flare elapses within few minutes, so that the found



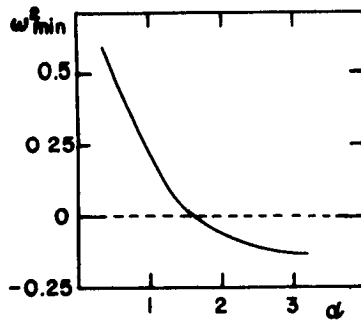


Fig.1. LL-Model:  
minimum eigenvalue  
 $\omega^2_{\min}$  as function  
of  $\alpha = \beta/2$ .

growth time may explain rather the evolution of the flare ribbons and the associated loop system which last several hours. The cause of the parameter shift in the quiescent prominence may reside in an external perturbation in form of a shock wave generated by a distant flare or in an internal perturbation in form of a newly emerging flux in the same active region. Our results can be considered as preliminaries because the studied two-dimensional models are still very simple to describe the complexity of quiescent prominences. However, further applications of our stability

method to more realistic models give the possibility of a better description of the impulsive phase of solar flares.

### References.

- [1] Bashkirtsev et al.: 1983, Solar Phys., 82, 443.
- [2] Bernstein, I. B. et al.: 1958, Proc. Roy. Soc., A244, 17.
- [3] Dungey, J. H.: 1953, MNRAS, 113, 180.
- [4] Galindo Trejo, J.: 1985, to be published.
- [5] Galindo Trejo, J. and Schindler, K.: 1984, Astrophys. J., 277, 422.
- [6] Hyder, C.: 1967, Solar Phys., 2, 49.
- [7] Kippenhahn, R. and Schlüter, A.: 1957, Z. f. Astrophys., 43, 36.
- [8] Kleczek, J. and Kuperus, M.: 1969, Solar Phys., 6, 72.
- [9] Lerche, I. and Low, B. C.: 1980, Solar Phys., 67, 229.
- [10] Menzel, D. H.: 1951, Proc. Conf. on Dynamics of Ionised Media, London.
- [11] Priest, E. R.: 1983, Solar Phys., 86, 33
- [12] Ramsey, H. E. and Smith, S. F.: 1966, Astron. J., 71, 197.

## THE STARTING CONDITIONS FOR AN OPTICALLY SMALL SOLAR GAMMA RAY FLARE

G. M. Simnett

Department of Space Research, University of Birmingham  
Birmingham B152TT, United Kingdom

J. M. Ryan

Space Science Center, University of New Hampshire  
Durham, New Hampshire 03824 USAABSTRACT

We suggest that optically small  $\gamma$ -ray flares result from gradual pre-flare acceleration of protons over  $\sim 10^3$  s by a series of MHD shocks in the low corona. A fraction of the accelerated protons are trapped in the corona where they form a seed population for future acceleration. If the shock acceleration is sufficiently rapid proton energies may exceed the  $\gamma$ -ray production threshold and trigger  $\gamma$ -ray emission. This occurs without the total flare energy being necessarily large. Magnetic field geometry is an important parameter.

1. Introduction

Now that the statistics of  $\gamma$ -ray flares have improved to the point where meaningful comparisons can be made with other flare data it has become clear that not only the large, spectacular H $\alpha$  flares are associated with prompt nuclear line emissions (e.g.,  $^{12}\text{C}$  and  $^{16}\text{O}$ ). Such flares require the presence of protons  $> 10$  MeV and generally exhibit the  $p(n,\gamma)d$  neutron capture line requiring protons  $\sim 30$  MeV. Results from SMM [1] have shown that a significant portion of the  $\gamma$ -ray events have onset times of  $\gamma$ -rays and hard X-rays ( $> 28$  keV) coincident to within  $\sim 1$  s with the total hard X-ray integrated flux well correlated with that of the  $\gamma$ -rays [2]. A process for producing hard x-rays from  $\gamma$ -ray producing protons is discussed in another paper [3]. Our model for such flares must be capable of producing such quasi-simultaneity, and it should also be capable of delaying  $\gamma$ -ray production without having to resort to a separate model. In extreme cases there is evidence of proton (ion) acceleration up to 1 GeV within a few s of the hard X-ray onset [4].

If we concentrate on the more common case where protons only up to 30 MeV are required, this still represents a significant energy gain if the protons start with a thermal distribution at  $\sim 10^7\text{K}$  (1 keV). Although mechanisms have been examined theoretically to achieve such rapid accelerations [5], the necessary physical conditions for the required acceleration efficiency are very severe and appear to be improbable at the Sun. We suggest that such rapid acceleration is not necessary, and that  $\gamma$ -ray emission represents the end product of a much more gradual ( $\sim 10^3$  s) acceleration process.

2. The Acceleration of Protons

There are few observational constraints on proton acceleration up to  $\sim 1$  MeV, somewhat below the  $\gamma$ -ray production threshold. However, we

SH 1.3-2

know from range/energy considerations that the acceleration cannot take place at high densities, thus restricting the acceleration site to the high corona. For example, at a density of  $2 \times 10^9 \text{ cm}^{-3}$ , which is representative of the base of the corona [6], a 100 keV proton has a range of only  $4 \times 10^9 \text{ cm}$ , which it would cover in  $\sim 8 \text{ s}$ . Therefore not only would any acceleration process at these densities result in excessive heating - most of the available energy would be dissipated as heat - but protons which did manage to get accelerated to 100 keV would have a short lifetime. However, a 400 keV proton has a range of  $10^{12} \text{ cm}$  at a density of  $10^8 \text{ cm}^{-3}$ , and therefore a lifetime  $\sim 10^3 \text{ s}$ . From these considerations we suggest that any proton acceleration region should be at a density at least as low as  $3 \times 10^8 \text{ cm}^{-3}$  corresponding to an altitude of  $\sim 10^5 \text{ km}$ . We believe the most plausible mechanism for proton acceleration is coronal shock acceleration. The basic theory of particle acceleration in shocks has been given by Bell [7] and most subsequent work has developed from his suggestions.

Fig. 1 outlines the scenario that appears most appropriate for the development of  $\gamma$ -ray flares. The magnetic field configuration is likely to be complex, with a series of small scale loops (shown left inset), plus some overlying magnetic structure with an overall size  $\sim 10^5 \text{ km}$ . We suggest that evolution of the lower lying loop structure, possibly caused by emerging flux, causes small energy releases, heating and a succession of small shocks. A fraction of the protons accelerated in these shocks are trapped in the overlying field and are available for further acceleration as seed particles in subsequent shocks. The acceleration we believe requires and is enhanced through the development of resonant turbulence, illustrated schematically in the center inset of Fig. 1. Throughout the whole process there is feedback between the accelerated particles, the MHD waves and shocks. This drives the energy release process harder. The latter is probably due to induced additional magnetic field reconnection. In the  $\gamma$ -ray

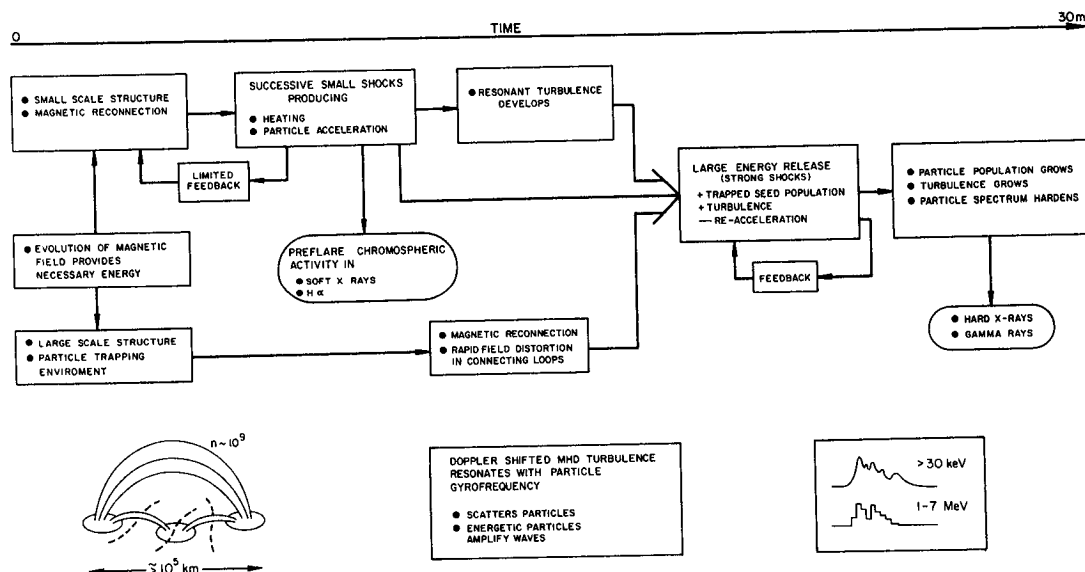


Figure 1. Schematic of pre-flare and flare particle acceleration and activity.

flare the build up of the proton population is eventually sufficient for a significant precipitation of protons near or below the transition zone, producing the signature of a  $\gamma$ -ray flare. This is illustrated schematically in the right inset of Fig. 1. The whole process takes  $\sim 10^3$  s. This is consistent with the coronal acceleration model discussed by Lee and Ryan [8].

There are some observable consequences of the scenario we have outlined. First, some of the more energetic protons from the early accelerations will not be stably trapped but will impact the top of the chromosphere, causing heating but little else. This heating should be visible prior to the flare as small soft X-ray and EUV brightenings from the appropriate impact points along the base of the loops indicated in the left inset (Fig. 1). Second, the protons that are stably trapped will, in fact, continue to lose energy to the coronal gas, thereby heating it. It has recently been suggested [9] that such heating may destabilize a coronal mass ejection, thus opening the magnetic field and releasing the trapped protons. This would also drive the energy release harder, causing a flare but probably not a  $\gamma$ -ray flare because the particle trapping environment has been lost.

### 3. Supporting Observations

The model is well supported by observations of the M4  $\gamma$ -ray flare near the solar limb on 1980 June 29, 10:41 UT. Fig. 2 shows the intensity-time profile of 3.5-8.0 keV X-ray, emission from 10:20-10:45 UT. The onset of the impulsive phase we take to be 10:40:10UT. It is obvious from the soft X-ray observations that there was considerable pre-flare activity for some 20 m before the impulsive phase. The OV transition region UV line intensity exhibits the same general behavior while hard X-rays and  $\gamma$ -rays are undetectable until after 1041 and peaking at about 1042. Spatially resolved data show that there were a number of resolved bright points in OV over a region of the limb covering a projected distance of  $> 10^5$  km. A large X-ray emitting structure extending  $\sim 1.5 \times 10^5$  km above the limb (in projection) was reported for the period of June 29 [10].

The general conclusion from these data is that before the  $\gamma$ -ray flare there was non-impulsive, but substantial emission from the transition zone over a widespread area near the solar limb. There was also evidence of a large scale magnetic structure of the type we believe is suitable for trapping moderate energy protons (few hundred keV) for periods of many minutes. Although there is some evidence for small disturbances in the corona during the flare, there was no major coronal transient as there was from other non- $\gamma$ -ray flares from this region.

Prior to the impulsive phase significant plasma turbulence was observed in Ca XIX emission indicating random velocities  $> 150$  km/s. Also there is very little evidence of radio emission before the impulsive phase. This is all consistent with energy deposition and wave generation by non-thermal protons in the low corona. Clearly this is a feature of our gradual acceleration model, which would predict proton energies of a few hundred keV, which are sufficient to drive the plasma turbulence, some 10s of seconds before the 10 MeV energies required for the  $\gamma$ -rays.

#### 4. Conclusions

We believe that the mechanism resulting in  $\gamma$ -ray emission from an otherwise optically small flare is the slow build-up of particle energy

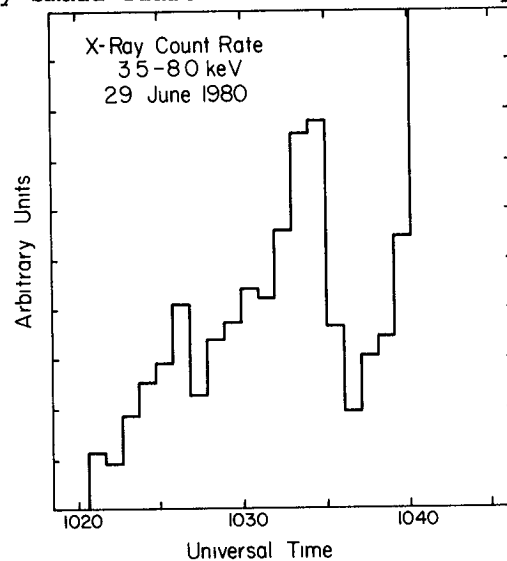


Figure 2. Soft X-ray count rate measured by HXIS on SMM. The impulsive phase is well off scale.

over a time scale of  $10^3$  s before the impulsive phase. The magnetic field configuration is very important and requires the presence of stable magnetic structures in the corona reaching to altitudes in excess of  $10^5$  km. Such magnetic structures are used to trap accelerated particles. During the pre-flare period energy is transferred to non-thermal protons by a series of small MHD shocks, gradually re-accelerating the surviving protons. A signature of this acceleration is the excitation of weak EUV and soft X-ray emission where some of the accelerated protons impact the chromosphere.

5. Acknowledgements We are grateful to Drs. D.J. Forrest, B.R. Dennis, J. Lemon and R.A. Shine for SMM data.

#### 6. References

1. Forrest, D.J. and Chupp, E.L., 1983, *Nature*, **305**, 5932, 291.
2. Forrest, D.J., 1983, AIP Conf. Proc. No. 101 (Ed. M.L. Burns et al.) 3.
3. Simnett, G.M., 1985, Proc. Intl. Cosmic Ray Conf. (LaJolla), SH 1.2-13.
4. Chupp, E.L., et al., 1982, *Ap. J.*, **263**, L95.
5. Achterberg, A., and Norman, C.A., 1980, *Astron. & Astrophys.* **89**, 359.
6. Vernazza, J.E, et al., 1981, *Ap. J. Suppl.*, **45**, 635.
7. Bell, A.R., 1978, *MNRAS* **182**, 147 and 443.
8. Lee, M.A. and Ryan, J.M., 1985, submitted to *Astrophys. J.*
9. Simnett, G.M. and Harrison, R.A. 1985, *Adv. Sp. Res.*, **4**, 7, 279.
10. Harrison, R.A., et al., 1984 Proc. STIP Symp. on Sol. Interplanet. Intervals (Eds., M.A. Shea, D.F. Smart and S.M.P. McKenna-Lawlor) 287.

ON THE DETECTABILITY OF KEV-MEV SOLAR PROTONS  
THROUGH THEIR NONTHERMAL LYMAN-ALPHA EMISSION

Richard C. Canfield and Ching-Ray Chang  
Center for Astrophysics and Space Sciences, C-011  
University of California, San Diego  
La Jolla, California 92093, USA

ABSTRACT

We investigate the intensity and timescale of nonthermal Doppler-shifted hydrogen  $L\alpha$  photon emission as diagnostics of 10 keV-10 MeV protons bombarding the solar chromosphere during flares. We determine the steady-state excitation and ionization balance of the proton beam, taking into account all important atomic interactions with the ambient chromosphere. For a proton energy flux comparable to the electron energy flux commonly inferred for large flares, we find  $L\alpha$  wing intensities orders of magnitude larger than observed nonflaring values. Our investigation of timescales for ionization and charge exchange leads us to conclude that over a wide range of values of mean proton energy and beam parameters, Doppler-shifted nonthermal  $L\alpha$  emission is a useful observational diagnostic of the presence of 10 keV-10 MeV superthermal proton beams in the solar flare chromosphere.

1. Introduction. Gamma-ray and hard X-ray observations of solar flares imply that, at energies  $\geq 10$  MeV, the number of energetic protons exceeds that of energetic electrons by several orders of magnitude [6]. This is currently understood [4] to be the consequence of an acceleration mechanism (e.g., a stochastic Fermi mechanism) in which the acceleration rate is proportional to momentum, acceleration takes place in a tenuous medium (the corona), and the emission is produced when the energetic particles are stopped fully in a thick target (the chromosphere and photosphere). However, this mechanism operates effectively only if some particles are already accelerated above a threshold energy by some other mechanism. Orrall and Zirker [5] have shown that charge-exchange  $L\alpha$  emission may be useful for the detection of relatively low energy ( $E < 1$  MeV) superthermal protons, which do not produce a significant level of nuclear emission. In this paper we extend the work of Orrall and Zirker to energetically significant values of beam flux, and address the question of the range of values of beam flux for which the intensity and timescale of  $L\alpha$  charge-exchange emission may fall into observationally relevant ranges.

2. Atomic Physics. To simplify our study of the emission of  $L\alpha$  by superthermal protons we represent the protons injected into the chromosphere by a vertical beam directed away from the observer. Some superthermal protons become superthermal hydrogen atoms in excited states, and subsequently radiate before they stop. Potentially relevant atomic processes that we have examined include charge exchange between beam protons and ambient hydrogen atoms, excitation of beam hydrogen atoms by collisions with ambient electrons, hydrogen atoms and protons, spontaneous radiative de-excitation of beam hydrogen atoms, stimulated radiative de-excitation of beam hydrogen atoms, collisional ionization of beam hydrogen

atoms by ambient electrons, protons and hydrogen atoms, and spontaneous radiative recombination of beam hydrogen atoms.

We have examined the relative importance of these various competing atomic processes, with the following conclusions. The dominant destruction process for superthermal beam protons is charge exchange with ambient chromospheric hydrogen atoms. Ionizing collisions of superthermal hydrogen atoms with ambient electrons, protons, and neutral hydrogen atoms are of comparable importance in creating superthermal protons. The main source of  $L\alpha$  emission is charge exchange from the proton beam. The dominant slowing process is Coulomb collisions with ambient electrons [7].

**3. Computed  $L\alpha$  Spectra.** Our chosen value of the hydrogen ionized fraction in our uniform chromospheric model atmosphere is guided by Orrall and Zirker, who used a detailed empirical model [8] to show that 10-1000 keV proton nonthermal  $L\alpha$  emission originates in the chromosphere. Our assumed 10% ionized fraction is an appropriate mean value. We have adopted a simple monoenergetic proton beam at input. The values of the input energy  $E_0$  and the total input energy flux  $F_E(0)$  are free parameters.

In Figure 1 we show the computed nonthermal  $L\alpha$  spectrum generated by monoenergetic proton beams of input energy flux  $F_E(0) = 10^{11} \text{ erg cm}^{-2} \text{ s}^{-1}$  (an upper limit to plausible values), for values of  $E_0$  ranging from 3 keV to 30 MeV. If we examine a single curve, say for  $E_0 = 30 \text{ keV}$ , we see a sharp

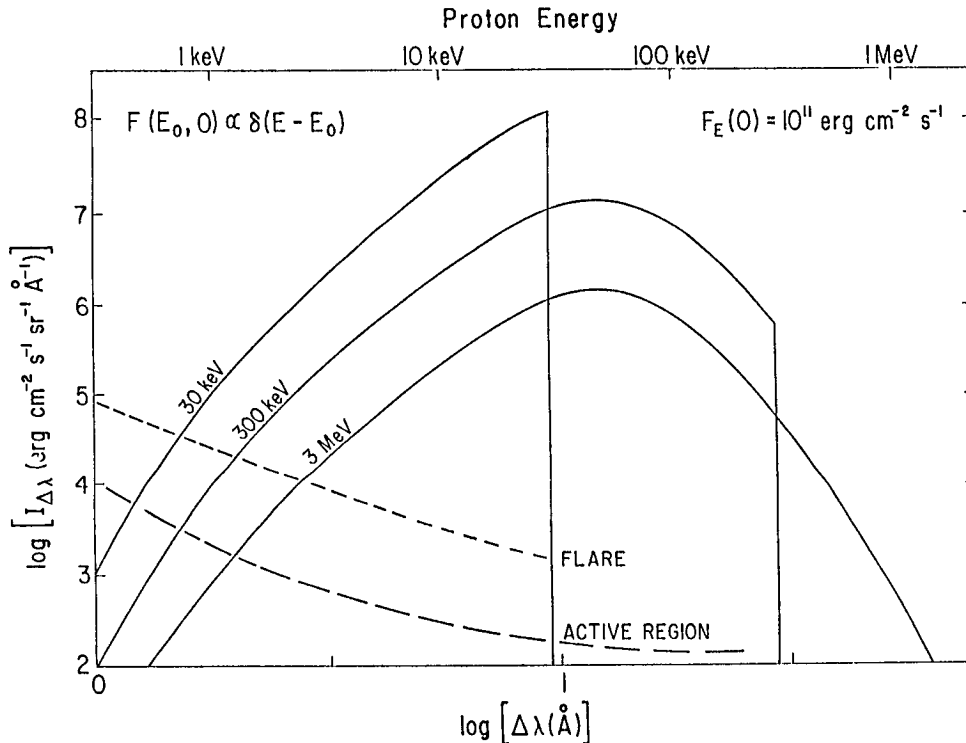


Fig. 1. - Theoretical nonthermal  $L\alpha$  spectra for protons of initial energy  $E_0$ .

peak in the spectrum at the wavelength shift  $\Delta\lambda$  appropriate to the velocity of protons of initial energy  $E_0$ , corresponding to emission from near the top of the chromosphere. At lesser values of  $\Delta\lambda$  the emission comes from slower protons that have penetrated some distance  $z$  into the target, where their velocity (and hence Doppler-shift) has dropped. If we consider the spectra in Figure 1 for  $E_0 = 300$  keV and 3 MeV, we see that the curves peak somewhat below  $E = 100$  keV (somewhat above  $\Delta\lambda = 10$  Å). This peak  $L\alpha$  intensity corresponds to the peak in the charge-exchange cross-section in this same energy range. It is interesting to compare the computed spectra to an observed solar active region  $L\alpha$  spectrum [3] and an observed (presumably thermal) solar flare  $L\alpha$  spectrum [2]. Throughout much of the energy range considered in Figure 1 the intensity of the computed nonthermal  $L\alpha$  emission exceeds the observed active region emission by several orders of magnitude.

**4. Timescales.** Our equilibrium computations of  $L\alpha$  emission will not be applicable unless the ionization structure of the chromosphere remains substantially unchanged within the time required for charge exchange. If the chromosphere becomes highly ionized within the collisional range of the protons, little charge exchange between superthermal protons and ambient hydrogen atoms can take place. Because recombination is several of orders of magnitude less efficient than charge exchange, per ambient particle, much less nonthermal  $L\alpha$  emission will be created if the atmosphere becomes ionized.

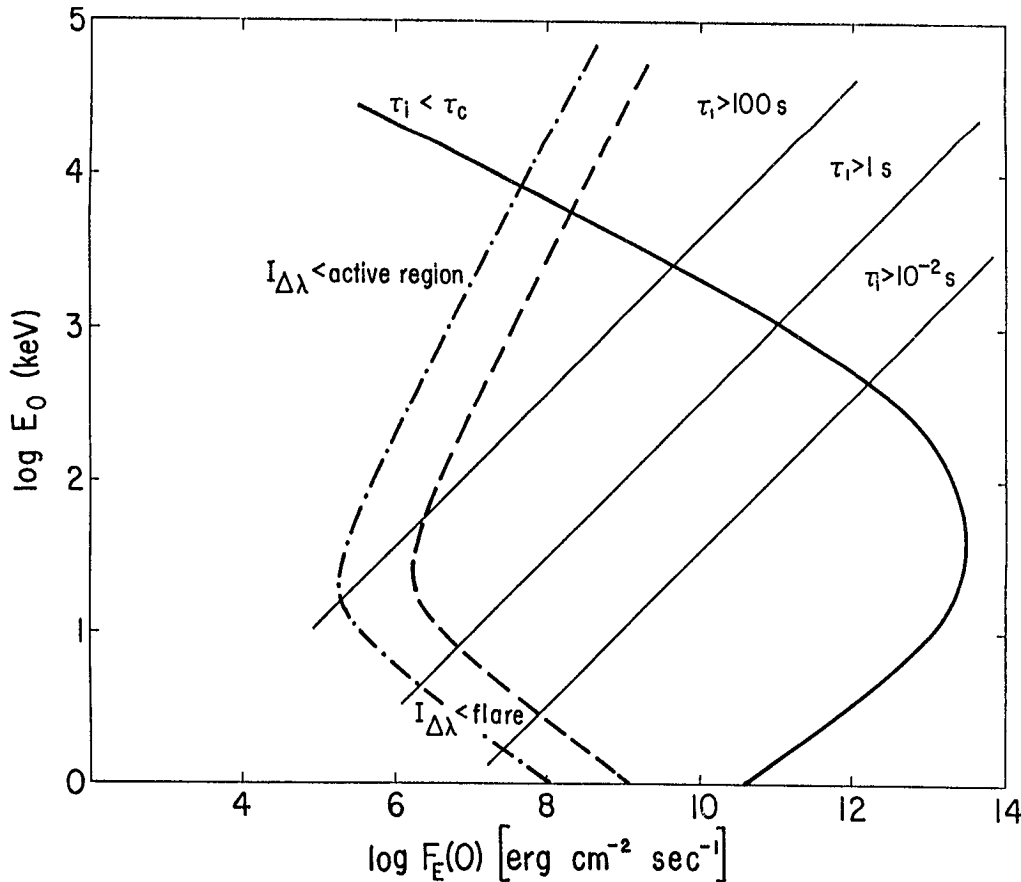


Fig. 2. The range of relevance of the equilibrium  $L\alpha$  spectra in Figure 1.



The range of relevance of the  $L\alpha$  spectra of Figure 1 is explored in Figure 2. The thick solid curve is that for which the ionization timescale  $\tau_i$  equals the charge exchange timescale  $\tau_c$ . The thin lines indicate various values of  $\tau_i$ . On the long-dashed curve the peak intensity of nonthermal  $L\alpha$  emission equals that of observed flare  $L\alpha$ -wing emission. On the dot-dashed curve the peak computed intensity of nonthermal  $L\alpha$  emission matches that of observed active-region  $L\alpha$ -wing emission. We see that at an energy of interest (say 100 keV), the intensity of nonthermal  $L\alpha$  emission exceeds the observed active-region background for all  $F_E(0)$  values above about  $10^6$  erg  $\text{cm}^{-2} \text{s}^{-1}$ , and the charge-exchange mechanism is effective up to around  $F_E(0) \sim 10^{13}$  erg  $\text{cm}^{-2} \text{s}^{-1}$ . Over this range of  $F_E(0)$  values the ionization time ranges from about 1000 s to very small values. Obviously at the lowest detectable intensities the equilibrium calculation given above is physically relevant throughout the duration of typical flares; at the high end of the  $F_E(0)$  range, the duration of validity becomes inconsequentially small. Figure 2 also serves to show that at input proton energies above about 10 MeV and below about 1 keV the equilibrium calculation is not both physically and observationally relevant at any value of the total energy flux.

**5. Conclusions.** We conclude that if the sun's chromosphere is bombarded suddenly from above by superthermal protons of energy 10 keV - 1 MeV, with energy fluxes consistent with the hypothesis that such protons are a significant component of the population of superthermal particles in flares, charge exchange would lead to an intense but brief burst of Doppler-shifted  $L\alpha$  emission. At much lower proton flux levels the emission would still exceed preflare background, but last much longer. In other work [1] we consider power-law and thermal forms of the input proton energy spectrum, the generation of emission in the hydrogen  $H\alpha$  line, and the details of the atomic physics.

**6. Acknowledgements.** We thank Edward Shoub, William Thompson, and Jack Zirker for stimulating discussions. This research has been supported by NASA grant NSG-7406 and National Science Foundation grant AST 83-20306.

#### References

1. Canfield, R. C., and Chang, C.-R. 1985, *Astrophys. J.*, 295, in press.
2. Canfield, R. C., and VanHoosier, M. E. 1980, *Solar Phys.*, 67, 339.
3. Cohen, I. 1981, An Atlas of the Solar Spectrum Between 1175 and 1950 Angstroms Recorded on Skylab with NRL's Apollo Telescope Mount Experiment, NASA Reference Publication 1069 (Washington: U. S. Government Printing Office).
4. Heyvaerts, J. 1981, in *Solar Flare Magnetohydrodynamics*, ed. E. R. Priest (New York: Gordon and Breach Publ.).
5. Orrall, F. Q., and Zirker, J. B. 1976, *Astrophys. J.*, 208, 618.
6. Ramaty, R. et al. 1980, in *Solar Flares*, ed. P. A. Sturrock (Boulder: University of Colorado Press), p. 117.
7. Trubnikov, B. A. 1965, *Reviews of Plasma Physics*, Consultants Bureau, New York, 1, 105.
8. Vernazza, J. E., Avrett, E. H., and Loeser, R. 1981, *Ap. J. Suppl. Ser.*, 45, 619.

## OBSERVATIONS OF SOLAR FLARE GAMMA-RAYS AND PROTONS

M. YOSHIMORI and H. WATANABE

Department of Physics, Rikkyo University,  
Toshima-ku, Tokyo 171, JAPAN.

## ABSTRACT

Solar flare gamma-rays (4 - 7 MeV) and protons (8 - 500 MeV) were simultaneously observed from six flares on 1 Apr., 4 Apr., 27 Apr. 13 May 1981, 1 Feb. and 6 June, 1982 by the Hinotori and GMS satellites. The relationship between 4 - 7 MeV gamma-ray fluences and peak 16 - 34 MeV proton fluxes for these flares are analyzed. It does not reveal an apparent correlation between these two parameters. The present result implies that the protons producing gamma-rays and the protons observed near the Earth do not always belong to the same population.

## 1. Introduction

The particle acceleration mechanism in solar flares has been studied through observations of radiowaves, X-rays, gamma-rays, neutrons and flare particles. The energetic photon observations provide a clue on the particle acceleration through interaction processes in the flare region. On the other hand, the particle observations provide the clue through propagation effects in the corona and interplanetary space. Hence, we need simultaneous observations of the photons and the particles to understand deeply the particle acceleration mechanism and the photon emission processes in solar flares. To study the acceleration of nuclei, it is important to investigate the relationship between the particles producing gamma-ray lines and the particles observed near the Earth. This investigation provide diagnostics for the following question: Are these two kinds of accelerated particles the same population? In addition, it provides the clue on the interaction model (thin-target or thick-target interaction model), together with observations of fragments such as deuterons, tritons and He-3 nuclei.

The gamma-ray observations were successfully performed during the solar maximum period from 1981 Feb. to 1982 June by the Hinotori satellite (Yoshimori et al., 1983). The Hinotori satellite observed 8 gamma-ray line flares during the above period. On the other hand, the GMS (Geostationary Meteorological Satellite) observed 23 solar proton events during the same period. Several observations of solar particles associated with gamma-ray line flares have been reported so far by the ISEE-3 (Pesses et al., 1981) and the IMP-8 (McGuire et al., 1981) satellites. These observations indicated that the solar proton fluxes were not always correlated with the gamma-ray line fluxes. Furthermore, Cliver et al. (1983) showed a lack of correlation between the peak 10 MeV proton fluxes and the 4 - 8 MeV gamma-ray excesses for western hemisphere flares.

In this paper, we analyze the relationship between flare-associated gamma-ray lines and interplanetary proton events observed from Apr., 1981 to June, 1982. The gamma-ray data are from the gamma-ray spectrometer on board the Hinotori satellite. The proton data are from the solid state Si detector on board the GMS.

## 2. Gamma-Ray and Proton Observations

The flares in which gamma-rays and protons were simultaneously observed are listed in Table 1. The flare date, maximum time, location, H $\alpha$  importance and GOES X-ray class are presented there. The detailed characteristics of these flares were described by Yoshimori (1984).

The time histories of gamma-ray count rate in the 4.0 - 6.7 MeV band were observed for the 1 Apr., 4 Apr., 27 Apr., 13 May, 1981, 1 Feb. and 6 June, 1982 flares. The 4.0 - 6.7 MeV gamma-rays are mostly dominated by prompt nuclear deexcitation lines of C-12 at 4.44 MeV and of O-16 at 6.13 MeV (Yoshimori, 1984). A few additional gamma-ray lines were reported for these flares. Of these flares the Feb. 1, 1982 flare did not reveal an apparent gamma-ray emission. The corresponding time histories of proton fluxes in the 8 - 500 MeV bands were observed.

The 1 Apr., 1981 flare showed the gradual time history with a long duration of 26 min. The 4.0 - 6.7 MeV gamma-ray fluence and the peak 16 - 34 MeV proton flux were  $(20 \pm 4)$  photons / cm<sup>2</sup> and  $(2.5 \pm 0.3)$  protons / cm<sup>2</sup> s sr, respectively. This flare is considered to be magnetically well-connected to the Earth; this flare occurred within the so-called preferred connection helio-longitude range. Protons with high energies of 200 - 500 MeV also were observed (Yoshimori, 1985). These 200 - 500 MeV protons revealed a fast rise and fall time history.

The 4 Apr., 1981 flare showed the impulsive time history with a short duration of 80 s. The 4.0 - 6.7 MeV gamma-ray fluence and the peak 16 - 34 MeV proton flux were  $(25 \pm 5)$  photons / cm<sup>2</sup> and  $(3.4 \pm 0.4)$  protons / cm<sup>2</sup> s sr, respectively. This flare is also considered to be magnetically well-connected to the Earth.

The 27 Apr., 1981 flare showed the gradual time history with long duration of 25 min, but the Hinotori satellite was eclipsed by the Earth at 0815 UT. This flare revealed the intensive gamma-ray line emission (Chupp, 1982, 1983; Yoshimori et al. 1983). However, this flare did not reveal the apparent proton increase in the 8 - 500 MeV band, in spite of the magnetically well-connected flare. Further, three large proton events which occurred in the same sunspot were reported on 24, 26 and 28 Apr., 1981. These results may imply that protons accelerated in the 27 Apr. flare could not escape into interplanetary space. The 4.0 - 6.7 MeV gamma-ray fluence is  $(30 \pm 5)$  photons / cm<sup>2</sup>, and the upper limit of the peak 16 - 34 MeV proton flux is 3 protons / cm<sup>2</sup> s sr.

The 13 May, 1981 flare showed the gradual time history with long duration of 18 min. This flare revealed a small increase of gamma-ray emission, but did not reveal the increase of proton flux. The absence of the apparent increase of proton flux may be due to the bad propagation condition in interplanetary space; this flare did not occur within the preferred connection helio-longitude range. The 4.0 - 6.7 MeV gamma-ray fluence is  $(50 \pm 9)$  photons / cm<sup>2</sup>, and the upper limit of the peak 16 - 34 MeV proton flux is 2 protons / cm<sup>2</sup> s sr.

The 6 June, 1982 flare showed the impulsive and multi-peak time history with duration of 6 min. The proton flux revealed the very gradual increase and the peak reached on 9 June. In addition, protons with energies above 68 MeV were not observed with statistical significance. It implies that protons could not be accelerated to energies above 70 MeV during the flare. The 4.0 - 6.7 MeV gamma-ray fluence and the peak 16 - 34 MeV proton flux are  $(35 \pm 6)$  photons / cm<sup>2</sup> and  $(6.0 \pm 0.7)$  protons / cm<sup>2</sup> s sr, respectively.

An unusual event was the 1 Feb., 1982 flare, in which intensive proton flux was observed, but gamma-ray line emission was not significant. The 16 - 34 MeV peak proton flux is  $(80 \pm 9)$  protons /  $\text{cm}^2 \text{ s sr}$ , and the upper limit of 4.0 - 6.7 MeV gamma-ray fluence is 13 photons /  $\text{cm}^2$ . This flare shows an opposite trend to the 27 Apr., 1981 flare, although this flare is also considered to be magnetically well-connected to the Earth.

### 3. Discussion

As shown in the previous section, the Hinotori and GMS data do not always reveal the apparent correlation between the gamma-ray line fluences and the peak 16 - 34 MeV proton fluxes. The scatter diagram of the 4.0 - 6.7 MeV fluence versus the peak 16 - 34 MeV proton fluxes is shown in Fig. 1 to see the correlation between these two parameters. The most of the 4.0 - 6.7 MeV gamma-rays consist of the C-12 line at 4.44 MeV and of the O-16 line at 6.13 MeV. The 16 - 34 MeV protons should contribute greatly to the production of these prompt gamma-ray lines. As shown in Fig. 1, there is no compelling evidence for the correlation for both eastern and western hemisphere flares. It is easily understood that there is not good correlation for the eastern hemisphere flares of 13 May, 1981 and 6 June, 1982. It is because the bad propagation condition in interplanetary space. Furthermore, the correlation is neither always found for the western hemisphere flares, which occurred within the preferred connection helio-longitude range. The present result is consistent with the Cliver et al.'s result (1983). These results seem to suggest that the protons producing the gamma-ray lines in the flare site and the protons observed near the Earth do not always belong to the same population.

Two gamma-ray line production models (thick- and thin target interaction models) have been proposed (Ramaty et al., 1975). If the gamma-ray lines are produced from the thin-target interaction, the gamma-ray line fluence should be nearly proportional to the 16 - 34 MeV proton flux. On the other hand, the thick-target model should predict that there is not always apparent correlation, because the gamma-ray lines are produced by the accelerated nuclei streaming down to the denser chromosphere and photosphere. The thick-target model is also supported from the absence of spallation products such as deuterons, tritons and He-3 nuclei (McGuire et al., 1977; Mewaldt et al., 1983). In the thick-target model, the spallation products that accompany the production of gamma-ray lines, are slowed down in the denser solar atmosphere and hence are not expected to be observed in interplanetary space.

The scattering diagram suggests that the directivity of accelerated nuclei in the flare site varies from flare to flare. The directivity may depend on the configuration of magnetic field of the flare region. If the directivity is isotropic, both gamma-ray lines and accelerated nuclei should be observed. However, if most of the accelerated nuclei stream down to the chromosphere, only gamma-ray lines will be observed. For example, the 27 Apr., 1981 flare showed the significant gamma-ray line fluences, but did not show the apparent solar proton flux. No increase of solar protons associated with this flare was interpreted in terms of some particle confinement mechanism (Sakurai, 1983). This confinement mechanism asserts that most of accelerated nuclei were trapped for long time in the acceleration region and were little released into interplanetary space. On the contrary, if most of the accelerated nuclei move upward, only solar particles will be observed. For example, the 1 Feb., 1982

flare showed the appreciable solar proton flux, but did not show gamma-ray line emission. Another similar result was reported from the 9 Dec., 1981 flare (Cliver et al., 1983). These two flare data may indicate that the upward moving protons are so dominant that gamma-ray lines are not observed. Much more data of solar gamma-rays and protons are needed to establish the detailed relation between the gamma-ray line fluences and the peak solar proton fluxes.

The authors wish to acknowledge the Meteorological Satellite Center for providing the solar proton data. The authors thank Dr. T. Kohno for his analysis of solar proton fluxes.

#### References

- Chupp, E.L.: 1982, *Gamma-Ray Transients and Related Astrophysical Phenomena*, ed. R.E. Lingenfelter, H.S. Hudson and M.M. Worrall (American Institute of Physics, New York, 1982) p.363.
- Chupp, E.L.: 1983, *Solar Phys.* **86**, 383.
- Cliver, E.W., Forrest, D.J., McGuire, R.E., and von Rosenvinge, T.T.: 1983, 18th Int. Cosmic Ray Conf., Bangalore, **4**, 84.
- McGuire, R.E., von Rosenvinge, T.T., and McDonald, F.B.: 1977, 15th Int. Cosmic Ray Conf., Plovdiv, **5**, 54.
- McGuire, R.E., von Rosenvinge, T.T., and McDonald, F.B.: 1981, 17th Int. Cosmic Ray Conf., Paris, **3**, 65.
- Mewaldt, R.A., and Stone, E.C.: 1983, 18th Int. Cosmic Ray Conf., Bangalore, **4**, 52.
- Pesses, M.E., Klecker, B., Gloeckler, G., and Hovestadt: 1981, 17th Int. Cosmic Ray Conf., Paris, **3**, 36.
- Ramaty, R., Kozlovsky, B., and Lingenfelter, R.E.: 1975, *Space Sci. Rev.* **18**, 341.
- Sakurai, K.: 1983, 18th Int. Cosmic Ray Conf., Bangalore, **4**, 93.
- Yoshimori, M., Okudaira, K., Hirasima, Y., and Kondo, I.: 1983, *Solar Phys.* **86**, 375.
- Yoshimori, M.: 1984, *J. Phys. Soc. Jpn.* **53**, 4499.
- Yoshimori, M.: 1985, *J. Phys. Soc. Jpn.* **54**, 1205.

Table 1

No.	Date	Maximum Time (UT)	Location	H <sub>α</sub> / GOES
1.	1 Apr., 1981	0154	S43 W52	2B/X2.3
2.	4 Apr., 1981	0502	S44 W85	3B/X1.9
3.	27 Apr., 1981	0813	N15 W90	--/X5.5
4.	13 May, 1981	0418	N11 E58	3B/X1.5
5.	1 Feb., 1982	1402	S14 W09	3B/X2.6
6.	6 June, 1982	1633	S09 E25	3B/X12

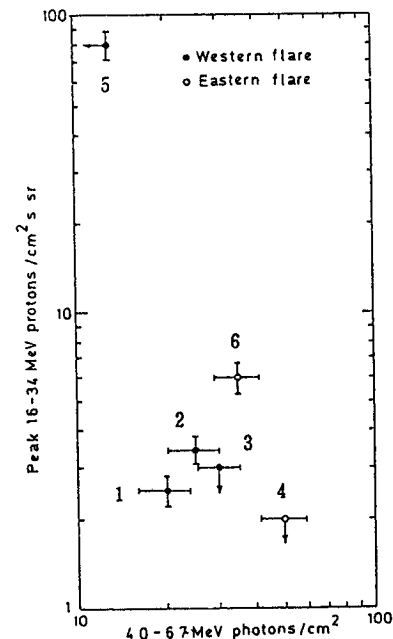


Fig. 1 Numbers attached to data correspond to flare numbers in Table 1.

## ENERGETIC PROTONS FROM A DISAPPEARING SOLAR FILAMENT

S.W. Kahler

Emmanuel College, Boston, Massachusetts 02115 USA

E.W. Cliver

Air Force Geophysics Laboratory, Hanscom AFB, Massachusetts 01731 USA

H.V. Cane\* and R.E. McGuire\*

Laboratory for High Energy Astrophysics, Goddard Space Flight Center  
Greenbelt, Maryland 20771 USA

R.G. Stone

Laboratory for Extraterrestrial Physics, Goddard Space Flight Center  
Greenbelt, Maryland 20771 USA

and N.R. Sheeley, Jr.

Naval Research Laboratory, Washington, D.C. 20375 USA

## ABSTRACT

A solar energetic ( $E > 50$  MeV) particle (SEP) event observed at 1 AU began about 1500 UT on 1981 December 5. This event was associated with a fast coronal mass ejection observed with the Solwind coronagraph on the P78-1 satellite. No metric type II or type IV burst was observed, but a weak interplanetary type II burst was observed with the low frequency radio experiment on the ISEE-3 satellite. The mass ejection was associated with the eruption of a large solar quiescent filament which lay well away from any active regions. The eruption resulted in an H $\alpha$  double ribbon structure which straddled the magnetic inversion line. No impulsive phase was obvious in either the H $\alpha$  or the microwave observations. This event indicates that neither a detectable impulsive phase nor a strong or complex magnetic field is necessary for the production of energetic ions.

1. Introduction. The conventional view of energetic (tens of MeV) solar particle acceleration is that it occurs only during flares in active regions (see Svestka (1981) for a general review). In many flares impulsive hard X-ray and microwave bursts indicate a rapid acceleration of electrons to energies of tens of keV. The  $\gamma$ -ray observations from the Solar Maximum Mission have shown that MeV ion production can also occur during the impulsive phase (Forrest and Chupp 1983). Acceleration of ions to tens of MeV then sometimes occurs in a subsequent "second phase" characterized by metric type II and type IV radio bursts and long-enduring soft X-ray and microwave events. The active regions producing these energetic flares are characterized by strong and complex magnetic fields, and the flares themselves are usually H $\alpha$  double ribbon structures (Svestka 1981).

Some exceptions to this conventional picture are known. The most convincing published example of a nonflare source for a prompt SEP event was discussed by Sanahuja *et al.* (1983). They attributed a  $1 < E < 15$  MeV SEP event to the disappearance early on 1979 April 23 of a large filament

\*Also: University of Maryland, College Park, Maryland 20742 USA

at least partially located in a small and weak active region. A pair of double-ribbon flares, one in McMath region 15956, accompanied the filament disappearance. However, they argued that the filament eruption, rather than the flares, was the important factor in this SEP event.

**2. Observations.** The SEP event of 1981 December 5 was observed with the GSFC cosmic ray experiment on the ISEE-3 spacecraft (Figure 1). The MeV electron onset was between 1415 and 1430 UT, followed by the proton onset between 1500 and 1530 UT. The velocity dispersion and rapid rise to maximum are evidence of an impulsive injection of particles from a well connected solar longitude. The 11-22 MeV proton flux measured by the Helios 1 spacecraft ( $\sim 13^\circ$  behind the west limb) on December 6 was a factor of 10 lower than that measured simultaneously by the GSFC experiment on IMP-8 at the Earth, consistent with our association of the SEP event with the disappearance of the disk filament, rather than with a source from behind the limb.

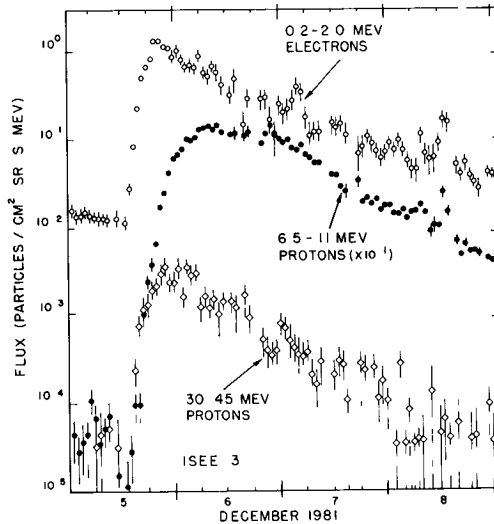


Figure 1. Flux-time plots of energetic particles for the SEP of 1981 December 5.

Several H $\alpha$  filtergrams obtained by the Haute Provence Observatory (provided courtesy of P. Simon) and reproduced in Figure 2 show the key times in the eruption of a large filament on 1981 5 December. The filament, located at  $\sim W35-45^\circ$ ,  $N15-30^\circ$  became active and began to erupt at  $\sim 1215$  UT. H $\alpha$  brightenings were first observed at 1315 UT, forming a classic double-ribbon pattern along the filament channel. The filament was not at the location of a former active region, and it lay at least 25 heliographic degrees from the nearest plage region.

Figure 3 shows the ejected filament and coronal material observed by the NRL white-light coronagraph (SOLWIND) on the P78-1 satellite. The first of these difference images shows that the coronal disturbance was not yet visible at 0658 UT, but was in progress during the next available image at 1447 UT. At this time the leading edge of the coronal material was already located at  $6.2 R_\odot$  in the northwest quadrant while the much smaller prominence was near the edge of the occulting disk at  $2.5 R_\odot$ . During the subsequent images the ejected coronal material left the  $2.5-10.0 R_\odot$  field of view, and the prominence moved uniformly outward in the plane of the sky. Its apparent latitude  $30^\circ$  north of west is consistent with the original location of the filament on the disk. From these observations, we found that the prominence was moving with a speed of  $305 \pm 20$  km/s in the plane of the sky. Extrapolated back to the  $0.65 R_\odot$  location of the disk filament, this speed gives a starting time of  $1329 \pm 0010$  UT, or approximately 1 hr after the disk filament began to disappear. This 1-hr time delay suggests that the erupting filament accelerated during the first hour after its initial disappearance from the H $\alpha$  spectral bandpass, as is usually observed for erupting prominences.

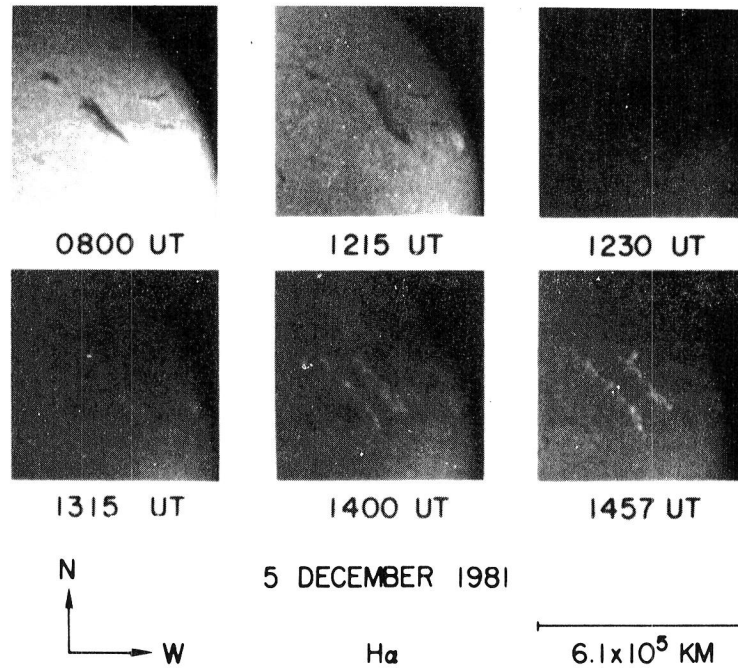


Figure 2. H $\alpha$  images from the Haute Provence Observatory showing the filament disappearance (top) and subsequent two-ribbon brightening (bottom) on 1981 December 5. Comparison of the top three images shows a clear outward motion of the northernmost part of the filament.

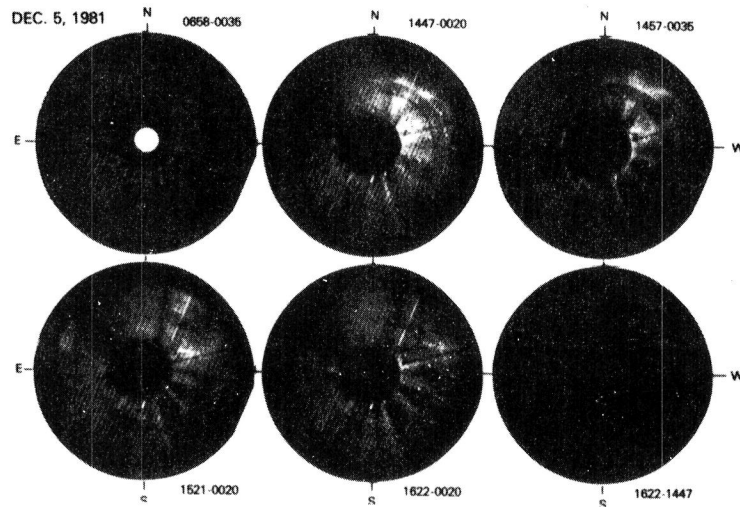


Figure 3. Subtracted images from the NRL Solwind coronagraph showing the CME of December 5. The H $\alpha$  filament can be seen as the small bright structure at the inner core of the CME.



No impulsive microwave or hard X-ray bursts accompanied the filament disappearance. There were, however, weak gradual soft X-ray and microwave events that appeared to accompany the eruption. A faint and very gradual GOES 1-8 Å enhancement began shortly after 1300 UT, rising from a C2.5 background to a peak level of only C3.5 at 1430-1450 UT. A gradual rise-and-fall event was observed in the Sagamore Hill Observatory 4995 MHz record beginning at ~ 1300 UT with a peak flux of  $21 \pm 3$  s.f.u. at ~ 1400 UT. Metric type III bursts observed from 1316 to 1326 UT were also detected in the ISEE-3 radio data, but these were not due to the filament activity because the deduced position of the 1980 kHz position was east of central meridian. An apparent shock-associated (SA) event (Cane *et al.* 1981) was observed at 1980 kHz in the ISEE-3 radio data from the end of the type III emission at about 1328 UT until 1352 UT. By tracking the centroid of the emission out to about 0.7 AU, we estimate that the source longitude for this event was in the range W10°- W40°, indicating a spatial as well as temporal association with the filament disappearance and CME. The SA event was followed by a weak interplanetary type II burst (Cane 1985).

**3. Discussion and Conclusion.** The  $E > 50$  MeV SEP event of 1981 December 5 has been associated with a filament disappearance well removed from any active region. The motion of the filament was observed in H $\alpha$  as shown in the second and third images of Figure 2 and later in the coronagraph images shown in Figure 3. Besides the filament disappearance, the prominent solar signatures of the December 5 event were the H $\alpha$  double-ribbon emission shown in Figure 2 and the accompanying weak gradual thermal soft X-ray and microwave event. The H $\alpha$  ribbons appear to be the footpoints of cool loop arcades overlain by hot soft X-ray loops.

In addition, we found no evidence of any impulsive phase microwave emission from this event. This indicates that neither active regions nor obvious impulsive phase phenomena are necessary for energetic particle production (cf. Cliver *et al.* 1983). The good association of SEPs with H $\alpha$  flares and with flare impulsive phase bursts is most likely not a direct cause-and-effect relationship but rather a manifestation of the Big Flare Syndrome (Kahler 1982), which states that, statistically, energetic flare phenomena are more intense in larger flares, regardless of the detailed physics.

**Acknowledgements.** This work was supported at Emmanuel College by AFGL contract AF 19628-82-K-0039, at NRL by NASA DPR W 14,429, and at GSFC/University of Maryland by NASA grant NGR 21-002316.

#### REFERENCES

- Cane, H.V. 1985, *J. Geophys. Res.*, **90**, 191.  
 Cane, H.V., *et al.* 1981, *Geophys. Res. Letters*, **8**, 1285.  
 Cliver, E.W., *et al.* 1983, *Astrophys. J.*, **264**, 699.  
 Forrest, D.J., and Chupp, E.L. 1983, *Nature*, **305**, 291.  
 Kahler, S. 1982, *J. Geophys. Res.*, **87**, 3439.  
 Sanahuja, B., *et al.* 1983, *Solar Phys.*, **84**, 321.  
 Svestka, Z. 1981, in *Solar Flare Magnetohydrodynamics*, ed. E.R. Priest (New York: Gordon and Breach), p.47.

# HELIOS I ENERGETIC PARTICLE OBSERVATIONS OF THE SOLAR GAMMA RAY FLARE EVENTS OF 7, 21 JUNE 1980 and 3 JUNE 1982

Frank B. McDonald, NASA Headquarters/Code P, Washington, DC 20546  
M.A.I. Van Hollebeke, Musee National des Sciences, Technique et Industrie  
PARC de La Villette, Paris, France  
James H. Trainor, NASA/GSFC, Code 600, Greenbelt, MD 20770

## ABSTRACT

The observed characteristics of the energetic particles associated with the solar  $\gamma$ -ray events of 3, 21 June 1980 and 3 June 1982 differ in several important aspects from the typical solar particle increases. They have flat energy spectra, are electron rich and have small precursor increases that begin some hours before the impulsive flare increase.

1. Introduction. Solar flare  $\gamma$ -rays and neutrons provide a direct means of determining the flux and energy spectra of those energetic particles accelerated by the flares which impact the lower coronae and photosphere (Ramaty et al., 1982, 1983; Chupp, 1984). The  $\gamma$ -ray time histories, when compared to those of x-rays, establish limits on the time required for particle acceleration. The flux and energy spectra of those flare accelerated particles which escape from the Sun can be determined by interplanetary observations. Comparing these two complimentary particle populations provides further understanding of the particle acceleration and transport processes in the flare region.

The Solar Maximum Mission Gamma Ray experiment of Chupp and his co-workers have made detailed observations of a number of solar  $\gamma$ -ray events (cf Chupp, 1984). Three of these flare increases are of special importance: 3 June 1982 and 21 June 1980 which are large intense  $\gamma$ -ray events that also produced a detectable flux of solar neutrons at 1 AU (Chupp et al., 1982, 1983); the 7 June 1980 event was more moderate in size, was accompanied by a small  $H\alpha$  flare, but the near simultaneity of the onset of  $\gamma$ -ray and soft x-ray emission implies that the particles are accelerated on a time scale of less than 2 seconds.

The Helios I spacecraft was in a favorable location at the time of each of these flares (Table 1). The small heliocentric distance

TABLE 1

SOLAR EVENT	FLARE LOCATION & $H\alpha$ CLASS	PEAK TIME FLARE IMPULSIVE PHASE (1)	HELIOS I HELIOCENTRIC DISTANCE	HELIO LONGITUDE SEPARATION (2)	PROTON SPECTRAL INDEX $\gamma$	ELECTRON/PROTON	Fe/O	He/H	$^3\text{He}/\text{He}^4$
3 June 1982	S09 E72 2B	1143 5	0 57 AU	3°	1 2 (3-200 MeV)	1 (3-6 MeV)	2 5± 5	132	02± 014
21 June 1980	N19 W88 1B	0118	0 54 AU	33°	2 6 (8-200 MeV)	0 25 (3-6 MeV)	0 9± 02	29	03± 013
7 June 1982	N12 W74 1B	0312	0 37 AU	14°	2 3 (3-30 MeV)	0 7 (1-2 MeV)	NOT OBSERVED	4	< 02

(1) Earth Observed Time

(2) Helio longitude Separation Between Helios I and Nominal Field Line

(Based on measured plasma velocity) Connecting to the Region of the Flare Site

between the spacecraft and the flare site significantly enhances the observations of the source region characteristics. The detailed observations of the energetic particles associated with these  $\gamma$ -ray flare events by the Goddard cosmic ray experiment on Helios I are presented in the following discussion along with their implication for the acceleration process. This present study builds on the previous reports based on both ISEE-3 and Helios I energetic particle data (Evenson, et al., 1980; Pesses et al., 1979; von Rosenvinge et al., 1981; McDonald and Van Hollebeke, 1985).

**2. Helios-I Energetic Particle Observations.** Both the 3 June 1982 and 21 June 1980 proton and electron data exhibit a "classical form" with a rapid rise to peak intensity followed by a relatively smooth exponential decay (Fig. 1). The peak fluxes at 50 MeV of 10.5 and 0.3 MeV protons mark these as moderate sized increases. For both events there is a definite precursor increase that begins some 3 hours before the major flare (McDonald and Van Hollebeke, 1985).

The time history of the 7 June 1980 event is remarkably different from those of the other two increases (Fig 2). The solar energetic particle time histories are complex and the peak intensities are small (Fig. 2). The 1-2 MeV electrons arrive promptly at  $\sim 0307$  (Helios time), have a step increase at  $\sim 0400$  and there is a new injection at  $\sim 0715$ . The integral electron channel for electrons  $> 250$  keV is a single parameter measurement which also responds to x-rays and  $\gamma$ -rays. The time history of these electrons indicate flare activity at  $\sim 0120$ ,  $0307$  and  $0715$ . The dashed line at  $0300$  (Helios time) is before the onset of the  $H_{\alpha}$  flare producing the gamma-rays observed by SMM. The 1.25-6 and 3.7-21 MeV proton channels both show a precursor event in progress at the time of the flare (Fig. 2a, 2b). Unlike the MeV electrons, the onset time for protons appears to be delayed until  $\sim 0400$  (the transit time is  $\sim 17$  minutes for 15 MeV protons and 31 minutes for 3.6 MeV protons). The sharp decrease that occurs in all proton channels between  $0400$  and  $0500$  appears to be produced by a change in declination of the interplanetary magnetic field of  $\sim 22^{\circ}$ . The proton anisotropies from

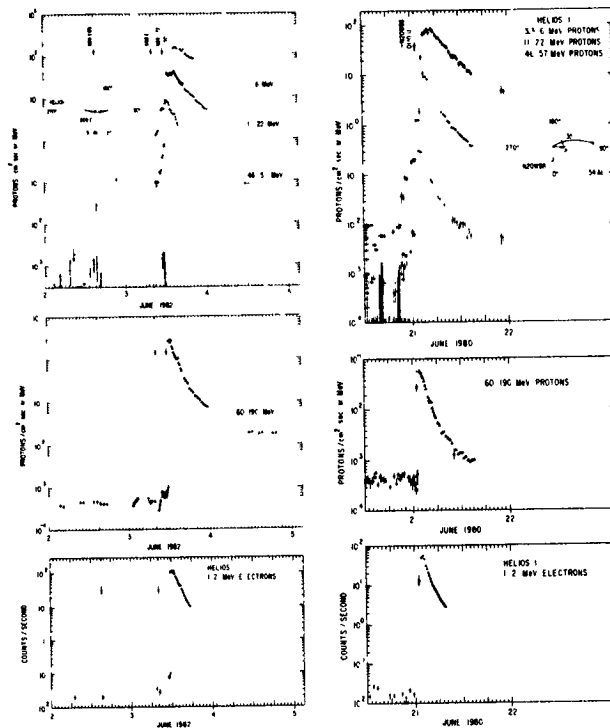


**Fig.1 Energetic particle time histories.** Vertical lines with arrows represent flare on-set times. The top insert shows the separation between Helios I and the nominal field line connecting to the flare site based on the measured plasma velocity.

3-20 MeV and 6-20 MeV are remarkably high from 0300-0900 so the observed proton intensities are very sensitive to the field direction. Fortunately the IP magnetic activity is usually quiet for this period and the field is in the plane normal to the spacecraft spin axis except for this deviation. There is also a new injection of 1.2-20 MeV protons at ~0720.

These three  $\gamma$ -ray events (Table 1) have flat-energy spectra, are electron rich, have high Fe/O ratios, no clear pattern for H/He but two contain modest amounts of  $^3\text{He}$ . Previous studies have shown that a significant fraction of the accelerated ions are confined at the flare site and have noted the high e/P ratio (Evenson et al., 1979, 1983; von Rosenvinge et al., 1979; Pesses et al., 1979; McDonald and Van Hollebeke, 1985). All three events are preceded by precursors some hours before the main event. In general, these precursor events would not have been observable at 1 AU.

**3. Discussion.** For the 3 June 1982 event the precursor can be identified with a flare in the same active region producing the primary event and extended to energies  $> 60$  MeV as well as MeV electrons. The time history for the precursor event is very different from that observed in the impulsive phase of the main event. Since the particle intensity and anisotropy are still increasing at the onset of the large flare and in view of the short transit time of the 1.5 MeV electrons, it is unlikely that there were significant changes in the interplanetary propagation conditions between the precursor event and the large event at 11:34. The slow continuing increase in energetic particles between 8:40 and 11:30 must reflect the effects of leakage from a coronal source region. For the June 21, 1980 event, the time history or the precursor proton increase is remarkably similar to that of 3 June 1982. The 7 June preflare increase resembles a pulse-like injection feature.

The precursor events described here imply that MeV ions (with energies extending to above 60 MeV along with MeV electrons in one case) are present in the corona prior to the onset of the main flare.

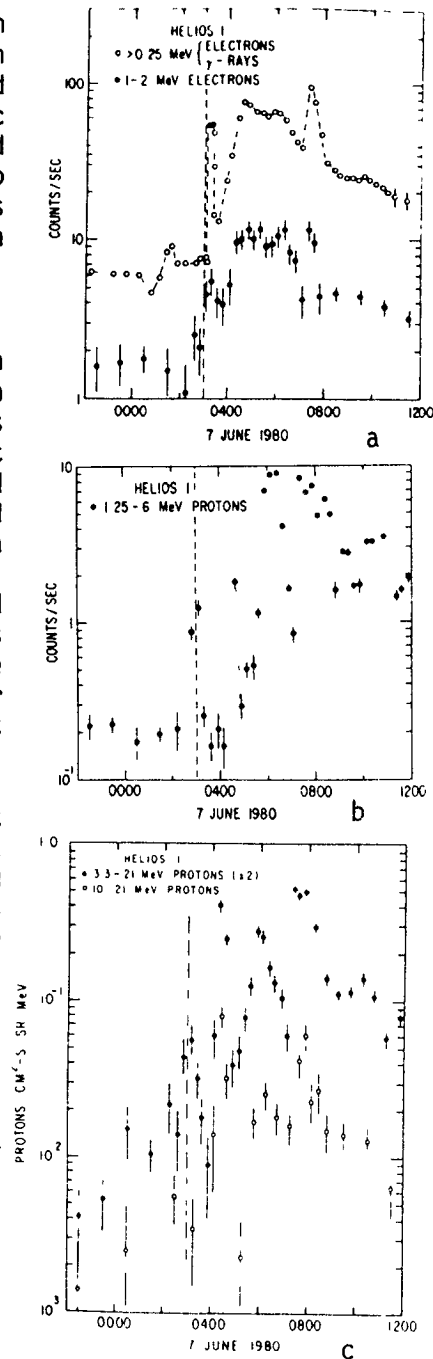


**Fig.2** Energetic particle time histories for 7 June 1980 events. The DASHED line represents the flare on-set time

The presence of these energetic particles allows the consideration of models where the impulsive phase and the resulting shock both further accelerate and precipitate this existing reservoir of stored energetic particles. The possibility of a continual acceleration process over the 3 hrs. prior to the main flare cannot be ruled out.

The problem of the storage of ions in magnetic loops has been examined by Zweibel and Haber (1983). They found that particles with small pitch angles at the top of the loop, i.e., particles that mirror closer to the photosphere, will be lost much more rapidly. Using their calculations, it is found that an average electron density,  $n_e < 10^8 \text{ cm}^{-3}$  is required if 5 MeV protons, mirroring near the top of the loop, are to lose  $< 2 \text{ MeV}$  in 2 hr. On this time scale, particle drifts become important but may be reduced by twisting the loop. The shock acceleration of these particles in a closed loop structure will preferentially increase the velocity component along the field line and lead to enhanced particle precipitation.

#### References

1. Block, G.M., and Kuzhevskii, B.M., (1979), Proc. 16th Internat. Cosmic Ray Conf. (Kyoto), 5, 1.
2. Chupp, E.L., et al. (1982), Ap.J. (Letters), 263, L95.
3. Chupp, E.L., Forrest, D.J., Kanbach, G., Share, G.H., DeBrunner, H., and Fluckiger, E. (1983), Proc 18th Internat. Cosmic Ray Conf. (Bangalore), 4, 75.
4. Chupp, E.L., (1984), Ann. Rev. Astr. Ap., 22, 359.
5. Evenson, P., Meyer, P., and Yanagita, S., (1981), Proc. 17th ICRC 3, 32.
6. Evenson, P., Meyer, P., and Pyle, K.R. (1983), Ap.J., 274, 875.
7. Forrest, D.J., and Chupp, E.L. (1983), Nature, 305, 291.
8. McDonald, F.B. and Van Hollebeke, M.A.I., (1985), Ap.J., 290, L67.
9. Pesses, M.E., Klecker, B., Gloeckler, G., and Hovestadt, D., (1981), Proc. 17th ICRC, 3, 36.
10. Ramaty, R., Lingenfelter, R.E., and Kozlovsky, B. (1982), in Gamma Ray Transients and Related Astrophysical Phenomena, ed. R. E. Lingenfelter et al. (New York: AIP), p.211.
11. Ramaty, R., Murphy, R.J., Kozlovsky, B., and Lingenfelter, R.E., (1983), Ap.J. (Letters), 273, L41.
12. Reinhard, R., and Wibberenz, G. (1974), Solar Phys., 36, 473.
13. Van Hollebeke, M.A.I., Ma Sung, L.S., and McDonald, F.B., (1975), Solar Phys., 41, 189.
14. von Rosenvinge, T.T., Ramaty, R., and Reames, D.V., (1981), Proc. 17th ICRC (Paris), 3, 28.
15. Zweibel, E.G., and Haber, D.A., (1983), Ap.J., 264, 648.

# INJECTION OF ENERGETIC PARTICLES FOLLOWING THE GAMMA-RAY FLARES ON JUNE 7, 1980, AS OBSERVED ON HELIOS-1.

Neustock, H.-H., Wibberenz, G., Iwers, B.  
Institut für Reine und Angewandte Kernphysik, Universität Kiel  
Olshausenstr. 40 - 60, 2300 Kiel, FR Germany

## ABSTRACT

On June 7, 1980, two flares with impulsive gamma-ray emission were observed at 0117 UT and 0312 UT. We present measurements of the University of Kiel cosmic-ray experiment on HELIOS-1. The first  $\sim 0.5$  MeV electrons escaped from the sun to interplanetary space simultaneously with the hard X-ray burst. For the 0312 UT flare the protons and  $\alpha$ -particle in the 3 - 20 MeV/nucleon range were injected from the sun with a delay of  $\sim 40$  min, followed by two subsequent new emissions.

1. Introduction. For a long time it was postulated in most models that the ion and relativistic electron acceleration takes place in the "second phase" of a flare, some ten seconds after the impulsive phase. But gamma-ray observations on SMM demonstrated (1) that these particles can be accelerated very rapidly and appear almost simultaneously with the non-relativistic electrons within time scales of seconds.

Correlations between the emission of hard electromagnetic radiation and the escaping energetic charged particles should give important clues for the acceleration mechanism. However, first studies showed that the number of nucleons escaping into space is only a small fraction of the number required to explain the observed gamma emission (2). A lack of correlation was found between the nuclear gamma emission of the flare and the size of the interplanetary proton events (3). These observations were explained by a highly variable ratio of particles moving upwards and downwards after acceleration, or by the existence of two independent populations.

In this paper we study the injection of energetic electrons, protons, and helium nuclei following a series of flares on June 7, 1980. The small distance of the HELIOS spacecraft to the sun and the unusually smooth interplanetary magnetic field allow a temporal resolution of the solar injection process which has not been reached before.

2. Observations. Energetic particle data were obtained with the University of Kiel cosmic ray experiment on HELIOS-1 (4,5). The instrument measures electrons with energies  $\gtrsim 0.3$  MeV, nucleons above 1.3 MeV/N in eight sectors each  $45^\circ$  wide in the ecliptic plane. For selected energy channels pulse height analysis allows particle identification and precise energy measurement for a representative sample of all incoming particles.

HELIOS-1 was in an ideal position to study the solar events on June 7, 1980, which occurred in Hale plage region 16886. The spaceprobe was located at 0.37 AU distance from the sun and was magnetically connected to a coronal region about  $2 - 11^\circ$  apart from the active region. Solar wind data indicate that HELIOS-1 was inside a "hole" in the solar

wind (Schwenn, private communication). The interplanetary magnetic field (courtesy F.M. Neubauer, G. Musmann) was exceedingly smooth. As a consequence, solar energetic particles arrive totally collimated and were practically confined to the sector which contained the magnetic field direction leading towards the sun. This allows to reduce the isotropic background considerably and to reconstruct directly the injection profile at the sun.

Figure 1 shows three minute averages of the particle intensities from the solar oriented sector for a 12 hour period on June 7. Time and location of the three solar flares are given in the inserts in the upper panel. The first two flares are also observed at  $\gtrsim 0.3$  MeV gamma energies, the third one is not. It is remarkable that this event shows the largest intensity in electrons. Because of the scatter free interplanetary propagation we can directly construct the total number of injected particles by integrating the observed directional intensities over time. The total electron numbers for the three events vary as 1:6:29. In contrast, the X-ray emission in the 1.6 to 12.4 keV range varies as 1:3:0.2.

In Figure 2 we have corrected for the interplanetary travel time of each particle group by subtracting  $t = s/v$  from the time of observation. Here  $s$  is the curved path length along the smooth interplanetary magnetic field spiral, as determined from the measured solar wind speed. The velocity  $v$  is determined from identification and energy measurements of the various particles. Results are plotted as a function of "solar release time" (SRT). Earth bound electromagnetic observations have been corrected accordingly. On this scale, the emission of electrons and X-rays occurs simultaneously, whereas for the first two flares the protons are delayed. In case of the 0315 flare we also find a multiple injection, with the first proton injection starting at 0345 SRT, the second at 0440 SRT. The last release at 0635 SRT is superimposed by a fresh injection of particles from the 0725 flare. In this case, protons and electrons are injected simultaneously and also coincident with the optical flare.

The temporal relation between X-ray and electron emission for the three flares is shown on an extended time scale in Figure 3. It shows that within about one minute the electron injection onset matches the impulsive X- and gamma-ray emission of the flare which marks the particle acceleration. The number of injected electrons has reached their maximum ( $I_{\max}$ ) in several minutes, but the injection lasts in any case much longer than the electromagnetic emission (see Figure 2). The steps in the electron onset in Figure 3 correspond to the temporal resolution of the data transmission of HELIOS at the time of observation. The uncertainty in fixing the release time by uncertainties in the path length is below one minute.

Figure 4 shows the injection of nucleons of different energy/nucleon, ordered from top to bottom with decreasing velocity. For the three separate injections following the 0315 flare we find that higher energy nucleons are injected later. This inverse velocity dispersion is not observed for the 0725 flare. Here nucleons are released simultaneously with the electrons.

Energy spectra can be fitted by power laws in kinetic energy over the range of observation (see Table 1). The electrons resulting from the gamma-flares show a harder spectrum. This is in accordance with results in (6). We see that also the proton energy spectrum for the 0725 flare which was not accompanied by gamma-rays is steeper than the first injections for the other cases. For the three consecutive injections following the 0315 flare the spectrum steepens from one injection to the next.

In summary, we find the following observations:

- (1) The  $\sim 0.5$  MeV electrons are released simultaneously with the hard X-ray bursts for all three events, within the temporal uncertainty of about one minute.
- (2) The electron injection continues for 15 - 20 minutes, much longer than the duration of the X-ray bursts.
- (3) There is no correlation between the number of electrons in interplanetary space and the emission in 1 - 8 Å X-rays or  $\gtrsim 0.3$  MeV gamma-rays.
- (4) For the flares at 0118 and 0315 nucleons are released from the sun with a considerable delay.
- (5) We find repeated injections of nucleons after the 0315 flare. For each of the three subsequent injections the proton spectrum gets steeper.
- (6) After correcting for interplanetary travel times we find that the injection starts later for nucleons of higher energy/nucleon.

3. Discussion. The delayed emission of nucleons confirms the view that the nucleons observed in interplanetary space need not be identical with the component responsible for the gamma-ray generation. Nevertheless the emitted nucleons may have been accelerated simultaneously with a gamma producing component, followed by storage in closed magnetic field regions with subsequent repeated release, possibly connected to the bird cage model (7). However, in this model the immediate release of electrons would be hard to understand. An alternate explanation for two independent populations is the acceleration of nucleons by a coronal shock wave. A type-II radio burst suggestive for a coronal shock had been observed after the 0312 flare, but not for the 0725 flare. In this event not accompanied by gamma-ray production the release of electrons and nucleons occurs simultaneously.

4. Acknowledgements. We are grateful to all members of the HELIOS team at the University of Kiel, principal investigator H. Kunow, who contributed to the success of the cosmic ray experiment. Unpublished X-ray data from the SMM gamma-ray experiment (see Figure 3) have been kindly supplied by E. Rieger, Garching. This work was supported by the German Bundesminister für Forschung und Technologie.

#### References

- (1) Chupp, E.L. et al., Ap. J. 244, L171-L174, 1981.
- (2) Von Rosenvinge, T.T. et al., Proc. 17th ICRC, 3, 28-31, 1981.
- (3) Cliver, E.W. et al., Proc. 18th ICRC, 4, 84, 1983.
- (4) Kunow, H. et al., Raumfahrtforschung 19, 253-258, 1975.
- (5) Kunow, H. et al., BMFT-FB-W81-016, 1981.
- (6) Evenson, P. et al., Ap. J. 283, 439-449, 1984.
- (7) Newkirk, G., and Wentzel, D.G., J. Geophys. Res. 83, 2009-2015, 1978.



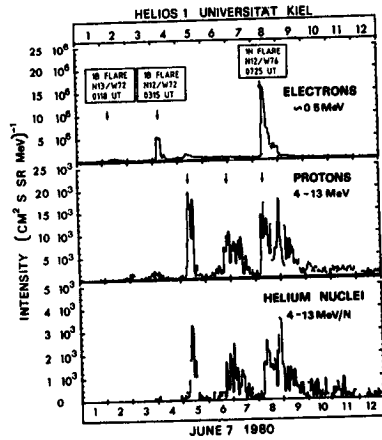


Figure 1: Particle intensities from the solar direction on a linear scale.

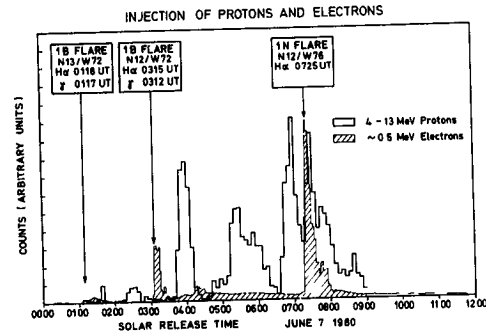


Figure 2: Solar injection of electrons and protons after correction for interplanetary travel time along the smooth interplanetary magnetic field. Solar Release Time (SRT) = UT - s/v.

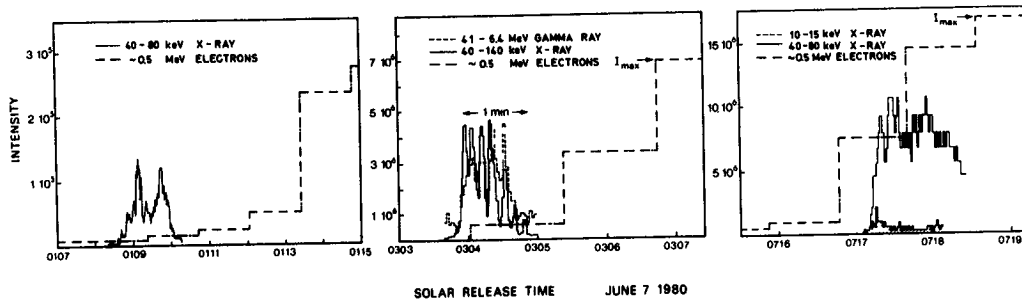


Figure 3: Temporal correlation between hard electromagnetic radiation and the release of relativistic electrons.

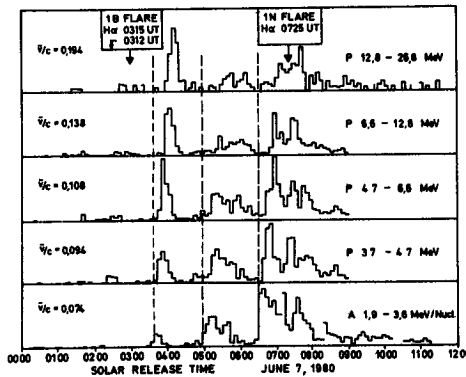


Figure 4: Energy dependence of solar release of protons (P) and Helium nuclei (A). The energy range is indicated on the right side. The dashed vertical lines give the injection onset for the lowest velocity channel.

Particle type	time interval	spectral index
electron (0.3 to 4 MeV)	0113 - 0154 UT	$3.50 \pm 0.11$
	0307 - 0330 UT	$3.48 \pm 0.07$
	0720 - 0804 UT	$3.93 \pm 0.05$
proton (4 to 37 MeV)	0138 - 0317 UT	$2.29 \pm 0.25$
	0416 - 0449 UT	$2.67 \pm 0.13$
	0513 - 0646 UT	$3.04 \pm 0.15$
	0712 - 0745 UT	$3.66 \pm 0.24$
	0745 - 0858 UT	$3.18 \pm 0.13$

Table 1: Spectral indices for a power law fit of the measured spectra. Proton spectra: The second to fourth time interval represent the three injections following the 0315 flare.

ULTRARELATIVISTIC ELECTRONS AND SOLAR FLARE  $\gamma$ -RADIATION.

P.E.Semukhin, G.A.Kovaltsov

Ioffe Physico-Technical Institute Academy of Sciences  
of the USSR, 194021 Leningrad, USSR

About ten solar flares accompanied with  $\gamma$ -radiation with the quantum energy  $>10$  MeV have been observed by now [1]. Practically all these flares took place within the heliolongitude  $\lambda > 60^\circ$ , i.e. close to the solar limb, which is indicative of an essential anisotropy of high-energy  $\gamma$ -radiation. Such radiation may be generated on one hand, by the decay of  $\pi^0$ , produced by nuclear interactions of accelerated protons with the matter of solar atmosphere. On the other hand, it may be generated by the deceleration of ultrarelativistic electrons in the solar atmosphere. The directivity diagram of  $\gamma$ -radiation during the  $\pi^0$ -decay is rather wide. Accordingly, in order to explain the anisotropy of radiation we must postulate a monodirectional beam of energetic protons moving towards the Earth parallel to the solar surface [2,3]. It is evident that in a major flare, the spectrum of accelerated protons being hard enough, the radiation produced by the  $\pi^0$ -decay may be predominant for high-energy radiation, the instance of which must have been the flare on 3.06.82 [3,4]. However, we think that the distribution of flares along heliolongitude is determined by the fact that in most cases the major part of radiation was generated by ultrarelativistic electrons. The bremsstrahlung of an ultrarelativistic electron with an energy  $E$  is concentrated in a narrow cone  $\sim E/m_e c^2$ . Accordingly the intensity of radiation emitted in a definite direction depends only on the thickness traversed by electrons in this direction. It is common knowledge the evolution of solar flares starts in closed magnetic arcs. Such arcs are the traps for energetic charged particles. Accelerated electrons will oscillate between two bottoms of the arc. They move parallel to the solar surface near the mirror points traversing maximum thickness in unit time, because

ambient density increases with depth. Thus the accelerated electrons regardless of its pitch-angle at the arc top generate  $\gamma$ -radiation of maximum intensity along the solar surface tangential line. For this reason the radiation will be anisotropic provided that the acceleration of electrons at the arc top is isotropic.

For the quantitative analysis of the model in question we have calculated the  $\gamma$ -radiation of ultrarelativistic electrons decelerating inside the magnetic arc. The coronal part of the arc was assumed to be semitoroidal with the radius of the axis line  $R$ , a magnetic field  $B_0$  and the ambient density  $n_a$ . At either bottom of the arc the field is directed along the solar radius and increases with depth:  $B=B_0(1+Z/Z_0)$ ; the density is  $n=n_0 \exp(Z/h)$ .  $Z$  being equal to 0, the density goes up ( $n_0 \gg n_a$ ) which corresponds to the transition region "corona-chromosphere". The calculation includes ionization and synchrotron energy loss of electrons. To simplify the calculation a loss cone  $\alpha_{\min}$  was introduced ( $\alpha$  is the pitch-angle at the arc top). Its value is so large that the electron trapped in the arc loses a minor part of its energy at one bounce. Fig. 1 gives an example of the calculation of the temporal behaviour of radiation with the quantum energy  $\xi=10$  MeV in the case of isotropic instantaneous injection of accelerated electrons at the arc top. The spectral index of power law injection spectrum  $\gamma_e=3.5$ . It is evident that the radiation is highly anisotropic during the first 10-20 sec. Within this period the intensity falls by 10-50 times and the radiation becomes unobservable at the contemporary level of experimental technique. This result corresponds to the observed duration of  $\gamma$ -ray impulses [1,5]. It is worth mentioning that the decrease of the loss cone increases the anisotropy of  $\gamma$ -radiation and steepness of the impulse fronts. Fig. 2 shows the radiation directivity at the moment of impulse maximum, the model parameters varying in value. It is evident that the radiation intensity from the limb to the center of the solar disk falls by 20-100 times. The radiation intensity of a major

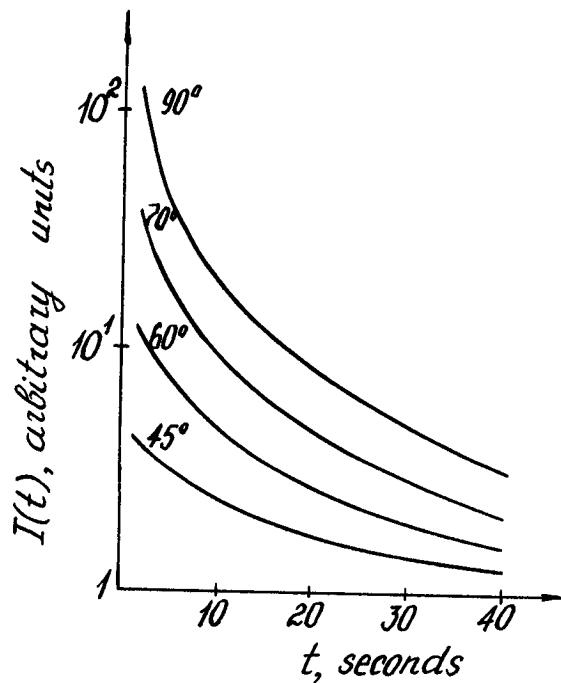


Fig. 1  
Temporal behavior of  $\gamma$ -radiation with the quantum energy of  $>10$  MeV for an instantaneous injection of accelerated electrons into the arc with the parameters:  $h = 2 \cdot 10^7$  cm,  $Z_0/h = 4$ ,  $R = 10^9$  cm,  $n_d = 10^{11} \text{ cm}^{-3}$ ,  $n_o = 10^{12} \text{ cm}^{-3}$ ,  $B_0 = 500$  the loss cone  $\cos \alpha_{\text{min}} = 0,8$ . Helio-longitude of the flare is indicated above the curves.

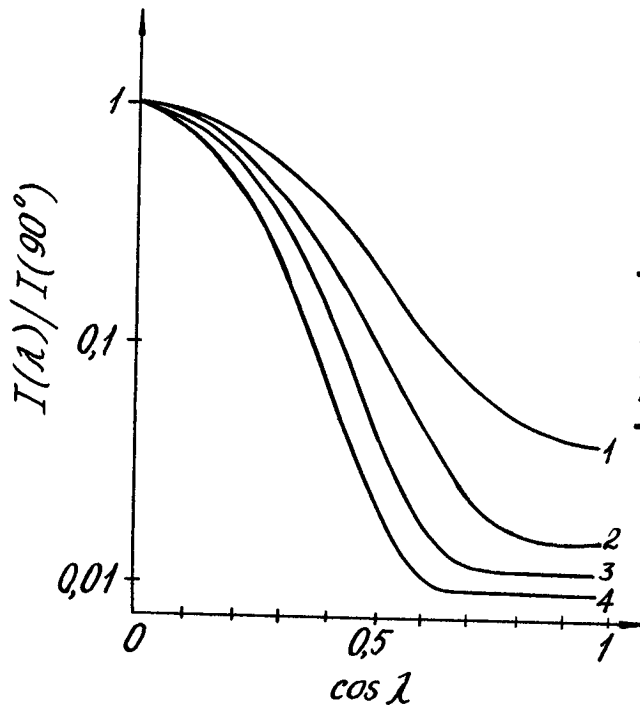


Fig. 2  
The radiation intensity at the moment of impulse maximum in variation with heliolongitude.

	$Z_0/h$	$\cos \alpha_{\text{min}}$
1.	1	0,94
2.	4	0,8
3.	8	0,68
4.	12	0,6

The other parameters correspond to those in Fig. 1.

flare that took place on 21.06.80 on the limb, would have been lower or comparable on the disk with the threshold of response of modern equipment.

In calculating the  $\gamma$ -radiation of the flare on 21.06.80 within the range of 0,2-1 MeV a complete number of accelerated electrons was obtained,  $N_e(>1 \text{ MeV})=5 \cdot 10^{33}$ , the index of spectrum being  $\gamma_e=3,5$  [6]. Extending this spectrum into higher energies,  $\gamma_e$  being constant, we calculated the  $\gamma$ -ray fluence with the quantum energies  $> 10 \text{ MeV}$  which corresponds to the observed value  $F_\gamma(>10 \text{ MeV})= 18 \text{ cm}^{-2}$  [1], the model parameters being equal to those in figure 1. The electron spectrum in interplanetary space during the flare on 21.06.80 was power law,  $\gamma_e$  being constant within the range of energies 0,5-20 MeV [7]. This fact justifies our extrapolation of the electron spectrum. During this flare only  $\sim 10\%$  of high-energy electrons escaped the solar atmosphere [7], which confirms our assumption that electrons are trapped by the magnetic arc in the solar atmosphere.

Thus the observation data of high-energy  $\gamma$ -radiation of flares can be explained by the specific features of the bremsstrahlung of ultrarelativistic electrons trapped within the magnetic arc even if the acceleration of electrons is isotropic.

### References.

1. E.Rieger et al. Proc. 18-th ICRC, 1983, v.4, p.83.
2. G.E.Kocharov, N.Z.Mandzhavidze, Pis'ma v AZh, 1984, v.10, p.771.
3. G.E.Kocharov, N.Z.Mandzhavidze, Izv.ANSSSR, ser.fiz., 1984, v.48, p.2212.
4. R.Ramaty, R.J.Murphy, Proc. Plasma Astrophysics school and workshop, Varenna, 1984, p.83.
5. E.L.Chupp, Solar Phys., 1983, v.86, p.383.
6. G.A.Kovaltsov, G.E.Kocharov, Preprint FTI AN SSSR, 1982, N.799.
7. P.Evenson et al. Astrophys.J., 1984, v.283, p.439.

# SOURCE ENERGY SPECTRA FROM DEMODULATION OF SOLAR PARTICLE DATA BY INTERPLANETARY AND CORONAL TRANSPORT

J. Pérez-Peraza\*, M. Alvarez-Madrigal\*, and F. Rivero\*  
Instituto de Geofísica, UNAM, 04510- C.U., México 20, D. F., MEXICO

L. I. Miroshnichenko  
IZMIRAN, Troitsk, Moscow Region, 142092, USSR

1. Introduction. The data on source energy spectra of solar cosmic rays (SCR), i.e. the data on the spectrum form and on the absolute SCR are of great interest at least for three reasons: 1) the SCR contain the energy comparable to the total energy of electromagnetic flare radiation ( $\leq 10^{32}$  ergs); 2) the source spectrum form indicates to a possible acceleration mechanism (or mechanisms); and 3) the accelerated particle are efficiently involved in nuclear electromagnetic and plasma processes in the solar atmosphere. Therefore the data on SCR source spectra are necessary for theoretical description of the processes mentioned and for the formulation of the consistent flare model. Below it is attempted to sound solar particle sources by means of SCR energy spectrum obtained near the Sun, at the level of the roots of interplanetary field lines in the upper solar corona. We consider data from  $\sim 60$  solar proton events (SPE) between 1956-1981 [1]. These data were obtained mainly by the interplanetary demodulation of observed fluxes near the Earth. Further, we used our model of coronal azimuthal transport to demodulate those spectra, and to obtain the source energy spectra.

2. Interplanetary Demodulation. Several methods are used for the interplanetary demodulation of SCR fluxes observed near the Earth. Most of them are traditionally based on the different modifications of the diffusion model of the full transport equation. In addition, at present the possibility exists to reconstruct the source spectrum by the gamma-ray and flare neutron data. The diffusion methodics of interplanetary demodulation was described in detail in another works [2, 3]. This methodics rest upon the extrapolation of intensity time profiles of SCR fluxes observed near the Earth to the momentum of their injection from the solar corona. Each of modifications of such a methodics is applicable only to a limited time interval or to a limited range of particle energy. Besides that, our Catalogue [1] contains some discrepancies and gaps in spectrum parameter estimations obtained by the different researchers. Because of these reasons we were able to use for the coronal demodulation only the data of 26 events.

3. Coronal Demodulation. The coronal transport model of solar flare particles was discussed in [4] and extensively described in [5]. Basically two transport steps take place in azimuthal coronal transport of particles: (a) a velocity-independent transport in a fast propagation region (FPR) which is associated with an expanding magnetic structure, (b) an energy-dependent transport in a low propagation region (LPR), dominated by transversal diffusion, drifts and gradual escape into the interplanetary space. The initial condition for the 2nd transport state, when particles are globally liberated from the FPR, at  $t=0$  is  $N(X,0)=N_a(E)/X_0$ , if  $X$  is within the width  $X_0$  of the FPR centered at the flare site, and  $N(X,0)=0$  elsewhere, where  $N_a(E)$  is the flare source energy spectrum. The azimuthal evolution of the number density of particles at time  $t$  and position  $X$  during the 2nd transport step is [4, 5].

\*On leave for the INAOE, Tonanzintla, A.P. 51. 72000-Puebla, México

$$\begin{aligned}
N(X,t) = 2.5N_a \exp(-\Gamma t - \frac{(X-v_d t)^2 + (X_o/2)^2}{8\kappa_\ell t}) \{ \exp[-\frac{(X-v_d t)(X_o/2)}{4\kappa_\ell t} + \\
\frac{(X-v_d t - X_o/2)^2}{8\kappa_\ell t}] \operatorname{erf}(\frac{X-v_d t - X_o/2}{(4\kappa_\ell t)^{0.5}}) - \exp[-\frac{(X-v_d t)(X_o/2)}{4\kappa_\ell t} + \\
\frac{(X-v_d t + X_o/2)^2}{8\kappa_\ell t}] \operatorname{erf}(\frac{X-v_d t + X_o/2}{(4\kappa_\ell t)^{0.5}}) \} \quad (1)
\end{aligned}$$

where  $\kappa_\ell$  and  $v_d$  are the transversal diffusion coefficient and drift velocity. Here after we will refer our results to the flare position ( $X_f$ ), such that  $X_i = X - X_f$ . For coronal demodulation we adopted the following procedure. We assume that the observed particle flux proceeds from a coronal longitude at  $\sim 60^\circ W$ ; so, at the coronal level the observed flux corresponds at the position  $X_c = X(60^\circ W) - X_f$ , and an ejection time from the corona ( $t_e$ ) given as  $t_e = 0$  if  $|X_c| \leq X_o/2$  and  $t_e = |X_c|/v_d$  if  $|X_c| > X_o/2$ ; next we equate (2) with the demodulated energy spectra  $N(E)$  from [3], [that for the task of simplicity we translated from rigidity to kinetic energy, Figs.(1) and (2)]:

$$2.5N_a(E)f[X_c, t_e, v_d(E), \kappa_\ell(E), X_o] = N(E) \text{ (part/MeV)} \quad (2)$$

so that the source energy spectrum  $N_a(E) = N(E)/2.5f[X_c, t_e, v_d, \kappa_\ell, X_o]$ , where the function  $f$  has been normalized. Once we have determined  $N_a(E)$  (part/MeV) we build the time-profiles by fixing the positions  $X_i$  and energy  $E_i$  in eq.(1), and making vary time relative to  $t_{on}$ ,  $(t - t_{on})$ , where  $t_{on} = (|X_i|/v_d) - X_o/2$  is the onset time of particle arrival at that particular position  $X_i$ , so that the time-origin occurs at  $t = t_{on}$ . The coronal time-profiles were built for several coronal positions and energy values. To build the particle azimuthal distributions we fixed energy and time in eq.(1) and evaluated for  $X_i \leq \pm 180^\circ$  taking the flare position as the coordinate-origin. Further, we evaluated for other times and different energies. For calculations we assumed for the FPR, an azimuthal width at its opening of  $80^\circ$  at  $0.9 R_\odot$  above the photosphere. For  $v_d = (60-250)\beta^2/(1-\beta^2)^{0.5}$  (cm/s) depending on whether the observational peak intensity was very late or early respectively, where  $\beta = v/c$ ,  $v$  and  $c$  are the particle and light velocities. We used  $\kappa_\ell = 6.7 \times 10^6 v$  (cm<sup>2</sup>/s). For the task of illustration we have chosen an event which FPR contains the connecting position  $X_c$  (23/VI/1956) and other which FPR does not contain  $X_c$  (22/VIII/1958). On the next figures we have illustrated linear azimuthal positions  $X_i$  in terms of angular coordinates  $\psi_i$ ; on Fig.(2) we show along with the demodulated spectrum the energy spectra that we have built for two others coronal longitudes. On figures(3)-(8) it is shown the azimuthal distributions of both events for several times at three different energies. It can be observed that the observational W-E asymmetry is confirmed by our results: the higher the particle energy the sharper the effect. Theoretically this is the translation of particle drift in the model. On figs. (9)-(11) it is show the time profiles of

the event for which  $X_c$  is outside of its FPR, for 3 different energies and several longitudinal positions. Out of the FPR profiles show the characteristic diffusive shape, whereas at locations within the FPR they show a peculiar decreasing shape. On Fig. (12) it is shown the regression in time from the corona back to the top of the FPR: since regression in time is equivalent to regression in distance to the FPR, for a given value of  $\psi$  any other  $\psi'$  such that  $\psi_f < \psi' < \psi$  can be seen as a time regression toward the time of particle liberation from the FPR. In fact time profiles at  $\psi_f \pm 40^\circ$  begin at  $t=0$ . Out of the FPR the onset is delayed proportionally to the distance from the flare site, such as indicated by observations. Fig. (13) shows the west-asymmetry effect relative to the profile on Fig. (9): at  $50^\circ$ -distance from the flare on the East side there is more of  $10^2$  time less particles than at the same distance on the West side, and at  $60^\circ$ -distance the flux has fallen to negligible levels relative to the West side. On figs. (14)-(16) we show time profiles for the 23/11/1956 event. Concerning source energy spectra, it is obvious that according to the coronal transport model the observational and the source spectra are basically the same when the FPR contains the connection longitude. So, among the studied 26 events, only in 8 events the FPR does not contain  $X_c$ . We have tabulated on Table 1, the source spectra characteristics of these 8 events along with one (23/11/1956) of the remaining 18 events where  $N_a = N(E)$ . On Fig. (17) we show the source spectrum  $N_a = D_0 E^{-\gamma} = 4.18 \times 10^{45} E^{-6.36}$  (part./MeV) of the 22/VIII/1958 event. Finally, on Fig. (18) it is illustrated the source spectrum  $N_a / \delta \psi_f$  (part./MeV cm) under the assumption of a finite flare width  $\delta \psi_f = 8^\circ$  and the spectrum at the top of the FPR at  $t=0$ ,  $N(X, t, E) = N_a / X_0$  (part./MeV cm).

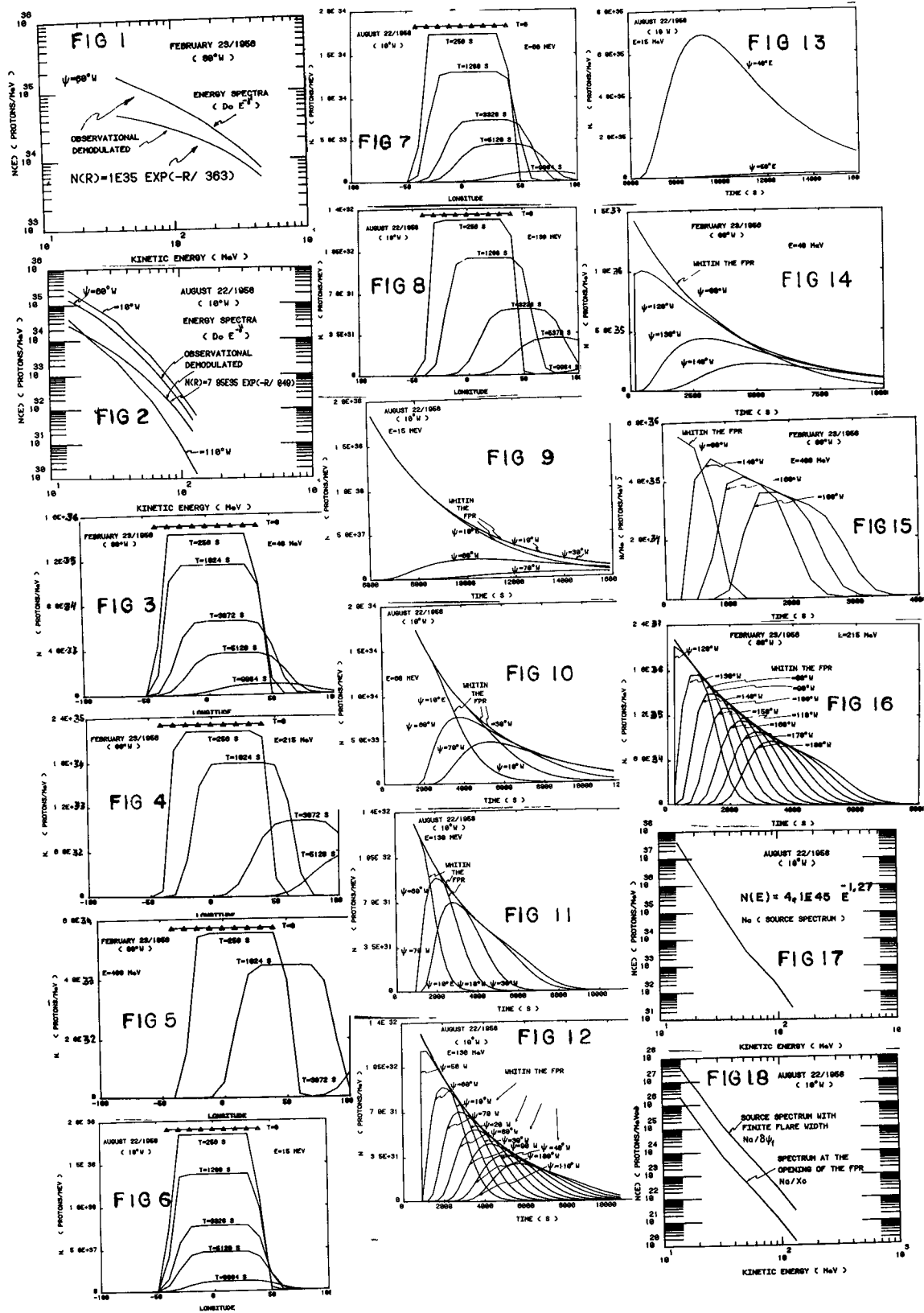
4. Conclusions. Though results are model-dependents they furnish a clear picture of the evolution of particle energy spectra from the source till their ejection into the interplanetary space, for those events where the observational-connecting-longitude is out of the FPR: it can be seen in Table 1 that energy spectra flattens at the coronal level relative to the source spectra; when particles move in the W-E direction, as in the 1/IX/1971 event, the change in spectrum slope is more important. It is interesting to analyze our results within the frame of the observational effects and model predictions summarized in [5]. We believe that this approach must be taken into account within the frame of solar particle acceleration theory and solar flare phenomena, such as for the evaluation of flare neutrons and electromagnetic radiation of non-thermal origin.

#### References

- [1] Miroshnichenko, L. I., Preprint IZMIRAN, 15, 548, 1985.
- [2] Miroshnichenko, L. I., Geomagn. and Aeron. 13, 26, 1973.
- [3] Miroshnichenko, L. I. et al., Dynamics of Radiation Conditions in Space, Energoatmizdat, Moscow, 1985 (with Petrov V M.)
- [4] Pérez-Peraza, J. and Martinelli, J., Proc. 17th Int. Cosmic Ray Conf. 3, 55, 1981. and Pérez-Peraza J. in
- [5] Invited Lecture, 9th European Cosmic Ray Symposium, Kosice, 1985.

C O R O N A L				S O U R C E			
				$N_a$			
E V E N T	L O N G I - T U D E	R A N G E MeV	$D_0$ PART/MeV	$\gamma_E$	$D_0$ PART/MeV	$\gamma_E$	
23/02/1956	23N80W	35 - 480	$2.10E37$	1.27	$2.1E37$	1.27	
22/08/1958	18N10W	15 - 115	$5.77E30$	3.74	$4.1E45$	6.36	
03/09/1960	18N89E	10 - 410	$2.91E36$	2.02	$1.4E53$	8.76	
28/09/1961	13N29E	15 - 470	$1.97E30$	3.20	$4.6E53$	8.76	
28/01/1967	150E	75 - 410	$5.16E34$	1.25	$1.1E40$	3.11	
29/09/1968	13N13W	10 - 160	$1.04E34$	1.49	$2.8E43$	5.76	
01/09/1971	12N130W	10 - 55	$1.43E30$	2.25	$4.9E45$	6.33	
28/05/1972	09N30E	30 - 75	$1.22E37$	2.62	$4.1E40$	4.14	
23/11/1956	-	30 - 120	$1.00E34$	2.20	$2.6E38$	4.03	





# SPECTRA OF SOLAR PROTON GROUND LEVEL EVENTS USING NEUTRON MONITOR AND NEUTRON MODERATED DETECTOR RECORDINGS

P.H. Stoker  
PU-CSIR Cosmic Ray Research Unit  
Department of Physics  
Potchefstroom University for CHE  
POTCHEFSTROOM 2520  
South Africa

## ABSTRACT

Recordings on relativistic solar flare protons observed at Sanae, Antarctic, show that the percentage increase in counting rates of the neutron moderated detector (4NMD) is larger than the percentage increase in counting rates of the 3NM64 neutron monitor. These relative increases are described by solar proton differential spectra  $j_s(P) = AP^{-\beta}$ . The power  $\beta$  is determined for each event and the hardnesses of the temporal variations of  $\beta$ , found for the GLE's of 7 May, 1978 and 22 November, 1977, are related to the results of Debrunner et al. (1980).

1. Introduction. Neutron monitors record at ground level solar protons of energies  $\lesssim 0.5$  GeV, while satellite data generally covers the energy range below 0.5 GeV. Debrunner et al. (1984) combined the two sets of observations for the solar proton events on 7 May, 1978 and 22 November, 1977, and deduced for various phases the solar proton energy spectra from 50 MeV to about 10 GeV.

These two events and several other solar proton events were recorded during the present solar cycle at Sanae with a cutoff rigidity of 0.86 GV in Antarctica. When looking at an event from only a single position on Earth, a particular spectral function has to be assumed in order to deduce the spectrum of solar protons entering the atmosphere. Since rigidity is the appropriate parameter for the combined effect of protons,  $\alpha$ -particles and heavier particles for earth bound recordings, a rigidity dependent spectral function was considered. A power law rigidity spectrum  $j = AP^{-\beta}$  appears to fit the spectra given by Debrunner et al. (1984) in the rigidity range  $\sim 0.5$  GV - 10 GV better than the exponential rigidity spectrum  $j = A \exp(-P/P_0)$ .

The neutron moderated detector 4NMD and super neutron monitor 3NM64 record at Sanae primary cosmic rays with different rigidity dependent sensitivities. In order to derive solar proton spectra for ground level events from these recordings, the specific yield functions of these two detectors have to be obtained accurately for rigidities  $\lesssim 1$  GV. Solar proton ground level events recorded at Sanae during the present solar activity cycle are analyzed accordingly in this paper.

2. Method. A specific yield function was computed for each detector from  $S(P) = n(P,t)/j(P,t)$ . The primary differential rigidity spectrum  $j(P,t)$  was obtained from the 1965 cosmic ray proton and helium particle spectra compiled by Webber (1973), while the differential response functions  $n(P,t)$  were deduced from a least square fitting (Van der Walt, 1983) of the Dorman function  $N(P) = N_0(1 - \exp(-\alpha P^{-k}))$  to the data of the 1976 sea level survey (Potgieter et al., 1980). The differential response functions for the NMD

and NM64 thus obtained were applied to reproduce correctly the relative counting rates recorded for the 15 February, 1978 Forbush decrease (Stoker and Louw, 1983).

If  $j_s(P,t)$  represents the primary solar proton differential spectrum, the enhanced counting rate due to a solar proton GLE is given by

$$\Delta N_s(P,t) = \int_{P_c}^{\infty} S(P) j_s(P,t) dP$$

with  $j_s(P) = AP^{-\beta}$ . The ratio of the enhanced counting rates recorded by the two detectors then becomes

$$\frac{\Delta N_s^{NMD}}{\Delta N_s^{NM64}} = \frac{\int_{P_c}^{\infty} S^{NMD} P^{-\beta} dP}{\int_{P_c}^{\infty} S^{NM64} P^{-\beta} dP}$$

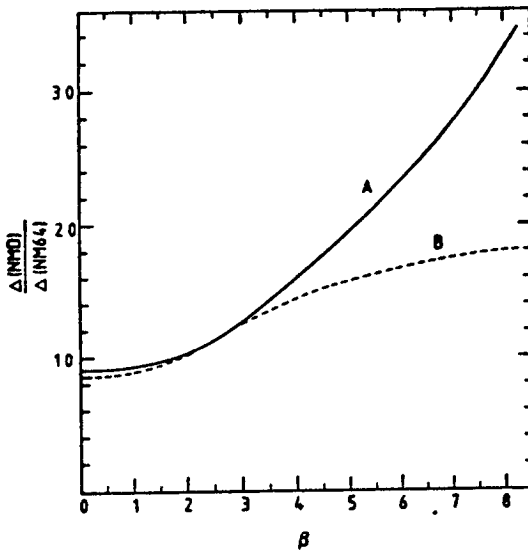


Figure 1

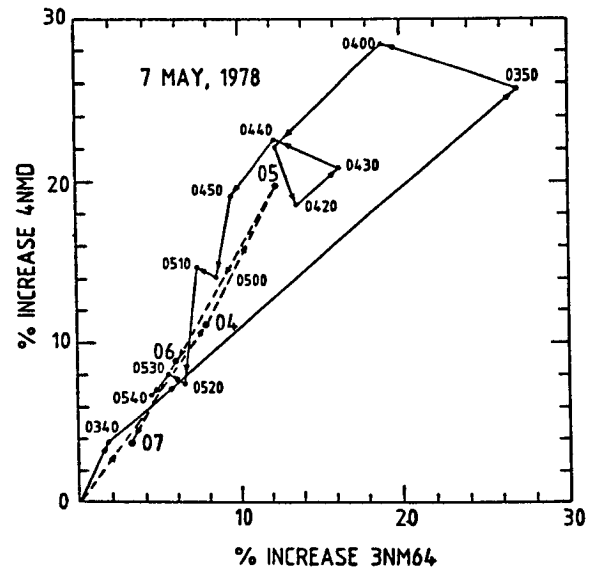


Figure 2

In Figure 1 the calculated ratio of enhanced counting rates is shown as a function of the power  $\beta$ , with  $P_c = 0.86$  GV. The constants of the Dorman function used in calculating  $S(P)$  are  $N_0 = 151.67$ ,  $\alpha = \exp 2.13$  and  $k = 0.894$  for the 3NM64, while for the 4NMD the values are  $N_0 = 157.68$ ,  $\alpha = \exp 1.99$  and  $k = 0.898$  and  $0.940$  respectively for the solid and broken lines A and B in the Figure. For both of these two sets of constants the Dorman functions lie within the statistical regression limits determined from fittings to latitude survey data for the NMD. The ratio of enhanced counting rates is not 1.00 for  $\beta = 0$  because the two differential response functions for the 4NMD and that of the 3NM64 are normalized at  $P = 17$  GV. The two curves in Figure 1 are considered to present the upper and lower limits of the ratio of the enhancements at a particular power  $\beta$ .

3. The GLE of 7 May, 1978. In Figure 2 the enhanced pressure corrected ten minute and hourly counting rates for the 4NMD are plotted as a function of the similar counting rates of the 3NM64, for the GLE of 7 May, 1978. The galactic contributions have been normalized to 100. From this Figure it follows that the first particles arrived at Sanae in the time interval 0335-0340 UT (signified by 0340) followed by a fast rise in counting rates during 0340-0350 UT. With  $\Delta\text{NMD}/\Delta\text{NM64} = 0.95$  for the enhancement until 0350 UT,  $\beta \approx 1.3$ , suggesting a flat initial spectrum, which presumably is the result of the earlier arrival of the more energetic protons. Subsequently the intensity of the slower particles are increasing, causing the displacement in the plot from 0350 to 0400, with the ratio  $\Delta\text{NMD}/\Delta\text{NM64}$  changing to 1.49, giving  $\beta = 3.4-3.5$  from Figure 1 for curves A and B respectively. After 0400 the solar proton spectrum becomes even softer. The average of the enhanced counting rates for the hour 0400-0500, indicated by 05 in the Figure, represents a ratio  $\Delta\text{NMD}/\Delta\text{NM64} = 1.63$ , giving  $\beta = 3.8-4.2$ . At 0450 UT  $\Delta\text{NMD}/\Delta\text{NM64} = 1.99$ , and  $\beta = 4.9$  for the upper curve A in Figure 1.

When the 7 May, 1978 solar proton spectra of Debrunner et al. (1984), for the rigidity interval of about 0.8 - 5 GV, are represented by the power law  $J_s \propto P^{-\beta}$ , the power values are  $\beta \approx 3.3, 3.6, 4.0$  and  $4.9$  respectively for the time periods 0335-0345, 0345-0400, 0400-0415 and 0430-0500. These values are about the same as we have obtained from Figure 1.

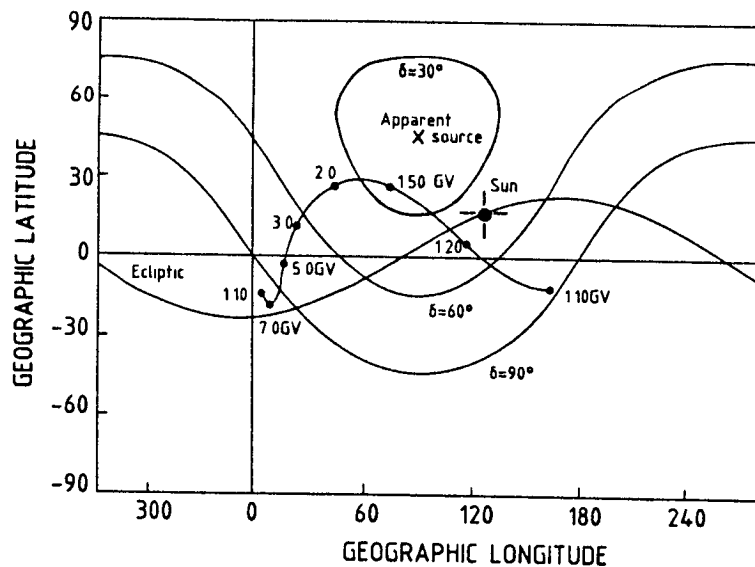
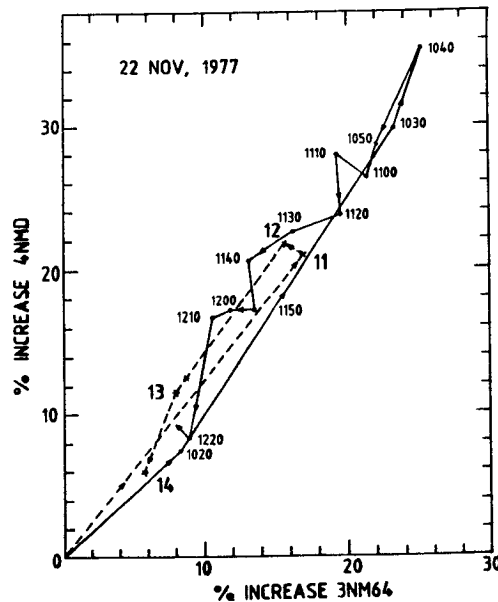


Figure 3 is in part a reproduction of Figure 3 of Debrunner and Lockwood (1980). The apparent source position and contours for angular distances of  $30^\circ$ ,  $60^\circ$  and  $90^\circ$  are shown for the 7 May, 1978 event. Added to the Figure are the asymptotic directions of vertical incident particles for Sanae (Shèa and Smart, 1971). From this Figure follows that the proton spectrum incident on top of the atmosphere at Sanae should be equivalent to the free space spectrum at 1 AU.

4. The GLE of 22 November, 1977. In Figure 4 the enhanced pressure corrected ten minute and hourly counting rates for the 4NMD are plotted as a function of corresponding counting rates of the 3NM64 for the GLE of 22 November, 1977. Here again the spectrum appears to soften from the eleventh to the twelfth hour UT. The ratio  $\Delta\text{NMD}/\Delta\text{NM64}$  for the first ten minutes 1010-1020 UT is  $\sim 0.9$ , suggesting  $\beta \lesssim 0$ , presumably again due to the earlier arrival of the more energetic protons. The ratio  $\Delta\text{NMD}/\Delta\text{NM64} = 1.30$  at 1030 which is also the average for the hour 1000-1100, implies  $\beta = 2.7 \pm 0.1$ . At 1040 the ratio of the enhancements = 1.41, with  $\beta = 3.1$ . For the decaying phase of this event the ratios of the enhancements show fluctuations around these values. For 1050-1100,  $\Delta\text{NMD}/\Delta\text{NM64} = 1.23$ , and  $\beta = 2.5$ ; 1100-1110, the ratio increased to 1.48 and  $\beta$  to 3.4. For the twelfth and thirtieth hour, the average ratio = 1.38 and  $\beta = 3.0$ .



When representing the 22 November, 1977 solar proton spectra of Debrunner et al. (1984) by a power law for the rigidity range  $\sim 1-6$  GV, the power values are  $\beta = 5.5, 4.6$  and  $4.9$  respectively for the time periods 1035-1046, 1055-1105 and 1200-1215. These values are larger than we found, but the fluctuations in hardness follow the same trend as we are observing. The lower power values deduced for Sanae may be attributed to an apparent source direction to the left  $0^\circ$  geographic longitude in Figure 3, favouring the higher rigidity protons to enter the atmosphere. Thus a harder solar proton rigidity spectrum was possibly incident at Sanae comparing to the free space spectrum as 1 AU.

5. Conclusions. Spectra of relativistic protons recorded at Sanae may be deduced from the relative enhancements in counting rates of the 4NMD and 3NM64 detectors. For GLE solar proton spectra of 23 September, 1978, 8 December, 1982 and 16 February, 1984 average powers  $\beta = 4.5 \pm 0.2, 2.8 \pm 0.1$  and  $2.6 \pm 0.1$  were obtained respectively.

Acknowledgements. The financial contribution and logistic support by the Department of Transport for Antarctic research are gratefully acknowledged.

#### References

- Debrunner, H., Flückiger, E., Lockwood, J.A. and McGuire, R.E., J. Geophys. Res. **89**, 769, 1984.
- Debrunner, H., and Lockwood, J.A., J. Geophys. Res. **85**, 6853, 1980.
- Potgieter, M.S., Raubenheimer, B.C., Stoker, P.H., and Van der Walt, A.J., S. Afr. J. Phys. **3**, 77, 1980.
- Shea, M.A., and Smart, D.F., AFCRL-TR-75-0247, May, 1975.
- Stoker, P.H., and Louw, P.A., 18th ICRC, Bangalore, Conf. Papers **4**, 181, 1983.
- Van der Walt, A.J., 18th ICRC, Bangalore, Conf. Papers **10**, 287, 1983.
- Webber, W.R., 13th ICRC, Denver, Conf. Papers **5**, 3568, 1973.

GROUND INCREASE OF COSMIC RAY INTENSITY  
ON FEBRUARY 16, 1984

Belov A.V., Blokh Ya.L., Eroshenko E.A., Ishkov V.N.,  
Yanke V.G.

Institute of Terrestrial Magnetism, Ionosphere and Radio  
Wave Propagation, USSR Academy of Sciences, 142092 Troitsk,  
Moscow Region, USSR

The event of February 16, 1984 is one of the two largest ground increases of solar cosmic rays (CR) in the last two cycles of solar activity. This event happened at a decrease of the 21-st cycle against a quiet background. Although at the beginning of 1984 the observed indices of solar activity  $/I/$  were higher than those at the end of 1983, the day of February 16 may be characterized as very quiet. On that day the geomagnetic perturbation ( $\Sigma K_p=14$ ,  $A_p=7$ ) was the lowest in February. After a small Forbush decrease due to the magnetic storm of February 12-13, the CR intensity almost completely recovered by February 16. Thus, the solar particles that came to the Earth on February 16 got into a practically unperturbed magnetosphere, and the variations of secondary CR induced by these particles were not superimposed on any other substantial variations of extraterrestrial or magnetospheric origin.

In the first half of February 1984 the solar flare activity was determined mainly by two active regions and was at a rather low level. This activity was somewhat heightened beginning from February 9, when the two active regions, AR 4408 (CD 25: S 12 L 340) and AR 4413 (CD 30: S 14 L 264) increased sharply in size and within 3 days each gave two flares of medium force. The second of the active regions rapidly lowered its activity and went beyond the western disk on February 19, 1984 and practically died away. The region AR 4408 went behind the disk increasing its area, it was in the phase of increasing activity. The activity of the region AR 4421 on the eastern disk did not give noticeable effects in CR observed on the Earth.

The solar flare responsible for the ground increase of solar CR on February 16 occurred most probably in the region AR 4408 three days after it went behind the western disk. That the flare occurred far beyond the disk is probably the most important specific feature of this event. Due to this, besides the CR from the indicated flare, it was only radio emission that reached the Earth, no emission at all being observed in the optical, UV, X-ray and  $\gamma$ -ranges.

According to radio data, the flare of February 16 occur-

red not later than 0858 T and was accompanied by intensive bursts of types IV, III, and II. For this event the western disk is a screen for all emissions that occur below  $\sim 150 \cdot 10^3$  km. The microwave burst was therefore small, whereas in the metric wave band, for which the radiation source is high in the corona, the event was rather powerful.

Figure 1 presents ground increases of February 16 for a number of neutron monitors of the world-wide net (five-minute data). The time of the beginning of the increase differs strongly for different stations. But within the second five-minute interval of the tenth hour (0905-0910 UT) a large effect was observed already for several stations. Analyzing the time variation of the counting rate for different monitors, one can obtain the following estimate of the time of arrival of first solar particles to the Earth:  $t_i = (0906 \pm 01)$  UT. Thus, if one does not assume the existence of an essential delay of radio bursts relative to the time of CR generation, one may state that having rapidly overcome the 60-degree's difference between the heliolongitude of the flare and IMF lines passing near the Earth, the first flare protons came to the Earth, in fact, without any delay.

Figure 2 presents the data of the neutrino monitor on the ship "Academician Kurchatov" which was at that time in the Atlantic Ocean at the point with coordinates (at 0900 UT)  $46^\circ 11'N$ ,  $53^\circ 02'W$ . By means of interpolation of the calculations made by Shea and Smart [2], we estimated the vertical cutoff rigidity for this point to be  $R_c = 1.62$  GV.

By many characteristics the flare of February 16, 1984 turned out close to the largest ground increase of the last cycle, to the event of May 7, 1978. In both cases one should note a rapid arrival of particles from the Sun, a small duration of the increase, a fast rise ( $< 10$  min. for stations with a large cutoff rigidity) and a sharp decrease of intensity. The decrease of intensity on the ship "Academician Kurchatov" can be represented in the period 0915-1015 UT in the form  $\exp(-t/\tau)$ , where  $\tau = 15$  m (Fig.2).

The increase of February 16, 1984, the same as the increase of May 7, 1978 is characterized by a large (close to 100 %) degree of anisotropy. The anisotropic phase of the flare was positive and occupied almost the whole period when the increase was large. The largest effect was observed in the stations, which at 9 h UT "looked" along the IMF lines towards the Sun. North-American stations and the research ship "Academician Kurchatov" appeared to be in an advantageous position for recording the ground increase. The dependence on the longitude and latitude of the point of observation turned out to be even stronger than the dependence

on the cutoff rigidity, and the value of the increase (57.4 %) on the research ship "Academician Kurchatov" ( $R_c = 1.62$  GV) exceeded, in particular, the value of the increase in high-latitudinal stations Alert and Thule ( $R_c = 0.00$  GV) situated in the same longitudinal zone /1/.

The large anisotropy of the effect and the large duration of its anisotropic phase do not allow us in this case to determine the form of the energy spectrum of the solar CR which came to the Earth by analyzing the dependence of the increase on the cutoff rigidity. In this case the analysis of the distribution of the effect on neutrons of different multiplicity /4/ may prove to be the most effective means for determining the slope of the energy spectrum. The observations of multiple neutrons were carried out in an expedition on the research ship "Academician Kurchatov".

It seems to us that the arrival to the Earth of charged particles from a flare beyond the disk can be explained by a particle drift in the neutral layer of heliomagnetosphere. By the indirect magnetospheric data /1/, on February 16 the Earth was in the positive sector of IMF, and the neutral layer was crossing the helioequator plane  $40-50^\circ$  to the west. The line of force which goes out of the flare region of heliolatitude  $\sim 10$  can come closer to the neutral layer, which at this heliolongitude must be projected onto the southern hemisphere of the Sun. Having drifted about  $60^\circ$  eastward (the drift of protons in 1984 in the neutral layer near the Sun must have just this direction), the protons could get (already in the northern hemisphere) onto the IMF line which was coming to the Earth. The hypothetical way of charged particles from the flare of February 16 to the Earth is shown in Fig.3.

#### REFERENCES

1. Solar Geophysical Data, 476, Part I, 1984, Boulder, Colorado, USA 80303.
2. Shea M.A., Smart D.F., Proc. 18-th ICRC, v.3, 415, 1983.
3. Belov A.V., Blokh Ya.L., Gushchina R.T., Dorman L.I., Eroshenko E.A., Inozemtseva O.I., Kaminer N.S. Libin I.Ya. Izv.AN SSSR, ser.fiz., 43, 12, 2512, 1979.
4. Dorman L.I. Experimental and Theoretical Bases of Cosmic Ray Astrophysics. Moscow, Nauka, 1975.





THE SCR FLARE OF 16 FEBRUARY 1984 AS RECORDED  
BY THE SAYAN SPECTROGRAPH

S.A.Kozlov, N.I.Pakhomov, L.A.Shapovalova, A.L.Yanchukovsky (Siberian Institute of Terrestrial Magnetism, Ionosphere and Radio Wave Propagation, USSR Academy of Sciences, Irkutsk 33, P.O.Box 4, USSR)

**ABSTRACT.** The Sayan cosmic ray (CR) spectrograph recorded an SCR flare that occurred on 16 February 1984. We present data from both 1-hour and 10-minute duration measurements in 10 channels with different energy sensitivity (of neutron monitors HM-64 located at different depths in the atmosphere, and of a neutron, multiple neutron and rigid mu-meson component lead-less detector). The parameters of the SCR variation spectrum are evaluated and it is shown that the recording of multiple neutrons at the same geographic point and at the same level in the atmosphere provides information similar to that from a spectrographic complex of instruments.

**INTRODUCTION.** The Sayan CR spectrograph /1/ is designed to provide data on the CR variations in different portions of the primary spectrum. This is achieved through: recording two components of secondary cosmic radiation (nucleon and muon), spacing the detectors in the depth of the atmosphere and the different geometry of neutron detectors. The CR geomagnetic cut-off rigidity at the site where the detectors are located is 3.9 GV.

A complex treatment of spectrographic measurements makes it possible to separate the CR variations into the components of interplanetary, magnetospheric and atmospheric origin and to determine the parameters of a primary spectrum ( $\Delta D/D$ ), the variations of geomagnetic cut-off rigidity ( $\Delta r$ ) and the variations of atmospheric temperature ( $\Delta R_c$ ) /2/.

Since 1983 the spectrograph incorporates the 6HM-64-selector instrument that provides multiple neutron records according to two discrimination criteria " $\geq m$ " and " $= m$ " ( $m$  - neutron multiplicity) /3/.

**RESULTS OF THE RECORDING OF THE SCR FLARE.** In February 1984, there occurred an SCR flare that was recorded by all the detectors of the complex.

The CR intensity increase according to five-minute measurements lasted for the first 10 minutes 10:00 UT on 16 February 1984 and almost immediately afterwards there was the onset of a decrease which, within 25 minutes, reached 1/2 its maximum value.

Table 1 summarizes the results of measurements of SCR flare amplitudes.

In order to intercompare the values of the amplitudes recorded, these are also plotted in Fig. 1. Straight line "A" indicates the values of flare amplitudes with five-minute intervals of averaging. These are recorded data on the neutron component obtained by three detectors HM-64 located at 3000, 2000 and 435 m above sea level and results of measurements of multiple neutrons at 3000 m according to the discrimination criterion of  $m \geq 1$  and  $m \geq 2$ . The values of amplitudes for one-hour intervals of the neutron component measurements as recorded by the lead-less detector and HM-64 instruments at different depths of the atmosphere, the values of multiple neutrons according to the discrimination criteria of  $m \geq 1$ ,  $m \geq 2$ ,  $m = 1$ ,  $m = 2$ , and  $m = 3$  and of the values of the rigid mu-meson component are indicated on straight line "B".

Table I

Instrument : Height above:		Flare amplitude (in %) at different times of data averaging		
(component): sea level of:		detector, m : 5 minutes : 10 minutes: 1 hour		
Lead-less detector	3000	-	-	3.3±0.2
6HM-64	3000	5.2±0.4	4.8±0.3	2.6±0.1
12HM-64	2000	4.7±0.4	4.5±0.3	2.4±0.1
18HM-64	435	4.0±0.5	4.0±0.4	2.2±0.2
Rigid mu-meson	435	-	-	0.0±0.2
6HM-64	3000	-	-	2.6±0.1
$m \geq 1$	3000	5.0±0.4	4.8±0.3	2.5±0.1
$m \geq 2$	3000	4.6±1.0	4.6±0.7	2.2±0.3
$m = 1$	3000	-	-	2.6±0.1
$m = 2$	3000	-	-	2.5±0.3
$m = 3$	3000	-	-	1.5±0.8

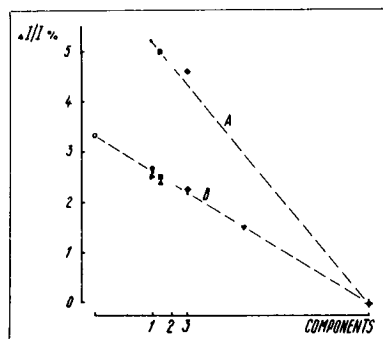


Fig. 1. Dependence of the recorded amplitudes of the SCR flare for five-minute (A) and one-hour (B) data of averagings. • - flare amplitude in the neutron component, as recorded by standard instruments at different depths in the atmosphere: 1 - 3000 m, 2 - 2000 m, 3 - 435 m; ○ - amplitude in the neutron component, as recorded by the lead-less detector; ● - amplitude in the total count rate of neutrons, as measured by the instrument 6HM-64-selector; flare amplitudes in multiple neutrons:

■ -  $m \geq 1$ , ◆ -  $m \geq 2$ , ► -  $m = 1$ , ▲ -  $m = 2$ , ◀ -  $m = 3$ ; + - flare amplitude, as measured in the rigid mu-meson component).

EVALUATION OF PRIMARY SPECTRUM PARAMETERS DURING THE FLARE. The analysis of the ratio of increase amplitudes averaged over a one-hour interval to those recorded by different detectors of the complex reveals that the energy spectrum of the variations for particles incident on the atmospheric boundary over Irkutsk cannot be represented by a simple exponential function. Thus, from the ratio of the amplitudes recorded by the neutron exponent of the exponential spectrum  $\delta$  must be  $\sim 0.35$  while for detectors 6HM-64 (3000 m) and 18HM-64 (435 m),  $\delta \sim 0.7$ . With such values of  $\delta$ , the effect of CR intensity increase was to be observed in the rigid mu-meson component. However, no such effect was recorded. It is interesting to note that according to the ratio of the amplitudes in 6HM-64 (3000 m) and 18HM-64 (435 m) averaged over the five-minute interval for a maximum SCR flux, the exponent of the spectrum was found to be  $\sim 1.7$ .

The observed peculiarities of the variation spectrum seem to be due to a significant anisotropy of the SCR flux density. In this case, because the particles of various energies have different asymptotic directions, the energy spectra of the particles arriving at the boundary of the atmosphere will depend on the location of the recording point, on local time and on SCR anisotropy characteristics. Within these considerations it is possible to explain both the anomalies in the spectrum of particles at some or another point of the Earth's surface and their dependence on the time interval of data averaging (on account of the anisotropy dynamics).

COMPARATIVE ANALYSIS OF THE MEASUREMENTS FROM THE SAYAN SPECTROGRAPH AND THE INSTRUMENT 6HM-64-SELECTOR. The instrument 6HM-64-selector is designed to record multiple neutrons of up to  $m \geq 6$  and  $m = 6$ .

An increase in CR intensity in the channels recording multiple neutrons during the flare was observed up to  $m = 3$  (channel  $m \geq 3$  was not operative during this period).

A comparison of the amplitudes recorded during the flare by the Sayan spectrograph and the instrument 6HM-64-selector reveals that the amplitude measured by a standard neutron monitor 18 HM-64 at 435 m is equal to the value of the intensity increase of secondary multiplicity neutrons as measured by the instrument 6HM-64-selector at 3000 m ( $m \geq 2$ , see Fig. 1). Temporal profiles of these components are also quite similar (see Fig. 2).

For the recording of third-multiplicity neutrons, the amplitude value is 1.5 % which is significantly smaller than that measured by a standard neutron monitor ( $\Delta \mathcal{I}/\mathcal{I} = 2.6\%$ ). This indicates a shift of the energy sensitivity of channel "m = 3" towards the region of larger energies of primary particles.

**CONCLUSIONS.** The SCR flare of 16 February 1984 showed a significant CR anisotropy which makes it difficult to represent the primary CR variation spectrum using a simple exponential function.

The SCR amplitude as measured at 3000 m and by recording multiple neutrons according to the discrimination criteria of  $m \geq 1$ ,  $m \geq 2$ ,  $m = 1$ , and  $m = 2$ , correspond to those recorded by standard neutron monitors at 3000, 2000 and 435 m.

The energy sensitivity of third-multiplicity neutrons (as compared with measurements of the neutron component by standard detectors HM-64) is shifted towards the region of larger energies of primary CR.

The recording of multiple neutrons at 3000 m provides information about CR variations similar to that from the Sayan CR spectrograph.

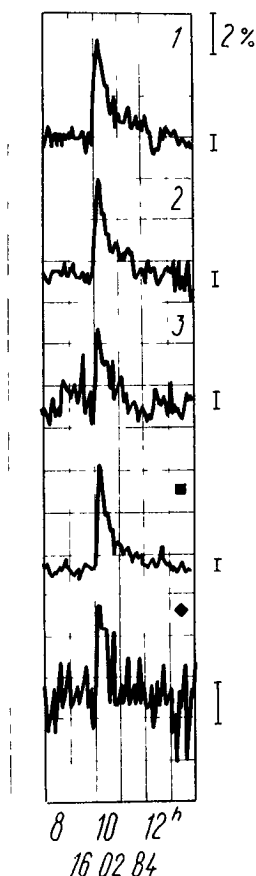


Fig.2. Results of recording the 16 February 1984 SCR flare from five-minute duration measurements with the Sayan spectrograph and the instrument 6HM-64-selector. 1, 2, 3 - neutron component as measured by standard neutron monitors at 3000, 2000 and 435 m, respectively; 4, 5, 6 - multiple neutrons as measured at 3000 m according to the discrimination criterion of  $m \geq 1$  and  $m \geq 2$ , respectively (measurement errors are shown at right).

#### REFERENCES

1. A.L.Yanchukovsky, A.A.Luzov, A.V.Sergeev. A spectrographic complex of instruments for studying the cosmic ray intensity variations. - In: Issl. geomagn., aeron. fiz. Solntsa, v.20, Irkutsk, Nauka, 1971, p.389-395.
2. V.M.Dvornikov, Yu.Ya.Krestyannikov, V.E.Sdobnov, A.V.Sergeev. Informativity of the spectrographic method. Izv. AN SSSR, 44, 1980, p.2640-2644.
3. A.L.Yanchukovsky, V.L.Yanchukovsky. An adaptive method of recording cosmic ray variations. - In: Issl. geomagn., aeron. fiz. Solntsa., v.68, Moscow, Nauka, 1984, p.201-210.

# TIME EXTENDED PRODUCTION OF NEUTRONS DURING A SOLAR FLARE

Chupp, E. L., Forrest, D. J., Vestrand, W. T.  
University of New Hampshire, Durham, NH 03824, USA

Debrunner, H., Flückiger, E.  
Universität Bern, Bern, Switzerland

Cooper, J. F., Kanbach, G., Reppin, C.  
Max-Planck-Institute für extraterrestrische Physik, 8046 Garching, FRG

Share, G. H.  
E.O. Hulburt Center for Space Research, Naval Research Laboratory,  
Washington, D.C. 20375, USA

**1. Introduction.** The most energetic neutral emissions expected from solar flares are  $\gamma$ -rays ( $>10$  MeV) from relativistic primary and secondary electron bremsstrahlung, from  $\pi^0$  meson decay, and from neutrons ( $>50$  MeV). Bremsstrahlung photon energies extend to that of the highest energy electron present, but the shape of the  $\pi^0$   $\gamma$ -ray spectrum, peaking at 69 MeV, does not depend strongly on the proton spectrum above threshold, which is  $\sim 292$  MeV for meson production on protons. The highest energy neutrons observed indicate directly the highest energy ions which interact at the Sun, and the presence or absence of an energy cutoff in the acceleration process. The high-energy proton spectrum shape can be determined from the neutron spectrum.

Detection of solar neutrons at the Earth with energies from 10 MeV to 1000 MeV have been reported from observations by the Gamma-Ray Spectrometer (GRS) on the Solar Maximum Mission (SMM) satellite (1,2), and from ground level neutron monitors (3), and through observations of the neutron-decay protons (4,5,6). By the use of new Monte Carlo calculations of the neutron and  $\gamma$ -ray responses of the SMM GRS (7) we have reevaluated the GRS neutron observations taking into account the effect of continuous production of rays and neutrons. This analysis has been carried out for two intense major solar flares; on 1980 June 21 and 1982 June 3, hereafter referred to as event I and II. The  $\gamma$ -ray results are given in (8). We find that the revised neutron efficiencies and background determination require some modification of the neutron results reported for event I (1). We also find that when continuous production of neutrons is taken into account that previous interpretation regarding event II must be revised (2,3).

**2. Methods.** We first reestablish that the SMM GRS high-energy detector has detected a neutron flux in the delayed phase of the 1980 June 21 impulsive limb flare. The high-energy detector portion in the SMM GRS, described in (9), consists of the 7 NaI elements and a single 24 cm X 7.5 cm CsI element, and records energy loss events in all elements, in 4 windows between 10 MeV and 100 MeV. In Figure 1 we show the excess GRS count rate in high-energy elements for energy losses  $> 10$  MeV. These excess rates are averaged over 65.54 s and are found by subtracting a measured background from the total GRS counts obtained during the flare. The principal characteristic in this plot is that the high-energy excess count rate rises steadily after the impulsive phase has fully terminated at 0122 UT. Since there is an absence of excess counts after this time at all energy losses ( $< 10$  MeV), we

attribute these excess counts to the arrival of solar neutrons at the SMM GRS. If a short burst of neutrons were released at the Sun during the impulsive phase, the count rate grows with time as progressively lower energy neutrons arrive at the Earth. This interpretation is the same as given earlier for this event (1) but we can now compare the GRS observations with the results of the Monte Carlo calculations of the GRS response (7), which predict that energy loss events due to high-energy neutrons should be confined to individual detector elements rather than produce simultaneous losses in both NaI and CsI. On the other hand, any  $\gamma$ -ray spectrum will produce a significant fraction of "mixed" events; that is, energy loss in both the NaI and CsI detector elements.

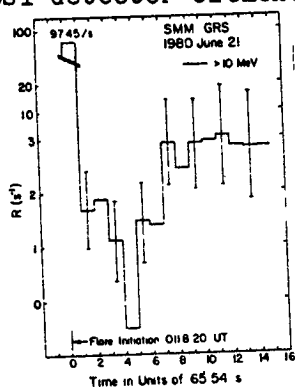


Fig. 1. GRS High-Energy detector average excess count rate during and after the impulsive limb flare at 0118.20 UT on 1980 June 21. The main impulsive phase at all energies occurs within the first time interval indicated but extends for about 3 minutes for all events  $> 10$  MeV. The neutron event commences in interval 5. SMM GRS

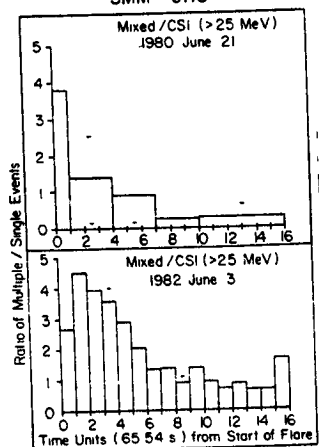


Fig. 2. The observed ratio of multiple events (NaI and CsI) to single events (CsI) for events I and II as a function of time during each event.

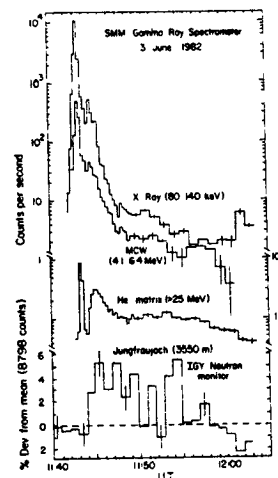


Fig. 3. The time histories for several GRS data channels are shown for the 1982 June 3 flare (event II) at 1143 UT and the corresponding response from the Jungfraujoch neutron monitor.

In Figure 2 we show, for events I and II, the observed behavior of the ratio of "mixed" high-energy events to those in the CsI element alone (above 25 MeV energy loss) from the impulsive phase until the end of the daylight portion of the flare orbit. During event I this ratio is initially about (0.3-0.4), but during the delayed phase it falls to  $0.047 \pm 0.023$  when averaged over a full 10 minutes of delayed emission. For a spectrum due only to  $\pi^0$   $\gamma$  rays and the associated meson decay electron bremsstrahlung, this ratio is expected to be rather large, 0.5-0.6, while primary electron bremsstrahlung spectra give a ratio ranging from 0.4-0.1 for power laws with exponents 1 to 5, respectively. As mentioned above, Monte Carlo calculations show this ratio is essentially zero for a pure flux of neutrons, and we conclude that the neutron interpretation for the delayed phase of event I is valid. No other reasonable explanation has been found for the delayed emission in this event.

**3. Results.** Observations of solar neutrons at the Earth were first reported for event II on 1982 June 3 from neutron-decay proton observations (4). Further reports came from GRS observations (2), and from ground level neutron monitors (3). In Figure 3 we show the count rate time histories for several GRS data channels, and for the Jungfraujoch neutron monitor which has a one minute sampling time.

It has been previously reported (3) that

the Jungfraujoch neutron monitor recorded high-energy neutrons in the time interval  $> (1144-1155)$  UT. Two other European neutron monitors, at Lominicky Stit and Rome, also recorded simultaneous increases, averaged over five minutes. Since the neutron monitors have an efficiency that increases continuously above 300 MeV but falls sharply below this energy, the early response of the Jungfraujoch monitor at 1144-1145 UT must be due to neutrons of GeV energy, if they were produced at the Sun at the time of the impulsive 1143 UT  $\gamma$ -ray peak shown in Figure 3. It should be noted that the neutron monitor response (Figure 3) above background, continues until  $\sim 1155$  UT. This observation requires that significant production of high-energy neutrons ( $> 300$  MeV) at the Sun must have continued well after the initial impulsive burst, since arriving neutrons from this emission would have energies well below that required to develop a significantly large atmospheric nucleon cascade (10).

In the case of the GRS rates, during event II the ratio of "mixed" to single events is initially large ( $\sim 0.4$ ) and falls to  $\sim 0.1$  at  $\sim 1149$  UT (Figure 2). Based on the GRS response to neutrons in event I, and assuming that the Monte Carlo calculations are correct in predicting no "mixed" events for neutrons, we would conclude that the GRS is responding to a combined flux of photons and neutrons. This circumstance alone indicates that photon production also continues throughout the post-impulsive phase. Earlier it was suggested (2) that the GRS was responding to a combined flux of  $\gamma$ -rays and neutrons between 1144-1147 UT, and that from 1147-1206 UT the energy loss spectrum was basically characteristic of high-energy neutron interactions in the GRS scintillators. We must now reevaluate the earlier conclusions on neutron observations in event II using a model for combined high-energy photon and neutron production throughout the event.

We have used several approaches to study the neutron and  $\gamma$ -ray contributions to the GRS rates in the post-impulsive phase. One approach assumes that  $\gamma$ -ray and neutron production rates are proportional throughout the flare and that spectral shapes do not change with time. Using this assumption, and  $\pi^0$  fluence versus time, (8), we can test any assumed neutron spectrum against the Jungfraujoch and GRS data. As an example we have used a neutron production spectrum at the Sun (11), based on a Bessel function accelerated proton spectrum (parameter  $\alpha T$ ). To perform this test we calculate the expected unnormalized count rate of the Jungfraujoch neutron monitor versus time using its known neutron sensitivity (3). This rate is then normalized to the observed monitor rates (Figure 3) by a  $\chi^2$  minimization for a given neutron production spectrum. Each best fit absolute continuous production solar neutron spectrum shape is then used to predict the GRS count rate versus time using the Monte Carlo results for the GRS sensitivity. Because of the limited statistics of the 1 minute neutron monitor rates, the normalization of the predicted curves is not better than a factor of 2.

Figure 4 shows a comparison of the predicted GRS count rate versus time for  $\alpha T = 0.03$  and  $0.05$ , compared with the GRS total high-energy detector rates averaged over 65.54 sec. Calculations of predicted rates for other  $\alpha T$  spectral shapes are in progress.

**4. Discussion** We have confirmed that the delayed emission observed by the GRS in event I is due to neutrons with energies from 50 MeV to  $> 250$  MeV,



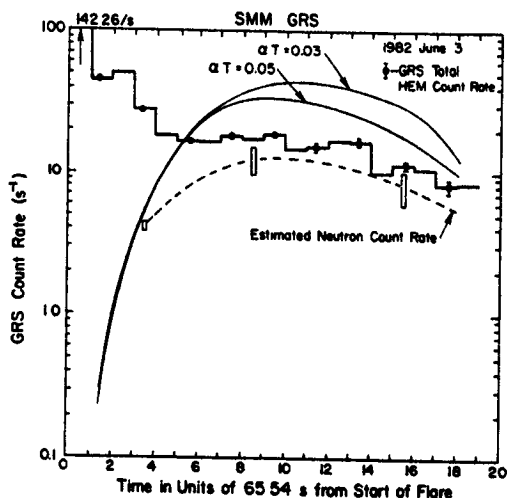


Fig. 4. The total GRS high-energy count rates for energy loss  $> 10$  MeV compared with predicted  $\alpha T$  fits determined from a time extended production of neutrons and normalized to Jungfraujoch neutron monitor rates. The estimated neutron count rate (dashed) is based on subtracting meson  $\gamma$ -ray contributions from the total rate (8). Error ranges are  $1\sigma$  - count statistics only.

assuming a delta function emission of neutrons at the Sun. Over this limited energy range, a neutron spectrum at the Sun of power law form ( $\alpha = 3.6$ ), or that produced by a proton Bessel function spectrum ( $\alpha T = 0.02$ ) is sufficient to fit the observed neutron flux at the Earth. This result is not changed significantly if the neutron emission is spread over the short time interval of the impulsive emission (1).

In the case of event II, we have confirmed that a time extended production of neutrons at the Sun is required to account for the response of the GRS and the Jungfraujoch neutron monitor throughout the delayed phase. Therefore a delta function production in the impulsive phase cannot account for the observations of the neutron monitors and the GRS to solar neutrons. As a consequence there is not a one to one

correspondence of arrival time to neutron energy, and this complicates the determination of a neutron spectrum. Also, a neutron production spectrum at the Sun resulting from a Bessel function flatter than  $\alpha T = 0.05$  may be required to pull the predicted neutron count ratio down to that required for the GRS simultaneous response to both neutrons and  $\gamma$  rays. This is indicated by the dashed curve in Figure 4. As previously pointed out (11, 12) a power-law spectral shape which is constant from 1 GeV down to 50 MeV is not viable.

**5. Conclusions.** Reanalysis of the GRS neutron observations taking into account time extended production of  $\gamma$  rays and neutrons and the neutron monitor results has led to a reinterpretation of event II. Theoretical results we have used here had assumed isotropic production of neutrons and an invariant spectral shape with time. It may be necessary to consider the effects of nonisotropic neutron production and a time varying spectral shape to satisfy all observational constraints including those provided by the neutron-decay protons.

**6. Acknowledgements.** We wish to thank Mary Chupp for and Robin Tuttle for preparation of this manuscript; Karen Dowd, Sabrina Kirwan, and Bao Li for data analysis assistance. This work was partially supported by contract NAS 5-28609 at the University of New Hampshire; NASA contract S.70926A at NRL; contract 010K017ZA/WS/WRK 0275:4 at the MPI, FRG; and the Swiss National Science Foundation Grant 2.876.80 at the U. of Bern.

#### References

1. Chupp, E. L., et al. (1982) Ap. J. (Letters) 263, L95.
2. Chupp, E. L., et al. (1983) Proc. 18th ICRC, 10, 33.
3. Debrunner, H., et al. (1983) Proc. 18th ICRC, 1, 75.
4. Evenson, P., et al. (1983) Ap. J. 274, 875.
5. Evenson, P., et al. (1983) Proc. 18th ICRC, 4, 97.
6. Meyer, P., et al. (1985) Bull. Am. Phys. Soc. 30, 780.
7. Cooper, J. F., et al. (1985) This Conference SH 9.1, 1.
8. Forrest, D. J., et al. (1985) This Conference SH 1.4-7
9. Forrest, D. J., et al. (1980) Solar Physics 65, 15.
10. Debrunner, H., et al. (1984), Presented at the 9th European Cosmic Ray Symposium, Kosice.
11. Murphy, R. J. and Ramaty, R., (1985) Advances in Space Research 4, 127.
12. Ramaty, R., et al. (1983), Solar Physics 86, 395.

FURTHER OBSERVATIONS OF PROTONS RESULTING FROM THE  
DECAY OF NEUTRONS EJECTED BY SOLAR FLARES\*

Paul Evenson<sup>+</sup>, Richard Kroeger<sup>x</sup>, and Peter Meyer<sup>x</sup>

<sup>+</sup>Bartol Research Foundation, University of Delaware  
Newark, Delaware 19716 USA

<sup>x</sup>Enrico Fermi Institute and Department of Physics  
University of Chicago, Chicago, Illinois 60637 USA

**ABSTRACT.** The solar flare of 1984 April 24 produced a large  $\gamma$ -ray fluence with energy  $>2\text{MeV}$ . The time profile of the interplanetary proton flux from this flare indicates the presence of decaying solar neutrons. This makes a total of three neutron flares so far observed by this method. The three flares are used to place constraints on the fluence and spectra of neutrons emitted by the sun.

1. **INTRODUCTION.** Neutrons emitted from the sun by large solar flares have been observed by two methods; direct detection as the neutrons pass the earth<sup>1-3</sup>, and detection of protons which result from the decay of the neutrons<sup>4,5</sup>. The first unambiguous identification of decay protons was made during the 1982 June 3 event<sup>4</sup>. More recently, on 1984 April 24 at 2354 UT, another solar event occurred showing a similar behaviour that fully confirms the earlier interpretation. This flare was located on the sun at S12 E43 and had the largest gamma ray fluence ( $>2\text{MeV}$ ) thus far detected by ISEE-3. A third neutron flare occurred on 1980 June 21<sup>5</sup>.

In this paper, we use the decay proton method to interpret data collected from the University of Chicago experiment onboard the ISEE-3 spacecraft. The energy of the decay protons is essentially the same as that of the parent neutrons. Thus, we can obtain precise neutron energy spectra near 1 AU in the range 25-138 MeV. These results yield information on the propagation of charged particles in the inner heliosphere as well as the fluence and spectrum of emitted neutrons.

2. **MEASUREMENTS.** The signature of neutron production is a flux enhancement prior to the expected arrival of the flare protons. Neutrons travel in straight lines from the flare site, hence their travel time is simply distance divided by velocity. Protons are influenced by the solar and interplanetary magnetic field. On a scale large compared with the proton gyro radius, their motion appears diffusive resulting in significant travel time delays. In flares which are poorly connected magnetically to the spacecraft these delays can be on the order of several hours. This is evident for the flares of 1984 April 24 (located at E55 relative to ISEE-3) and 1982 June 3 (located at E72). The measured proton rates from 25.7-47.5 MeV for these two flares are in figures 1 and 2. In both flares we observe a large initial gamma ray burst followed by a rise in the proton flux approximately 20-30 minutes later - the expected delay

---

\*Supported, in part, by NASA contract NAS 5-26680 and NASA grant NGL 14-001-005.

for the arrival of neutrons. The initial rise in the proton flux is rapid, corresponding to the time when the expanding shell of neutrons passes the instrument. This is followed by a slow decline in flux as the decay protons diffuse away. Protons produced directly by the flare cause the flux to rise again about 4 hours after the initial gamma ray burst in the 1984 flare, 16 hours in the 1982 flare, and only 1 hour in the neutron flare of 1980 June 21 (not shown here). The solid line in these two figures is a result of modeling proton propagation in the inner heliosphere using a mean free path of 0.3 AU and an isotropic emission of neutrons.

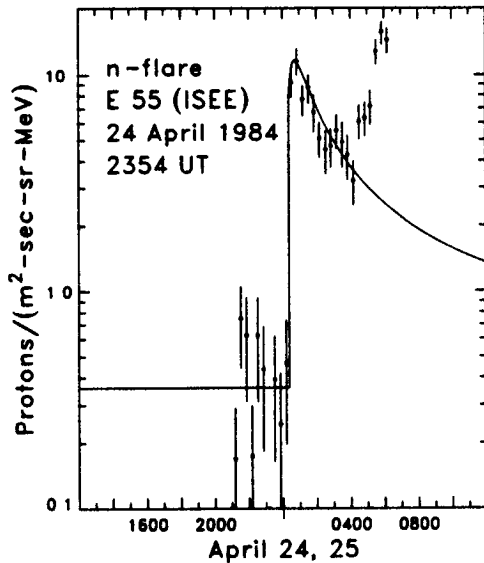


Figure 1

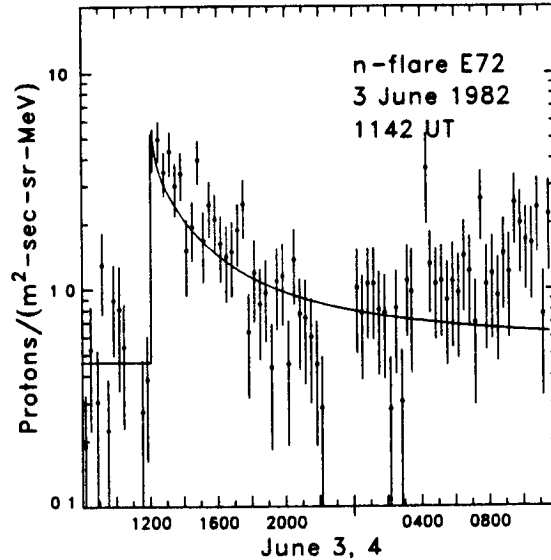


Figure 2

The intensity at the onset of the decay proton flux depends only on the number of neutrons emitted in the direction of the spacecraft. This flux is determined by decay protons which were produced in the vicinity of the spacecraft. In figure 3 we show the spectrum of decay protons collected from 30 to 90 minutes after the initial gamma ray burst. During this time the flux of decay protons is expected to vary by less than about 30% from its initial value. Most of the protons have undergone several scatterings and are nearly isotropic in their pitch angle distribution.

**3. DISCUSSION.** We consider two models which both are able to describe the profile of the decay proton fluxes. In one model, the neutrons are emitted from the sun isotropically in all directions. The sun blocks all downward moving neutrons. The remaining neutrons form an expanding hemispherical shell. In the other model, the neutrons are all emitted in the plane parallel to the local horizon at the flare site, half of which escape the sun. The models are referred to as the isotropic and the pancake model. For both models, we assume that the neutrons are produced impulsively at the time of the gamma ray burst. As they move outward they decay to form energetic protons in the inner heliosphere. We assume

that these protons rapidly become isotropic in pitch angle. Propagation is treated using a spherically symmetric diffusion model with negligible cross field diffusion.

The rate of decline in the decay proton flux depends primarily on the scattering mean free path for protons along the direction of the solar magnetic field. We find that the same mean free path fits our data in both models and that it is impossible to distinguish between them on the basis of our measurements alone. Described physically, the number of neutrons moving outward falls exponentially with distance from the sun. In both models, the density of decay protons is greatest at the inner most exposed portion of the magnetic field line connected to the spacecraft.

For both models we calculate the number of neutrons required to fit our measured fluxes. These results are shown in figures 4 and 5 for the isotropic and pancake emission models respectively. We indicate the spectral index of the power law that best fits the data in both figures. The calculated neutron fluence differs by a factor of 2.3 depending on which of the two models is used.

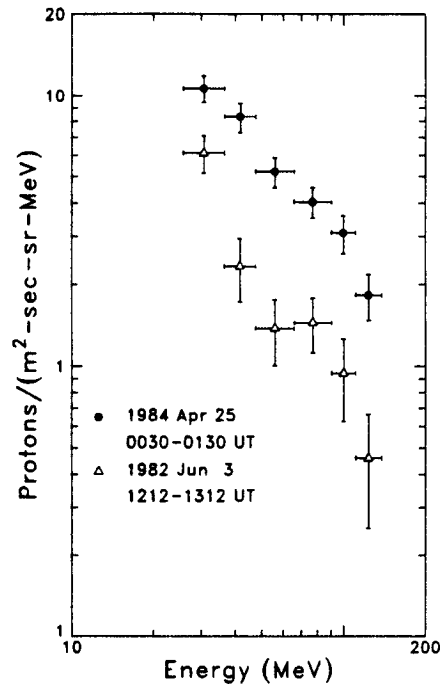


*Figure 3*

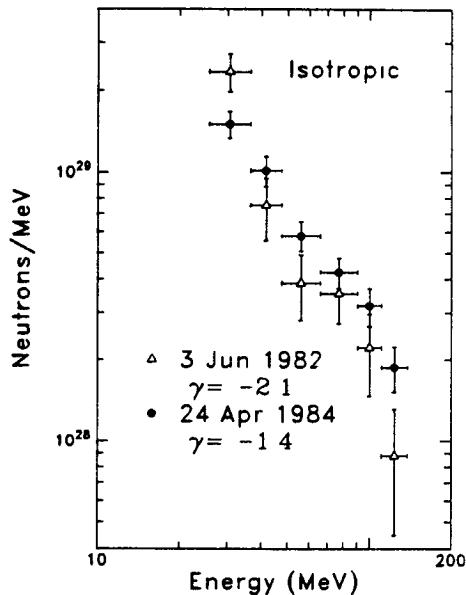


*Figure 4*

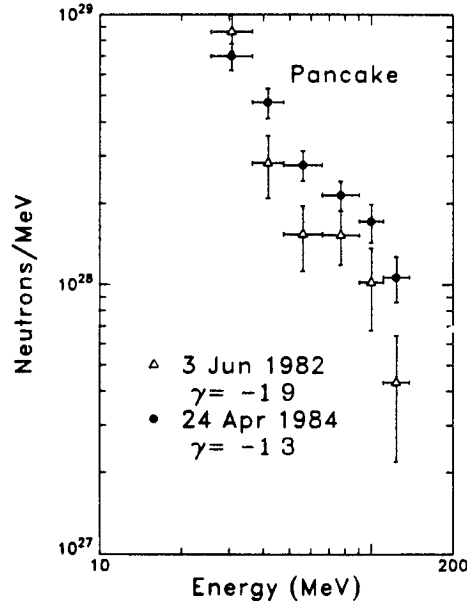


*Figure 5*

Figure 6 relates the neutron fluence (25.7-47.5 MeV) to the gamma ray fluence ( $E > 2\text{MeV}$ ). We have not observed neutron emission from small gamma ray flares. Results from all large gamma ray flares are included in this figure except for one when the proton background was very high due to a previous flare. The 1983 flare occurred at 2217 UT on May 7.

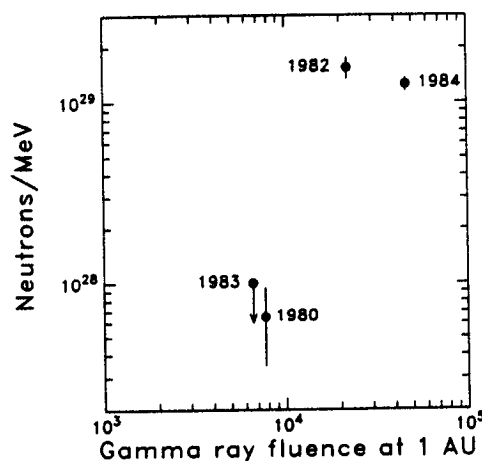


*Figure 6*

**4. CONCLUSION.** All three neutron flares have similar neutron emission spectra. Neutrons, along with  $\gamma$ -rays, result from a primary population of particles accelerated in the flare which most likely interact in the solar corona<sup>7</sup>. Since the neutrons result mostly from higher energy particles than the  $\gamma$ -rays, the correlation in figure 6 is related to the shape of the primary particle spectrum. Our results suggest that the shape of this spectrum is relatively invariant in the three flares though possibly somewhat harder in the larger flares.

The scattering mean free path of protons in the inner heliosphere does not depend strongly on the isotropy of the neutron emission. Therefore, the 1982 and 1984 neutron flares offer a unique and clean chance to study charged particle propagation in the inner heliosphere without being affected by phenomena that occur near the sun. A mean free path of roughly 0.3 AU fits the decay proton profile in both flares quite well suggesting this value may be applicable to other propagation problems too.

#### 5. REFERENCES.

1. E. L. Chupp, D. J. Forrest, J. M. Ryan, J. Heslin, C. Reppin, K. Pinkau, G. Kanbach, E. Rieger, and G. H. Share, 1982, *Ap. J.*, **265**, L95
2. H. Debrunner, E. Flueckiger, E. L. Chupp, D. J. Forrest, 1983, 18th ICRC (Bangalore), **4**, 75
3. E. L. Chupp, D. J. Forrest, G. H. Share, G. Kanbach, H. Debrunner, E. Flueckiger, 1983, 18th ICRC (Bangalore), **10**, 334
4. P. Evenson, P. Meyer, K. R. Pyle, 1983, *Ap. J.*, **274**, 875
5. P. Evenson, R. Kroeger, P. Meyer, D. Müller, 1983, 18th ICRC (Bangalore), **4**, 97
7. R. J. Murphy and R. Ramaty, *Advances in Space Research*, Proc. of the Solar Maximum Analysis Symposium, COSPAR, Graz, Austria, (1984)

# SUGGESTIONS FOR IMPROVING THE EFFICIENCY OF GROUND-BASED NEUTRON MONITORS FOR DETECTING SOLAR NEUTRONS

N. IUCCI, M. PARISI, C. SIGNORINI, M. STORINI and G. VILLORESI  
 Istituto di Fisica dello Spazio Interplanetario del CNR  
 Dipartimento di Fisica - Università "La Sapienza"  
 Piazzale Aldo Moro, 2 - 00185 ROMA, ITALY

1. Introduction. On the occasion of the June 3, 1982 intense gamma-ray solar flare a significant increase in counting rate due to solar neutrons was observed by the neutron monitors of Jungfraujoch/1/ and Lomnický Štít/2/ located at middle latitudes and high altitudes. In spite of a larger detector employed (12-NM64) and of the smaller solar zenith angle, the amplitude of the same event observed at Rome (see Figure 1) was much smaller and the statistical fluctuations of the galactic cosmic ray background higher than the ones registered at the two mountain stations, because of the greater atmospheric depth at which the Rome monitor is located. We will study here the efficiency for detecting a solar neutron event by a NM-64 monitor as a function of the Sun zenith angle, atmospheric depth and threshold rigidity of the station; some suggestions for improving remarkably the detection efficiency will be given.

2. The efficiency of a standard neutron monitor for the detection of solar neutron events. The increase  $\Delta I(X_\theta)$  produced by a solar neutron event in the neutron monitor counting rate will depend on the amount of atmospheric matter in the Sun's direction,  $X_\theta = X/\cos\theta$ , where  $X$  is the actual atmospheric depth in  $\text{g}/\text{cm}^2$  and  $\theta$  the solar zenith angle (see Figure 2). The observed relative amplitude is  $\Delta I(X_\theta)/I(X, P_T, t)$ , where the nucleonic intensity background  $I(X, P_T, t)$  is a function of atmospheric depth, threshold rigidity  $P_T$  and modulation level at the observation time  $t$ .

The standard error  $\sigma$  of the relative amplitude is produced by the fluctuations in the cosmic ray background [ $\sigma(X, P, t) = \bar{m}(X, P, t)/\sqrt{I(X, P, t)}$  where  $\bar{m}$  is in first approximation the mean detected multiplicity], therefore will depend also on the size and type (IGY or IQSY) of monitor employed. In Figure 3 we show the expected change of the relative amplitude  $\Delta I/I$  for a solar neutron event registered at the rigidity threshold of Rome ( $P_T = 6.3 \text{ GV}$ ), as a function of  $X$  and  $\theta$ . For this computation we used the attenuation lengths  $\lambda(X)$  of the nucleonic component estimated by BACHELET et al./3/ for a modulation level  $I(1033, 0, t) = 0.9 I(1033, 0, \text{May } 1965)$ . For the secondary neutrons of the solar neutron event a tentative attenuation length  $\lambda_n = 110 \text{ g}/\text{cm}^2$  was used. This value of  $\lambda_n$  was derived from the June 3, 1982 solar neutron event (see Figure 3). The expected change of the relative amplitude for a change  $\Delta X = (X'' - X')$  in atmospheric depth as a function of  $\theta$  is comp-

uted by

$$\frac{\Delta I(X', \theta)}{I(X')} \bigg/ \frac{\Delta I(X'', \theta)}{I(X'')} = \frac{\exp[\Delta X / (\lambda_m \cdot \cos \theta)]}{\exp\left[\int_{X'}^{X''} dX / \lambda(X)\right]}$$

In Figure 3 the variation of the inverse of the standard error of the relative amplitude is also plotted. From this plot we may estimate that the value of the signal to noise ratio  $[\Delta I/I] \cdot \sigma^{-1} \approx 3$  obtained for the June 3, 1982 event registered at Rome ( $\theta \approx 20^\circ$ ) becomes  $\approx 14$  for the same NM-64 placed at an intermediate altitude of  $750 \text{ g/cm}^2$ . In Figure 3 the computations relative to  $\theta = 0^\circ$  are also reported because the results obtained here for  $P_T = 6.3 \text{ GV}$  can be applied to any rigidity threshold by simply taking into account the latitude effect of the nucleonic component.

3. Modifications of the standard neutron monitor for improving the efficiency of detecting solar neutron events. The relative amplitude of the event  $\Delta I/I$  for a given  $X, \theta, t$  and  $P_T$  can be increased by decreasing the background cosmic ray intensity  $I$ . This could be done in two different ways: (a) - by changing the energy response of the standard neutron monitor towards lower energies and (b) - by modifying the omnidirectional property of the standard neutron monitor in order to have the maximum response for particles approaching the monitor from the Sun direction. A simple way to increase the low energy response and decrease the cosmic ray background is suggested by the energy dependence of the number of neutrons emitted by the nuclear disintegration in lead /4/ ; the number of detected correlated neutrons (multiplicity) will be also function of the energy of the colliding neutron /5/. It is expected that the secondaries produced by solar neutrons of energy  $< 1 \text{ GeV}$  /6/ should influence mainly the intensity  $I_1$  of the channel of detected multiplicity 1; for this channel the relative amplitude of a solar neutron event can be estimated as:

$$\frac{\Delta I_1(X, \theta)}{I_1(X)} \approx \frac{\Delta I(X, \theta)}{I(X)} \cdot K(X) \quad \text{where } K(X) = I(X)/I_1(X) ;$$

$$\sigma_1(X) = 1/\sqrt{I_1(X)} = \sigma(X) [\sqrt{K(X)} / \bar{m}(X)]$$

The signal to noise ratio increases by a factor  $\bar{m}(X) \cdot \sqrt{K(X)}$ , which is  $\approx 2$  for a NM-64 at sea level. In Figure 3 we show the expected change of the relative amplitude  $\Delta I/I_1$  and of its  $1/\sigma_1$  for a solar neutron event registered by a NM-64 at  $6.3 \text{ GV}$ , as a function of  $X$  and  $\theta$ . The attenuation length  $\lambda_1(X)$  of the detected multiplicity 1 was taken from /7/;  $K(X)$  is found to increase with altitude because  $\lambda_1(X) > \lambda(X)$ . When only the events with detected multiplicity 1 are registered, it is convenient to increase the probability of detect-

ing the locally produced neutrons; this could be obtained by adding some  $\text{BF}_3$ -counters to the standard geometry without increasing the amount of lead; for instance, if the detection probability is increased by a factor 2, the signal to noise ratio  $[\Delta I_1/I_1] \cdot G_1^{-1}$  will increase by a factor 1.5-2.0. Moreover the background cosmic ray intensity can be largely decreased, at least at middle latitudes, by shielding the monitor with an appropriate structure able to reduce the flux of cosmic ray particles which approach the monitor from the portion of the sky never scanned by the Sun. For instance at 42N geographic latitude we might shield the monitor from  $\sim 20\text{S}$  to  $90\text{N}$ . If the background intensity is reduced by a factor  $\sim 2$  the signal to noise ratio increases by a factor  $\sim 1.4$ . This effect can be improved remarkably if the monitor is mounted on a platform which rotates with the Sun; in this case the shielding structure may also cover the lateral sides of the monitor; a possible geometry of this solar neutron telescope is given in Figure 5. With this telescope the cosmic ray background can be reduced by a factor 10. In Figure 6 we show, for a proper network of 9 near-equatorial solar neutron telescopes, located at mountain altitude, measuring the intensity of the detected multiplicity 1 and with increased (by a factor 2) probability of detecting the locally produced neutrons, the contour-lines of  $(\Delta I_1/I_1) \cdot G_1^{-1} = A$ , 2A and 4A respectively, as a function of time (day and hour); the value of A given in Figure 6 was computed for an event with observed relative amplitude  $\Delta I/I = 0.5\%$  for  $P_T = 6.3\text{GV}$ ,  $X = 1010 \text{ g/cm}^2$ ,  $\theta = 20^\circ$ .

#### References.

- /1/ H. DEBRUNNER et al.: 18th I.C.R. Conf. 4,75,1983.
- /2/ G.E. KOCHAROV: 8th E.C.R. Symp. Tecnoprint, p.51,1983.
- /3/ F. BACHELET et al.: Nuovo Cimento 35, 23,1965.
- /4/ M. BERCOVITCH et al.: Phys. Rev. 119, 412, 1960.
- /5/ E.B. HUGHES and P.L. MARSDEN: J.Geophys.Res.71,1435,1966.
- /6/ E.L. CHUFF et al.: 18th I.C.R. Conf. 10,334,1983.
- /7/ N. JUCCI et al.: Nuovo Cimento 6B,111,1971.

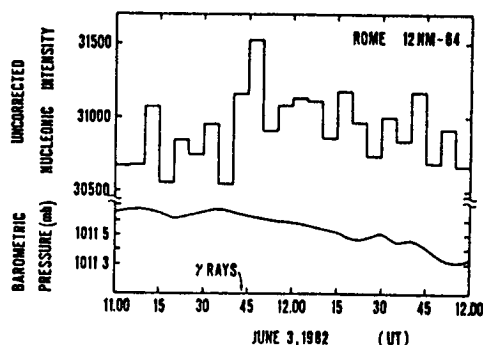


Figure 1

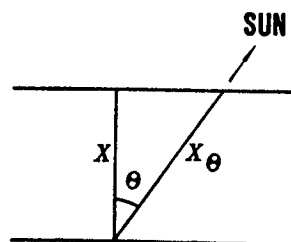


Figure 2



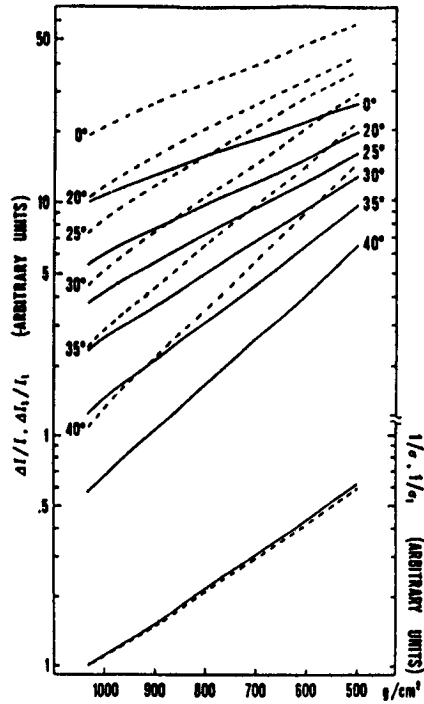


Figure 3: Changes of the observed relative amplitude and of the inverse of its standard error, for a solar neutron event registered by a neutron monitor located at  $R_p = 6.3$  GV vs. atmospheric depth for different Sun zenith angles (total counts registered; full lines; multiplicity 1 counts registered; broken lines).

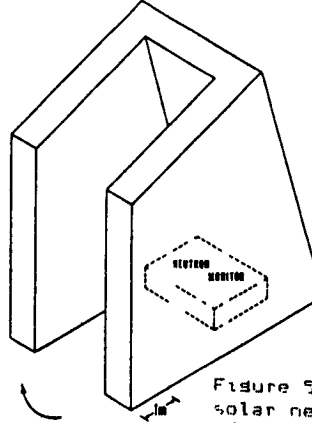


Figure 5: Sketch of a possible solar neutron telescope for middle latitudes ( $\sim 40^\circ$ ).

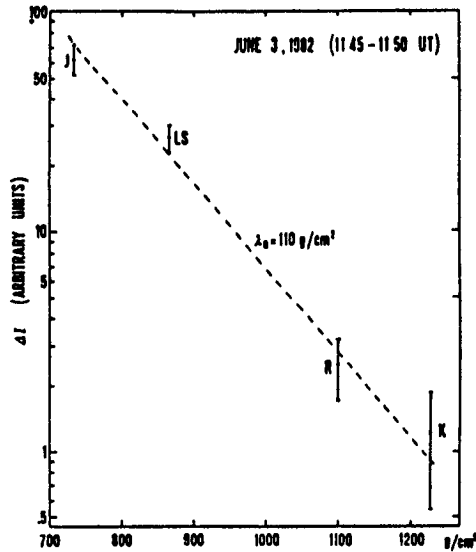


Figure 4: The absolute amplitude  $\Delta I$  of the June 3, 1982 event for the Jungfraujoch (J), Lomnický štít (LS), Rome (R) and Kiel (K) stations vs. atmospheric depth to Sun  $X_0$ . The  $I$  are computed from the  $\Delta I/I$  by applying the latitude and altitude changes of  $I$ .

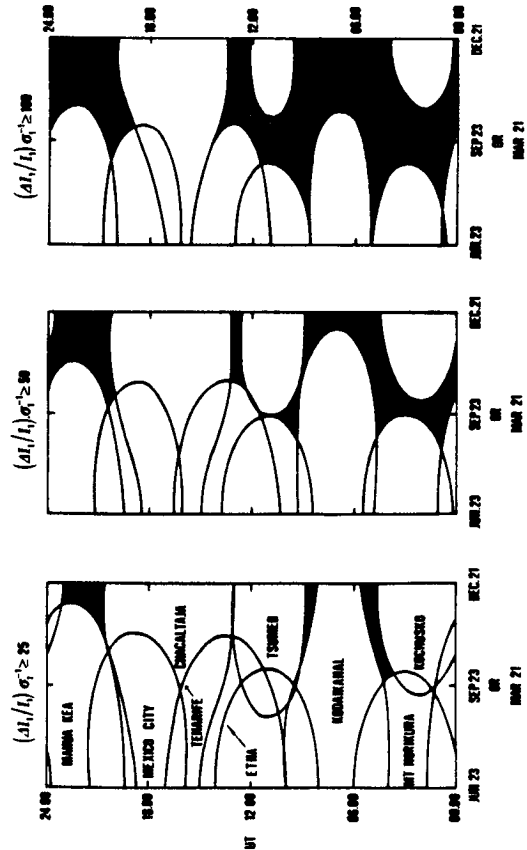


Figure 6

## SEARCH FOR SOLAR NEUTRONS USING NM-64 EQUIPMENT

N.J. Martinic, A. Reguerín, E. Palenque, M.A. Taquichiri  
 Chacaltaya Cosmic Ray Laboratory, University of La Paz  
 M. Wada, A. Inoue, K. Takahashi  
 Institute of Physical and Chemical Research, Tokyo

## ABSTRACT

Two years (1980-1982) neutron monitor data from the Chacaltaya (geographic coordinates: N16.32°, W68.15°; cutoff rigidity: 13.1 GV; altitude: 5,300 m a.s.l.) station has been scanned; the sampling time of the 12NM-64 neutron monitor is 5 min. The nucleonic component increases have been correlated with 66 hard X-, gamma-rays satellite data from solar origin, as reported by several groups. We present typical neutron monitor time profiles of the events. Chree-analysis was performed discriminating the events according its solar coordinates. Ground data from solar limb loci are more enhanced at the time of the onset than other geometrically visible flares. We present also Chree histograms of neutron monitor out-put profiles from geometrically invisible events from the Chacaltaya station.

1. Introduction

The search for solar neutrons using evaporation neutrons of the nucleonic components of the cosmic rays detected by ground based instruments has led to scan out-puts of high altitude, high cutoff rigidity stations. The low attenuation length of such stations makes it possible to recognize additional, from solar origin, neutron enhancements one is expected to identify. On the solar surface neutrons are available as secondary particles of the interactions of energetic nuclei in the base of the corona; also,  $^1\text{H}$  capture of neutrons radiate gamma lines of 2.22 MeV (Prince et. al., 1983). Other photons: the 0.5 MeV positron annihilation and the  $\pi^0$  decay furnishes the other gammas; the hard X-rays are produced via bremsstrahlung from the energetic electrons.

We assume that a solar flare is related with some kind of acceleration mechanisms for electrons or/and protons and other species; and that neutrons (or the energetic photons) shall, in general, follow the trajectories of the accelerated parents. The latter has, in general, preferred directions, say, parallel to the solar surface. Less energetic neutrons and X-rays may be produced isotropically.

In this phenomenological analysis we assume that the neutron generation is impulsive (typical life-time:  $\approx 100$  s) and that at least 0.5 of the neutrons can escape the solar atmosphere. We present below statistical analyses of 66 solar events correlated to the ground based 12 NM-64 of the Chacaltaya station.

2. Data treatment

From the 66 solar events we investigate, we show in Fig. 1 a typical time profile as seen by the 5-min Chacaltaya monitor. The short sample of 3 hours exhibit an increase synchronic with the onset time of the reported satellite data; however, notice other increases more important than the former one. The sigma,  $\sigma$ , of this short sample is 0.3 % taken during 6 hours data. As can be checked on Table III, the parent flare was a limb one and the onset was on 21:15 of Dec. 23th 1980. It was a short lived

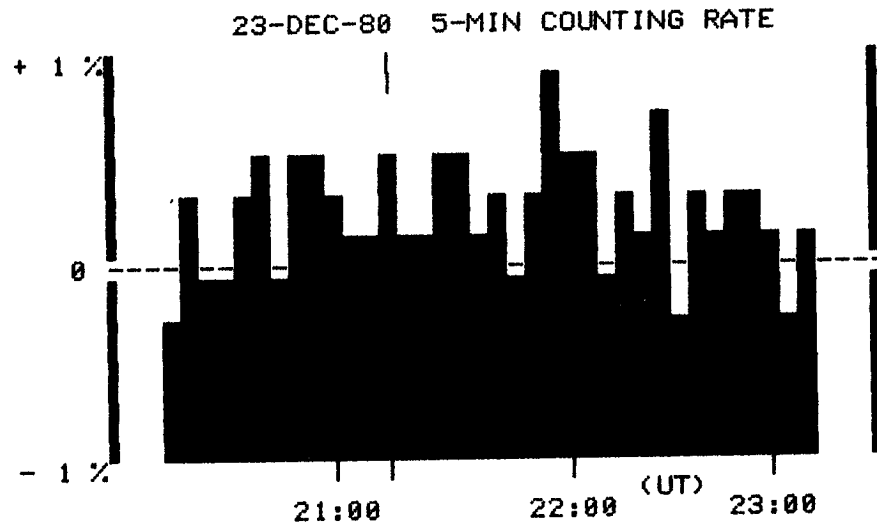


Fig.1: Nucleonic component NM-64 time profile.  
The solar gamma ray event is shown with a dash.

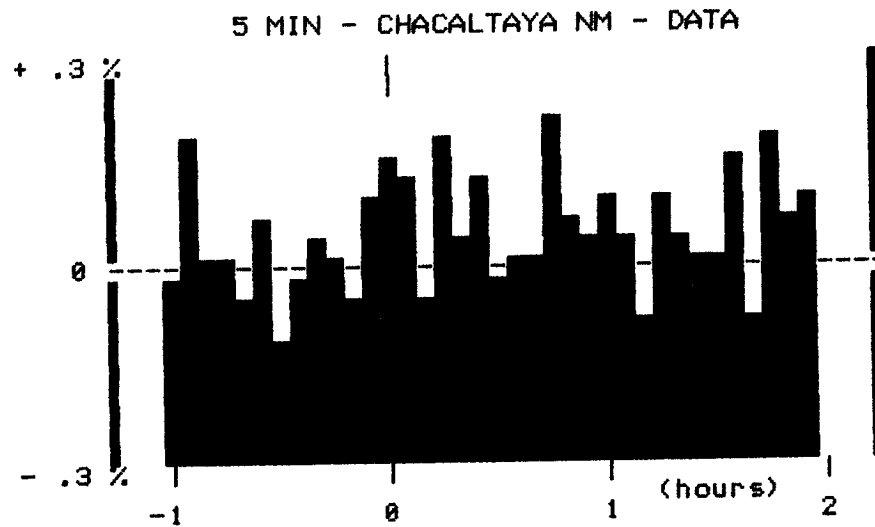


Fig.2: Chree Analysis of 11 visible gamma or X- flares (see Table III).  
The ordinates are given in % of 6-hour mean value. The total length of the plotted data is three hours. The onset of the event is shown with a dash.

flare ( 15 s ) with a peak emission above 0.3 MeV photons according to the SMM data; the GOES classification is M3. A special feature of this profile is that it appears an enhancement more or less continuous of the monitor data one hour before and one hour after the flare onset.

Fig. 2 illustrates a Chree analysis of 11 solar events when the sun is above the horizon ( see Table III ); the flare location is correlated with the limb of the sun. The criterion: If the solar longitudes are larger than  $70^\circ$ , then they belong to this group. The increases associated with these flares can be seen clearly on the onset of the event, above the statistical fluctuations. In Fig. 3 we present a superposed epoch analysis centered on the onset of the parent flares with coordinate positions on the disk

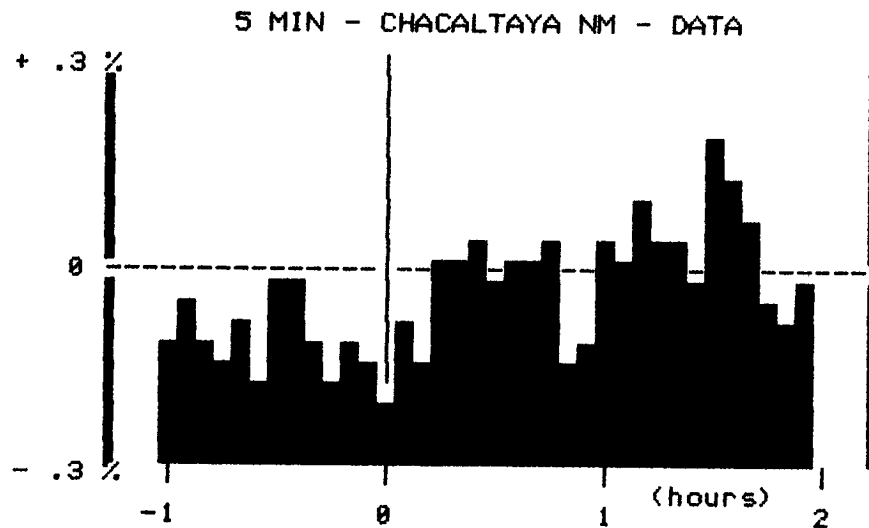


Fig.3: Chree Analysis of 21 visibles gamma or X- flares (see Table II ). The ordinates are given in % of 6-hour mean value. The total length of the plotted data is three hours. The onset of the event is shown with a dash.

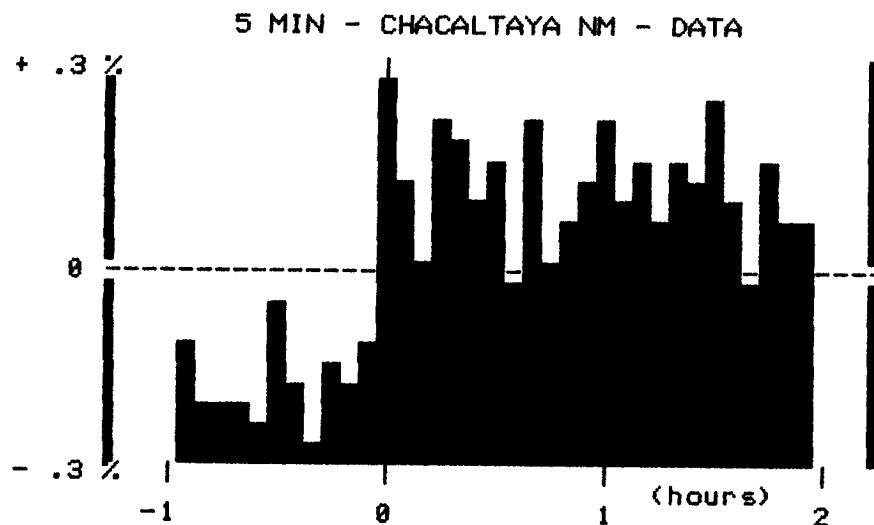


Fig.4: Chree Analysis of 16 invisible gamma or X- flares (see Table I ). The ordinates are given in % of 6-hour mean value. The total length of the plotted data is three hours. The onset of the event is shown with a dash.

when the sun is above the Chacaltaya horizon. ( Cf. Table II ). The short plotted sample illustrates a smooth increase, starting at the onset time; no peaks can be observed. Among these events no discrimination was taken into account with the solar zenith angle as seen by Chacaltaya. Finally, Fig. 4 illustrates the histogram of a superposed epoch analysis of 16 solar events with coordinates on the solar disk (their solar longitudes are less than  $70^\circ$ ) when the sun is below the Chacaltaya horizon and shows a step-like behaviour, well above the statistical fluctuations, of the mean value before and after the onset of the events. Other 'nocturnal' events, not shown here, do not present any special feature and its analysis shall be omitted.

### 3. Discussion

7. Discussion  
Although satellite data is not available in order to discriminate solar sources of neutrons visible from the Chacaltaya neutron monitor, say according to its integral neutron intensity (which is model dependent), type of photon emission, and the like, we have presented a preliminary superposed epoch analysis of 66 events pint-pointed mainly via satellite flare survey. We concentrated on solar events of disk or limb parent flares location, and when the sun is above or below the Chacaltaya horizon. The search of solar neutrons via neutron monitor by other authors and known to us (Debruenner et al., 1983; Iucci et al., 1984) show positive identification of solar effects.

We summarize our work: The limb flares, when the sun is above or below the Chacaltaya horizon a) for local nocturnal flares no feature can be noticed and b) for diurnal ones the histogram may produce a peak. For parent flares located on the disk they produce an enhancement of the neutron monitor intensity before and after the onset times, when the sun is below the Chacaltaya horizon; otherwise no particular features can be seen.

## References

- REFERENCES
- Prince et al., 1983, 18th ICRC, Bangalore, 4, 79  
Debruenner et al., Chupp et al., 1983, 18th ICRC, Bangalore, 4, 75  
Iucci et al., 1984, Rome, IFSI-report

## A SEARCH FOR SOLAR NEUTRONS ON A LONG DURATION BALLOON FLIGHT

R. Koga  
Space Sciences Laboratory, The Aerospace Corporation  
El Segundo, CA 90245, USA

G. M. Frye, Jr. and A. Owens  
Physics Department, Case Western Reserve University  
Cleveland, OH 44106, USA

B. V. Denehy, O. Mace, and J. Thomas  
RAAF Physics Department, Melbourne University  
Parkville, Victoria, Australia

## ABSTRACT

The EOSCOR III detector, designed to measure the flux of solar neutrons, was flown on a long duration RACoon balloon flight from Australia during Jan - Feb, 1983. The circum-global flight lasted 22 days. No major solar activity occurred during the flight and thus only an upper limit to the solar flare neutron flux is given. The atmospheric neutron response is compared with that obtained on earlier flights from Palestine, Texas.

1. Introduction. A solar neutron detector, EOSCOR III, (1) was launched from Alice Springs, Australia (23.5° S) at 2040 UT Jan. 19, 1983 on a  $0.44 \times 10^6 \text{ m}^3$  zero pressure polyethylene balloon. As first pointed out by Lally (2), during the summer months at low latitudes, a zero pressure balloon will descend to a stable float altitude after sunset without any ballast drop and then return to its original float altitude after sunrise. Because the magnitude of the day-night altitude excursion is determined primarily by the difference in the radiation seen by the balloon in the day and night environments, Lally (2) has christened this the RACoon (Radiation-controlled balloon) technique. Since we are interested only in a solar observation, the RACoon method is admirably suited to achieving a multi-day observing period at a few mbar altitude with a standard balloon (3).

2. The Flight Characteristics. The circum-global flight was scheduled for the summer to take advantage of the zonal winds which are characteristically uniform both in bearing and velocity, during the three summer months at mid-latitudes. The flight path is shown in Figure 1. The day and night altitudes were initially about 130 and 70 k ft, respectively. The night altitudes remained nearly constant during the flight except when over a very cold cloud deck near Tahiti. The day altitude, however, gradually decreased, reaching approximately 110 k ft one day before termination. The ambient air temperature varied between -20° and -75°C during the flight.

Power for the detector instrumentation was provided by silicad batteries, continuously charged during the day by an array of solar panels. Processed data from the experiment were telemetered to the

ground through the METEOSAT and GOES satellites and the position of the balloon continuously monitored by the ARGOS satellite network.

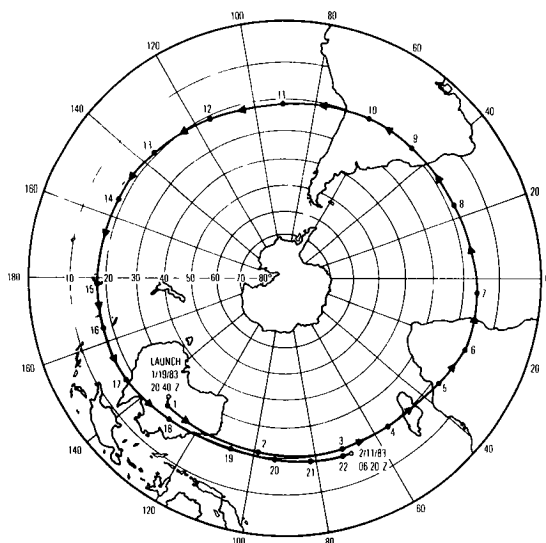


Fig. 1. RACOON Flight Trajectory.

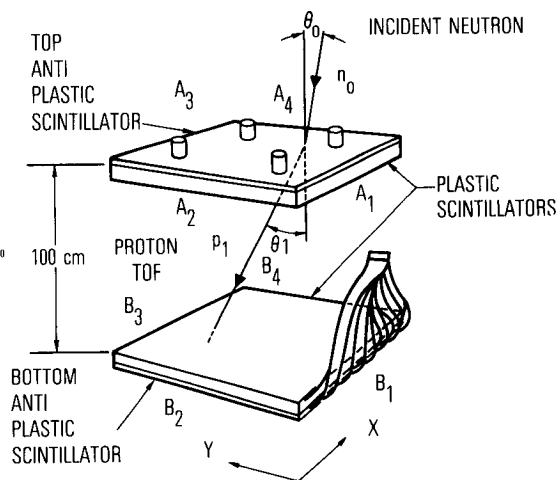


Fig. 2. The EOSCOR III Detector. Adiabatic, Isochronous Light Pipes with 7.8 cm PMT's View the Edges  $A_1 \dots B_4$ . (only  $B_1$  shown).

**3. Experimental.** The detector was designed to measure solar flare neutrons in the energy range 20 to 150 MeV (4). It consisted of two 1 m<sup>2</sup> scintillators separated by a 1 m time-of-flight (TOF) path, as shown in Figure 2. Proton energies from n-p scatters and  $^{12}\text{C}(n,pX)$  interactions in the upper scintillator were determined by pulse height and TOF measurements. TOF is also used to discriminate the slower moving protons from the more numerous, downward moving Compton electrons. This is shown in Figure 3 where pu, eu, ed, and pd denote upward moving (albedo) protons and electrons, and downward moving electrons and protons, respectively. The separation of these components was made possible by use of a light time compensation technique (1) carried out by an on-board computer. The FWHM of the electron peak was 2.2 ns, which was very close to that obtained during the earlier calibration run at the Indiana University Cyclotron Facility. Raw data related to events within the pd group are telemetered for further analysis.

Solar neutron events are identified by an increase in the neutron counting rate over the atmospheric background, correlated in time with the solar flare. From the gondola position and orientation, the angle  $\theta$  between the vertical detector axis and the neutron arrival direction is known and therefore the neutron energy is given by  $E_n = E_p / \cos^2 \theta$ , where  $E_n$  and  $E_p$  are the incident neutron and the measured proton energies, respectively.

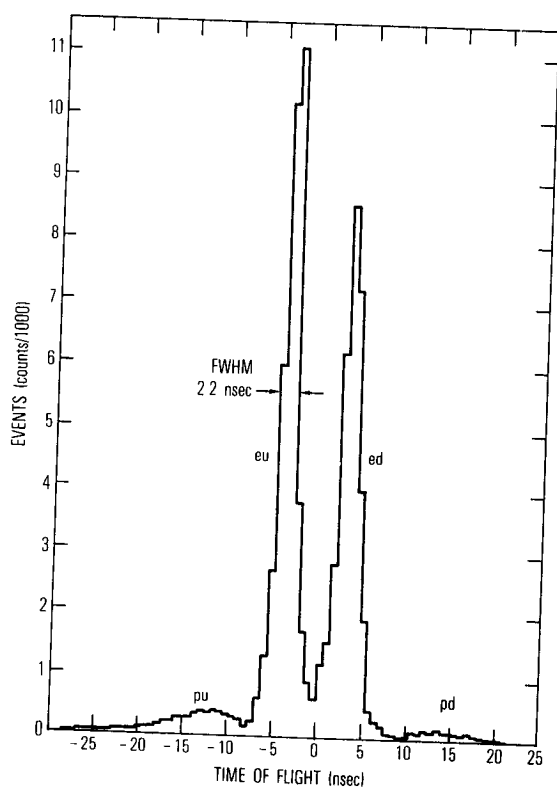


Fig. 3. TOF Spectrum at  $3.1 \text{ g/cm}^2$  above Alice Springs.

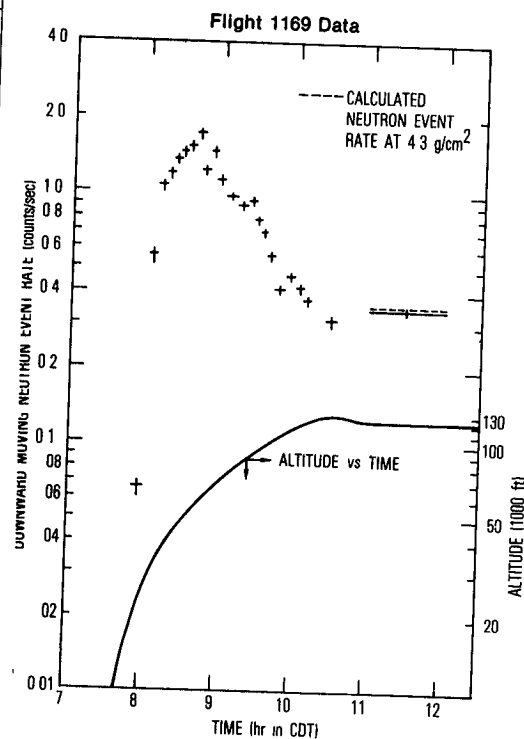


Fig. 4. Event rates of downward moving neutrons at Palestine, Texas (September 25, 1979).

4. Atmospheric Neutrons. Because the atmospheric neutrons are omnidirectional the proton spectrum cannot be unfolded to yield the atmospheric neutron spectrum. However, the counting rates as a function of altitude and geomagnetic cutoff give a measure of the variation of the atmospheric neutron intensity with these parameters. The rate of downward moving neutrons is obtained from group pd in Figure 3. Measurements of high energy neutrons near the top of the atmosphere have been reported for geomagnetic cutoffs 0.4 GV (Thompson, Manitoba), 4.5 GV (Palestine, Texas), and 11.6 (Parana, Argentina) (5,6). The downward moving neutron flux measured by Preszler et al. (6) was used to calculate the expected counting rates for the EOSCOR III detector. The expected rate is shown in Figure 4 along with the measured rates. For comparison the downward moving neutron rates from several previous flights are also listed in Table 1.



Table 1. EOSCOR III Downward Moving Neutron Event Rates

LOCATION	DATE	ALTITUDE (g/cm <sup>2</sup> )	RATE (event/sec)
Palestine	25 Sept 1979	4.3	0.34 ± .02
Palestine	17 Oct 1979	9.0	0.61 ± .03
Palestine*		4.6	0.35
Alice Springs	19 Jan 1983	3.1	0.16 ± .01
Alice Springs	19 Jan 1983	4.3	0.22 ± .01

\*Calculated from the measured 1971 neutron flux of Preszler et al. (6).

5. Solar Neutrons. The sun was quiet during the observational period of the flight (7) with the exception of normal sporadic C class flares. On January 20, 1983, for instance, there were a few such flares. From our derived neutron counting rates we place a  $3\sigma$  limit on the solar neutron flux of  $3 \times 10^{-3}$  neutrons cm<sup>-2</sup> s<sup>-1</sup>.

6. Acknowledgments. This work was supported by NSF grant ATM 82-06044, the Australian Research Grants Committee, and the RAAF. The work of one of the authors (R.K.) was supported by The Aerospace Corporation-sponsored Research Program.

#### References

1. Koga, R., et al.; Proc. of the 17 ICRC, 9 (1981) 328.
2. Lally, V.; Proc. XXIV COSPAR conf. Ottawa, I.1.4 (1982).
3. Frye, G. M., Jr.; Adv. Space Sci., 3, no. 6 (1983) 117.
4. Koga, R., et al.; Nuc. Instr. and Meth., 165 (1979) 47.
5. Nazarets, M. A.: PhD thesis CWRU (1976).
6. Preszler, A. M., et al.; J. Geophys. Res., 81 (1976) 4715.
7. Solar-Geophysical Data, 467B, Boulder, Colorado (1983).

# NEUTRAL PION PRODUCTION IN SOLAR FLARES

Forrest, D. J., Vestrand, W. T., Chupp, E. L.  
University of New Hampshire, Durham, NH 03824 USA

Rieger, E., Cooper, J.  
Max-Planck-Institut für extraterrestrische Physik, 8046 Garching, FRG

Share, G.  
E.O. Hulburt Center for Space Research, Naval Research Laboratory, USA

## ABSTRACT

The Gamma-Ray Spectrometer (GRS) on SMM has detected more than 130 flares with emission  $>300$  keV. More than 10 of these flares were detected at photon energies  $>10$  MeV (1). Although the majority of the emission at 10 MeV must be from electron bremsstrahlung, at least two of the flares have spectral properties  $>40$  MeV that require gamma rays from the decay of neutral pions. We find that pion production can occur early in the impulsive phase as defined by hard X-rays near 100 keV. We also find in one of these flares that a significant portion of this high-energy emission is produced well after the impulsive phase. This extended production phase, most clearly observed at high energies, may be a signature of the acceleration process which produces solar energetic particles (SEP's) in space.

**1. Introduction.** Gamma-ray production in solar flares at energies  $>10$  MeV is only expected from a few mechanisms. These are bremsstrahlung by primary accelerated electrons, bremsstrahlung by positrons and electrons from the decay of charged pions, and directly from the decay of neutral pions. Each process has secondary characteristics other than its spectrum at energies  $>10$  MeV. These include intense low-energy X-ray emission from any continuous spectrum of primary electrons, emission of the 0.511 MeV gamma-ray line for charged pions, and the emission of high-energy neutrons for neutral pions. These secondary signatures can be used to confirm a spectral interpretation and they can also be used to extract more information concerning the primary particle spectra at the Sun. In particular we note that while the spectral shape of the pionic gamma rays does not depend strongly on the details of the accelerated particle spectrum, its intensity is a strong indicator of the nuclear reaction rate which must produce both neutrons and pions (2, 3). Hence, combined measurements of both pions and neutrons will yield information on both the directivity and spectra of the very high-energy accelerated ions.

**2. The High-Energy Monitor on GRS.** The high-energy monitor on the SMM GRS (4) consists of 2 separate sensors. The top or sunward sensor consists of seven 7.6 cm X 7.6 cm NaI detectors and the bottom sensor consists of a 24 cm X 7.5 cm CsI back detector. Neutral events producing energy losses between (10-100) MeV are recorded in 4 energy bands in each of the sensors for three different cases. These are events which occur only in the NaI, only in the CsI, and events which occur in both (called "mixed" events). By appropriately summing these energy-loss bands we can define a five-channel energy-loss spectrum. The nominal energy edges of these channels are 10, 25, 40, 65, 100 and 140 MeV. The effective area for both gamma rays and

neutrons have been calculated by Cooper et al. (5). These calculations have also shown that only gamma rays are effective in producing "mixed" events. Hence, the ratio of the "mixed" to the NaI only and/or CsI only events is an effective separator of neutrons and gamma rays. We note that events in the (100-140) MeV band, which only uses "mixed" events, requires gamma rays with energies greater than 100 MeV.

**3. Flare Observations.** The high-energy neutron observations from the flare at 01:18:20 UT on 21 June 1980 have been presented earlier (6,7) and have been reanalyzed with improved neutron efficiencies in a companion paper (8). The basic high-energy observations shows strong emission  $>10$  MeV in the 65 s impulsive phase, followed by a low-intensity excess lasting to the end of the orbit (see Figure 1; ref. 8). Figure 1 shows the photon spectrum measured during the impulsive phase of this flare. The solid curves in this figure are the best-fit photon spectrum, determined by combining both power-law and pion gamma-ray spectra. The power-law spectrum is  $(5.0 \pm 0.1) (E/10 \text{ MeV})^{(2.7 \pm 0.1)}$  photons  $\text{MeV}^{-1} \text{ cm}^{-2}$  and the integral of the neutral pion spectrum is  $0.6 \text{ photons cm}^{-2}$ . The statistical test used to determine these values shows that while the overall fit is better with the pion spectra, the improvement is not sufficiently large to require it. Hence, the above pion flux must be considered an upper limit. The only way to get a larger pion flux would be to introduce a spectral break in the power law near 40 MeV. Note however, that the data do require photons  $>100$  MeV. In the extended emission phase we find that neither the spectral properties nor the observed ratio of "mixed" to CsI counts (8) is consistent with gamma rays. We find that only  $13 \pm 6\%$  of the observed counts in this phase can be due to photons with a resulting upper limit neutral pion photon flux of  $0.5 \pm 0.2 \text{ cm}^{-2}$ .

The time history in several energy bands for the flare of 3 June 1982 is shown in Figure 3 by Chupp et al. (8). Again the high-energy observations show strong emission in a 65 s impulsive phase. However, in this event the impulsive phase is followed by a stronger extended emission phase. Figure 2 shows the photon spectrum observed during the 65 s impulsive phases. Again, these data indicate an intense power-law continuum but in this case the data show a strong hardening at energies  $>40$  MeV which is described by a neutral pion photon spectrum with a integrated flux of  $12 \text{ photons cm}^{-2}$ . Figure 3 shows a 65 s spectrum from the beginning of the extended phase. As can be seen all of the data in this interval can be fit with a combined charged and neutral pion photon spectra. We have used these data to experimentally determine the charged-to-neutral pion ratio and find it to be  $3.1 \pm 0.2$ .

Finally, in Figure 4 we show a 65 s spectrum further into the extended phase. In this case an attempt was made to fit the data, under the assumption that all the counts are due to photons. The data in Figure 4 show that a pion-photon spectrum is a good fit in the lowest and the highest channel but the observations exceed the pion-photon model in the three middle channels. Both the spectral shape and the time dependence of this mid-energy excess is what is expected from the high energy neutrons which must accompany any pion emission. It is just this process which allows us to separate the gamma-ray and neutron components versus time within the GRS data. Chupp et al. (8) have used these separated data to study the high-energy neutron production from this flare.

As a confirmation of the pion intensities deduced from gamma-ray spectral shape arguments, we note that these intensities are a predictor of the 0.511 MeV line flux from charged pions. As an example we use the spectrum shown in Figure 3, which requires an integrated neutral pion-photon flux of  $7.8 \pm 0.4 \text{ cm}^{-2}$ . With our observed charged-to-neutral pion ratio of  $3.1 \pm 1$ , and a positive-to-total charged pion ratio of 0.70, our predicted 0.511 MeV flux, during this interval, from charged pions is  $0.12 \pm 0.02 [f(0.511)] \text{ photons cm}^{-2} \text{ s}^{-1}$ . Here,  $f(0.511)$  is the 0.511-to-positron ratio (3). Share et al. (9) found that the total flux at this time  $0.35 \pm 0.05 \text{ photons cm}^{-2} \text{ s}^{-1}$ . Murphy et al. (3) found that only  $0.15 \text{ photons cm}^{-2} \text{ s}^{-1}$  could be accounted for by the radioactive positron emitters produced mainly in the impulsive phase. The difference between the measured value and Murphy's values is  $0.20 \text{ photons cm}^{-2} \text{ s}^{-1}$ , which is in agreement with our predictions for charged pions produced well after the impulsive phase for a  $f(0.511) = 1.6 \pm 0.2$ .

Our analysis shows a integrated flux of  $45 \text{ cm}^{-2}$  neutral pion photons measured after 11:46:00 UT. When compared to the  $12 \text{ cm}^{-2}$  measured in the impulsive phase, we find that >80% of the pion emission was observed in the extended phase.

**4. Discussion.** We have presented spectral evidence for pion production in 2 flares. During the impulsive phase this emission is always accompanied by intense primary electron bremsstrahlung. In the larger of these two flares, 3 June 1982, the pion production continued well after the impulsive phase. The properties of this extended phase are distinctly different from the impulsive phase. Specifically, the extended phase seems to be ion enriched and spectrally hardened.

It is interesting to speculate that this newly discovered phase is associated with the acceleration process that generates SEP's in space. Surprisingly, there is poor correlation between the nuclear gamma-ray intensity and the size of the well-connected SEP's (10). This argues against a close link between impulsive phase acceleration and SEP acceleration. McDonald et al. (11) have shown that the cosmic-ray event associated with the 3 June 1982 flare had an unusually hard spectrum. It is intriguing that the spectrum associated with the extended gamma-ray phase is also unusually hard.

**5. Acknowledgements.** We wish to thank Mary Chupp and Robin Tuttle for preparation of this manuscript; Karen Dowd and Sabrina Kirwan for data analysis assistance. This work was in part supported by contract NAS5-28609 at the University of New Hampshire; NASA contract S.70926A at the NRL; contract 010K017ZA/WS/WRK 0275:4 at the MPI, FRG; and the Swiss National Science Foundation Grant 2.876.80 at the University of Bern.

#### References

1. Rieger, E., et al., (1983) Proc. 18th ICRC 10, 338.
2. Ramaty, R., et al., (1975) Space Sci. Rev. 18, 341.
3. Murphy, R. J. and Ramaty R., (1985) Advances in Space Research 4, 127.
4. Forrest, D. J., et al., (1980) Solar Physics 65, 15.
5. Cooper, J. F., et al., (1985) This Conference, SH 9 1, 1.
6. Chupp, E. L., et al., (1982) Ap. J. 263, L95
7. Ramaty, R., et al., (1983) Ap. J. (Letters) 273, L41.
8. Chupp, E. L., et al., (1985) This Conference, SH 1.4-1.
9. Share, G., et al., (1983) Positron-Electron Pairs in Astrophysics, eds. M. Burns, A. Harding, and R. Ramaty, (American Institute of Physics New York) p. 15.
10. Cliver, E., et al., (1983) Proc. 18th ICRC 10, 342.
11. McDonald, F. B. and Van Hollebeke, M., (1985) Ap. J. (Letters) 290, L67

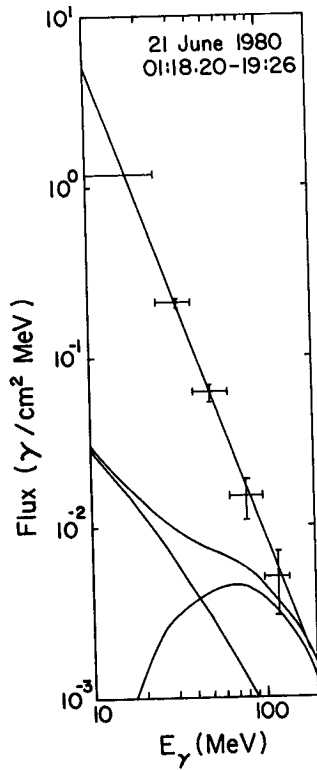


Fig. 1. The (10-140) MeV photon spectrum for the impulsive phase of the 21 June 1980 flare

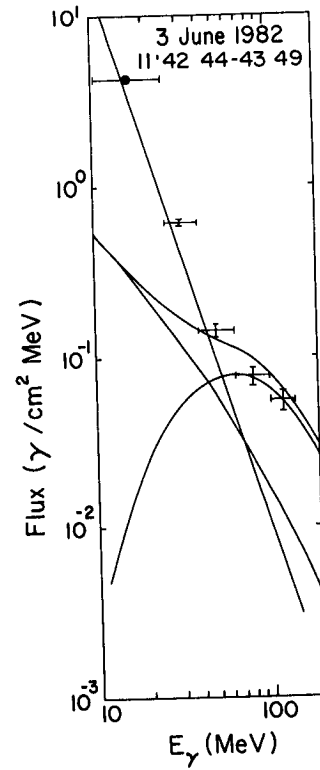


Fig. 2. The (10-140) MeV photon spectrum for the impulsive phase of the 3 June 1982 flare.

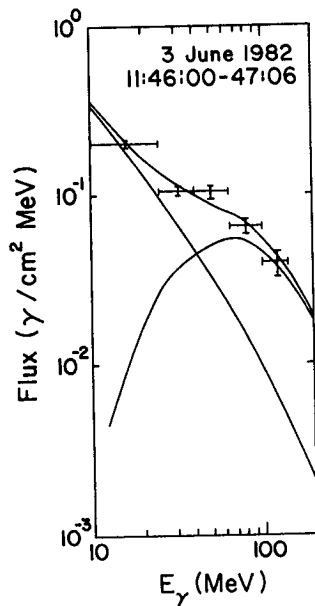


Fig. 3. The (10-140) MeV photon spectrum early in the extended phase of the 3 June 1982 flare.

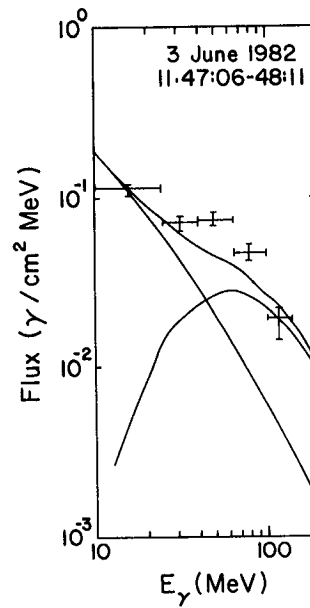


Fig. 4. The (10-140) MeV spectrum showing the photon spectrum and the effects of the high-energy neutrons in the extended phase of the 3 June 1982 flare

SH-1.4-8

# HIGH ENERGY NEUTRON AND GAMMA-RADIATION GENERATED DURING THE SOLAR FLARES

G.E.Kocharov, N.Z.Mandzhavidze

Ioffe Physico-Technical Institute Academy of Sciences of  
the USSR, Leningrad, 194021,USSR

Problem of high energy neutrons and gamma rays generation in the solar conditions is considered. It is shown that due to a peculiarity of generation and propagation of neutrons corresponding solar flares should be localized at high helio-longitudes.

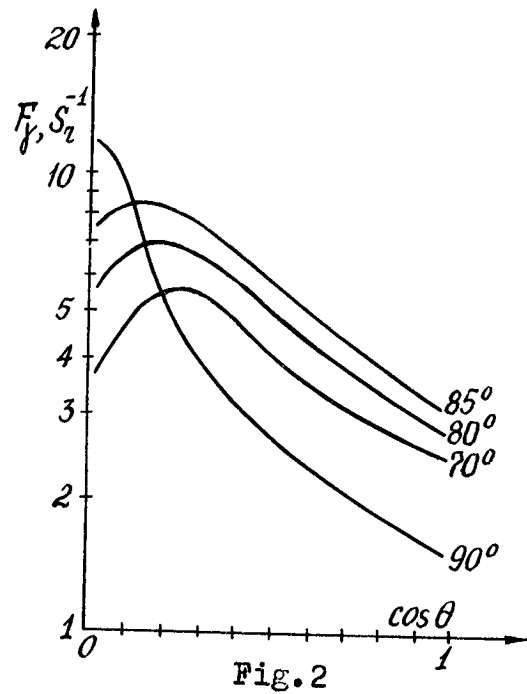
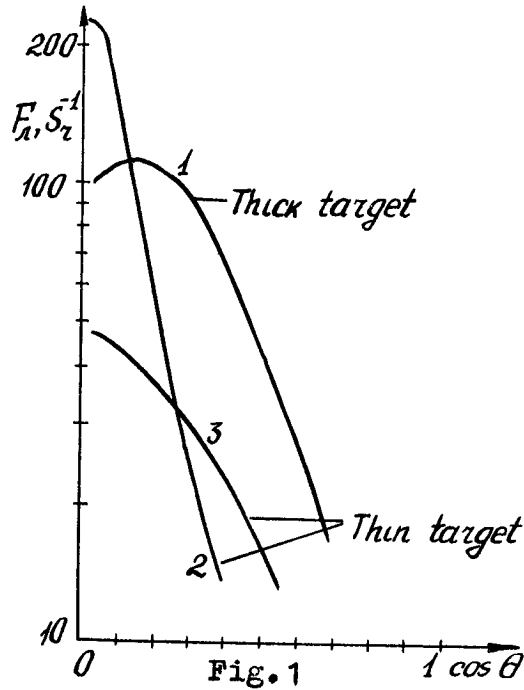
Solar neutrons have been detected only for two flares: for June 21 1980 on board of the SMM satellite by Chupp et al. [1] and for June 3 1982 simultaneously in several experiments by SMM [1,2], neutron monitors [3,4,5] and registration of protons of solar neutron decay origin [6] .

Experimental data allow to establish that energy spectra of neutrons generated in a flare may be described as power law in wide energy interval 50 to 1000 MeV with the spectral indexes 3 and 3.5 for the flares 21.06.80 and 3.06.82 accordingly.

In contrast to  $\gamma$ -lines which are formed by low energy particles (10-30 MeV) neutrons contain an information on energy spectra and angular distributions of accelerated particles in wider energy interval. Calculations of charged-particle energy spectra based on the observed neutron spectra have been made by Ramaty et al. and by us [7-13]. Ramaty et al. considered thick-target model and assumed that in the interaction region the distribution of accelerated particles is isotropic. They have also assumed that after their production the neutrons escape freely from the Sun. But because the neutrons have mean free paths comparable to the stopping range of the protons which produce them, the protons should be trapped magnetically in the region at column depths significantly less than their ranges. It was shown that both  $\gamma$ -line and neutron experimental data might be explained if charged particle spectrum is described by the Bessel function.

In our calculations we tried to refuse the assumption on magnetic trap and considered a beam configuration of accelerated particles. In this case for any direction of beam the flux of solar neutrons increases with an increase of a flare heliolongitude. It can be easily shown for the beam directed to the observer. Really, the thickness of matter traversed by accelerated particles in the solar atmosphere into Earth's direction for limb flare is higher than for disc flare about  $(\pi R_{\odot} / 2h_0)^{1/2} \approx 30-100$  times ( $h_0$  - is the scale height,  $R_{\odot}$  - is the solar radius). If the accelerated particles move to the Sun the neutrons which are scattered on  $90^\circ$  for the limb flare and on  $180^\circ$  for the disc flare are detected. The probability of backscattering is less relative to the scattering on  $90^\circ$ . However, as in this case nuclear reactions occur in deep regions of the solar atmosphere an absorption of neutrons may be essential. This effect was considered by us and it is shown that the limb retains an advantage.

All calculations of neutron generation and their escape from the Sun were made using Monte-Carlo method taking into account the angular and energy characteristics of (PP) and (pHe) reactions which are the main source of high energy ( $>50$  MeV) neutrons. The beams with different angles relative to solar radius were considered. Particle spectra were presented as power law with different spectral indexes. For different heliolongitudes total yield of neutrons and their energy spectrum have been calculated. Fig. 1 shows the dependence of the fluxes of the neutrons ( $>50$  MeV) on flare heliolongitude for 3 cases. It is seen that for all cases the neutron fluxes are decreased strongly from the limb to the disk. If we consider the beam directed to the Sun the experimental spectra for the flares 21.06.80 and 3.06.82 may be explained if  $\gamma_p = 3-3.5$  for  $E_p > 100$  MeV. In this case using experimental figures for total flux of neutrons:  $2.8 \cdot 10^{28}$  and  $2.5 \cdot 10^{29}$  we obtain for the total number of accelerated particles the following values:  $N_p(>30) = 7 \cdot 10^{32}$  and  $7.5 \cdot 10^{33}$ ,



Dependence of neutron fluxes on flare heliolongitude for the beams with different angles relative to solar radius.  
 1.  $\alpha=0$ ,  $\gamma_p=3,5$ ,  $N_p(>30\text{MeV})=10^6$   
 2.  $\alpha=90^\circ$ . 3. Isotropic yield to upper hemisphere  $\gamma_p=2.5, 23$ ,  $n N_p(>30\text{ MeV})/h_p^{1/2} = 1.5 \cdot 10^{23}$ ,  $n$  is number density in an interaction region.

Dependence of gamma-ray flux on flare heliolongitude for beams with different angles relative to solar radius.

accordingly. These figures are in good agreement with the total number of accelerated particles obtained by using  $\gamma$ -line data (see [13] and references therein). So, supposing a beam configuration it is possible to explain particle spectrum as power law from 10 MeV to 1000 MeV with single spectral index. Definitive conclusion can be made after obtaining of experimental distribution on heliolongitude for flares with measurable neutron fluxes.

Now we concern with the problem of high energy  $\gamma$ -rays. At the present time 14 solar flares with high-energy ( $>10\text{ MeV}$ )  $\gamma$ -rays are registered [14]. These events have a strong solar limb preference with 13 of 14 occurring in flares with a heliocentric angle  $>72^\circ$  [14].

If high energy gamma-rays are generated by ultrarelativ-



vistic electrons then the radiation is directed along of electron velocity and above considered arguments are correct. Let us consider the case when the source of high energy gamma-rays are  $\pi^0$ -mesons, which are generated in the same reactions as energetic solar neutrons.

It is seen (Fig.2) that the dependence for  $\alpha < 90^\circ$  is weaker than for the neutrons. For tangent beams an advantage of limb is obvious. But in this case the flare should occur in dense region  $n \geq 10^{13} \text{ cm}^{-3}$ . According to [14] all high energy  $\gamma$ -ray flares are characterized by fast impulses ( $\leq 2\text{s}$ ) which is in favour of high density of interaction region. Thus we cannot exclude a nuclear origin of high energy  $\gamma$ -rays. To make a definitive conclusion on the source of high-energy  $\gamma$ -rays it is very important to measure an energy spectrum of gamma-radiation.

#### References.

1. Chupp E.L. et al. *Astrophys. J. Letts.*, 1982, v. 263, p. 135.
2. Chupp E.L. et al. *Proc. 18-th ICRC, Bangalore*, 1983, v. 4, p. 97.
3. Efimov Yu.E. et al., *ibid.*, v. 13, p. 240.
4. Debrunner H. et al., *ibid.*, v. 4, p. 75.
5. Iucci N. et al., 1984, Preprint, IFSI, Italy, N 84-1.
6. Evenson P. et al. *Astrophys. J.*, 1983, v. 274, p. 875.
7. Ramaty R. et al. *Astrophys. J.*, 1983, v. 273, p. L41.
8. Ramaty R. et al., *Solar Phys.*, 1983, v. 86.
9. Lingenfelter R.E. et al. *Proc. 18-th ICRC, Bangalore*, 1983, v. 4, p. 101.
10. Ramaty R., Murthy R.J., *Proc. of the Plasma Astrophys. School and Workshop, Varenna*, 1984, p. 83.
11. Kocharov G.E., Mandzhavidze N.Z. *Izv. AN SSSR, ser. fiz.*, 1984, v. 48, N. 11, p. 2212.
12. Kocharov G.E., Mandzhavidze N.Z., *Pis'ma v Astron. Journ.*, 1984, v. 10, p. 771.
13. Kocharov G.E., *Proc. of the Plasma Astrophys. School and Workshop, Varenna*, 1984, p. 65.
14. Rieger E. et al. *Proc. 18-th ICRC, Bangalore*, 1983, v. 4, p. 83, paper presented at 164-th AAS Meeting, Baltimore, Maryland, 1984.

ON THE ANGULAR AND ENERGY DISTRIBUTION OF SOLAR  
NEUTRONS GENERATED IN P-P REACTIONS

Yu.E.Efimov, G.E.Kocharov

Ioffe Physico-Technical Institute Academy  
of Sciences of the USSR, 194021, Leningrad  
U S S R

Problem of high energy neutron generation in P-P reactions in the solar atmosphere is reconsidered. It is shown that the angular distribution of emitted neutrons is anisotropic and the energy spectrum of neutrons depends on the angle of neutron emission.

Solar neutrons have been detected for two flares June 21 1980 and June 3 1982 in direct experiments on board of the SMM satellite [1,2]. P.Evenson et al. [3] have observed fluxes of energetic protons in interplanetary space which they interpret as the decay products of neutrons generated in a solar flare on June 3 1982. High energy neutrons from this flare have been observed by high mountain neutron monitors at Jungfraujoch (Switzerland) and Lomnitsky Stit (Czechoslovakia) and by ground-based station in Roma [4-7].

The problem of neutrons generation and their escape from the solar atmosphere have been considered by R.Lingenfelter et al. [8]. They assumed that an angular distribution of the neutrons is isotropic and the probability of neutron generation in proton-nucleus collisions does not depend on energy. However this assumption for the energies higher than 100 MeV is not valid for P-P and p-He collisions. For example, generated in p-p reactions neutrons with a kinetic energy 500 MeV are concentrated in apex angle of cone of  $30^\circ$ . As at the experiments solar neutrons are registered up to 1000 MeV we reconsider a problem of neutron generation taking into account available data on the differential cross sections of corresponding nuclear reactions. Here we consider only the results of the calculations for P-P interaction with

one pion generation. Neutron escape from solar atmosphere was calculated using Monte-Carlo method. Total and differential cross-sections for elastic and inelastic P-P-interactions were approximated by polynoms based on the available data. Details of calculations are given in [9]. Results of calculations are shown in Fig.1 and 2.

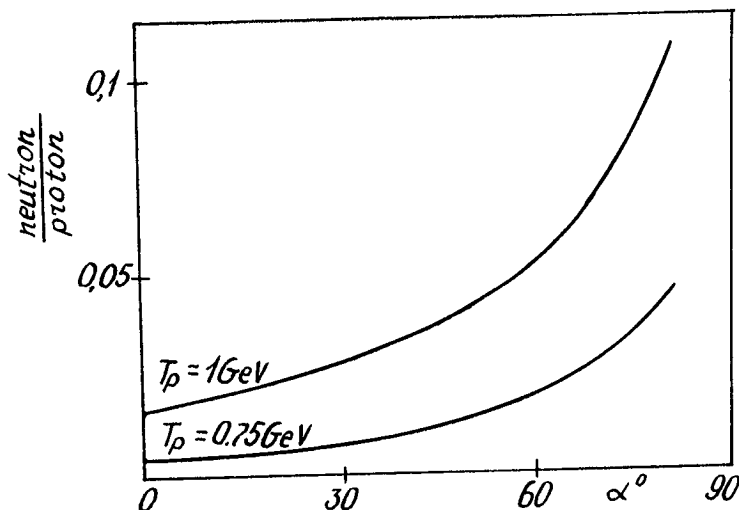


Fig.1. Dependence of neutron yield from the Sun (for energy interval 1-350 MeV) on angle of incidence  $\alpha$ -is the angle between the Sun outward and proton velocity direction).  $T_p$ -is kinetic energy of protons.

It is seen that neutron emission is anisotropic and their energy spectrum depends on neutron emission angle. Neutrons with energy  $\geq 100$  MeV are emitted only at angles  $60^\circ$  and more. It is natural that only neutrons generated by protons with high  $\alpha$  can escape the solar atmosphere without collision or with one or two collisions.

Based on the obtained data one can show that very few neutrons emit at the angles  $\Delta\theta = 0^\circ - 15^\circ$  to solar normal and there is no neutrons with the energies  $\geq 100$  MeV. This fact helps to clarify that the neutrons were discovered in the flares with high heliolongitudes. The protons moving to the upper hemisphere practically have not ionization losses and the products of their reactions do not interact. Neutrons yield in this case depends on the thickness of the matter

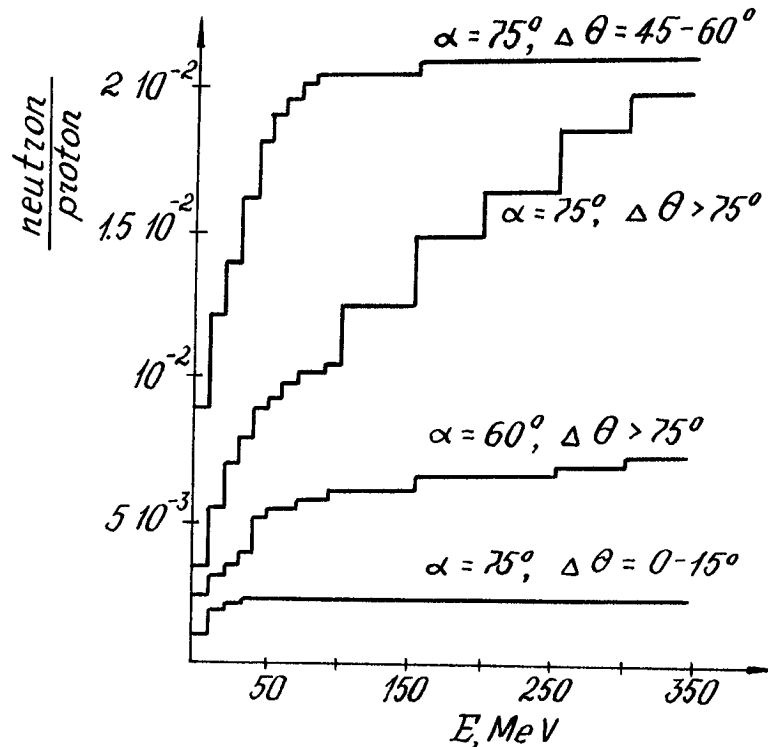


Fig.2. Energy spectrum of neutrons escaping into interplanetary medium (normalized to one proton).  $T_p = 1$  GeV and for the given point of observation on angular distribution of neutrons. The difference of neutron fluxes from the protons moving at  $0^\circ$  to solar surface and at large angle to it, will be mainly connected with different path of protons in the outer atmosphere of the Sun. Considering in first approximation that passing thickness of matter  $\sim 1/\cos \alpha$  we obtain that for protons moving at the angle  $72^\circ$ , the neutron flux should be 3.2 times higher than for the protons at the angle  $0^\circ$ . Protons with the angles up to  $15-20^\circ$  take part in generation of neutron flux for disc flare ( $0^\circ$ ), and for the flare E72 $^\circ$ -protons with angles less  $72^\circ$  are the main source of neutrons. So the difference in neutron fluxes from two such type of flares is not substantial (although, spectrum for the flare E72 will be more rigid). But the possibilities of observation of neutrons generated by protons moving to the lower hemisphere are substantially different for consi-

sphere are substantially different for considered two flares. Based on these facts, one may conclude that in flare 3.06.82(E72) the neutrons are generated by protons moving to the lower hemisphere. If in the acceleration region number density is  $10^{12} \text{ cm}^{-3}$ , the relative yield of neutrons for  $72^\circ$  in the case of thin target will be  $10^{-2}$ - $10^{-3}$  from the yield for the thick target.

We can conclude also (not taking into consideration magnetic field), that in the flare of 3.06.82, accelerated particles did not form sufficiently narrow beam, directed bottom at the angles  $0$ - $30^\circ$ .

The fact that the fluxes of neutrons with the energies  $> 100 \text{ MeV}$  and the energy spectra depend on the direction of motion of accelerated particles allow to obtain the information on angular distribution of accelerated high energy particles by the registration of high energy neutrons.

#### References.

1. E.L.Chupp et al. Astrophys.J.Lett. 263, L95, 1982.
2. E.L.Chupp et al. Proc.ICRC Bangalore, v.4, p.74, 1983.
3. H.Debrunner et al. Proc.ICRC, Bangalore, v.4, p.75, 1983.
4. Yu.E.Efimov et al., Proc.18-th ICRC, Bangalore, v.13, p.185, 1983.
5. P.Evenson et al. Proc.18-th ICRC, Bangalore, v.4, p.97, 1983.
6. R.E.Lingenfelter et al., Journ.Geophys.Res., v.70, p.4077, 1965.
7. R.E.Lingenfelter, R.Ramaty in High Energy Nuclear Reactions in Astrophys., ed.B.S.Shen, New York, W.A.Benjamin, 1967, p.99.
8. G.V.Voskresenskaya et al., Preprint FTI, N.896, 1984, Leningrad.

POSSIBLE DETECTION OF FLARE-GENERATED  
POSITRONS BY HELIOS 1 ON 3 JUNE 1982

E. Kirsch, E. Keppler, K. Richter  
Max-Planck-Institut für Aeronomie,  
D-3411 Katlenburg-Lindau, FRG

1. Introduction. The production of neutrons and  $\gamma$ -ray lines by solar particles in the photosphere has been studied by (1,2,3) and others. In the meantime  $\gamma$ -line measurements were reported (4,5,6,7). The principal positron emitters which lead to the 0.51 MeV  $\gamma$ -line are  $^{11}\text{C}$ ,  $^{14}\text{O}$ ,  $^{15}\text{O}$ ,  $^{13}\text{N}$ ,  $^{19}\text{Ne}$ . The energies of the positrons from radioactive nuclei are of the order of few hundred keV. Positrons resulting from the  $\pi^+$  decay have energies of  $\sim 10$ -100 MeV and cannot be measured by the MP Ae-detector.

Most of the positrons annihilate in the photosphere. A fraction however should be able to escape into the interplanetary space (2). It is the purpose of this paper to present proton, electron and, for the first time, positron measurements ( $E = 152$ -546 keV) obtained by the MP Ae-particle detector on board of Helios 1.

2. Experiment description and method of detection. The MP Ae-detector was designed to measure ions ( $E \geq 80$  keV), electrons ( $E \geq 20$  keV) and positrons ( $E = 152$ -546 keV) with high energy (16 channels) and angular (16 sectors) resolution (8,9). Ions, electrons and positrons are separated by a inhomogeneous magnetic field and then detected by several semiconductor detectors.  $S_7$  (125 mm<sup>2</sup> area, 322  $\mu$  thickness) is the ion detector and  $S_8$  (300 mm<sup>2</sup>, 274  $\mu$ ) its anticoincidence detector. The positron detector  $S_6$  (200 mm<sup>2</sup>, 1000  $\mu$ ) is anticoincidence shielded by  $S_9$  (300 mm<sup>2</sup>, 322  $\mu$ ). A fully anticoincidence shield was not possible due to weight limitations. Various coincidence conditions lead to the following channels:  $S_{6.1} \cdot S_{6.2} \cdot S_9 = e^+$  (152-546 keV);  $S_{6.1} \cdot S_{6.2} \cdot S_9 = e^+$  ( $> 546$  keV),  $S_7 \cdot S_8 = p$  ( $> 80$  keV) and x, $\gamma$  rays,  $S_7 \cdot S_8 = p, e$  ( $\geq 6$  MeV);  $S_9 = p, e$  ( $\geq 30$  MeV) and x, $\gamma$ -rays;  $S_{1,2,3,4} = e^-$  ( $\geq 20$  keV) and x, $\gamma$  rays. The x and  $\gamma$ -ray sensitivity results from the Compton scattering process of photons in the detectors. In interplanetary space positrons must be identified in the presence of relativistic particles, x and  $\gamma$ -rays and high energy neutrons produced by the same flare.

3. Observations. The 2B white light flare (S 09°, E 72°) on 3 June had its optical emission from 11:41 - 13:26 UT (H $\alpha$  max = 11:48 UT) and produced X rays (Solar Geophysical Data, June 1982),  $\gamma$ -rays and neutrons (6). Helios 1 was at a distance of 0.57 AU from the sun and at  $\sim 99^\circ$  heliographic longitude i.e. well connected to the flare region. The time resolution of the measurements was 107 sec. Fig. 1 shows from top to bottom  $\geq 30$  MeV protons and electrons ( $S_9$ ),  $\geq 6$  MeV protons, electrons ( $S_7 \cdot S_8$ ) and measurements of the 2 positron channels. It can be seen that the positron channels are disturbed by particles which penetrate the shielding of the instrument and cannot be eliminated by the anticoinci-

dence detector  $S_9$ . Thus the only chance to separate positrons against the background exists before the main increase. The low energy positron channel has a small premaximum followed by a short minimum (Fig. 1). The increase phase is shown in Fig. 2 with 107 sec time resolution. The main event starts to increase in intervals 4, 5 and 6 and only interval 4 may be suitable for a possible positron identification. If we take the maximum of the radio burst (Solar Geophysical Data, June, 1982) 11:43:20 UT at earth (minus 500 sec at the sun) as the start of the nuclear interaction and the production of the positron emitters the first positrons of 150-550 keV will be expected  $\sim 425-310$  sec later at Helios, i.e. 11:40:10 - 11:42:05 UT which is interval 4 of Fig. 2.

From other observations it is known that the event starts with a  $\gamma$  and x-ray peak (6) which is in time coincidence with interval 3 of Fig. 2. About 100 sec later (corresponding to interval 4 and 5 of Fig. 2) the x ray and 4.1-6.4 MeV  $\gamma$ -line flux is smaller by approximately a factor of 10. However the delayed  $\gamma$ -ray lines (2.2 MeV see (10) their Fig. 1) and 0.51 MeV see (11) their Fig. 6)) contribute to the background of interval 4 and 5 of Fig. 2 and must be eliminated. The curves 1 and 2 (Fig. 2) present measurements of the electron detectors for the solar (1) and antisolar (2) direction. Different operation modes of the ion detector ( $S_7 \cdot \bar{S}_8$ ) are shown in curves 3-6 for the solar (3,5) and antisolar (4,6) direction which measure the x and  $\gamma$ -ray background in this early phase. Curve 7 presents protons, electrons and  $\gamma$ -rays measured by the single detector  $S_9$  whereas curve 8 ( $S_7 \cdot \bar{S}_8$ ) shows the increase phase of charged particles. Thus charged particles and  $\gamma$ -rays contribute to the count rate of the positron channels also in interval 4 (curves 9,10). In comparison to the pre-event intervals ( $I_0, I_1, I_2$ ) the interval 4 shows the following increases

- 1)  $p, \gamma, (S_7 \cdot \bar{S}_8, \Delta E \geq 80 \text{ keV})$ , curve 5 and 6

$$I_4 / (I_1 + I_2) / 2 = \frac{182}{133} = 1.368$$

- 2)  $p, e, \gamma, (S_9, \Delta E \geq 80 \text{ keV})$ , curve 7

$$I_4 / (I_0 + I_1 + I_2) / 3 = \frac{816}{645.33} = 1.264$$

- 3)  $e^+, p, \gamma, (S_{6.1} \cdot \bar{S}_{6.2} \cdot \bar{S}_9, \Delta E = 152 - 546 \text{ keV})$ , curve 9

$$I_4 / (I_0 + I_1 + I_2) / 3 = \frac{106}{65} = 1.63$$

The second positron channel (curve 10,  $\Delta E \geq 546 \text{ keV}$ ) will not be considered since the magnetic system of the experiment does not quantitatively deflect the positrons of such energies.

By comparing the proton (5+6) and the positron channel (9) it follows that  $1.368/1.63 = 0.839$  of the positron count rates results from background radiation. The positron count rate in interval 4 would then be

$$106 - 0.839 \cdot 106 = 17 \pm 14$$

(14 = statistical error calculated after quadratic error propagation). The flux above the statistical error may be considered as positrons. It follows for a geometric factor of  $G = 3.2 \cdot 10^{-2} \text{ cm}^2 \text{ sterad}$  and 107 sec measuring time

$$\frac{3}{107 \cdot 3.2 \cdot 10^{-2}} = 0.876 \text{ e}^+ / \text{cm}^2 \text{ sec ster}$$

or extrapolated to 1 AU distance =  $0.28 \text{ e}^+/\text{cm}^2 \text{ sec ster}$ . It is assumed that positrons are confined by the interplanetary magnetic field to, say  $\sim 1$  sterad. The same flux distributed over  $2\pi$  steradian would then be  $4.4 \cdot 10^{-2} \text{ e}^+/\text{cm}^2 \text{ sec ster}$ . Model calculations (3; their fig. 5) reveal that about 40 % of the positron emitters have decayed in  $\sim 100$  sec. The totally emitted positron flux is therefore  $\sim 11 \text{ e}^+/\text{cm}^2$ .

4. Discussion and conclusion. The flare of 3 June 1982 has been investigated by (6, 10, 11). It is of interest to compare the flux of the emitted positrons with the flux of totally generated positrons. After Share and Rieger (private communication) the time integrated flux of the 0.51 MeV line was  $\sim 100 \gamma/\text{cm}^2$ . According to (11, their fig. 6) the flare of 3 June 1982 has a high  $\alpha \cdot T$  value ( $\alpha$  = stochastic acceleration efficiency of the flare region,  $T$  = particle residence time in the acceleration region) namely  $\alpha \cdot T = 0.04$ . For such an  $\alpha \cdot T$  a ratio of the generated positrons to the 4-7 MeV  $\gamma$  flux of

$$\frac{\text{e}^+}{4-7 \text{ MeV}} \sim 0.7$$

can be derived from (3, their fig. 4). From the 4-7 MeV flux of 305 photons/cm<sup>2</sup> (11) follows then  $213 \text{ e}^+/\text{cm}^2$  have been generated.

A further possibility to calculate the flux of the positrons is to compare the total proton flux  $\geq 30$  MeV of  $3 \cdot 10^{33}$  protons (11) with model calculations of (3, their fig. 5). It follows  $\sim 5.5 \cdot 10^{-32}$   $3 \cdot 10^{33} = 165$  photons/cm<sup>2</sup> (when  $\alpha T = 0.02$ ) and more than 165 would be expected for  $\alpha T = 0.04$ .

Thus assuming the "thick target" interaction model and the here derived positron flux ( $11 \text{ e}^+/\text{cm}^2$ ) it can be concluded that  $\leq 10$  % of the positrons can escape into the interplanetary space.

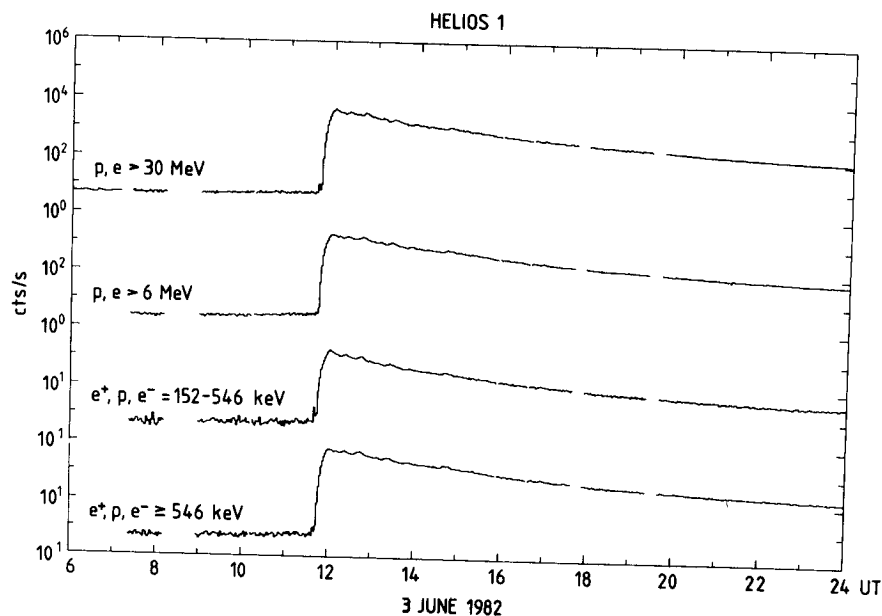


Fig. 1 Proton, electron and positron measurements on June 3, 1982, 06:00 - 24:00 UT.



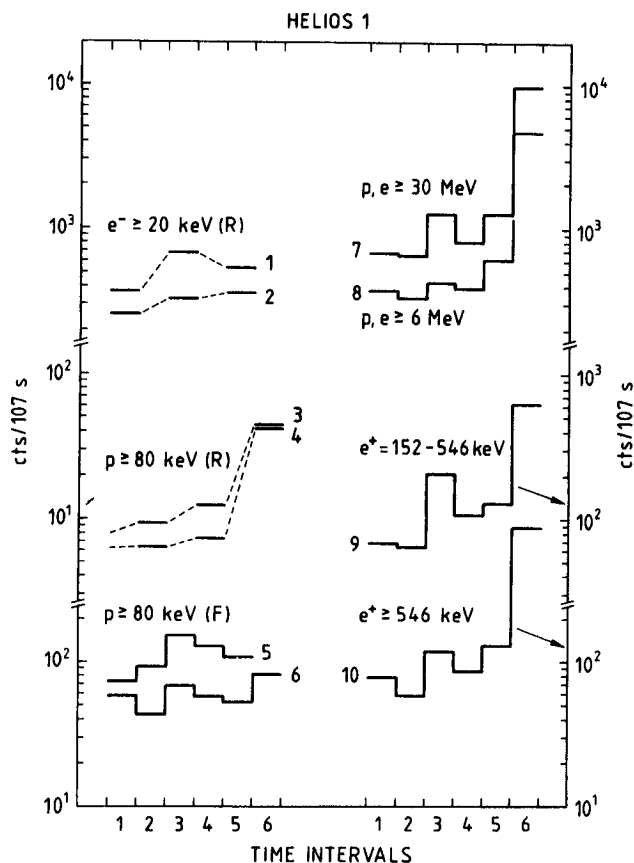


Fig. 2 Increase phase of the June 3, 1982 particle event.

Interval 1 = 11:35:24 UT  
 2 = 11:37:11 UT  
 3 = 11:38:58 UT  
 4 = 11:40:45 UT  
 transmit time  
 5 = 11:42:32 UT  
 $\Delta T = 107 \text{ sec}$

### References

1. Lingenfelter, R.E. and R. Ramaty, (1967), Ed. B.S.P. Shen, University of Pennsylvania, USA, pp.99
2. Ramaty, R., et al., (1975), Space Science Rev. 18, 341
3. Ramaty, R., et al.; (1983), Sol. Phys. 86, 395
4. Chupp, E.L., et al., (1973), Nature 241, 333
5. Chupp, E.L., et al., (1982), The Astrophysical Journal 263, L95
6. Chupp, E.L., et al., (1983), 18th International Cosmic Ray Conf., Bangalore 1983, Vol. 10, 334
7. Yoshimori, M., et al., (1983), 18th International Cosmic Ray Conf., Bangalore 1983, Vol. 4, 85
8. Keppler, E., et al., (1976), Bundesministerium für Forschung und Technologie, BMFT-FBW 76-14
9. Keppler, E., et al., (1977), J. Geophys. - Zeitschrift für Geophysik, 42, 633
10. Prince, T.A., et al., 18th International Cosmic Ray Conf., Bangalore 1983, Vol. 4, 79
11. Murphy, R.J. and R. Ramaty, (1984), Adv. Space Res., Vol. 4, No.7, 127

# SHOCK AND STATISTICAL ACCELERATION OF ENERGETIC PARTICLES IN THE INTERPLANETARY MEDIUM

Valdés-Galicia, J.F.<sup>1</sup>, Moussas, X.<sup>2</sup>, Quenby, J.J.<sup>3</sup>, Neubauer, F.<sup>4</sup>, Schwenn, R.<sup>5</sup>

1. Instituto de Geofísica, UNAM, 04510 Coyoacán, D.F., México
2. Astrophysics Lab., National Univ. of Athens, Panepistimiopolis, GR 15771 Athens, Grece.
3. The Blackett Lab. Imperial College, London SW7 G.B.
4. Inst. für Geophysik und Meteorologie, Univ. Köln, F.R.G.
5. Max Planck Inst. für Aeronomie, Katlenburg-Lindau, F.R.G.

1. Introduction. Definite evidence for particle acceleration in the solar wind came around a decade ago (Mc Donald et al, 1976, Barnes et al, 1976). Since then a considerable amount of data have been taken at different distances from the sun confirming and extending the first findings and it is now widely accepted that particles are accelerated in the Solar Wind (Quenby, 1983). Two likely sources are known to exist: particles may be accelerated by the turbulence resulting from the superposition of Alfvén and Magnetosonic waves (Statistical Acceleration) or they may be accelerated directly at shock fronts formed by the interaction of fast and slow solar wind (CIR's) or by traveling shocks due to sporadic coronal mass ejections. Naturally both mechanisms may be operative.

Shock acceleration has been widely investigated theoretically (Axford, 1981 and references therein) and there is substantial evidence of this as an operative mechanism in the Heliosphere (Scholer, 1984). However there are also experimental observations not obviously consistent with shock acceleration v.g. (Van Ness et al, 1984) and some ion enhancements only explained in terms of statistical acceleration (Richardson, 1984).

Previous treatments of statistical acceleration involved theoretical methods based on power spectral representations of the electromagnetic field (see Quenby, 1983 and references therein).

In this work the acceleration problem was tackled numerically using Helios 1 and 2 data to create a realistic representation of the Heliospheric plasma as will be described in the next section. Two 24 hour samples were used: one where there are only wave like fluctuations of the field (Day 90 Helios 1) and another with a shock present in it (Day 92 of Helios 2) both in 1976 during the STIP II interval. Transport coefficients in energy space have been calculated for particles injected in each sample and the effect of the shock studied in detail.

2. Interplanetary Medium Model. The magnetic field used is defined from  $\mathbf{B}_i$  three dimensional vectors where each one corresponds to the 8 sec. measurements of Helios 1 or 2. Every point in space is also furnished with a solar wind velocity vector  $\mathbf{V}_i$  where these are the corresponding velocities in the solar wind frame. Consequently because all parts of the solar wind are moving there is an electric field  $\mathbf{E}_i = -\mathbf{V}_i \times \mathbf{B}_i$  associated to every point in space. For every sample we have divided the space in a series of layers where both the electric and magnetic fields are constant. Trajectories are integrated based on analytical

solutions of the equations of motion for each layer. For more details see Moussas et al, (1982).

Because we require layers of roughly  $1/20$  of a cyclotron radius only 100 MeV protons have been used in this work, lower energies require smaller IMF sampling time to keep a reasonable number of layers per gyroradius.

3. Calculation of Transport Coefficients in Energy Space. First and second order coefficients ( $D_T$  and  $D_{TT}$ ) were calculated in energy space by two different techniques. One is based upon the construction of a steady state distribution by injecting particles with a single energy  $T_0$  (100 MeV in this case) and removing them when they reach any of the two preset boundaries "above" and "below" the injection point (see Moussas et al, 1982 for details).

Another method is based upon the time evolution of the energy distribution.  $D_T$  is calculated via a least square fit of successive distributions first order momenta vs. time. If we take the diffusion equation in energy, integrate for injection at  $T=T_0$ , assume a first order Taylor expansion in energy for  $D_{TT}$ , and make a determination of the spread  $\langle(T-\langle T \rangle)^2\rangle$  we arrive at

$$\langle(T-\langle T \rangle)^2\rangle = 2D_{TT}(T_0)t + 2(D_T)^2$$

from where  $D_{TT}$  can be calculated.

Both methods are generalizations of those initially developed by Jones et al (1978) to study pitch angle scattering on a randomly generated IMF.

The effect of the shock is traced by counting every particle encounter with it and recording the resulting energy change. The average energy change is given by the ratio of the total gain and the number of shock encounters. Transport coefficients can be calculated using the time an average particle takes to get back to the shock  $t_B = 2\lambda/v$  where  $\lambda$  = mean free path = 0.03 AU (see Valdés-Galicia et al, 1984) and  $v$  = particle velocity.

4. Shock Characteristics. The shock used in this study passed through Helios 2 on day 92 of 1976 when the spacecraft was at 0.45 AU from the Sun. It is a perpendicular shock  $\Theta_{Bn} = 89^\circ$  (Lepping et al, 1971) with a high Alfvén Mach number  $M_A = 7.5$ . The magnetic field overshoot is some 24 Gammas which is around 50% of the downstream field.

It was assumed to be a plane shock and data were transformed to a frame where the  $Y-Z$  plane coincides with that of the shock so that it is parallel to our layer planes.

5. Results and Discussion. In figure 1 we present a result of a time stationary distribution of particles for an experiment carried out using data from day 90/Helios 1. It can be easily appreciated the asymetry of the distribution towards the "right" of the injection energy  $T_0$  showing strong acceleration by waves. Boundaries were put at  $\pm 2$  MeV from  $T_0 = 100$  MeV. It should be noted that the mean free path these particles is very small ( $\lambda = 0.006$  AU, Valdés-Galicia et al, 1984).

Figure 2 shows an evolution diagram of the distribution function of particles in energy and time. Contours are drawn for different density levels. Areas with zero density within the distribution are shown black. Injection energy is at the middle of the figure and energy increases downwards. Full extension from top to bottom is 6 MeV. The horizontal scale covers 2000 sec. Black diamonds represent first order momenta of particle distributions every 100 secs.

In table I we show the main results of this work. Transport coefficients are average values of the calculations done by the two different methods. Although not shown individually both values agree within 15%. The second row of table I shows results for all particles (85) used with Helios 2 day 92 sample including 79 shock crossings so they are representative of the two processes involved (shock and statistical acceleration),

We can appreciate that even though average energy changes corresponding to statistical and statistical plus shock acceleration are greater than the shock produced average, transport coefficients for this process are greater by an order of magnitude. In the last column of the table we have calculated the the e-folding times ( $\tau$ ) corresponding to every experiment (Wibberenz et al, 1972). If we calculate the time for adiabatic deceleration at 0.45 assuming  $V_{sw} = 400$  Km/sec and radial expansion we get  $\tau_{ad} = 35.3$  hours. Thus although statistical acceleration can have an effect in reducing the adiabatic cooling only the shock accelerated particles are able to overcome it at these energies.

Unfortunately we were limited by the time resolution of the data and could not explore lower energies in a similar manner,

## 6. Conclusions.

- a) The time evolution and time stationary methods to calculate transport coefficients agree quite well.
- b) Statistical acceleration at particle energies of 100 MeV in the inner Heliosphere is not able to overcome the effects of adiabatic cooling.
- c) Shock acceleration as opposed to statistical acceleration may be a source of particles at these places and energies.

- d) Statistical acceleration may be a more efficient process at lower energies.

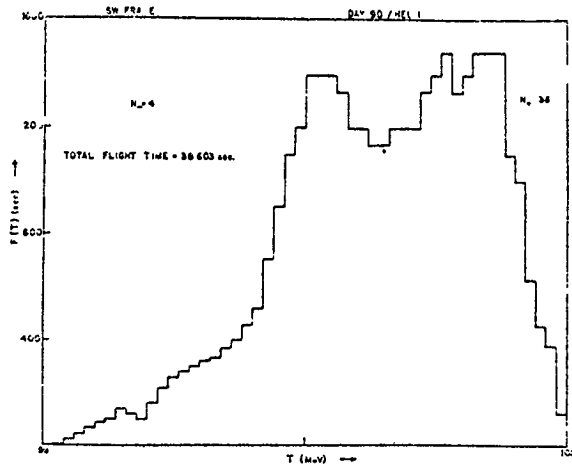


FIG 1

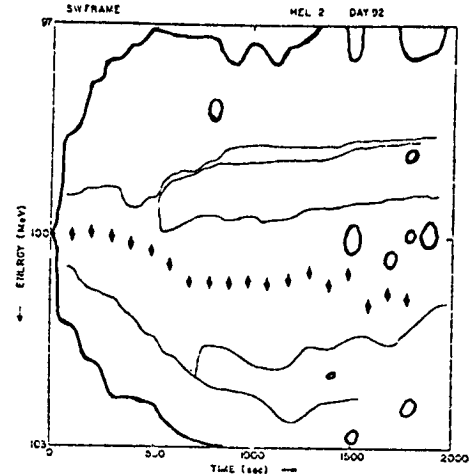


FIG 2

TABLE I

LOY/SC	POSITION (AU)	ACCELERATION PROCESS	$\langle \Delta T \rangle$ ( $\mu\text{eV}$ )	$D_T$ ( $\text{MeVs}^{-1}$ )	$D_{TT}$ ( $\text{MeVs}^{-2}$ )	$\tau$ (Hrs)
90/HEL 1	0.31	STATISTICAL	0.76	$(3.6 \pm 2.1) \times 10^{-4}$	$(4 \pm 3) \times 10^{-4}$	76.5
92/HEL 2	0.45	SHOCK+STATISTICAL	0.83	$(5.2 \pm 2) \times 10^{-4}$	$(5 \pm 3.5) \times 10^{-4}$	53.
92/HEL 2	0.45	SHOCK	0.26	$(3.4 \pm 1.5) \times 10^{-3}$	$(1 \pm .9) \times 10^{-4}$	10.9

## REFERENCES

- AXFORD I. (1981) Proc. XVII I.C.R.C., 12, 155.  
 BARNES J. ET AL. (1976) ASTROPHYS. J. LETT., 210, L91.  
 JONES ET AL. (1978) PHYS. FLUIDS, 21, 361.  
 LEPPING ET AL. (1971) J.G.R., 76, 4349.  
 MC. DONALD F. ET AL. (1976) ASTROPHYS. J. LETT., 203, L 149.  
 MOUSSAS ET AL. (1982) ASTROPHYS. SP. SCI., 85, 99.  
 QUENBY J. (1983) SP. SCI. REV., 34, 137.  
 RICHARDSON I. (1984) PLANET. SP. SCI., 32, 1179.  
 SCHOLER M. (1984) PROC. INT. SYMP. ON C.R. MOD., M'ORIOKA, JAPAN, 161.  
 VALDES-GALICIA ET AL. (1984) SOLAR PHYS., 91, 399.  
 VAN NISS P. ET AL. (1984) J.G.R., 89, 2122.  
 WIBBERENZ ET AL. (1972) IN COSMIC PLASMA PHYSICS (ED. K. SCHINDLER) 399.

## ENERGETIC ION ACCELERATION AT COLLISIONLESS SHOCKS

R. B. Decker and L. Vlahos  
 The Johns Hopkins University, Applied Physics Laboratory  
 Laurel, MD 20707  
 USA

1. Introduction. Spacecraft observations have shown that ions are routinely accelerated to energies from  $\sim 10$  keV to  $\sim 10$  MeV at interplanetary shocks (1). Of particular relevance in understanding how such ion events are produced are the angle  $\bar{\theta}_{Bn}$  between the mean shock normal and mean upstream magnetic field and the level of magnetic fluctuations in the shock's vicinity. When  $\bar{\theta}_{Bn} < 90^\circ$  (i.e., a nearly perpendicular shock) and the magnetic field quasi-laminar, pitch angle scattering is infrequent, and ions are accelerated primarily via the scatter-free shock drift process by drifting along the  $\vec{U} \times \vec{B}$  electric field parallel to the shock surface (2). When  $\bar{\theta}_{Bn} > 0^\circ$  (i.e., a nearly parallel shock) and the level of magnetic wave activity is high, pitch angle scattering is frequent, and ions are accelerated primarily via the diffusive shock acceleration process by being compressed between converging magnetic irregularities fixed in the upstream and downstream flows (3).

Although a small minority of ion events observed near 1 AU have features indicative of the acceleration process being predominantly either scatter-free shock drift or diffusive, most events are more complex, and are associated with shocks having intermediate values of  $\bar{\theta}_{Bn}$  and various levels of wave activity. To model these cases, we have developed a test particle simulation that integrates along ion orbits in a system described below.

2. Model. Let  $K[X,Y,Z]$  denote a system fixed with the shock, with the shock lying in the  $Y-Z$  plane, and the unit vector  $\hat{X} = -\hat{n}$  ( $\hat{n}$  = shock normal), so that  $X < 0$  upstream (subscript 1) and  $X > 0$  downstream (subscript 2). The vectors  $\vec{U}_1 = U_1(\cos \delta_1, 0, \sin \delta_1)$  and  $\vec{B}_{01} = B_{01}(\cos \theta_1, 0, \sin \theta_1)$  denote the upstream plasma velocity and mean magnetic field ( $\theta_1 = \bar{\theta}_{Bn}$ ), respectively. In  $K$  the  $\vec{U} \times \vec{B}_0$  electric field is along  $Y$ . Given in addition the upstream Alfvén Mach number  $M_{A1}$  and plasma beta  $\beta_1$ , the mean downstream conditions are obtained by solving the MHD jump equations (with a ratio of specific heats of 5/3).

We assume that the injected ions are true test particles (i.e., they are not coupled self-consistently to the shock and/or waves), and neglect shock structure by requiring (ion gyroradius)  $\gg$  (shock transition). Pitch angle scattering is introduced by superposing upon  $\vec{B}_{0i}$  ( $i = 1$  or  $2$ ) a zero-mean, random magnetic field component  $\vec{b}_i(z)$  which, in either the upstream or downstream plasma frame, varies only with coordinate  $z$  along  $\vec{B}_{0i}$ , is transverse to  $\vec{B}_{0i}$ , and is static (i.e., scattering is elastic in either plasma frame). The field  $\vec{b}_i(z)$  is a superposition of  $N$  circularly polarized plane waves with wavevectors along  $\vec{B}_{0i}$ . The amplitude of each Fourier component with wavenumber  $k$  is derived from a power spectrum  $P(k)$  using a well-known technique (4).

SH 1.5-3

The simulation proceeds first by constructing the  $\vec{b}_1(z)$ , then by solving the Lorentz force equation for the particle orbit using the field  $\vec{B}_1(z) = \vec{B}_{01} + \vec{b}_1(z)$  in the appropriate plasma frame, performing a Lorentz transformation between plasma frames at shock crossings, and continuing until pre-set spatial and/or temporal boundaries are crossed, whereupon the process is repeated for a new particle.

**3. Results.** Acceleration at interplanetary shocks was simulated using the form  $P(k)$  in Figure 1, which shows sample upstream spectra with  $B_0 = B_{01} = 5$  nT. Wavenumber  $k$  in the solar wind or plasma frame (top and right axes) was related to frequency  $f$  in the spacecraft frame (bottom and left axes) via  $k = 2\pi f/V_{SW}$  for a solar wind speed  $V_{SW} = 4 \times 10^7$  cm/s. Spectrum A (correlation length  $2 \times 10^{11}$  cm) represents that of ambient transverse Alfvénic fluctuations in the interplanetary medium (5). Spectra B and C (correlation length  $1.3 \times 10^8$  cm) represent transverse MHD waves presumably driven by ions streaming upstream from the shock (6,7). To model the observed spectra, we damped the upstream shock-associated field amplitude with the function  $[1 + |X|/X_1^*]^{-1}$ , where  $X_1^* = D_1 \cos \theta_1$ , with  $D_1$  measured along  $\vec{B}_{01}$  from the shock. For  $D_1 = 1.5 \times 10^{11}$  cm  $= 0.01$  AU ( $\gg 1.3 \times 10^8$  cm), the integrated power or variance  $\sigma^2$  of C at  $|X| = X_1^*$  is  $0.06 B_{01}^2$ , 1/4 that of spectrum B at  $X = 0$ , where  $\sigma^2 = 0.25 B_{01}^2$ . Downstream spectra used were similar to those in Figure 1, except  $D_2 = 1.5 \times 10^{13}$  cm  $= 1$  AU, and  $\sigma^2 = 0.36 B_{02}^2$  to model the enhanced wave levels observed downstream of shocks. Realizations of spectra A and B for  $N = 4096$  were superposed to form  $\vec{b}_1(z)$ , with linear interpolation used between grid points during orbit integrations. The upper scale in Figure 1 shows the resonant proton energy at which proton gyroradius  $\rho \sim k^{-1}$ .

Figures 2 and 3 show results for  $\delta_1 = 0^\circ$ ,  $\theta_1 = 60^\circ$ ,  $U_1 = 4 \times 10^7$  cm/s,  $B_{01} = 5$  nT,  $M_{A1} = 8$ ,  $\beta_1 = 1$ , and protons injected upstream with energy  $E_0 = 10$  keV in the upstream plasma frame. For this case,  $B_{02}/B_{01} = 3.2$  and the plasma density jump  $r = 3.7$ . We define the scale time  $\tau_{01} = eB_{01}/m_0c = 13$  sec (upstream proton gyroperiod) and scale length  $\rho_{01} = v_0\tau_{01}/2\pi = 2.8 \times 10^8$  cm (upstream gyroradius of a 10 keV proton with speed  $v_0 = 1.3 \times 10^8$  cm/s).

In Figure 2(a) kinetic energy  $E/E_0$  in the shock frame is shown versus distance  $X/\rho_{01}$  from the shock (upstream at left, downstream at right of  $X = 0$ ). In 2(b) and 2(c)  $E/E_0$  and  $X/\rho_{01}$  are shown versus time  $t/\tau_{01}$  during the orbit. Periods A-H in 2(a) are marked atop 2(b). The largest and most rapid

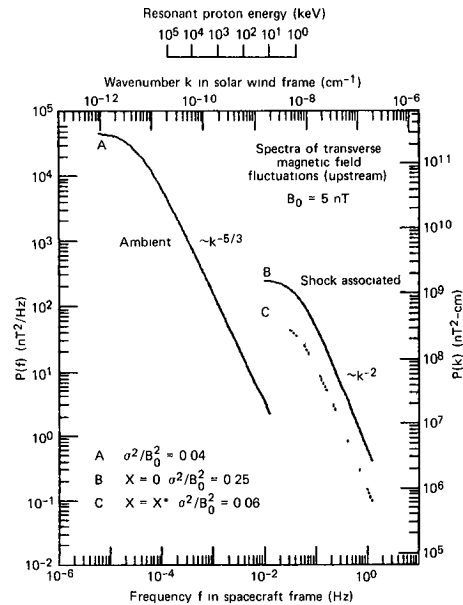


Fig. 1. Wave power spectra

SH 1.5-3

energy gains clearly occur during the shock drift phases of acceleration (e.g.,  $t/\tau_{01} = 8$  to 9, 11 to 14, 24 to 30, and 40 to 42). In comparison, diffusive energy gains due to compression between the inflowing upstream plasma and the shock are relatively small (e.g.,  $t/\tau_{01} = 14$  to 24 and 30 to 40). The particle in Figure 2 crossed the shock 42 times and was accelerated from 10 to 560 keV in  $43 \tau_{01} = 9.4$  min. This orbit shows features typical of the case  $\theta_1 = 60^\circ$ .

In Figure 3 we show the energy spectra that result after an elapsed time of  $300 \tau_{01} = 66$  min for 2900 injected protons. The quantity  $\Delta f(E)/\Delta E$  is the fraction of particles with energy  $E$  within  $\Delta E$  centered at the logarithmically-spaced plot points. The upstream (solid) and downstream (dashed) spectra denote sums over all particles with  $X < 0$  and  $X > 0$ , respectively. Error bars are two statistical standard deviations in length.

**4. Discussion.** The most striking aspect of Figure 3 is that well-formed energy spectra spanning more than two decades in energy are produced within only one hour after injection and that these spectra bear remarkable qualitative and quantitative resemblance to observations. For example, the downstream spectrum from 10 keV to 1 MeV is well-described by a power law with spectral exponent  $\sim 2.2$ , which is quite close to some observed values (1). In addition, the upstream

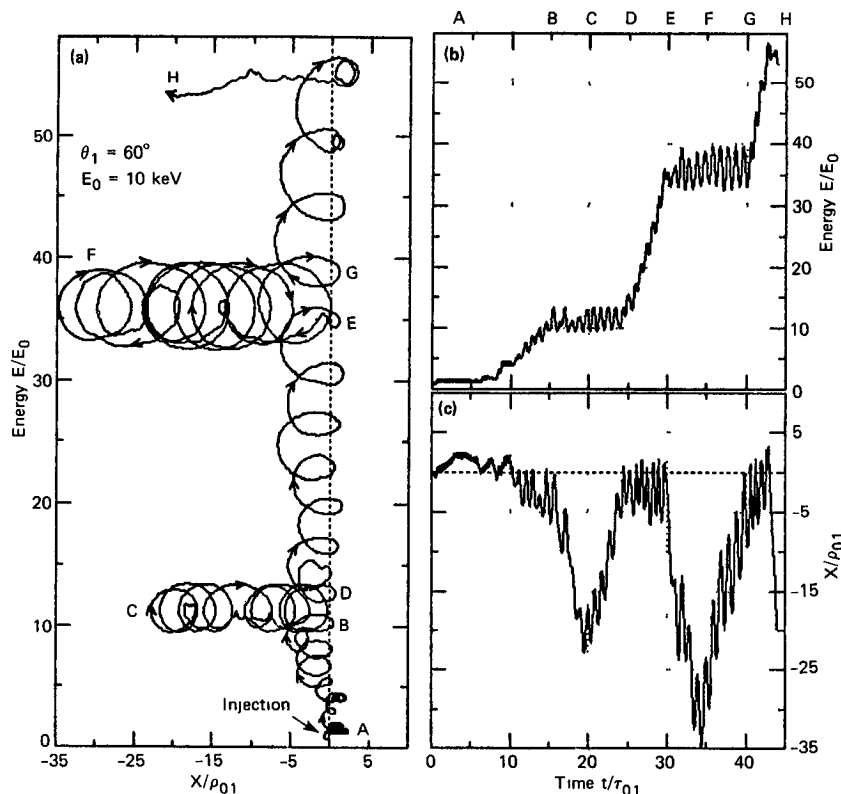


Fig. 2. Sample proton orbit



spectrum folds over with decreasing energy, similar to observed events (8). The cutoff time as well as the upstream escape boundary at  $X = 0.5$  AU produce the steepening of the upstream spectrum beyond  $\sim 1$  MeV.

We emphasize that the spectra in Figure 3 are primarily the products of the shock drift acceleration process, with pitch angle scattering simply providing the means to return particles to the shock for multiple drift acceleration phases, as in Figure 2. Diffusive acceleration contributes little to acceleration in this case. To estimate the maximum effect expected from diffusive acceleration, we set  $\theta_1 = 0^\circ$ , and keeping all other parameters fixed as in the  $\theta_1 = 60^\circ$  case, injected particles at 10 keV ( $B_{02}/B_{01} = 1$  and  $r = 3.85$  in this case). After  $300 \tau_{01}$  the spectra extended no further than  $E/E_0 = 10$  or 100 keV, illustrating, as one might expect, that 300 gyroperiods is far too short a period for diffusive acceleration alone to produce an extended energy spectrum. Examples of energy spectra for various values of  $\theta_1$  from  $0^\circ$  to  $75^\circ$  are shown by reference 9.

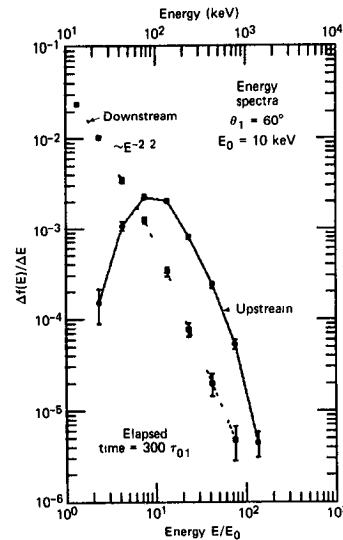


Fig. 3. Proton energy spectra

**5. Conclusions.** We have presented an example from a test particle simulation designed to study ion acceleration at oblique turbulent shocks. For conditions appropriate at interplanetary shocks near 1 AU, we have found that a shock with  $\theta_{Bn} = 60^\circ$  is capable of producing an energy spectrum extending from 10 keV to  $\sim 1$  MeV in  $\sim 1$  hour. In this case total energy gains result primarily from several separate episodes of shock drift acceleration, each of which occurs when particles are scattered back to the shock by magnetic fluctuations in the shock vicinity.

**6. Acknowledgements.** This work was supported in part by the JHU/APL Independent Research and Development Program under Navy Contract N00024-83-C-5301 and in part by NSF Grant ATM-83-05537.

#### References

1. van Nes, P., et al.: 1984, JGR, **89**, 2122.
2. Decker, R. B.: 1983, JGR, **88**, 9959.
3. Lee, M. A.: 1983, JGR, **88**, 6109.
4. Owens, A. J.: 1978, JGR, **83**, 1673.
5. Hedgecock, P. C.: 1975, Solar Phys., **42**, 497.
6. Tsurutani, B. T., et al.: 1983, JGR, **88**, 5645.
7. Sanderson, T. R., et al.: 1985, JGR, **90**, 3973.
8. Decker, R. B., et al.: 1981, JGR, **86**, 8819.
9. Decker, R. B. and Vlahos, L.: 1985, paper SH 1.1-6, these proceedings.

**ACCELERATION OF IONS AND ELECTRONS TO NEAR-COSMIC RAY ENERGIES  
IN A PERPENDICULAR SHOCK: THE JANUARY 6, 1978 EVENT**

S. M. Krimigis  
Applied Physics Laboratory, The Johns Hopkins University  
Laurel, MD 20707

E. T. Sarris  
The University of Thrace  
Polytechnic School  
Xanthi, Greece

**ABSTRACT**

Acceleration of energetic ions to  $\sim 200$  MeV and electrons to  $\sim 2$  MeV were detected by the Low Energy Charged Particle (LECP) instrument on Voyager 2 in association with a quasi-perpendicular shock of  $\theta_{Bn} = 87.5^\circ$  at 1.9 AU. The measurements, obtained at a time resolution of  $\sim 1.2$  sec, reveal structure of the energetic particle intensity enhancements down to a scale of the order of the particle gyroradius, and suggest that acceleration takes place within a gyrodiameter of the shock. The observations are consistent with the predictions of the shock drift acceleration (SDA) mechanism. The absence of any fluctuations in the magnetic field during the shock passage suggests that turbulence is not essential to the shock acceleration process in the interplanetary medium.

1. Introduction. It is a well documented observational fact that even weak ( $M_A \approx 1.5$ ) quasi-perpendicular shocks readily accelerate ions to relatively high energies (up to  $\sim 50$  MeV, Sarris et al., 1976), while quasi-parallel shocks rarely accelerate ions to rather modest ( $\sim 200$ - $300$  keV maximum) energies, if such shocks are more or less supercritical ( $M_A \approx 2.8$ , Kennel et al., 1984). Surprisingly, theoretical work on shock acceleration of cosmic rays has concentrated on quasi-parallel shocks (Axford et al., 1977; Blandford and Ostriker, 1978), despite the fact that such shocks are demonstrably incapable of producing high energy particles in the interplanetary medium. In an earlier paper (Sarris and Krimigis, 1985) we reported the details of a high mach number shock ( $M_A \approx 3.4$ ) observed by Voyager 2 at 1.9 AU. In this paper we examine further the development of the energy spectrum and the time variability of the intensity at the time of shock passage. For details of the detector system and instrument operation see Krimigis et al., 1977.

2. Results. Figure 1 shows the count rate profile of several channels from the LECP instrument from January 1 - 7, 1978, following a 2N flare at 2145 UT on January 1, 1978. The shock wave intercepted the Voyager 2 spacecraft on January 6, 1978 at 00:01:30 UT, as is evident from the intensity-time profile in the figure. The energy extent of the enhancement can be seen from the fact that the iron channel in the range  $\sim 2$ - $12$  MeV/nuc (i.e. a total energy  $> 112$  MeV) increased in intensity by well

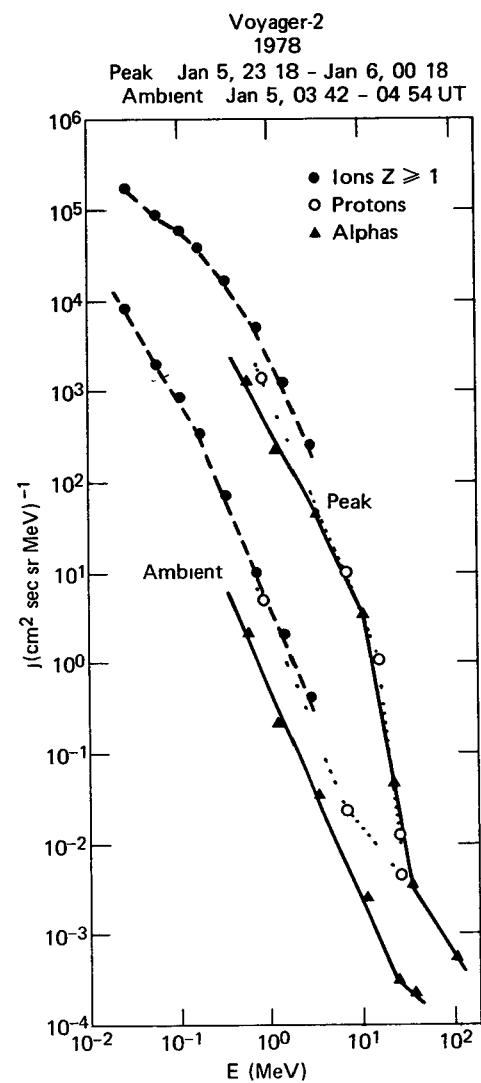
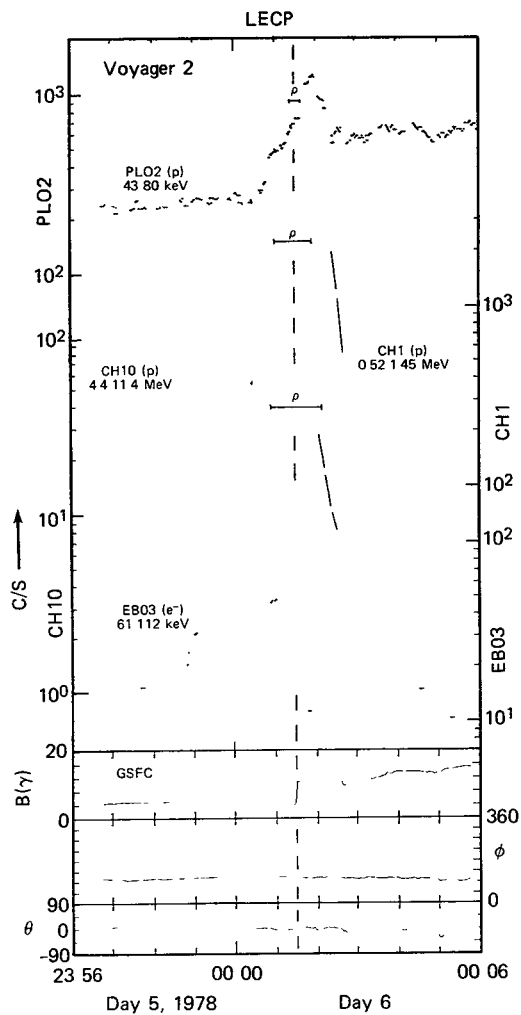
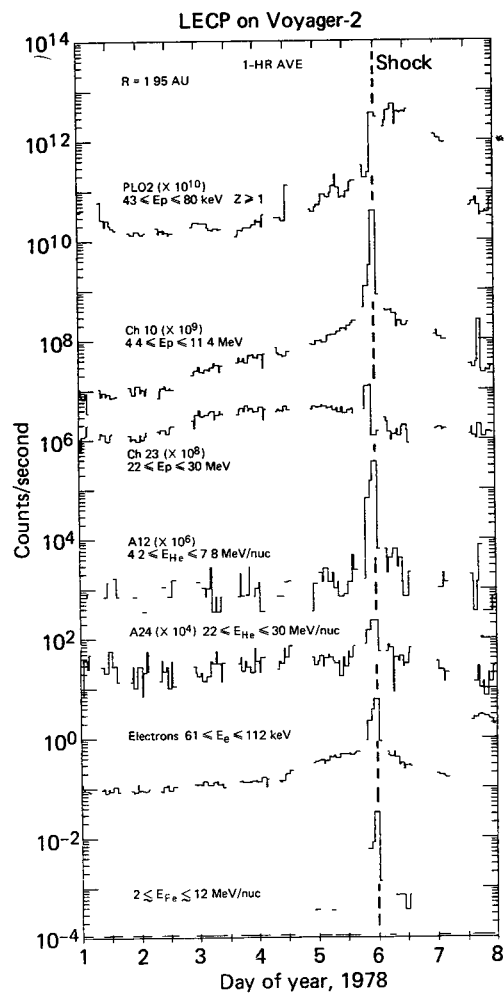


Figure 1 Hourly averages of the responses of selected channels from the LECP instrument on Voyager-2 following the January 1, 1978 solar flare event; the shock wave (dashed line) encountered the spacecraft on January 6, 1978 at 00:01:30 UT.

Figure 2 Expanded time scale of ion and electron counting rates with a time resolution of 1.2 sec. for channels PL02 and EB03 and ~ 10 sec. for Channel CH1 and CH10. The length of time corresponding to the particle gyroradius as convected past the spacecraft is marked for each channel with the exception of EB03. The magnetic field measurements are shown in the bottom three panels (Courtesy of Drs. N. F. Ness and R. P. Lepping).

Figure 3 Energy spectra of ions  $Z > 1$  at lower energies and protons and He at higher ( $> 100$  MeV) energies, when shock effects were weak (ambient) and around the shock (peak).

---

over 2 orders of magnitude.

The detailed time interval to within  $\pm 5$  minutes of the passage of the shock is shown in Figure 2. The magnetic field parameters (courtesy of N. F. Ness and R. P. Lepping) are shown in the bottom three panels. The top curve in the upper panel shows that the enhancement for the lowest energy ions ( $\sim 40$  keV) occurs immediately after the passage of the shock; at an energy about a factor of 10 higher (second curve), however, the intensity peaks at the shock passage with more of the increase upstream rather than downstream of the shock. At an energy one order of magnitude higher still (third curve from the top) the increase is most notable upstream of the shock while the intensity drops by well over an order of magnitude downstream within a gyro-diameter of the shock. We also note that the energetic electrons are essentially attached to the shock itself with the intensity being higher upstream than downstream. It is important to note that this energy separation effect is distinct in both the general large scale structure of the energetic particle intensity enhancements seen in Figure 1, as well as in the fine scale intensity structure which is attached to the shock. The peak intensities of the fine structure are found downstream (low energies) or upstream (high energies) at distances from the shock of the order of the particle gyroradius. It is essential to note that measurements of the magnetic field with a time resolution of 1.92 sec. indicate that the magnetic field is very quiet upstream from the shock front and show no evidence for the presence of significant magnetic turbulence in the frequency range from  $\sim 0.2$  Hz to  $\sim 10^{-3}$  Hz.

Figure 3 shows the energy spectra of ions with  $Z > 1$  up to  $\sim 3$  MeV, and of protons and alpha particles at energies  $> 0.5$  MeV where the elements can be clearly separated (Sarris and Krimigis, 1985). The ambient population some twenty hours prior to the passage of the shock is shown for comparisons. It is evident that the enhancements were largest for helium ions, especially at the higher energies ( $\sim 10$  MeV). Although not shown here, the enhancements for the heavier elements extended to total energies  $\sim 200$  MeV (Sarris and Krimigis, 1985).

3. Discussion. The shock acceleration event described above is remark-

able in that not only did it accelerate nuclei and electrons to almost cosmic ray energies, but that it did so in the absence of any discernible level of turbulence in the magnetic field. Further, the data demonstrate that all intensity enhancements and fine structure occur within a gyrodiameter of the shock from the lowest ( $\sim 40$  keV) to the highest ( $> 20$  MeV) energies. This event and many other similar ones (Armstrong et al., 1985) demonstrate that turbulence is not a necessary condition for particle acceleration in shocks, to the highest energies observed in the interplanetary medium.

Recent simulation work on quasi-perpendicular and quasi-parallel shocks in the presence of turbulence (Decker and Vlahos, 1985) shows that magnetic fluctuations have a tendency to cause a test particle to encounter the shock more than once. In each of these encounters, however, the energy gain is mostly through drift acceleration along the shock surface, rather than compression. This result helps to explain the observation that maximum energies attained in quasi-parallel shocks are at most  $\sim 300$  keV. The apparent maximum energy gain is likely due to the fact that the time during which the instantaneous magnetic field-shock normal geometry is near-perpendicular is rather small and consequently the energy gain through shock-drift is low. This energy gain "saturation" effect at relatively low energies suggests that the particle escapes the shock turbulence region after only a few encounters with the shock.

Similarly in the astrophysical case, quasi-perpendicular shocks would energize the ions to several hundred MeV. Such particles would then become the seed population; further energization would obtain through scattering in magnetic field fluctuations which may cause the ions to undergo additional encounters with the shock for further energy gains. At some point (relativistic energies?) compression may begin to become an appropriate description for the process.

4. Acknowledgements. We are grateful to Dr. A. Vinas of GSFC for providing us with the shock parameters. This work was supported by NASA under Task I of Contract N00024-83-E-5301.

5. References. Armstrong, T. P. et al., Shock Drift Acceleration, Proceedings of the Chapman Conference on Collisionless Shocks, AGU, 1985.

Axford, W. I. et al., The acceleration of cosmic rays by shock waves, Proceedings, International Conf. of Cosmic Rays 15th, 11, 132, 1977.

Blandford, R. D. and J. P. Ostriker, Particle acceleration by astrophysical shocks, Astrophys. J., 221, L29, 1978.

Decker, R. B. and L. Vlahos, Energetic ion acceleration at collisionless shocks, 19th ICRC Conference, SH 1.5-3, 1985.

Krimigis, S. M. et al. The Low Energy Charged Particle (LECP) experiment on the Voyager spacecraft, Space Sci. Rev., 21, 329, 1977.

Kennel, C. F., et al., Structure of the November 12, 1978 quasi-parallel interplanetary shock, J. Geophys. Res., 89, 5435, 1984.

Sarris, E. T. and S. M. Krimigis, Quasi-perpendicular shock acceleration of ions to  $\sim 200$  MeV and electrons to  $\sim 2$  MeV observed by Voyager 2, Astrophys. J., \_\_, (in press) November 15, 1985.

Sarris, E. T. et al., Observations of a high-energy ion shock spike in interplanetary space, Geophys. Res. Lett. 3, 133, 1976.

PARTICLE ACCELERATION DUE TO SHOCKS  
IN THE INTERPLANETARY FIELD:  
HIGH TIME RESOLUTION DATA AND SIMULATION RESULTS.

R.L. Kessel, T.P. Armstrong, R. Nuber, J. Bandle  
University of Kansas, Lawrence, KS, 66045, U.S.A.

## INTRODUCTION

In this study, data is examined from two experiments aboard the Explorer 50 (IMP 8) spacecraft. The Johns Hopkins University/Applied Physics Lab Charged Particle Measurement Experiment (CPME) provides 10.12 second resolution ion and electron count rates as well as 5.5 minute or longer averages of the same, with data sampled in the ecliptic plane. The Goddard Space Flight Center Magnetic Field Experiment provides the high time resolution magnetic field data (15.36 sec). IMP 8 spends about half its nearly circular (32 to 38 Re) orbit in the interplanetary field. The high time resolution of the data allows for an explicit, point by point, merging of the magnetic field and particle data and thus a close examination of the pre- and post-shock conditions and particle fluxes associated with large angle oblique shocks in the interplanetary field. A computer simulation has been developed wherein sample particle trajectories, taken from observed fluxes, are allowed to interact with a planar shock either forward or backward in time. Shock normals are determined from the single spacecraft method of Lepping and Argentiero (1) using the Imp 8 magnetic field data and OMNI plasma data (J.W. King, NSSDC). One event, the 1974 Day 312 shock, is examined in detail.

## DETERMINATION OF THE SHOCK NORMAL

The method of Lepping and Argentiero is based on the coplanarity theorem (2) in which the normal is determined by the magnetic fields:

$$\hat{n} = \frac{(\vec{B}_2 - \vec{B}_1) \times (\vec{B}_1 \times \vec{B}_2)}{|(\vec{B}_2 - \vec{B}_1) \times (\vec{B}_1 \times \vec{B}_2)|}$$

Instead of using the average values calculated from the data, "best estimate" values are determined in a manner to be explained below. Two assumptions are necessary to use this method: first, that the Rankine-Hugoniot equations are valid for interplanetary shocks; second, that the shock is a step-function increase in all parameters, with superimposed noise. Figure 1 lends credibility to the second assumption. The first assumption is necessary because certain of the

Rankine-Hugoniot equations are used as a constraint on the shock normal. The equations in the shock rest frame are:

$$\begin{aligned} [\rho V_n]_1^2 &= 0 \\ \left[ \rho V_n V_t - \frac{B_n B_t}{4\pi} \right]_1^2 &= 0 \\ [V_n B_t - V_t B_n]_1^2 &= 0 \\ [B_n]_1^2 &= 0 \end{aligned}$$

Eleven variables can be identified from these equations:

$$\rho_1, \rho_2, \vec{W}(\vec{V}_2 - \vec{V}_1), \vec{B}_1, \vec{B}_2$$

Three of these variables are isolated in terms of the other eight. In the Lepping and Argentiero study any three variables could be isolated. Their data consisted of 30 sec averaged magnetic field data and approximately 90 sec averaged plasma data. In this study 15 sec averaged magnetic field data was used along with 5 min averaged plasma data. Because of the large standard deviations associated with the solar wind data ( $W_x, W_y, W_z$ ), partly due to the low resolution of the data, it was necessary to isolate these three variables. To use them in the Rankine-Hugoniot equations to solve for the other variables produced inconsistent results or no convergence.

The method uses the eight "known" variables and the three variables calculated from the Rankine-Hugoniot equations in a type of least squares fit which is minimized by use of an iteration process. The solution should converge to the "best estimate" values relatively quickly. Many starting values should be used and these compared to assure convergence to the same minimum.

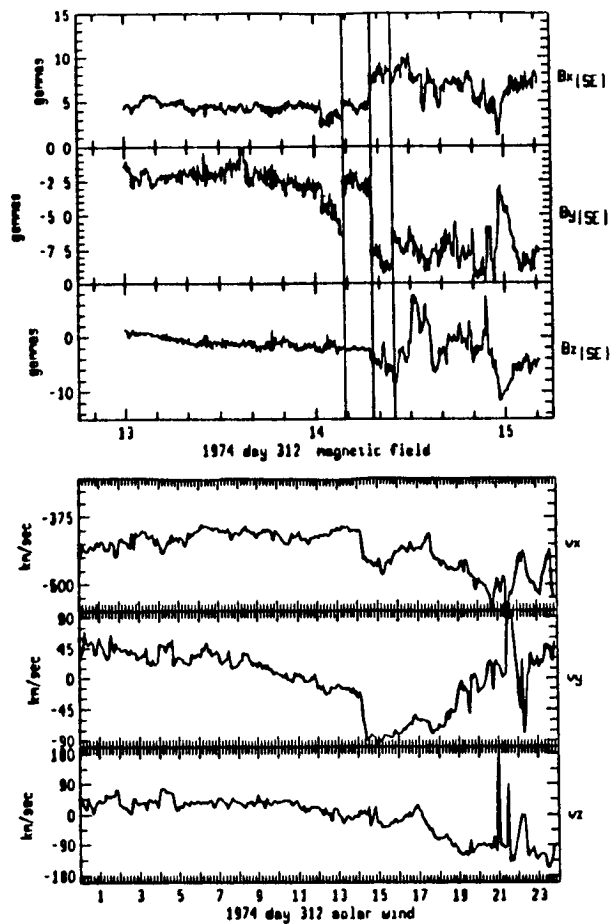


Fig. 1. a) Magnetic field in solar ecliptic coordinates. Vertical lines separate field into pre- and post- shock regions which were used in the shock normal determination. b) Solar wind in solar ecliptic coordinates. Shock occurs at 14 30 hours.

This normal determination method was tested in several ways. Multiple runs were made with different starting values (particularly, different numbers of plasma points were used from 15 min to 40 min of data), and these were checked against each other. Three events were used; one, the 1974 day 312 shock to be used in the remainder of this work, and two others which were checked against thetabn angles supplied by Tsurutani (private comm.)--thetabn being the angle between the magnetic field and the shock normal. The 1979 day 93 thetabn was calculated at  $39^\circ$  which is within  $4^\circ$  of that calculated by Tsurutani, and the 1979 day 95 thetabn is within  $6^\circ$  of the Tsurutani value. The 1974 day 312 shock was not included in the Tsurutani study. It was further checked by calculating the time of propagation of the shock from the spacecraft along the shock normal to the Earth and comparing against the reported SSC time. For a calculated thetabn of  $60^\circ$  and a shock speed of 470 km/sec, the time of arrival at Earth was 14.29 hours compared to the reported 14.23 hours.

#### DESCRIPTION OF THE COMPUTER SIMULATION

The computer simulation is a further development of the work of Chen (3). The frame of reference is as follows. A plane shock is assumed moving in the direction of the shock normal (x direction). The magnetic field is in the x-z plane ( $B_y=0$  upstream forces  $B_y=0$  downstream). The upstream plasma moves in the -x direction, the downstream plasma in the x-z plane. The electric field is in the y direction and constant across the shock. Data for a particular shock can be made to fit these conditions by suitable rotations and galilean transformations. The best estimate values from the previous section provide a consistent set for this work since they obey the Rankine-Hugoniot equations (as they must since they were determined from these equations). With this framework established, individual particles are allowed to spiral in along magnetic field lines and be reflected upstream or transmitted downstream due to the change in magnetic field at the shock surface and the initial conditions. The particles move according to the Lorentz force; each time a particle crosses the shock the final conditions at the crossing point become the new initial conditions, and the appropriate magnetic field is inserted into the force equation. The gain or loss in energy is monitored, along with the number of times the particle crosses the shock before being reflected or transmitted. Particles can be inserted either upstream or downstream from the shock and can move either forward or backward in time.

#### DISCUSSION

Figure 2 shows the CPME data used in the study. This is the 290 keV to 500 keV sectorized proton data. It is highly structured on a short time scale particularly in the post shock region. Associated with each of the eight data channels is a direction consistent with the midpoint in the



ecliptic plane of the 45 degree sampling angle. Plasma flow collected for each of these channels will be in the opposite direction. Magnetic field data is also available on this high resolution time scale. For several of the peaks the magnetic field is identified, and associated pitch angles are determined for each of the eight channels. Then, using a linear distribution of phase angles for each pitch, an ensemble of particles is sent backward in time to the shock surface.

The objective of this study is a quantitative determination of the particle kinematics in the vicinity of interplanetary shocks, in particular the 1974 day 312 shock. The anisotropy of the particle data at certain peaks together with the phase averaged energy changes, and comparisons, will be presented.

#### ACKNOWLEDGEMENTS

The authors wish to thank Dr. P. R. Briggs for helpful suggestions and technical assistance. This work was supported in part by the NSF through grant ATM-7925987.

#### REFERENCES

1. R.P. Lepping and P.D. Argentiero, "Single Spacecraft Method of Estimating Shock Normals", J. Geophys Res., 76,19, 1971.
2. D.C. Colburn and C.P. Sonett, "Discontinuities in the Solar Wind", Space Sci. Rev., 5,439, 1966.
3. G. Chen, "Numerical Simulation of the Interaction of Charged Particles with Oblique Magnetohydrodynamic Shocks", PhD Thesis, University of Kansas, 1975.

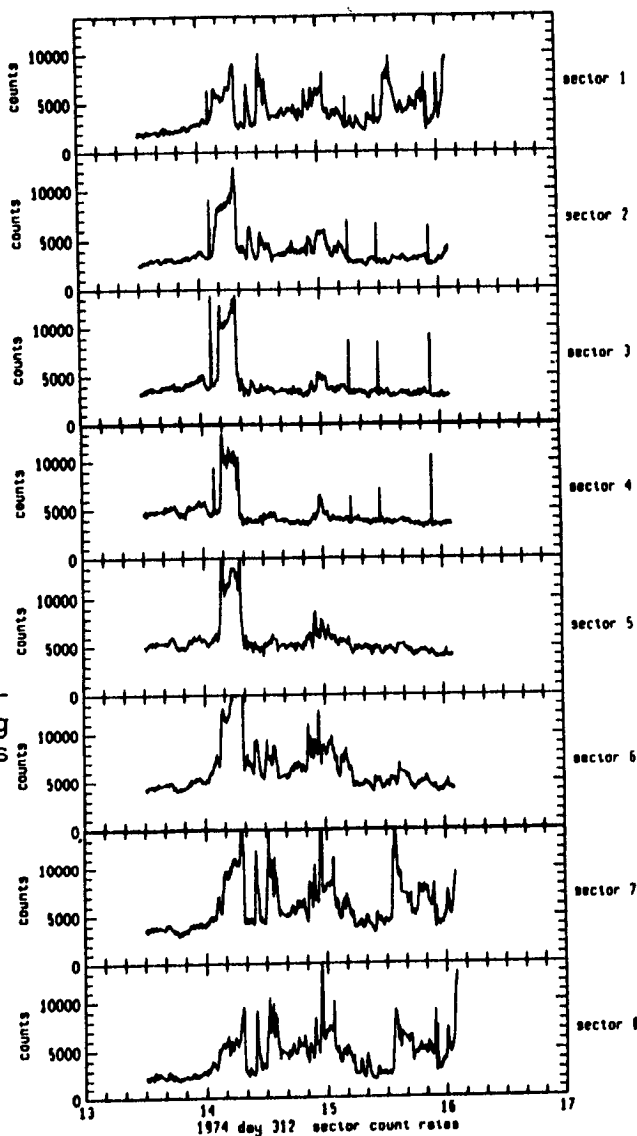


Fig 2 8 sectors in the ecliptic plane of 290 keV to 500 keV proton data from the JHU/APL Charged Particle Measurement Experiment (CPME) Shock occurs at 14 30 hrs

PITCH ANGLE DISTRIBUTIONS OF 35-1000 keV PROTONS  
AT QUASI-PERPENDICULAR INTERPLANETARY SHOCKS

A. Balogh  
Physics Department  
Imperial College, London, UK

and

G. Erdős  
Central Research Institute for Physics  
Budapest, Hungary

ABSTRACT

The characteristic features of the scatter-free acceleration process near perpendicular shocks are examined in the upstream and downstream pitch angle distributions of 35-1000 keV protons. Reasonable quantitative agreement is found between theoretical predictions and observations. The role played by "bottle" geometries, leading to enhanced acceleration, is highlighted.

1. Introduction. The mechanisms responsible for particle events associated with the passage of interplanetary shock waves have received much experimental and theoretical attention (Axford, 1981; Sanderson et al., 1985). In particular, the relative importance of scatter-free and diffusive acceleration models has been subjected to close scrutiny, much of the recent evidence coming from the observations made by the low energy charged particle experiment on the ISEE-3 (now ICE) spacecraft in orbit around the Lagrange point L1 during the period 1978-80. In this paper we examine the behaviour of the pitch angle distributions of 35-1000 keV protons associated with five interplanetary shocks which exhibited some of the most characteristic features of the scatter-free (gradient drift) acceleration model, as discussed by Sanderson et al. (1985).

Shock spikes, sharp increases in the intensity of low energy ions in close proximity to the passage of quasi-perpendicular interplanetary shocks, are normally attributed to particles accelerated in a single interaction with the shock wave, during which they drift along the electric field due to the motion of the shock in the frame of the plasma. Numerous, increasingly refined numerical simulations and analytical calculations have clarified many features of the process (see Decker, 1983). The behaviour of the anisotropy, in terms of spherical harmonics, was examined by Sanderson et al. (1985).

Observations presented in this paper were obtained with the low energy proton experiment onboard the ISEE-3 spacecraft (Balogh et al., 1978), which provides a 180-point measurement of the distribution function of 35-1000 keV protons every 16 seconds. The technique for describing the distribution function in terms of pitch angle distribution in the frame of the solar wind was worked out by Erdős (1981).

Time-reversed trajectory calculations for various shock parameters have been used to derive the qualitative features of the pitch angle distribution upstream and downstream of the shock. In Figure 1, results are shown for a shock of velocity  $w_s = 200$  km/s, with an angle  $\alpha = 80^\circ$  between the shock normal and the upstream magnetic field, and therefore a transformation velocity into the electric field free frame (e.g. Axford, 1981)  $w = w_s \sec \alpha \approx 1100$  km/s. We assumed a particle velocity  $v = 3000$  km/s and an exponent of the differential power law spectrum  $\gamma = 2.5$ .

Peak intensities (in the solar wind frame) can be derived from adiabatic theory. The critical pitch angle for reflection upstream of the shock in the E-free frame is  $\mu_c = \sqrt{1 - B_u/B_d}$ , where  $B_u$  and  $B_d$  are the magnetic field strengths upstream and downstream of the shock, respectively. The transformation into the solar wind frame gives

$$\mu_u = \frac{\mu_c + w/v}{\sqrt{1 + 2\mu_c w/v + (w/v)^2}} \quad (1) \quad \text{and} \quad \mu_d = \frac{w/v}{\sqrt{1 + (w/v)^2}} \quad (2)$$

as the cosine of the pitch angle for which the maximum occurs in the distributions, respectively upstream and downstream of the shock. We note that the maxima in the distributions occur at pitch angles which depend on particle velocity. For oblique shocks and low energy particles the downstream distributions do not peak exactly at  $90^\circ$ , although as the particle energy increases, the peak of the distribution for given shock velocity and geometry moves to  $90^\circ$ , or  $\mu = 0$ .

For simple shock geometries, the gradient drift model predicts a sharp peak in the upstream pitch angle distribution at a value of  $\mu$  given by (1) and the existence of a loss cone due to particles transmitted through the shock.

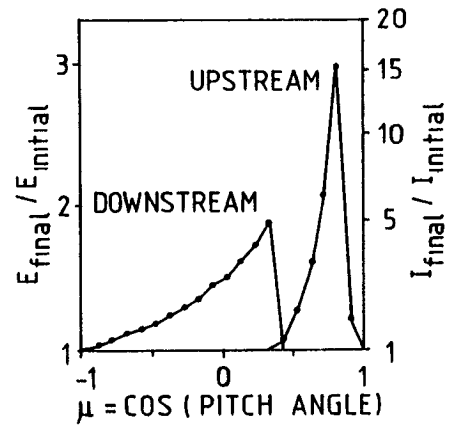


Fig. 1. Time-reversed calculation of upstream and downstream pitch angle distributions.

2. Observations. Pitch angle distributions upstream and downstream of five shock associated events are shown respectively in Figures 2 and 3. The energy dependence of upstream distributions is illustrated qualitatively in Figure 2, where pitch angle distributions are shown from two energy channels (35-56 keV and 91-147 keV, respectively).

The transformation velocity  $w$  can be estimated, using (2), from the position of the peak in the downstream pitch angle distributions, and compared to the value calculated from  $w_s$  and  $\alpha$  as determined by Sanderson et al. (1985). The two sets of values,  $w(\text{peak})$  and  $w(w_s, \alpha)$  respectively, are shown in Figure 3.

The shift in the peak of the pitch angle distribution towards  $\mu = 0$  for increasing energies was clearly identifiable on 26.7.79 and

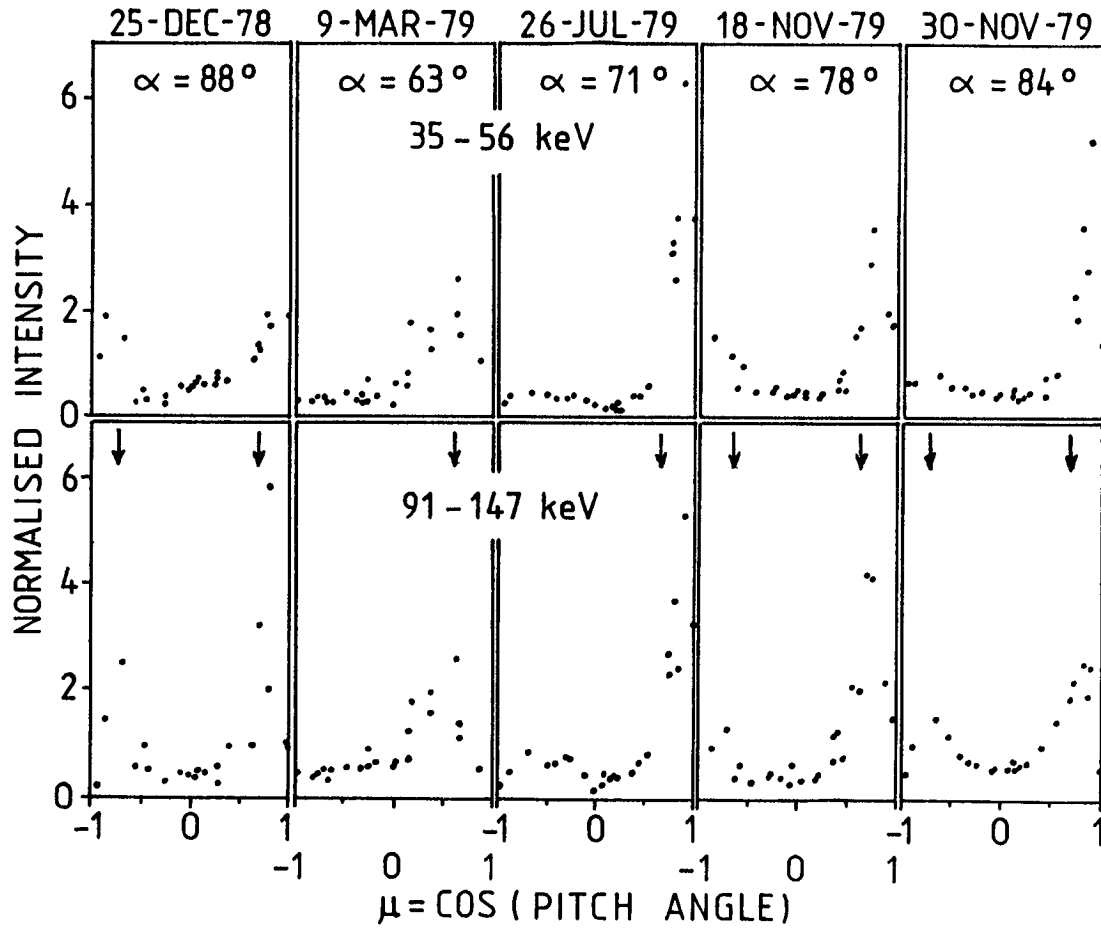


Fig. 2. Upstream pitch angle distributions in five shock-spike events. The arrows indicate the calculated values of  $\mu_c$ .

$\mu_d$	0.53	0.04	0.81	?	0.68
$w(\text{peak})$	1800	100	4000	?	2700 km/s
$w(w_s, \alpha)$	3800	370	330	700	900 km/s

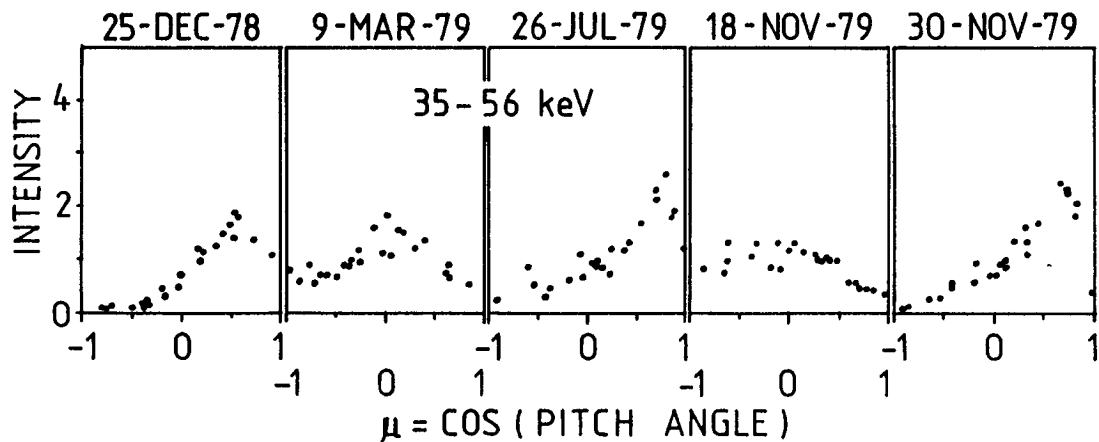


Fig. 3. Downstream pitch angle distributions.

30.11.79, illustrated in Figure 4 for the second of these events. On 9.3.79 and 18.11.79 the peak of the distribution was at  $\mu = 0$  for all energies. On 25.12.78, the behaviour of the peak could not be ascertained due to poor statistics at high energies.

3. Discussion and Conclusions. For particles reflected upstream of the shock we observe a sharp cut-off in the pitch angle distribution, characteristic of a loss-cone in the distributions even at the lowest ( $\sim 35$  keV) energies, corresponding to  $v \approx 3000$  km/s. The existence of upstream reflected particles implies that the transformation velocity is in all cases less than about 3000 km/s.

The existence of a bi-directional loss cone as shown in Figure 2 at higher energies in at least two, possibly three events (25.12.78, 30.11.79, possibly 18.11.79), corresponding to the largest values of  $\alpha$ , appears to indicate that the upstream magnetic field lines intersected the shock in such a way as to form a short-lived magnetic "bottle" as discussed by Balogh and Erdős (1983).

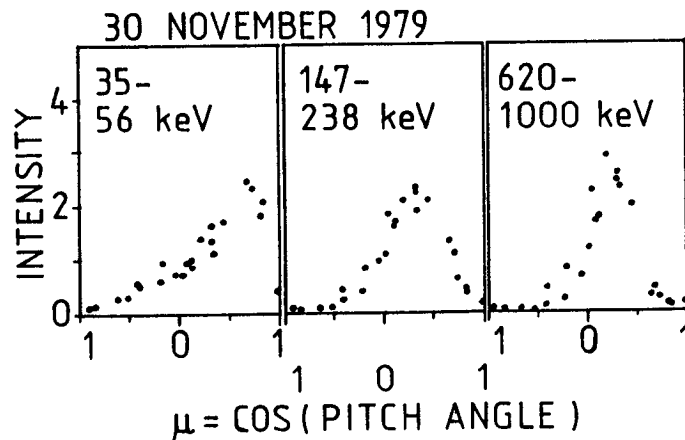


Fig. 4. Energy dependence of the downstream pitch angle distribution.

The effective shock velocity, determined from the position of the peak in the downstream pitch angle distribution, is different from that determined using  $w_s$  and the time-averaged value of the angle  $\langle \alpha \rangle$  between the upstream magnetic field and the shock normal. This can be explained by either a small error (a few degrees) in the determination of the shock normal, or possibly by the sensitivity of pitch angle distribution to  $w_s \langle \sec \alpha \rangle$  whereas the calculated velocity is  $w_s \sec \langle \alpha \rangle$ .

Overall, the shape and energy dependence of pitch angle distributions support the identification of these five events as examples of the gradient-drift acceleration process. However, the model should include the effect of fluctuations in the angle between the shock normal and the upstream field. Furthermore, at close-to-perpendicular shocks, the special geometry identified as a possibly short-lived magnetic "bottle" (as proposed by Balogh and Erdős, 1983) is likely to contribute significantly to the intensity of the shock spike.

#### References

- Axford, W. I., (1981), 17th ICRC (Paris), 12, 155.
- Balogh, A., et al., (1978), IEEE Trans. Geosci. Electronics GE-16, 176.
- Balogh, A., and Erdős, G., (1983), Planet. Space Sci., 31, 1389.
- Decker, R. B., (1983), J. Geophys. Res., 88, 9959.
- Erdős, G., (1984), 17th ICRC (Paris), 8, 197.
- Sanderson, T. R., et al., (1985), J. Geophys. Res., 90, 19.

SPATIAL DEPENDENCE OF THE LOCAL DIFFUSION COEFFICIENT MEASURED UPSTREAM  
OF THE NOVEMBER 12, 1978 INTERPLANETARY TRAVELING SHOCK

G. Gloeckler<sup>1</sup>, F.M. Ipavich<sup>1</sup>, B. Klecker<sup>2</sup>, D. Hovestadt<sup>2</sup> and M. Scholer<sup>2</sup>

<sup>1</sup>Dept. of Physics & Astronomy, Univ. of MD, College Park, MD 20742 USA  
<sup>2</sup>MPI für Extraterrestrische Physik, 8046 Garching, FRG

1. Introduction. Characteristics of suprathermal particles accelerated by quasi-parallel interplanetary traveling shocks have been generally explained in terms of a first order Fermi mechanism (e.g. see review in ref. 7). Such models require diffusive scattering of particles upstream of the shock. This scattering is characterized by a local diffusion coefficient,  $\kappa$ , which is determined by the local power density of waves in the upstream region as described by Lee (7). A number of studies have investigated the behavior of  $\kappa$  of  $\lesssim 1$  MeV upstream ions close to interplanetary shocks. Scholer et al. (8) have used results of first order Fermi shock acceleration theory (e.g. ref. 1) to derive the diffusion coefficient and its energy dependence from the measured gradient of the upstream particle intensity. Van Nes et al. (9), using the same approach, obtained the spatial and energy dependence of  $\kappa$  for 3 interplanetary shocks over a more extended energy and distance range. Klecker et al. (6) deduced the spatial dependence of  $\kappa$  in the upstream region for 30 and 130 keV protons from the measured first-order anisotropies and intensity gradients.

In this paper we examine the dependence of the diffusion coefficient of suprathermal upstream protons on distance from the November 12, 1978 interplanetary traveling shock using a different approach. Unlike previous studies our method, which is based on measurements of particle streaming and intensity gradients, does not rely on predictions of shock acceleration theories or require first-order expansions. We have chosen to examine the local spatial variations of  $\kappa$  upstream of the November 12, 1978 shock because the characteristics of this quasi-parallel shock have been extensively studied (e.g. ref. 5), and also because of its favorable geometry (i.e. B field nearly radial). The initial results of this study have been reported by Gloeckler et al. (3).

2. Instrumentation and Method of Analysis. For this study we use the counting rate data from the University of Maryland/Max-Planck-Institut-Garching ULECA sensor (see ref. 4 for details) on ISEE-3 which was placed in a halo orbit at a radial distance of  $\sim 230 R_E$  upstream of the earth. Of relevance to the present discussion are the capabilities of the electrostatic deflection vs energy ULECA sensor to reliably separate protons from alpha particles and to determine their differential intensities in three energy bands centered on energies  $\bar{E}$  of 33, 66 and 132 keV/e, and respective band widths  $\Delta E/\bar{E}$  of 20, 27 and 37%. The sensor has a  $60^\circ$  fan-like acceptance aperture with its wide angle in a plane perpendicular to the ecliptic. The three proton counting rates are available every 128 sec in each of eight  $45^\circ$  sectors of the ecliptic plane.

For the present analysis we use the 33 and 66 keV sectorized proton counting rate data to derive the proton distribution function,  $f$ , in the

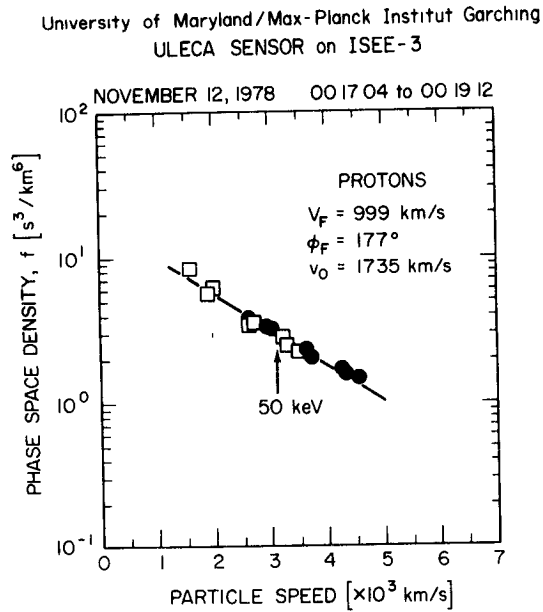


Figure 1. Rest frame proton phase space density,  $f(v)$ . For  $V_F = 999$  km/s and  $\phi_F = 177^\circ$  segments of  $f(v)$  from the 33 keV proton rate channel (open squares) and the 66 keV channel (solid circles) join smoothly to form a common spectrum.

frame of reference (rest frame) in which  $f$  is assumed to be isotropic, and find the velocity,  $\vec{V}_F$ , of that rest frame relative to the spacecraft. We follow the technique of Gloeckler et al. (2) for mapping the sectorized counting rate data into segments of the rest frame distribution function  $f(v)$ , where  $v$  is the particle speed in the rest frame, making use of the invariance properties of  $f$ . When the proper rest frame velocity,  $\vec{V}_F$ , is chosen, the two segments of  $f(v)$  join up and the resulting spectrum becomes smooth, as shown in Figure 1. We note in particular that our method requires no prior knowledge of the shape of the rest frame energy spectrum nor need  $V_F/v$  be small.

3. Observations. Using a least-squares technique we derive for each available 128 sec interval the rest frame velocity and the rest frame distribution function (over a range of particle speeds from  $\sim 1000$  to  $5000$  km/s). Figure 1 shows an example of a 128 sec averaged distribution function  $f(v)$  obtained  $\sim 4 \cdot 10^{10}$  cm upstream of the shock. We note that the shape of  $f(v)$  tends to be between that of a pure power law and an exponential, and that the spectrum becomes harder with distance from the shock (3). In the present analysis an exponential form is assumed and the e-folding speed,  $v_0$ , is computed from a linear fit to the data as shown in the figure.

In Figure 2 we plot the derived speed,  $V_F$ , (solid circles) and direction of motion,  $\phi_F$ , (upper panel) of the suprathermal proton rest frame for each available 128 sec interval as a function of time as the shock is approached. Notice that the direction of  $\vec{V}_F$  is generally within  $\sim 10^\circ$  antisunward. Also shown is the sum of the solar wind,  $V_{SW}$ , and Alfvén,  $V_A$ , speeds taken (or derived) from data published in (5). While far ahead of the shock  $V_F$  exceeds  $(V_{SW} + V_A)$  by as much as  $1000$  km/s, close to shock this difference is about a few hundred km/s, and behind the shock the two velocities are the same within experimental errors, implying pure convection at a speed equal to the sum of solar wind and Alfvén speeds. If we interpret the difference between the speeds  $V_F$  and  $(V_{SW} + V_A)$  upstream of the shock to be the diffusive streaming of suprathermal ions along the magnetic field  $B$  (nearly radial for this shock) which results from the observed upstream particle density gradient, the local diffusion coefficient along  $B$ ,  $\kappa_{\parallel}(r_1, v)$  at a distance  $r_1 = (t_{sh} - t_i)V_{sh}$  from the shock ( $V_{sh}$  and  $t_{sh}$  are the shock

speed and arrival times respectively) may be related to quantities measured at  $r_i$  as follows:

$$(1) \quad \vec{S} = 0 = \left[ \frac{1}{3} v \left( \frac{\partial f}{\partial v} \right) \right] * \vec{e}_B \cdot [\vec{V}_F(v) - (\vec{V}_{SW} + \vec{V}_A)] + \kappa_{\parallel}(r_i, v) * \vec{e}_B \cdot \vec{\nabla} f(v).$$

$\vec{S}$  is the differential streaming (which in zero is the particle rest frame), and  $\vec{e}_B$  is the unit vector along  $\vec{B}$ . Since for the November 12, 1978 shock  $\vec{B}$  and  $\vec{V}_{SW}$  were nearly radial, and assuming that  $\vec{V}_A$  was directed along  $\vec{B}$  in the upstream region, and that  $f(v)$  has an exponential dependence on  $v$  with e-folding speed  $v_0$ , eq. (1) may be simplified to

$$(2) \quad \kappa_{\parallel}(r_i, v) = \left[ \frac{v}{3v_0} \right] * \left[ \frac{256 \cdot 10^{10}}{\ln(f_{i+1}/f_{i-1})} v_{sh} \right] * [V_F - (V_A + V_{SW})].$$

To obtain  $\kappa$  at a distance  $r_i$  upstream of the shock values for  $v_0$  are obtained from the slope of the  $i$ th distribution function, and the particle density gradient is determined from the neighboring values of  $f$  at  $v = 3100$  km/s (50 keV).  $V_F$  and  $(V_A + V_{SW})$  are those plotted in Figure 1 at times  $t_i$  related to  $r_i$  by  $r_i = (t_{sh} - t_i) V_{sh}$ , where we used values for  $V_{sh}$  of 612 km/s and  $t_{sh}$  of 0:28:18 as given in (5).

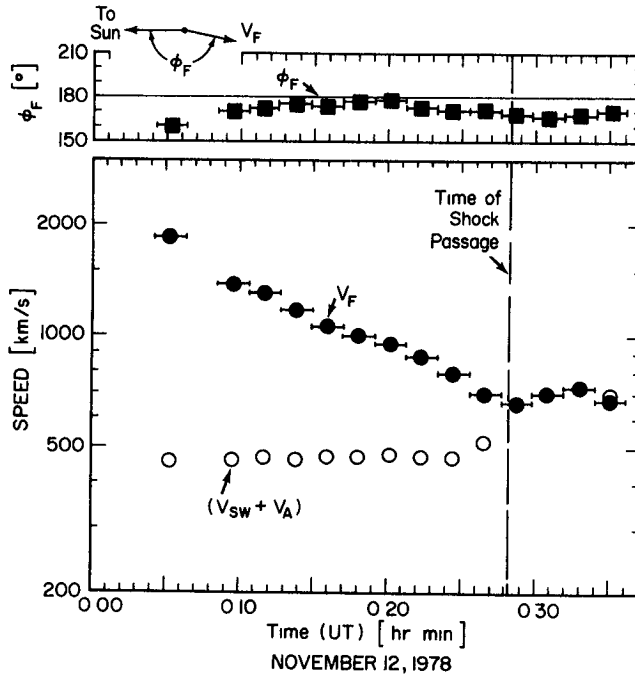


Figure 2. Speed and direction of motion of the rest frame (solid symbols) and the solar wind plus Alfvén speed ( $V_{SW} + V_A$ ) vs time before and immediately after shock passage. The difference between  $V_F$  and  $(V_{SW} + V_A)$  is interpreted in terms of diffusive streaming. Behind the shock  $V_F \approx (V_{SW} + V_A)$  implying pure convection of 50 keV protons at that speed.

4. Spatial Dependence of  $\kappa_{\parallel}$ . In Figure 3 we show values of  $\kappa_{\parallel}$  for  $\sim 50$  keV protons as a function of distance from the shock, where  $\kappa_{\parallel}$  is computed using eq. (2). The uncertainties shown come

primarily from inaccuracies in determining the local density gradients. We note that there may be systematic errors ( $\lesssim 30\%$ ) in the values of  $\kappa$  resulting from using the simpler eq. (2) rather than eq. (1) which incorporates vector quantities. Consistent with expectations (7) we find that  $\kappa$  increases exponentially from a value of  $\sim 7 \cdot 10^{17}$  cm<sup>2</sup>/s near the shock to  $\sim 2.5 \cdot 10^{18}$  cm<sup>2</sup>/s at  $\sim 4.5 \cdot 10^{10}$  cm from the shock with an e-folding distance of  $3.4 \cdot 10^{10}$  cm. What is surprising is the subsequent decrease (again exponential, with e-folding distance of  $\sim 1.1 \cdot 10^{10}$  cm) in



the value of  $\kappa$  with distance from the shock.

**5. Discussion and Conclusions.** The factor of  $\sim 4$  increase in  $\kappa$  over a distance of  $\sim 4.5 \cdot 10^{10}$  cm is consistent with a comparable decrease in the power spectral density of waves at  $2 \cdot 10^{-2}$  Hz (see Fig. 8 of ref. 7).

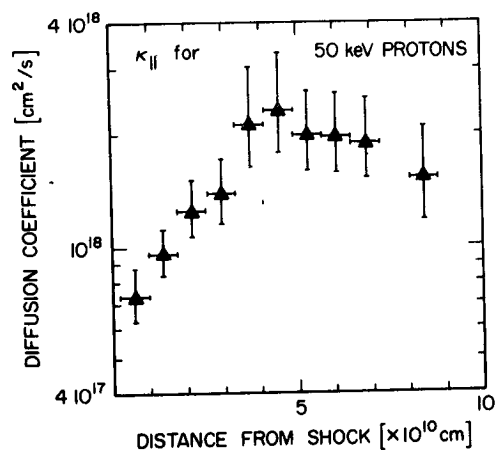


Figure 3. Spatial dependence of  $\kappa_{||}$  on upstream distance from the shock.

The value of  $7 \cdot 10^{10}$  cm<sup>2</sup>/s of  $\kappa_{||}$  (50 keV) near the shock is in excellent agreement with prediction (for this shock) based on a self-consistent theory for wave excitation and particle acceleration upstream of interplanetary shocks (7). Our values of  $\kappa$  and its spatial dependence are also in qualitative agreement with those reported in (6,9). What is puzzling is the decrease of  $\kappa_{||}$  (50 keV) at larger distances which is not predicted by current theory. To pursue this point further we computed  $\kappa_{||}$  (100 keV) following the procedure outlined above but now using the 66 and 132 keV proton counting rate data. We found that the rest frame speeds  $V_F$  characteristic of  $\sim 100$  keV protons are smaller than those shown in Figure 1 for 50 keV protons.

Ratios of  $\kappa_{100}/\kappa_{50}$  were determined to be  $\sim 3.0$ , 1.2 and 1.8 near the shock, at  $r = 4 \cdot 10^{10}$  cm and  $8 \cdot 10^{10}$  cm respectively. Assuming a simple power law dependence of  $\kappa$  on particle energy these values correspond to  $\kappa \propto E^{+1.6}$ ,  $E^{+0.26}$ ,  $E^{+0.85}$  respectively. We therefore conclude in agreement with (9) that one cannot characterize the energy dependence (or the spatial dependence) of  $\kappa$  in a simple way. Our results indicate an increase in the wave power density beyond  $r \sim 5 \cdot 10^{10}$  cm and in general a more effective scattering of 50 keV protons compared to 100 keV protons. This hypothesis can be checked using local wave power spectrum measurements as a function of distance from the November 12, 1978 interplanetary traveling shock.

**Acknowledgements.** We are grateful for helpful discussions with Dr. M.A. Lee, and to the many individuals at UMD and MPE who made our ISEE experiments a success. This work was supported by NASA under contract NAS5-28704 and grants NAGW-101, NGR 21-002-224/316, and by the BMFT contract RV 14-B8/74 in West Germany.

## References

1. Axford, W.I. *et al.* 1977, Plovdiv ICRC, 11, 132.
2. Gloeckler, G. *et al.* 1984, Geophys. Res. Letters, 11, 603.
3. Gloeckler, G. *et al.* 1984, Trans. Am. Geophys. U. (EOS), 65, 1035.
4. Hovestadt, D. *et al.* 1978, IEEE Trans. Geo. El., GE-16, 166.
5. Kennell, C.F. *et al.* 1984, J. Geophys. Res., 89, 5436.
6. Klecker, B. *et al.* 1984, private communication.
7. Lee, M.A. 1983, J. Geophys. Res., 88, 6109.
8. Scholer, M. *et al.* 1983, J. Geophys. Res., 88, 1977.
9. van Nes, P. *et al.* 1984, Adv. Space Res., 4, 315.

## LATITUDE DEPENDENCE OF CO-ROTATING SHOCK ACCELERATION

R. E. Gold,<sup>1</sup> L. J. Lanzerotti,<sup>2</sup> C. G. MacLennan,<sup>2</sup> S. M. Krimigis<sup>1</sup>

<sup>1</sup> The Johns Hopkins University Applied Physics Laboratory, Laurel, MD, 20707 USA

<sup>2</sup> AT&T Bell Laboratories, Murray Hill, NJ, 07974 USA

### ABSTRACT

We briefly discuss energetic particle observations in the outer heliosphere ( $\geq 12$  A.U.) by the LECP instruments on the Voyager 1 and Voyager 2 spacecraft that show a definite latitude dependence of the number and intensity of particle enhancements produced by co-rotating interplanetary regions during an interval when no solar energetic particle events were observed. The particle enhancements are fewer in number and less intense at higher ( $\sim 20^\circ$ ) heliolatitudes. However, the similar spectral shapes of the accelerated particles at the two spacecraft indicate that the acceleration process is the same at the two latitudes, but less intense at the higher latitude.

*1. Introduction.* Particles accelerated in various regions of the heliosphere -- e.g., planetary bow shocks and magnetospheres, interplanetary traveling shocks, co-rotating interaction regions -- have been studied extensively near Earth (1 A.U.) [e.g., review by Gloeckler, 1984]. The progression of the two Voyager spacecraft deep into the outer heliosphere, beyond the orbit of Saturn, at nearly the same heliolongitude provides the opportunity to study interplanetary shock acceleration processes in the outer heliosphere as well as to search for heliolatitude dependences of the acceleration processes.

This brief note presents the results of some initial analyses of Voyager data during the period when the Voyager 1 (V1) spacecraft was at high heliolatitudes. The data used are from the Low Energy Charged Particle (LECP) instrument flown on both Voyager spacecraft [Krimigis et al., 1967]. Ion and proton data from selected sub-systems of the instrument are used.

*2. Observations.* Plotted in Figure 1 are the daily average fluxes of low energy ions and higher energy protons for the interval 1981 to mid-1984. The higher energy fluxes shown provide information on the occurrences of solar energetic particle events. The lower energy fluxes provide information on the occurrences of co-rotating interplanetary regions which can accelerate particles. The enhanced co-rotating particle fluxes are seen to occur sporadically at each spacecraft.

While there are a number of interesting intervals in the data (see Gold et al., 1985 for discussions of other aspects of these data), we concentrate specifically on the  $\sim 200$  days of data between day 243, 1983, and day 75, 1984. During this interval of 1983-84 the two Voyager spacecraft were at approximately the same heliolongitude, with Voyager 1 increasing in heliolatitude from  $\sim 20.5$  to  $\sim 22.5^\circ$  and in distance from  $\sim 17.2$  to  $\sim 19$  A.U. while Voyager 2 remained approximately in

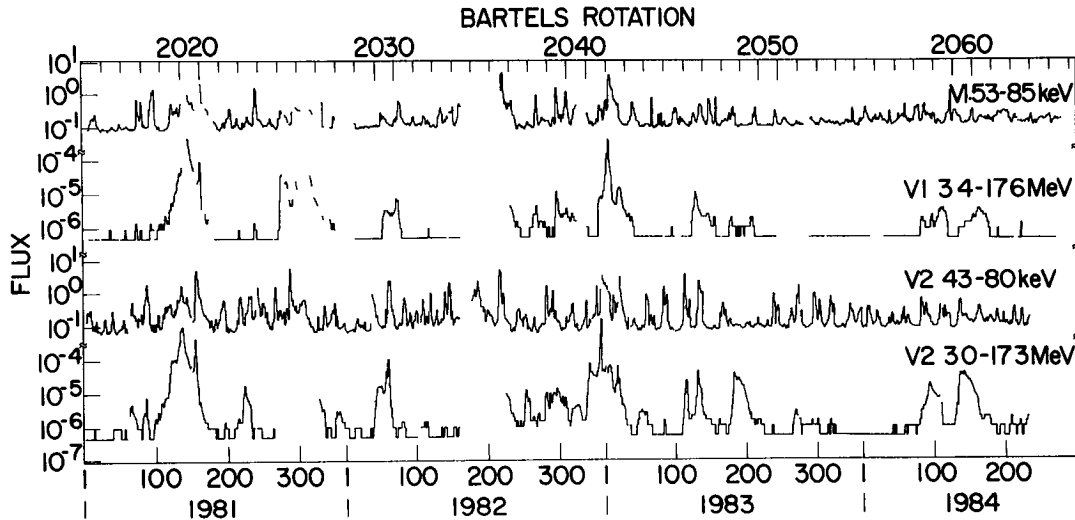


Fig. 1 Plot of daily average fluxes in ion and proton channels from LECP experiment on Voyager 1 and Voyager 2 spacecraft, 1981 to mid-1984.

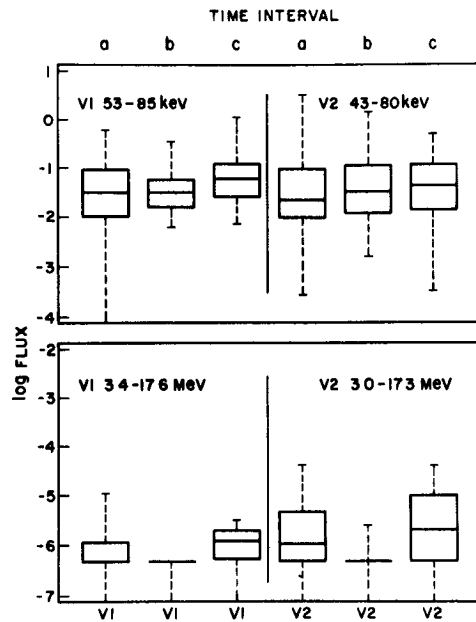


Fig. 2 Statistical distributions (represented as box plots) of fluxes in ion and proton channels on the two Voyager spacecraft for three time intervals. The interval (b) corresponds to day 243, 1983, to day 75, 1984. Intervals (a) and (c) correspond to a 200 day period preceding and a 150 day period following interval (b).

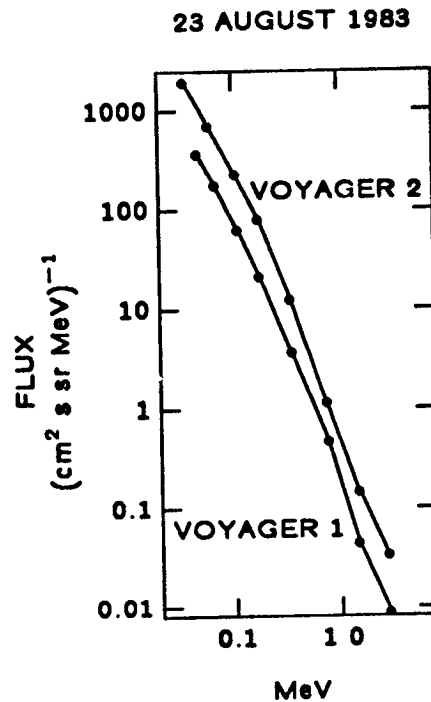


Fig. 3 Daily average ion spectra from Voyager 1 and Voyager 2 on day 235, 1983.

the ecliptic plane, moving from  $\sim 12.3$  to  $13.7$  A.U. Within this time interval essentially no enhancements indicative of transient solar particle events were seen in the  $3.4$ - $17.6$  MeV proton fluxes on Voyager 1. Voyager 2, in the ecliptic plane, observed some proton activity at about day 270, but in general the activity of the higher energy protons during this interval was considerably suppressed compared to that before and after.

In contrast to the higher energy protons, the low energy ion fluxes are enhanced sporadically throughout the interval of interest. The enhancements, produced by co-rotating interplanetary interaction (shock) regions, are less numerous and less intense at Voyager 1 (Figure 1).

The distinction between the ion and proton fluxes for time intervals before and after the interval of special interest (i.e., day 243, 1983 to day 75, 1984) is illustrated by the statistical box plots of Figure 2. The intervals denoted as (a), (b), and (c) correspond to 200 days preceding the special interval, the interval of interest, and 150 days following. Each box represents 50% of the distribution of particle fluxes during each time interval, with the median indicated by the line across the middle or lower edge of the box. The "error bars" indicate the distributions of fluxes for the upper 25% and lower 25% of the fluxes. A background, consisting of linear interpolations between the lowest flux rate in each respective Bartels rotation, has been subtracted from the data before compiling the statistics. The statistical distributions show clearly that the low energy ion fluxes have essentially the same distributions for each time interval at each spacecraft. The distributions of the higher energy protons are vastly different, quantitatively, in interval (b) than in the other two intervals. At Voyager 1, the fluxes in interval (b) were all basically near background, as is qualitatively evident from Figure 1.

Daily average ion spectra from both spacecraft on day 235, 1983, during a co-rotating event at each location, are shown in Figure 3. (A different co-rotating region, of course, is seen at each location.) The spectral shapes at the two locations are similar. The similarity in the spectra together with the statistical result showing decreased amplitudes at higher latitudes indicates that the co-rotating acceleration process is the same in and out of the ecliptic, but less effective at higher latitudes.

**3. Discussion.** During the  $\sim 200$  days of quiescence in the outer heliosphere, when the interplanetary environment was essentially undisturbed by intermittent solar energetic particle events and the accompanying transient interplanetary disturbances, the particle enhancements associated with co-rotating interaction regions were more intense in the ecliptic plane than at latitudes  $\sim 20^\circ$  above the plane. This conclusion was also reached by the Voyager cosmic ray instrument team studying  $> 0.5$  MeV protons [Christon and Stone, 1985]. The acceleration process, however, appears to be the same at both locations. For the  $\sim 200$  days, the medium may have resembled the prediction of Burlaga [1983], who speculated that beyond  $\sim 10$  A.U. the large scale dynamics of the interplanetary medium could be dominated by pressure waves; the originating coronal signatures would be lost. The solar wind would therefore be more homogeneous on a large scale [see also Smith et al., 1985, and Whang and Burlaga 1985]. Finally, Lanzerotti et al. [1985] suggested that the undisturbed (by transient events) outer heliosphere during this interval facilitated the detection of the enhanced levels of 3 kHz plasma waves that Kurth et al. [1984] attributed to plasma processes produced at the heliosphere boundary between the interaction of the solar

wind with the interstellar medium.

**4. Acknowledgements.** The work at The Johns Hopkins University Applied Physics Laboratory was supported by NASA under Contract N00024-83-C-5301.

**5. References**

- Burlaga, L. F., (1983), *J. Geophys. Res.*, **88**, 6085-6094.  
Christon, S. E., and Stone, E. C., (1985), *Geophys. Res. Lett.*, **12**, 109-112.  
Gloeckler, G., (1984), *Adv. Space Res.*, **4**, 127-137.  
Gold, R. E., et al. (1985), in preparation.  
Krimigis, S. M., et al. (1977), *Space Sci. Rev.*, **21**, 329-354.  
Kurth, W. S., et al. (1984), *Nature*, **312**, 27-31.  
Lanzerotti, L. J., et al. (1985), *Nature*, submitted.  
Smith, Z. K., et al. (1985), *J. Geophys. Res.*, **90**, 217-220.  
Whang, Y. C., and Burlaga, L. F., (1985), *J. Geophys. Res.*, **90**, 221-232.

## ELEMENTAL ABUNDANCES IN COROTATING EVENTS

T. T. von Rosenvinge and R. E. McGuire\*  
 NASA/Goddard Space Flight Center, Greenbelt, MD 20771, U.S.A.

1. Introduction. Large, persistent solar-wind streams in 1973 and 1974 produced corotating interaction regions which accelerated particles to energies of a few MeV/nucleon. The proton to helium ratio (H/He) reported in reference (1) was remarkably constant at a value  $(22 \pm 5)$  equal to that in the solar wind  $(21 \pm 3)$ , suggesting that particles were being accelerated directly out of the solar wind. In this paper we report on preliminary results from a similar study approximately 11 years (i.e., one solar cycle) later. Corotating events have been identified by surveying the solar wind data, energetic particle time-histories and anisotropies. This data was all obtained from the ISEE-3/ICE spacecraft. These events also show H/He ratios similar to that in the solar wind. In addition, we have examined other corotating events at times when solar flare events could have injected particles into the corresponding corotating interaction regions. We find that in these cases there is evidence for H/He ratios which are significantly different from that of the solar wind but which are consistent with the range of values found in solar flare events.

2. Results. In Figure 1 we present a 27-day recurrence plot of the solar wind speed obtained from the Los Alamos National Laboratory Solar Wind Experiment on the ISEE-3 spacecraft (now renamed ICE); this data was processed by a simplified algorithm adequate for this purpose and is not to be considered definitive. ICE at this time was near 1 AU, leading the Earth in its orbit. Figure 1 shows the formation of two recurrent solar wind streams. A similar plot for the interplanetary magnetic field direction shows that these two streams are in opposite portions of a two sector magnetic field pattern. Using Figure 1 and particle time-history plots, we identified eight different time intervals as candidate corotating events. Low energy electron rates and high energy proton rates were scanned for any evidence of impulsive (solar) origin. In addition, anisotropy data was examined for apparent flow from the east. (Corotating events typically have particle flow from the east. This results from the vector sum of the radial Compton-Getting anisotropy due to the outward flow of the solar wind and the backward flow along the interplanetary magnetic field lines from the presumed acceleration region at several AU from the Sun.) The H/He ratio was evaluated for each interval in the energy range 4.5-6.5 MeV/nucleon. Also the C/O ratio was evaluated in the energy range 1.8-2.8 MeV/nucleon. Averaged over all eight intervals we find  $H/He = 20 \pm 8$  and  $C/O = .8 \pm .2$  (to be compared with  $H/He = 22 \pm 5$  and  $C/O = .8 \pm .2$  in reference (1)).

Other time periods since the launch of ISEE-3 in 1978 have been examined in a similar manner. A long-lived high-speed stream gave rise to a brief but apparently clean corotating event August 1-4, 1979. The

\* Also Department of Physics and Astronomy, University of Maryland College Park, MD 20742, U.S.A.

## ELEMENTAL ABUNDANCES IN COROTATING EVENTS

T. T. von Rosenvinge and R. E. McGuire\*  
 NASA/Goddard Space Flight Center, Greenbelt, MD 20771, U.S.A.

1. Introduction. Large, persistent solar-wind streams in 1973 and 1974 produced corotating interaction regions which accelerated particles to energies of a few MeV/nucleon. The proton to helium ratio (H/He) reported in reference (1) was remarkably constant at a value  $(22 \pm 5)$  equal to that in the solar wind  $(21 \pm 3)$ , suggesting that particles were being accelerated directly out of the solar wind. In this paper we report on preliminary results from a similar study approximately 11 years (i.e., one solar cycle) later. Corotating events have been identified by surveying the solar wind data, energetic particle time-histories and anisotropies. This data was all obtained from the ISEE-3/ICE spacecraft. These events also show H/He ratios similar to that in the solar wind. In addition, we have examined other corotating events at times when solar flare events could have injected particles into the corresponding corotating interaction regions. We find that in these cases there is evidence for H/He ratios which are significantly different from that of the solar wind but which are consistent with the range of values found in solar flare events.

2. Results. In Figure 1 we present a 27-day recurrence plot of the solar wind speed obtained from the Los Alamos National Laboratory Solar Wind Experiment on the ISEE-3 spacecraft (now renamed ICE); this data was processed by a simplified algorithm adequate for this purpose and is not to be considered definitive. ICE at this time was near 1 AU, leading the Earth in its orbit. Figure 1 shows the formation of two recurrent solar wind streams. A similar plot for the interplanetary magnetic field direction shows that these two streams are in opposite portions of a two sector magnetic field pattern. Using Figure 1 and particle time-history plots, we identified eight different time intervals as candidate corotating events. Low energy electron rates and high energy proton rates were scanned for any evidence of impulsive (solar) origin. In addition, anisotropy data was examined for apparent flow from the east. (Corotating events typically have particle flow from the east. This results from the vector sum of the radial Compton-Getting anisotropy due to the outward flow of the solar wind and the backward flow along the interplanetary magnetic field lines from the presumed acceleration region at several AU from the Sun.) The H/He ratio was evaluated for each interval in the energy range 4.5-6.5 MeV/nucleon. Also the C/O ratio was evaluated in the energy range 1.8-2.8 MeV/nucleon. Averaged over all eight intervals we find  $H/He = 20 \pm 8$  and  $C/O = .8 \pm .2$  (to be compared with  $H/He = 22 \pm 5$  and  $C/O = .8 \pm .2$  in reference (1)).

Other time periods since the launch of ISEE-3 in 1978 have been examined in a similar manner. A long-lived high-speed stream gave rise to a brief but apparently clean corotating event August 1-4, 1979. The

\* Also Department of Physics and Astronomy, University of Maryland College Park, MD 20742, U.S.A.

SOLAR AND INTERPLANETARY PARTICLES AT 2 TO 4 MEV  
DURING SOLAR CYCLES 21, SOLAR CYCLE VARIATIONS  
OF EVENT SIZES, AND COMPOSITIONS

T.P. Armstrong, J.C. Shields, P.R. Briggs and S. Eckes  
University of Kansas, Lawrence, Kansas 66045 U.S.A.

## I. INTRODUCTION

In this paper we study 2-4 MeV/nucleon protons, alpha particles, and medium (CNO) nuclei in the near-Earth interplanetary medium during the years 1974-1981. Since this period contains both the solar activity minimum in 1976, and the very active onset phase of Solar Cycle 21, we have searched for characteristic compositional differences between the solar minimum and solar maximum ion populations.

Previous studies of interplanetary particle composition at these energies have concentrated on well-defined samples of the heliospheric medium. During flare particle events, the ambient plasma is dominated by ions accelerated in specific regions of the solar atmosphere; observation of the proton/alpha and alpha/medium ratios for flare events shows that there is marked compositional variability both during an event [1] and from event to event [2,3], suggesting the complicated nature of flare particle production and transport. Longer-term studies of non-flare activity have uncovered non-impulsive flux increases that recur with the same frequency as the Sun's 27-day rotational period; indeed, there appears to be a strong spatial relationship between these particle populations and the global structure of the interplanetary magnetic field [4,5]. The unusual spectral and compositional features of these non-flare events may point toward an interplanetary acceleration mechanism [6].

Beneath this overlying activity is a substrate of low-level flux which can be examined during so-called "quiet" periods. The characterization of quiet-time plasma carries some of the same difficulties as any null measurement, i.e. the need to remove ALL external effects; however, a continuous outflow of suprathermal solar particles has been observed and analyzed during less-active portions of the previous Solar Cycle [7].

Our aim is to examine the compositional characteristics of these separate particle populations at Solar Minimum, and to track the evolution of those characteristics during the transition to the Solar Active phase.

## II. TECHNIQUE

The observations for this paper come from the Charged Particle Measurement Experiment aboard the Explorer 50 (a.k.a. IMP-8) satellite. The CPME is a telescope stack of



solid-state detectors, with fixed discriminator voltages on each detector and on-board channel logic; the raw data is in the form of passbands in  $dE$ -vs- $E$  space, and these passbands have been structured to provide for very "pure" single-species channels in the 2-4 MeV/nucleon range: channel P4 for protons, channel A3 for alphas, and channels Z1 and Z2 for medium nuclei. A complete description of the CPME has been presented elsewhere [8].

Daily-average count rates for the four channels mentioned above are used to produce values of the proton/alpha and alpha/medium ratios at 2-4 MeV/nucleon [8]. At this temporal resolution, data coverage is essentially complete from IMP-8 launch in 1973 up to the present; from examination of the entire data set, we have selected two continuous intervals: day 300 1974 to day 200 1977 (Solar Minimum), and day 1 1978 to day 365 1981 (Solar Active).

These two intervals have been subdivided into three categories of solar activity: 1) FLARE days, when the observed flux can be traced to a solar particle event or events; 2) QUIET time, when the daily-averaged flux is below a specified upper limit; and 3) non-flare, non-quiet (NFNQ) periods, when non-flare acceleration mechanisms may be operating. We have taken considerable care to identify flare-related flux enhancements, using earlier catalogues of particle flare observations [9,10] and extending these techniques for the identification of flares in the 1978-81 "Solar Active" period. The criterion for labeling daily-averaged flux as QUIET was a count rate in channel A3 (1.8 - 4.2 MeV/nucleon) less than  $4 \times 10^{*-4}$  counts/sec; this threshold lies well above the instrumental background level, but below the typical level of activity observed by the CPME.

### III. RESULTS

The sampling statistics for the Solar Minimum and Solar Active intervals appear in Table 1. As expected, the percentage of "quiet" days decreases when the Solar Active phase commences (from 53% to 8%), and the number of flare-dominated days increases (from 14% to 24%). However, our analysis also shows that the average flux increases for both flare and non-flare days during the Solar Active period. Median FLARE proton flux at Solar Active time is 4.20 protons/( $cm^{*2}$  sec sr MeV), about 250 times as large as at Solar Minimum (0.017 protons/( $cm^{*2}$  sec sr MeV)); the median alpha particle flux increases by a factor of 144, and the medium nuclei flux increases by a factor of 138. Even for non-flare periods, the average intensity increases from Solar Minimum to Solar Active intervals: by a factor of 80 for protons (from 0.00098 to 0.081 protons/( $cm^{*2}$  sec sr MeV)) and by a factor of 25 for alphas and medium nuclei. Clearly, the active onset of a new Solar Cycle is very broad-based for medium-energy solar ions; the general level of particle production rises, while the number and intensity of solar particle flares increases.

Composition ratios of FLARE, NFNQ, and QUIET intervals

for Solar Minimum and Solar Active periods appear in figures 1 and 2. We have formed histograms of the logarithm of H/He and He/CNO for these sets, and indicate the median of each distribution by an arrow. These median values are displayed in the figures, along with uncertainties representing the limits of two-thirds of the total range of values.

At Solar Minimum, the distributions are obviously distinct, with the QUIET flux having a relatively higher content of  $Z > 1$  ions. Notice that the FLARE and NFNQ are also distinct, with the FLARE composition ratios showing wide variations. Apparently, the products of non-flare acceleration processes have different compositional signatures from flare particles, though the greatest differences exist between quiet and non-quiet flux.

The situation changes at the Solar Active period, with the H/He ratios increasing for all classes of activity. The NFNQ distribution is now almost identical with the FLARE distribution. Since the sheer number of samples makes it extremely unlikely that the NFNQ set is dominated by undocumented flare events, we suggest that the majority of NFNQ particles in the Solar Active phase may have their origin in flare acceleration processes.

#### ACKNOWLEDGMENTS

This work was supported in part by the NSF through grant ATM-83-05537 to the Johns Hopkins University Applied Physics Laboratory and the University of Kansas, and by a University of Kansas Undergraduate Research Award.

#### REFERENCES

1. Armstrong, T.P. et al, "Variations in the Charge Composition of the July 2-12, 1974 Solar Particle Event", Proceedings XIV Int. Cosmic Ray Conf., Munich, 1975, p. 1592
2. Lanzerotti, L.J. et al, "Abundance of solar cosmic ray alpha particles", J. Geophys. Res., 78, 1973, p. 3935
3. Mason, G.M. et al, "A survey of 1 MeV/nucleon solar flare particle abundances,  $1 < Z < 26$ , during the 1973-1977 solar minimum period", Ap. J., 239, 1980, p. 1070
4. Pesses, M.E. et al, "Energetic protons associated with interplanetary active regions 1-5 AU from the Sun", J. Geophys. Res., 83, 1978, p. 553
5. Briggs, P.R. et al, "Observations of interplanetary energetic ion enhancements near magnetic sector boundaries", GRL, 11, 1984, p. 27
6. Gloeckler, G. et al, "Observed distribution functions of H, He, C, O, and Fe in corotating energetic particle streams ...", Ap. J. (Lett.), 230, 1979, p. L191
7. Krimigis, S.M. et al, "Measurements of the quiet time low energy proton, alpha, and M nuclei component in cosmic rays", Proceedings XIII Int. Cosmic Ray Conf., Denver, 1973, p. 1656

8. Armstrong, T.P., "Handbook and reference manual for Charged Particle Measurement Experiment data from Explorer 47 and 50", Rep. JHU/APL 76-02, Appl. Phys. Lab., Johns Hopkins Univ., Laurel, Md., 1976
9. Briggs, P.R., "Solar and interplanetary ions near Earth", dissertation, University of Kansas, 1981
10. Nonnast, J.H. et al, "A study of solar flare soft X-rays and their relation to particle events observed with IMP 8", J. Geophys. Res., 87, 1982, p. 4327

TABLE 1. Sampling Statistics

	Solar Minimum	Solar Active
QUIET	493	116
NFNQ	401	948
FLARE	132	346

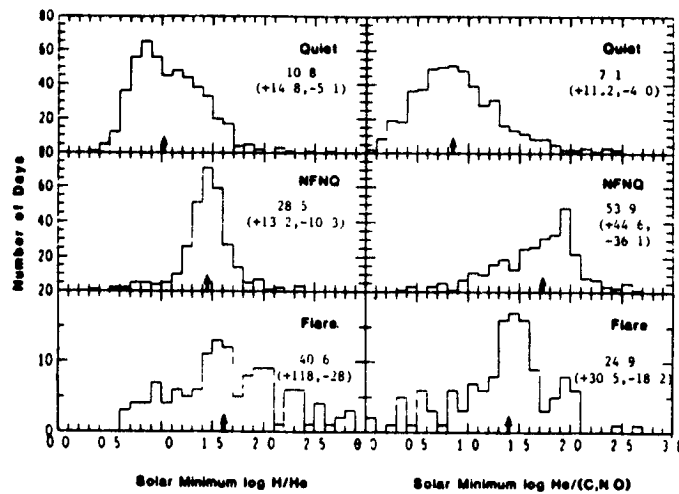


Figure 1

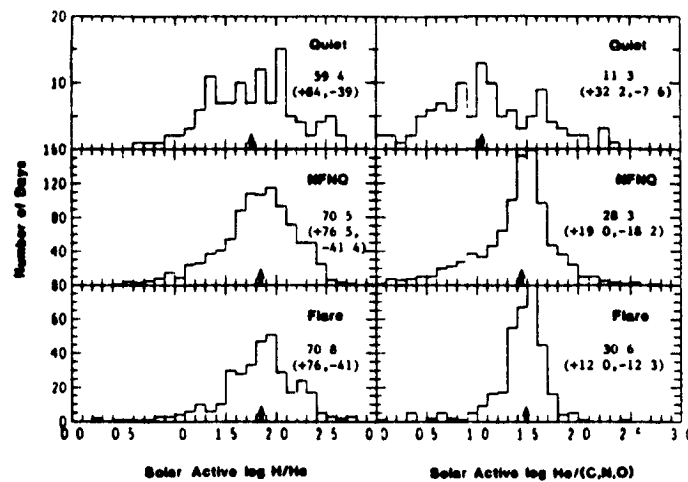


Figure 2

COSMIC RAY ACCELERATION BY STELLAR WIND.  
SIMULATION FOR HELIOSPHERE

S.I.Petukhov, A.A.Turpanov, V.S.Nikolaev

Institute of Cosmophysical Research and Aeronomy,  
Lenin Ave., 31, 677891 Yakutsk, USSR

ABSTRACT

It is shown that the acceleration of the solar wind particles at the solar wind terminal shock is capable of providing the total flux, spectrum and radial gradients of the low-energy protons close to ones observed in the interplanetary space.

1. Introduction. The solar wind deceleration by the interstellar medium may result in the existence of the solar wind terminal shock [1]. In this case a certain fraction of thermal particles after being heated at the shock would obtain enough energy to be injected to the regular acceleration process [2-5]. An analytical solution for the spectrum in the frame of a simplified model that includes particle acceleration at the shock front and adiabatic cooling inside the stellar wind cavity has been derived in [6].

A more realistic model is discussed in the present paper in order to estimate whether this process might occur the main source of the low-energy cosmic rays in the heliosphere.

2. Model. Let the solar wind velocity  $u(r)$  in a steady state spherically symmetric model be equal to  $u_1 = \text{const}$  at  $r < R$  and  $u_2(R/r)^2$  at  $r > R$ , where  $R$  is the solar wind terminal shock radius,  $\sigma = u_1/u_2$  - the compression ratio of the shock. Cosmic ray propagation in the diffusive approximation is governed by the transport equation:

$$\frac{1}{r^2} \frac{\partial}{\partial r} (r^2 u \frac{\partial n}{\partial r}) - \frac{1}{r^2} \frac{\partial}{\partial r} (r^2 u n) + \frac{1}{3r^2} \frac{\partial}{\partial r} (r^2 u) \frac{\partial}{\partial p} (np) = 0 \quad (1)$$

where  $n(r, p)$  is the particle number density per unit inter-

val of momentum  $p$ ,  $\mathcal{K}(r, p)$  - cosmic ray diffusion coefficient. At  $r < R$  and  $r > R$  (subscripts 1 and 2, respectively) it is given by

$$\mathcal{K}_{1,2} = \mathcal{D}_{1,2}(p) \cdot (r/R)^{\beta_{1,2}}$$

The matching conditions are that the particles current and the number density should be continuous at the shock. The other conditions are the absence of source or sink at  $r=0$  ( $r \cdot n(r, p) \rightarrow 0$  as  $r \rightarrow 0$ ) and a given spectrum at infinity ( $n(r, p) \rightarrow N_{\infty}(p)$  as  $r \rightarrow \infty$ ).

Integrating (1) with respect to  $r$  from 0 to  $R-0$  and using the analytical solution to (1) at  $r > R$ , the matching condition might be reduced to the following:

$$\begin{aligned} \frac{\epsilon-1}{3\epsilon} \cdot \frac{\partial}{\partial p} [p \cdot n(R, p)] + \frac{n(R, p)}{\epsilon[1-\varphi(p)]} = \\ = \frac{1}{u_1 R^2} \int_0^{R-0} \frac{1}{3r^2} \frac{\partial}{\partial r} (r^2 u_1) \frac{\partial}{\partial p} [p \cdot n(r, p)] r^2 dr + \frac{\varphi(p) N_{\infty}(p)}{\epsilon[1-\varphi(p)]} \end{aligned} \quad (2)$$

where  $\varphi(p) = \exp[-u_2 R / (1+\beta_2) \mathcal{D}_2(p)]$

Hence, the problem is to solve the equation (1) at  $r \leq R$  with respect to the boundary condition (2). The equation (1) is valid at particle momentum  $p$  higher than some limiting value, say  $p_0$ . One more condition is necessary to make the system (1), (2) being completed, namely  $n(R, p_0) = n_0$ . This condition relates the injection rate to the spectrum amplitude  $p=p_0$ .

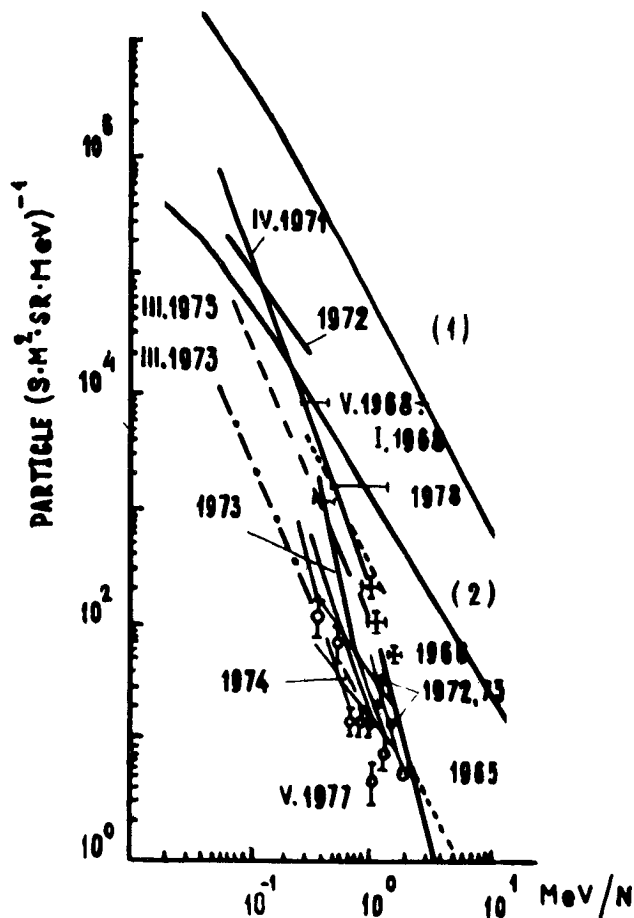
It has been shown [7-9], that the shock acceleration is efficient enough to transfer a significant fraction ( $\sim 50\%$ ) of the inflowing plasma kinetic energy to the accelerated particles. The accelerated particles spectrum takes on the power law form with the index equal to that one given by the linear theory at particles velocity  $v \simeq 3 u_1$  [9]. The corresponding values for the solar wind particles are  $T \simeq 10$  keV or  $p_0 \simeq 3 \cdot 10^{-3} m_p c$ . Particles of energy correspon-

ding to the cutoff velocity diffuse far upstream and suffer catastrophic adiabatic cooling.

3. Results and Discussion. The results of the numerical calculations are presented in Figure in comparison with the observational data [10]. The curve labelled "1" is the differential proton flux near the shock, "2" - that one at the orbit of the Earth. The following parameters were used:  $u_1 = 5 \cdot 10^7$  cm/s,  $R = 7,5 \cdot 10^{14}$  cm,  $\sigma = 4$ . The solar wind energy density near the shock  $E_k$  has been taken equal to  $5 \text{ eV/cm}^3$ . The value of  $n_0$  has been defined so, that accelerated particles ( $T \gtrsim 10 \text{ keV}$ ) contain 10% of the kinetic energy density  $E_k$ . The diffusion coefficients are  $\kappa_1 = 6,5 \cdot 10^{22} (p/m_p c)^{0,3} (r/R)^{0,2} \text{ cm}^2 \cdot \text{s}^{-1}$ ,

$\kappa_2 \ll \kappa_1$ . The diffusion coefficient in the outside vicinity of the shock might be significantly reduced due to the magnetic field compression and convection of the turbulence excited by the accelerated particles. This leads to the strong modulation of the galactic proton flux at  $T \lesssim 10 \text{ MeV}$ . Radial gradient  $n^{-1} \partial n / \partial r$  takes on a value of 15%/AU at  $T = 10 \text{ keV}$  and 5%/AU at  $T \approx (1-10) \text{ MeV}$ .

The comparison of the results with the observations shows that under the above assumptions the acceleration rate (source  $\mathcal{Q}_1$ ) is capable of providing the



registered intensity of the low-energy particles in the interplanetary space. In the energy range  $T < 100$  KeV the solar cosmic rays might contribute significantly to the total intensity, especially during the maximum of solar activity [11]. This would cause the complicated variations of the low-energy cosmic ray intensity: in the energy range  $T < 100$  KeV the intensity is correlated with the solar activity level [10]; at the energy  $T=6$  MeV/nuc. the anticorrelation takes place [11]. The relative contribution of the source  $Q_1$  increases with the heliocentric distance  $r$ .

The cutoff energy for the accelerated particles spectrum is determined by  $\mathcal{E}_c(T_{\max}) \simeq Ru_1$ ; on the other hand,  $T_{\max} \simeq$

10 MeV/nuc. as is observed for different nuclear species. That should be consistent with our model if  $\mathcal{E}$  is a function of  $T$  per nucleon only. The verification of this suggestion should be based on the treatment of the cosmic ray chemical composition.

4. Acknowledgements. The authors are grateful to Dr.E.G.Berezhko for useful discussions.

#### References

1. Baranov, V.B., Krasnobayev, K.V., (1977), Gidrodinamicheskaya Teoriya Kosmicheskoi Plasmy, Moskva, Nauka.
2. Krymsky, G.F., (1977), Dokl. AN SSSR, 234, 1306.
3. Axford, W.I. et al., (1977), Proc.15-th ICRC, Plovdiv, 11, 132.
4. Bell, A.R., (1978), Mon.Not.Royal Astron.Soc., 182, 147.
5. Blandford, R.D., Ostriker, J.P., (1978), Ap.J., 221, 29.
6. Webb, G.M. et al., (1983), Proc.18-th ICRC, Bangalore, 2, 263.
7. Eichler, D., (1979), Ap.J., 229, 419.
8. Krymsky, G.F., (1981), Izv. AN SSSR, Ser.fiz., 45, 450
9. Berezhko, E.G. et al., (1983), Proc.18-th ICRC, Bangalore, 2, 259.
10. Zeldovich, M.A., Logachev, Yu.I., (1983), Kosmicheskiye Issledovaniya, 21, No.5, 803.
11. Zamow, R., (1975), Ap.J., 197, 167.

## The Energy Spectrum of Jovian Electrons in Interplanetary Space

S. P. Christon, A. C. Cummings, and E. C. Stone

*California Institute of Technology, Pasadena, CA 91125 USA*

W. R. Webber

*University of New Hampshire, Durham, NH 03824 USA*

In this paper we report on the energy spectrum of electrons with energies  $\sim 10$  to  $\sim 180$  MeV measured with the electron telescope on the Voyager 1 and 2 spacecraft [Stone *et al.*, 1977] in interplanetary space from 1978 to 1983. The kinetic energy of electrons is determined by double  $dE/dx$  measurements from the first two detectors ( $D_1$ ,  $D_2$ ) of a stack of eight solid state detectors and by the range of particle penetration into the remaining six detectors ( $D_3$  to  $D_8$ ) which are interleaved with tungsten absorbers.

From 1978 to 1983 (radial range  $\sim 2$  to  $\sim 12$  AU) electrons of jovian origin were clearly observable for electrons stopping in  $D_3$  ( $E \geq 4$  MeV) and in  $D_4$  ( $E \geq 8$  MeV). For electrons stopping in  $D_5$  ( $E \geq 12$  MeV), the jovian flux dominated the galactic electron flux for a period of approximately one year near the encounter with Jupiter [Christon *et al.*, 1985]. Jovian electrons were also observed in  $D_6$  ( $E \geq 21$  MeV) but not in  $D_7$  ( $E \geq 28$  MeV). A detailed interpretation of the electron variations in all energy channels depends on an accurate subtraction of background induced by energetic protons of a few 100 MeV. This subtraction is facilitated by laboratory calibration results at several energies. Further results on the differential energy spectrum of jovian electrons and limits on the maximum detected energies will be reported.

This work was supported in part by NASA under contract NAS 7-918 and grant NGR 05-002-160.

### References

- Christon, S. P., A. C. Cummings, E. C. Stone, and W. R. Webber, *19th Internat Cosmic-Ray Conf, La Jolla*, paper SH4.7-4, 1985.
- Stone, E. C., R. E. Vogt, F. B. McDonald, B. J. Teegarden, J. H. Trainor, J. R. Jokipii, and W. R. Webber, *Space Sci. Rev.*, **21**, 355, 1977.



## THE JOVIAN ELECTRON SPECTRUM: 1978-1984\*

Paul Evenson<sup>+</sup>, Peter Meyer<sup>x</sup>, and Dan Moses<sup>x</sup><sup>+</sup>Bartol Research Foundation, University of Delaware  
Newark, Delaware 19716 USA<sup>x</sup>Enrico Fermi Institute and Department of Physics  
University of Chicago, Chicago, Illinois 60637 USA

**ABSTRACT.** Observations of Jovian electrons through six consecutive 13-month Jovian synodic periods from 1978 to 1984 have been made by the University of Chicago electron spectrometer onboard the ISEE-3 (ICE) spacecraft. The Jovian electron spectrum was determined from 5 to 30 MeV and was found to have a shape which is not a power law in kinetic energy, but cuts off at approximately 20 MeV. The average shape of the spectrum over each of the six intervals of best magnetic connection remains the same for all intervals within uncertainties.

1. **INTRODUCTION.** Observation of interplanetary electrons of Jovian origin at 1 AU provides a unique opportunity to study the propagation of charged particles in the inner heliosphere. Jupiter is a point source of particles imbedded in the solar cavity which sweeps through a range of magnetic connection to the earth with a well defined period. Previous investigators of Jovian electrons at 1 AU during the period of solar minimum (1,2) successfully applied a convection-diffusion model of propagation, determined the value of the "cross-field" diffusion coefficient, and demonstrated the modulation properties of corotating interaction regions. The study presented in this paper goes beyond the previous work into the time of solar maximum with observations by the University of Chicago spectrometer onboard the ISEE-3 spacecraft.

2. **METHOD.** A detailed description of the University of Chicago electron spectrometer onboard ISEE-3 is given in reference (3). The observations from ISEE-3 are unique in two aspects: the large change in the level of solar activity during the active life of the spacecraft and the absence of magnetospheric effects as the spacecraft was positioned at the inner Lagrangian point during most of the flight. Also, the instrument was very stable over the six years of observations. The single factor restricting continuous coverage of Jovian electrons is contamination by solar flare electrons. Elimination of solar flare contamination periods is handled by monitoring the spectral index of electrons observed on IMP-8 at lower energy (1-3 MeV). A better solar flare monitor is being developed using data from the Max-Planck-Institute ULEWAT instrument on ISEE-3 which is also free from magnetospheric effects.

The question of instrument stability in time is critical for solar modulation studies. The solid state detectors and plastic anticoincidence detectors show stability at the 3% level in all calibration and consistency checks over the duration of the flight. The ethylene gas Cerenkov detector used for proton rejection has a small gas leak, and loses approximately 1 atm of pressure per year from an initial pressure

\*Supported, in part, by NASA contract NAS5-26680 and NASA grant NGL-14-01-005

of 18 atm. The change in Cerenkov threshold is continually measured by a change in the pulse height distribution of the Cerenkov signal. The CsI calorimeter also exhibits a drift due to gain changes in the photomultiplier tube for which a correction is made using pulse height analysis of the signal from minimum ionizing protons.

Excellent background rejection is obtained with the requirement of a Cerenkov signal coincident with a stopping particle. The modulation of the flux of Jovian electrons at 1 AU due to changes in the degree of magnetic connection of the spacecraft to Jupiter can be used to further improve background rejection of particles which are not electrons, as well as electrons which are not Jovian in origin. The 10 MeV energy bin was chosen to monitor the Jovian modulation because it is the bin with the highest background rejection efficiency and because solar flares only rarely emit electrons at 10 MeV. A regression of daily rates of each energy bin relative to the 10 MeV bin determines the spectral shape of the Jovian component.

3. **RESULTS.** An example of a Jovian electron energy spectrum determined by the regression technique during the first epoch of best connection (Oct. 27, 1978 to Feb. 24, 1979) is shown in Figure 1. The spectrum is normalized by the average flux in the 10 MeV bin with the assumption that the flux in that bin is totally free of background. One characteristic of the Jovian electron spectral shape of particular interest is the roll off at energies above 20 MeV. The existence of a high energy limit to the Jovian interplanetary emission was first suggested in (4) and has implications for the acceleration of Jovian electrons, as will be discussed in a separate paper.

The form of the energy spectrum of Jovian electrons determined by the regression technique is found to be the same for each epoch of best connection. Therefore, within statistical errors, the average spectral shape of the Jovian quiet-time increases is constant over the period of observation covering six Jovian seasons. Further, the correlation of the daily rates of each energy bin with the reference 10 MeV bin is better fit by a linear regression than by any higher order polynomial during any one epoch of best connection, implying that the spectral shape is constant over a time scale as short as one day. The chi-square goodness of fit parameter degrades with the separation in mean energy of a bin from the reference 10 MeV bin. Because of limited statistics, the interpretation of this uniform scatter about the regression fit line as fluctuations of the spectral shape about an average shape cannot be quantified. Specifically, 10 hour variations in

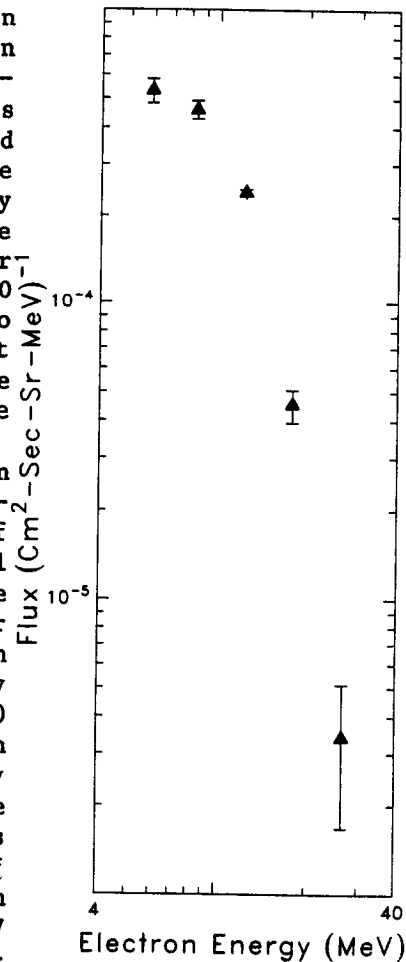


Fig. 1: Jovian electron spectrum determined by regression fit technique during Dec. 1978 epoch.

the spectral shape were searched for using several techniques and none were found.

4. DISCUSSION. The spectral shape of Jovian electrons below 10 MeV presented in this paper is flatter than the kinetic energy power law index of 1.5 reported in (5). However, the spectral index reported at lower energies (.2-1 MeV) of -1.3 or less (6) coupled with the observed roll off above 20 MeV demonstrates that a power law spectrum is a poor approximation in this energy regime. Relying on the background rejection efficiency of the instrument, an average spectrum over the same time interval can be generated which includes the electron component not modulated by the change in the magnetic connection of the spacecraft to Jupiter (and therefore excluded from the spectrum obtained by the regression technique) (Figure 2). This spectrum more closely matches that of Eraker and Simpson (5) and, in comparison with the spectrum obtained by the regression technique, suggests the existence of a significant non-Jovian component at lower energies which would probably be of solar origin. A low energy solar electron component could also explain the degradation of the goodness of fit parameter at these energies.

The constancy of the spectral shape from epoch to epoch during the onset of solar maximum activity demonstrates the lack of solar cycle modulation of the Jovian electron spectrum. This lack of solar modulation is consistent with the conclusions from the radial gradient measurements of cosmic rays (7) that during solar maximum activity 99% of modulation occurs at a solar distance  $>31$  AU. The difference in solar modulation of galactic particles and the relatively local Jovian particles is very clearly seen in the intensity-time plots in Figure 3. While galactic relativistic protons of significantly higher rigidity undergo an obvious solar cycle intensity variation, the Jovian electrons continue with the same 13-month cycles fit by the same convection-diffusion model envelope as observed during solar minimum activity. The only solar cycle effect in the Jovian electrons noted to date is a more impulsive rise and fall of individual increases.

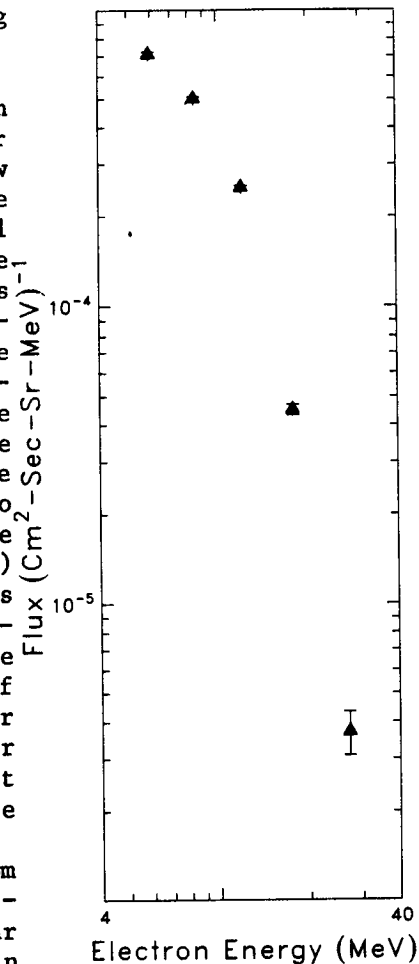
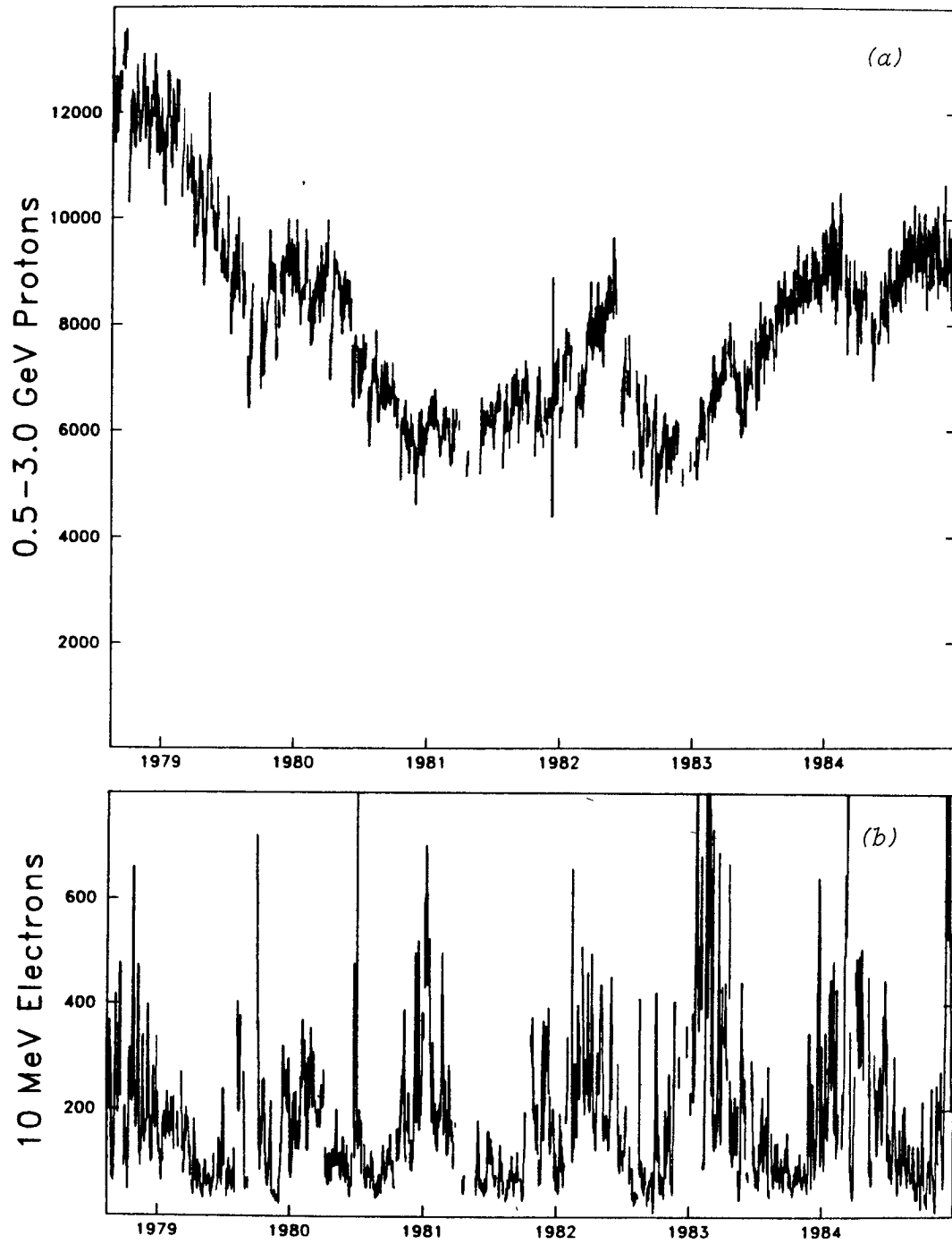


Fig. 2: Spectrum of all electrons during December 1978 epoch.

#### REFERENCES

1. Conlon, T. 1978, JGR 83, 541.
2. Chenette, D. 1980, JGR 85, 2243.
3. Meyer, P. and Evenson, P. 1978, IEEE Trans. GE16, 180.
4. L'Heureux, J. and Meyer, P. 1976, Ap.J. 209, 955.
5. Eraker, J. and Simpson, J. 1979, Ap.J. 232, L131.
6. Mewaldt, R., Stone, E. and Vogt, R. 1975, Proc. of 14th ICRC, 2, 758.
7. McKibben, B., Pyle, R. and Simpson, J. 1985, Ap.J. 289, L35.



*Fig. 3: Daily rates of protons (a) and electrons (b) observed by ISEE-3. No flare subtraction has been made in these plots.*

OBSERVATION OF THE FLUXES OF NUCLEI WITH ENERGIES 10-20 MEV  
PER NUCLEON DURING THE SOLAR FLARE OF APRIL 26, 1984

Bobrovskaya V.V., Grigorov N.L., Zhuravlev D.A., Kondratyeva M.A.,  
Nymnik R.A., Tretyakova Ch.A., Alekseev N.V., Vakulov P.V.,  
Sechinov V.P.

Institute of Nuclear Physics, Moscow State University,  
Moscow, USSR

ABSTRACT

Observations of the fluxes of low energy nuclei in the Earth's magnetosphere are reported. The energy distribution and the composition of the nuclear component of cosmic rays observed during the Solar flare of April 26, 1984 are presented.

I. Introduction. The nuclei (C,N,O) with energies 5-10 MeV per nucleon at altitudes 350-450 km within  $-52^\circ < \lambda < 52^\circ$  were observed on the Skylab (1973-1974) and Salyut-6 (1981) scientific orbital stations [1, 2]. The question now is what is the origin of these particles.

Indeed, the magnetic rigidity of the nuclei is so small that the Earth's magnetic field inhibits the access of these nuclei to the noted latitude from the interplanetary space. The assumption [1] that the observed particles are the singly charged ions which are "stripped" at the altitudes of hundreds of kms and trapped by the earth magnetic field seems to us unsound because the carbon ion  $C^+$  with an energy of 5 MeV per nucleon will have the rigidity 1.2 GV and can be trapped on the shell with  $L \geq 3.5$  only. At the altitudes 350-450 km within the latitudes  $\pm 52^\circ$  there are no regions where the particles trapped at  $L \geq 3.5$  could be observed.

The assumption that the observed particles are the nuclei accelerated in the magnetosphere and accumulated in the internal Earth radiation belt [3] is not obvious either. The fact is that at the noted altitudes the maximum of the intensity of the trapped particles corresponds to  $L = 1.2 - 1.5$ . If the particles are accelerated while radial drifting from the more

removed L-shells to  $L=1.2-1.5$ , they will fail to reach the observing level, because of the low drift velocity they lose the total energy to ionization in the residual atmosphere at heights of 400-700 km. The assumption that the particles are accelerated at the observed altitudes would imply the existence of an unknown acceleration mechanism.

The consideration of the situation led us to the assumption that there are short-time periods when the radial drift velocity is by several orders of magnitude higher than that of mean one typical for small L. During these short-time periods the particles could jump from  $L = 2$  to  $L = 1.2$  without energy losses. This assumption leads inevitably to the consequence on strong intensity variations of the flux of low energy nuclei observed at low altitudes near the Earth.

2. Methods. To obtain the information on the stability of the fluxes we regularly exposed small stacks of solid detectors to the near-earth space. The stacks consisted of several 100 mkm cellulose nitrate sheets. The area of the stacks was  $10-20 \text{ cm}^2$ . The stacks were wrapped about with two Al mylar layers, each 5 mkm in thickness.

3. Results and discussion. The results of observations during the 1984 year are presented in Table I.

Table I.

No. of the stack	:	Exposure time	:	Angle of in- clina- tion of orbit	:	Mean height	:	Flux of nuclei (C,N,O): $\text{cm}^{-2}\text{day}^{-1}$	:	Notes
I	:	April-May 1984	:	$72.9^\circ$	:	400 km	:	$\sim 2000$	:	Solar flare
2	:	June 1984	:	$72.8^\circ$	:	400 km	:	$1.3^{+0.1}$	:	
3	:	June-July 1984	:	$62^\circ$	:	260 km	:	$2.4^{+0.2}$	:	
4	:	September-October 1984	:	$70^\circ$	:	400 km	:	$15^{+1.0}$	:	
"Salyut-6"	:	May 1981	:	$52^\circ$	:	350 km	:	$\sim 200$	:	Solar flare

The fluxes of nuclei in the 5th column refer to the particles coming to rest in the upper layer of the stacks. The 1981-year data are given in the last line of the Table. It is seen from the Table that during the 1981-1984 year period the flux of nuclei at the Earth magnetosphere at heights of  $\sim 300$  km changed by a factor of  $\sim 10^2$ . During the 1984 year the flux also varied (the data from the stacks No. 2, 3, and 4).

We failed to identify the charges of nuclei registered in the stack No.2 and No.3 because their paths were small. The spectra of particles stopping in the top sheet of these stacks were, therefore, identified from their total ranges on the assumption that all the nuclei registered are the oxygen ones. The obtained spectra are presented in Fig. 1 and 2. Typical is a very "soft" spectrum such as

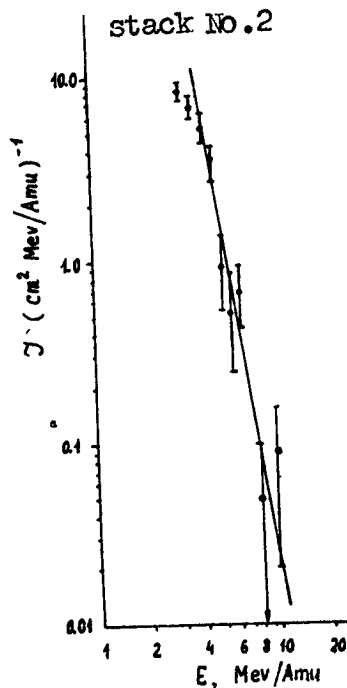


Fig. 1

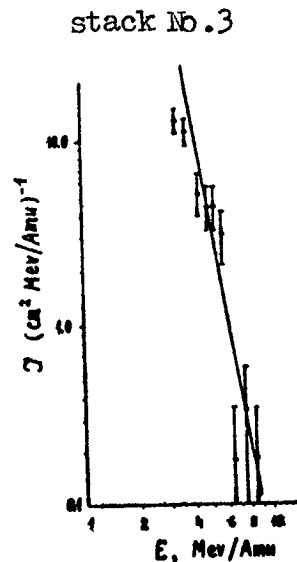


Fig. 2

$I(E) \sim E^{-\gamma}$  with  $\gamma \approx 6$ . It is similar in shape to the spectrum of the particles observed in the Earth's magnetosphere on the Salyut-6 station, but the flux intensities differ sharply. The bending of the

spectrum at  $E < 4$  MeV per nucleon is due to the threshold effect.

In April 1984 the exposure time of the stack No. I coincided with a powerful solar flare. The particles observed in the stack

No. I are seemingly the particles from the flare detected during the short-time periods when the satellite (inclination to the equatorial plane  $\sim 73^\circ$ ) arrived into the region with a low rigidity of the magnetic cut-off. The charge identification was made from the dependence of the etched cone length on the residual range. The energy of the nuclei with a known charge was determined from the total path in the stack. Fig. 3 presents the energy spectrum of C and O nuclei observed during the flare. It will be noted that both flare particles and nuclei observed in the magnetosphere have the same energy distribution (large  $\gamma$ ).

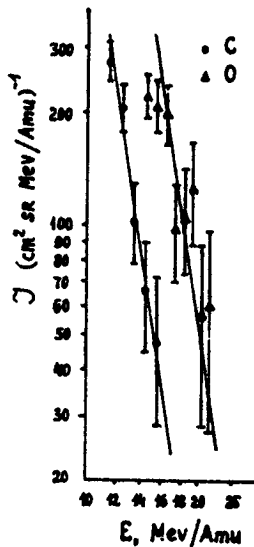


Fig. 3

4. Conclusions. In order to contribute to an increased understanding of the nature of low energy nuclei at low altitudes near the Earth it is necessary to obtain information on the spatial distribution of the observed fluxes.

References.

1. Biswas, S., Durgaprasad, N., Nevatia, J., and Venkatavaradan, V.S., (1975), Proc. 14th ICRC, 2, 816.
2. Bobrovskaya, V.V., Gorchakov, E.V., Grigorov, N.I. et al., (1983), Proc. 18th ICRC, 2, 2.
3. Chan, J.H., and Price, P.B., (1975), Proc. 14th ICRC, 2, 831.



ENERGETIC PARTICLE OBSERVATIONS OF THE SOLAR-GAMMA RAY/NEUTRON  
FLARE EVENTS OF 3 JUNE 1982 AND 21 JUNE 1980  
ISOTOPIC AND CHEMICAL COMPOSITION

M.A.I. Van Hollebeke, Musee National des Sciences, Technique et Industrie  
PARC de La Villette, Paris, France  
Frank B. McDonald, NASA Headquarters/Code P, Washington, DC 20546  
James H. Trainor, NASA/GSFC, Code 600, Greenbelt, MD 20770

ABSTRACT

Studies of the charge composition of two solar gamma-ray/neutron-flare events reveal a striking enrichment of Iron relative to Oxygen with a smaller enrichment of intermediate nuclei. He/O is also enhanced and moderate amounts of  $^3\text{He}$  are detected but there is no evidence for  $^2\text{H}$  or  $^3\text{H}$ .

1. Introduction. The extensive studies of the charge composition of flare-associated energetic particles (McGuire et al., 1979, 1985; Cook et al., 1980, 1984; Mason et al., 1980) have shown there are large changes in the relative abundances of the various elements from event-to-event. J.P. Meyer (1985) has established that this data can be organized to first order by the assumption that there is a basic composition pattern (that differs from the photospheric composition by a simple bias related to an elements first ionization potential) with a superimposed additional bias which is a monotonic function of  $Z$  for  $Z = 6 - 26$  and which varies from event-to-event.

It is of interest to compare these basic patterns with the charge and isotopic composition measured for the flare events of 3 June 1982 and 21 June 1980. Both of these events produced nuclear gamma-rays and solar neutrons that were detected by the Solar Max Mission gamma-ray experiment (Chupp 1984). These observations of nuclear gamma-rays and energetic neutrons require that a significant fraction of the solar energetic ions accelerated in conjunction with the flare event must have undergone nuclear interactions as they traversed the region of the lower corona and solar photosphere. It is especially useful to examine the isotopic composition of hydrogen and helium for the presence of the generally rare isotopes  $^2\text{H}$ ,  $^3\text{H}$  and  $^3\text{He}$  that could have been produced by spallation processes. Furthermore, the near simultaneity of the x-ray and  $\gamma$ -ray emission (Forrest & Chupp 1984) characterize these as very impulsive events that place stringent constraints on the particle acceleration time.

As reported previously (McDonald & Van Hollebeke, 1985a, b) the observed characteristic of the energetic protons and electrons accelerated in these events differ in several important aspects from typical solar particle increases. They had flat energy spectra ( $\gamma = 1.22$  from 3-200 MeV for 3 June 1982 and  $\gamma = 2.7$  for 21 June 1980), are electron rich ( $P/e = 1$  at 4 MeV for 3 June 1980) and both have small but well-defined precursor events that begin some 3 hours before the impulse flare increase.

The principal detector used in these composition studies was the Low Energy Telescope (LET-1) of the Goddard Helios I cosmic-ray experiment. This 4 element multi-parameter system (two 150 micron Si dE/dx detectors, one 0.25 cm total energy solid-state detector and an anti-coincidence element) has a geometric factor of  $0.13 \text{ cm}^2\text{-sr}$  and is identical to that flown on Pioneer 10/11 except that the gain settings and priority selection system on Helios were modified to provide full scale coverage from  $Z = 1\text{-}26$ . Webber et al., 1975 has discussed in detail the excellent charge resolution of this telescope.

On 3 June 1981, Helios I was at a heliocentric distance of 0.57 AU and  $\sim 3^\circ$  in heliolongitude from the nominal interplanetary field-line connecting to the region above the flare site (S09, E72). On 21 June 1980 the spacecraft was  $\sim 33^\circ$  from the nominal field line joining the flare site (N20, W88) at a heliocentric distance of 0.54 AU.

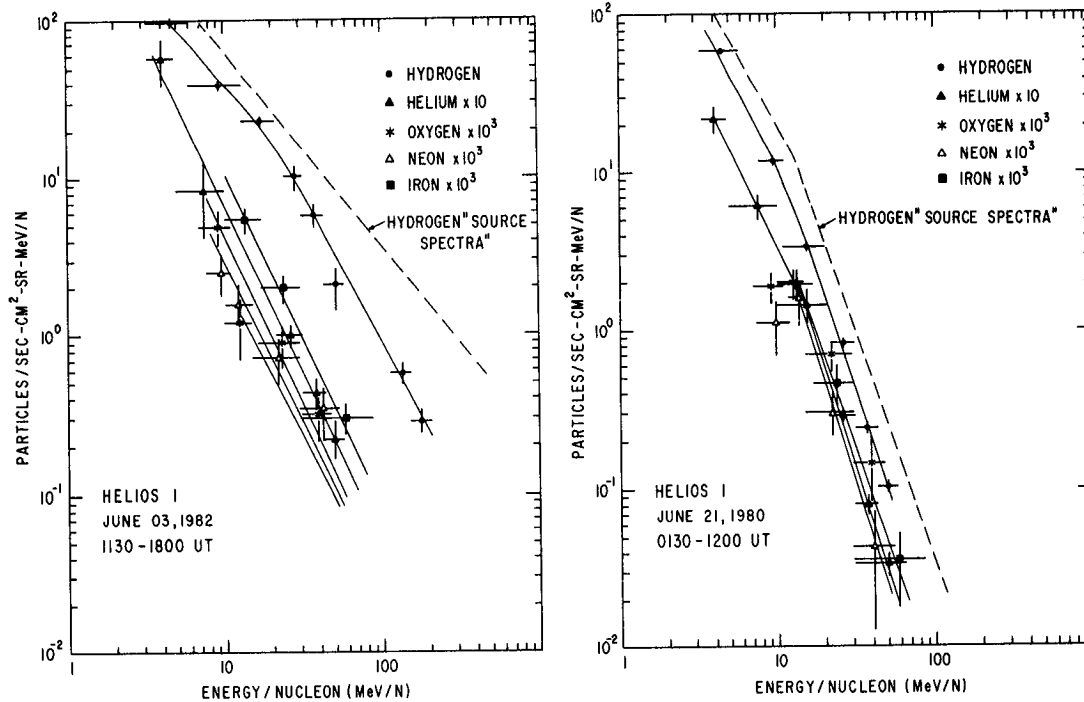
2. Isotopic Composition. The detection of nuclear gamma-rays and neutrons from these two flare events indicate that nuclear interactions are occurring in the solar atmosphere and photosphere. At higher particle energies, nuclear spallation processes should result in the production of  $^2\text{H}$ ,  $^3\text{H}$  and  $^3\text{He}$ . The presence of these otherwise rare isotopes would provide additional information on the acceleration and transport of these energetic particles. From Table 1, it is seen that no  $^2\text{H}$  or  $^3\text{H}$  was detected except for one candidate  $^2\text{H}$  on 3 June 1982. The upper limits in Table 1 are comparable to those of Mewaldt and Stone 1983 and McGuire et al., 1985 for single solar events but are substantially larger than their upper limits obtained by averaging over many events.

TABLE 1

	$^2\text{H}/\text{H}$ 3.3-39 MeV/nuc	$^3\text{H}/\text{H}$	$^3\text{He}/^4\text{He}$ 30-50 MeV/nuc
3 June 1982	$<4 \times 10^{-4}$	$<4 \times 10^{-4}$	$.02 \pm .014$
21 June 1980	$<5 \times 10^{-4}$	$<4.5 \times 10^{-4}$	$.03 \pm .013$

From the thin-target calculation of Ramaty and Kozlovsky, 1974, with  $\gamma = 1.3$ , an upper limit of  $\sim 0.25 \text{ g/cm}^2$  is obtained for the solar material traversed by 30 MeV ions. There is a small but finite amount of  $^3\text{He}$  detected for both of these events suggesting preferential injection and/or acceleration of this component rather than production by nuclear spallation processes.

3. Charge Composition. As in other studies of the elemental abundances, it is necessary to extend the analysis period beyond the time of peak intensity. However, because of the impulsive nature of the events, unusually short integration periods have been used (6.5 hrs for 6/3/82 and 10.5 hrs for 6/21/81). The resulting energy spectra for the more abundant species are shown in Fig 1. The H, He, C, O and Mg have a spectral index,  $\gamma \approx 1.4$  for 3 June 1982 event and  $\gamma = 2.0 \pm .1$  for Fe. For 21 June 1980 the corresponding  $\gamma$  values are 2.2 and 2.75. This steepening may result from the fact that the Iron spectra extends to higher energies (the H data is in agreement with this interpretation).



The details of the charge composition (Table 1) reveal a striking overabundance of Fe. The Fe/O of  $2.5 \pm .5$  for the 3 June 1982 event is a factor of 34 above the baseline SEP value of McGuire et al., while the value of 0.91 for the 21 June 1982 increase is 14x the SEP baseline. The final line in Table 2 is an enhancement factor using the GSFC solar energetic particle baseline which is an average of events with little or no Fe enrichment. J. P. Meyer has derived a "mass-unbiased" baseline using a different criteria for selecting events. By either measure these events display a remarkable Fe/O enrichment. The Ne/O, Mg/O are enhanced by more modest amounts. The Si/O ratio is substantially less than would be expected but the poor statistics for this element do not permit any definite conclusions.

TABLE 2

SOLAR ENERGETIC PARTICLE ABUNDANCES 10-47 MeV/nuc									
	H/He	He/O	C/O	N/O	O/O	Ne/O	Mg/O	Si/O	Fe/O
3 June 1982 1130-1800	132	102±14	0.38±1	-----	1	0.87±.2	0.62±.18	0.2±.08	2.5±.5
21 June 1980 0130-1200	29	79±10	0.53±1	16±.06	1	0.46±.13	0.19±.06	0.4±.1	0.91±.02
McGuire et al. SEP Baseline	66	53±5	0.45±.02	13±.01	1	0.13±.01	0.18±.01	0.15±.01	0.066±.006
Enrichment Factor 3 June 1980	2	1.9±.27	0.84±.2	-----	1	6.7±1.5	3.4±.1	1.3±.5	38±7.6

4. Discussion. The general pattern of  $Z$  enrichment for  $6 < Z < 26$  appears to be consistent with that proposed by Meyer (1985). The high value of Fe/O correlate remarkably with the data of McGuire et al., 1985, showing a strong inverse relation between the spectral index  $\gamma$  and the Fe/O ratio (Fig. 2). This effect may be a key factor in understanding  $Z$  enrichment. It is also interesting that the He/O ratio of  $102 \pm 14$  for 2 June 1982 is very high and is consistent with the previously reported positive correlations between the He/O and Fe/O (Meyer et al., 1985). This correlation does present difficulties with interpreting the  $Z$ -enrichment as a rigidity effect.

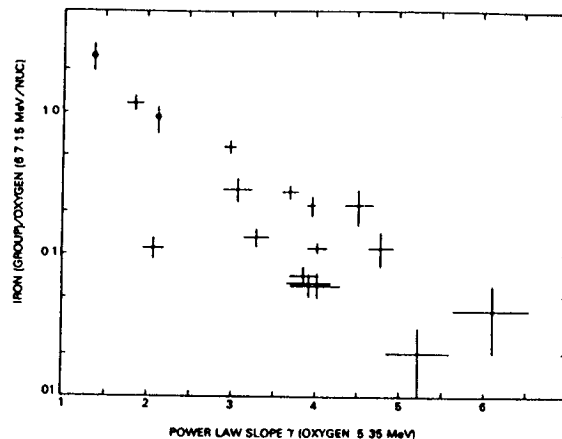


Fig. 2 Compilation by McGuire et al., 1985, of Fe/O vs Power Law Slope  $\gamma$  with the two added values (black dots) from this paper.

Solar neutrons are probably produced mainly by the spallation of He nuclei, but the large overabundance of Iron means Fe nuclei will make a substantial contribution to these events. Further studies are now underway to determine this relative role of He and Fe.

#### References

1. Chupp, E.L., (1984), *Ann. Rev. Astron. Astrophysics*, **22**, 359
2. Cook, W.R., Stone, E.C., and Vogt, R.E., (1980), *Ap.J.*, **238**, L97; (1984), *Ap. J.* **279**, 827
3. Forrest, D.J., and Chupp, E.L., (1984), *Nature*, **305**, 291
4. Mason, G.M., Fisk, L.A., Hovestadt, D., and Gloeckler, G., (1980), *Ap.J.* **239**, 1970
5. McDonald, F.B., and Van Hollebeke, M.A.I., (1985a), *Ap.J.*, **290**, L67; (1985b), *Proc. 19th ICRC*, Paper # SH1.3-8
6. McGuire, R.E., von Rosenvinge, T.T., and McDonald, F.B., (1979), *Proc. 16th ICRC*, Kyoto, **5**, 61; (1985) submitted for publication to *Ap.J.*
7. Mewaldt, R.A. and Stone, E.C., (1983), *Proc. 18th ICRC*, Bangalore, **4**, 52
8. Meyer, J.P., (1985), *Ap.J. Supplement*, **57**, 1515.
9. Ramaty, R. and Kozlovsky, B., (1974), *Ap.J.*, **193**, 1974
10. Ramaty, R., Lingenfelter, R.E., and Kozlovsky, B., (1982), *Gamma Ray Transients and Related Phenomena*, Ed. R.E. Lingenfelter, et al., (N.Y. AIP) P211
11. Webber, W.R., Roelof, E.C., McDonald, F.B., Teegarden, B.J., and Trainor, J.H., (1975), *Ap.J.*, **199**, 482.

## Precision Measurements of Solar Energetic Particle Elemental Composition

*H. Breneman and E. C. Stone*

California Institute of Technology  
Pasadena, California 91125 USA

### 1. Introduction

Using data from the Cosmic Ray Subsystem (CRS) aboard the Voyager 1 and 2 spacecraft (Stone et al 1977), we have determined solar energetic particle abundances or upper limits for all elements with  $3 \leq Z \leq 30$  from a combined set of 10 solar flares during the 1977-1982 time period. Statistically meaningful abundances have been determined for the first time for several rare elements including P, Cl, K, Ti and Mn, while the precision of the mean abundances for the more abundant elements has been improved by typically a factor of  $\sim 3$  over previously reported values. When compared to solar photospheric spectroscopic abundances, these new SEP abundances more clearly exhibit the step-function dependence on first ionization potential previously reported by Cook et al (1979, 1984) and Meyer (1981, 1985).

### 2. Observations

Each CRS includes four Low Energy Telescopes (LET) and two High Energy Telescopes (HET) employing silicon solid-state detectors and covering a combined incident energy range for oxygen of 3.5 - 50 MeV/nucleon. A scatterplot of LET data from the  $Z = 14 - 20$  charge range is shown in Fig. 1. Even relatively rare elements such as Ar and Ca are clearly resolved. For the rarer elements (e.g., P, Cl, K), the abundances were determined by performing maximum-likelihood fits to the rare element peak and its two usually more abundant neighbors. For the most abundant elements (C, N, O, Ne, Na, Mg, Al, Si, S, Ar, Ca, Cr, Fe), the abundances could be determined in each of the flares; these values were averaged to obtain mean abundances using a weighting technique that takes into account both statistical variations and real abundance variations from flare to flare.

### 3. Results

The average SEP abundances relative to silicon for elements with  $3 \leq Z \leq 30$  are listed in Table I. In Fig. 2, these results for the more abundant elements are compared to those obtained by other recent investigations. It can be seen that the new abundances agree well with the previously determined values but have about a factor of three higher precision.

### 4. Discussion

An ordering by first ionization potential (FIP) of SEP composition relative to "solar system" or photospheric composition has been noted in the past (Hovestadt 1974, Webber 1975, McGuire et al 1979). In particular, Cook et al (1979, 1984) found a step-function dependence on FIP, with elements with  $FIP > 10$  eV depleted by a factor of  $\sim 5$  in SEPs and elements with  $FIP < 8$  eV approximately equally abundant in SEPs and the photosphere. This behavior may be expected on the basis of

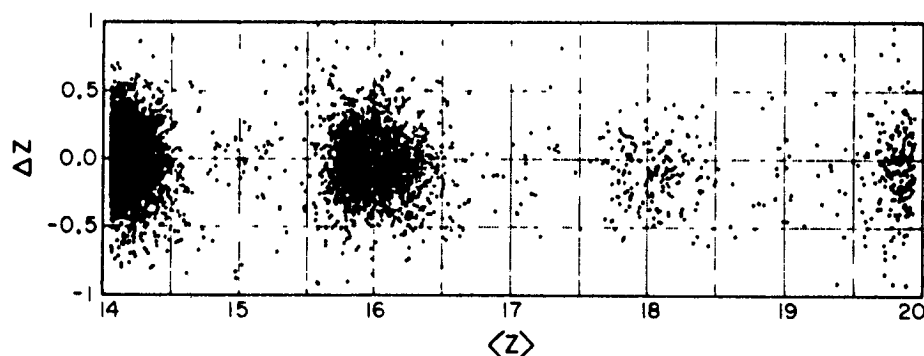


Fig 1. Scatterplot of SEP data from LET in the  $Z = 14 - 20$  charge range  $\langle Z \rangle$  is the average, and  $\Delta Z$  the difference, of two essentially independent charge determinations obtained from the LET data for each analyzed particle

dynamical ionization models such as that of Geiss and Bochsler (1984) for the formation of the corona. Fig 3 shows that the step-function ordering by FIP is more clearly defined in the new data, including the elements P, Cl, K, Ti, and Mn. However, Fig 3 also discloses statistically significant enhancements and depletions of several elements such as Na, Fe and Ni, which are discussed by Breneman and Stone (1985) in the context of an acceleration/propagation fractionation of SEPs based on the ionic charge-to-mass ratio of the species making up the SEPs.

In Fig 4, the SEP abundances are compared to galactic cosmic ray source (GCRS) abundances (Lund 1984). The absence of a FIP-dependence in the SEP/GCRS ratio indicates that the GCRS may have a FIP-dependent step-function fractionation like that of the SEPs (Cook et al 1979, Meyer 1981, Lund 1984). Both may exhibit a depletion of elements with FIP greater than  $\sim 10$  eV because of the smaller flux of ionizing photons with energies greater than that of Ly- $\alpha$  (10.2 eV). Both C and N appear to be distinctly different in SEPs and the GCRS.

Table I SEP average elemental abundances ( $S_1 = 1000$ )

Z	abundance	Z	abundance	Z	abundance	Z	abundance
3	< 1.36	10	887 $^{+91}_{-88}$	17	2.01 $^{+0.63}_{-0.62}$	24	14.3 $^{+2.9}_{-2.4}$
4	< 0.17	11	73.3 $^{+7.2}_{-6.6}$	18	20.7 $^{+3.5}_{-3.0}$	25	5.0 $^{+2.7}_{-1.9}$
5	< 0.34	12	1206 $^{+84}_{-81}$	19	2.95 $^{+1.01}_{-0.93}$	26	959 $^{+105}_{-94}$
6	2710 $^{+270}_{-240}$	13	87.4 $^{+4.3}_{-4.1}$	20	68 $^{+12}_{-10}$	27	< 13.5
7	775 $^{+54}_{-51}$	14	1000	21	(0.22 $^{+0.39}_{-0.22}$ )*	28	33.6 $^{+6.9}_{-5.9}$
8	6230 $^{+360}_{-340}$	15	478 $^{+0.94}_{-0.70}$	22	3.5 $^{+1.4}_{-1.1}$	29	(0.40 $^{+0.64}_{-0.40}$ )*
9	(0.29 $^{+0.29}_{-0.29}$ )*	16	222 $^{+8}_{-7}$	23	(0.34 $^{+0.48}_{-0.34}$ )*	30	1.09 $^{+0.92}_{-0.85}$

\* Abundances for these elements are based on fewer than 5 particles and are highly uncertain

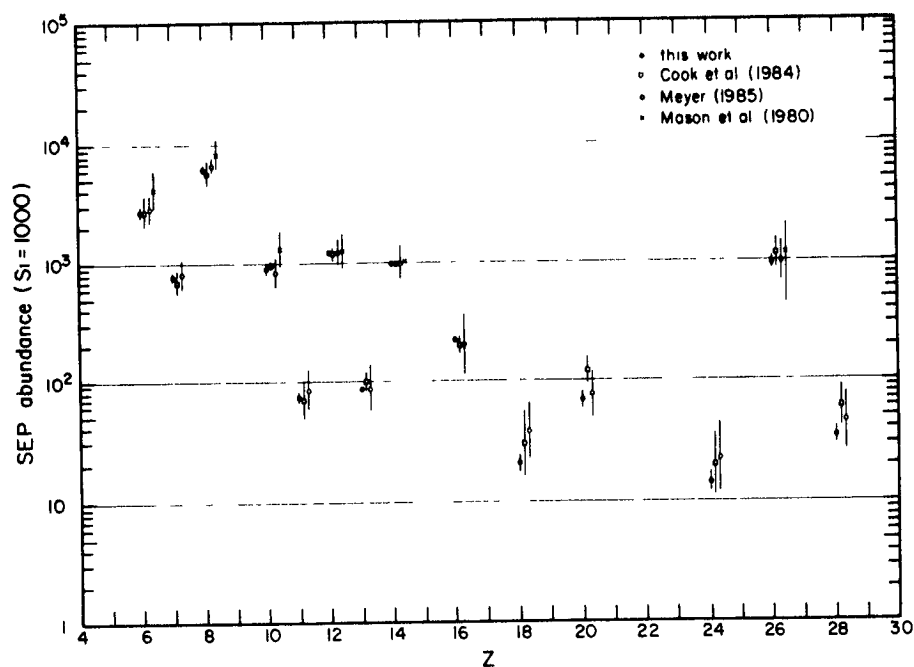


Fig 2 Comparison of the new SEP abundances with other recent SEP abundance measurements

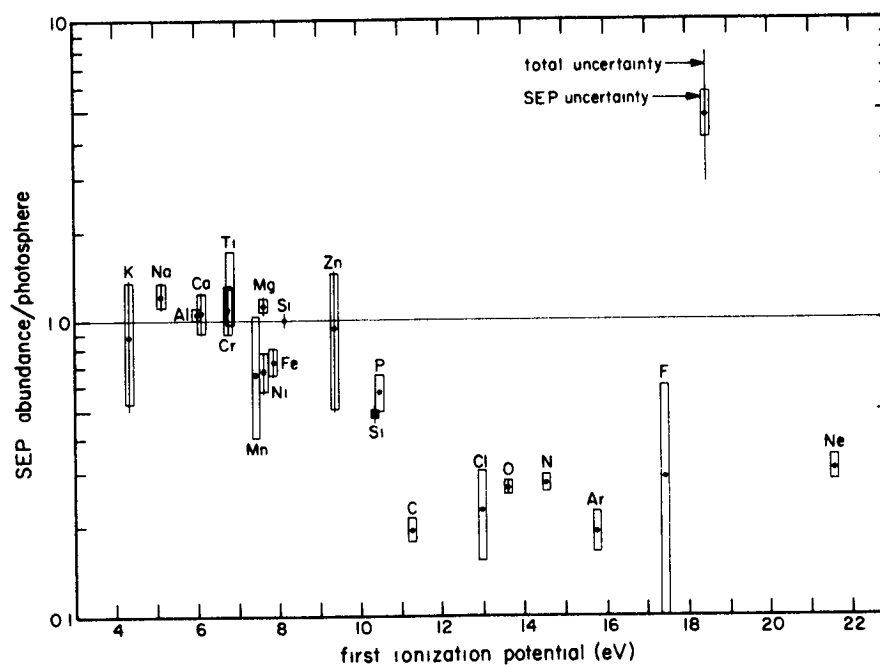


Fig 3 SEP abundances ( $S_i = 1$ ) relative to spectroscopic photospheric abundances (Grevesse 1984), plotted vs FIP

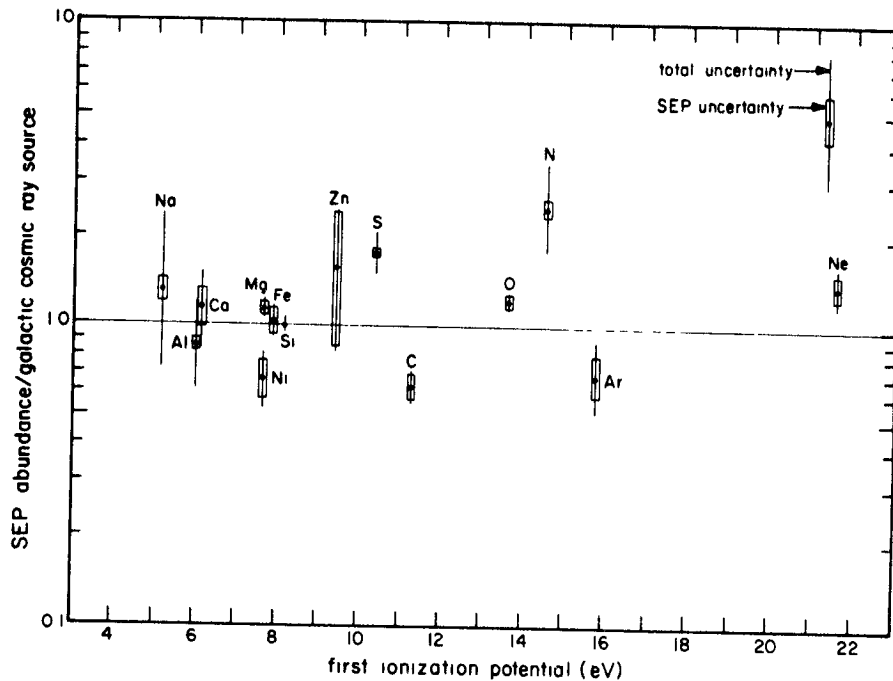


Fig 4 SEP abundances ( $S_1 = 1$ ) relative to galactic cosmic ray source abundances (Lund 1984), plotted vs FIP

### 5. Acknowledgements

This work has been supported in part by the National Aeronautics and Space Administration under contract NAS7-918 and grant NGR 05-002-160

### References

- Breneman, H., and Stone, E. C. 1985, *Proc 19th Int Cosmic Ray Conf* (La Jolla), paper SH 2 1-5
- Cook, W. R., Stone, E. C., Vogt, R. E., Trainor, J. H., and Webber, W. R. 1979, *Proc 16th Int Cosmic Ray Conf* (Kyoto), 12, 265
- Cook, W. R., Stone, E. C., and Vogt, R. E. 1984, *Ap. J.* **279**, 827
- Geiss, J., and Bochsler, P. 1984, International Conference on Isotopic Ratios in the Solar System, Paris
- Grevesse, N. 1984, *Physica Scripta* **T8**, 49.
- Hovestadt, D. 1974, in *Solar Wind III*, ed by C. T. Russell, University of California, Los Angeles.
- Lund, N. 1984, Invited Lecture at the Symposium on Nucleosynthesis and Acceleration of Cosmic Rays, XXV COSPAR Plenary Meeting, Graz, Austria
- Mason, G. M., Fisk, L. A., Hovestadt, D., and Gloeckler, G. 1980, *Ap. J.* **239**, 1070
- McGuire, R. E., von Rosenvinge, T. T., and McDonald, F. B. 1979, *Proc 16th Int Cosmic Ray Conf.* (Kyoto), 5, 61
- Meyer, J.-P. 1981, *Proc 17th Int Cosmic Ray Conf* (Paris), 3, 145
- Meyer, J.-P. 1985, *Ap. J. Suppl.* **57**, 151
- Stone, E. C., Vogt, R. E., McDonald, F. B., Teegarden, B. J., Trainor, J. H., Jokipii, J. R., and Webber, W. R. 1977, *Sp. Sci. Rev.* **21**, 355
- Webber, W. R. 1975, *Proc 14th Int Cosmic Ray Conf* (Munich), 5, 1597



# Solar Coronal and Photospheric Abundances from Solar Energetic Particle Measurements

*H. Breneman and E C Stone*

California Institute of Technology  
Pasadena, California 91125 USA

## 1. Introduction

Solar energetic particle (SEP) elemental abundance data from the Cosmic Ray Subsystem (CRS) aboard the Voyager 1 and 2 spacecraft (Breneman and Stone 1985) are used to derive unfractionated coronal and photospheric abundances for elements with  $3 \leq Z \leq 30$ . We find that the ionic charge-to-mass ratio ( $Q/M$ ) is the principal organizing parameter for the fractionation of SEPs by acceleration and propagation processes and for flare-to-flare variability, making possible a single-parameter  $Q/M$ -dependent correction to the average SEP abundances to obtain unfractionated coronal abundances. A further correction based on first ionization potential allows the determination of unfractionated photospheric abundances

## 2. Results

The composition of individual flares relative to the average SEP composition can be described by a function that is roughly monotonic in  $Z$  but variable in magnitude from flare to flare (Cook et al 1979, 1984, McGuire et al 1979, Meyer 1981,

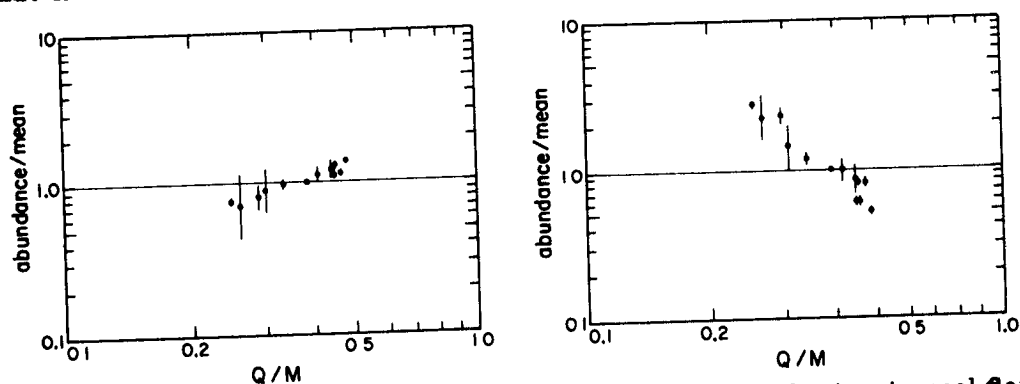


Fig. 1. Abundances relative to the mean SEP abundance for two typical flares, plotted vs.  $Q/M$ .

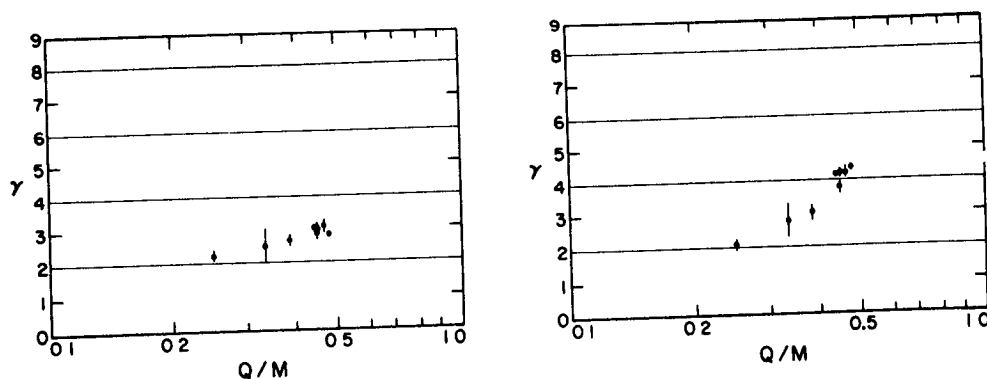


Fig 2 Spectral index  $\gamma$  vs.  $Q/M$  for two typical flares.

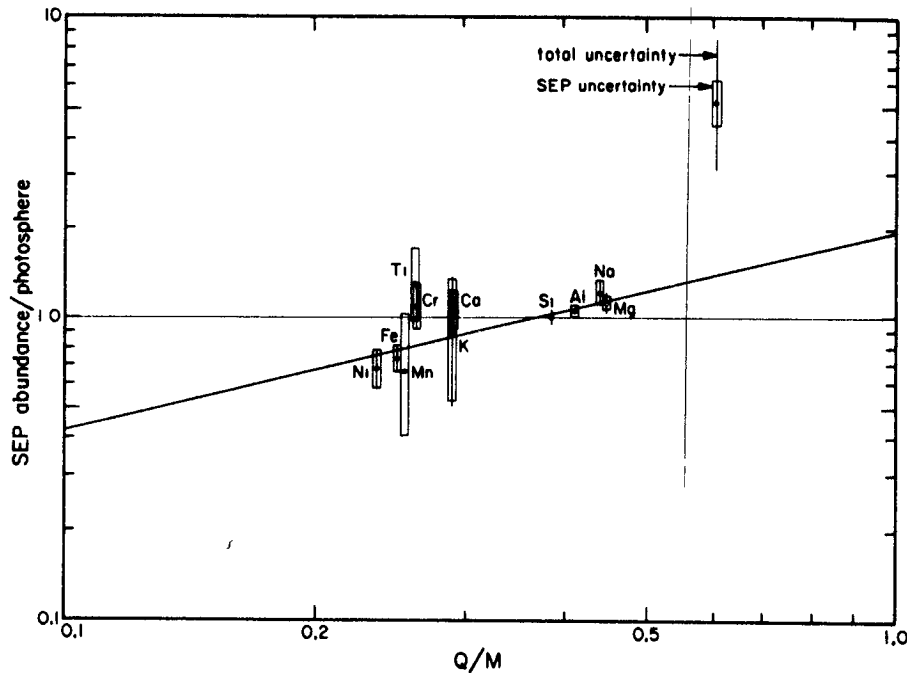


Fig 3 Mean SEP abundance relative to the photosphere (Grevesse 1984) for the low-FIP elements, plotted vs.  $Q/M$ . The best-fit power-law has a reduced  $\chi^2$  of 1.0.

1985) Using the recently reported SEP ionic charge states (Luhn et al. 1984), we find that this compositional variability exhibits a monotonic dependence on the ionic charge-to-mass ratio  $Q/M$  of the particles, as illustrated in Fig 1. Such a dependence is not unexpected for acceleration and propagation effects. The spectral indices of the elemental differential energy spectra for a given flare also tend to be ordered by  $Q/M$  (Fig 2). Thus we derive an unfractionated coronal composition by applying a  $Q/M$ -dependent correction to the average SEP abundances.

### 3. Discussion

The correction factor has been determined by comparing the SEP abundances of elements with low first ionization potential (FIP), which display no FIP-dependent fractionation (Breneman and Stone 1985), to the photospheric spectroscopic abundances (Grevesse 1984) (see Fig 3). The derived correction function, which is a power-law in  $Q/M$  with a slope of  $0.66 \pm 0.17$ , may be applied to the SEP abundances for *all* elements, resulting in SEP-derived coronal abundances (see Table 1). As Fig 4 shows, they agree well with coronal abundances obtained by XUV/X-ray spectroscopy, but have much higher precision and are available for many more elements.

The derived coronal abundances can also be corrected for the FIP-dependent fractionation suggested by the dynamical ionization model of Geiss and Bochsler (1984). In this model, the high-FIP elements such as N, O, F, Ne, Cl and Ar are depleted because their ionization times are longer than the time individual atoms spend in a rising spicule. Thus, their abundances are corrected by the depletion factor of oxygen in SEPs relative to the photosphere ( $4.03 \pm 0.26$ ), P and S are corrected by the depletion factor of sulfur ( $1.89 \pm 0.17$ ), C is corrected by the mean of the oxygen and sulfur depletion factors, since its proper depletion factor is uncertain, and the low-FIP elements, which are quickly ionized, are left

Table 1. SEP-derived coronal and photospheric abundances relative to silicon

Z	SEP-derived corona	SEP-derived photosphere	Z	SEP-derived corona	SEP-derived photosphere
6	2350 $^{+250}_{-230}$	6490 $^{+280}_{-270}$	19	3.9 $^{+2.1}_{-1.6}$	3.9 $^{+2.1}_{-1.6}$
7	700. $^{+52}_{-48}$	2775 $^{+53}_{-50}$	20	82. $^{+14}_{-12}$	82. $^{+14}_{-12}$
8	5680 $^{+390}_{-340}$	22900	21	(0.31 $^{+0.55}_{-0.31}$ )*	(0.31 $^{+0.55}_{-0.31}$ )*
9	(0.28 $^{+0.29}_{-0.28}$ )*	(1.1 $^{+1.2}_{-1.1}$ )*	22	4.9 $^{+1.6}_{-1.3}$	4.9 $^{+1.6}_{-1.3}$
10	783. $^{+84}_{-77}$	3140 $^{+205}_{-195}$	23	(0.48 $^{+0.69}_{-0.48}$ )*	(0.48 $^{+0.69}_{-0.48}$ )*
11	67.0 $^{+8.8}_{-8.2}$	67.0 $^{+8.8}_{-8.2}$	24	18.3 $^{+3.9}_{-3.3}$	18.3 $^{+3.9}_{-3.3}$
12	1089. $^{+84}_{-82}$	1089 $^{+84}_{-82}$	25	6.8 $^{+3.9}_{-2.7}$	6.8 $^{+3.9}_{-2.7}$
13	83.7 $^{+4.2}_{-4.0}$	83.7 $^{+4.2}_{-4.0}$	26	1270 $^{+170}_{-150}$	1270 $^{+170}_{-150}$
14	1000	1000	27	< 18.1	< 18.1
15	4.89 $^{+0.66}_{-0.72}$	9.24 $^{+1.46}_{-1.54}$	28	46.5 $^{+8.1}_{-7.4}$	46.5 $^{+8.1}_{-7.4}$
16	242. $^{+10}_{-9}$	460. $^{+42}_{-36}$	29	(0.57 $^{+0.87}_{-0.57}$ )*	(0.57 $^{+0.87}_{-0.57}$ )*
17	2.38 $^{+0.84}_{-0.80}$	9.6 $^{+3.5}_{-3.3}$	30	1.61 $^{+0.87}_{-0.76}$	1.61 $^{+0.87}_{-0.76}$
18	24.1 $^{+4.2}_{-3.6}$	102 $^{+20}_{-17}$			

\* Based on fewer than 5 particles and highly uncertain

unchanged. The resulting SEP-derived photospheric abundances (Table 1) involve fewer modeling parameters than spectroscopic determinations and are available for some elements (e.g., C, N, Ne, Ar) that cannot be observed spectroscopically. The main differences (Fig. 5) are a significantly higher abundance of Cr (and possi-

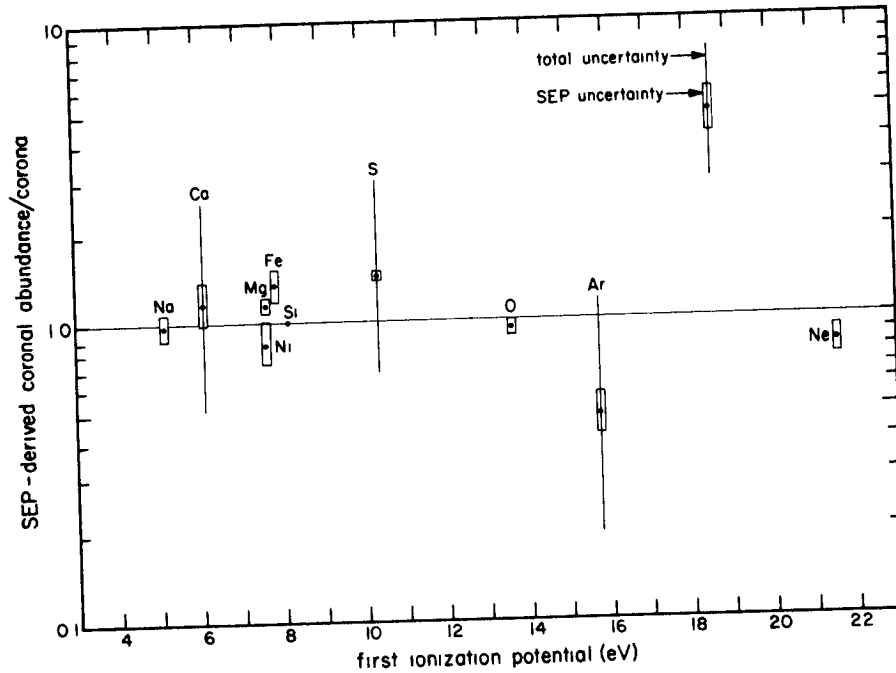


Fig. 4 SEP-derived coronal abundances relative to spectroscopically-derived coronal abundances (Veck and Parkinson 1981), plotted vs FIP

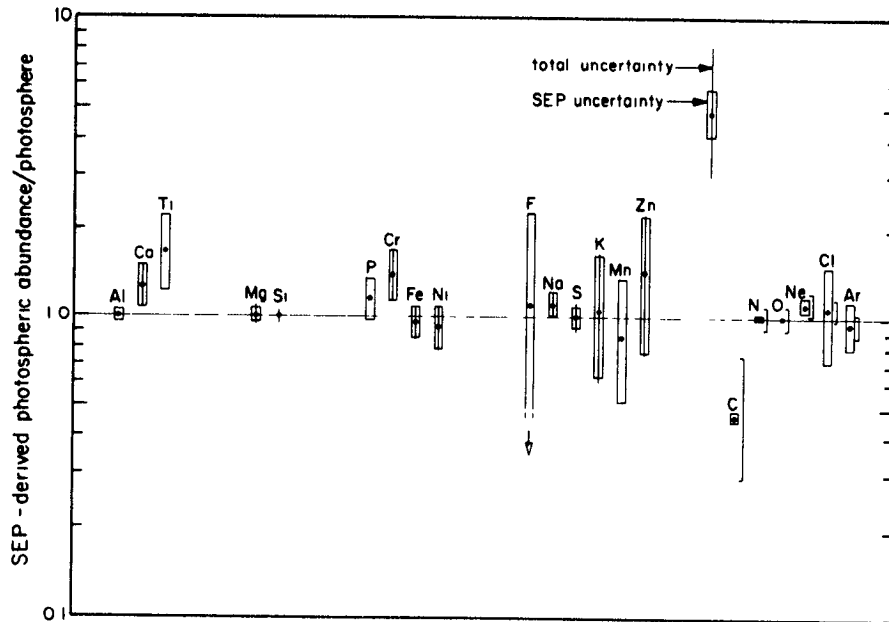


Fig 5 SEP-derived photospheric abundances relative to spectroscopically-derived photospheric abundances (Grevesse 1984) The estimated uncertainty in the FIP fractionation correction is indicated by the vertical brackets

bly Ca and Ti) and a C abundance that is about half of the commonly assumed solar abundance. The SEP-derived Fe/Si ratio is in agreement with the recent photospheric value (Grevesse 1984), which is 50% larger than the meteoritic value.

#### 4. Acknowledgements

This work has been supported in part by the National Aeronautics and Space Administration under contract NAS7-918 and grant NGR 05-002-160.

#### References

- Breneman, H., and Stone, E. C. 1985, *Proc 19th Int Cosmic Ray Conf* (La Jolla), paper SH 2 1-4.
- Cook, W. R., Stone, E. C., Vogt, R. E., Trainor, J. H., and Webber, W. R. 1979, *Proc 16th Int Cosmic Ray Conf* (Kyoto), **12**, 265.
- Cook, W. R., Stone, E. C., and Vogt, R. E. 1984, *Ap J* **279**, 827.
- Geiss, J., and Bochsler, P. 1984, International Conference on Isotopic Ratios in the Solar System, Paris.
- Grevesse, N. 1984, *Physica Scripta* **T8**, 49.
- Luhn, A., Klecker, B., Hovestadt, D., Gloeckler, G., Ipavich, F. M., Scholer, M., Fan, C. Y., and Fisk, L. A. 1984, *Adv Space Res* **4**, No 2-3, 161.
- McGuire, R. E., von Rosenvinge, T. T., and McDonald, F. B. 1979, *Proc 16th Int Cosmic Ray Conf* (Kyoto), **5**, 61.
- Meyer, J.-P. 1981, *Proc 17th Int. Cosmic Ray Conf* (Paris), **3**, 145.
- Meyer, J.-P. 1985, *Ap J Suppl.* **57**, 151.

# SILICON TO IRON ABUNDANCES IN SOLAR COSMIC RAYS AND IN THE SUN

M.N. Vahia, S. Biswas and N. Durgaprasad  
Tata Institute of Fundamental Research, Bombay 400005  
INDIA

## ABSTRACT

Differential spectra of even charged nuclei between Si and Fe in the August 4, 1972 event are made in the energy region of 10 to 40 MeV/n-1 using rocket borne plastic detectors. The resultant relative abundances of elements and low energy ( $E < 25$  MeV n-1) enhancements are obtained. Comparison with spectroscopically determined photospheric abundances is also made. The implications of these relative abundances on the acceleration mechanisms is discussed.

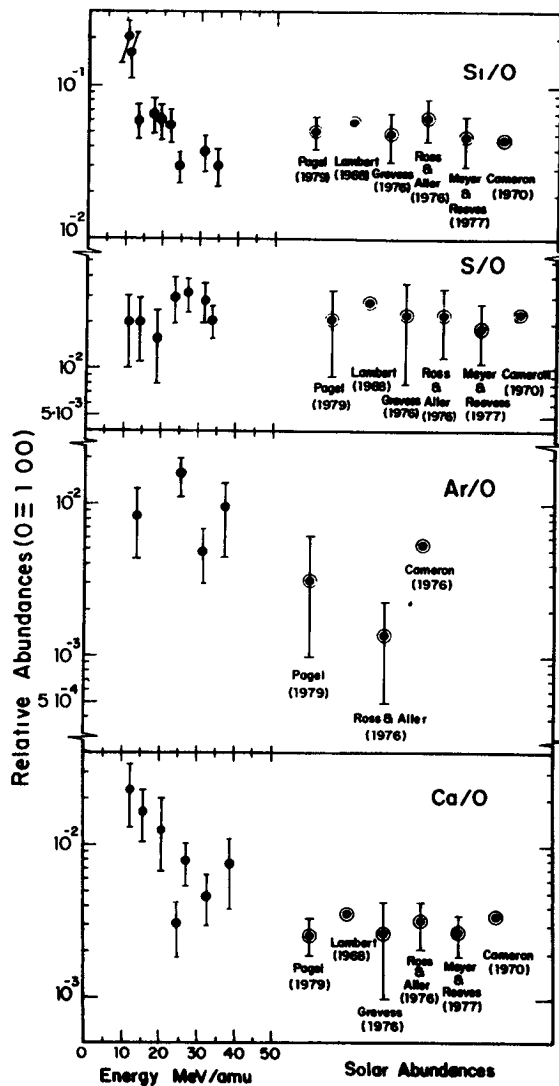
1. Introduction. With rocket flights and solid state nuclear track detectors, large flares have been studied in great details and it has been shown that at the higher energies ( $E > 25$  MeV/amu) the relative abundances tend to match the photospheric abundances (Bertsch et al 1974; Biswas et al., 1983; Crawford et al., 1975). August 4, 1972 was amongst the largest events with large heavy ion fluxes. Data of good statistics on relative abundances for even charged nuclei between  $Z = 14$  to 26, were obtained in this flare. The results are discussed in this paper.

2. Experimental Method. The study of the August 4, 1972 event was done with a stack of 23 sheets of Lexan polycarbonate flown on a sounding rocket in NASA's SPICE programme from Ft. Churchill, Canada at 1916 UT to study the emission from an optical flare of 0617 UT the same day. The rocket was spin stabilised and reached an altitude of 160 kms above earth. The rocket nose cone was opened at an altitude of 60kms on ascent and closed at 85 kms on descent giving a total of 245 seconds of exposure (see Durgaprasad et al., 1982).

The plastics were recovered and processed in 6.25 N NaOH solution at  $(40 \pm 0.1^\circ\text{C})$  for 4 hours to reveal the tracks of  $Z > 12$  elements. A total area of 30 sq. cms. was studied at different depths to determine

the spectra. The details of the technique are discussed elsewhere (Vahia, 1983).

Fractional charges were assigned to the tracks using the constant energy contours. The Gaussian of all charge values for all the events had FWHM for Si as 0.24 and for Fe as 0.33 charge units. From this the differential spectra were determined. The differential spectrum of Fe obtained by us was compared with that obtained by other investigators on the same flight and good agreement was found. The oxygen spectra were taken from the measurements by Bertsch et al (1974) made in the same flight. The relative abundances are plotted in Fig. 1



**3. Results.** In the case of odd charges, only 13 Al, 15 P, 17 Cl, 23 V and 25 Mn have observable flux values. It should however be noted that since the processing of the sheets was done to study  $Z > 14$  elements, the aluminium events are subject to detection efficiency and its relative abundances need not be considered for the present study.

Fig. 1a Variation of relative abundances as compared to oxygen of Si, S, Ar and Ca nuclei with energy and comparison with photospheric value.

As for other observed elements, with the notable exception of Mn, they are seen in very small numbers and no definite flux measurements can be attempted. The Mn fluxes can be determined only approximately by the method of histogram subtraction. In the entire energy range Mn/O ratio is about 0.10. This is a factor of about 10 above the spectroscopic determination of  $0.008 \pm 0.005$ . In our study we observed a high Mn/Fe ratio of 0.15 (~20 events) in sheets 2 and 3 (energy 10-25 MeV/amu). In the sheets 4-5 and 8-9 we saw no appreciable flux of Mn implying  $\text{Mn/Fe} < 0.01$ . Hence it seems that Mn must be having a steeply falling spectrum. This would result in a steeply falling enhancement between 10 and 40 MeV/amu. Therefore the Mn observations seem to be consistent with the

photospheric determinations within experimental approximations. The elements Si, S, Ar, Ca, Ti, Cr and Fe are seen in sufficiently large numbers to help in determining detailed spectra of these elements. Their charge histograms are also distinct and devoid of possible contaminations. Hence flux determination can be made accurately and with a high degree of confidence.

At low energy, the more abundant elements for which detailed study is possible show varying degrees of enhancements.(Figure 1 )

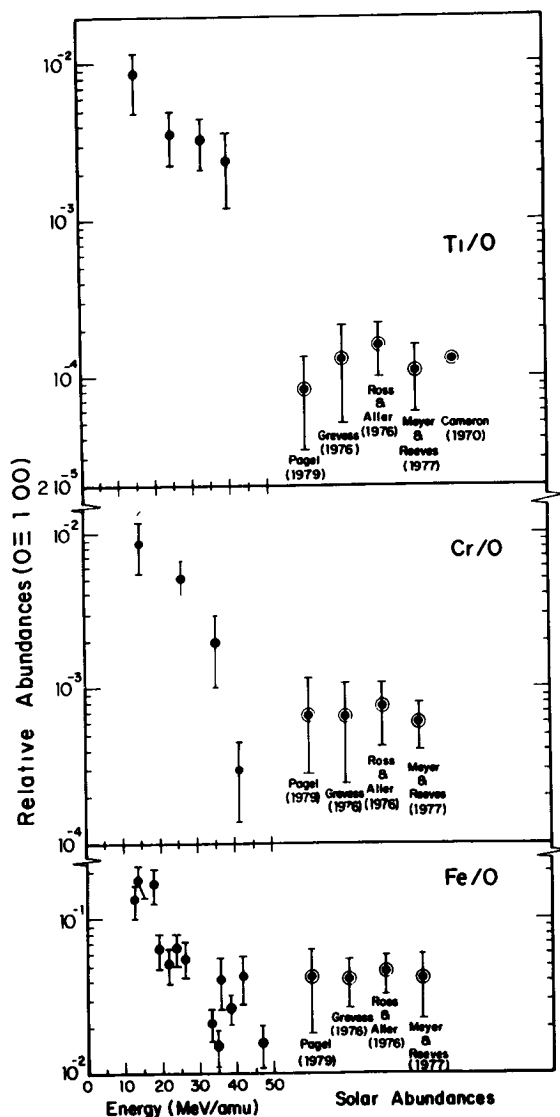


Fig.1b Variation of relative abundances as compared to oxygen of Ti, Cr and Fe nuclei with energy and comparison with photospheric value.

This is given in Table 1 for E between 10 and 20 MeV/amu.

Table 1 : Enhancement factors of Si-Fe elements in  
August 4, 1972 event

Element	Solar abundance Pagel (1979)	Energy Interval	Abundance rela- tive to oxygen	Enhance- ment factor
Si	(0.052 $\pm$ 0.013)	10-16	(0.12 $\pm$ 0.05)	2.31 $\pm$ 1.12
		16-20	(0.058 $\pm$ 0.024)	1.12 $\pm$ 0.54
S	(0.021 $\pm$ 0.012)	10-20	(0.020 $\pm$ 0.009)	0.95 $\pm$ 0.69
Ar	0.0031	10-20	(0.0097 $\pm$ 0.0055)	3.06 $\pm$ 1.25*
Ca	(0.0026 $\pm$ 0.0007)	10-20	(0.020 $\pm$ 0.009)	7.69 $\pm$ 4.03
		10-20	(0.131 $\pm$ 0.052)	3.12 $\pm$ 2.17
Fe	(0.042 $\pm$ 0.024)	20-25	(0.085 $\pm$ 0.035)	2.02 $\pm$ 1.42

**4. Conclusions.** In this study the differential spectra of Si, S, Ar, Ca, Ti, Cr and Fe were determined between 10-40 MeV/amu during Aug. 4, 1972 event. The Fe differential spectra were checked with those determined by other investigators using the same flight exposure. The agreement was found to be good. The oxygen spectra determined by Bertsch et al (1974) in the same flight were used to determine the relative abundances with respect to oxygen. At low energies (10-20 MeV/amu) the abundances were found to be enhanced over the photospheric value and at high energies ( $E > 25$  MeV/amu) the values agree with the solar photospheric values in general. In most cases this study has resulted in more accurate determination of the high energy SEP compositions which may be used interchangeably with the solar photospheric abundances as representative of the solar surface matter.

#### References

1. Bertsch, D.L. et al., 1974, Solar Phys., 39, 479.
2. Biswas, S. et al., 1983, Solar Phys., 89, 163.
3. Cameron, A.G.W., 1970, Space Sci. Rev., 15, 121.
4. Cook, W.R. et al., 1979, Proc. 16th ICRC, 10, 265.
5. Crawford, H.J., et al., 1975, Ap.J., 195, 213.
6. Durgaprasad, N., et al., 1982, Nucl. Inst. and Methods, 199, 573.
7. Grevesse, N., 1976, Trans. of IAU, vol. XVI B, 116.
8. Lambert, D.L., 1968, MNRAS, 138, 79.
9. Meyer, J.P. and Reeves, H., 1977, Proc. 15 ICRC, 2, 137.
10. Pagel, B.E.J., 1973, Space Sci. Rev., 15, 1.
11. Pagel, B.E.J., 1979, in Origin and Distribution of Elements, Ed. L.H. Ahrens, Pergamon Press, 79.
12. Ross, J.E. and Aller, L.H., 1976, Science, 191, 1223
13. Vahia, M.N., Thesis submitted to the Bombay University.



# VARIATIONS IN ELEMENTAL COMPOSITION OF SEVERAL MEV/NUCLEON IONS OBSERVED IN INTERPLANETARY SPACE

R.E. McGuire<sup>†</sup>, T.T. von Rosenvinge, and D.V. Reames  
NASA/Goddard Space Flight Center,  
Greenbelt, MD 20771 USA

## ABSTRACT

We have surveyed six years of accumulated ISEE-3 and IMP-8 data to study variations in elemental relative abundances among the different populations of energetic (1.5 to >10 MeV/nuc) ions seen in interplanetary space. We present evidence suggestive that heavy ion enrichments may be organized (with substantial scatter) by a rigidity scaling factor  $A/Z^*$  over the range H to Fe. We also show some data to support the hypothesis that shock-associated particles are probably accelerated from ambient energetic fluxes.

**1. Introduction.** The elemental composition of solar energetic particle (SEP) events has been the subject of a number of recent studies [1,2,3,4,5,6]. This paper is a report of results from a new, ongoing study of low energy (1-10 MeV/nucleon) elemental composition with combined data from the Goddard particle experiments on ISEE-3 and IMP-8.

**2. Abundance Distributions.** We have identified nearly 150 separate events, which occurred between 1978 and 1983, with >50 Oxygen counts in the ISEE-3 energy band 1.9 to 2.8 MeV/nucleon. Of these events, we can associate about one-half with solar flares. The other periods are either shock-associated or of unknown origin. Figure 1 contains histograms of the abundance ratios H/O, He/O, C/O, Si/O and Fe/O constructed from event averages of the flare events. The arrows indicate median values in the distributions. Data for He and heavier ions comes from the ISEE-3 experiment, data for H and again He comes from IMP-8. We note that the He/O, C/O and Si/O distributions are narrow compared to H/O or Fe/O and that there is a high abundance tail in the Si/O distribution. Histograms constructed using our identified shock events or from those increases that are of unknown origin tend to follow the same

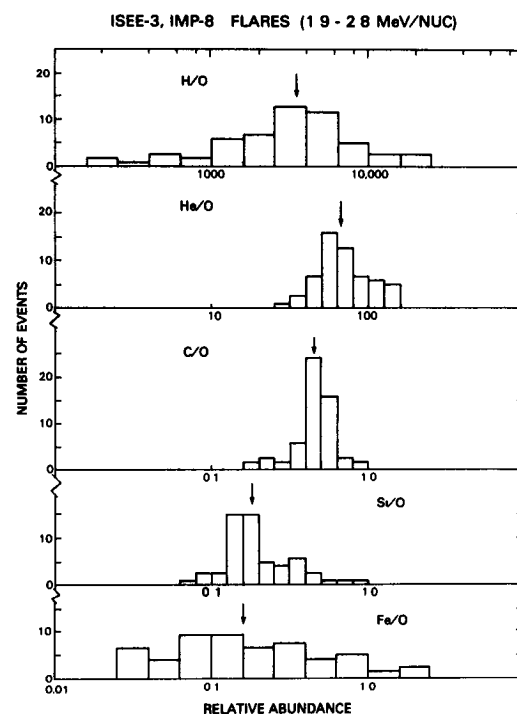


Fig. 1. Abundances in flare events.

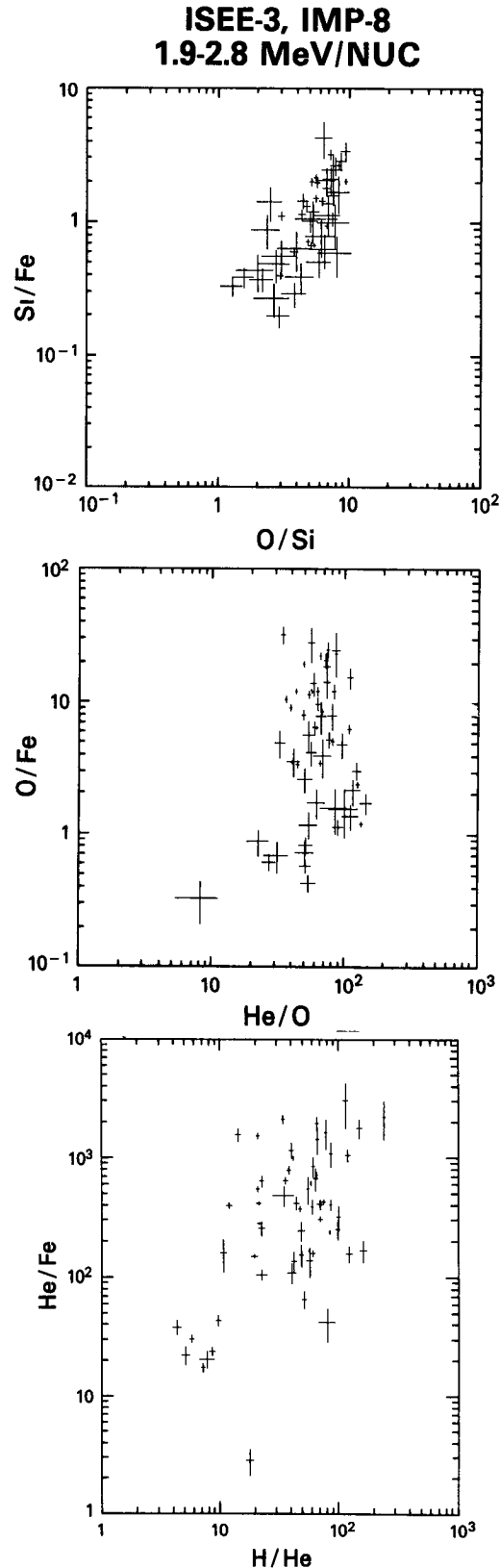
<sup>†</sup>Also Dept. of Physics and Astr., U. of MD, College Park, MD 20742 USA

general range and distribution of values as the flare events in Figure 1, except that there are fewer Fe-enriched events.

**3. Abundance Correlations.** An important question in the interpretation of heavy-ion enrichments is whether atomic number ( $Z$ ), atomic mass ( $A$ ) or the rigidity-scaling factor mass divided by effective charge ( $A/Z^*$ ) best organizes the enrichment factors for different elements. Note that  $A/Z^*$  for H:He:O:Si:Fe fall in the approximate ratios 1.0:2.0:2.2:2.6:4.0, using the charge state measurements of [7]. Thus the relative histogram widths in Figure 1 are consistent with  $A/Z^*$  as the organizing parameter, in that largest differences in  $A/Z^*$  give rise to the widest distributions.

To further explore this idea, we present a series of scatter plots of the flare data in Figures 2a-2c. Figure 2a shows O/Si versus Si/Fe. The trend as seen (larger O/Si imply larger Si/Fe, a positive slope) is the trend expected given that heavy ion enrichments increase monotonically with e.g. increasing  $A/Z^*$  [1,2,3,4,6]. Note the common factor of the Si abundance in the denominator of O/Si and the numerator of Si/Fe. If variations (from whatever cause) in O and Fe were not correlated with variations in Si, we might still find an apparent correlation in the ratios because of this common factor but with a negative slope. The amplitude of the random variations determines whether such an effect will be seen. Figure 2b shows He/O versus O/Fe. Given the narrow distribution of He/O in Figure 1, it is not surprising that we find,

Fig. 2. Scatter plots of flare abundance ratios: (a) O/Si vs Si/Fe, (b) He/O vs O/Fe, and (c) H/He vs He/Fe.



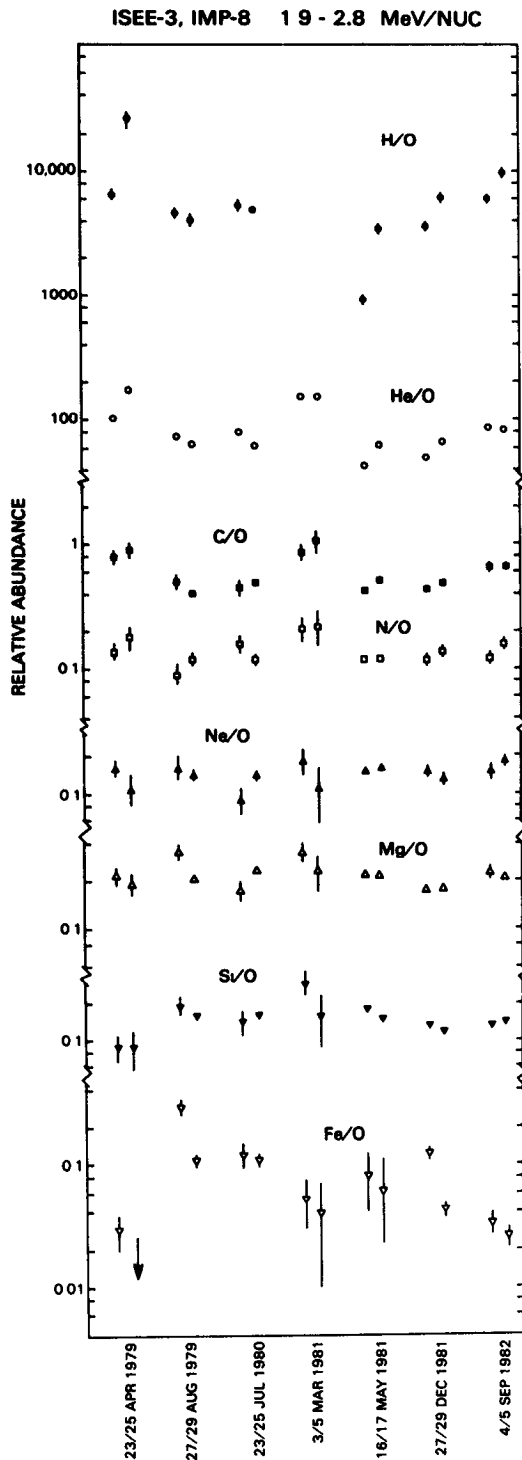


Fig. 3. Abundances for 7 pairs of events (ambient energetic flare particles and shock-associated particles).

at best, only a slight positive slope to the correlation. This plot is also consistent with  $A/Z^*$  organization since the scaling factors for He and O are similar. It is not easily understood in terms of organization by Z or A separately. Random variations would again give a negative slope, if any, to the plot.

A plot of higher energy (7.2-12.5 MeV/nucleon) He/O to O/Fe in fact shows such a negative slope. This higher energy data is consistent with the published ratios of McGuire et al. (1979,1985) but we emphasize that such a negative slope is ambiguous because of the common factor in the ratios. That the nature of these plots changes with energy may be only a consequence of the increased scatter in the relative fluxes at the higher energies.

Figure 2c shows H/He versus He/Fe. Here too there is a suggestion of positive slope (possibly larger in magnitude than that of He/O versus O/Fe) but the trend is obscured by the overall scatter in the data. If  $A/Z^*$  organizes the data overall, we would expect H/He to be positively correlated with He/Fe or O/Fe. We note that H and He spectral slopes are generally not equal [2,8,9]; the unequal spectral slopes may be largely responsible for the scatter. Other explanations for a general coincidence of low H/He ratios with higher Fe abundances (for instance, special plasma conditions required in the source region for an Fe enrichment to take place [10]) are also clearly possible.

4. A Source Population for Shock-associated Particles. A quite different question of concern to us is that of the source population in shock-associated energetic particle

flux increases. In particular, if these particles are locally accelerated, then we might expect the shock particles to mirror the abundances of ambient energetic particle fluxes. In Figure 3, we have plotted elemental abundances as pairs of events (event-averaged abundances preceeding the shock particles and abundances in the flux peak associated with the shock) for a select set of events. In these events, the ambient peak was separable from the shock peak (at the energy range of the composition data, again from 1.8-2.8 MeV/nucleon) and both averaged fluxes were sufficient to satisfy the >50 Oxygen count limit. Those events with unusual composition (e.g. high C/O ratios) were expected to be the most useful in testing the hypothesis. Unfortunately, few events satisfied the selection criteria and these had mostly average composition. In general, we do believe the abundance pairs as plotted are consistent with local acceleration of the shock-associated particles from the ambient energetic populations. The plot does not however provide strong positive evidence for the idea. We note that variation in H/O between the ambient and shock particles might be expected because the energy spectra are steepened generally at shocks and because the ambient H and He spectra do not have the same slope. Fe/O is complicated by the kind of temporal variations that occur in many events [6,11,12], specifically where Fe/O is higher at the event onset than near the shock arrival time.

5. Acknowledgments. This work was supported in part under NASA Grant NGR 21-002-316.

#### References.

1. McGuire, R.E. et al., 1979, Proc. 16th ICRC, 5, 61.
2. McGuire, R.E. et al., 1985, submitted to Ap. J..
3. Cook, W.R. et al., 1980, Ap. J. (Lett.), 238, L97.
4. Cook, W.R. et al., 1984, Ap. J., 279, 827.
5. Mason, G.M. et al., 1980, Ap. J., 239, 1070.
6. Reames, D.V. and T.T. von Rosenvinge, 1981, Proc. 17th ICRC, 3, 162.
7. Luhn, A. et al., 1984, Adv. Space Res., (Graz, COSPAR Proceedings).
8. McGuire, R.E. et al., 1981, Proc. 17th ICRC, 3, 65.
9. McGuire, R.E. et al., 1984, Adv. Space Res., 4, 117.
10. Fisk, L.A., 1978, Ap. J., 224, 1048.
11. O'Gallagher, J.J. et al., 1976, Ap. J. (Lett.), 209, L97.
12. Scholer, M. et al., 1978, J. Geophys. Res., 83, 3349.

ON THE RETENTION OF HIGH-ENERGY PROTONS AND  
NUCLEI WITH CHARGES  $Z \geq$  OR EQUAL TO 2 IN LARGE  
SOLAR FLARES AFTER THE PROCESS OF THEIR  
ACCELERATION

N.N. Volodichev, B.M. Kuzhevsky, O.Yu. Nechaev, I.A. Savenko

Institute of Nuclear Physics, Moscow State University;  
Moscow 119899, USSR

Abstract. The available experimental data obtained from ground-based neutron monitors and from satellites suggest that the protons with energies of up to several GeV should be retained on the Sun after the process of their acceleration. The protons are on the average retained for 15 min, irrespectively of the solar flare heliolatitude and of the accelerated particle energy ranging from 100 MeV to several GeV. One of the explanation for the phenomenon is that the particles are retained in a magnetic trap formed in a solar active region. However, there does not exist information on how the nuclei with charges  $Z \geq 2$ , whose fraction in the Sun's atmosphere is  $\sim 10\%$ , behave during the retention time. The Prognoz experiments failed to find any  $Z \geq 2$  nuclei of solar origin during large solar flares. The upper limit of the number of such nuclei does not exceed 1% of the number of  $\geq 500$  MeV solar protons and may be accounted for by the features of the experimental methods. The absence of the  $\geq 500$  MeV/nucleon nuclei with  $Z \geq 2$  may be due to their retention in the magnetic trap which also retains the high-energy protons. During the trapping time (15 min on the average) the  $\geq 500$  MeV/nucleon nuclei with  $Z \geq 2$  may escape due to nuclear interactions and ionization loss. In this case the H concentration should be  $\sim 10^{12} \text{ cm}^{-3}$ , which is observed in the lower chromosphere.

1. Introduction. The period between the moments of generation of particles in a flare and their emergence in interplanetary space is understood here to be the time of particle retention by the flare. The particle generation moment is meant to be onset time of the radio, X-ray, and gamma-ray emissions. If a particular event is rapid, the time of electromagnetic radiation maximum is taken to be the particle generation moment.

The time of accelerated-particle runaway to the interplanetary space was determined in [1, 2] using the information concerning the time of the first arrival of the  $\geq 100$  MeV and  $\geq 500$  MeV protons at the Earth. Considering that the diffusive mode of particle propagation does not get stationary as yet and making the natural assumptions that the  $\geq 100$  MeV and  $\geq 500$  MeV particles are injected to the interplanetary space simultaneously and traverse the same path by the moment of their detection, we may find the moment of particle runaway to interplanetary space using the known time of the initial detection of the  $\geq 500$  MeV and  $\geq 100$  MeV protons.

2. Results and discussion. The table below presents the

various data for the events detected on board Prognoz satellites. The main conclusion following from the data is that the moment of particle injection to the interplanetary space is delayed relative to the particle generation moment, irrespectively of whether the microwave radio, X-ray, or gamma-ray emission maximum times are taken to be the particle generation moment. The delays vary from several minutes to several tens of minutes for different events.

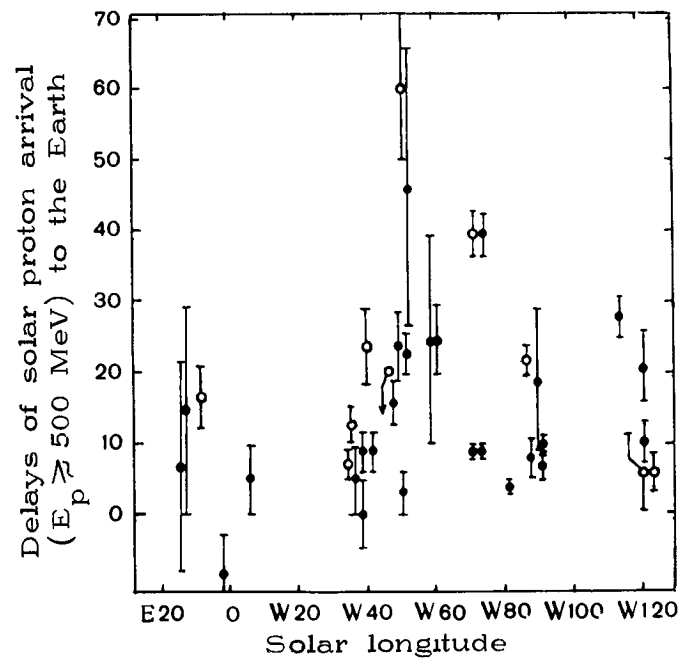
Fig. 1 shows the results of analyzing the dependence of the delay on the flare heliolatitude. The dark circles show the measurement results of [3], the light circles are the Prognoz measurements. It may be concluded that in case of the Sun's western hemisphere the delay is independent of flare longitude. The delays for most of the events range from 10 to 20 min. The comparison between the delays inferred from the satellite and neutron monitors data shows that the delay is also independent of particle energy in the 100 MeV - 2 GeV range.

Table

The delays of the  $\geq 100$  MeV and  $\geq 500$  MeV solar protons injections to interplanetary space relative to the maxima of the microwave radio, X-ray, and gamma-ray emissions

N	$E_p \geq 100$ MeV, $\geq 500$ MeV							$E_p \sim 2$ GeV
	Ref.	Date	Region McMath	Helio- coordi- nates	Flare class	Satellite	Delay, min	Delay, min [3]
1	/1/	July 7, 1966	8362	Post-limb flare	2B	Proton-3	$\leq 20$	$24 \pm 5$
2	/1/	July 22, 1972	11976 ?		-	Prognoz-2	$0 \div 12$	-
3	/1/	Aug. 4, 1972	11976		3B	Prognoz-2	$17 \pm 4$	-
4	/1/	Aug. 7, 1972	11976		3B	Prognoz-2	$\approx 6$	$9 \pm 3$
5	/1/	April 29, 1973	12322		2B	Prognoz-3	$\approx 40$	$40 \pm 3$
6	/1/	Sept. 24, 1977	14942 or ? 14943	Post-limb flare	-	Prognoz-6	$4 \div 8$	$10 \pm 3$
7	/1/	Nov. 22, 1977	15031		2B	Prognoz-6	$24 \pm 5$	$9 \pm 3$
8	/2/	April 1, 1981	17539		2B-3B	Prognoz-8	$60 \pm 10$	-
9	/2/	April 4, 1981	17539		3B	Prognoz-8	$22 \pm 2$	-
10		April 10, 1981	17568		2B-3B	Prognoz-8	$13 \pm 3$	-

3. Discussion. Two reasons for the particle delays may be indicated. The first is the particle retention in closed magnetic fields of solar active regions [4]. The second reason is that the



• - /3/ , ◦ - the present work

Fig.1. The high-energy solar proton delays versus flare heliolongitude

delay may correspond to the time interval between the accelerations from low to high-energies. The gamma-ray line emission and the X-rays from the flares are generated by particles with energies of several MeV [5], whereas the particle delays were determined for the  $\geq 100$  MeV and  $\geq 500$  MeV protons. In case of neutron monitors, the mean effective energy is some 1 GeV. The entire solar cosmic ray spectrum was found in a flare region, whereas the time intervals between the moments of the emergence of low-energy protons and the associate gamma-ray line emission and high-energy protons are determined by the rate of energy gain. The  $\geq 30$  MeV gamma-ray data and the flare-generated neutron detection [6] indicate that the period within which the particles are accelerated up to hundreds and thousands of MeV may not exceed a minute.

It is not excluded, however, that the particles are accelerated in the solar corona or even in the interplanetary medium by the moving shocks. In such cases the time interval between the electromagnetic radiation generation and the high-energy particle generation may reach tens of minutes.

It should be noted that the solar nuclei  $Z \geq 2$  and energies  $\geq 500$  MeV/nucleon were not in practice detected in large solar flares. The upper limit for the number of such nuclei relative to the  $\geq 500$  MeV protons was found to be a fraction of one percent in the Prognoz data, and this level may well be accounted for by the methodical features of the experimental design.

It may be assumed that the solar nuclei with  $Z \geq 2$  (mainly the He nuclei), just as the solar protons, are retained in a magnetic trap and, within the retention time ( $\sim 15$  min) are lost for nuclear collisions and ionization. From the gamma-ray data it follows that the density of matter in the gamma-ray production region is  $n \sim 10^{12} \text{ cm}^{-3}$ . Then the total thickness of matter traversed by He nuclei within 15 min is  $X \sim 20 \text{ g cm}^{-2}$ , i.e. exceeds the nuclear and ionization paths of He nuclei in hydrogen. But the protons with energies of up to  $\sim 200 \text{ MeV}$  must also be lost within the same period, the fact that must affect the solar proton energy spectrum in this energy range.

If the acceleration is assumed to take place up to the same rigidities, the flux of nuclei with  $Z \geq 2$  and  $E \geq 500 \text{ MeV/nucleon}$  should be compared with the  $\geq 1.4 \text{ GeV}$  proton flux of the same rigidity.

4. Conclusion. It should be noted in conclusion that the delay of high-energy proton runaway from the Sun and the absence of high-energy nuclei with  $Z \geq 2$  found by the Prognoz measurements during large solar flares may be combined within a unified model relevant to particle retention in a magnetic trap located in an active region on the Sun. In this case, however, the solar proton energy spectrum should exhibit a feature at  $\sim 200 \text{ MeV}$ . At the same time, if the charged particles are accelerated in large flares up to a certain rigidity, one must compare between the fluxes of protons and heavier nuclei of the same rigidity. If in this case the solar particle flux ratio replicates the solar atmospheric composition, the delay of the particle runaway from the Sun may be explained by, for example, a durable acceleration mechanism.

#### References

1. Volodichev N.N., Savenko I.A. Proc. 17-th ICRC, Paris, 1981, v. 3, p. 45.
2. Volodichev N.N. Kosmich. Issl., 1983, v. 21, p. 731.
3. Cliver E.W., et al. Astroph. J., 1982, v. 260, p. 362.
4. Mullan D.J. Astrophys. J., 1983, v. 269, p. 765.
5. Kuzhevsky B.M. Uspekhi Fiz. Nauk, 1982, v. 137, No 2, p. 235.
6. Chupp E.L. Conference proceedings U.S. - Japan Seminar on "Recent Advances in the Understanding of Solar Flares", 1982, Tokyo, Japan.



DIFFUSION IN THE CHROMOSPHERE , AND THE COMPOSITION OF THE SOLAR CORONA  
AND ENERGETIC PARTICLES

Sylvie VAUCLAIR

Observatoire du Pic-du-Midi et de Toulouse, France

Jean-Paul MEYER

Service d'Astrophysique, Centre d'Etudes Nucléaires de Saclay, France

1. Introduction. Composition observations, (i) in the Solar Photosphere, and (ii) in the upper Transition Region (TR) and Corona (as well as in Solar Wind, SW, and Solar Energetic Particles, SEP) imply a change of composition of the solar atmosphere somewhere between the Photosphere and the upper TR ( $T > 70000$  K) /7,8,25,26,46/. Heavy elements with First Ionization Potential (FIP)  $> 9$  eV (hereafter "high-FIP elements") are  $\sim 4$  times less abundant in the TR and Corona than in the Photosphere, as compared to both Hydrogen and heavy elements with lower FIP ("low-FIP elements").

These observations suggest a separation between neutral and ionized elements in a region where the high-FIP elements are mostly neutral, and the low-FIP elements ionized /25,26/. This occurs in the Chromosphere at altitudes above 600 km and below 2000 km above Photosphere (in the average quiet chromospheric model VAL C of /43/, used throughout this paper; fig. in /13/). Here we shall investigate whether diffusion processes can explain the observed change in composition.

2. The diffusion equation - Possible processes. When a gas mixture is subject to pressure, temperature or concentration gradients, or to selective forces, the gas components diffuse with respect to one another. This process, believed to be the reason for chemically peculiar A and B stars /e.g. 28, 29,27,45/, has already been invoked to explain the He depletion in the Solar Wind /19,27,12,13/. Thermal diffusion in the TR has also been studied by /9,30,42,36,33,34,35,12,13/. The diffusion velocity for a gas with negligible abundance in a gas mixture may be written /6,10/

$$v_D = D (\nabla \ln c - k_p \nabla \ln p - k_T \nabla \ln T + F/kT)$$

where  $D$  is the diffusion coefficient,  $k_p$  the pressure diffusion factor (the  $\nabla \ln p$  term is equivalent to the gravitational settling),  $k_T$  the thermal diffusion factor,  $F$  any selective forces (e.g. the radiative force), and  $c$  the concentration of the element.

In solar-type stars, the radiative acceleration is never large enough to compete with gravitational settling /28/: the last term is negligible. In the chromospheric plateau, the temperature gradient is small, and the thermal term is also negligible. In the TR this term is large. However, all elements become 100 % ionized as  $T$  increases and the neutral-ionized element separation therefore cannot work there. As the concentration gradient is also generally small the diffusion velocity reduces to

$$v_D = D k_p \nabla \ln p \quad (\text{gravitational settling term})$$

In case of partial ionization of an element, the atoms spend part of their time in the various ionization states, and the resulting velocity may be written, in first approximation /29,1/, as  $v_D = \eta_k v_{Dk}$ , where  $\eta_k$  is the fraction of atoms in the ionization state  $k$ , and  $v_{Dk}$  the corresponding diffusion velocity.

If the elements have to diffuse across a magnetic field, the transverse diffusion velocities of the ions are reduced by a factor of  $(1 + \omega^2 t_{col}^2)^{-1}$ , where  $\omega$  is the Larmor pulsation and  $t_{col}$  the characteristic time between two collisions /44,1/. If this factor is large, the transverse diffusion of ions is stopped, while the diffusion velocity of neutrals is unchanged. Thus the

diffusion velocity of any element reduces to  $v_D = \eta_n v_{Dn}$ , where the index  $n$  refers to the neutral fraction.

Now, a large fraction of the solar surface is always covered with horizontal magnetic fields anchored in the network, from altitudes of  $\sim 700$  km /3,11,47,14,20,15/ up to above the H $\alpha$  emitting region ( $>1500$  km) /22,23/. Their typical intensity is  $\sim 5$  to 25 G. At a typical chromospheric temperature of  $\sim 6000$  K, the factor  $\omega^2 t_{col}^2 \approx (4.6 \cdot 10^{13}/n_H)^2$  for ions becomes  $>1$  for altitudes above  $\sim 950$  km, reaching values of  $\sim 10$  and  $\sim 100$  at  $\sim 1100$  and  $\sim 1300$  km. Above these altitudes, ions are effectively prevented from settling gravitationally, while neutrals are not.

3. The diffusion coefficient for neutral heavies. The diffusion coefficient  $D$  for neutral heavy nuclei of mass  $A$  on the dominant neutral H gas of the chromosphere can be expressed as /6,10/

$$D = 3\sqrt{2}\pi /16 \cdot 1/(n_H \cdot \sigma_{eff}) \cdot \sqrt{kT/m^*}$$

$$D = 4.287 \cdot 10^{18} \cdot 1/(n_H \cdot \sigma_{15}) \cdot \sqrt{T \cdot \sqrt{1+1/A}} \quad (\text{cm}^2 \text{ s}^{-1})$$

where  $n_H$  is the neutral H number density,  $T$  the temperature,  $m^* = m_H A/(A+1) \approx m_H$  the effective mass of the interaction,  $\sigma_{eff}$  an "effective" collision cross section to be discussed below, and  $\sigma_{15} = \sigma_{eff}$  in units of  $10^{-15} \text{ cm}^2$ . (The diffusion coefficient in ionized H is not very different; a small admixture of  $H^+$  therefore does not affect the picture). The effective cross-section  $\sigma_{eff}$  can conveniently be expressed as  $\sigma_{eff} = \pi r^{*2} \Omega^{(1,1)*}$ , where  $r^*$  is some typical range of the interaction potential, and  $\Omega^{(1,1)*}$  is the reduced collision integral describing the collision kinematics in the actual potential /6,10,32,41,31/.

The noble gas-H interaction potentials are characterized by a steep repulsive part and a tiny Van der Waals attractive well, whose depth  $\epsilon \sim 10^{-3}$  eV is extremely small as compared to the mean thermal energy  $kT = 0.52$  eV of the atoms in the  $\sim 6000$  K chromospheric gas (fig.1). So, only the repulsive part is important. The key information on these potentials comes from /5/, whose results have been by and large confirmed by more recent work /4,39,40,17,38/. The repulsive part of the potential is most realistically fitted by a modified Buckingham-type potential /21,5,6,10/, and we have adopted the potential parameters of /5/. On this basis the collision integrals  $\Omega^{(1,1)*}$  have been interpolated from the tables of /21/ (reproduced in /6,10/), yielding the effective cross-sections  $\sigma_{eff}$  given in Table 1 (or the effective collision radii  $r_{eff}$  such that  $\sigma_{eff} = \pi r_{eff}^2$  shown in fig.1).

In reactive element-H potentials, the tiny Van der Waals minimum is completely swamped out by a  $\sim 4$  eV attractive well associated with the covalent bond (fig.1). The characteristics of these potentials have been derived from the data tabulated in /18/, using the formalism of /16/. They can be reasonably well fitted with Morse-type potentials /16,10/. The collision integrals  $\Omega^{(1,1)*}$  have been interpolated from the tables of /37/ (reproduced in /10/), yielding the values of  $r_{eff}$  and  $\sigma_{eff}$  given in fig.1 and Table 1, the latter being  $\sim 2.4$  times as large as the  $\sigma_{eff}$ 's for noble gases.

Table 1	Interaction	He-H	Ne-H	Ar-H	C-H	N-H	O-H	S-H
	$\sigma_{eff} (10^{-15} \text{ cm}^2)$	0.89	1.05	1.45	2.84	2.17	2.35	3.27

4. The neutral element diffusion velocity and time scale. The diffusion velocity due to the gravitational force for neutral elements is /6,10/

$$v_D = D \cdot (A-1) \cdot \nabla(\ln p) \cdot \eta_n$$

$$v_D = 3.70 \cdot 10^{18} \cdot \sqrt{T} \cdot (A-1) \sqrt{1+1/A} / \sigma_{15} \cdot 1/n_H \cdot \nabla(\ln p) \cdot \eta_n \quad (\text{km/day})$$

where we have inserted  $D$  and  $n_H$  is in  $\text{cm}^{-3}$  and  $\nabla(\ln p)$  in  $\text{cm}^{-1}$ . This velocity has been evaluated in the framework of model VAL C /43/.  $\eta_n$  is close to 1 for most high-FIP elements up to  $x \approx 1900$  km (see fig. in /13/), except for C (and probably S) for which ionization reduces the diffusion velocity by factors up to  $\sim 2.5$  within the chromospheric plateau. Fig.2 shows the calculated  $v_D$ 's vs.

altitude  $x$ , for the two extreme elements Ar and C. All other high-FIP elements have intermediate diffusion velocities.

From these velocities, we derive for each element A diffusion time scales  $t_{D,A}(x) = N_H / (S_\odot v_{D,A}(x) \cdot n_H(x)) / 2$ . This time is the time needed for a mass of  $N_H$  H-atoms above an altitude  $x$ , assumed completely mixed, to be depleted in atoms A by a factor of  $1/e$  by downward diffusion at its base  $x$  ( $S_\odot$  = solar surface area). These diffusion times  $t_D$  are plotted vs. altitude  $x$  in fig.3, for Ar and C.

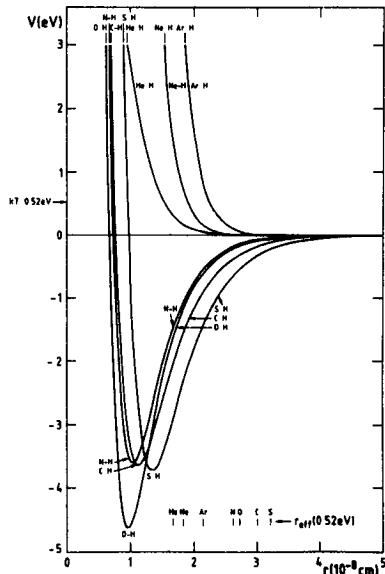


Fig.1

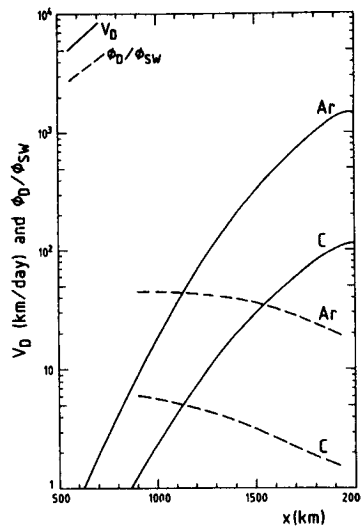


Fig.2

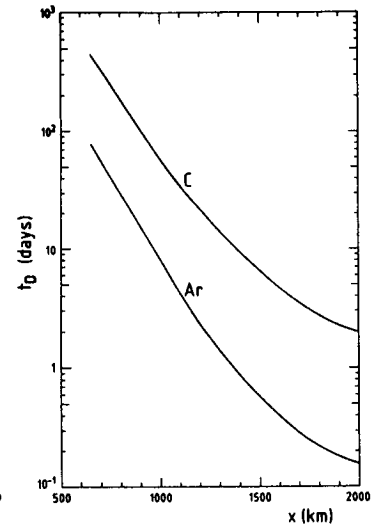
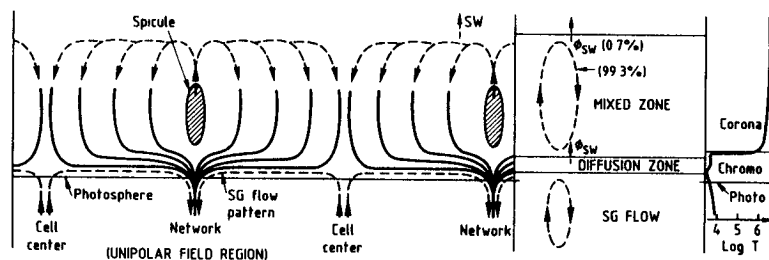


Fig.3

**5. Discussion - A tentative scheme.** The surface of the quiet Sun at altitudes of ~700 to 2000 km is believed to be largely covered, above the Supergranulation (SG) cells, by horizontal magnetic fields of intensity ~5 to 25 G, whose energy density exceeds that of the gas above ~1000 km (fig.4) /3,11,47,14,20,15,22,23/. Above ~1000 km, the gas may therefore be stabilized by the field, and we may have in the chromospheric plateau a "diffusion region" with an horizontal field, which remains stable, isolated from lower lying material, over some unknown time scale  $\tau$ . Gravitational settlement of heavy neutrals takes place there, but the horizontal field acts as a filter against ions. Starting in the upper Chromosphere above the network (SG boundaries), spicules are probably the major upward carrier of material from Chromosphere into Corona. Almost all the material they lift later falls back, either in the spicule itself, or as a rain along the more vertical configuration of the field at higher altitudes (fig.4). Only 0.7 % of it leaves the system in the form of SW /above ref./. Above the quiet "diffusion region" at altitude  $x$ , we therefore have an apparently fully "mixed region" comprizing the entire TR and Corona (fig.4). The material leaving the "mixed zone" as SW (flux  $\phi_{SW,H}$ ) is treated as constantly replenished by fresh matter from the underlying "diffusion region" at an average effective velocity  $U(x) = \phi_{SW,H} / n_H(x)$ , in a steady state fashion lasting over the stability time  $\tau$  of the "diffusion region".

By and large, the abundance of an element A in the "diffusion zone" (and hence in the "mixed zone") can be kept low if its downward diffusion velocity  $v_{D,A}(x)$  relative to the bulk H gas is larger than the effective upward velocity  $U(x)$  of this bulk gas :  $v_{D,A}(x) / U(x) = n_H(x) \cdot v_{D,A}(x) / \phi_{SW,H} = \phi_{D,A}(x) / \phi_{SW,A} \gtrsim 1$  (since  $n_A/n_H = \text{cst}$  throughout the "mixed zone"). Fig. 2 shows that this ratio is indeed  $>1$  (~30 for Ar, and ~3 for C, our worst case), and does not depend much on the altitude  $x$  of the interface between the quiet and the mixed-up zones. This strong constraint is thus satisfied.

Fig. 4



Other constraints lead to limits to the altitude  $x$  of the "diffusion region". An upper limit  $x \lesssim 2000$  km is imposed by the fact that the high-FIP elements must still be mostly neutral /43,13/. A lower limit  $x \gtrsim 1000$  km comes from the requirement that ions be prevented to diffuse by the horizontal magnetic fields ( $\omega^2 t_{\text{col}}^2 \gg 1$ ). In addition the stability time of the required structure (i.e. the time during which the diffusion region is effectively isolated from the denser lower lying material, so that the zones above and below it remain unmixed) must be longer than the diffusion time  $t_D$  (fig.3). The higher the altitude, the more easily this constraint can be fulfilled. For our worst case, C, the required stability time decreases from  $\sim 60$  days at 1000 km to 7 days at 1500 km and a minimum of  $\sim 2$  days at 2000 km. These times are longer than the stability time of the low lying SG and network, which is of the order of 1 day /3/.

**6. Conclusion.** The heavy element composition anomalies in the TR, Corona, SW and SEP can be explained in terms of gravitational settling of the heavy neutrals in the Chromosphere, provided that a large fraction of the solar surface is covered by quiet, presumably field stabilized, regions at high altitude in the chromospheric plateau ( $\sim 1500$  to 2000 km). These regions must effectively shield the coronal reservoir from the denser, lower chromospheric gas. They must be stable over at least a few days, and must therefore not be strongly perturbed by the daily changes of the SG pattern at lower altitude. Unless a different scheme is found to explain it, the odd coronal composition therefore permits to set stringent limits to the degree of chaos of the Chromosphere, to the turbulent exchange of matter between the lower and the upper chromospheric layers.

**Acknowledgements.** We wish to thank Pierre Mein, Georges Michaud and Bernard Sayer for important discussions.

#### References

1. Alecian, G. et al 1983, *Fund Cosmic Phys* **8**, 369
2. Aller, L.H. et al 1960, *Ap J* **132**, 461
3. Athay, R.G. 1976, *The Solar Chromosphere and Corona Quiet Sun* (Reidel)
4. Bassi, D. et al 1976, *Phys Rev A* **13**, 584
5. Bickes, R.W. et al 1973, *Faraday Disc Chem. Soc.* **55**, 167
6. Chapman, S. et al 1970, *The Mathematical Theory of Non-Uniform Gases* (Cambridge U. Press)
7. Cook, W.R. et al 1980, *Ap J Letters* **238**, L97
8. Cook, W.R. et al 1984, *Ap J* **279**, 827
9. Delache, P. 1967, *Ann d'Ap* **30**, 827
10. Ferziger, J.H. et al 1972, *Mathematical Theory of Transport Processes in Gases* (North Holland)
11. Gabriel, A.H. 1976, *Phil Trans. R Soc Lond A* **351**, 339
12. Geiss, J. 1982, *Space Sci Rev.* **33**, 201
13. Geiss, J. et al 1984, in *Isotopic Ratios in the Solar System*, Paris, (CNES), in press
14. Giovanelli, R.G. 1980, *Solar Phys* **68**, 49
15. Giovanelli, R.G. et al 1982, *Solar Phys* **79**, 267
16. Herzberg, G. 1950, *Spectra of Diatomic Molecules* (Van Nostrand)
17. Hishinuma, N. 1981, *J Chem Phys* **75**, 4960
18. Huber, K.P. et al 1979, *Constants of Diatomic Molecules* (Van Nostrand)
19. Jokipii, J.R. 1966, in *The Solar Wind*, ed. R.J. Macklin et al (Pergamon), p 215
20. Jones, H.P. et al 1983, *Solar Phys* **87**, 37
21. Mason, E.A. 1954, *J Chem. Phys.* **22**, 169
22. Mein, P. et al 1982, *Astr Ap* **111**, 136
23. Mein, P. et al 1984, Preprint
24. Meyer, A. et al 1979, *Astr. Ap.* **78**, 33
25. Meyer, J.P. 1981, 17th ICRC, Paris, **3**, 149
26. Meyer, J.P. 1985, *Ap J Suppl.* **57**, 173
27. Michaud, G. 1980, *Astron J* **85**, 589
28. Michaud, G. et al, 1976, *Ap J* **210**, 447
29. Montmerle, T. et al 1976, *Ap J Suppl* **31**, 489
30. Nakada, M.P. 1969, *Solar Phys.* **7**, 302
31. Pauly, H. 1979, in *Atom-Molecule Collision Theory*, R.B. Bernstein ed. (Plenum Press)
32. Pauly, H. et al, 1965, in *Advances in Atomic and Molecular Physics*, vol 1, D.R. Bates ed (Academic)
33. Roussel-Dupré, R. 1980, *Ap J* **241**, 402
34. Roussel-Dupré, R. 1981, *Ap J* **243**, 329
35. Roussel-Dupré, R. 1981, *Ap J* **252**, 393
36. Shine, R. et al 1975, *Ap J Letters* **202**, L101
37. Smith, F.J. et al 1964, *J Chem Phys* **41**, 3560
38. Theodorakopoulos, G. et al 1984, *J Phys. B* **17**, 1453
39. Toennies, J.P. et al 1976, *Chem. Phys. Letters* **44**, 5
40. Toennies, J.P. et al 1979, *J Chem Phys* **71**, 614
41. Torrens, I.M. 1972, *Interatomic Potentials* (Academic)
42. Tworowski, A.S. 1975, *Ap Letters* **17**, 27
43. Vernazza, J.E. et al 1981, *Ap J Suppl* **45**, 635
44. Vauclair, S. et al 1979, *Ap J* **227**, 526
45. Vauclair, S. et al 1982, *Ann Rev Astr Ap* **20**, 37
46. Webber, W.R. 1982, *Ap J* **255**, 329
47. Withbroe, G.L. et al 1977, *Ann Rev. Astr. Ap.* **15**, 363

# ANOMALOUS ABUNDANCES OF SOLAR ENERGETIC PARTICLES AND CORONAL GAS: COULOMB EFFECTS AND FIRST IONIZATION POTENTIAL (FIP) ORDERING

D. J. Mullan  
Bartol Research Foundation  
University of Delaware  
Newark, DE 19716  
USA

## ABSTRACT

We argue that FIP ordering of elemental abundances in solar energetic particles and in the corona can both be explained Coulomb effects.

1. Introduction. Solar energetic particles (SEP) and coronal gas have anomalous abundances relative to the photosphere (1). The anomalies are similar in both cases: this led Meyer (1) to conclude that SEP acceleration is not selective, but merely preserves the source abundances (in the corona). Here, we argue that SEP acceleration can be selective, because identical selectivity operates to determine the coronal abundances.

The abundance anomalies are ordered by first ionization potential (FIP). Meyer (1) claims that this requires source temperatures of  $T=8000$  K. However, we find that FIP ordering occurs even if  $T > 10^6$  K.

2. Coulomb effects in SEP. SEP pre-acceleration in magnetic reconnection (e.g. in a solar flare) favors ions with low Coulomb losses (2) (hereafter ML). Pre-acceleration selects ions with charge  $Z < R A^{0.5}$ . (A is atomic weight, R is a critical number.) ML argued that in a hydrogen dominated corona, where coronal heating itself depends on reconnection, R should lie close to the proton value,  $R=1.0$ . Then the pre-acceleration time scale  $t_b$  would be marginally shorter than the proton Coulomb loss time  $t_p$ . With  $R=1$ , pre-acceleration of (e.g.) iron ions will favor ions with  $Z \leq 7$ . This selection of certain (low) charge states gives rise to abundance anomalies in SEP (see (2)).

ML discussed two cases of reconnection in a coronal magnetic loop. Case A had  $t_b < t_p$  only at the top of the loop; case B had  $t_b < t_p$  at all points in the loop. Abundance anomalies in Case A were found to be quite large in some cases: to agree with observations, the anomalies would require dilution with non-processed material. Meyer (1) criticizes Case A because different flares would apparently require rather similar dilution factors. However, Case B yields anomalies which are much closer to the observed values. Dilution is irrelevant in Case B. In this paper, we refer only to Case B.

ML predicted that Na/Si, Mg/Si, Ca/Fe, and Ni/Fe should be less in flares than in the photosphere by factors of 2-3. Meyer (1) claims that SEP data do not support these predictions. However, the observed ratios have a large scatter in different flares (see Fig. 3 in (1)). The scatter is such that the lower limit on the above ratios can be smaller than photospheric by factors of 2-3 (as Case B predicts) except for Na/Si. Thus, the Na/Si ratios might present a problem for Case B: perhaps the ionization equilibrium of Na are incorrect. Apart from Na, however, the data can be reconciled with Case B predictions, contrary to the claim in (1) that the ML

scenario disagrees with the data. (Meyer (1) did not discuss Case B of ML).

As an indication of how the ML scenario succeeds, both qualitatively and quantitatively, in reproducing the observed elemental anomalies in energetic particles, we show Case B predictions and data in Fig. 1, as a function of FIP. (Both cases are normalized to Si). Experimental points in Fig. 1 are taken mainly from (1), but in the case of elements which have not yet been detected in solar cosmic rays, we took data from (3) for the galactic cosmic rays. (Elemental anomalies are quite similar in solar and galactic cosmic rays (1).) As regards the ML predictions plotted in Fig. 1, we note that no specific values were predicted in Case B for H and He. The nature of the ML scenario (marginal heating of H) is such that the amount of hydrogen selected for pre-acceleration depends in detail on the extent to which the margin is exceeded. This is not known: however, a firm prediction is that, since H and He in the corona have identical values of  $Z^2/A$ , the abundances of both H and He (whatever they are) should be identical. To show this in Fig. 1, we join the H and He predictions by a horizontal dashed line. The vertical placing of this line cannot be determined at the present level of detail: we have chosen to plot it so as to overlap with the error bars of the data for H and He.

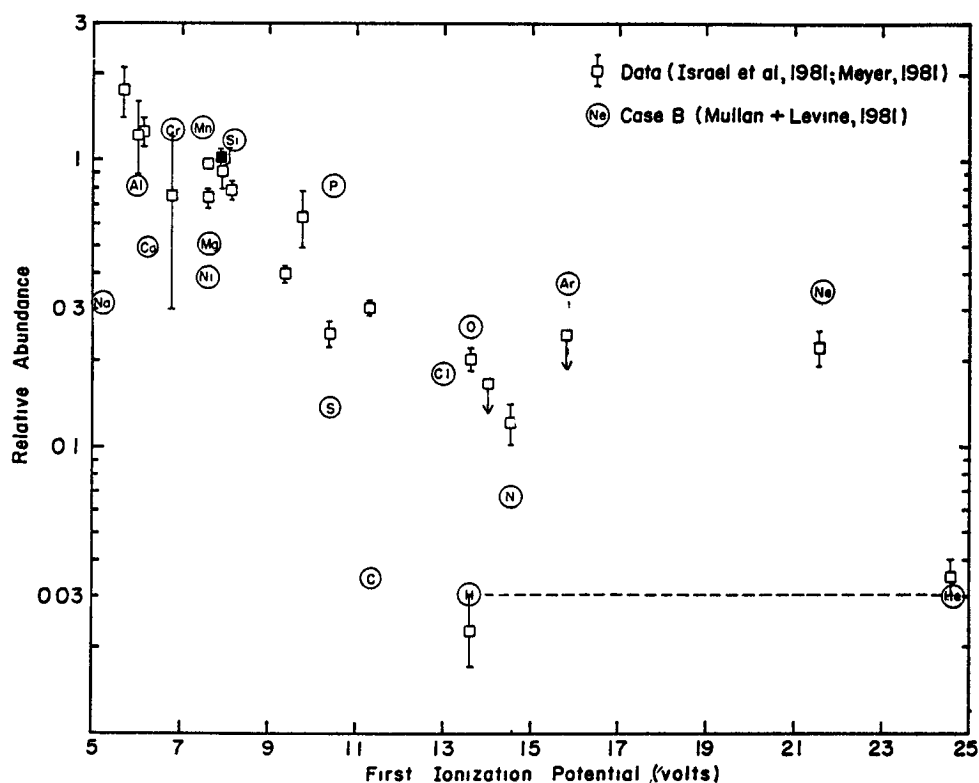


Fig. 1. Relative abundances of elements as a function of FIP.

The agreement between Case B predictions and data in Fig. 1 is quite good. Thus, both show maximum values of the abundance anomalies (around values of 1) at low FIP (except for Na), and both show a pronounced "step"

down to lower values at about 10 volts. The lower abundances at large FIP are down for both by factors of 3-10 relative to those at low FIP. The "step" is well-defined in the Case B predictions: for the elements P, S, and C, the FIP values differ by < 10%, but their abundances differ by factors of ~ 1000%. The H and He data can be reconciled with the prediction of equal abundances: H need not be regarded as an exception in the Case B scenario. Note that the only free parameter in Case B is the loop thermal structure.

Since the ML predictions in Fig. 1 were obtained for coronal loops with  $T > 10^6 K$ , an important conclusion from Fig. 1 is that FIP ordering of elemental abundances does not require a chromospheric phenomenon: it may occur even in the corona.

We stress that the predicted anomalies in Fig. 1 arise from a selection of ions with  $Z^2/A$  less than a critical ratio, viz.  $R=1.0$ . Abundance anomalies similar to those shown in Fig. 1 are expected to occur in any loop where ions with  $Z < A^{0.5}$  are preferentially selected. This will be important to keep in mind when we consider the accumulation of minor ions in the solar corona due to solar wind outflow.

3. Solar Wind: Minor Ions. The solar wind consists mainly of protons, but minor ions are dragged along by Coulomb effects if the proton flux is sufficiently large. In order that ions of atomic weight  $A$  and charge  $Z$  be dragged out of the sun, the proton flux must exceed the minimum value

$$F_{\min} = 3.4 \times 10^8 (T/10^6)^{3/2} G(A, Z) \text{ cm}^{-2}\text{s}^{-1} \text{ (cgs)}. \quad [1]$$

Coronal temperature  $T$  will be taken to be  $10^6 K$  here.  $G$  is a function of  $A$ ,  $Z$ , and  $T$  (see (4)): in the limit of heavy ions,  $G \approx A/Z^2$ .

The actual solar wind flux is not infinitely large: therefore, some ions will not be dragged out by the protons, but will instead be left behind to accumulate in the corona. Which ions are left behind? To answer this, we refer to the actual value of the solar wind flux. During the years 1962-1975, in low speed solar wind, the flux was  $3.9 \times 10^8$  cgs on average; in high speed wind, it was  $2.7 \times 10^8$  cgs on average; in a long term average, it was  $3.8 \times 10^8$  cgs (5). As mentioned in (5), these fluxes are uncertain by factors of order 30%, and there is a rather large spread in the fluxes: the standard deviation in the long term average is  $2.4 \times 10^8$  cgs (5). In a sample of solar wind recorded near solar maximum (August 1978 to February 1980) by ISEE-3, we have examined a series of 2117 "snapshots" of the solar wind, each lasting 3 seconds, with one "snapshot" every 5-6 hours throughout a 550-day interval. The mean flux we found was  $3.2 \times 10^8$  cgs. This lies within the 30% uncertainty of the long term average in (5). It appears safe to adopt a mean solar wind flux of  $(3-4) \times 10^8$  cgs.

The interesting aspect of these fluxes for our purposes can be seen from eq. [1]. The mean flux apparently suffices to drag out only those ions which have  $G < (3-4)/3.4 = 0.9-1.2$ , i.e. ions with  $Z > (0.92-1.06)A^{0.5}$ . The remaining ions, those with  $Z \leq (0.92-1.06)A^{0.5}$ , are left behind to enrich the corona.

There is no a priori reason why the solar wind flux should have any relationship whatever to the coefficient in eq. [1]. Thus, the mean value

of the upper limit on the ratio  $R = Z^2/A$  of the ions which would enrich the corona could be arbitrary, in principle. We draw attention to the fact that, in practice, however, the upper limit on  $R$  in the enriched coronal gas is equal to unity (within the uncertainties of the solar wind measurements). Thus, ions of (e.g.) iron with  $Z \leq 7$  will accumulate in the solar corona.

4. Discussion. We have found that ions which are selectively preaccelerated in SEP (i.e. those with  $R < 1$ ) are the same as those which enrich the coronal gas because the average solar wind leaves them behind. Therefore, abundance anomalies which appear in SEP because of the Coulomb selectivity are also expected to appear in the coronal gas. Thus, the predictions in Fig. 1 should also be relevant for abundances in the coronal gas, provided thermal structures are not too different. (Note that Case B predictions, which appear in Fig. 1, are insensitive to source temperature, as long as  $T \geq 10^6$  K; see Fig. 8 of (2). Hence, differences in temperature between a solar flare site and the source region of the solar wind will not affect the predictions in Fig. 1, since both temperatures in all likelihood are  $\geq 10^6$  K.) We suggest that coronal abundances are anomalous relative to the photosphere because of Coulomb losses in the solar wind, while SEP anomalies are due to Coulomb losses at a flare site. Hence, SEP acceleration can be selective: but since it enhances the selection which has already occurred in the corona, the anomalies appear similar. Different classes of Fe-richness in SEP may reflect situations in the sun where SEP selectivity and/or solar wind selectivity have operated and reinforced each other to varying extents.

The enrichment of the solar corona will not proceed indefinitely: at times, the solar wind flux becomes considerably larger than average. Thus, in the data set discussed in (5), the 5-95% range limit on the solar wind flux is  $(1.5-7.8) \times 10^8$  cgs. In 550 days of ISEE-3 data, we found 9 samples (out of 2117) with fluxes of  $(9.0-9.9) \times 10^8$  cgs. each separated by an average interval of about 60 days. At such times, the accumulated enrichment of 60 days is flushed out, such that only ions with very small  $Z$  are left behind ( $Z < (0.5-0.6)A^{0.5}$ ). But on the average, enrichments of coronal gas will build up with abundance anomalies as shown in Fig. 1.

5. Conclusions. Elemental abundances are observed to be anomalous (relative to the photosphere) in both SEP and in coronal gas. Here we propose that Coulomb effects can explain both sets of anomalies. The Coulomb loss scenario makes predictions of elemental anomalies as a function of FIP and these predictions agree well both qualitatively and quantitatively with the observed data for energetic particles (see Fig. 1). FIP ordering is not a sign that the source material is at  $T=8000$  K: we find that the source material can have  $T \geq 10^6$  K, and still preserve FIP ordering.

#### References

1. Meyer, J. P., (1985), *Ap. J. Suppl.*, 57, 151.
2. Mullan, D. J. and Levine, R. H., (1981), *Ap. J. Suppl.* 47, 87 (ML).
3. Israel, M. et al., (1981), *Proc. 17th ICRC*, 2, 36.
4. Hollweg, J., (1981), *J. Geophys. Res.*, 86, 8899.
5. Feldman, W. et al., (1977), in: *The Solar Output and Its Variations* ed. O. R. White (Colorado Univ. Press), p. 357.



# THE MEAN IONIC CHARGES OF N, NE, MG, SI, AND S IN SOLAR ENERGETIC PARTICLE EVENTS

A. LUHN, D. HOVESTADT, B. KLECKER, M. SCHOLER

Max-Planck-Institut für extraterrestrische Physik, 8046 Garching, F.R.G.

G. GLOECKLER, F. M. IPAVICH, A. B. GALVIN

University of Maryland, College Park, MD 20742, U.S.A.

C. Y. FAN

University of Arizona, Tucson, AZ 85721, U.S.A.

L. A. FISK

University of New Hampshire, Durham, NH 03824, U.S.A.

## ABSTRACT

The mean ionic charges of Nitrogen, Neon, Magnesium, Silicon, and Sulfur in solar flare particle events have been determined for 12 flares during the time interval from September 1978 to September 1979. The observations were carried out with the MPI/UoMd ULEZEQ Sensor on the ISEE-3 satellite. Comparing the results with mean charge states established in a hot coronal plasma under equilibrium conditions, we derive different temperatures for different elements. These range from approx  $2 \cdot 10^6$  K to  $7 \cdot 10^6$  K in a single flare. From flare to flare the variation in temperature for each element is less than the variation between different ion species.

1. Introduction The ionic charge state distributions of solar energetic particles provide important information about both the conditions at the source region and the nature of acceleration, coronal, and interplanetary propagation processes. The processes involved in general depend on the particle's rigidity, thus, a knowledge of the particles mass to charge ratio  $A/Q$  is essential for comparing observations of solar energetic particles with theoretical models of acceleration and propagation processes. Since charge states are not altered during the passage of the ions to earth<sup>1</sup>, measurement of the charge state distributions can be used to diagnose the conditions of the plasma at the source region of the energetic particles.

We report measurements of the mean ionic charges for the elements C, N, O, Ne, Mg, Si, S, and Fe in 12 flare associated solar energetic particle events in the time period from September 1978 to September 1979. Mean ionic charges of C, O, and Fe have been published before for all but two of the flares considered here<sup>2,3</sup>. In <sup>4</sup> the other elements have been analysed for three of the flare events. For completeness these results are included in this work.

2. Instrument and Data Analysis. The data presented in this paper have been obtained with the Max-Planck-Institut / University of Maryland ULEZEQ Sensor onboard the ISEE-3 spacecraft. During the period of the measurements from September 1978 to October 1979 this satellite was positioned at the Lagrangian point  $L_1$  between the Earth and the Sun, at a distance of about  $230 R_E$  from the Earth. By combining an electrostatic deflection system with a position sensitive solid

state detector and a proportional counter, the ULEZEQ sensor is capable of determining separately the energy  $E$  and nuclear charge  $Z$  of an incoming ion in the energy range from  $\sim 0.3$  to  $\sim 4$  MeV/nucleon as well as measuring its ionic charge  $Q$ . Because of the poor counting statistics, especially for the rarer elements (N, Ne, Mg, Si, and S) and the limited charge resolution of the sensor, we present only the mean values of the charge state distributions. The determination of the ionic charge is, apart from statistical errors, subject to a systematic uncertainty of less than 5%. The resolution of the sensor with respect to elemental species is such that within the Iron group, individual elements cannot be separated. However, since most particles in this group are in fact Iron, we stay with the common practice to designate them by "Fe". For a detailed description of the sensor and data analysis see Hovestadt et al.<sup>5</sup>

Table 1. *Selected SEP events*

ID	Accumulation period
1	1978 doy 266.12 00- 271.00 00
2	doy 314.06 00- 321.00 00
3	doy 346.06 00- 355.00 00
4	1979 doy 48.18 00- 55.06 00
5	doy 87.06 00- 90.00 00
6	doy 93.12 00- 98.00 00
7	doy 113.06 00- 117.12 00
8	doy 147.12 00- 152.12 00
9	doy 157.06 00- 165.00 00
10	doy 213.06 00- 218.00 00
11	doy 231.12 00- 239.00 00
12	doy 258.06 00- 272.00 00

For our analysis we selected 12 well identified flare associated solar energetic particle events from September 1978 to September 1979 (see Table 1). The start and end times for the accumulation periods were chosen as to maximize the counting statistics, that is from the onset of the energetic particle flux well into the declining phase. We assume here that the charge states are not affected by post-acceleration of the flare generated shock wave during the passage to earth. The energy ranges for the accumulation of the different elements represent a compromise between charge resolution and counting statistics. They are 0.45-2.34 MeV/N for C, 0.45-2.62 MeV/N for N, 0.54-2.64 MeV/N for O, 0.56-3.14 MeV/N for Ne, 0.56-3.37 MeV/N for Mg, 0.55-2.97 MeV/N for Si, 0.55-3.17 MeV/N for S, and 0.34-1.78 MeV/N for Fe.

**3. Results and Discussion** In Table 2 we summarize the results for the mean charges in all of the observed flares. We also give the weighed average of the 12 periods. From the measured mean charge and ionization equilibrium tables<sup>6,7,8,9</sup> one can derive for each ion the electron temperature of the source plasma of these ions. This should give consistent results if the following assumptions hold: 1) Conditions are such that charge equilibrium can be established, 2) the distribution function of the plasma electron is a Maxwellian (this is assumed in the calculation of the tables), and 3) charge exchange processes are negligible during acceleration and propagation. As an example we show in Fig 1 mean equilibrium charge states as a function of temperature for O, Ne, Mg, Si, and S. The values of the mean charge for accumulation period 1 are indicated by heavy lines. For the elements shown as well as for C and N there is no difference in the mean values of the charge state distributions as calculated from the tables of Jordan<sup>(6,7)</sup> and Shull and van Steenberg<sup>(8,9)</sup> above temperatures of  $\sim 10^6$  K. We do not show Iron, because for this ion the difference in the inferred temperatures for the two tabulations is significant. We attribute this to the inherent difficulties in estimating the ionization and recombination rates for a many electron system (as Iron in this temperature range) and the errors introduced in the simple analytical interpolation formulae for the rate coefficients used in<sup>8</sup>. In Fig 2 we compile

Table 2 Mean charges in solar energetic particle events

period ID	mean charge									
	C	N	O	Ne	Mg	Si	S	Fe		
1	576 ± 0.05*	631 ± 0.11	713 ± 0.04	923 ± 0.15	108 ± 0.16	111 ± 0.21	112 ± 0.42	144 ± 0.16		
2	590 ± 0.06	659 ± 0.13	717 ± 0.05	920 ± 0.25	114 ± 0.20	120 ± 0.31	105 ± 0.47	163 ± 0.24		
3	579 ± 0.09	653 ± 0.16	719 ± 0.06	953 ± 0.29	110 ± 0.28	119 ± 0.37	129 ± 1.31	157 ± 0.26		
4	566 ± 0.13	674 ± 0.26	711 ± 0.11	974 ± 0.27	105 ± 0.38	115 ± 0.67	---	177 ± 0.62		
5	581 ± 0.16	706 ± 0.41	676 ± 0.16	889 ± 0.88	112 ± 0.69	100 ± 0.82	---	122 ± 1.35		
6	572 ± 0.05	637 ± 0.09	701 ± 0.04	906 ± 0.16	107 ± 0.16	114 ± 0.28	110 ± 0.82	151 ± 0.24		
7	582 ± 0.07	679 ± 0.14	705 ± 0.10	914 ± 0.44	106 ± 0.36	117 ± 0.17	---	136 ± 0.86		
8	580 ± 0.15	625 ± 0.34	689 ± 0.18	947 ± 0.48	972 ± 0.70	117 ± 1.41	---	163 ± 1.34		
9	559 ± 0.04	619 ± 0.07	683 ± 0.04	877 ± 0.14	104 ± 0.15	983 ± 0.23	955 ± 0.90	142 ± 0.22		
10	558 ± 0.16	665 ± 0.43	710 ± 0.20	846 ± 0.71	102 ± 0.67	---	---	145 ± 0.51		
11	562 ± 0.07	634 ± 0.17	684 ± 0.06	891 ± 0.21	105 ± 0.24	106 ± 0.33	112 ± 0.59	147 ± 0.26		
12	540 ± 0.11	625 ± 0.22	671 ± 0.12	821 ± 0.48	108 ± 0.53	111 ± 0.57	897 ± 1.25	146 ± 0.74		
average	570 ± 0.02	637 ± 0.04	700 ± 0.02	905 ± 0.07	107 ± 0.07	110 ± 0.10	109 ± 0.24	149 ± 0.09		

\* Errors are 1σ statistical errors only. Additionally, the mean charges are subject to a systematic error of ± 5%  
 \*\* No values are given if less than 3 counts are detected

the inferred equilibrium temperatures for all of the 12 periods. It is evident that 1) different elements apparently reflect different equilibrium temperatures and 2) these values remain fairly constant from flare to flare. This is a strong indication that at least one of the above three assumptions is not applicable.

Recently calculations have been performed to allow for 1) non steady state charge states and 2) a non-Maxwellian tail of the electron distribution function determining the charge state distributions (<sup>10</sup>), as well as 3) for charge states by interactions of fast ions with a hot coronal plasma (<sup>11</sup>). Neither of these relaxations from the original assumption of charge equilibrium can explain the observed variations in the mean charge states for the different elements. To resolve this discrepancy one possibly has to invoke a combination of the above three effects and also take into account the x-ray radiation field, which is negligible in the quiet solar corona, but might not be in solar flares <sup>12</sup>.

**5 Acknowledgements** We are grateful to the many individuals at the Max-Planck-Institut für extraterrestrische Physik and the Space Physics group of the Department of Physics and Astronomy at the University of

Maryland, who developed the hardware and software for our ISEE experiments. This work is supported in part by NASA under contract NAS5-20062, grants NGR-21-002-224 and NGR-21-002-316, and by the Bundesministerium für Forschung und Technologie, contract RV 14B8/74 and 0101 017-ZA/WF/WRK 175/4.

Fig 1 Mean charge of O, Ne, Mg, Si, and S as a function of temperature as calculated from 8.9. Heavy lines mark the temperature ranges compatible with the 95% confidence interval of the charge state measurements of solar energetic particle event 1

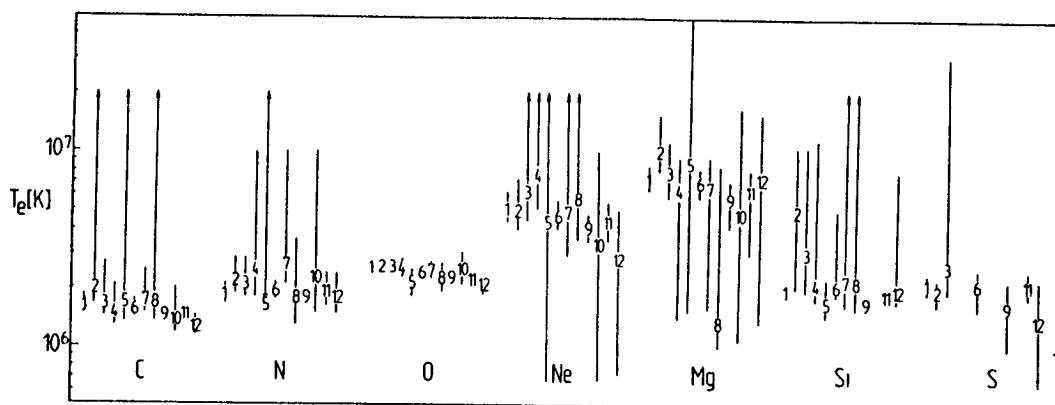
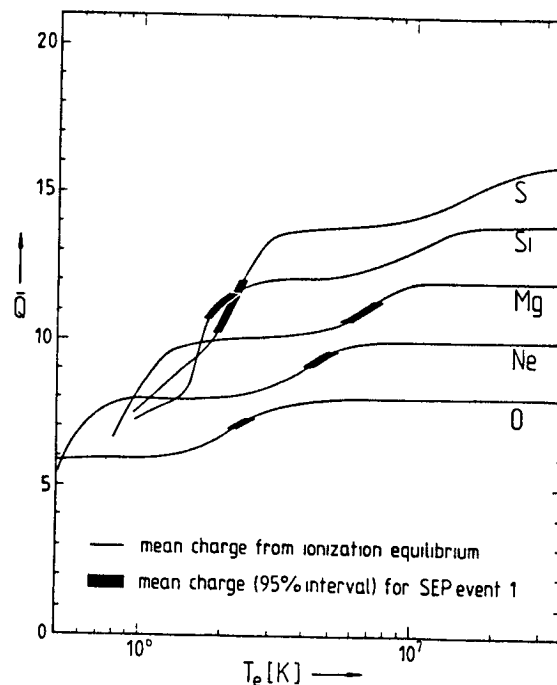


Fig 2 Equilibrium temperatures (95% confidence intervals or lower limits) for the 12 SEP periods of Table 1, derived from 8.9.

#### References

1. D. Hovestadt et al. *Ap J* **281**, p 463 (1984)
2. G. Gloeckler et al. *Proc 17th Int. Cosmic Ray Conf (Paris)*, **3**, p 136 (1981)
3. D. Hovestadt et al. *Adv. Space Res* **1**, p 61 (1981)
4. A. Luhn et al. *Adv. Space Res* **4**, p 161 (1984)
5. D. Hovestadt et al. *IEEE Trans Geos. Electr.* **GE-16**, p 166 (1978)
6. C. Jordan *M.N.R.A.S.* **142**, p 501 (1968)
7. C. Jordan *M.N.R.A.S.* **148**, p 17 (1969)
8. M. J. Shull, M. v. Steenberg *Ap. J. Suppl.* **48**, p 95 (1982)
9. M. J. Shull, M. v. Steenberg *Ap. J. Suppl.* **49**, p.351 (1982)
10. A. Luhn, D. Hovestadt. paper SH 2.1-12 (this conference)
11. A. Luhn. Ph.D. Thesis, Technische Universität München (1985)
12. D. J. Mullan. priv. comm. (1985)

# CALCULATIONS OF HEAVY ION CHARGE STATE DISTRIBUTIONS FOR NONEQUILIBRIUM CONDITIONS

A. Luhn, D. Hovestadt

Max-Planck-Institut für extraterrestrische Physik

8046 Garching, F R G

## ABSTRACT

Numerical calculations of the charge state distributions of test ions in a hot plasma under nonequilibrium conditions are presented. In particular, we derive the mean ionic charges of heavy ions for finite residence times in an instantaneously heated plasma and for a non-Maxwellian electron distribution function. Comparing the results with measurements of the charge states of solar energetic particles, we find that neither of the two simple cases considered can explain the observations.

1 Introduction Recent measurements of the charge states of heavy ions in solar energetic particle events<sup>1</sup> indicate that nonequilibrium conditions at the source of the solar energetic particles (presumably an active region in the lower corona) are likely to play a key role in establishing the charge state distribution observed at earth. In particular, the temperature as derived from the equilibrium tables of charge state distributions<sup>2,3,4</sup> differed significantly for different ion species. Calculations of equilibration times for impurity ions in a fusion plasma<sup>5</sup> indicate that, as a function of plasma temperature, the time for initially neutral atoms to reach their equilibrium charge state distribution can vary by approximately two orders of magnitude. We have therefore calculated the mean ionic charges for elements of relevance to solar flare studies which are expected a) for a finite residence time of the ions after an instantaneous heating of the plasma, and b) for a non-Maxwellian distribution function for the electrons in the plasma.

2 Methods The rate of change of the abundances  $n_i$  of the ionization states  $i$  of an ion with nuclear charge  $Z$  is given by the following system of equations

$$\begin{aligned}\dot{n}_1 &= n_e (-n_1 S_1 + n_2 \alpha_2), \\ \dot{n}_i &= n_e (n_{i-1} S_{i-1} + n_{i+1} \alpha_{i+1} - n_i (S_i + \alpha_i)), \quad (i=2 \dots Z), \\ \dot{n}_{Z+1} &= n_e (n_Z S_Z - n_{Z+1} \alpha_{Z+1}).\end{aligned}\tag{1}$$

For vanishing time dependence this becomes

$$n_i S_i = n_{i+1} \alpha_{i+1}, \quad (i=1 \dots Z)\tag{2}$$

$S_i$  denotes the total ionization rate coefficient from ionization state  $i$  to  $i+1$ ,  $\alpha_i$  the total recombination rate coefficient from  $i$  to  $i-1$ , and  $n_e$  is the electron density. The rate coefficients are obtained by multiplication of the relevant cross sections with the electron velocity, averaged over the electron distribution function. For the time dependent calculations with a Maxwellian electron distribution we use the fit parameters for the rate coefficients given in 2 and 3. These are calculated using the corona approximation, i.e. neglecting any density dependent terms in the

cross sections and photoionization by the radiation field, which is valid for the parameter range considered here. The processes included are collisional ionization and radiative and dielectronic recombination together with corrections taking into account autoionization after collisional excitation and dielectronic recombination. For the calculation of the charge states produced by a non-Maxwellian distribution, however, we need the cross sections  $\sigma$  as a function of electron impact velocity. To obtain these, we use the analytical forms of the rate coefficients for a Maxwellian distribution given by <sup>6</sup> and solve numerically for the parameters of the cross sections by comparing them with the rate coefficients given by <sup>2,3</sup>. We then can find the rate coefficients for an arbitrary electron distribution  $f_e$  by calculating  $\int v \sigma(v) f_e(v) dv$ , where  $v$  denotes the electron velocity.

The equations (1) are solved by numerical integration with an algorithm suited for the widely differing time scales of the abundance changes for the different ionization states. The initial charge distributions and the equilibrium distributions for a non-Maxwellian electron distribution function are calculated using the equilibrium equations (2). In view of the accuracy of the parameters given by <sup>2</sup> for the interpolation formulæ for the rate coefficients, conclusions based on the values of specific ionization ratios have to be made with caution. However, the mean values of the charge distributions, which are used for this work, are much less affected.

**3 Results and Discussion** We first discuss the time development of the mean ionic charge of different ions after an instantaneous heating of the plasma. This is motivated by the observation that in the initial phase of a solar flare the temperature rises by a factor of approx. 10 over the ambient coronal temperature of about  $10^6$  K within a time of the order of 1 second (see for instance <sup>7</sup> and <sup>8</sup>). The subsequent acceleration of protons, alpha particles, and heavier ions may

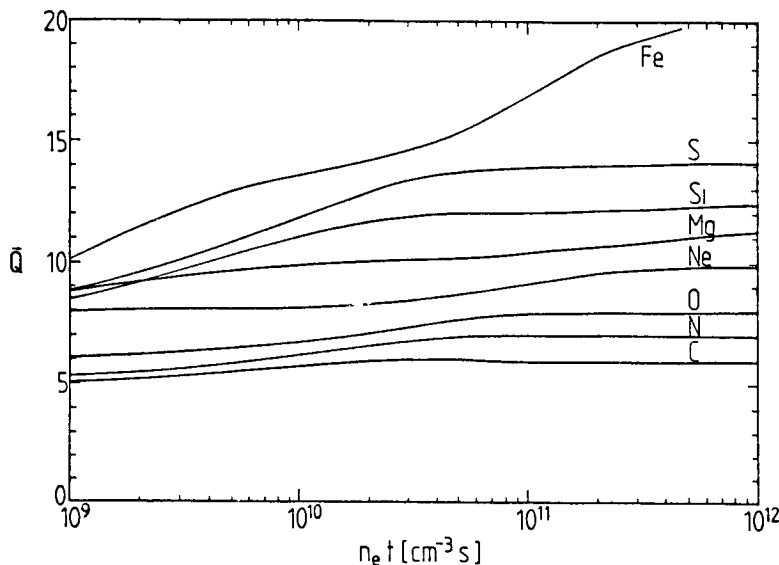


Fig 1 Time development of mean charges after an instantaneous heating of the plasma from  $10^6$  K to  $10^7$  K at time  $t=0$

remove the ions in a timescale comparable to the equilibration time for the ionic charge. In Fig. 1 we plot the mean charge as a function of  $n_e t$  for the case of a temperature rise from  $10^6$  K to  $10^7$  K. Note that the time for Neon and Magnesium to reach their new equilibrium charge state distribution is a factor of ten larger than that for e.g. Oxygen if one assumes a typical electron density of  $10^9$   $\text{cm}^{-3}$ , it is of the order of 100 s.

This is a consequence of the high ionization potential for the K shell electrons of these elements, which in this temperature range cannot be removed for ions with a higher atomic number  $Z$ . The differences in the equilibration times contrast with the observation of rather high charge states for Ne and Mg<sup>1</sup>, which on the basis of the notion sketched above would be expected for elements with short equilibration times. For different initial and final temperatures the equilibration times change. However, their ratios for the different ions remain approximately the same. We can therefore conclude, that the simple model of the freezing in of nonequilibrium charge states due to the escape of the particles from the heated coronal material cannot explain the ionic charges of solar energetic particles.

The second case considered is the calculation of equilibrium charge distributions for a non-Maxwellian electron distribution function of the coronal plasma. The existence of a non-thermal tail of electrons in the transition zone and the lower corona is supported both by theoretical calculations for the quiet sun (e.g. 9,10) and observations in flaring regions (e.g. 11,12). Owocki and Scudder (6) have considered this case and derived the ionization ratios  $O^{+6}/O^{+7}$  and  $Fe^{+11}/Fe^{+12}$ . They find that an estimation of the temperature based on these ratios overestimates or underestimates the true temperature of the plasma depending on the ratio  $k_B T_m / I$ , where  $k_B$  is the Boltzmann constant,  $T_m$  the temperature inferred with a Maxwellian distribution, and  $I$  the ionization potential of the state considered. We follow (6) in employing the "kappa" (generalized Lorentzian) distribution as a convenient one parameter representation of a Maxwellian with a power law tail. Our result is that the mean charge changes in general by considerably less than the ionization state ratios, especially if states are compared which constitute the flanks of the charge distribution.

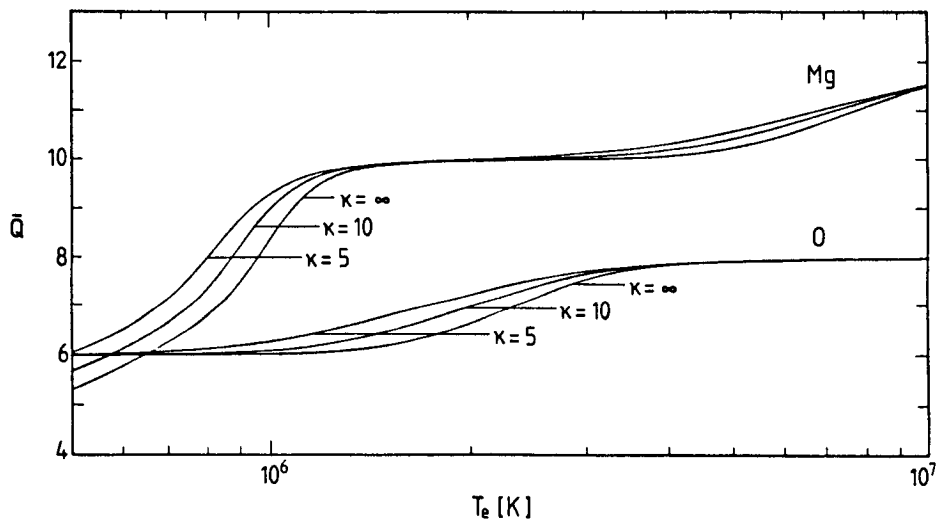


Fig 2 Mean equilibrium charges of O and Mg for a  $\kappa$  electron distribution function with  $\kappa=5$  and 10 and a Maxwellian ( $\kappa=\infty$ )

In Fig 2 we compare the mean equilibrium charges of O and Mg as a function of temperature (defined for the  $\kappa$  distribution as corresponding to the mean electron energy) for values of the parameter  $\kappa$  of 5, 10, and  $\infty$  (corresponding to a strong and moderately pronounced electron tail

and a purely Maxwellian distribution). Fig 3 shows the mean charges for various heavy ions for a  $\kappa$  distribution with  $\kappa=5$ . Although the effect of the energetic tail of the electron distribution is to raise the mean charge above that of a Maxwellian with the same temperature, the variation of this effect for the different ions is not pronounced enough to explain the variation of the temperature inferred for the different ions from a Maxwellian

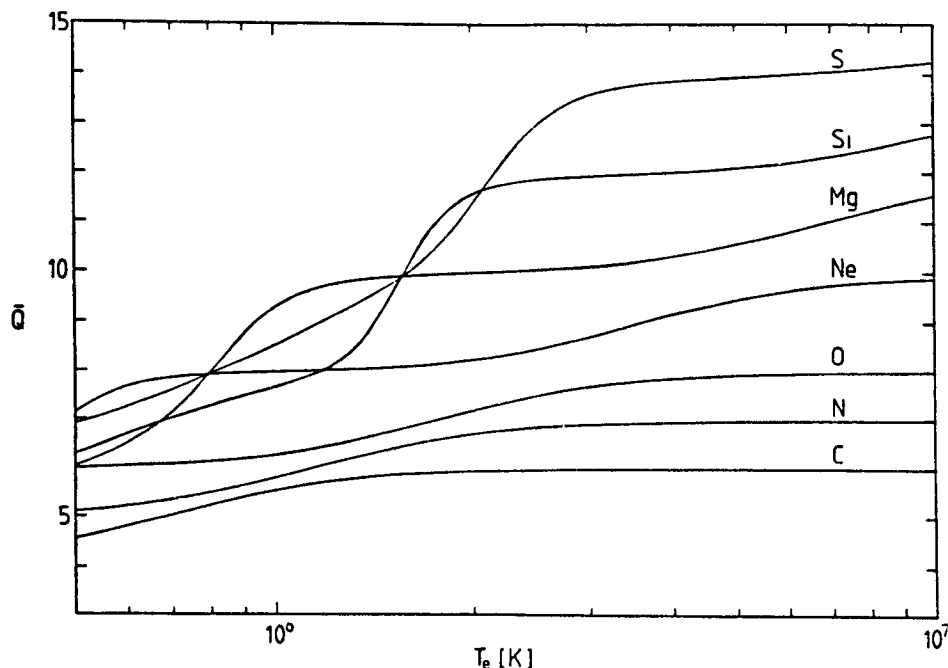


Fig 3 Mean equilibrium charges as a function of electron temperature for a  $\kappa$  distribution with  $\kappa=5$

In closing we conclude that neither of the above two simple models is able to explain the observed discrepancy in the temperatures derived from the mean ionic charge states for the heavy constituents of flare generated solar energetic particles.

#### References

- 1 A. Luhn et al. paper SH 2.1-11, this conference
- 2 M. J. Shull, M. v. Steenberg. Ap J. Suppl **48**, p 95 (1982)
- 3 M. J. Shull, M. v. Steenberg. Ap J. Suppl **49**, p 351 (1982)
- 4 C. Jordan MNRAS **142**, p 501 (1969)
- 5 P. G. Carolan, V. A. Piotrowicz Plasma Phys **25**, p 1086 (1983)
- 6 S. P. Owocki, J. D. Scudder. Ap J **270**, p 758 (1983)
- 7 R. P. Lin, H. S. Hudson. Solar Phys **50**, p 153 (1976)
- 8 D. M. Rust et al. Ap. J. **288**, p 401 (1985)
- 9 R. Roussel-Dupré. Sol. Phys **68**, p. 243 and p. 265 (1980)
- 10 E. C. Shoub. Ap J **266**, p.339 (1983)
- 11 S. F. Smerd, in AAS-NASA Symposium on Solar Flares, NASA SP-50 (1964)
- 12 P. L. Dufton, A. E. Kingston, F. P. Keenan. Ap. J. **280**, L35 (1984)



## ABUNDANCES FROM SOLAR-FLARE GAMMA-RAY LINE SPECTROSCOPY

R. J. Murphy  
University of Maryland  
College Park, MD 20742

R. Ramaty  
NASA/GSFC  
Greenbelt, MD 20771

D. J. Forrest  
University of New Hampshire  
Durham, NH 03824

B. Kozlovsky  
Tel Aviv University  
Tel Aviv, ISRAEL

## ABSTRACT

Elemental abundances of the ambient gas at the site of gamma-ray line production in the solar atmosphere are deduced using gamma-ray line observations from a solar flare. The resultant abundances are different from local galactic abundances which are thought to be similar to photospheric abundances.

1. INTRODUCTION. Gamma-ray emission from solar flares consists of lines from nuclear reactions and continuum primarily from relativistic electron bremsstrahlung (1,2). These gamma rays are produced in thick-target (3) interactions of energetic particles with ambient gas, most likely in the chromosphere or the transition region. A particularly good gamma-ray spectrum has been observed (4) by the gamma-ray spectrometer (GRS) on SMM from the April 27, 1981 flare. This spectrum shows several narrow lines: at 6.13, 4.44, 1.78, 1.63, 1.37 and 0.85 MeV from deexcitations of  $^{16}\text{O}$ ,  $^{12}\text{C}$ ,  $^{28}\text{Si}$ ,  $^{20}\text{Ne}$ ,  $^{24}\text{Mg}$  and  $^{56}\text{Fe}$ , respectively, at 2.22 MeV from neutron capture, at 0.51 MeV from positron annihilation and at  $\sim 0.45$  MeV from  $\alpha$ - $\alpha$  fusion. While earlier work (5,6) predicted that these should be the strongest lines, the observed line ratios are inconsistent (4) with our calculations which assume local galactic (7) abundances for the ambient gas (see Table 1). These local galactic abundances are believed (7) to be similar to photospheric abundances.

2. ANALYSIS. We have calculated deexcitation spectra resulting from thick-target nuclear reactions. These spectra, binned into photon energy channels  $j$  defined in ref.(6), can be expressed as  $\sum_{\ell} n(\ell)A(j,\ell)$ , where  $n(\ell)$  is the abundance of element  $\ell$  (with  $\ell$  defined in Table 1) and  $n(\ell)A(j,\ell)$  is the contribution of interactions of all the energetic particles with this element. To these spectra we add bremsstrahlung, the neutron capture line and positron annihilation radiation. For the bremsstrahlung we assume a power law with adjustable index, for the neutron capture we take an infinitely-narrow line at 2.223 MeV and for the

annihilation radiation we assume an infinitely-narrow line at 0.511 MeV along with the orthopositronium continuum corresponding to 67% of the positrons annihilating via positronium. We transform the photon spectra into pulse-height spectra using a numerical model of the detector response which will be presented elsewhere. The total pulse-height spectrum can then be written as  $\rho(i) = \sum_{\ell} n(\ell) \mathcal{A}(i, \ell) + \mathcal{A}_b(i) + \mathcal{A}_n(i) + \mathcal{A}_p(i)$ , where  $i$  denotes pulse-height channel number,  $\mathcal{A}(i, \ell)$  is the partial pulse-height spectrum of element  $\ell$ , and  $\mathcal{A}_b(i)$ ,  $\mathcal{A}_n(i)$  and  $\mathcal{A}_p(i)$  are the bremsstrahlung, neutron capture and positron annihilation pulse-height spectra. We derive the abundances by comparing  $\rho(i)$  to the observed pulse-height spectrum and varying the  $n(\ell)$ 's and  $\mathcal{A}_b$ ,  $\mathcal{A}_n$  and  $\mathcal{A}_p$  until a best fit is obtained. We only consider one isotope for each element except for C, Ne and Mg, for which we include the contributions of  $^{13}\text{C}$ ,  $^{22}\text{Ne}$  and  $^{26}\text{Mg}$  but with fixed isotopic ratios (8).

The partial spectra  $\mathcal{A}(i, \ell)$  depend on the energetic-particle composition, spectrum and angular distribution. The particle composition that we use is given in Table 1. Because in the solar atmosphere interactions amongst nuclei heavier than He are expected to be negligible and because no gamma-ray lines are produced in p-p or p- $\alpha$  interactions, the  $\mathcal{A}(i, \ell)$ 's for  $\ell > 2$  depend only on the energetic protons and  $\alpha$ -particles and consist mostly of narrow lines. For the same reason,  $\mathcal{A}(i, 1)$  depends only on the energetic C and heavier nuclei and consists mostly of broad lines.  $\mathcal{A}(i, 2)$  depends on the energetic  $\alpha$ -particles and heavier nuclei and consists of the narrow feature at  $\sim 0.45$  MeV in addition to broad lines. The dominant contribution to the total pulse-height spectrum is from the  $\mathcal{A}$ 's with  $\ell > 2$ . The contributions of  $\mathcal{A}$  with  $\ell = 1$  and 2 are relatively small, since in a thick target the interactions of the heavier nuclei are suppressed by the  $Z^2/A$  dependence of the Coulomb energy loss. In addition, a good fit of the calculated pulse-height spectrum to the observed spectrum can only be achieved if the observed narrow lines are adequately accounted for. As just mentioned, the narrow lines are produced mostly by the energetic protons and  $\alpha$ -particles. Thus, uncertainties in the abundances of the energetic heavy nuclei relative to each other and relative to the protons do not significantly affect the determination of ambient C and heavier element abundances. The ambient H abundance, however, does depend on the ratio of energetic heavy nuclei to protons and therefore cannot be determined reliably. Information on the ambient He abundance is obtained primarily by fitting the  $\sim 0.45$  MeV feature and therefore depends on the  $\alpha/p$  ratio which is also very uncertain. This uncertainty, however, does not significantly affect the heavy element abundance determinations as long as the  $\alpha/p$  ratio is not much larger than  $\sim 0.1$ .

For the energy spectrum of the April 27, 1981 flare we use a Bessel function with  $\alpha T = 0.02$ , a value close to the average  $\alpha T$  determined (3) for several flares using the 2.22 to 4-7 MeV fluence ratio or the high-energy neutron arrival-time profile. We cannot use either method for this flare because the 2.22 MeV line was strongly attenuated owing to the location of the flare on the solar limb and no neutrons were observed. Our calculations, however, indicate that variations in the spectrum do not affect the abundance determinations significantly. The angular distribution of the energetic particles affects the shapes and central energies of the lines, but since the Doppler shifts of the

narrow lines are not expected to exceed the energy resolution of the SMM/GRS detector, we assume that the energetic particles are isotropic.

3. RESULTS. The abundances deduced by optimizing the fit of the calculated spectrum to the data are given in Table 1. This optimization method is discussed in the accompanying paper. Here we derive values of reduced  $\chi^2$ ,  $\chi_v^2$ , from the comparison of the gamma-ray abundances shown in Table 1 with both the local galactic and coronal abundances. We have renormalized the gamma-ray abundances using multiplicative factors determined by minimizing  $\chi_v^2$ . For the local galactic case, this factor is 1.4, leading to  $\chi_v^2 = 3.6$  ( $v = 11$ ). This implies that the gamma-ray abundances are different from the local galactic abundances. For the coronal case, the factor is 1.1 and  $\chi_v^2 = 1.1$  implying that the gamma-ray and coronal abundances are consistent within the errors. The closed circles in Figures 1 and 2 show the ratios of the renormalized gamma-ray abundances to the mean local galactic and coronal abundances. The error bars reflect the  $1-\sigma$  errors of the gamma-ray abundances. The open boxes represent the errors in the local galactic and coronal abundances.

With the renormalization that we have adopted, the principal difference between the gamma-ray and the local galactic abundances is the underabundance of C and O in the gamma-ray sample. The Fe, Si, Mg and Ne abundances in the two samples are in good agreement, but the statistical errors for Ca, S, Al and N and the systematic error for He (due to the uncertain  $\alpha/p$  ratio) are too large to permit a quantitative conclusion. As discussed above, the gamma-ray determination of the H abundance is also subject to a large systematic error. A similar suppression of C and O has been found (7) in the coronal abundances relative to the local galactic abundances (which are thought to be similar to photospheric abundances). It has been pointed out that this suppression may be caused by charge-dependent mass transport from the photosphere to the corona. Since the photosphere is collisionally ionized at a relatively low temperature, the transport could depend on the first ionization potentials of the elements. While the gamma-ray sample probably pertains to the chromosphere or transition region, similar fractionation effects could be influencing these sites as well. However, if the Ne abundance in the photosphere (where it cannot be measured) is the same as in the local galactic sample, then the difference between the gamma-ray and photospheric abundances must be due to additional processes, because correlation with first ionization potential alone would predict a lower Ne abundance than that derived here.

#### 4. REFERENCES

1. Ramaty, R. et al., 1983, Solar Physics, 86, 395.
2. Chupp, E. L., 1984, Ann. Rev. Astron. Astrophys., 22, 359.
3. Murphy, R. J. and Ramaty, R., 1985, Adv. in Space Res., 4, 127.
4. Forrest, D.J., 1983, in Posi.-Elec. Pairs in Astrop., AIP, NY, p.3.
5. Lingenfelter, R. E. and Ramaty, R., 1967, in High-Energy Nuclear Reactions in Astrophysics, Benjamin, NY, p.99.
6. Ramaty, R., et al., 1979, Ap. J. (Supp), 40, 487.
7. Meyer, J. P., 1985, Ap. J. (Supp), 57, 173.
8. Cameron, A. G. W., 1982, in Essays in Nuc. Astrop., Cambridge, p.23.

5. ACKNOWLEDGEMENTS. We would like to acknowledge discussions with E. L. Chupp and the rest of the GRS team, as well as with R. E. Lingenfelter. The work of DJF was supported by NASA, contract NAS 5-28609.

TABLE 1

## Elemental Abundances

$\lambda$	Element	Local Galactic	Corona	Energetic Particles	Abundances from Gamma Rays
1	H	$2.71 \times 10^6 (1.1)$	$2.55 \times 10^6 (1.4)$	$8.66 \times 10^5$	$(5.61 \pm 3.49) \times 10^5$
2	He	$2.60 \times 10^5 (1.25)$	$2.50 \times 10^5 (3.0)$	$5.86 \times 10^4$	$(1.92 \pm 0.25) \times 10^5$
3	C	1260(1.26)	600(3.0)	270	$288 \pm 50$
4	N	225(1.41)	100(1.7)	75	$117 \pm 91$
5	O	2250(1.25)	630(1.6)	600	$422 \pm 62$
6	Ne	325(1.50)	90(1.6)	85	$199 \pm 27$
7	Mg	105(1.03)	95(1.3)	144	$68 \pm 25$
8	Al	8.4(1.05)	7(1.7)	8	$-15 \pm 52$
9	Si	100(1.03)	100(1.3)	100	$100 \pm 28$
10	S	43(1.35)	22(1.7)	19	$48 \pm 83$
11	Ca	6.2(1.14)	7.5(1.5)	7	$17 \pm 15$
12	Fe	88(1.07)	100(1.5)	99	$76 \pm 18$

Local galactic and coronal abundances from ref.(7). The quantities in parantheses are multiplicative errors, f. We take  $m(f-1)$  as an estimate for a  $1-\sigma$  error about the mean value  $m$ . For the energetic particles,  $p/\alpha$  and  $p/O$  are the same as those of ref.(8) and C through Fe relative to O or Si are similar to the mass-unbiased solar energetic particle abundances of ref.(7). The gamma-ray abundance errors are  $1\sigma$ .

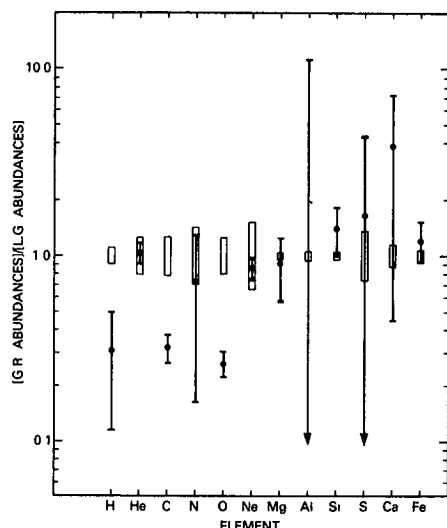


Figure 1. Ratios of renormalized gamma-ray abundances to local galactic abundances (closed circles).

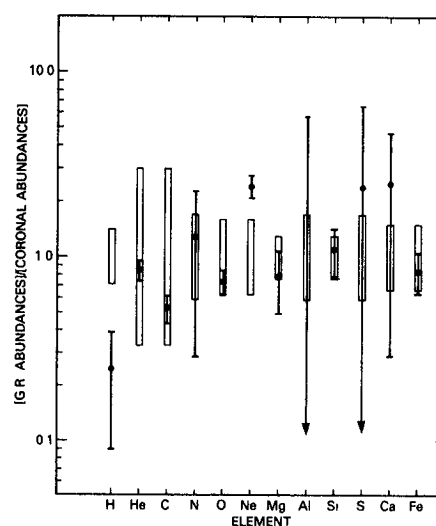


Figure 2. Ratios of renormalized gamma-ray abundances to coronal abundances (closed circles).

## SOLAR FLARE GAMMA-RAY LINE SPECTROSCOPY

R. J. Murphy  
University of Maryland  
College Park, MD 20742

D. J. Forrest  
University of New Hampshire  
Durham, NH 03824

R. Ramaty  
NASA/Goddard Space Flight Center  
Greenbelt, MD 20771

B. Kozlovsky  
Tel Aviv University  
Tel Aviv, ISRAEL

1. INTRODUCTION. In a previous paper (1), we have outlined the techniques and presented the results of solar elemental abundance determinations using observations of gamma-ray lines from the April 27, 1981 solar flare. Here, we elaborate on these techniques, present the observed and the best-fitting theoretical spectra, present numerical values for the photon fluences and derive the total number of protons involved in the thick-target production of these gamma rays.

2. DETECTOR RESPONSE. The gamma-ray spectrometer (GRS) on SMM is an actively-shielded, 7-crystal NaI scintillation detector (2) with 476 pulse-height channels. Its pulse-height resolution corresponds to an energy resolution of ~7% at 662 keV and its effective area is energy-dependent, varying from ~20 to ~200 cm<sup>2</sup>. Using a numerical model for the detector response, a photon spectrum  $a(j)$  incident on the detector can be transformed into a pulse-height spectrum  $p(i) = \sum_j D(i,j) a(j)$ , where  $D(i,j)$  represents the detector response, and  $i$  and  $j$  are the pulse-height and photon energy channel numbers, respectively. This numerical model takes into account the effective area, the pulse-height resolution and the photopeak, first escape peak and Compton continuum fractions. In particular, the Compton continuum includes an edge feature resulting from the escape of photons through its unshielded aperture. The details of this model will be published elsewhere.

3. ANALYSIS. We have calculated deexcitation spectra resulting from thick-target nuclear reactions and combined them with spectra expected from bremsstrahlung, neutron capture and positron annihilation. The total spectrum, binned into photon energy channels  $j$  defined in ref. (3), can be expressed as  $a(j) = \sum_{\ell} n(\ell) A(j,\ell)$ , where, for  $1 \leq \ell \leq 12$ ,  $n(\ell)$  is the abundance of element  $\ell$  and  $n(\ell) A(j,\ell)$  is the contribution of interactions of all the energetic particles with this element (see ref.(1)),  $n(13) A(j,13)$  is the bremsstrahlung spectrum,  $n(14) A(j,14)$  is the neutron capture spectrum taken to be a delta-function at 2.223 MeV and  $n(15) A(j,15)$  is the positron-annihilation spectrum assumed to be the sum of a delta-function at 0.511 MeV and the orthopositronium annihilation function normalized such that 67% of the positrons annihilate via positronium. For a power-law bremsstrahlung spectrum, we

find that a good fit to the data is obtained with an index equal to 2.1. Using the detector response, we obtain the pulse-height spectrum,  $\rho(i) = \sum_{\ell} n(\ell) A(i, \ell)$ , where  $A(i, \ell)$  are partial pulse-height spectra.

To obtain the best fit between the calculated pulse-height spectrum,  $\rho(i)$ , and the observed spectrum,  $c(i)$ , we minimize  $\chi^2_v$  by varying the  $n(\ell)$ 's. Here,  $\chi^2_v = \sum_i \omega(i) [c(i) - \rho(i)]^2 / v$ , where  $v$  is the number of degrees of freedom (450 usable detector channels less the 15 free variables  $n(\ell)$ ),  $\omega(i)$  is the statistical weight of channel  $i$  and  $c(i) = O(i) - fB(i)$ , where  $O(i)$  is the number of counts accumulated during the flare integration time,  $B(i)$  is the number of counts accumulated during the background integration time and  $f$  is a factor adjusting background integration time to flare integration time. We take  $\omega(i)$  to be  $1/\sigma^2(i)$ , where  $\sigma^2(i)$  is the mean-square error for channel  $i$ . For the Poisson statistics assumed here,  $\sigma^2(i) = O(i) + f^2 B(i)$ .

The values of  $n(\ell)$  which minimize  $\chi^2_v$  are obtained by solving the set of equations resulting from taking partial derivatives of  $\chi^2_v$  with respect to each of the  $n(\ell)$ 's and setting them to zero. The solutions of these equations can be written as  $\vec{n} = E A^+ W \vec{c}$ , where  $\vec{n}$  is a vector whose elements are the  $n(\ell)$ ,  $A$  is a matrix whose elements are  $A(i, \ell)$ ,  $A^+$  is its transpose,  $W$  is a diagonal matrix whose elements are the statistical weights  $\omega(i)$ ,  $\vec{c}$  is the vector of the observed pulse-height spectrum and  $E = (A^+ W A)^{-1}$  is the error matrix. If the only source of error is observational counting statistics (i.e., fluctuations in  $c(i)$ ), then the mean-square errors of the  $n(\ell)$ 's are the diagonal elements of  $E$  multiplied by  $\chi^2_v$  (4,5).

The off-diagonal elements of  $E$  give information on the interference between the partial spectra. Interference arises when two partial spectra contribute significantly to an observed spectral feature. The interference coefficient is  $F(k, \ell) = [E(k, \ell)]^2 / [E(k, k)E(\ell, \ell)]$ . When  $F(k, \ell)$  is much less than 1, the interference is negligible. However, when  $F(k, \ell)$  is large,  $n(k)$  and  $n(\ell)$  cannot be determined independently. Their sum can be determined with an error  $[E(k, k) + E(\ell, \ell)] \chi^2_v$ , but the overall fit will remain just as good if either  $n(k)$  or  $n(\ell)$  is varied by a factor  $F(k, \ell)$  while keeping the sum  $n(k) + n(\ell)$  constant.

**4. RESULTS.** The resultant  $n(\ell)$ 's for  $1 \leq \ell \leq 12$ , together with their respective mean-square errors, are given in the last column of Table 1 of ref.(1). As discussed there, the statistical errors in the derived abundances of C, O, Ne, Mg, Si and Fe are sufficiently small to allow meaningful comparisons with the local galactic and coronal abundances, but the statistical errors for N, Al, S and Ca, as well as the systematic errors for H and He, preclude such comparisons. In addition to these 12 elements, the fit of the calculations to the data also provides information on the bremsstrahlung and the neutron-capture and positron-annihilation radiation. We present this information in terms of photon fluences incident on the detector. We find that the  $>0.3$  MeV bremsstrahlung fluence is  $(1060 \pm 14)$  photons/cm<sup>2</sup> for the power law index of 2.1, the neutron capture line fluence is  $(4.3 \pm 2.9)$  photons/cm<sup>2</sup> and the 0.51 MeV line fluence is  $(25.8 \pm 2.6)$  photons/cm<sup>2</sup>. In comparison, the fluences resulting from interactions with ambient H, He, C, N, O, Ne, Mg, Al, Si, S, Ca and Fe are 27, 59, 15, 6.7, 30, 62, 35,  $<1.3$ , 56,

4.2, 1.9 and 56 photons/cm<sup>2</sup>, respectively, with the same relative errors as given in ref.(1).

We have also considered the interference coefficients between the 15 components given above. We find that between the six reliably determined elements (C, O, Ne, Mg, Si, Fe) these coefficients are all less than 0.1. Interference, therefore, should introduce little additional uncertainty in the determination of the abundances of these elements. However, we find interference between S and neutron capture ( $F=0.3$ ), and He and positron annihilation ( $F=0.21$ ), resulting from the detector's inability to adequately resolve the 2.22 MeV line from the 2.23 MeV line of <sup>32</sup>S and the 0.511 MeV line from the  $\alpha$ - $\alpha$  feature at  $\sim 0.45$  MeV, respectively. There is also interference between C and N ( $F=0.27$ ), resulting from contributions to the 4.44 MeV line from C and N spallation. But, as already discussed, the abundances of S, N and He are not well determined. Also, the 2.22 MeV line fluence cannot be adequately determined because, for the April 27, 1981 flare, this line is strongly attenuated by Compton scattering in the photosphere.

The observed spectrum of the April 27, 1981 flare is compared to the calculated spectrum in Figure 1. Here, the lines of <sup>16</sup>O, <sup>12</sup>C, <sup>20</sup>Ne, <sup>24</sup>Mg and <sup>56</sup>Fe can be clearly seen. The feature marked n is due to the 2.22 MeV line, with additional contributions from <sup>14</sup>N (at 2.31 MeV) and <sup>32</sup>S. The lack of significant interference between the 2.22 and 2.31 MeV lines indicates that adequate detector resolution is available to distinguish between them. Even though the <sup>28</sup>Si line at 1.78 MeV is not clearly visible, the Si abundance can nevertheless be well determined since in the calculation the bulk of the photons above the line center energy are produced by interactions with Si. The dip just below the second <sup>56</sup>Fe line is probably due to the effects of a calibration line of <sup>60</sup>Co at 1.17 MeV.

From the fluences for the various components given above, the total nuclear radiation (including the 2.22 MeV line and all the positron annihilation radiation) is 372 photons/cm<sup>2</sup> and its ratio to the total observed bremsstrahlung above 0.3 MeV is 0.35. This value is of considerable importance for studies of the angular distribution of gamma rays from solar flares (6). Likewise, we find that in the 4-7 MeV band, 77 photons/cm<sup>2</sup> are from nuclear interactions and 28 photons/cm<sup>2</sup> are from bremsstrahlung. The fractional contributions of the various ambient elements to this 4-7 MeV nuclear radiation are the following: 0.1, 0.08, 0.18, 0.03, 0.30, 0.13, 0.06, 0.0, 0.08, 0.0, 0.0, 0.04 for the 12 elements from H through Fe. Thus, about 1/2 of the nuclear emission in the 4-7 MeV band is from interactions with ambient C, N and O.

To determine the total number of protons involved in the gamma-ray production, we must assume a ratio of H to the heavier elements in the ambient medium. Using the abundances deduced from the gamma rays in ref.(1), we obtain  $N_p(>30 \text{ MeV}) = 3.8 \times 10^{32}$  protons, where  $N_p(>30 \text{ MeV})$  is the number of protons with kinetic energy greater than 30 MeV. But, as we have discussed, the H abundance in this sample is uncertain. Assuming abundances similar to the local galactic abundances (for which the ratio of H to heavier nuclei is higher than for the gamma-ray sample (1)),  $N_p(>30 \text{ MeV}) = 6.7 \times 10^{32}$ .

## 5. REFERENCES

1. Murphy, R. J. et al., this publication.
2. Forrest, D. J. et al., 1980, Solar Phys., 65, 15.
3. Ramaty, R., Kozlovsky, B. and Lingenfelter, R. E., 1979, Ap. J. (Supp.), 40, 487.
4. Trombka, J. I. and Schmadebeck, R. L., "A Numerical Least-Square Method for Resolving Complex Pulse Height Spectra", NASA SP-3044, 1968.
5. Bevington, P. R., "Data Reduction and Error Analysis for the Physical Sciences", McGraw Hill, NY, 1969.
6. Dermer, C. D. and Ramaty, R., 1985, submitted to Ap. J.

6. ACKNOWLEDGEMENTS. We would like to acknowledge discussions with E. L. Chupp and the rest of the GRS team, as well as with R. E. Lingenfelter. The work of DJF was supported by NASA, contract NAS 5-28609.

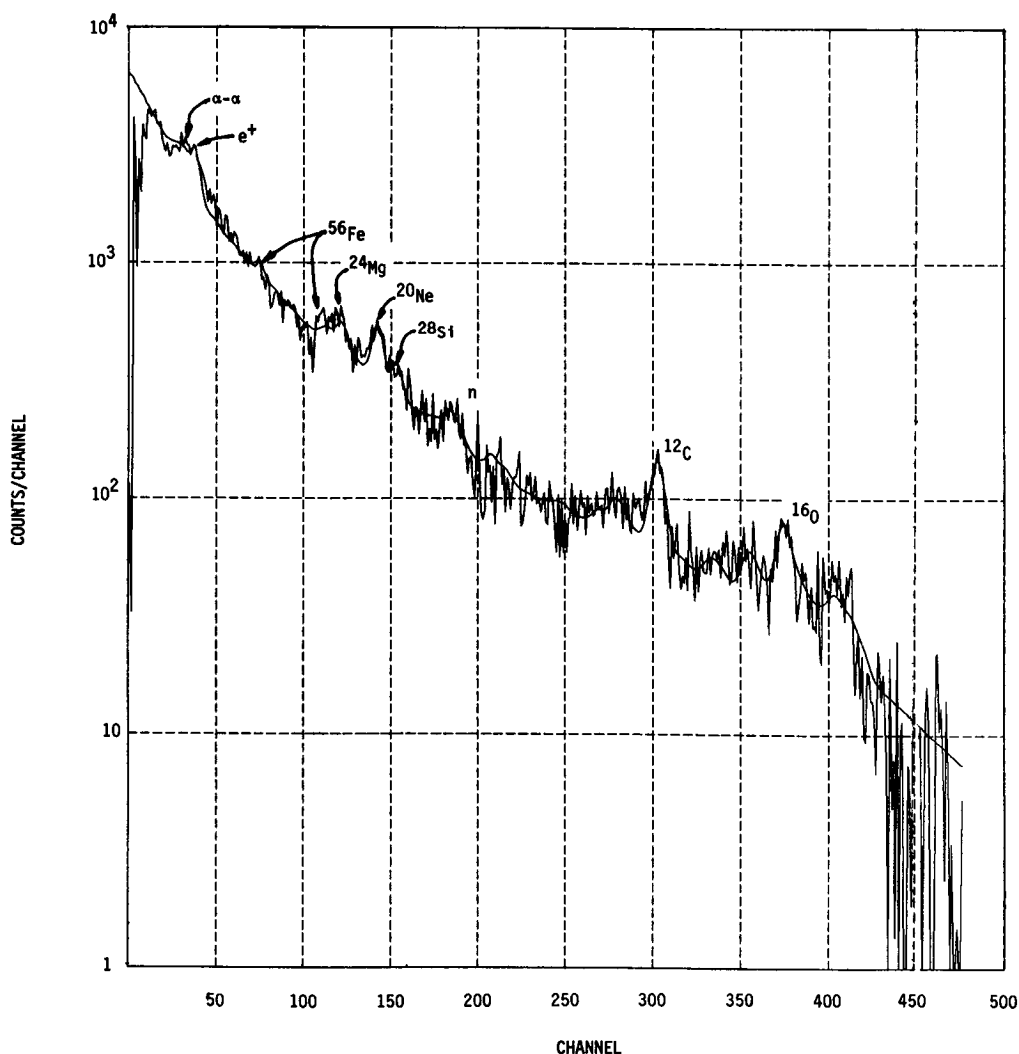


Figure 1. Observed and calculated (smooth curve) spectra of the April 27, 1981 solar flare.



# ISOTOPIC OVERABUNDANCES AND THE ENERGETIC PARTICLE MODEL OF SOLAR FLARES

R. Pérez-Enríquez and S. Bravo  
Instituto de Geofísica, UNAM, Ciudad Universitaria  
México D.F., 04510, MEXICO

## ABSTRACT

According to the energetic particle model of solar flares particles are efficiently accelerated in the magnetic field loop of an active region (AR) by hydromagnetic turbulence. Based on this picture, we shall demonstrate that the isotopic overabundances observed in some flares are not a consequence of the flare itself but they are characteristic of the plasma in the AR. Only in the event of a flare releasing the plasma into the interplanetary space it is possible to observe this anomalous composition at spacecraft locations.

**1. Introduction.** The observation of an anomalous composition of solar flare particles from some events began as early as 1962 when Schaeffer and Zahringer measured a ratio of  $^3\text{He}/^4\text{He} \sim 0.2$  for the Nov. 12, 1960 event, compared to the normal ratios in the solar atmosphere and in the solar wind of about  $10^{-4}$  (Geiss and Reeves, 1972). Since then, ratios of about one have been measured for these isotopes and substantial overabundances of Fe and another heavy elements have also been observed in the solar energetic particle flux. The characteristic features of the "rich" events have been reviewed by Ramaty et al. (1980), and Kocharov and Kocharov (1984).

Several models have been proposed for the explanation of such overabundances. The most successful are those in which the anomalous composition observed is the result of the acceleration of a preferentially preheated population at the time of the flare, the selective heating been caused by various instabilities generated in the plasma. There are two such plasma instabilities that seem to explain both the  $^3\text{He}$ , and heavier ions overabundances observed: the Fisk's (1978) model which assumes that a current electrostatic instability leads to ion cyclotron waves which heat the ions by a resonant process, and the Ibragimov and Kocharov (1978) model which assumes that a high level of turbulence is present in the flare plasma giving rise to the production of ion sound waves with the consequent heating of the isotopes. The physical characteristics of the plasma assumed in both models are somewhat similar: They both required that the relative abundance of  $^4\text{He}$  to H is already larger than normal -so the characteristic frequency of the plasma is closer to the gyrofrequency of the isotopes to be preferentially heated- and a value of  $\beta$  (the plasma to magnetic pressure ratio) smaller than one -to assure that the plasma remains confined to the magnetic field. There is, however, an important difference in the ratio of electron to ion temperatures ( $T_e/T_i$ ) required by each mechanism to operate: ion cyclotron waves in Fisk's model require a value of about 10, while for the ion sound waves in the Ibragimov and Kocharov's model this ratio should be about 100.

Some observations seem to present problems to the requirements of these models. On the one hand, the X-ray emission detected by the SMM and Hinotori satellites (see reviews by Yoshimori et al., 1983; Chupp, 1983; Svestka and Shadee, 1983) seems to indicate that the  $\beta$  value of the plasma before and at the time of the flash of the flare is very near to one and not as low as required by both models. On the other hand, the coexistence of two different isotopes of Fe ( $\text{Fe}^{11,12}$  and  $\text{Fe}^{17-20}$ ) has been observed in the flare particle flux by MaSung et al. (1981), and Klecker et al. (1984), (see Table I), thus implying two different temperatures at the flare site. We shall show in the following sections that for the energetic particle model (EPM) no such difficulties exist, and that it can give an overall explanation of the observations.

TABLE I

Event	Overabundant Isotopes	Underabundant Isotopes
14-15 May, 1974 (MaSung et al. 1981)	$^3\text{He}, \text{Ne}, \text{Mg}, \text{Si},$ $\text{O}, \text{S}, \text{Fe}^{11,12}$ and $\text{Fe}^{16,17,18}$	C
Average of five events during 1978 and 1979 (Klecker et al. 1984)	$^3\text{He}, \text{Fe}^{19+20}$	

2. The Plasma in AR's According to the Energetic Particle Model of Solar Flares. Here we shall limit ourselves to describe the characteristics of the energetic particle model (EPM) which are relevant to the problem of the production of the overabundances of  $^3\text{He}$  and heavier nuclei in an AR; (for a more detailed discussion of the model see Pérez-Enríquez, 1985). In this model, particles from the coronal plasma are efficiently accelerated by hydromagnetic waves from the convective zone, as discussed by Hollweg (1984) in the context of coronal heating, while they remain trapped in the intense bipolar magnetic field of an AR. Hence both the density and temperature of the plasma increase with time since the very appearance of the magnetic loop. In other words, the trapped plasma undergoes a dynamic evolution which may eventually lead to the occurrence of a flare, in contrast with those models which assume that the plasma plays a passive role in the generation of the flare and remains undisturbed until the flash.

Since the electrons move faster than the protons by a factor of  $\sim 43$  at the same energy, a Fermi type of acceleration within the theory of Kulsrud and Ferrara (1971) will be efficient only for the ions and the electron population will gain its energy mainly from its interaction with the ions. Now, according to the theory of Kennel and Petschek (1966), the stable trapping of the particles can be maintained as long as their energy  $E$  is below  $E_c = B^2/8\pi n$ , where  $B$  is the magnetic field, and  $n$  is the electron number density. As a consequence of the Fermi acceleration there are everytime more ions beyond  $E_c$  which try to escape and as they do they generate their own resonant waves. The wave instability so produced will depend on the physical characteristics of the plasma in the AR such as the  $T_e/T_i$  ratio, the  $\beta$  of the

plasma and the relative abundance of  $^4\text{He}$  to  $\text{H}$ .

a) The  $T_e/T_i$  and  $\beta$  values: As the energy of the electrons is "purely" of thermal nature, and the energy of the ions is mainly convective there will be a relative streaming between them, and thus, as described by Pérez-Enríquez (1985), a Buneman instability will take place with a growth rate  $\gamma_B = \sqrt{3}/2 (m_e/m_i)^{1/3} \omega_{pe}$ . Here  $m_{e,i}$  are the electron and ion masses respectively, and  $\omega_{pe} = (4\pi n_e e^2/m_e)^{1/2}$  is the electron plasma frequency. For a value of  $n_e = 3 \times 10^9 \text{ cm}^{-3}$ ,  $\gamma_B \approx 2.2 \times 10^8 \text{ s}^{-1}$  and  $T_e$  grows very fast while  $T_i$  does it much slower; so  $T_e/T_i$  increases with time reaching values as high as several hundreds as observed. In a similar manner, as the number density of particles in the region also tends to increase, so it does  $\beta$ . In other words, both  $T_e/T_i$  and

$\beta$  are growing functions of time and their schematic evolution is shown in Fig. (1). Notice that these functions are quite arbitrary, but here we are only interested in showing the increase of  $T_e/T_i$  and  $\beta$  with time. In the figure,  $t_F$  and  $t_{IK}$  correspond to the times where Fisk's or Ibragimov and Kocharov's models operate, respectively.

b) The  $^4\text{He}$  to  $\text{H}$  ratio: Since  $^4\text{He}$  is four times heavier than  $\text{H}$ , it is expected to be more abundant at the bottom of the AR. In fact, from simple thermodynamic considerations, we obtain that the relative abundance of  $^4\text{He}$  to  $\text{H}$  at the feet of a typical AR can be greater than that at the top by a factor as high as 100. So, the value of the  $^4\text{He}$  to  $\text{H}$  ratio can be of about 10 at lower parts of the AR.

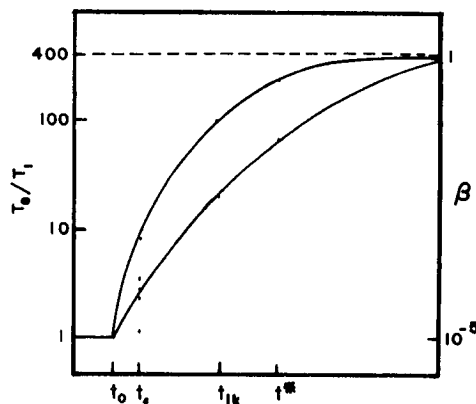


Fig.(1). Evolution of  $T_e/T_i$  and  $\beta$  in the active region(AR) from the initial time  $t_0$  to a time  $t^*$ , the time of the flare.

3. Isotopic Overabundances and Conclusions. The picture that comes out from all this is the following: due to the dynamic evolution of the plasma in the AR as described by the EPM, the requirements of the overabundance model are fulfilled at times  $t_F$  (for Fisk's model), and  $t_{IK}$  (for Ibragimov and Kocharov's model) as a consequence of such evolution (see Fig. 1). That is, the composition of the plasma in AR's also presents an evolution and so the specific composition to be observed in the interplanetary space will depend on how late in the life of the AR the flare takes place. A flare happening in the early stages of the development of an AR will send out into the interplanetary medium energetic particles with normal composition for no time has been given to the plasma to grow an overabundance ( $t^*$  before  $t_F$  in the Figure), whereas if the flare happens later the energetic particles will present an anomalous composition. In other words, the overabundances observed are indeed a characteristic of the plasma in AR's and are not produced by the flare proper. The existence of two isotopes of iron (Table I) is also easily explained within the context of our model because different

temperatures are reached by the plasma at different stages of its evolution.

### References.

- Chupp, E.L., (1983), Solar Phys., 86, 383.  
 Fisk, L.A., (1978), Astrophys. J., 224, 1048.  
 Geiss, J. and Reeves, H., (1972), Astron. Astrophys., 18, 126.  
 Hollweg, J.V., (1984), Astrophys. J., 277, 392.  
 Ibragimov, I.A., Kocharov, G.E. and Kocharov, L.G., (1978), Joffe Phys. Techn. Inst., No. 588.  
 Kennel, C.F. and Petschek, H.E., (1966), J. Geophys. Res., 71, 1.  
 Klecker, B. et al., (1984), Astrophys. J., 281, 458.  
 Kocharov, L.G. and Kocharov, G.E., (1984), Space Science Rev., 35, 89.  
 Kulsrud, R.M. and Ferrara, A., (1971), Astrophys. Space Sci., 12, 302.  
 Ma Sung, L.S. et al., (1984), Astrophys. J. Lett., 245, L45.  
 Pérez-Enríquez, R., (1985), (accepted for publication in Solar Phys.).  
 Ramaty, R. et al., (1980), in P.A. Sturrock (ed.), Solar Flares, Boulder, Co., Assoc. Univ. Press, p.117.  
 Schaeffer, O.A. and Zahringer, J., (1962), Phys. Rev. Letters, 8, 389.  
 Svestka, Z. and Schadee, A., (1983), Solar Phys., 86, 267.  
 Yoshimori, M. et al., (1983), Solar Phys., 86, 375.

## NUCLEOSYNTHESIS IN THE TERRESTRIAL AND SOLAR ATMOSPHERES

Chuanzan Yu    Renming Zhou    Shijie Zhan  
Department of Physics, Yunnan University, Kunming  
P R C

## ABSTRACT

Variations of  $\delta D$ ,  $\delta^{13}C$ ,  $\Delta^{14}C$  and  $\delta^{18}O$  with time have been measured by a lot of experiments. Many abnormalities of isotope abundances in cosmic rays have been found by balloons and satellites. We hold that these abnormalities are related to nucleosynthesis in the terrestrial and solar atmospheres and are closely related to solar activities.

1 Introduction    In recent years, radiative  $\Delta^{14}C$  in annual rings of trees with different ages at different places<sup>[1]</sup>, the contents of  $\delta^{18}O$  in different ice-layers<sup>[2]</sup>, the contents of  $\delta^{13}C$  in organic layers at the bottom of the sea<sup>[3]</sup>, The ratios of (D/H) and the contents of  $^3H$  at different altitudes of the terrestrial atmosphere<sup>[4]</sup> and the ratios of (D/H) in rain<sup>[5]</sup>, snow<sup>[6]</sup> and tree<sup>[7]</sup> have been determined. Variations of the Earth's environment (Temperatures, the contents of  $CO_2$  and the heights of the sea level) for several hundred thousand years can be inferred from these data. This kind of research has provided very important informations for meteorology, archaeology and environmental science.

Recently high altitude balloon experiments have observed that the relative abundances of isotope D and  $^3H$ <sup>[8]</sup>,  $^{15}N$ ,  $^{22}Ne$  and  $^{26}Mg$ <sup>[9]</sup> increase greatly, each nucleus has energy of several hundred Mev and most of them come from the outside of the terrestrial atmosphere. At the same time, satellites have observed that the contents of  $^3He$ , when solar flares burst, increase by  $\sim 10^4$  times or even exceeds the contents of  $^4He$ <sup>[10]</sup>.

We hold that variations of isotopic contents mentioned above are related to nucleosynthesis in the terrestrial and solar atmospheres.

2 Nucleosynthesis in the Terrestrial Atmosphere    The main reactions are,

(1) The bombardment of cosmic rays with the terrestrial atmosphere and its secondary particles can cause many nuclear reactions and the intensity of cosmic rays is modulated by solar activities.

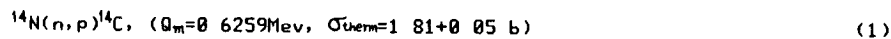
(2) High energy particles produced by solar flares can cause various nuclear reactions in the terrestrial atmosphere.

(3) Protons, in the inner radiative zone of the Earth, can be accelerated to 1--100Mev. They can interact with nuclei in the terrestrial atmosphere to bring about nucleosynthesis.

(4) All three processes mentioned above can produce secondary neutrons and will make neutrons to have a certain intensity, which will change with the

period of solar activities and the terrestrial magnetic latitudes

Radiative  $^{14}\text{C}$  and  $^3\text{H}$  are obviously the direct evidence of nucleosynthesis in the terrestrial atmosphere. They can be produced by following reactions,



The reaction rate in the terrestrial atmosphere is

$$r = N_N \cdot \sigma \cdot N_n \quad (3)$$

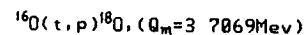
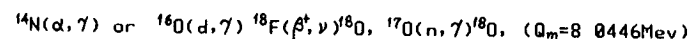
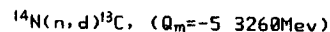
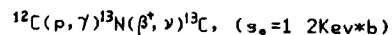
where  $N_N$  is the density of nitrogen-cylinder in the terrestrial atmosphere and  $N_n$  neutron flux. Near the equator,  $N_n^{\text{min}}(1) = 0.110/\text{cm}^2 \cdot \text{sec}$  for the minimum solar activity years and  $N_n^{\text{max}}(1) = 0.105/\text{cm}^2 \cdot \text{sec}$  for the maximum solar activity years. At regions with high latitude,  $N_n^{\text{min}}(2) = 1.367/\text{cm}^2 \cdot \text{sec}$  for the minimum solar activity years and  $N_n^{\text{max}}(2) = 0.709/\text{cm}^2 \cdot \text{sec}$  for the maximum solar activity years.

The amount of  $^{14}\text{C}$  produced at high latitude region is usually 2--5 times as high as that at middle and low latitude regions. Therefore, the results of [1] can be reasonably explained.

By (1), (2) and (3) the average reaction rate forming  $^{14}\text{C}$  in the terrestrial atmosphere at the sea level can be calculated to be  $\sim 6/\text{cm}^2 \cdot \text{sec}$  and the reaction rate for  $^3\text{H}$  at stratosphere  $\sim 0.3/\text{cm}^2 \cdot \text{sec}$  (spallation products included).

The main composition of the terrestrial atmosphere are N and O. Their cross sections producing D, bombarded by incident protons with energy 40Mev, are measured to be 25mb and 38mb, respectively. The cross section producing  $^3\text{H}$  is about 5 times smaller. The cross sections producing D and  $^3\text{H}$  increase with energy of the incident protons.

$^{13}\text{C}$  accounts for 1.1% of element C and  $^{18}\text{O}$  0.2% of element O. In the terrestrial atmosphere, reactions producing  $^{13}\text{C}$  and  $^{18}\text{O}$  are as follows,

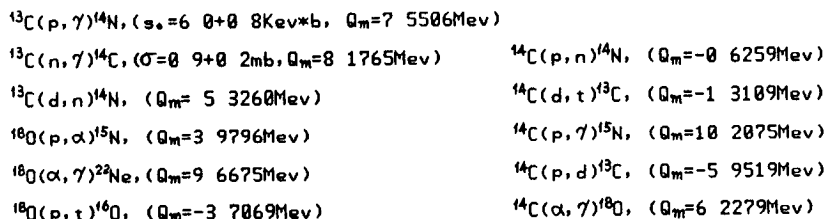


Only several Mev kinetic energy is needed for newly produced D and  $^3\text{H}$  to penetrate the Coulomb barrier and to make nuclear reactions possible. The half-time of  $^3\text{H}$  is  $T_{1/2}=12.25\text{y}$  and reaction  $^3\text{H}(p, \gamma)^4\text{He}$  is easy to take place. Thus for different times there are different  $\delta^3\text{H}$ . It is easy for D in water vapour and newly produced D to react with protons,  $\text{D}(p, \gamma)^3\text{He}$ . Thus, D will decrease

SH 2 2-2

greatly and there are different D for different times and at different atmosphere heights. Combined with ions OH, D and  $^3\text{H}$  fall on to the ground as rain and snow, and can be investigated as an index of precipitation and meteorology.

By same reason, the contents of  $^{13}\text{C}$ ,  $^{14}\text{C}$  and  $^{18}\text{O}$  in the terrestrial atmosphere, after nuclear interaction, will change. The main reactions are as follows,



Owing to different times of their production and destruction and different diffusion taking place in the atmospheric circulation, there are different  $\delta\text{D}$ ,  $\delta^{13}\text{C}$ ,  $\Delta^{14}\text{C}$  and  $\delta^{18}\text{O}$ . By determining them, variations of solar activities and the Earth's environments for hundred thousand years can be inferred.

3 Nucleosynthesis in the Solar Atmosphere. Thermonuclear reactions in the interior of the Sun carry on in the "reactor" with  $T = 15 \times 10^6 \text{ K}$ . The photospheric surfaces with  $T < 10^6 \sim 6000 \text{ K}$  are intense convective layers (photosphere), within which there are many kinds of processes of nucleosynthesis. The main processes are,

(1) n, D and  $^3\text{H}$  leaked out from the "reactor" into the convective layers are no longer nuclear fuels. Passing through the chromosphere and corona, D and  $^3\text{H}$  are accelerated by magnetic field to enter the terrestrial atmosphere. Passing through convective layers and chromosphere, reactions of n, D and  $^3\text{H}$  will take place, such as  $p(n, \gamma)\text{D}$ ,  $\text{D}(n, \gamma)^3\text{H}$ ,  $\text{D}(\text{D}, p)^3\text{H}$ ,  $\text{D}(p, \gamma)^3\text{He}$ ,  $^3\text{H}(p, \gamma)^4\text{He}$ ,  $^{14}\text{N}(n, \gamma)^{15}\text{N}$ ,  $^{14}\text{N}(\text{D}, p)^{15}\text{N}$ ,  $^{14}\text{N}(p, \gamma)^{15}\text{O}(\beta^+, \nu)^{15}\text{N}$ ,  $^{20}\text{Ne}(\text{D}, \gamma)^{22}\text{Ne}(\beta^+, \nu)^{22}\text{Ne}$ ,  $^{20}\text{Ne}(^3\text{H}, p)^{22}\text{Ne}$ . That is the reason why remarkable increases in D and  $^3\text{H}$  have been observed [8]. It has also been observed that the abundances of  $^{15}\text{N}$  exceeds that of  $^{14}\text{N}$  and the relative abundances of  $^{22}\text{Ne}$  increase by 2.75 times [9].

(2) There is a good number of high energy particles jetted out at the bottom of the photosphere during solar flares. Thus they can cause many kinds of nucleosynthesis. IMP-8 recorded on May 7th-12th, 1974 that  $^3\text{He}$  increases by  $10^4$  times and exceeds  $^4\text{He}$ , Ne, Mg and Si increase by 10 times [10]. They are caused by reactions  $\text{D}(\text{D}, p)^3\text{He}$ ,  $\text{D}(p, \gamma)^3\text{He}$ ,  $^3\text{H}(p, n)^3\text{He}$  and  $^{16}\text{O}(\alpha, \gamma)^{20}\text{Ne}$ ,  $^{14}\text{N}(\alpha, \gamma)^{18}\text{O}(\alpha, \gamma)^{22}\text{Ne}$ ,  $^{20}\text{Ne}(\alpha, \gamma)^{24}\text{Mg}$ ,  $^{24}\text{Mg}(\alpha, \gamma)^{28}\text{Si}$ , i.e.  $\alpha$ -processes caused by temperature-rising at some solar flares. Owing to the fact that  $^4\text{He}$  have been consumed greatly and  $^3\text{He}$  have reached the low temperature regions, the abundances of  $^3\text{He}$  exceeds that of  $^4\text{He}$  and Ne, Mg and Si increase.

(3) There is so called "granulation" with diameter of 1500km. Its magnetic field is about dozens of Gauss, by which protons in convection can be accelerated to knock out neutrons from CNO nucleus. Thus neutron rich isotopes increase to some extent.

#### 4 Discussions

(1) The counting rate recorded at the middle latitude sea level is 20% slower in the maximum solar activity years than the minimum solar activity years. M. Stuiver and P. D. Quay<sup>[11]</sup>, by determining  $^{14}\text{C}$ , have found Maunder, Spörer and Wolf minimums of solar activities. We hold that the rule of older solar activities might be found by comprehensive studies on  $\delta\text{D}$ ,  $\delta^{13}\text{C}$ ,  $\Delta^{14}\text{C}$  and  $\delta^{18}\text{O}$ .

(2) Variations of  $\delta\text{D}$ ,  $\delta^{13}\text{C}$ ,  $\Delta^{14}\text{C}$  and  $\delta^{18}\text{O}$  are related to nucleosynthesis in the terrestrial atmosphere. In most cases, the experimental data give "-" values, i.e. the amounts of destruction are more than that of production. In order to find out their relations, experiments on the change of  $\delta^{15}\text{N}$  and  $\delta^{17}\text{O}$  contents should be carried on.

(3)  $^{22}\text{Ne}$  super-abundance experiments also observed large increase in abundances of neutron rich isotopes, such as  $^{15}\text{N}$ ,  $^{17}\text{O}$ ,  $^{18}\text{O}$ ,  $^{21}\text{Ne}$ ,  $^{25}\text{Mg}$ ,  $^{26}\text{Mg}$ ,  $^{29}\text{Si}$  and  $^{30}\text{Si}$ . They should be regarded as a whole and have same origin of non-thermal nucleosynthesis in the solar atmosphere.

(4) The abundance of  $^3\text{He}$  increased by  $10^4$  times is not a result of selective acceleration<sup>[10]</sup>, but a result of large amounts of consumption of  $^4\text{He}$  and  $^3\text{He}$  jetted out to low temperature regions. Thus  $^3\text{He}$  exceeds  $^4\text{He}$ . Increases in  $^3\text{H}$  and  $\text{D}$  observed by balloons are results of nucleosynthesis in the solar atmosphere at different conditions.

5 Conclusions Following conclusions can be drawn from this paper,

- (1) There are many kinds of nucleosynthetic processes in the terrestrial and solar atmospheres. They are different to each other.
- (2) Variations of  $\delta\text{D}$ ,  $\delta^{13}\text{C}$ ,  $\Delta^{14}\text{C}$  and  $\delta^{18}\text{O}$  are related to solar activities.
- (3) The super-abundance of  $^{22}\text{Ne}$  has the solar origin.
- (4) Abnormalities of abundances in cosmic rays observed in recent years are caused by nucleosynthesis of non-thermal nuclear reactions.

#### 6 References

- [1] C. Y. Fan, et al., 18th ICRC, V3(1983)82-85
- [2] P. I. Abell, Nature, 297(1982)321
- [3] N. J. Shackleton, et al., Nature, 306(1983)319-322
- [4] W. Pollock, et al., J. Geophys. Res., V85, C10(1980)5555
- [5] J. R. Lawrence, et al., Nature, 296(1982)638-640
- [6] I. Friedman & G. I. Smith, Science, 176(1972)790
- [7] J. R. Lawrence & J. W. C. White, Nature, 311(1984)558
- [8] W. R. Webber & S. M. Yushak, Ap. J., 275(1983)391-404
- [9] W. R. Webber, 17th ICRC, V2(1981)261-264
- [10] E. Möbius & D. Hovestadt, IAU Symp. No. 94, <<Origin of Cosmic Rays>>(1980)395
- [11] M. Stuiver & P. D. Quay, Science, 207(1980)11



TYPE III SOLAR RADIO BURSTS AND  $^3\text{He}$ -RICH EVENTS

D. V. Reames and R. G. Stone  
NASA/Goddard Space Flight Center,  
Greenbelt, MD 20771 USA

## ABSTRACT

We investigate the kilometric radio data for  $^3\text{He}$ -rich events during the 1979-82 time period. Type III bursts are present for each event as expected from the previous electron/ $^3\text{He}$ -event association. A list of identified solar events is presented.

1. Introduction The association of solar  $^3\text{He}$ -rich events and non-relativistic electron events by Reames, von Rosenvinge and Lin (RvL, 1985) allowed the precise timing and velocity dispersion of the electron data to be used to identify the solar events responsible for the acceleration of particles with such anomalous isotopic abundances. However, these non-relativistic electron data are only available for the first 15 months of the ISEE-3 mission while many of the larger and more interesting  $^3\text{He}$  events occurred during the next several years of the mission. Fortunately, these same electrons are responsible for the rapidly drifting radio features called Type III bursts as they propagate at high velocity through the decreasing density of the interplanetary medium.

In this paper we show the relationship between the Type-III radio observations and the particle data in  $^3\text{He}$ -rich events and then use this association to identify the source region for many of the events.

2. Observations and Analysis The helium observations described in this paper were obtained with the very-low-energy telescope (VLET) in the GSFC cosmic-ray experiment on ISEE-3. In a few events it was possible to observe energetic (0.25 to 2 MeV) electron increases in the high-energy telescope of the same experiment.

The kilometric radio data used to study the interplanetary portion of the Type III radio emissions were obtained from the Radio Astronomy Experiment aboard ISEE-3. These radio observations provide not only timing of the electron release at the sun but also directional information that can track the electron population in interplanetary space and locate the solar longitude of the source within 10 to 20 degrees.

A list of  $^3\text{He}$ -rich time periods (Kahler et al., 1985) was re-examined for well-defined particle increases during the Dec. 1979 to Aug. 1982 study period. Dynamic radio spectra and single-frequency time histories were then examined during each of these events for the related Type III emission and the onset

times and spectral characteristics of the events were determined.

In Figure 1 we show the particle and radio data for two  $^3\text{He}$  time periods in 1982. Two events are seen in Fig. 1a, the Type III emission for the first event begins at 0533-0536 UT on June 25. There is no obvious increase in the energetic electrons from this event but the 2.2 - 3.4 MeV/AMU He nuclei begin to increase at 0745 and the 1.3 - 1.6 MeV/AMU nuclei arrive at 0830. The second event in Fig 1a begins in the radio data at 1945 and is seen minutes later (particle data are averaged in 15-min intervals) in the energetic electron data but He-nuclei from the event are not seen until after the data gap at about 2330.

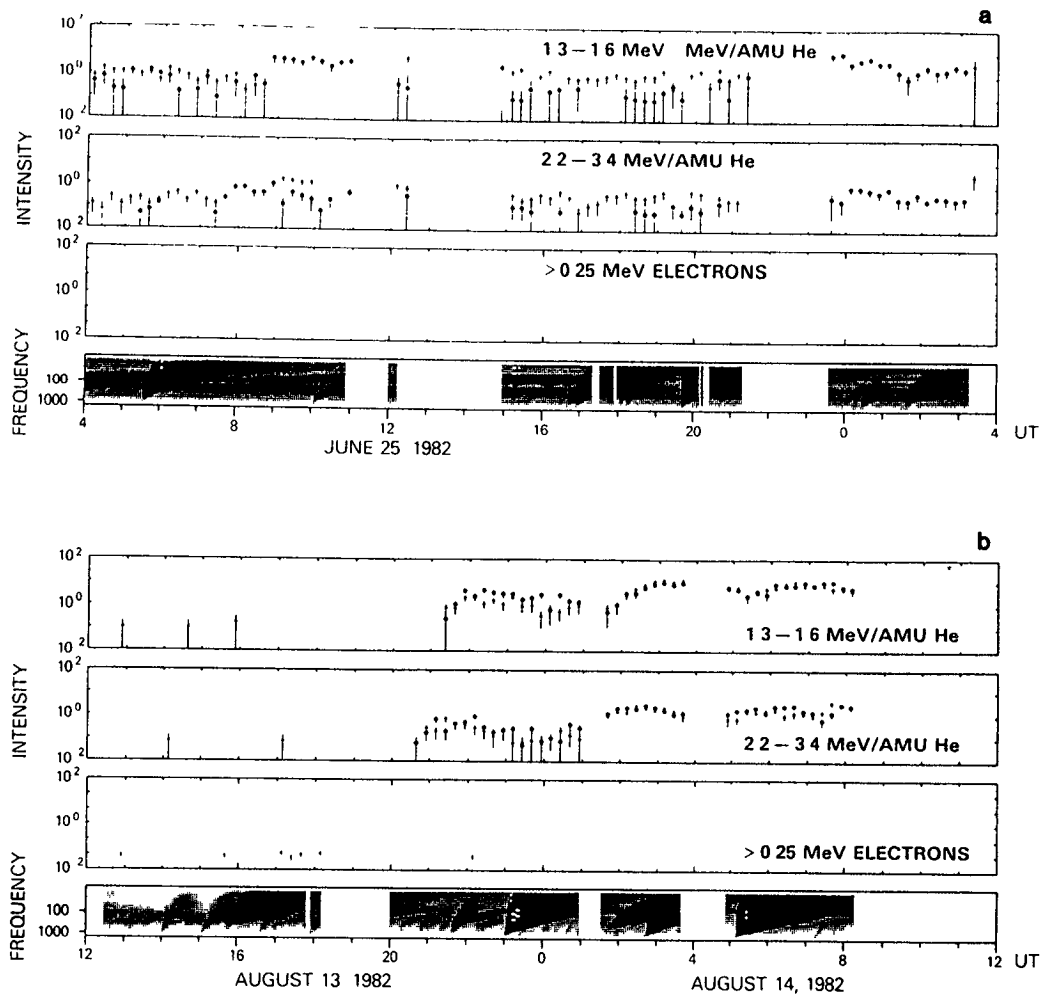


Fig. 1 Dynamic radio spectra and electron and He time histories for (a) Jun 25-26, 1982 and (b) Aug 13-14, 1982.

In Fig. 1b we show the striking series of  $^3\text{He}$ -rich events on Aug 13 - 14, 1982 that include the gamma-ray event (also  $^3\text{He}$  rich) at 0506 on Aug 14. The first Type-III event, is masked by the ubiquitous data gap at 1800-2000. Helium in the two energy intervals arrive at 2030 and 2115. The next three events beginning in the radio data at 2302, 0241 and 0509 each inject energetic electrons that are seen at 1 AU, and each inject fresh He nuclei that are observed after they propagate to 1 AU 2-3 hrs later as described by RvL (1985). Only the higher-energy He nuclei are seen from the large gamma-ray event before the data gap; all energies are seen again at 1200, just off the plot.

Note the difference in size and character of the Type III dynamic spectra in Fig. 1b for those events that contribute electrons and He at 1 AU and for those that do not. The other, weaker events in the same time period drift slowly to low frequencies because they lack sufficient intensities of faster, more-energetic electrons that would propagate outward more rapidly. Lacking energetic electrons, these events also lack measurable intensities of  $^3\text{He}$  (see also Reames and Lin, 1985).

Note also the quiet conditions in the particle observations prior to the first Aug 13 event. During the first 6 hrs in Fig 1b (excluding data gaps seen as white areas in the radio data) only 5  $^4\text{He}$  particles enter the telescope in both energy bands. In fact, no  $^3\text{He}$  particles enter the telescope in the 24-hr period prior to the first event.

The major  $^3\text{He}$ -rich events in the Dec 1979 to Aug 1982 for which we can identify the likely radio onset time are shown in Table 1. Also shown are the metric-radio and H-alpha flare data for most of the events. Many of the events occur in groups from the same active region, a fact that greatly simplifies their identification. In a few cases, where other candidate events do exist, they are always smaller events from the same active region.

3. Conclusion In conclusion we have shown that the solar electron- $^3\text{He}$  event association can be extended considerably by use of the kilometric radio data. Each  $^3\text{He}$ -rich event we examined was found to have a candidate Type III event and in most cases an unambiguous identification could be made. Of course these data do not provide the continuous and direct extrapolation of the velocity dispersion provided by the direct observation of non-relativistic electrons. On the other hand, the directional capability of the radio experiment provides the added spatial information that was only partially exploited in this work.

The prevalence of multiple events, usually with different isotope ratios, from the same solar active region is, once again, a striking result of this study. Each event is itself composed of groups at much higher time resolution in the radio data.

Table 1. Type III and Flare Associations of  $^3\text{He}$ -Rich Events

Date	1.3 He		2MHz Time	Metric		Flare		
	Onset	3/4		Time		Time	Site	Imp.
1979 Dec 14	2000	1.5	1552	1550	2GG	1553	N10W51	1B
			-1605	-1559		-1643		
1980 Nov 9	1930	0.9	1621	1620	3G	1621	S14W44	-N
				-1623		-1633		
Nov 10	0000	1.4	2035	2033	2GV	2028	S12W48	-N
				-2035		-2054		
Nov 10	0830	1.8	0448	0448	2GV	0446	S09W51	-N
				-0449		-0508		
Dec 16	1830	0.5	1455					
1981 Sep 15	2315	1.2	1935	1933	3GGV			
				-1937				
Nov 20	1330	0.2	1045	1041	2GG	several		
				-1043				
1982 Mar 10	1615	>1.4	gap	1220	3GG	1213	S06W32	1B
				-1255		-1308		
Mar 10	2300	0.7	1845	1844	3GGV	1845	S06W34	2B
				-1850		-1908		
Jun 25	0830	0.3	0533	0530	3SIS	0528	N13W50	1B
			-0536	-0535		-0615		
Jun 25	2330	0.4	1945	1944	3GGV	1941	N17W56	2B
				-1945		-2010		
Jun 30	1315	>1.0	0915					
Aug 13	2130	2.0	gap	1813	2GG			
				-1820				
Aug 14	0200	0.8	2302	2259	3GV	2301	N13W59	-N
				-2303		-2334		
Aug 14	0600	1.2	0241	0238	2GV	0237	N11W60	1B
			-0245	-0244		-0315		
Aug 14	0800	0.2	0509	0506	3GV	0507	N11W62	1B
				-0515	II	-0525	gamma-ray	

The event identifications begin to show a link between the impulsive electron-rich  $^3\text{He}$  events and the impulsive electron-rich solar gamma-ray events with the Aug 14 event.  $^3\text{He}$  has been observed in two other gamma-ray events by Van Hollebeke et al. (1985). The distinction between particle events with impulsive and long-duration X-ray events has been clearly demonstrated by Cane et al. (1985).

#### References

- Cane, H. V., R. E. McGuire and T. T. von Rosenvinge, 1985, XIX ICRC paper SH 1.2-12 and *Astrophys. J.* (to be published).  
 Kahler, S. et al., 1985, *Astrophys. J.* **290**, 742.  
 Reames, D. V., and R. P. Lin, 1985, XIX ICRC paper SH 2.2-5.  
 Reames, D. V., T. T. von Rosenvinge and R. P. Lin, 1985, *Astrophys. J.* **292**, 716.  
 Van Hollebeke, M. A. I., F. B. McDonald and J. H. Trainor, 1985, XIX ICRC paper 2.2-3.

SOLAR SOURCE REGIONS OF  $^3\text{He}$ -RICH PARTICLE EVENTS

S.W. Kahler  
Emmanuel College, Boston, Massachusetts 02115 USA

R.P. Lin  
Space Sciences Laboratory, University of California  
Berkeley, California 94720 USA

D.V. Reames  
Laboratory for High Energy Astrophysics, Goddard Space Flight Center  
Greenbelt, Maryland 20771 USA

R.G. Stone  
Laboratory for Extraterrestrial Physics, Goddard Space Flight Center  
Greenbelt, Maryland 20771 USA

M. Liggett  
Big Bear Solar Observatory, California Institute of Technology  
Pasadena, California 91125 USA

## ABSTRACT

We use  $\text{H}\alpha$ , X-ray, and metric and kilometric radio data to examine the solar sources of energetic ( $\sim 1$  MeV/nucleon)  $^3\text{He}$ -rich particle events observed near earth in association with impulsive 2 to 100 keV electron events. Each  $^3\text{He}$ /electron event is associated with a kilometric type III burst belonging to a family of such bursts characterized by similar interplanetary propagation paths from the same solar active region. The  $^3\text{He}$ /electron events correlate very well with the interplanetary low frequency ( $\sim 188$  kHz) radio brightnesses of these events, but progressively worse with signatures from regions closer to the Sun. When  $\text{H}\alpha$  brightenings can be associated with  $^3\text{He}$ /electron events, they have onsets coinciding to within 1 min of that of the associated metric type III burst but are often too small to be reported. The data are consistent with the earlier idea that many type III bursts, and now, by implication, the  $^3\text{He}$ /electron events, are due to particle acceleration in the corona, well above the associated  $\text{H}\alpha$  and X-ray flares.

1. Introduction. It is now clear that  $^3\text{He}$ -rich energetic particle events are distinguished from the solar energetic particle (SEP) events of greater fluxes and energies not only by their anomalous He composition, but also by their lack of association with metric type II bursts and coronal mass ejections (Kahler et al. 1985). A comparison of 12  $^3\text{He}$ -rich events with impulsive 2 to 100 keV electron events suggests that  $^3\text{He}$  ions are impulsively accelerated and injected into interplanetary space along with the electrons (Reames et al. 1985). The low fluxes and slow speeds of the  $E \sim 1$  MeV/nucleon  $^3\text{He}$  ions make injection times uncertain, but the close association of the particle events with fast-drift type III radio bursts provides the precision of timing needed to make the association of the particle events with solar phenomena.

To learn more about the sources of these events we examine the characteristics of the H $\alpha$  flares and type III bursts associated with the 12  $^3\text{He}$ -rich events studied by Reames et al. (1985)

**2. Observations and Analysis.** The times of the 12 events are given in Table 1. Several of these events occurred on the same day and in these cases are associated with H $\alpha$  flares in the same active region. In each case we give the time of the onset and the maximum reported burst size of the associated metric type III radio burst. The approximate flare sites and McMath region numbers, based on both reported H $\alpha$  flares and inspection of H $\alpha$  patrol films, are also listed. In three cases we give alternative suspected McMath regions in parentheses. All H $\alpha$  events were subflares except for the November 8 1B flare.

Each  $^3\text{He}$ /electron event was associated with a prominent kilometric type III burst observed with the Meudon/GSFC solar radio experiment on ISEE-3. An examination of the kilometric data during the few hours before and after the type III burst reveals that that burst is one of a family of such bursts, all of which show nearly identical solar elongation angles as a function of radio frequency. This suggests that the energetic electrons producing the bursts traverse similar paths from a single solar region through the interplanetary medium. Figure 1 shows an example of such bursts during a 6 hr interval on 1979 August 14. We have listed in Table 1 the number of prominent kilometric type III bursts in each such family during an 18 hr period around the time of the  $^3\text{He}$ /electron burst. The last column gives the number of bursts possibly associated on the basis of the timings with listed H $\alpha$  flares in the active region presumed to be the source of the  $^3\text{He}$ /electron event. Numbers in parentheses are the numbers of bursts possibly associated with listed H $\alpha$  flares in the alternative active regions for the three dates for which the active region is in some doubt.

TABLE 1							
Date	Type III Start UT	Class <sup>e</sup>	Approx. Location	H $\alpha$ Onset UT	McMath Region	Total km type III	Total with H $\alpha$ flares
1978							
Nov 8	1751	3GG	N18 E12	1751	643	2	2
Nov 27	2056	3GG	N26 W47 <sup>a</sup>	2055	672 (673)	6	0 (4)
Dec 26	1319 <sup>b</sup>	-	S21 W41 <sup>a,d</sup>	--	721	4	0
Dec 26	2122	WNG <sup>c</sup>	S21 W45 <sup>a</sup>	2104	721		
1979							
Feb 10	1818	3GG	N13 W23 <sup>a</sup>	< 1800	807 (808)	6	2 (1)
May 17	0558	2G	S35 W78 <sup>a</sup>	0551	996 (010)	13	3 (0)
Aug 14	1728	3GG	S18 W45	1728	205	4	2
Aug 14	2048	3GG	S17 W48	2048	205		
Sept 6	0906	2GG	N20 W62	0906	252	10	5
Sept 6	1148	3GG	N18 W67	1148	252		
Sept 6	1332	3GG	N16 W63	1332	252		
Sept 6	1851	2GG	N16 W65 <sup>a</sup>	1850	252		

<sup>a</sup> flare not listed in SGD, but found in visual inspection of H $\alpha$  films.

<sup>b</sup> start time of 1980 kHz burst.

<sup>c</sup> weak intermittent group.

<sup>d</sup> no confirmation with optical data.

<sup>e</sup> GG: > 10 type III bursts; G: < 10 type I&I bursts.

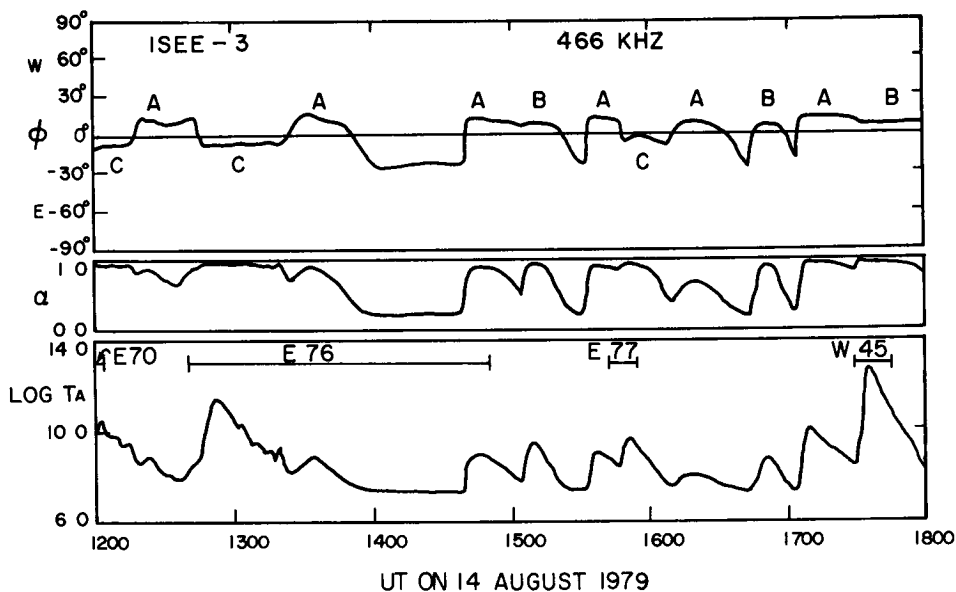


Figure 1. 466 kHz data from 1979 August 14. Three families of bursts labeled A, B, and C were present during the 6-hr interval. B events were associated with McMath 205.  $\phi$  is the solar elongation angle;  $\alpha$  a measure of the source size, with 1 being a point source; and  $T_A$  the antenna temperature. Associated H $\alpha$  flare reports are also shown.

In two of the three events with questionable active region associations we see that the H $\alpha$  flare associations of the alternative regions are worse than for the preferred active regions, although the statistics are limited. Using only these data, we could have selected the preferred region for all the  $^3\text{He}$ /electron events except for the November 27 event and the two on December 26. In the latter case no choice could be made. On the other hand, by simply looking for listed H $\alpha$  flares at well connected longitudes, we would have misidentified the source regions in two or three cases.

To get a better idea of the signatures of the  $^3\text{He}$ /electron events, we have compared reported H $\alpha$  flares, metric type III bursts, and antenna temperatures of the 1980 and 188 kHz bursts for the kilometric bursts with and without  $^3\text{He}$ /electron events. We omit the large sample of events on May 17, few of which are associated with H $\alpha$  flares or metric type III bursts. The results are shown in Figure 2. The contrast between the two groups increases as we consider first the H $\alpha$  flares and then the progressively lower frequencies of the type III bursts. At 188 kHz the logs of  $T_A$  of all but one of the 12  $^3\text{He}$ /electron events exceeded 10.5. On the other hand, this value was exceeded by only 3 of the 21 kilometric type III burst group.

**3. Discussion.** Each kilometric burst family is characterized by the degree of its association with reported metric type III bursts and H $\alpha$  flares as shown in Table 1. The families of November 8, August 14, and September 6 are well associated, while the others are not. This lack of observed associated H $\alpha$  activity with several  $^3\text{He}$ /electron events

suggests a coronal origin for the energetic  $^3\text{He}$  ions and electrons. Figure 1 shows that the correlation between the occurrence of a  $^3\text{He}$ /electron event and a solar/interplanetary event increases with increasing distance of the solar/interplanetary event from the sun. This suggests that  $\text{H}\alpha$  activity may have little to do with the acceleration of the  $^3\text{He}$  ions and electrons other than to reflect indirectly the presence of the overlying event, presumably as a result of the precipitation of some fraction of the energized particles as suggested by Kane et al. (1974). We also found a close coincidence between onsets of metric type III bursts and onsets of associated  $\text{H}\alpha$  and X-ray flares suggesting that the initial activity of the  $^3\text{He}$ /electron events begins in the high corona. Observations of type III emission from interplanetary electron beams are complicated by factors involving generation (Lin et al. 1981) and propagation of the bursts, so the situation may prove to be more complex.

4. Conclusions. Each  $^3\text{He}$ /electron event is associated with a kilometric type III burst which appears as a member of a family of bursts sharing similar interplanetary propagation paths. The members of each family differ from each other in their associated antenna temperatures at different frequencies and in their metric type III and  $\text{H}\alpha$  flare associations. In our study the best empirical indication of the occurrence of a  $^3\text{He}$ /electron event proved to be a high antenna temperature at 188 kHz. Reported  $\text{H}\alpha$  flare observations are a poor guide to the occurrence or origin of these events and in some cases are misleading, perhaps because of inaccurate reporting. The poor association of the  $^3\text{He}$ /electron events with  $\text{H}\alpha$  flares suggests a high coronal origin for at least some of the events.

Acknowledgements. This work was supported at Emmanuel College by AFGL Contract AF 19628-82 0039, at GSFC/University of Maryland by NASA grant HGR 21-002316, and at the University of California, Berkeley in part by NASA grant NAG 5-376.

#### REFERENCES

- Kahler, S. et al. 1985, *Ap. J.*, **290**, 742.  
 Kane, S.R., et al. 1974, *Solar Phys.*, **38**, 483.  
 Lin, R.P., et al. 1981, *Ap. J.*, **251**, 364.  
 Reames, D.V., et al. 1985, *Ap. J.*, in press.

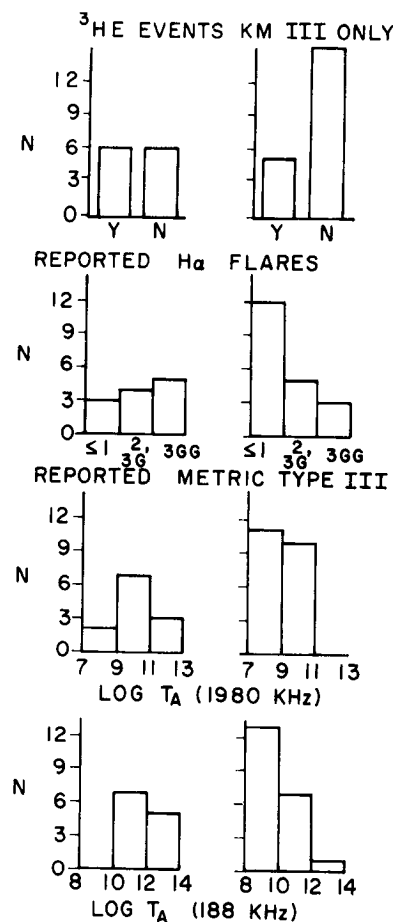


Figure 2. Histograms of  $\text{H}\alpha$  flares, metric type III bursts and  $\log T_A$  for kilometric type III bursts with and without  $^3\text{He}$ /electron events.



$^3\text{He}$  IN SOLAR NON-RELATIVISTIC ELECTRON EVENTS

D. V. Reames  
 NASA/ Goddard Space Flight Center, Code 661,  
 Greenbelt, MD 20771 USA

and

R. P. Lin  
 Space Sciences Laboratory, University of California,  
 Berkeley, CA 94720 USA

## ABSTRACT

We report on a systematic study of the presence of  $^3\text{He}$  in 187 solar electron events observed on the ISEE-3 spacecraft during a 9-month period beginning in Aug 1978.  $^3\text{He}$  is present in over half of the events and in 2/3 of events with 19 keV electrons, suggesting that  $^3\text{He}$  would be found in all electron events given somewhat greater collection efficiency.

1. Introduction In a recent paper Reames, von Rosenvinge and Lin (RvL, 1985) suggested a common origin for solar  $^3\text{He}$ -rich events and non-relativistic electron events. This association was based upon the close temporal relationship between the two species which share nearly scatter-free propagation from the sun and upon the observation of electrons in all of the  $^3\text{He}$ -rich event periods.

In this paper we examine the inverse relationship by asking the extent to which all solar electron events are accompanied by  $^3\text{He}$ . To this end, we have begun with a list of solar electron events observed by the Univ. of California experiment on the ISEE-3 spacecraft and, for each event, we have examined data from the very-low-energy telescope of the GSFC experiment on the same spacecraft for the presence of  $^3\text{He}$ .

2. Observations and Results The solar electron event list used in this study gives the onset time of each event and the intensity of electrons at 2 and 19 keV. Of the 187 events during the study period, 103 (55%) had measurable fluxes of 19 keV electrons, the remainder being observed only at lower energies. Where possible, the source of the event has been identified by the metric Type III radio emission and/or the H-alpha flare characteristics using Solar-Geophysical Data.

The measurements in RvL (1985) showed the 1.34-1.63 MeV  $^3\text{He}$  onset to occur 2-4 hrs after the electron onset and the  $^3\text{He}$  maximum to occur 1-2 hrs later. We therefore scanned the hourly-averaged  $^3\text{He}$  data during the 8-hr interval from 2 to 10 hrs after the electron onset and recorded the  $^3\text{He}$  intensity. This technique allowed us to press for the maximum sensitivity to  $^3\text{He}$  without introducing an unacceptable number of spurious events

from  $^3\text{He}$  background or from recounting multiple events. The  $^3\text{He}$  background estimated at about one particle every 3-4 days would be expected to contribute 2 to 3 spurious events out of the 85 observed.

In 34 (18%) of the 187 events it was not possible either to observe or to set meaningful limits on the  $^3\text{He}$ , usually because of a large particle event in progress but also occasionally because of data gaps. Of the subset of 103 events with 19-keV electrons, 17 were similarly excluded. The remaining events, 153 total and 86 with 19-keV electrons, are categorized by their  $^3\text{He}$  content in Table 1. In Table 1 we see that over half (56%) of the electron events have  $^3\text{He}$  and that fraction jumps to 2/3 (66%) for events with 19-keV electrons.

Table 1  $^3\text{He}$  in Electron Events

	$^3\text{He}$	no $^3\text{He}$	total
All electron events	85(56%)	68(44%)	153
19-keV elect events	57(66%)	29(34%)	86

We explore the  $^3\text{He}$  association as a function of electron intensity and spectral index in Tables 2 and 3. Here the highest electron intensities and flattest spectra show a high probability of  $^3\text{He}$  association. Otherwise, the correlation with intensity is weak, especially for 2-keV electrons. For those events with  $^3\text{He}$ , the  $^3\text{He}$  intensity is plotted versus the electron intensities in Figure 1. There appears to be no correlation with 2-keV electrons in Fig. 1a, however, a broad correlation seems to exist with the 19-keV electrons in Fig. 1b but the limited dynamic range of the instruments makes its observation difficult.

Table 2  $^3\text{He}$  Observation vs. Electron Intensity

(a) 2-keV Electrons			(b) 19-keV Electrons		
Intensity (x1000)	$^3\text{He}$	no $^3\text{He}$	Intensity	$^3\text{He}$	no $^3\text{He}$
>100	7(78%)	1	>10	9(78%)	1
10-100	28(55%)	23	1-10	26(65%)	14
1-10	36(54%)	31	0.1-1	22(61%)	14
<1	14(52%)	13	Total	57(66%)	29
Total	85(56%)	68	None(<0.3)	28(42%)	39

Table 3  $^3\text{He}$  Observation vs. Electron Spectral Index

Index	$^3\text{He}$	no $^3\text{He}$
<2.0	1	0
2.0-2.9	9(69%)	4
3.0-3.9	22(59%)	15
4.0-4.9	15(68%)	7
>5.0	2(50%)	2

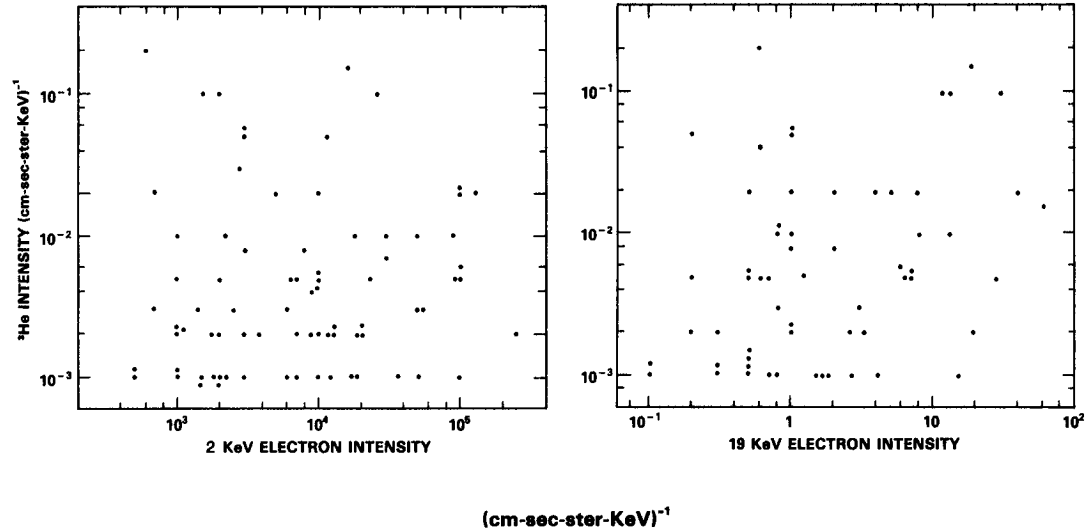


Fig. 1  $^3\text{He}$  vs. electron intensities for two electron energies.

With Figure 2 we address the question of the relative importance of electron intensity versus spectral index in determining the  $^3\text{He}$  intensity. Symbols on the plot denote the most intense 13  $^3\text{He}$  events, other  $^3\text{He}$  events, and events with no  $^3\text{He}$ . The tendency of the more  $^3\text{He}$ -rich events to lie toward the top of the plot (greater 19-keV intensity) is stronger than their tendency toward flatter spectra. Of the 23 events with 19-keV electron intensity above 3 ( $\text{cm}^2\text{-ster-sec-MeV/AMU}$ ) $^{-1}$  (30% of plotted data), 19 (83%) exhibit  $^3\text{He}$  and 8 (62%) of the 13 largest  $^3\text{He}$  events are found in this region.

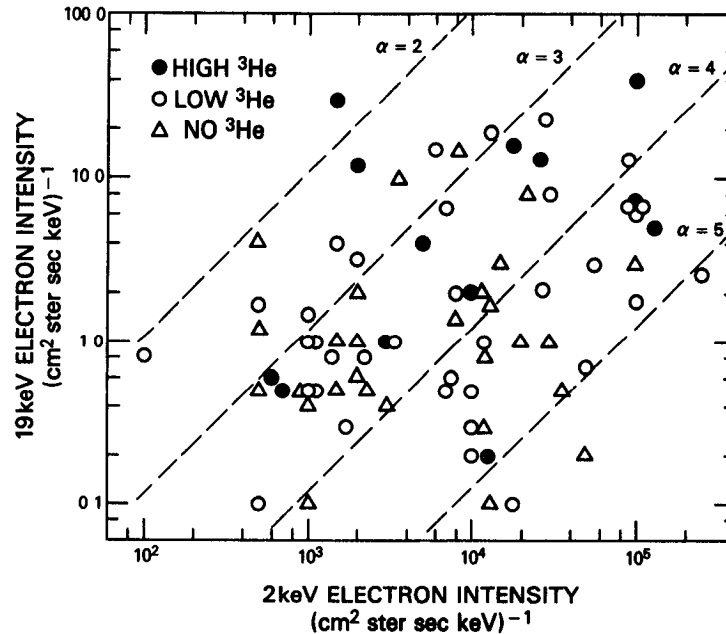


Fig 2. Electron intensity cross-plot with  $^3\text{He}$  content shown for each event. Electron power spectral indices are diagonal lines.

3. Relation to Solar Events The results of the preceding section lead to the conclusion that  $^3\text{He}$ -rich events are not unusual, but are, in fact, a further manifestation of the same mechanism that accelerates electrons in the impulsive phase of solar events. Our ability to associate these particles in space with the corresponding radio, optical and X-ray features at the sun depends upon the size and character of the events.

We have used our preliminary radio and optical event associations in table 4 to show how the likelihood of identification of such events depends upon the presence of  $^3\text{He}$  or 19-keV electrons in the event. We have included all radio events in the Type III column even though a small percentage of them are Type I.

Table 4 Number of Radio and Flare Associations for Events with Various Properties

	Type III	Flare	Total
$^3\text{He}$	61(72%)	40(47%)	85
No $^3\text{He}$	<u>41(61%)</u>	<u>18(26%)</u>	<u>68</u>
Total	102(66%)	58(40%)	153
19-keV Electrons	84(82%)	60(58%)	103
No 19-keV Electrons	<u>41(49%)</u>	<u>16(19%)</u>	<u>84</u>
Total	125(67%)	76(41%)	187

Since metric Type III radio emission is a signature of electron ejection from the solar corona, it is not surprising to find a good correlation (67%) for all electron events. This correlation is improved substantially for events with 19-keV electrons (82%) and slightly for the  $^3\text{He}$  events.

The correlation with H-alpha flares is not as good as with Type III events but again improves with both subsets of particle events. Particles accelerated on open magnetic field lines in the high corona may not have adequate access below the corona to produce significant H-alpha or X-ray events.

Of the 61 radio associations of the  $^3\text{He}$  events, 6 are Type I events and 55 Type III; 8 of the latter are Type III, V. Most of the events are groups (G or GG) and about half have radio intensity 2 or 3. None of the 61 events show Type II or IV emission or other shock-related features.

The 40 flares associated with the  $^3\text{He}$  events show the solar longitude distribution of typical impulsive well connected events with only 8 of the 40 in the eastern hemisphere. Two of the flares are importance 2, 6 are importance 1 and the remaining 32 are subflares.

#### REFERENCES

Reames, D.V., T.T. von Rosenvinge and R.P. Lin, 1985, *Astrophys. J.* 292, 716.

# ELEMENTAL ABUNDANCE DIFFERENCES BETWEEN NUCLEI ACCELERATED IN CIR SHOCKS AND SOLAR FLARES

W.F. Dietrich and J.A. Simpson

Enrico Fermi Institute, University of Chicago,  
Chicago, Illinois 60637, USA

**ABSTRACT.** By measuring the ratios of nuclear abundances H/He, CNO/Fe-group and the Fe-group/He for 51 passages of Corotating Interaction Regions (CIRs) at 1 AU, and also by measuring these ratios from 620 solar flares in the energy range 0.6 to 4 MeV per nucleon, it is concluded that CIR shock acceleration alone does not change significantly these ratios from the values they have for solar system abundances or the solar wind. On the other hand, the solar flare ratios continue to reflect strong biases in the abundances, consistent with requirements for multi-stage acceleration processes at the Sun.

**1. Introduction.** It was discovered that hydrogen and helium nuclei are accelerated in the interplanetary medium in association with corotating interaction regions (CIRs) mainly beyond 1 AU (McDonald et al. 1976; Barnes and Simpson 1976) and that the corotating shocks associated with the CIRs are the site of the acceleration process (e.g. Barnes and Simpson 1976; Pesses et al. 1978). McGuire et al. (1978), Gloeckler et al. (1979) and Scholer et al. (1979) then showed that at 1 AU, CIRs accelerate nuclei over the element range of hydrogen to iron with relative abundances that tend to be different from typical abundance distributions observed at low energies in solar flare accelerated nuclei.

The evidence by Tsurutani et al. (1982) that CIR shock acceleration of ions is due to quasi-perpendicular shocks mainly beyond 1 AU now provides the opportunity to investigate further; 1) the origin of the local (interplanetary) "seed" ion population which is accelerated by CIRs, and; 2) the question of whether an interplanetary quasi-perpendicular shock can reproduce the kinds of preferential enhancements of abundances frequently observed for solar flare accelerated nuclei. This latter question has a strong bearing on whether, in solar flares, shocks alone can account for the observed enhancements, or whether, for example, the ions in the solar flare site undergo a preliminary stage of injection which biases the relative abundances. Our investigation includes the measurement of selected abundance ratios (e.g., H/He, CNO/Fe, and Fe/He) for 51 passages of CIRs at 1 AU during the period 1973-79. We also have determined these abundance ratios for 620 solar flares observed during 1973-84, of which a subset of 100 flares are observed to be <sup>3</sup>He-rich.

**2. Experimental Aspects.** Because the spectra of CIR accelerated nuclei have steep negative slopes and are restricted to energies below a few MeV per nucleon, their measurement by means of single dE/dx parameter analysis is difficult (e.g. McGuire et al. 1978). These difficulties are reduced in the case of the IMP 7 and IMP 8 Low Energy Telescope (LET; Simpson et al., 1974) which, in addition to a thin dE/dx detector has: a) a second yes/no detector providing particle range information, and; b) a 256 channel pulse height analyzer that spans the range H to Fe (which is in saturation). Pulse discriminator levels are set for fluxes of four

major nuclear groups, mainly H, He, CNO and Mg-Fe. The latter group, dominated by the iron flux will be referred to as the Fe-group ("Fe") in this report. The pulse height analysis enables us: 1) to independently measure the energy spectrum of He nuclei; 2) to evaluate any contamination of low Z particles by higher Z nuclei (which is an insignificant factor for the CIR composition measurements) and; 3) to normalize the fluxes of H, He, CNO, and "Fe" to abundance ratios for the same energy per nucleon. For CIRs the principal source of error in the "Fe" group abundances is statistical fluctuations, however for the CNO group and He abundances, the largest errors are systematic (i.e. from uncertainties in the count rate discriminator levels, the spectral slope, and uncertainties of range-energy relations at these low energies). For solar flares the "Fe" contamination appearing in the CNO fluxes is the most significant factor. Since the same instrument and method of analysis are employed in obtaining both CIR and solar flare abundances, the systematic errors mostly cancel when determining the ratios of abundances. Further details on the analysis will be published elsewhere.

The identification of intervals for CIR passage were mainly based on CIRs identified in previous publications (see e.g., Christon and Simpson, 1979; Tsurutani *et al.*, 1982) with the constraints that: 1) the flux for the He at low energy must reach a factor 6 above the prevailing background counting rate of 0.0015 He/s; 2) the magnetic field and solar wind measurements confirmed the presence of a CIR; and 3) a recurrence period of 27 days could be identified. Our investigations with IMP 7 and 8 at 1 AU assume, as do the reports of McGuire *et al.* (1978), Gloeckler *et al.* (1979), and Scholer *et al.* (1979) that the 1 AU observations of CIR abundances are the result of the inward flow of the ions (e.g. Marshall and Stone, 1977) from the CIRs beyond 1 AU.

### 3. Comparison of CIR and Solar Flare Accelerated Nuclei.

The abundance ratios of "Fe"/He versus H/He in the energy interval 0.6-4 MeV/n are plotted in Figure 1 for CIRs, all solar flares, and the subset <sup>3</sup>He-rich solar flares. Figure 2 is the corresponding plot for "Fe"/He versus CNO/He. The data from Figures 1 and 2 have been

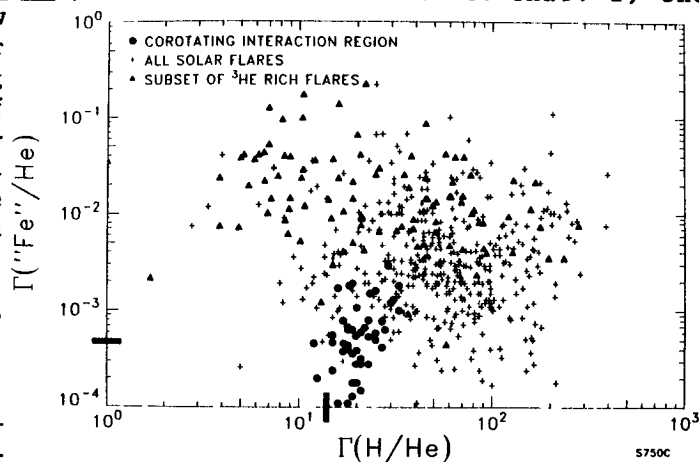


Figure 1

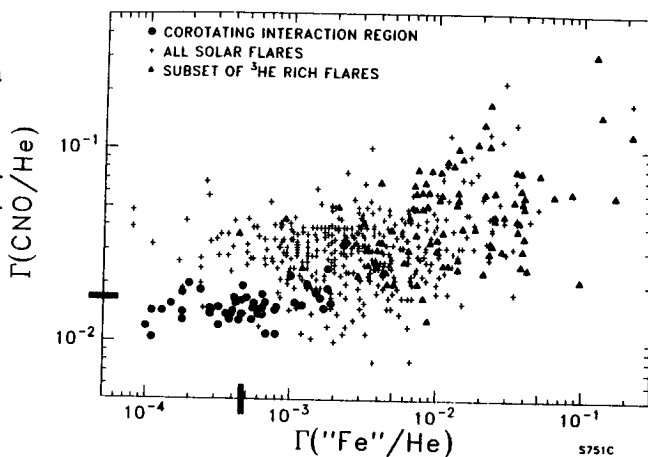


Figure 2

used to prepare the histograms in Figures 3 and 4. These plots reveal: 1) The range of variations for all 3 measured abundance ratios for CIRs (including experimental error) is seen in Figs. 1 and 2 to be small compared to that for the range of solar flare abundance ratios (i.e., the dynamic range of variation for CIRs is only a factor  $\sim 2$  for H/He and CNO/He and factor 30 for "Fe"/He, whereas the dynamic ranges for solar flare abundance ratios are 3000, 40, and 3000 for H/He, CNO/He and "Fe"/He, respectively). From the number distributions of the CIR H/He and "Fe"/He ratios in Figs. 3 and 4 we note the narrower distribution for the CIRs compared with the corresponding solar flare distributions. Unlike the case for solar flares, we have found no examples of large deviations from the mean abundance ratios for CIRs; 2) the mean H/He, CNO/He and "Fe"/He ratios for CIRs are 20, 0.015, and 0.00048 respectively, while the corresponding H/He, CNO/He and "Fe"/He ratios for flares are 52, 0.030, and 0.0028, respectively. The CIR average abundance ratios are close to the universal abundance ratios (Cameron, 1982) (marked as bars on the axes of Figs. 1 and 2) except the H/He ratio which is in somewhat better agreement with fast solar wind values. Average solar flare "Fe"/He abundances at 2-4 MeV/n are seen to be enhanced by a factor of six to seven over photospheric abundances, and He is seen to be depleted in solar flares relative to both H and CNO. In Fig. 1 and 2, very few solar flares ratios appear in the plot area occupied by the CIR data.

We have compared our results for the H/He, CNO/He and Fe/He ratios of CIR accelerated particles with previously reported abundance ratios in Table 1. We have converted published He/O ratios to a CNO/He ratio by using the the published CIR C/O ratios. Clearly our survey, when averaged over many CIRs, confirms the earlier published work based on relatively few CIRs and flares.

**4. Conclusions.** We find that: 1) for nuclei accelerated in corotating interaction region shocks the average values of the abundance ratios are close to the solar system abundances and are not inconsistent with the abundance ratios for the solar wind; 2) The variability of the abundance ratios for CIRs is more than an order of magnitude less than the variability observed in solar flares confirming McGuire *et al.* (1978); 3) there is no evidence for preferential enhancements of nuclear abundances in any CIR events.

From the above evidence we conclude that the "seed" nuclei for the CIR shock acceleration mechanism are ambient ions in the interplanetary medium with a composition which is similar to the solar system abundances. However, for solar flare nuclei we find, as reported by several

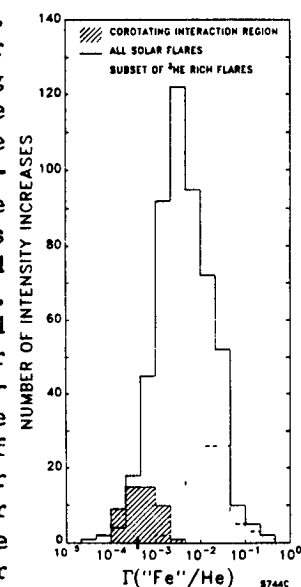


Figure 3

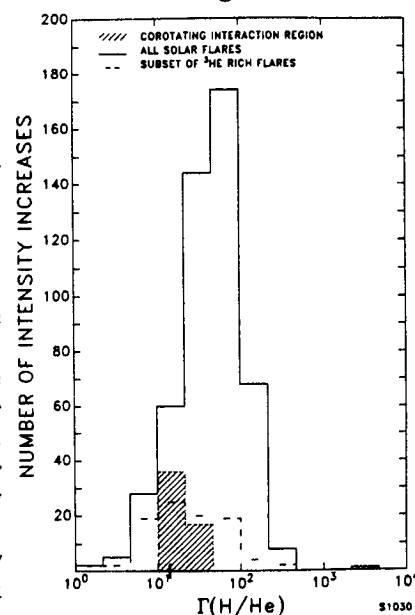


Figure 4

TABLE 1

Reference	Energy Range (MeV/n)	C/O	CNO/He $\times 100$	Fe/He $\times 10000$	p/He	Number of CIRs	Years
(7)	3.4 - 23.	$0.8 \pm .2$	$1.48 \pm .45^+$	NA	$22. \pm 5^*$	6	1973-1976
(9)	0.6 - 1.0	$0.91 \pm .03$	$0.98 \pm .045^+$	$7.1 \pm .6$	$11.9 \pm 0.2$	4	1974
		$0.90 \pm .07$	$0.80 \pm .084^+$	$1.8 \pm .6$	$11.2 \pm 0.2$	5	1976
(4)	0.3 - 5.0	$1.05 \pm .19$	$1.25 \pm .42^+$	$5.5 \pm 2.$	$16.6 \pm 3.5$	9	1974, 1976
This Work	0.6 - 4.0	NA	$1.5 \pm .25$	$5. \pm 3.$	$20. \pm 2.$	51	1973-1979
(2)		0.60	1.67	4.7	14.		

+ Ratios and errors calculated from C/O and He/O ratios and errors quoted in each paper.

\* Average of 17 events at 1.6-8.8 MeV/n

investigations, that the ambient source of nuclei reflects biases in the relative abundances of accelerated nuclei - i.e., preferential enhancements of some abundances. Thus, if shocks accelerate nuclei in solar flares, they probably represent the second stage of acceleration. The small variation in the CIR abundance ratios suggests that only shock acceleration is involved in the interplanetary medium, whereas the extreme variability of the solar flare ratios from solar flares points to a complex, multiple acceleration process.

5. **Acknowledgements.** We wish to acknowledge support of the staff in the Laboratory for Astrophysics and Space Research, particularly the aid given by S.P. Christon in identifying CIRs for this study. This work was supported in part by NASA Contract NAS 5-28422 and NSF Grant ATM 84-12382.

#### References

1. Barnes, C.W. and Simpson, J.A. 1976, Ap. J., **210**, L91.
2. Cameron, A.G.W., 1982, Essays in Nucl. Astrophysics, 23.
3. Christon, S.P., and Simpson, J.A., 1979, Ap. J. (Letters), **227**, L49.
4. Gloeckler, G., Hovestadt, D., Ipavich, F.V., and Mason, G.M. 1979, 16th ICRC, **5**, 368.
5. Marshall, F.E., and Stone, E.C., 1978, J. Geophys. Res., **83**, 3289.
6. McDonald, F.B., Teegarden, B.J., Trainor, J.H., Von Rosenvinge, T.T., and Webber, W.R. 1976, Ap. J. Lett., **203**, L149.
7. McGuire, R.E., Von Rosenvinge, T.T., McDonald, F.B. 1978, Ap. J., **224**, L87.
8. Pesses, M. E., Van Allen, J.A. and Goertz, C.K. 1978, JGR, **83**, 553.
9. Scholer, M., Hovestadt, D., Klecker, B., and Gloeckler, G. 1979, Ap. J., **227**, 323.
10. Simpson, J.A., Hamilton, D.C., McKibben, R.B., Mogro-Campero, A., Pyle, K.R., and Tuzzolino, A.J., 1974, JGR, **79**, 3522.
11. Tsurutani, B.T., Smith, E.J., Pyle, K.R., and Simpson, J.A. 1982, JGR, **87**, 7389.



THE HEAVY ION COMPOSITION IN  $^3\text{He}$ -RICH SOLAR FLARESG.M. Mason<sup>1</sup>, D.V. Reames<sup>2</sup>, D. Hovestadt<sup>3</sup> and T.T. von Rosenvinge<sup>2</sup><sup>1</sup>Dept. of Physics & Astronomy, Univ. of MD, College Park, MD 20742 USA<sup>2</sup>NASA/Goddard Space Flight Center, Greenbelt, MD 20771 USA<sup>3</sup>MPI fur Extraterrestrische Physik, 8046 Garching, FRG

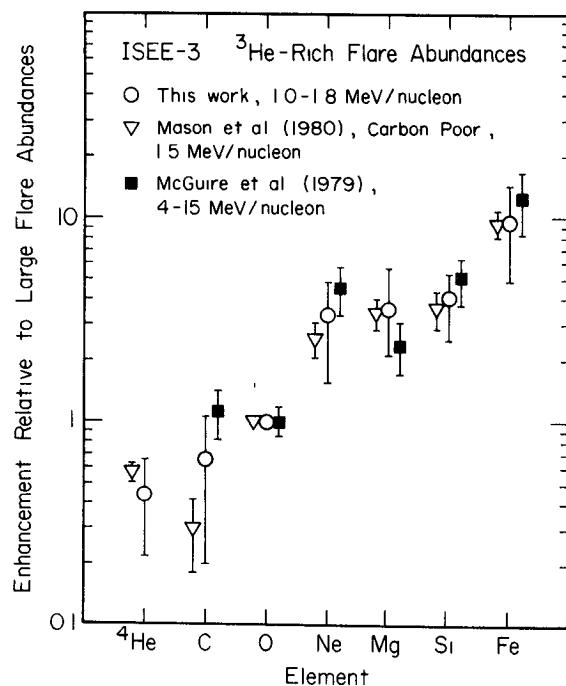
1. Introduction. It has been known for some time that  $^3\text{He}$ -rich flares show a tendency to be enriched in heavy ions (5), and that this enrichment covers the charge range through Fe (e.g. 3,8,10,14). The discovery of this association was responsible, in part, for the discarding of  $^3\text{He}$  enrichment models which involved spallation or thermonuclear reactions, since such models were unable to produce heavy nuclei enhancements (e.g. review in ref. 12). More attractive appeared to be plasma resonance models which offered the possibility of producing  $^3\text{He}$  and also heavy nucleus enrichments (e.g. 2,7). Previous studies of heavy nucleus enrichments in  $^3\text{He}$ -rich flares (8,10) have covered only a few, isolated cases, thereby precluding the identification of systematic features of these enrichments. In order to investigate this association more thoroughly, we present here results of a survey of heavy nucleus abundances observed in 66  $^3\text{He}$ -rich flares which occurred over the period October 1978-June 1982.

2. Observations. The measurements were carried out in interplanetary space using instruments on the ISEE-3 spacecraft.  $^3\text{He}$  and  $^4\text{He}$  data are from the Goddard VLET sensors (13), and the heavy nuclei abundances are from the MPI/UMD ULEWAT sensor (4). The flares studied, and their method of selection, have been described in reference 6. In the present study, considerable care was exercised to insure that the two instruments were properly intercalibrated (9).

Figure 1 shows the enhancements relative to large flare abundances (from ref. 8) for 32  $^3\text{He}$ -rich flares in which there were  $^4\text{He}$  flux increases. The energy ranges are 1.3-1.6 MeV/nuc for  $^4\text{He}$ , and 1.0-1.8 MeV/nuc for heavier ions. Although the enhancements are normalized to 0, the choice is arbitrary, and it can be seen from the figure that the enrichment increases with A or Z over the entire range  $^4\text{He}$  through Fe. Figure 1 includes data for three "carbon-poor" flares (8) and for a survey of 17 flares (10). Note the striking similarity of the enhancements reported in the three separate studies. Note also that the measurements in the figure cover the range 1-17 MeV/nuc, and that there is no evidence of an energy dependence in the abundance pattern--thus the composition appears to be a measure of the abundances in the pre-injection plasma, e.g. as in the model of Fisk (2).

The error bars for the new results in Figure 1 are not obtained from the averaging (as is the case in the earlier studies), but rather they show the range of values observed in 2/3 of the cases centered about the mean. Thus, the "1-sigma" errors in the present work give an idea of the spread of values observed over a number of flares.

In view of the large range of  $^3\text{He}/^4\text{He}$  enrichments (from  $\sim 10^3$  to  $>10^4$  times coronal values), one of the most surprising results of this survey was the discovery of a relatively narrow range of heavy nuclei enrichments. This can be seen from Figure 2, which shows histograms formed by least-squares fitting of each of 44 flares to the



84-40

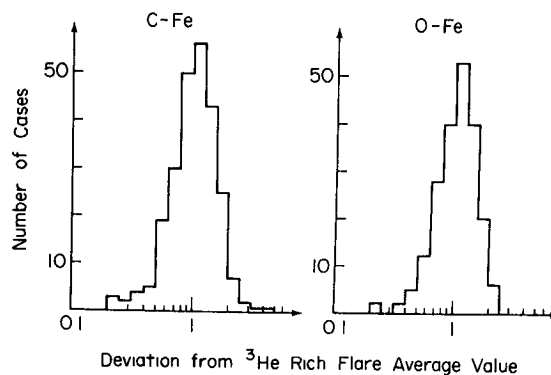
Figure 1

the same mechanism which causes the  $^3\text{He}$  enrichments, then we might expect a ratio such as  $\text{Fe}/\text{O}$  to correlate with the  $^3\text{He}/^4\text{He}$  ratio. Figure 3 shows that this is not the case: even though the  $\text{Fe}/\text{O}$  ratio is very large in these flares, the heavy least squares fit line in the figure has a slope of  $0.02 \pm 0.06$ , and thus we find no statistically significant correlation between the degree of Fe enrichment and the degree of  $^3\text{He}$  enrichment.

Flares showing extreme deviations from the average pattern may yield information about the acceleration mechanism(s). Therefore all the flares were examined for large  $\chi^2$  deviations from the average pattern. Only 4 of the 66 flares had significant deviations. The abundances in each of these is shown in Figure 4, where they are compared with large flare abundances (8) and the pattern from Fig. 1. Considering case (a) in the figure, the abundance anomaly is an enrichment of C by about 3 standard deviations compared with the  $^3\text{He}$ -rich flare pattern. This is the most

the abundance pattern shown in Fig. 1, and tallying the fractional deviations from the average values for each element. This fitting process results in histograms centered at 1.0, whose width is a measure of the deviations of individual elements from the average pattern (Fig. 1). Over the range C-Fe (left histogram) over 90% of the points fall within a factor of 2 of the mean, that is, between 0.5 and 2.0. Most of the large deviation points are from the element C, as can be seen from the right histogram, which shows fits over the range O-Fe, where 93% of the points fall within a factor of 2 of the mean.

If the heavy nucleus enrichment is caused by



84-47

Figure 2

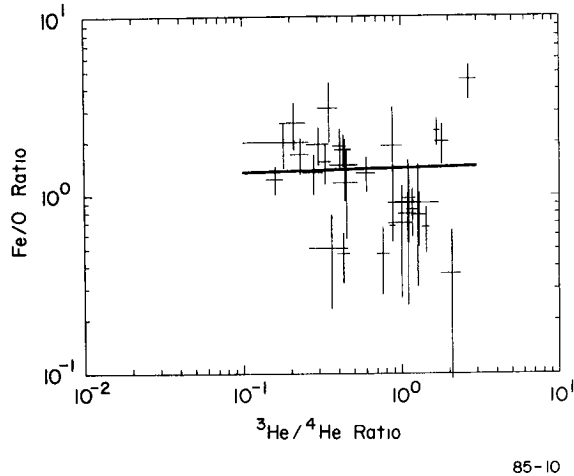


Figure 3

tant comments to be made about the search for deviations from the average pattern are: (1) such deviations are rather rare, and (2) when they occur, there is no trend for very large enhancements for single elements or limited ranges of elements.

**3. Discussion.** Figure 5 compares the heavy nucleus enrichment pattern observed here with predictions from several models. Panel (a) compares the present results with the calculations of ref. 7 for short (solid line) and long (dashed line) heating times. The fit is not particularly good, although a different set of model parameters might well improve it. Panel (b) shows a fit using a simple model (9) based on the Fisk mechanism. Although the fit in panel (b) is acceptable, it depends on a particular choice of plasma parameters which if varied slightly will

produce an enhancement pattern quite different from the result in our survey. In general, the plasma resonance models appear to need a very special set of parameter choices to yield the observed enrichments, and this is unsatisfying in view of the fact that virtually the same pattern appears from one flare to the next.

Figure 5(c) shows an enrichment pattern taken from the detailed calculations of Nakada (11) concerning the transport of heavy ions in the lower corona. Nakada's calculation includes effects of gravitational settling and thermal diffusion, assuming a temperature gradient of 1 K/cm at  $T = 10^5$  K. The line in Fig. 5(c) shows the range of enrichments (compared with the

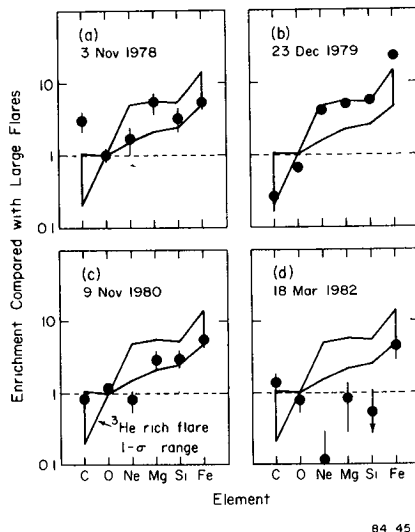
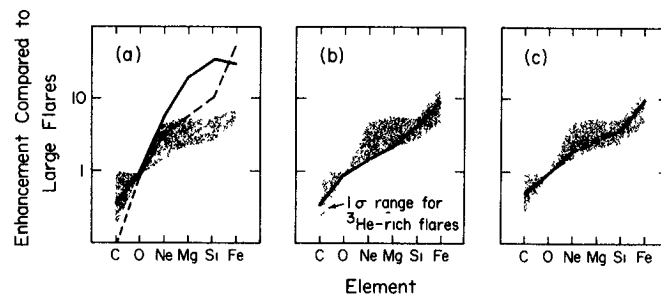


Figure 4

baseline photospheric composition) for the range  $5-9 \times 10^5$  K. The pattern is a surprisingly good fit to our results, and is all the more interesting because the mechanism in this case appears to produce basically the same result over a broad temperature range.

We interpret the observations presented here, along with previously reported work, to show that while a plasma resonance mechanism may account for the  $^3\text{He}$  enrichments observed in these flares, this mechanism does not appear to be an attractive one for explaining the heavy nuclei enrichments that are associated with these events. Rather, we suggest that the heavy nuclei enrichments are due to heavy ion enrichments in the ambient plasma at the sites where the  $^3\text{He}$  rich flares occur. We note that in plasma resonance models such as that of Fisk (2), a relatively high  $^4\text{He}/\text{H}$  ratio is required, and the same mechanism which produces this enhancement might also produce the heavy nucleus enrichments. Model calculations by Nakada (11) indicate that sites with such enrichments may routinely occur in the corona.



85-13

Figure 5.  $^3\text{He}$ -rich flare heavy nuclei enhancements (shaded areas) vs. model calculations: (a) Kocharov and Orishchenko, (b) "Fisk", (c) lower coronal enhancements from Nakada (1969).

4. Acknowledgements. We are grateful to the many individuals at GSFC, MPI and UMD who were responsible for the success of the ISEE-3 instruments. This work was supported by NASA under contract NAS5-28704, grants NGR 21-002-224/316 and NAGW-101, by the NSF under grant ATM-84-07546, and by the Bundesministerium fur Forschung und Technologie, contract RV 14-B8/74.

#### References

1. Anglin, J.D. *et al.* 1977, Plovdiv ICRC, 5, 43.
2. Fisk, L.A. 1978, *Ap.J.*, 224, 1048.
3. Gloeckler, G. *et al.* 1975, *Ap.J. (Letters)*, 200, L45.
4. Hovestadt, D. *et al.* 1978, *IEEE Trans. Geo. El.*, GE-16, 166.
5. Hurford, G.J. *et al.* 1975, *Ap.J. (Letters)*, 201, L95.
6. Kahler, S. *et al.* 1985, *Ap.J.*, 290, 742.
7. Kocharov, L.G. and Orishchenko, A.V. 1983, Bangalore ICRC, 4, 37.
8. Mason, G.M. *et al.* 1980, *Ap.J.*, 239, 1070.
9. Mason, G.M. *et al.* 1985, *Ap.J.* (submitted).
10. McGuire, R.E. *et al.* 1979, Kyoto ICRC, 5, 90.
11. Nakada, M.P. 1969, *Solar Phys.*, 7, 302.
12. Ramaty, R. *et al.* 1980, in "Solar Flares" (ed. P. Sturrock), 117.
13. von Rosenvinge, T.T. *et al.* 1978, *IEEE Trans. Geo. El.*, GE-16, 208.
14. Zwickl, R.D. *et al.* 1978, *Ap.J.*, 225, 281.

THE MEAN IONIC CHARGE OF SILICON IN  $^3\text{He}$ -RICH SOLAR FLARES

A. Luhn, B. Klecker, D. Hovestadt, E. Möbius  
 Max-Planck-Institut für extraterrestrische Physik  
 8046 Garching, F.R.G.

## ABSTRACT

In addition to the previously reported mean ionic charge of Iron in  $^3\text{He}$ -rich solar flares we have for the first time determined the average mean charge of Silicon for 22  $^3\text{He}$ -rich periods during the time interval from September 1978 to October 1979. The results indicate that the value of the mean charge state of Silicon is higher than the normal flare average by approximately 3 units and in particular it is higher than the value predicted by resonant heating models for  $^3\text{He}$ -rich solar flares.

1. Introduction. The  $^3\text{He}$  isotope was first measured as a constituent of solar energetic particle events in 1970 by Hsieh and Simpson <sup>1</sup>. Following this discovery, it has been firmly established by now that there exists a class of generally small solar flare events in which the abundance of the  $^3\text{He}$  isotope relative to  $^4\text{He}$  in solar cosmic rays is greatly enhanced relative to the normal solar abundance ratios. Enrichments of more than four orders of magnitude have been observed, leading to a  $^3\text{He}/^4\text{He}$  ratio of  $\geq 1$ . These unusually high enrichment factors can best be explained by a two-stage acceleration process with a first step highly selective in mass per charge and a second step acting only upon particles above a certain threshold in rigidity or velocity. Several plasma heating processes have been proposed as the first stage (2,3,4,5), which preferentially heat certain minor ion species like  $^3\text{He}$ . The effect of the preferential heating will be most pronounced in the tail of the ion distribution function. The second stage acceleration process will then (apart from introducing additional abundance changes, see <sup>6</sup>) mainly reflect the abundance ratios in the tails of the ion distribution functions. In all of the proposed heating processes the ionic charge states play a critical role for the largest attainable particle velocity and/or the heating rate. Measurements of the charge states of energetic ions in  $^3\text{He}$ -rich events are therefore crucial in understanding the nature of the enrichment process. For recent reviews of observational and theoretical aspects of  $^3\text{He}$ -rich flares see e.g. <sup>7,8</sup>.

2. Instrument and Data Analysis. The data presented in this paper have been obtained during the period from September 1978 to October 1979 with the Max-Planck-Institut / University of Maryland ULEZEQ Sensor onboard the ISEE-3 spacecraft (see also <sup>8</sup>). The instrument is described in more detail by Hovestadt et al. <sup>10</sup>. We performed the charge analysis of Fe and Si for 22 periods rich in  $^3\text{He}$  as determined from a systematic study of the composition of solar energetic particles with our wide angle particle telescope (ULEWAT) on the same spacecraft. We selected periods with a  $^3\text{He}/^4\text{He}$  ratio of  $\geq 0.1$ , lasting more than one day. The average  $^3\text{He}/^4\text{He}$  ratio of all 22 periods is 0.227. The energy range for which the charge analysis for Si and Fe is performed, is 0.55-3.0 and 0.34-1.8 MeV/N respectively. This represents a compromise between elemental and charge resolution and counting statistics.

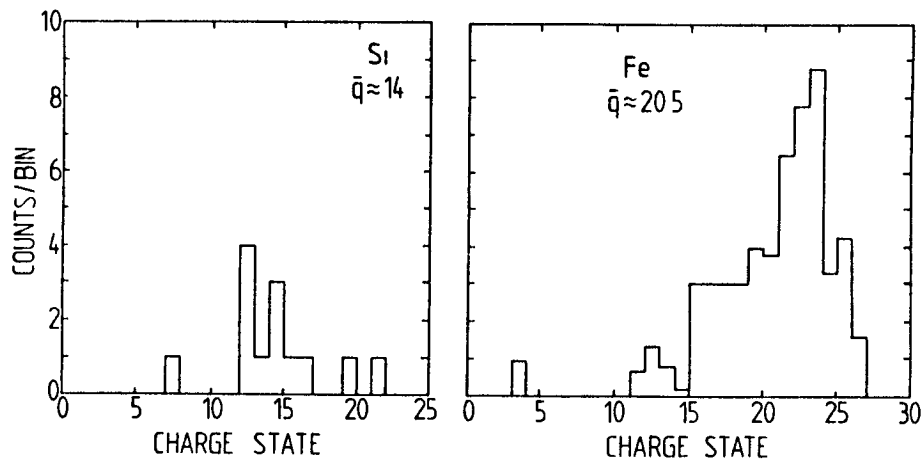


Fig 1 *Measured charge state distributions of Si and Fe for  $^3\text{He}$ -rich energetic particle events*

**3. Results.** Because of the poor counting statistics for heavy ions in the  $^3\text{He}$ -rich energetic particle events, it is impossible to give mean charge states for individual events. Instead, we have to accumulate the pulse height data for all of the observed events and derive an average charge

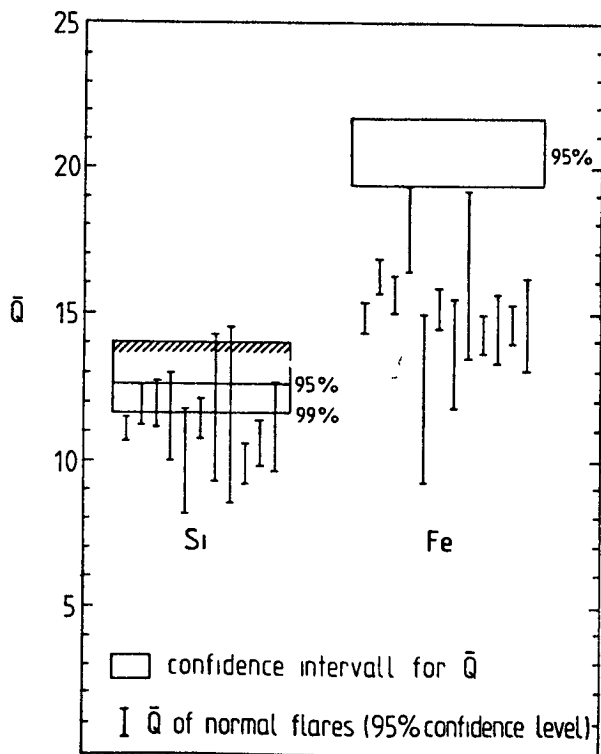


Fig 2 *Confidence levels for the average charge in  $^3\text{He}$ -rich periods compared with results for normal flares (<sup>9</sup>).*

state distribution. Still, we have only registered a total of 13 Silicon and 56 Iron ions. Fig 1 shows the resulting charge state histograms. The mean charge for Fe is  $20.6 \pm 1.2$  (95% confidence level). Compared to the average charge of  $14.9 \pm 0.2$  for normal solar energetic particle events<sup>9</sup>, it is significantly higher for this class of flares, confirming the result of Klecker et al.<sup>11,12</sup> for a subset of  $^3\text{He}$ -rich periods. The mean charge of Si is much less well determined. The value calculated from the measured distribution is compatible with fully ionized Si ions. In order to find lower boundaries for the mean charge, we performed a t test and obtain values of 12.6 and 11.7 for confidence levels of 95% and 99% respectively. Again this has to be compared with a value of  $11.0 \pm 0.2$  for normal flares. Although the statistical significance is less than in the case of Fe, one can conclude that also

Si shows higher charge states in  $^3\text{He}$ -rich flares Fig 2 gives the confidence intervals of the mean charges for Si and Fe together with results from normal flares. It should be noted that in addition to the statistical errors quoted above, the mean charges are subject to a systematic error of 5%. However this does not effect the comparison between this result and the mean charges of normal flares, since both measurements have the same systematic error.

**4 Discussion** We will concentrate on the comparison of the measurements with the implications of Fisk's  $^3$  model for the preferential heating of  $^3\text{He}$ . For a discussion of the other processes see <sup>12</sup> Fisk employs resonant heating by electrostatic ion cyclotron waves in connection with a second stage acceleration process as described in the introduction to account for the

$^3\text{He}$  enrichment factors observed. The condition for resonant interaction of an ion (mass  $m_i$ , charge  $q_i$ , velocity  $v_{\parallel}$  parallel to the magnetic field  $B$ , gyrofrequency  $\Omega = q_i B / m_i c$ ) with a wave of frequency  $\omega$  and parallel wavenumber  $k_{\parallel}$  is given by

$$|(\omega - n\Omega) / (k_{\parallel} v_{\parallel})| = 1 \quad (1)$$

$n$  is the number of the harmonic of the interaction. To be in resonance with the first harmonic of the gyrofrequency of  $^3\text{He}$  requires He-cyclotron waves with a frequency  $\omega \sim 1.2 \Omega_{\alpha}$ ,  $\Omega_{\alpha}$  being the gyrofrequency of  $^4\text{He}$ . To determine the charge states of heavy ions which interact resonantly with the wave, we follow Mason et al <sup>13</sup> in setting  $v_{\parallel} = (k_B T / 3 m_i)^{1/2}$  and requiring a value of  $k_{\parallel}$  such that the bulk of the wave-supporting  $^4\text{He}$  distribution does not fulfill the resonance condition (1). We then obtain the following expression for the resonant  $Q/A$  ratio ( $Q$ =charge in units of  $e$ ,  $A$ =atomic mass number of the ion)

$$2 \frac{\omega}{\Omega_{\alpha}} \left[ 1 - \frac{2}{\sqrt{A}} \left( 1 - \frac{1}{4 \omega / \Omega_{\alpha}} \right) \right] < n \frac{Q}{A} < 2 \frac{\omega}{\Omega_{\alpha}} \left[ 1 + \frac{2}{\sqrt{A}} \left( 1 - \frac{1}{4 \omega / \Omega_{\alpha}} \right) \right] \quad (2)$$

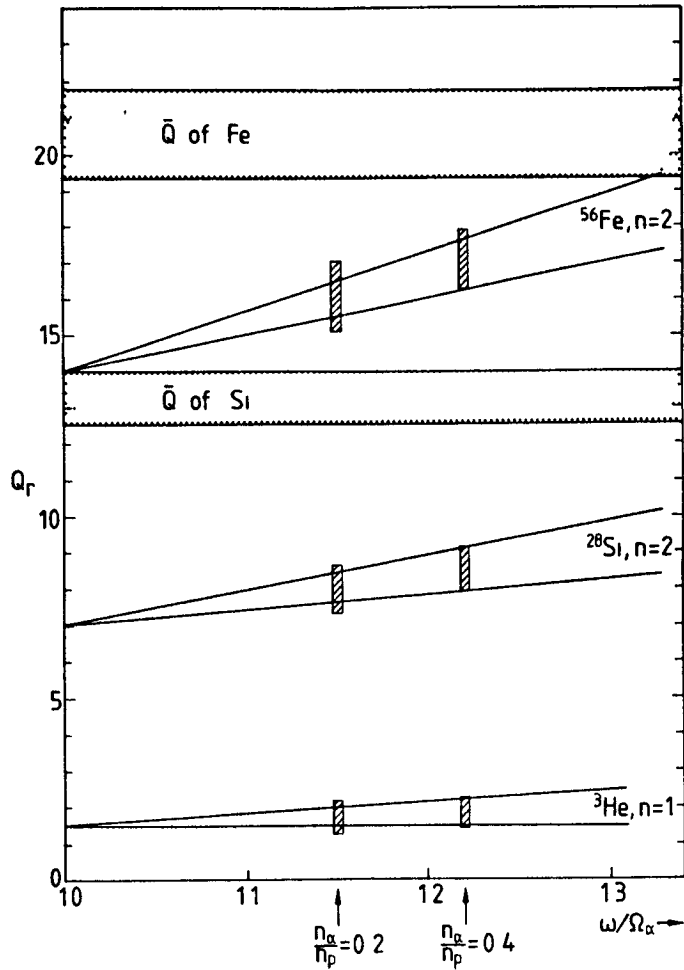


Fig 3 Allowed ranges of the ionic charge for resonant heating by He-cyclotron waves as a function of the wave frequency  $\omega/\Omega_{\alpha}$

In Fig 3 we plot the allowed range of the resonant charge  $Q_r$ , satisfying (2), as a function of the wave frequency. The hatched vertical bars represent the regions of  $Q_r$  calculated from a numerical solution of the dispersion relation for an electrostatic ion cyclotron wave in a Hydrogen - Helium plasma for two different values of the relative Helium concentration  $n_\alpha/n_p$ . Shaded regions mark the 95% confidence interval for the observed average mean charges. Resonant heating of Fe via the second harmonic would require charge states of approx 16 to 18, whereas for Si one would expect charge states around 8 to 9 (see also 13). Despite the poor counting statistics for Si, a mean charge of 8 to 9 is not compatible with the observations. For Fe too the measured mean charge is higher than that required for resonant interaction. However, the width of the charge distribution is wide enough to extend down to the resonant charge states. One may therefore conclude that if indeed the Fisk mechanism is acting as a first stage heating mechanism, it cannot be the only one. Significant portions of the source plasma of the energetic particles must stem from a different, as yet unspecified injection process. The high charge states of both Fe and Si imply a temperature of  $\sim 10^7$  K in the source region of  $^3\text{He}$ -rich flares. This is significantly higher than temperatures of  $\sim 3 \cdot 10^6$  K derived from Si and Fe charge states in normal flares<sup>9</sup>. A high temperature at the source region of  $^3\text{He}$ -rich flares also excludes selective heating by ion acoustic turbulence as proposed by Kocharov<sup>4</sup>, because in this model the heating site is located at the upper chromosphere with an ambient temperature of  $\sim 10^5$  K (8).

5 Acknowledgements We are grateful to the many individuals at the Max-Planck-Institut für extraterrestrische Physik and the Space Physics group of the Department of Physics and Astronomy at the University of Maryland, who developed the hardware and software for our ISEE experiments.

#### References

1. K.C Hsieh, J.A Simpson Ap J Lett **162**, L191 (1970)
2. J.A Ibragimov, G.E Kocharov Proc 15<sup>th</sup> Int Cosmic Ray Conf. (Plovdiv), **12**, p 221 (1977)
3. L.A. Fisk Ap. J **224**, p 1048 (1978)
4. L.G. Kocharov Proc. 17<sup>th</sup> Int. Cosmic Ray Conf (Paris), **3**, p 175 (1981)
5. H Vervoglīs, K Papadopoulos Ap J. Lett **270**, L95 (1983)
6. E Mobius et al Ap J **238**, p 768 (1980)
7. C.Y. Fan et al Space Science Rev **38**, p 143 (1984)
8. L.G Kocharov, G.E Kocharov Space Science Rev **38**, p 89 (1984)
9. A Luhn et al paper SH 2 1-11 (this conference)
10. D Hovestadt et al. IEEE Trans Geos Electr **GE-16**, p 166 (1978)
11. B Klecker et al Ap J **281**, p 458 (1984)
12. B. Klecker et al.. Proc 18<sup>th</sup> Int Cosmic Ray Conf (Bangalore), **4**, p 65 (1983)
13. G. Mason et al Ap. J **239**, p 1070 (1980)
14. A Luhn, Ph.D Thesis, Technische Universität München (1985)



# ON THE CONNECTION BETWEEN THE $^3\text{He}$ -ENRICHMENT AND SPECTRAL INDEX OF SOLAR ENERGETIC PARTICLES

L.G. Kocharov

Leningrad Polytechnical Institute, Leningrad, 195251, USSR

Ya.V. Dvoryanchikov

Ioffe Physico-Technical Institute of the Academy of Sciences of the USSR, Leningrad 194021, USSR

A model is presented which can explain the observed tendency of events with large  $^3\text{He}/^4\text{He}$  ratios to have steeper spectra [1]. In this model preferential injection of  $^3\text{He}$ , acceleration by Alfvén waves and Coulomb deceleration of ions are considered simultaneously. The observed tendency may be obtained as a result of competition between injection and acceleration processes.

## 1. Introduction

It was shown that preferential injection (preacceleration) of  $^3\text{He}$  by plasma waves can provide high  $^3\text{He}$ -enrichment levels observed in some solar energetic particle events (see [2] and references therein). All proposed theoretical models for  $^3\text{He}$  enrichment consider a two-stage acceleration process: a preacceleration (injection) stage due to wave-particle interaction at low energies and an acceleration process requiring a threshold injection velocity such as Fermi type acceleration by Alfvén waves. The high  $^3\text{He}/^4\text{He}$  ratio is proposed to arise at the first (preacceleration) stage, at the second stage the observed spectra are formed. Up to now these two stages were investigated separately [2,3]. Recently the tendency of events with large  $^3\text{He}/^4\text{He}$  ratios to have steeper spectra was found [1]. It is possible only if injection and acceleration processes are connected by some way. The model taking into consideration such connection will be presented here.

## 2. The Model.

The equation for the ion distribution function has the form:

$$\frac{\partial f}{\partial t} = \frac{1}{V^2} \frac{\partial}{\partial V} \mathcal{D} V^2 \frac{\partial f}{\partial V} - \frac{f}{T(V)} + \frac{1}{V^2} \frac{\partial}{\partial V} (F V^2 f). \quad (1)$$

Here the diffusion coefficient  $D = D^{(A)} + D^{(C)} + D^{(in)}$ , where  $D^{(A)}$  describes the acceleration by Alfvén waves,  $D^{(C)}$  is due to Coulomb collision,  $D^{(in)}$  is the injection diffusion coefficient due to wave-particle interaction at low energies. The second term in right-hand side of equation (1) describes diffusive escaping of particles; it plays role only at high velocities  $V \gg V_A$ , where  $T(V) = 3L^2 \mathcal{D}^{(A)} / V_A^2 V^2$ .

## SH 2.2-9

$V_A$  is the Alfvén velocity and  $L$  is a typical length scale of the acceleration region. The last term in (1) describes the deceleration of particles by Coulomb collisions. If we are interested in the injection problem the velocities from thermal up to observed in the interplanetary space should be considered. That is why we will use the diffusion coefficient  $D^{(A)}$  in the form [4] which is valid for arbitrary velocity of test particle:

$$D^{(A)} = \frac{4\pi z^2 e^2 V_A^2}{V(1+V_A^2/c^2) c^2 A^2 m_p^2} \int_{K_0}^{K_{max}} dK \frac{W_K}{K} \Phi(\alpha, \beta); \quad (2)$$

$$\Phi(\alpha, \beta) = \int_0^\infty du \int_0^1 dx \cos(\alpha u x) \left\{ \left[ s^2 \cos u - 3(1-x^2) \sin^2 u \right] \times \right. \\ \times \left( \frac{\sin(\beta s)}{\beta^2 s^5} - \frac{\cos(\beta s)}{\beta s^4} \right) + \frac{\sin(\beta s)}{s^3} (1-x^2) \sin^2 u \left. \right\}, \quad (3)$$

$$s = \sqrt{4(1-x^2) \sinh^2 \frac{u}{2} + u^2 x^2}, \quad \alpha = \frac{K V_A}{\omega_H}, \quad \beta = \frac{K V}{\omega_H},$$

Here  $Ze$  and  $Am$  are the charge and the mass of accelerated ion,  $K$  is the wave number,  $\omega_H = ZeH/Am_p c$ ,  $H$  is the magnetic field strength,  $W_K \propto K^{-\nu}$  is spectral density of Alfvén waves,  $K_0$  and  $K_{max}$  are the minimum and maximum wave numbers of wave spectrum. The diffusion coefficient  $D^{(c)}$  and deceleration coefficient  $F$  due to Coulomb collisions are given by expressions [5]:

$$D^{(c)} = \frac{z^2 e^2 \omega_{pe}^2 m_e \ln \Lambda}{A^2 m_p^2 V} \left[ G(u) + \frac{T_e}{T_p} G(\mu u) \right]; \quad (4)$$

$$F = 2 \frac{z^2 e^2 \omega_{pe}^2 \ln \Lambda}{A m_p^2 V_e^2} \left[ G(u) + \frac{T_e}{T_p} G(\mu u) \right];$$

$$u = V/V_e, \quad \mu = \sqrt{m_p T_e / m_e T_p}, \quad G(u) = \frac{\text{erf}(u) - u^2 \frac{d}{du} \text{erf}(u)}{2u^2};$$

$$\text{erf}(u) = \frac{2}{\sqrt{\pi}} \int_0^u e^{-x^2} dx. \quad (5)$$

Here  $V_e = \sqrt{2k_B T_e / m_e}$  is the thermal velocity of electrons,  $T_e$  and  $T_p$  - electron and proton temperatures,  $\omega_{pe}$  is electron plasma frequency. For simplicity at thermal velocities the injection diffusion coefficient was proposed to be constant.

To obtain preferential injection of  $^3\text{He}$  the diffusion coefficient  $D^{(in)}$  for it must be greater:  $D_{^3\text{He}}^{(in)}/D_{^4\text{He}}^{(in)}=3$ . At higher energies it was proposed that  $D^{(in)}$  increases sharply and then it decreases as  $V^{-3}$  (Fig.1).

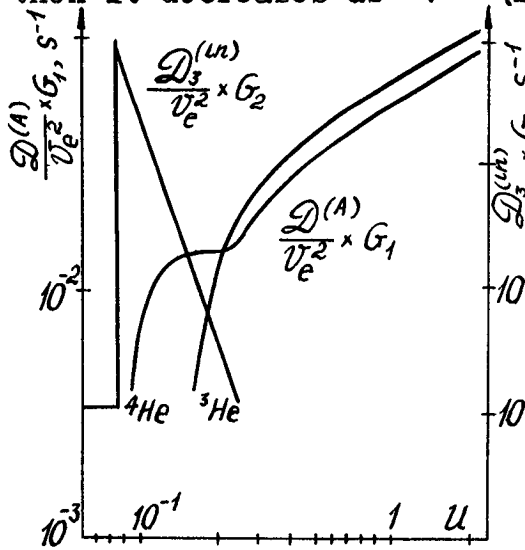


Fig.1. The diffusion coefficients  $D_{^3\text{He}}^{(in)}$  and  $D^{(A)}$  used in calculations.  $K_{\max}=0.35 \frac{\omega_{HP}}{V_A}$   
 $T = 6 \cdot 10^6 \text{ K}$ ,  $\nu = 1.5$   
Low loss case:  $n=4 \cdot 10^{10} \text{ cm}^{-3}$ ,  
 $L=5 \cdot 10^8 \text{ cm}$ ,  $H=70 \text{ Gs}$ ,  $\nu_0=1 \text{ Hz}$ ,  
 $\frac{W}{nk_B T_e} = 0.35$ ,  $G_1=2$ ,  $G_2=3.3$   
High loss case:  $n=5 \cdot 10^{11} \text{ cm}^{-3}$ ,  
 $L=2 \cdot 10^9 \text{ cm}$ ,  $H=260 \text{ Gs}$ ,  $\nu_0=1 \text{ Hz}$ .  
 $\frac{W}{nk_B T_e} = 0.35$ ,  $G_1=1$ ,  $G_2=0.1$

Such form has the diffusion coefficient for ion-sound turbulence used earlier in  $^3\text{He}$ -enrichment problem [4].

The solution of equation (1) has been found by the method described in [6], but at high energies we have obtained quasistationary solution. Theoretical parameters has been selected basing on observational data (for details see [7]).

### 3. Results and discussion

Calculations show that high  $^3\text{He}/^4\text{He}$  ratio is formed at the energies from 100 eV up to 10 keV due to injection and the ratio changes slowly at higher energies where the acceleration mechanism works. As can be seen from experimental data [3] for some  $^3\text{He}$ -rich solar particle events  $^3\text{He}/^4\text{He}$  ratio decreases with increasing of energy at  $E \geq 2 \text{ MeV/N}$ . For another events such decrease is not seen. To explain the  $^3\text{He}/^4\text{He}$  decrease at  $E \geq 2 \text{ MeV/N}$  we have proposed that the plasma density in the acceleration region is high. In this case higher Coulomb losses for  $^3\text{He}$  leads to steeper spectra of this helium isotope. As a result  $^3\text{He}/^4\text{He}$  ratio decrease with increasing of energy. For this high loss case the obtained parameters of acceleration region are: density  $n \approx 10^{12} \text{ cm}^{-3}$ ,  $L \approx 10^9 \text{ cm}$ ,  $H \approx 250 \text{ Gs}$ ,  $T \approx 6 \cdot 10^6 \text{ K}$  and if the lowest frequency of Alfvén wave spectrum  $\nu_0=1 \text{ Hz}$  the wave energy density

$W/nk_B T_e \approx 0.2$ . For events without  $^3\text{He}/^4\text{He}$  decrease at  $E \geq 2 \text{ MeV/N}$  lower values of  $n$  and  $H$  have been obtained (low loss case):  $n \approx 3 \cdot 10^{10} \text{ cm}^{-3}$ ,  $H \approx 70 \text{ Gs}$ .

Calculations show that the higher turbulent energy density  $W/nk_B T_e$  (shorter acceleration time) is, the lower energy particles may be accelerated. But at lower energies the  $^3\text{He}/^4\text{He}$  ratio is lower too (due to the injection mechanism). On the other hand, the shorter is the acceleration

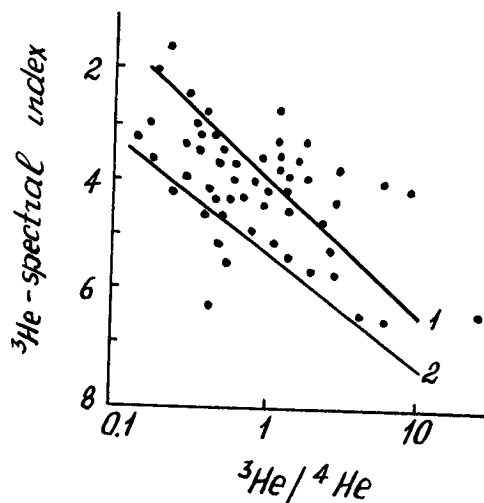


Fig.2.  ${}^3\text{He}$ -spectral index  
(at 2MeV/N) vs.  ${}^3\text{He}/{}^4\text{He}$   
ratio; solid lines-calculated  
for  $W/nk_B T_e$  varied  
from 0.1 to 0.5;  
1- high loss case;  
2- low loss case (see Fig.1).

time, the smaller is the power law index. In figure 2 the result of varying of wave energy density  $W/nk_B T_e$  is shown. The experimental scatter plot of event-averaged  ${}^3\text{He}$ -spectral index versus  ${}^3\text{He}/{}^4\text{He}$  ratio is shown too [1]. It is seen that the experimental tendency conforms the tendency obtained by varying the acceleration time. Thus the observed tendency may be explained as a result of competition between injection and acceleration processes at the intermediate energy region ( $U \approx 0.3$  in figure 1).

### References

1. D.V. Reames, T.T. von Rosenvinge, 1983, 18-th ICRC, 4, 48.
2. L.G. Kocharov, G.E. Kocharov, 1984, Space Sci. Rev., 38, 89.
3. E. Möbius et al., 1982, Astrophys. J., 259, 397.
4. V.N. Tsytovich, A.S. Tchyghachov, 1969, in "Fizika plasmy", v.2, Atomizdat, Moscow, p.87.
5. A.G. Sitenko, Isyan-Yu-Tay, 1962, J. Tech. Fiz., 32, 1324.
6. A.V. Gurevich, 1960, J. Exp. Teor. Fiz., 38, 1597.
7. L.G. Kocharov, Ya.V. Dvoryanchikov, 1984, in "Energichnie tchastitsy i fotony solnechnykh vspishek", Leningrad, p.63.

# THE PLASMA MECHANISM FOR PREFERENTIAL ACCELERATION OF HEAVY IONS

L.G. Kocharov

Leningrad Polytechnical Institute, Leningrad, 195251  
U S S R

A.V. Orishchenko

Ioffe Physico-Technical Institute, Leningrad, 194021,  
U S S R

The induced scattering of ion-acoustic waves on ions is considered for preferential preacceleration of heavy elements. The reconsidered diffusion coefficient in velocity space is used. If the threshold velocity for the main acceleration is linear in charge-to-mass ratio, the induced scattering can account for the observed heavy element abundances in solar cosmic rays.

## 1. Introduction.

In the paper [1] induced scattering of Langmuir waves on ions was considered as a mechanism by which heavy ion enrichment could be produced in solar cosmic rays. It was proposed that the threshold velocity for the main acceleration is linear in charge-to-mass ratio ( $V_{th} = (Z/A)V_1$ ) and the diffusion coefficient in the velocity space due to induced scattering of Langmuir waves on ions  $D_L \propto Z^4/A^2$ . Recently the dependence of diffusion coefficient of ions  $D_L$  on charge  $Z$  and mass  $A$  has been reconsidered by L. Kocharov [2] and J. Weatherall [3]. It was shown that for Langmuir waves the factor  $Z^4/A^2$  taken from [4] (expressions 5.107-5.109) should be replaced by factor  $Z^2/A^2$ . For ion-acoustic waves more complicated dependence on  $Z$  and  $A$  takes place (see below). As a result of this reconsideration J. Weatherall [3] concluded that induced scattering cannot lead to enrichment of  $^3\text{He}$  and heavy elements. For ion-acoustic waves this conclusion was based on examination of diffusion coefficient  $D_{ia}$  at thermal velocity for a very high ratio of the number of helium nuclei to protons in solar plasma:  $n(\text{He})/n(\text{H}) = 0.2$  (according to [5]  $n(\text{He})/n(\text{H}) = 0.07$ ). On the contrary in the paper [2] the attention was drawn

to the fact that in the significant for  $^3\text{He}$ -enrichment problem nearest superthermal region and for moderate  $n(\text{He})/n(\text{H})$  ratio the diffusion coefficient  $D_{ia}$  is greater for the lighter helium isotope. Thus the preferential acceleration of helium-3 can be explained on the base of the ion-acoustic heating as it was proposed earlier (see [4]). Here we will show that the induced scattering of ion-acoustic waves can produce observed enrichment of heavy ions too, while Langmuir heating leads to a normal abundances of elements.

## 2. The model.

We propose the ion-acoustic turbulence to be excited in a region with coronal temperature for a short time. As a result of interaction between waves and particles velocity distribution function of ions  $f(\vec{V})$  is altered. The change of  $f(\vec{V})$  is described by the diffusion equation in velocity space. At low velocities where the induced scattering of waves plays the main role the diffusion coefficient has the form:

$$D_{ia} = \frac{\hbar^2}{A^2 m_p^2} \int W_{\vec{V}}(\vec{k}_1, \vec{k}_2) N_{k_1} N_{k_2} \frac{(\vec{k}_- \cdot \vec{V})^2}{V^2} \frac{d\vec{k}_1 d\vec{k}_2}{(2\pi)^6} \quad (1)$$

where  $\vec{k}$  is a wavevector,  $\vec{k}_- = \vec{k}_1 - \vec{k}_2$ ,  $N_k$  is a wave occupation number,  $(Am_p)$  is ion mass,  $\vec{V}$  is ion velocity,  $W_{\vec{V}}(\vec{k}_1, \vec{k}_2)$  is probability for scattering a wavevector  $\vec{k}$  into a wavevector  $\vec{k}_2$  by a particle with velocity  $\vec{V}$  [2] :

$$W_{\vec{V}}(\vec{k}_1, \vec{k}_2) = \frac{Ze^4 (2\pi)^3}{m_p^2 \omega_{pp}^4} \frac{(\vec{k}_1 \cdot \vec{k}_2)^2}{k_1^2 k_2^2} \left[ \frac{Z}{A} \left( 1 - \frac{\vec{k}_1 \cdot \vec{V}}{\omega_{k_1}} \right)^{-2} - 1 \right]^2 \delta(\omega_- - \vec{k}_- \cdot \vec{V}) \quad (2)$$

Here  $(Ze)$  is ion charge,  $\omega_k$  is a frequency of wave with wavevector  $\vec{k}$ ,  $\omega_- = \omega_{k_1} - \omega_{k_2}$ ,  $\omega_{pp}$  is proton plasma frequency. At low velocities  $V \ll V_s$  ( $V_s = \sqrt{T_e/m_p}$  is ion sound velocity):

$$D_{ia} \approx \left[ \frac{Z}{A} \left( 1 - \frac{Z}{A} \right) \right]^2 D_0; \quad D_0 = \left( \frac{W_{ia}}{n T_e} \right)^2 \frac{\kappa}{\Delta K} \frac{V_s^2}{2} \omega_{pp}. \quad (3)$$

3.

Here  $W_{\omega}/nT_e$  is a ratio of wave energy to thermal one,  $\Delta K/K$  is relative width of wave spectrum,  $T_e$  is electron temperature. Similar to [1,4] the distribution function of ion species "i" at time t can be found as:

$$f_i(\vec{v}, t) = (\pi b_i^2)^{-\frac{3}{2}} \exp(-v^2/b_i^2); \quad b_i^2 = V_p^2 \left\{ \frac{1}{A_i} + x_0^{-2} \left[ \frac{Z}{A} \left( 1 - \frac{Z}{A} \right) \right]^2 \right\} \quad (4)$$

where  $V_p = \sqrt{2T_p/m_p}$  is proton thermal velocity,  $x_0^2 = V_p^2 (4Q_0 t)^{-1}$ ,  $T_p$  is initial proton temperature. If the threshold velocity for the main acceleration is linear in charge-to-mass ratio ( $V_{th}^i = \frac{Z_i}{A_i} V_1$ ), then the enrichment factor of ion species "i" relative to ion species "j" can be found:

$$Q_{ij} = \int_{V_{th}^i}^{\infty} v^2 f_i(\vec{v}, t) dV / \int_{V_{th}^j}^{\infty} v^2 f_j(\vec{v}, t) dV. \quad (5)$$

### 3. Discussion and summary.

From calculations of enrichment coefficients using different values of  $x_0$ ,  $V_1$  and ion ionization state it is seen that good accordance with experiment is possible when  $x_0 = 0.2-0.3$ ,  $V_1 \approx 6 V_{Tp}$  and ionization state is equilibrium conforming to temperature  $T_* \approx 5 \cdot 10^6 K$ . Calculated and observed enrichment factors for different elements relative to oxygen are shown in figure. The coincidence seems to be satisfactory.

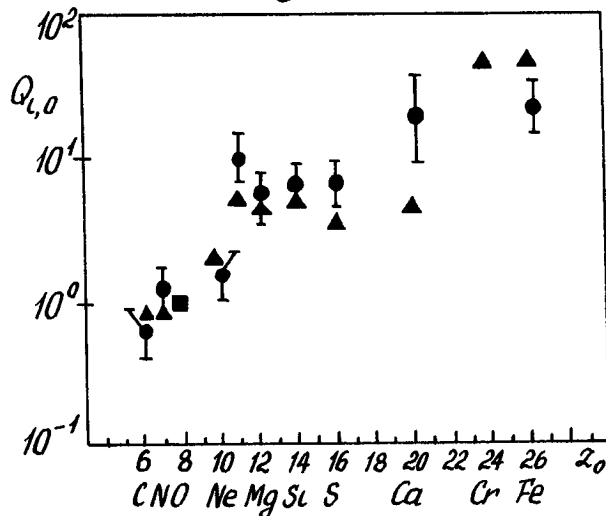


Figure. Enrichment factors relative to oxygen. Circles-observed for Sept. 24, 1977 event [6]. Triangles -calculated for  $x_0 = 0.25$ ,  $V_1/V_{Tp} = 6$ ,  $T_* = 5 \cdot 10^6 K$ .

Thus the reconsideration of scattering probability [2,3] is not crucial for induced-scattering mechanism of heavy

ion enrichment. Comparing to our previous model [1] now better agreement of theory and experiment is attained. In present model enrichment of heavy elements is a result of two reasons: (1) the induced scattering heats heavy ions up to a greater temperature ( $T \propto \frac{Z^2}{A} (1 - \frac{Z}{A})^2$ ); (2) the threshold velocity  $V_{th}$  is lower for heavier ions.

Note that induced scattering of Langmuir waves used in [1] combining with  $V_{th} = \frac{Z}{A} V_i$  leads to the normal abundances of elements even when the portion of accelerated particles is small (while equilibrium Maxwellian distribution at coronal temperature leads to a great depletion of heavy ions). Thus the model [1] is suitable for events with normal abundances of ions.

In conclusion, the mechanism of preacceleration by induced scattering has the sensitivity to ion charge and mass needed to account for observed solar cosmic-ray abundances. The contrast conclusion made by J. Weatherall [3] probably derives from an incorrect application of plasma theory to solar cosmic-ray problems.

#### References.

1. L.G. Kocharov, A.V. Orishchenko. 1983. 18th ICRC, 4, 37.
2. L.G. Kocharov, 1983, Soln. Dann. 9, 60.
3. J. Weatherall, 1984, Astrophys. J., 281, 468.
4. L.G. Kocharov, G.E. Kocharov, 1984, Space Sci. Rev., 38, 89.
5. A.G.W. Cameron, 1973, Space Sci. Rev., 15, 121; 1981, preprint N. 1357.
6. R.E. Mc Guire et al., 1979, 16-th ICRC, 5, 61.



## OBSERVATIONS OF SOLAR ENERGETIC PARTICLES AT A SYNCHRONOUS ORBIT

- T.Takenaka (a), Y.Ohi (b), T.Yanagimachi (b),  
 K.Ito (b), T.Kohno (c), and K.Sakurai (d)  
 (a) Science and Engineering Research Laboratory,  
 Waseda University, Shinju-ku, Tokyo 162, Japan  
 (b) Department of Physics, Rikkyo University,  
 Toshima-ku, Tokyo 171, Japan  
 (c) The Institute of Physical and Chemical Research,  
 Itabashi, Tokyo 173, Japan  
 (d) Institute of Physics, Kanagawa University,  
 Rokkakubashi, Yokohama 221, Japan

1. INTRODUCTION The Space Environment Monitors (SEM) on board the Japanese geostationary meteorological satellites (GMS-1 and GMS-2) observed energetic protons, alpha particles and electrons continuously for February 1978 to September 1984. The satellites were at 6.6 earth radii above 140°E equator. Observational items are shown in Table 1 [1].

In the propagation studies of solar energetic particles, statistical analyses for many events revealed on averaged picture of the propagation such as was reported by Reinhard et al.[2] and Van Hollebeke et al.[3]. They showed the existence of the fast propagation region (FPR:45°W  $\pm$   $\sim$ 60°, on an average) or the preferred connection region (PCR:20°W - 80°W) in the heliolongitude. We tried to study some characteristics of the propagation process of solar energetic particles by using the data provided by the GMS/SEM's for February 1978 to February 1983. Some preliminary results of the data analyses are reported in the present paper.

2. DISTRIBUTION OF THE SEP EVENTS Sometimes, the GMS/SEM's observed the solar energetic particle (SEP) events at their synchronous orbits. Two examples of the SEP events are shown in Fig.1(a) and 1(b). As seen in the figures, there was apparent increase in each channel, except for the P1 and EL channels. These two channels are omitted from our analyses because they are contaminated dominantly by the geomagnetically trapped or quasi-trapped particles.

About 50 SEP events were observed by the GMS/SEM's for the period (Fig.2). Hourly plots of the SEM data, first, indicate that the time profiles of flux intensities of the SEP events are different from event to event. It seems, however, that they are able to be classified roughly into two groups. One of them is the short rise time (SRT) event group. The rise time of

Table 1. Observational items of the GMS/SEM's.

GMS-1/SEM			GMS-2/SEM		
Channel Name	Particle Type	Energy Range (keV)	Channel Name	Particle Type	Energy Range (keV)
P1	protons	1.2 - 4	P1	protons	0.8 - 4
P2	protons	4 - 8	P2	protons	4 - 8
P3	protons	8 - 16	P3	protons	8 - 16
P4	protons	16 - 34	P4	protons	16 - 30
P5	protons	34 - 80	P5	protons	30 - 60
P6	protons	80 - 200	P6	protons	60 - 100
P7	protons	200 - 500	-	-	-
A1	alphas	9 - 70	A1	alphas	8 - 66
A2	alphas	30 - 70	A2	alphas	32 - 66
A3	alphas	65 - 170	A3	alphas	64 - 120
A4	alphas	130 - 250	A4	alphas	120 - 240
A5	alphas	320 - 370	A5	alphas	270 - 370
EL	electrons	> 2	EL	electrons	> 2

The data were obtained by the GMS-1/SEM for Feb 1978 to Dec.1981 and by the GMS-2/SEM for Dec.1981 to Feb 1983.

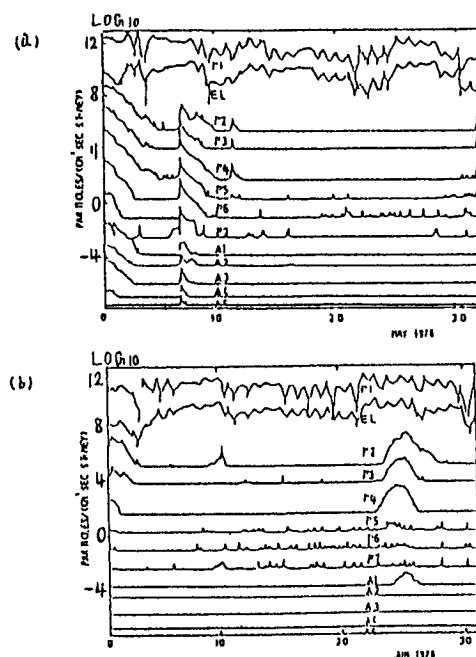


Fig 1 Two examples of the SEP events Hourly averaged SEM data are plotted for May 1978 (a) and Jun 1978 (b). The event of May 7, 1978 is classified as an SRT event, and Jun 23, 1978 event as an LRT event. Each channel is separated from others by multiplying factor 10

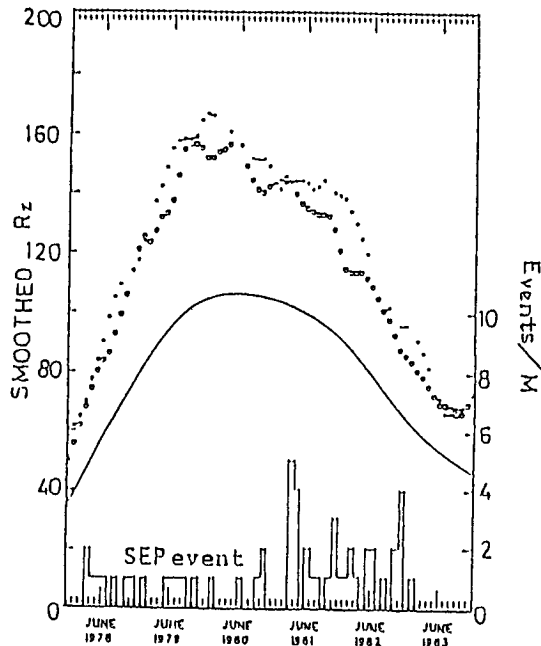


Fig 2. Distribution of the SEP events observed by the GMS/SEP's for the period of Feb 1970 to Feb 1983. This period just coincides with the maximum phase of solar activity cycle 21 (Sun spot data were taken from the SOLAR-GEOPHYSICAL DATA.)

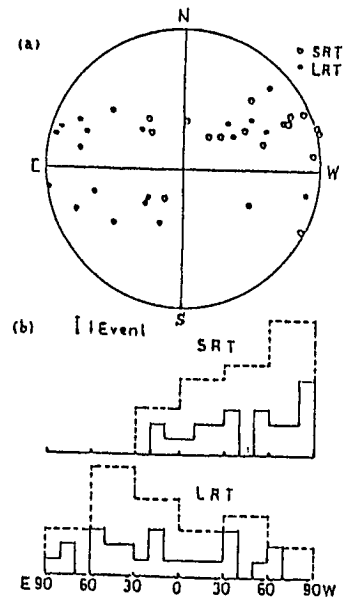


Fig 3. Distribution of the SEP events in the heliographic longitude. The parent flares are plotted on the solar disk (a). In the figure (b), heliographic bin is taken by  $10^\circ$  (solid line) or  $30^\circ$  (broken line).

an SRT event is relatively short. It has a clear peak, as shown in Fig.1(a). (Here the rise time is defined as the time from onset to maximum flux intensity.) The other group is composed of several events, alternatively, which do not belong to the SRT event group (such as in Fig.1(b)), that is, it includes long rise time events, those which have no clear peak, and those which have somewhat complex time profiles. We called the second group the long rise time (LRT) event group. The distributions of the SRT and the LRT events are shown in Fig.3. These figures indicate that the SRT events distribute dominantly on the western hemisphere and many of the LRT events on the eastern.

**3 CORRELATION BETWEEN THE SRT EVENTS AND THE PRECEDING SSC's** Temporal situation of the interplanetary space will become a very important factor in addition to the steady and averaged configuration of the space, when we consider the interplanetary propagation of solar energetic particles. Shock waves are one of the most dominant sources which affects the temporal situation of the space such as the IMF. Shocks also disturb the geomagnetic situation as sometimes observed as storm sudden commencement (SSC).

We examined the correlation between the SEP events and preceding SSC's. Fig.4 shows the frequency distribution of events which were accompanied by the SSC several days prior to onset of event. In the figure,  $\tau$  is the time needed for the sun to rotate  $180^\circ$ ; it is considered to be nearly double scale of the broadness of interplanetary shocks [5]. It can be seen in the figure that a reasonable correlation exists between the SRT events and their accompanied preceding SSC's, while no correlation exists for the LRT events. And  $\tau$  is considered as a limit of the correlation.

**4 TIME VARIATION OF P/ $\alpha$  -RATIO** It would be interesting to find tendencies of time variation of the proton-alpha ratio in the context of propagation study, because it is expected that there are some qualitative differences in the effects suffered during the propagation. We plotted

three ratios corresponding to three energy (per nucleon) ranges,  $R(L)$ ,  $R(M)$  and  $R(H)$  defined as

$$\begin{aligned} R(L;t) &= [P2(t)P3(t)]/A1(t), \\ R(M;t) &= P4(t)/A3(t), \\ \text{and } R(H;t) &= P5(t)/A4(t). \end{aligned}$$

Examples of these plots for an SRT and an LRT events are shown in Fig.5. In the figure, plots of  $R(H)$ , which is the one of highest energy, fluctuate significantly, because of poor statistics on  $P5$  and  $A4$ . From the plots of many events, we may be able to say that  $R(L)$  has a constancy in its value during a event for both the SRT and the LRT events but the values are different from event to event. And, for the SRT events,  $R(M)$  and  $R(H)$  have a tendency to decrease with time, while they were nearly constant for the LRT events. These tentatively identified tendencies are represented in Fig.5 by broken lines.

## 5. DISCUSSION

**5.1 Coronal Propagation:** The SEM data are hourly averaged ones and can not provide any information about anisotropy. Hence, it is not possible to discuss coronal propagation in detail. However, we can draw some suggestions about coronal propagation from the data. It is not natural that the mechanism of solar flare responsible for particle acceleration and release would change depending on the heliolongitude of flare position. Therefore, Fig.3 suggests as follows. The differences between the SRT and the LRT events are attributed to the differences of the propagation effects suffered during the propagation between the sun and the earth for each group. As is well known, the region of good connection is  $40^\circ - 50^\circ W$  in the heliolongitude. According to Reinhard et al., the predominantly well guided region is not so narrow, in fact, it is rather more wide; that is the FPR has a size of  $\sim 100^\circ$ . In section 2, we found that the width of distribution of the SRT event was about  $100^\circ$ . This may imply that the solar energetic particles, generated by the flare at a heliolongitude  $\lambda$ , fill up the region with a center of  $\lambda$  and radius of  $\sim 50^\circ$  in heliolongitude, and when the root of the IMF passing the earth is lying in this region, that event will be observed as an SRT event at 1AU. Fig.3 is an evidence of the existence of the FPR. Thus, we would be able to state that the SRT events are distributing in the FPR and many of the LRT events are far from this region. We should, here,

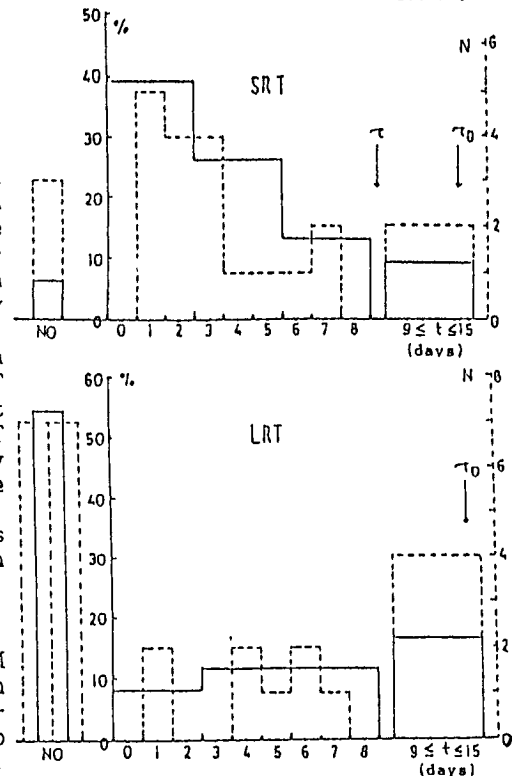


Fig 4 Correlation between the SEP events and their accompanied preceding SSC's. The frequency distribution is shown. The abscissa in the figure represents how many days does occur SSC prior to SEP event. And  $\tau$  is a limit of the correlation. Diagram indicated by broken line with right hand side ordinate represents the distribution of event number.

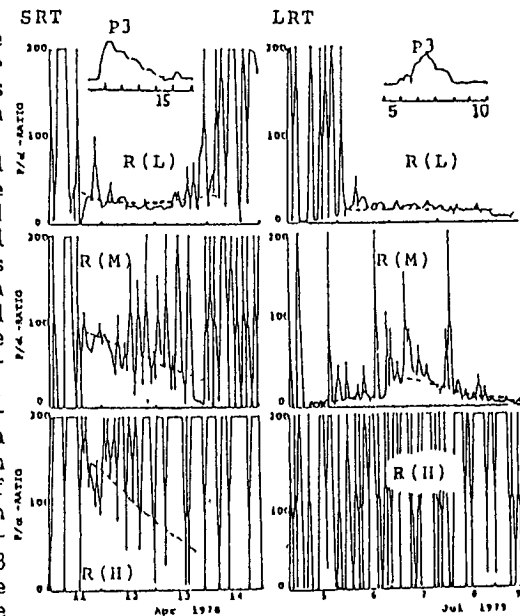


Fig.5 Time variation of  $P/d$ -ratio. Three ratios corresponding to three energy ranges are plotted. Tentatively identified tendencies are drawn by hand as broken lines.

note the fact that there are a few exceptions for both groups, and the statement is valid in the sense of averaged picture.

5.2 Interplanetary Propagation: Let us consider the space with distance less than 1AU when a shock has just passed, i.e., immediately after an occurrence of SSC. Observations show that, when a shock has passed in the space, the solar energetic particles propagate in the interplanetary space; then these particles are observed predominantly as an SRT event. This means that, for such an event, most of the energetic particles have suffered only little scattering through their propagation in the space. Therefore, the result is that mean free path, hence diffusion coefficient, is large for the energetic particles with energy (or rigidity) under consideration. And this may suggest the number density of scattering centers in the space decreased after passage of shock. When a shock wave that triggered off an SSC has propagated through the space, the irregularities of magnetic field which are scattering centers were swept out. Thus the density of scattering centers is minimized within several days after an occurrence of a SSC. At this time, it is considered that some region of the interplanetary space which has been swept out by a shock is a "clean space". The cleanness of the space will decay in two ways. One is due to the rotation of the sun. The other is due to the random motion of the roots of the IMF on the solar surface. Therefore, it is inferred that an upper limit in time between the SRT events and preceding SSC's. According to the statistics in Fig.4, this upper limit is 7-10 days.

We should, however, remember the following argument. If the interplanetary shock that is observed as a preceding SSC and the solar flare, that generates an SRT event occur in the same active region, then another possibility may exist other than the above mentioned. The active region that is responsible for a SRT event has been in the eastern hemisphere several days before. At this time, it is possible to imagine that such active region has generated a shock wave that is responsible for a SSC. In this case, the correlation between a western hemisphere event and its preceding SSC necessarily exists. Then, the essential condition of the occurrence of SRT events is that the parent flare occurs in the western hemisphere; and the correlation between SRT events and their preceding SSC's is not the cause but a result. If it were a result, it becomes more interested because subsequent occurrences of shock ejection and flare provides informations of prediction of an occurrence of flare and of flare mechanism itself. Continuous measurements of the power spectrum of the IMF will be able to solve this problem.

The time profiles of the LRT events significantly differ from each other. Moreover it is not possible that the LRT events can be understood by using one propagation model only (e.g., anisotropic diffusion model). These two facts may suggest that the interplanetary propagation effects modulate significantly the time profile. For example, when we tried to fit the time profiles by using an anisotropic diffusion model (e.g., Burlaga's ADB model [5]), fitting curve was in good agreement with the appropriate parameters for the SRT events, but for the LRT events, no reasonable agreement was obtained. In the case of the SRT event, time variations of  $P/\alpha$  -ratio for  $R(L)$ ,  $R(M)$  and  $R(H)$  are able to be understood by introducing appropriate energy (or rigidity) dependence of the mean free path of particles. On the other hand, for the LRT event, it is not possible to explain the time variation of  $P/\alpha$  by using diffusion theory only because it is considered that this kind of events was suffered the propagation effects other than diffusion effect. Though, it seems that constancy in  $P/\alpha$  restricts these effects such as that protons and alphas were modulated in a same manner.

The SEM data used in the present study were provided from the Meteorological Satellite Center, the Japanese Meteorological Agency.

- References
1. SOLAR-GEOPHYSICAL DATA, 1978.
  2. R.Reinhard et al., 1974, Solar Phys., 36, 473-494
  3. M.A.I. Van Hollebeke et al., 1975, Solar Phys., 41, 189-223.
  4. A.J. Hundhausen, 1974, 'Coronal Expansion and Solar Wind', Springer-Verlag, Berlin, Heidelberg.
  5. L.F. Burlaga, 1967, J. Geophys. Res., 72, 4449-4460.

# CORONAL PROPAGATION OF SOLAR FLARE PARTICLES OBSERVED BY SATELLITE

Tsuyoshi KOHNO, Nariaki NITTA, Masami WADA and Tomoshige SUDA\*

Institute of Physical and Chemical Research  
7-13, Kaga-1, Itabashi, Tokyo 173, Japan

Meteorological Research Institute\*  
1, Nagamine-1, Yatabe, Tsukuba, Ibaraki 305, Japan

## Abstract

Propagation of solar flare particles in corona was studied using the satellite data at the geostationary orbit. By selecting very fast rise time events only, the interplanetary propagation were assumed to be scatter free arrival. The results show that the propagation in corona does not depend on particle energy in 4 - 500 MeV protons, and the time delays from optical flare do not depend on the distance between the flare site and the base of the interplanetary magnetic field which connects to the earth.

## 1. Introduction

Energetic particles accelerated in a solar flare play an important role in the flare energetics. Because of the propagation effects, however, it is very difficult to know the total energy of all particles in a flare using particle data observed at interplanetary space. There are two propagation effects; one is coronal propagation from the flare site to the point where they are released from the sun to the interplanetary space, and the other is interplanetary propagation from that point to the earth. Many studies have been done for both propagation processes (Ma Sung et. al. 1975, Schatten and Mullan 1977, Mullan 1983 for coronal propagation and Jokipii 1971, Earl 1976, Ma Sung and Earl 1978, Owens 1983 for interplanetary propagation). Using 80 solar flare data, Ma Sung et. al. showed that particle propagation is independent of both rigidity and energy. This is very hard to understand with normal diffusion processes such as proposed earlier by Reid 1964. Schatten and Mullan proposed a magnetic bottle model to interpret the fast non diffusive propagation in the corona.

## 2. Observation and data presentation

The solar proton data were obtained from Japanese Geostationary Meteorological Satellite (GMS-1, GMS-2). The continuous data are available

from February 1978 GMS-1 was switched to GMS-2 on December 21, 1981. The energy range of data used here is 4 - 500 MeV and 4 - 100 MeV for GMS-1 and -2, respectively. The differentially divided energy channels are seven and five for each.

We assumed that the coronal propagation effect can be separated from interplanetary one by selecting very fast rise time event only, which can be considered as scatter free propagation in the interplanetary space. We have chosen 18 events in the period from September 1977 to December 1982. The criterion of "fast rise" is not so severe but we selected having a rise time (from start of increase to the maximum) of less than a few hours. We assume the time profiles at the base of the garden hose lines of interplanetary magnetic field which connect to the earth can be seen from these so-called scatter free events which means the modulation during the propagation in space can be neglected.

Table 1 Scatter free arrival events observed by GMS-1, -2.

Date	G	H $\alpha$ flare			SID		SWV km/sec	IMF deg	$\rho$ deg
		onset	location	imp	onset	imp			
Sep 19 77	G	0955	N08 W57	3B	1028	3	330	W69	12
Sep 24 77	G	0539?							
Apr 11 78		1334+8	N22 W56	3	1401	3	505	45	30
Sep.23 78	G	1944+3	N35 W50	3B	0945	2+	340	66	32
Feb 17 79		1905	N16 W28	SB	1905	1-	310	73	50
Aug 21 79	G	0550	N17 W40	2B	0607	1-	600	38	10
Apr 10 81	G	1632	N08 W36	2B	1642	3	380	59	27
Apr 24 81		1346	N20 W50	2B	1348	2+	780	29	32
May 10 81		0715	N06 W73	1B	0717	1	340	66	11
Jul 20 81		1310	S26 W75	1B	1310	1	410	55	37
Jan.31 82		0020E	S13 E08	2N	2329)	3	(380)	59	66
Mar. 7 82		0308E	N17 W53	2B	0303	2	370	61	25
Jul.22 82		1648	N16 W89	1F	1645	2+		55	35
Nov.22 82		1741	S11 W36	1N	1742	2		55	23
Nov 26 82		0230	S11 W86	2B	0235	2		55	33
Dec.17 82		1820	S07 W20	3B	1820	3		55	35

G: Ground level enhancement, SWV. Solar Wind Velocity

$\rho$ : angular distance between flare site and the base of IMF

Fig 1 gives intensity time profiles of typical example of a flare of August 21, 1979. Time A means the H $\alpha$  flare start. The two lines in the each energy channel indicate the time delay band from optical flare observation assuming the travelling distance of 1.2 AU with the particle speed corresponding to each energy band. In the bottom of Fig.1, we can see that the intensity time profiles and the onset times of increase of all channels nearly coincide after correction of the propagation time. For the other events, nearly the same tendency can be seen with two exceptions (May 7, 1978 and Dec 7, 1981), although the average shape of time profiles and the onset time delays from the optical flare are different from flare to flare. These 16 flare characteristics are

summarized in Table 1. We understand the two exceptions are special cases which can be interpreted by some interplanetary modulation as already reported by Kohno and Wada 1979.

Aug. 21, 1979

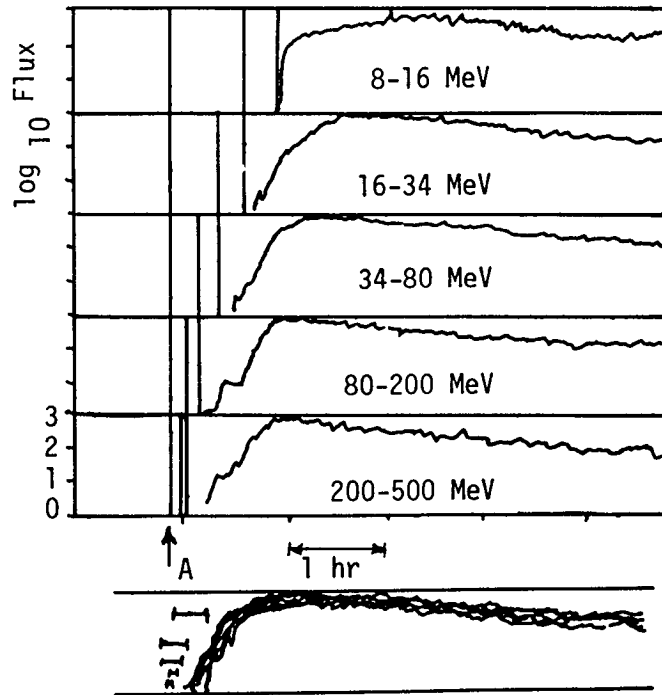


Fig 1 Examples of time profiles of two minutes averaged data normalized to the maximum flux. Time A shows the H $\alpha$  start. two vertical lines in each channel indicate the time delay from optical observation depending on particles velocity of each channel

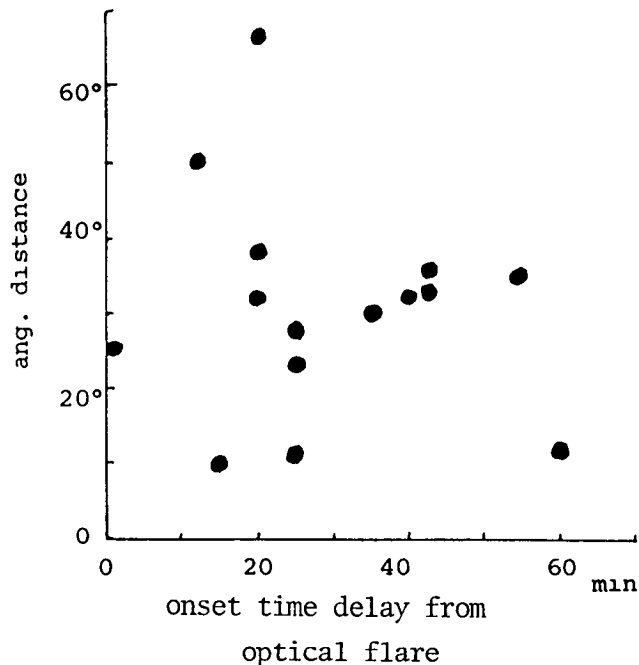
In order to see the dependence of the onset time delays from the optical flare on the distance between the flare site and the base of IMF which connects to the earth, we used the observed solar wind velocity data ( King 1977, 1979 ) if available and mean value of 410 km/sec if not available. These distances thus obtained are shown in the last column of Table 1. In Fig.2, the relation of this distance vs the onset time delay from optical flare is plotted. It is clear that there is completely no relation between the two parameters. The mean value of the onset time delay from optical flare is about 30 minutes.

### 3. Discussion and conclusion

What we have shown here can be summarized as ' 1 ) When the travel times between the sun and the earth are adjusted, the intensity time profiles and the onset times of 4 - 500 MeV protons are almost same in a flare. 2 ) Distribution of onset time delays from optical flare has a mean value of 30 minutes and there is completely no relation with the distance between the flare site and the base of the IMF. This is another proof of energy-rigidity independent propagation in corona in addition to the results of Ma Sung et. al. 1975. Schatten and Mullan have proposed the magnetic bottle model to interpret the rigidity-energy independent

propagation in corona. The bottles produced by flares serve as temporary traps of particles. They may have the dimension of half angle near  $60^\circ$ , which result in fast azimuthal propagation inside, and rather slow leakage from the bottle. The present results of analysis may match to this model. Our mean time scale of particle release from that bottle is 30 minutes while their model suggests about 60 minutes.

Fig 2  
Relation of particle increase onset time delays from optical flare vs the distance between the flare site and the base of IMF. As shown in Table 2, no appropriate flare was found for one sample out of 16.



Mason et al (1984) also showed that there is no correlation between the relative abundances and separation angle, nor is there a significant correlation between the sizes of the relative abundance fluctuations. They proposed from this results the possible large scale shock acceleration model. Our results also support their assumption.

We acknowledge the Meteorological Satellite Center for providing the data.

#### References

- Earl, J.A., *Ap.J.*, **206**, 301, 1976.  
 Jokipii, J.R., *Rev. Geophys. Space Phys.*, **9**, 27, 1971.  
 King, J.H., NSSDC/WDCA-R&S 77-04, 77-04a, 79-08, 1977, 1979.  
 Kohno, T. and M. Wada, *Geophys. Res. Lett.*, **6**, 421, 1979.  
 Mason, G.M., G. Gloeckler and D. Hovestadt, *Ap. J.*, **280**, 902, 1984.  
 Ma Sung, M.A.I., Van Hollebeke and F.B. McDonald, 14th ICRC, **5**, 305, 1975.  
 Ma Sung and J.A. Earl, *Ap.J.*, **222**, 1080, 1978.  
 Mullan, D.J., *Ap.J.*, **269**, 765, 1983.  
 Owens, A.J., *J. Geophys. Res.*, **84**, 4451, 1979.  
 Schatten, K.H. and D.J. Mullan, *J. Geophys. Res.*, **82**, 5609, 1977.



## CORONAL PROPAGATION OF FLARE ASSOCIATED ELECTRONS AND PROTONS

Schellert, G., Wibberenz, G., Kunow, H.  
 Institut für Reine und Angewandte Kernphysik, Universität Kiel  
 Olshausenstr. 40-60, 2300 Kiel, FR Germany

## ABSTRACT

A statistical study of characteristic times and intensities of 36 solar particle events observed between 1977 and 1979 by the Kiel Cosmic Ray Experiment on board HELIOS-1 and -2 has been carried out. For  $\sim 0.5$  MeV electrons we order the times of maximum and the absolute intensities with respect to angular distance from the parent flare. Discussion of coronal parameters in terms of Reid's model leads to typical time constants for coronal diffusion and escape.

1. Introduction. Particle intensities observed in interplanetary space are a superposition of coronal and interplanetary propagation effects which are difficult to separate. In this paper we use statistical studies of a large number of events to investigate the properties of solar transport of flare particles.

2. Coronal angular dependence of maximum times. Assuming only diffusive propagation in interplanetary space it can be shown that the maximum times of solar particle events can be approximated by (1)

$$T_{\max} = t_{\max}^{\text{ip}} + c_m \quad (2.1)$$

in good agreement with the full numerical solution of the convolutional integral.  $c_m$  is the time-to-maximum of the coronal injection and  $t_{\max}^{\text{ip}}$  would describe the interplanetary propagation for  $\delta$ -function injection.

Using the model of Reid (2) for solar particle transport and a simple model for interplanetary diffusion leads for sufficiently large angular distances  $\phi$  to

$$T_{\max} = t_{\max}^{\text{ip}} + \frac{\phi}{2} \sqrt{t_c t_L} \quad (2.2)$$

In this case  $c_m$  increases linearly with angular distance  $\phi$ .

Maximum times versus  $\phi$  for  $\sim 0.5$  MeV electrons with diffusive time intensity and time anisotropy profiles are shown in Figure 1. Only events were selected for which the coronal magnetic connection point of the spacecraft is west of the corresponding flare. The  $H_\alpha$ -onset has been chosen as acceleration time. Apparently the nearly constant propagation times for small angular distances  $\phi$  are described by a fast propagation region (3) with a mean extension of  $\sim 26^\circ$ . The time constants seem to increase linearly for larger angular distances as predicted in (2.2). A least squares fit to the data results in a geometrical mean of the two time constants for coronal diffusion and escape of

$$\sqrt{t_c t_L} \approx 7.5 \text{ h}$$

Coronal transport effects can be neglected within the fast propagation

region, so that measured maximum times would only be determined by interplanetary propagation. For a radially independent diffusion coefficient  $K$  we obtain with

$$t_{\max}^{\text{ipl}} = \frac{r^2}{6K}$$

an upper limit for the mean free path parallel to the average interplanetary field of  $\sim 0.12$  AU for  $r = 1$  AU in good agreement with earlier work (4).

3. Coronal angular dependence of maximum intensities. In the 1977 - 1979 period we were able to obtain maximum intensities from both spacecraft HELIOS-1 and -2 for 12 events. Differences due to interplanetary propagation are corrected by assuming an  $r^{-2}$  dependence of the absolute intensities. Although the actual radial dependence can be derived only if coronal and interplanetary effects are taken into account in a combined propagation model, our statistical analysis shows that the coronal distance dependence is much stronger than the effects of different normalization factors  $(r/r_E)^n$  for  $2 \leq n \leq 3$ . Radially normalized maximum intensities are therefore a measure of the number of particles at the injection maximum  $I_{\max}$  for the respective angular distance. Using Reid's model in the range of large  $\phi$   $I_{\max}$  is controlled only by the ratio of the time constants for coronal diffusion and escape:

$$I_{\max} = I(c_m) \sim \frac{1}{\phi} \exp \left\{ -\sqrt{\frac{t_c}{t_L}} \phi \right\} \quad (3.1)$$

Since the exponential term will dominate the  $\phi^{-1}$ -dependence, this leads to

$$I_{\max} \sim \exp \left\{ -\sqrt{\frac{t_c}{t_L}} \phi \right\} \quad (3.2)$$

Comparing the normalized maximum intensities for the same event as observed by two spacecraft at different coronal connection distances from the flare allows to determine the ratio  $t_c/t_L$ :

$$\frac{I_{\max}(\phi_2)}{I_{\max}(\phi_1)} = \exp \left\{ -\sqrt{\frac{t_c}{t_L}} (\phi_2 - \phi_1) \right\} \quad (3.3)$$

Figure 2 shows the amplitude variations with coronal angular distance for  $\sim 0.5$  MeV electrons. In order to disregard the different event sizes we normalize the respective maximum amplitudes to obtain  $I_{\max} = 1$  for  $\phi = 0^\circ$ .

The slope varies considerably, apart from a group of four events with similar behaviour. It is not useful to describe this amplitude variation with angular distance by an average value of  $t_c/t_L$ . Regarding individual events observed by at least two spacecraft at different solar longitude we always find intensity variations larger for protons than for electrons. Figure 3 shows an example for the event of April 11, 1978, as observed by HELIOS-1 and -2. The large difference in temporal delays for protons as compared to electrons is immediately evident. In general the difference in amplitude variation between the two particles is more pronounced than in this example (see e.g. 1).

4. Conclusions. For non-relativistic protons Ng and Gleeson (5) found  $t_c = 50 - 100$  h and  $t_L = 10 - 15$  h between 1 - 50 MeV. Mc Guire et al. (6) derived  $t_c \approx 90$  h and  $t_L \approx 9$  h for 3 - 60 MeV protons taking into account a typical extension of the fast propagation region of  $\sim 25^\circ$ .

SH 3.1-3

The value from (6) for protons  $t_c t_L \approx 810 h^2$  in contrast to our value  $t_c t_L \approx 55 h^2$  quoted above for electrons shows that coronal transport occurs much faster for electrons for which the average rate of increase  $\Delta T_m / \Delta \phi$  is almost a factor of 4 smaller. From the coronal transport models we can exclude electric field drift. This process proposed in (7) was based on (a) a linear rate of increase  $\Delta T_m / \Delta \phi$  with  $\phi$  and (b) the suggested independence of coronal transport from particle type (8). The simple Reid model leads to the observed linear dependence, based on the combination of coronal diffusion and escape, whereas diffusion alone would lead to  $T_{\max} \sim \phi^2$ . We also find clear evidence that electrons are transported faster through the corona.

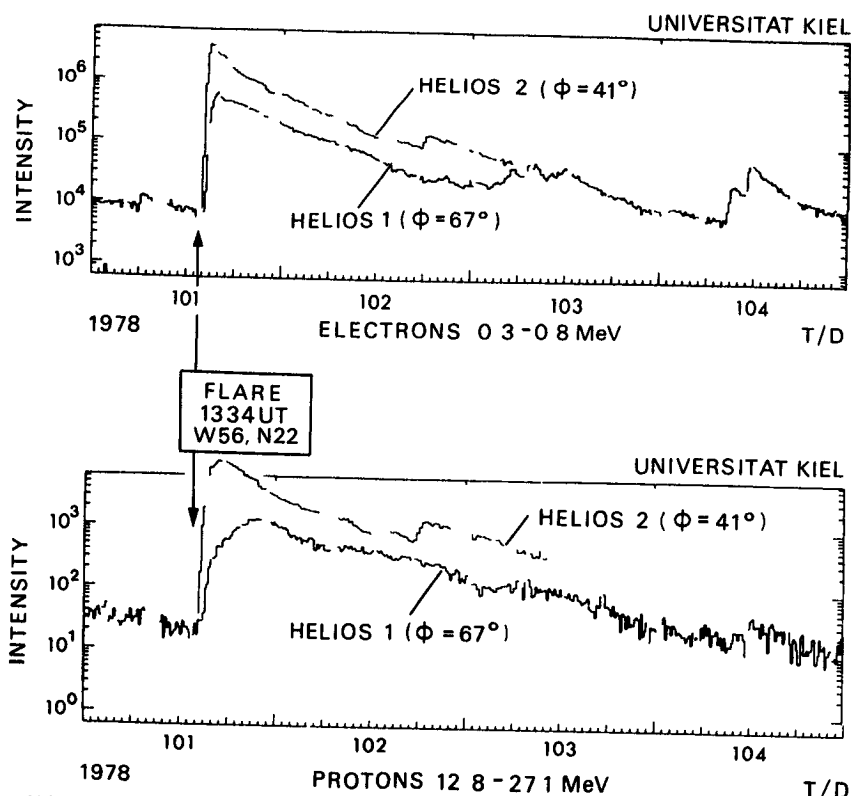
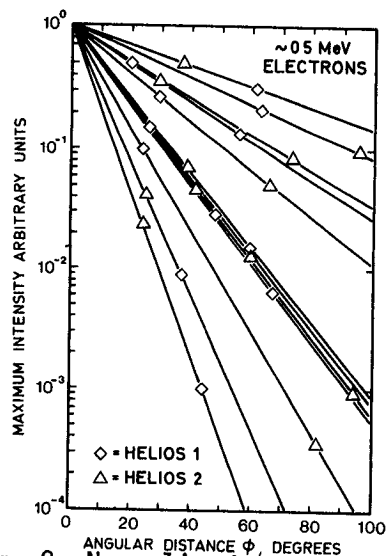
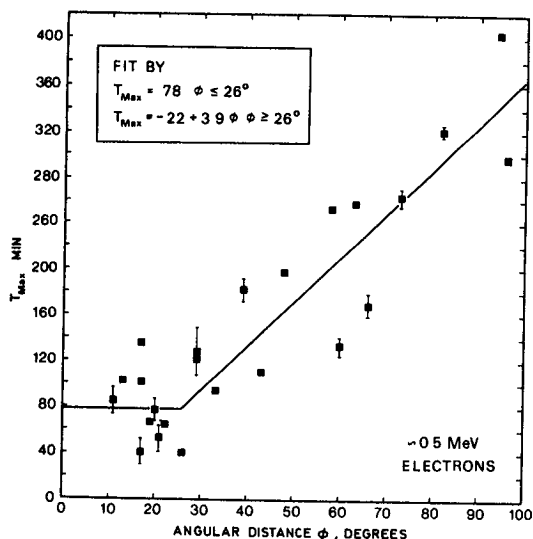
Any other process leading to coronal transport independent of particle type is also excluded by our observation (bird cage model (9) and coronal shock).

The considerable spread in the amplitude variation (Figure 2) precludes any simple classification scheme with coronal distance only. There is no apparent association of the size of the variation with the location of the coronal connection point inside or outside the fast propagation region. The observations suggest that we have no universal process for coronal diffusion as e.g. inherent in the Fisk and Schatten (10) model, but a process which varies highly with individual coronal magnetic field structures.

5. Acknowledgements. The authors appreciate the collaboration and support from the other members of the HELIOS-team from the Kiel University. This work was partly supported by the German Bundesminister für Forschung und Technologie.

#### References

1. Wibberenz, G., K. Kecskeméty, H. Kunow, A. Somogyi, B. Iwers, Y.I. Logachev, V.G. Stolpovskii, (1985), Coronal and interplanetary transport of solar energetic protons and electrons, to be published
2. Reid, G.C., (1964), J. Geophys. Res. 69, 2659 - 2667
3. Reinhard, R. and G. Wibberenz, (1974), Solar Phys. 36, 473 - 494
4. Palmer, I.D., (1982), Rev. Geophys. Space Phys. 20, 335 - 351
5. Ng, C.K. and L.J. Gleeson, (1975), Solar Phys. 46, 347 - 375
6. Mc Guire, R.E. et al., (1983), 18th Int. Cosmic Ray Conf. 10, 353 - 360
7. Reinhard, R. and E.C. Roelof, (1973), 13th Int. Cosmic Ray Conf. 2, 1378 - 1383
8. Ma Sung, L.S. et al., (1975), 14th Int. Cosmic Ray Conf. 5, 1767 - 1772
9. Newkirk, G. and D.G. Wentzel, (1978), J. Geophys. Res. 83, 2009 - 2015
10. Fisk, L.A. and K.H. Schatten, (1972), Solar Phys. 23, 204 - 210



# GEOMETRY OF THE DIFFUSIVE PROPAGATION REGION IN THE AUGUST 14, 1982, SOLAR ELECTRON EVENT

Paul Evenson  
Bartol Research Foundation of the Franklin Institute  
University of Delaware  
Newark, Delaware 19716 USA

**ABSTRACT** On August 14, 1982, relativistic electrons arrived promptly after an impulsive gamma-ray flare, indicating that very little scattering was taking place in interplanetary space. By ignoring anisotropy data the time profile of the event is well described by interplanetary diffusion except for the derived particle injection time. This discrepancy provides independent evidence that the particles are diffusing in a volume close to the sun rather than in interplanetary space. The flux at maximum method of determining the number of particles produced is still a good approximation when appropriately applied.

**1. INTRODUCTION** With the recent availability of high resolution gamma ray data from the solar maximum mission accurate counting of particles emitted by solar flares has assumed a new importance. Gamma ray fluences yield estimates for the number of particles interacting in the target which have been used to calculate the fraction of particles escaping the target by comparison with interplanetary observations (Von Rosenvinge et al. 1983, Evenson et al. 1984). To date these comparisons have been made using the time to maximum method (Parker, 1963) to estimate the number of escaping particles. It is well recognised that this method removes most sensitivity to the interplanetary diffusion coefficient but depends explicitly on the assumption that the particles are diffusing isotropically in interplanetary space and that the distance from the source to the observer is known.

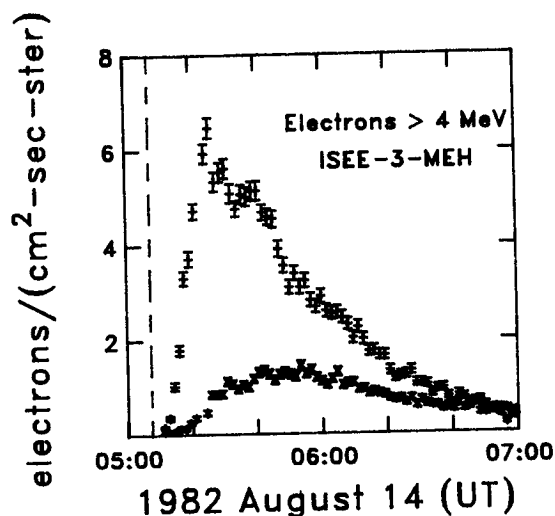


FIGURE 1

**2. THE 1982 AUGUST 14 ELECTRON EVENT** On the 14th of August, 1982, a solar flare located at a longitude of W66 produced an intense, highly impulsive burst of radiation (x-rays through MeV gamma rays) at 05:07:30 earth received time (Kane et al. 1985). The time profile of a relativistic electron event which followed this flare is shown in figure 1, where the dashed line gives the time of the photon impulse. A large anisotropy is evident -- the

upper trace gives the flux from the direction of the sun along the interplanetary magnetic field line and the lower trace gives the flux back toward the sun. When the observed anisotropy is considered it is obvious that isotropic diffusion in the interplanetary medium cannot be the source of the shape of the time profile. Kane et al. (1985) conclude that the time profile of this event can be explained by impulsive production of all electrons at the time of the photon impulse, followed by coronal diffusion (Reid, 1964) and interplanetary focused diffusion (Bieber et al., 1980).

**3. VOLUME OF THE DIFFUSION REGION** The combination of two dimensional diffusion with escape in the Reid model is in fact similar to three dimensional diffusion (Ford et al., 1977). Therefore if one ignores the anisotropy and models the average electron flux as a function of time by interplanetary isotropic diffusion a very good fit is obtained with an estimated mean free path of 0.15 AU. It is interesting to note that one can deduce that the particles have not in fact diffused in interplanetary space without reference to the anisotropy information. This conclusion is reached by considering plots of

$$\ln(I \cdot (t-t_0)^{3/2}) \text{ versus } 1/(t-t_0)$$

(e.g. Cline and McDonald, 1968). Data scaled in this manner lie on a straight line if and only if the correct choice for the origin time ( $t_0$ ) of the particles is made. The slope of the line then gives the diffusion coefficient and the intercept gives the total number of particles released. determining the particle number in this manner is exactly equivalent to using the time of maximum method. By stepping the

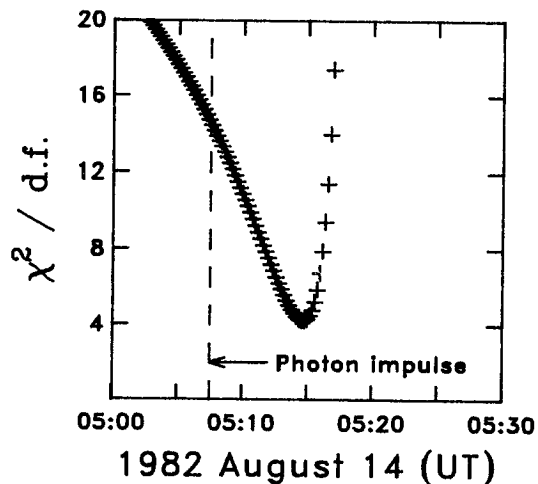


FIGURE 2

introduced by fluctuations in the magnetic field direction at the spacecraft rather than a systematic deviation from a diffusive shape.

assumed origin time in small increments and fitting a straight line to the rescaled data for each time one can generate the plot in figure 2 which shows the value of chi-squared for the best fit straight line at each time step. The estimated origin time of the particles is thus 05:15, the time at which the scaled data are best represented by a straight line. In generating this figure the fit was done to the sum of the two curves in figure 1. A minimum chi-squared of greater than one is a result of scatter in the data

The time axis of figure 2 has been adjusted to correspond to the arrival time at the spacecraft of a photon emitted from the sun at the time of the supposed acceleration of the particles. The time of the photon impulse is indicated with a vertical line. Not only is the time derived from the diffusion fit much later than the gamma ray flash, it actually is later than the arrival of the first electrons at the spacecraft. This seemingly absurd finding is actually the desired result; it indicates that the observer is not embedded in the diffusion volume but rather is seeing the diffusion process as reflected in the continuous escape of a small fraction of the diffusing particles which then propagate to the spacecraft nearly unimpeded by scattering in the interplanetary medium.

The error in the acceleration time estimate immediately provides a limit on the volume of the diffusion region. Since the transit time of an electron along the Parker field is eleven minutes it can be shown that an eight minute error implies that the radius of the diffusion region cannot be larger than 0.3 AU. Actually the situation is more complex than this because interplanetary scattering is influencing the shape of the time profile. Using the profile of the outward flux (upper trace of figure 1) yields a larger time error whereas a fit only to the backward flux interestingly gives an origin time very much closer to the gamma ray flash. This backward flux profile of course is produced predominantly by interplanetary scattering. In conjunction with other work (Bieber et al., 1985) I have done a detailed fit to this event with the conclusion that the time evolution is consistent with diffusion in the solar corona, although a diffusion region with dimensions as large as 0.1 AU probably can not be excluded.

4. NUMBER OF PARTICLES ACCELERATED The pitch angle distribution of the electrons at the spacecraft can be determined from the data, integrated over time, and projected in the radial direction to obtain the electron fluence at the spacecraft, 25200 electrons per square centimeter. Reid (1964) shows that the net outflow from any point on the surface can be determined analytically given the distance from the flare to the foot of the field line, the loss time constant and the diffusion coefficient. Using the solar wind speed (Bame, private communication) of 280 km/sec I estimate that the flare occurred 25 degrees from the best connection field line and then obtain a loss time constant of 1/hr and a mean free path of 500 km from the fit to the data. Scaling the spacecraft fluence to the solar surface by the square of the distance to the center of the sun and using the Reid expression for the fluence from the solar surface implies the production of  $3.1 \times 10^{31}$  electrons. This may be compared with an estimate of  $6.2 \times 10^{31}$  obtained using the directionally averaged flux and the time of maximum method.

The closeness of these two numbers is not completely fortuitous. As Reid (1964) points out, the fluence of particles leaving the sun is not nearly so strong a function of distance from the flare as is the maximum intensity. In the limit of slow escape the escaping fluence becomes independent of position. With the parameters derived for this event the fluence at a point 25 degrees removed from the flare site is only a factor of three more than the fluence obtained by dividing the total number of particles by the surface area of the sun. (The two fluences are approximately equal 55 degrees from the flare site.) If the subsequent diffusion in interplanetary space produces a time profile which is long compared to the duration of the injection then the time of maximum method can still yield reliable results even though the diffusion in connection longitude is taking place on the sun. In the 1982 August 14 event effects of interplanetary and coronal diffusion on the time profile are comparable. Therefore the two methods give consistent results. A good rule of thumb for counting particles from a flare would be that if the net fluence is easy to determine, i.e the event is very anisotropic, use the fluence and the Reid model. On the other hand, when an event is sufficiently isotropic that the fluence is statistically difficult to determine it is likely that the conditions for the validity of the time of maximum method are satisfied.

5. ACKNOWLEDGEMENTS I would like to thank Drs. J.A. Earl and J.W. Bieber for many helpful discussions. This work was supported in part by NASA grant NAG-374.

#### 6. REFERENCES.

- Bieber, J.W. et al., J. Geophys. Res., 85, 2313, 1980.  
 Bieber, J.W. et al., 19th ICRC paper SH 4.2-23, 1985.  
 Cline T. and F.B. McDonald, Solar Phys., 5, 507, 1968.  
 Evenson, P., et al., Astrophys. J., 283, 439, 1984.  
 Ford, T. et al., J. Geophys. Res., 82, 4704, 1977.  
 Kane, S.R., P. Evenson and P. Meyer, submitted, 1985.  
 Parker, E., Interplanetary Dynamical Processes, ed. R.E. Marshak, (New York: Wiley) 1963.  
 Reid G., J. Geophys. Res., 69, 2659, 1964.  
 Von Rosenvinge, T.T., et al., 17th ICRC, 3, 28, 1981.



# PECULIARITIES OF PROPAGATION OF CHARGED PARTICLES IN SOLAR CORONA

E.I.Morozova, N.F.Pisarenko, N.A.Mikryukova  
Space Research Institute, 117810 Moscow, USSR

V.V.Klimenko, V.E.Timofeev, Yu.G.Shafer  
Institute of Cosmophysical Research & Aeronomy  
Lenin Ave., 31, 677891 Yakutsk, USSR

## ABSTRACT

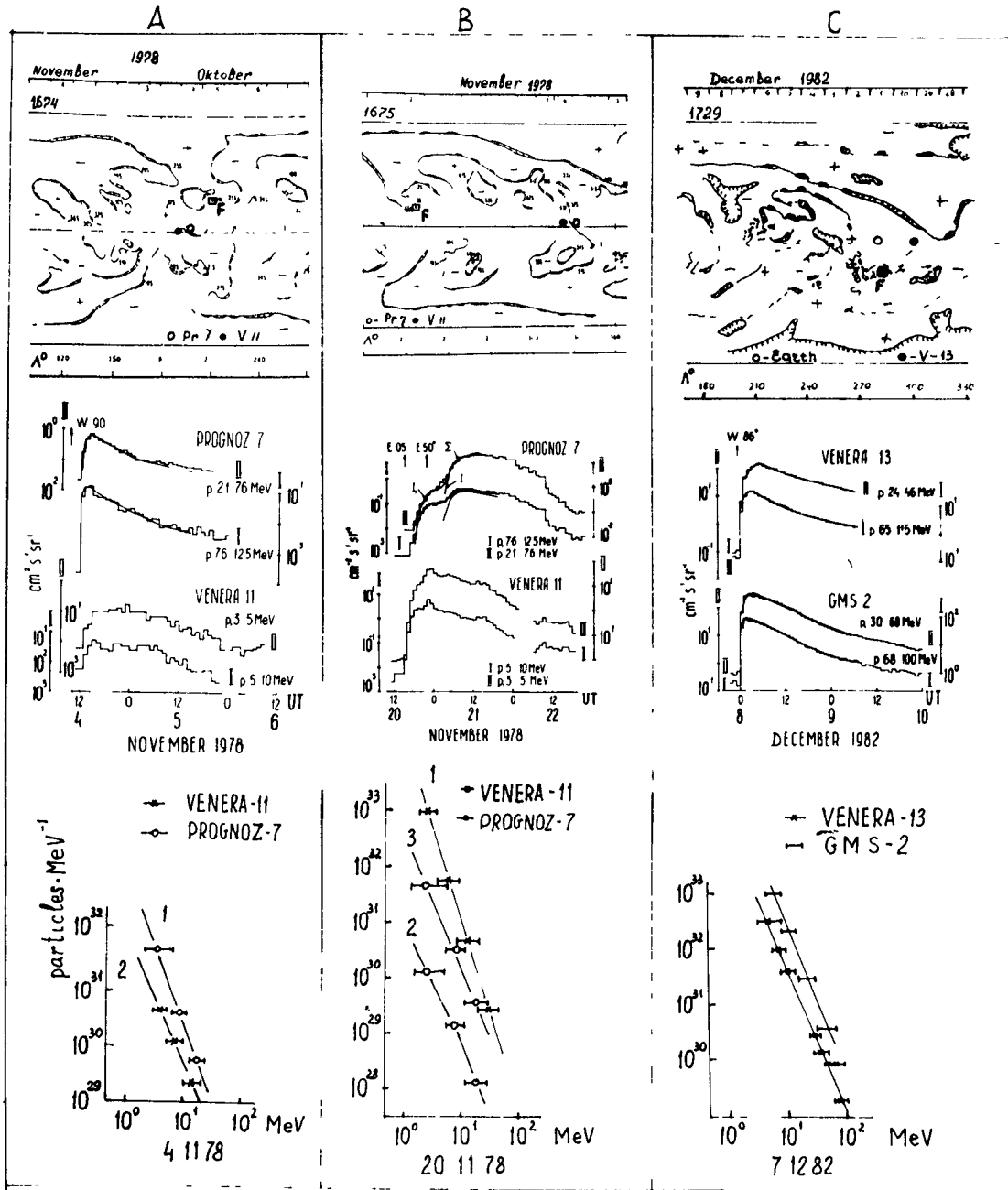
The influence of boundaries of the large-scale unipolar magnetic regions (UMR) on the Sun upon the charged particle propagation in the solar corona and interplanetary space is investigated. Increases of the charged particle fluxes from solar flares on November 4 and 20, 1978 detected by "Venera-11" and "Prognoz-7" and on December 7, 1982 by "Venera-13" and "GMS-2" were analyzed.

1. The investigations of a large number of solar flares located at various heliolongitudes revealed some regularity in dependence of time of the coronal particle transfer from the flare heliolongitude [1,2]. It was shown that out of the region of fast propagation of particles the speed of coronal transfer of particles is  $17 - 40^\circ/\text{hr}$  [2]. However, it is still unclear where the deceleration of a flux of particles propagating in corona occurs and with what the decrease of transfer speed is associated.

2. To estimate the influence of boundaries of the large-scale UMR upon temporal and spectral characteristics of charged particle fluxes the increases of fluxes associated with November 4 and 20, 1978 and December 7, 1982 solar flares were investigated (Figure). Each event was observed simultaneously at two spacecraft located at various azimuthal and radial distances from the Sun. In Figure the synoptical maps of photospheric magnetic fields are shown where  $\square F$  are places of the flares [3]. Here the projections of force line bases (injection points) associated with spacecraft are shown. The points of connection on the Sun are calculated taking into account the average speed of solar wind on Prognoz-7 and IMP-8 data.

The injection moment of particles into the force tube connected with spacecraft was determined on [5]. On difference between moments of injection and generation of particles (maximum in  $H_\alpha$ ) the speed of particle flux transfer in the corona is estimated.

For 4.11.78 event the fast arrival of particles to the point of connection with Prognoz-7 (flare and point of connection are in one UMR) is observed and the transfer speed



is  $\sim 145^\circ/\text{hr}$ . At the injection point Venera-11 (a connection point) a significant delay of particles is observed and an average particle transfer speed in the corona to the connection point with Venera-11 is only  $\sim 12^\circ/\text{hr}$ . It is obvious that such a decrease of the average speed is caused by the particle propagation across the UMR boundary. Since the azimuthal distance between injection points Prognoz-7 and Venera-11 is  $\sim 8^\circ$  the estimated transfer speed of particles across the UMR boundary is  $\sim 5^\circ/\text{hr}$ .

In 20.11.78 event (Figure, B) for Venera-11 the moments of injection and generation of particles coincide. The injection point Venera-11 is at one UMR with the flare and the fast transfer of particles inside UMR is realized. The particles from the flare into the force tube connected with Prognoz-7 are injected twice. The first moment of the injection (1525 UT) is delayed with respect to the moment of generation by  $\sim 33$  min which yields the speed of particle transfer in the corona to the injection point Prognoz-7

$\sim 135^\circ/\text{hr}$ . The second injection (the arrival of the main "mass" of particle flux) occurred at 1725 UT and the average speed particle transfer in the corona to the injection point Prognoz-7 is  $\sim 30^\circ/\text{hr}$ . Since the azimuthal distance between injection points Venera-11 and Prognoz-7 is  $\sim 6^\circ$  and they are located at various UMR near the boundary then the estimations of speed of particle flux transfer across the boundary yield  $\sim 2.5^\circ/\text{hr}$  [4]. In 7.12.82 event (Figure, C) the place of the flare and the injection point for Venera-13 and GMS-2 are located in one UMR. The moments of generation and injection of particles within measurement errors coincide, i.e. the fast particle transfer in the corona is realized.

3. To determine a total number of particles at the injection point and to estimate the efficiency of the UMR boundary consider the propagation character of charged particles in the interplanetary medium. The location of force line bases connected with Venera-11 and Prognoz-7 (Figure, A, B) near UMR boundary determined significantly a complicated structure of temporal profiles of particle fluxes. UMR boundaries influence not only upon particle propagation in the solar corona but indirectly upon the character of particle propagation in the interplanetary medium. For instance, more complicated than in Prognoz-7 temporal structure of particle flux increase on Venera-11 was caused by a prolonged particle injection (for 4.11.78) into the force tube connected with Venera-11 and by a presence of large-scale interplanetary magnetic field structures near the UMR boundary (for 20.11.78). For illustration the temporal profiles of intensities only at two energy ranges (the average graphs of Figure, A, B, C) were chosen.

Temporal profiles of intensity were approximated by a solution of the diffusion equation [6]. The differential energy spectra of particles at injection points are presented in Figure, A, B, C, bottom. In Figure, A, B the curves 1 show spectra at injection point located in one UMR with flare (the fast particle transfer in the corona). The curves 2 are the spectra at injection point observed behind UMR boundary (the curve 3 transfer across the boundary). The curve 3 is the spectrum of particles propagating fastly across the UMR boundary.

A comparison of a total number of particles before and after the boundary allows to estimate its "transparency". For proton energies  $E \sim 5$  MeV only  $\sim 15\%$  (4.11.78) and  $\sim 8\%$  (20.11.78) of a total particle flux penetrated across the boundary, for  $E_p \sim 20$  MeV this value is  $\sim 25\%$  (4.11.78) and

$\sim 20\%$  (20.11.78). It is interesting to compare the absolute particle fluxes detected at injection points of Venera-11 and Prognoz-7 20.11.78 propagating fastly in the corona (curves 1 and 2, Figure, B). The ratio of these fluxes determines actually the efficiency of fast particle transfer across the UMR boundary. For  $E_p \sim 5$  MeV only  $\sim 0.3\%$  of particles is observed behind the boundary, for  $E_p \sim 20$  MeV energies this value is  $\sim 0.7\%$ .

In the event of 7.12.82 (Figure, C) the absolute particle fluxes on GMS-2 are by an order of magnitude larger than on Venera-11. Here there are no influences of UMR boundaries upon charged particle transfer in the corona. Such a difference in a value of flux confirms the earlier found experimental fact [7] that on closed force lines of geomagnetic field ( $L \sim 6.6$ ) the measured particle flux is larger than its values beyond the Earth's magnetosphere due to the isotropization effect.

4. Thus, the boundary of the UMR decreases significantly the effective speed of particle transfer in the corona. Within the UMR boundary the speed of particle transfer is  $2 + 5^\circ/\text{hr}$ . Only insignificant portion of flare particle flux propagates across the boundary without the change of the speed and density. At estimation of absolute values of particle fluxes from the flare it is necessary to take into account the influence of not only boundaries of large-scale UMR on the Sun but also the peculiarities of processes of interaction of particles with interplanetary and geomagnetic fields.

The authors are grateful to Dr.M.Wada for the kindly presented GMS-2 data.

#### References

1. Reinhard, R., Wibberentz, G., (1974), Solar Phys., vol.36, p.473.
2. Ma Sung, L.S., Van Hollebeke, M.A., McDonald, F.B., (1975), Proc. 14-th ICRC, vol.5, 1979.
3. Solar Geophys. Data, (1978), No.412, Part 1; (1979), No.417, Part II; (1983), No.461, Part I; (1983), No.462, Part I.
4. Klimenko, V.V., i dr., (1982), Izv. AN SSSR, Ser. fiz., 46, No.9, 1702.
5. Walnichek, B.I. i dr., (1980), Geomagnetizm i aeronomiya, 20, No.5, 777.
6. Krimigis, S., (1965), J. Geophys. Res., 78, 1007.
7. Bezrodnykh, I.P. et al., (1981), Proc. 17-th ICRC, Paris, 3, 401.

## SOME CHARACTERISTICS OF THE SOLAR FLARE EVENT OF FEBRUARY 16, 1984

H. Debrunner and E. Flückiger  
Physikalisches Institut, University of Bern,  
3012, Bern, Switzerland

J. A. Lockwood  
Space Science Center, University of New Hampshire  
Durham, New Hampshire 03824 USA

R. E. McGuire  
NASA Goddard Space Flight Center  
Greenbelt, Maryland 20771 USA

1. Introduction In the morning of February 16, 1984 a solar cosmic ray event (GLE) was recorded by the world-wide network of neutron monitors (NM). In Fig. 1 we show the counting rate vs. time profile of the Goose Bay NM (geog. lat. = 53.3°N, geog. long. = 299.6°E) where the increase is expressed as percent of the counting rate of an equatorial sea level NM. The Goose Bay NM was observed to have the maximum response to the solar particles. Its counting rate vs. time profile exhibits a rapid increase to maximum, has a large amplitude (~ 170%) and decays rapidly to background in ~ 90 min. In Fig. 1 we also show the counting rate vs. time profile for the Tixie Bay NM (71.6°, 128.9°) which recorded an increase of only a few percent. Since the NMs at Goose Bay and Tixie Bay have asymptotic viewing directions ~ 180° apart in longitude, we can deduce the anisotropy of the solar particle flux at earth from these stations using the expression:

$$A = \frac{\Delta N_{GB} - \Delta N_{TB}}{\Delta N_{GB} + \Delta N_{TB}}.$$

The anisotropy shown in the lower part of Fig. 1 is ~ 1 for the first 45 min. of the event.

The signature of the GLE on February 16, 1984 is similar to that of the GLE on May 7, 1978 for which it has been shown that:

- a) the propagation of the solar particles was nearly scatter-free between the sun and the earth [1];
- b) the flare particles at the sun had relatively easy access to the footpoint of the magnetic field line connecting the sun and the earth [2].

2. Source of the Solar Flare Particles We have inspected the H $\alpha$  and solar magnetic field synoptic charts and the radio observations in order to locate the active region responsible for the solar flare in which the particles producing the GLS on February 16, 1984, were accelerated. The solar synoptic charts show three major active regions at heliocentric longitudes between 40°W and 150°W: Regions 4413 at ~ 50°W, 4410 at ~ 95°W and 4408 at ~ 130°W [3]. No H $\alpha$  flare was reported from the observations before or during the time of the GLE. We, therefore, conclude that the source of the particles was not on the visible disk of the sun.

On February 16, 1984 at 0858 UT a type III G, a type II metric and a microwave burst started. Since the microwave spectrum showed the spectral maximum below 3.2 GHz, the corresponding active region must have been behind the limb of the sun. An analysis of the Nançay radio

heliograph data [4] and the highest frequencies at which the burst was observed, excludes a flare position at  $40^\circ$  beyond the west limb of the sun corresponding to active region 4408.

The possibility that the active region 4408 was the source of the solar particles can also be excluded on the basis of the intensity-time (IT) profile of the GLE observed at earth. From an analysis of the fine-time resolution data from the cosmic-ray telescopes on IMP7 and Helios A for the May 7, 1978 GLE we have shown that the acceleration of the energetic flare protons can be described by a  $\delta$ -like process at the flare site and that the coronal propagation of the flare particles can be approximated by 2-dimensional diffusion with losses. We can write for the (IT) profile of the injection of the solar particles into the interplanetary medium [2]:

$$I^E(b,t) = \frac{A(E)}{t} \exp \left\{ - \frac{b^2}{4D_S^E t} - \beta^E t \right\} \quad (1),$$

where:

- $b$  = longitudinal component of the position vector on the surface of the sun with respect to the flare site;
- $D_S^E$  = the solar diffusion coefficient for protons of energy  $E$ ;
- $\beta^E$  = loss rate for protons of energy  $E$ ;
- $A(E)$  = constant factor.

In the interval  $20 < E < 500$  MeV the diffusion coefficient was found to be  $D_S^E [\text{cm}^2/\text{s}] \sim 4.4 \times 10^{15} \{E[\text{MeV}]\}^2$ . The loss rate for  $90 < E < 500$  MeV was  $\beta^E \sim (2.9 \pm 0.5) \text{hr}^{-1}$ . Using the results of this model for the flare particle propagation at the sun we calculated the expected (IT) profiles of the solar particles at earth for the GLE on February 16, 1984 assuming the flare position at  $95^\circ\text{W}$  in one case and  $130^\circ\text{W}$  in the other case. The diffusion of the solar particles in the interplanetary magnetic field (IMF) between the sun and the earth has been neglected because the high anisotropy of the GLE indicates scatter-free propagation.  $D_S^E$  was evaluated by extrapolating the energy dependence to 2 GeV.  $\beta^E$  was taken as  $\sim 2.9 \text{hr}^{-1}$ , which is probably too small because there is evidence that  $\beta$  is increasing with energy [2]. The position parameter  $b$  depends on the position of the footpoint at the sun of the IMF line connecting the earth to the sun. Unfortunately, no solar wind speed ( $V_{\text{SW}}$ ) data were available to us to determine this footpoint. We, therefore, evaluated  $V_{\text{SW}}$  from the time delay of the sudden commencement observed on February 10, 1984, most probably produced by the shock front of the solar flare on February 16, 1984. For the deduced value of  $V_{\text{SW}} \sim 400 \text{ km/s}$ , the footpoint of the IMF to earth was  $\sim 33^\circ$  from an assumed flare site at  $95^\circ\text{W}$  and  $\sim 68^\circ$  from a site at  $130^\circ\text{W}$ .

The theoretical (IT) profiles of the solar particles at earth are shown in Fig. 2 along with the NM count rate profile at Goose Bay. From an inspection of Fig. 2 we conclude that a source location of  $130^\circ\text{W}$  can be excluded. The only possible source is located at  $95^\circ\text{W}$ . Furthermore, the agreement between the observed and the theoretical (IT) profiles is very good if we consider that  $D_S^E$  was extrapolated, the value of  $\beta^E$  used for  $E \sim 2 \text{ GeV}$  was determined for lower energy protons and both these parameters may vary from event to event [2].

### 3. Energy Spectrum and Pitch Angle Distribution of the Solar Particles

We recognize that the GLE of February 16, 1984 shows a normal signature for a flare event in which the particles at the sun have relatively easy access to the footpoint of the IMF line connecting the

earth to the sun and the IMF conditions are quiet so that the flare particle propagation from the sun to the earth is essentially scatter-free. In order to determine the rigidity spectrum and pitch angle distribution of the relativistic solar protons at earth we followed the method given by [5]. The response of a neutron monitor to the anisotropic solar proton flux as a function of time,  $\Delta N(t)$ , can be expressed [6]:

$$\Delta N(t) = \sum_{P_c}^{\infty} S(P) \cdot I(P, t) \cdot F(\delta[P], t)$$

where  $P_c$  is the effective cutoff rigidity,  $S(P)$  is the specific yield as a function of rigidity,  $I$  is the solar proton rigidity spectrum, and  $F$  is the pitch angle distribution assumed here to be independent of rigidity. The angle  $\delta(P)$  represents the angular distance between the asymptotic direction of vertically incident particles at the NM and the direction of the IMF near the earth. By a trial and error procedure we can determine the apparent source position and  $I$  and  $F$  which give the best fit of the calculated to the observed data. We used NM data from Akad. Kurchatov, Alert, Alma Ata, Deep River, Durham, Goose Bay, Hermanus, Inuvik, Irkutsk, Jungfraujoch, Kerguelen, Kiel, Kiev, Leeds, Magadan, McMurdo, Moscow, Mt. Washington, Potchefstroom, Rome, Sanae, Terre Adelie, Tixie Bay, and Tsumeb and data from [7]. First results of the analysis give the apparent source direction in a region centered at the geographic coordinates  $\sim 5^\circ S$ ,  $\sim 5^\circ E$ , which is  $45^\circ W$  of the earth-sun line.

The deduced pitch angle distribution  $F(\delta)$  at the time of maximum intensity, is plotted in Fig. 3. Clearly  $F(\delta)$  is very narrow, demonstrating that the propagation of the relativistic solar protons in the IMF from the sun to the earth was practically scatter-free (m.f.p. for pitch-angle scattering  $> 1$  AU). At the time of maximum intensity the rigidity spectrum is given by  $I(P)$  [ $p/m^2$  ster s GV]  $\sim 7.25 \times 10^4 \{P[GV]\}^{-4.25}$  for  $1 < P < 10$  GV, where  $I(P)$  is the flux averaged over  $4\pi$ . The corresponding energy spectrum is shown in Fig. 4 along with the spectrum at lower energies deduced from the cosmic-ray telescope onboard IMP8. The agreement between the two spectra is very good. Unfortunately IMP8 was in the earth's magnetotail so that no direct anisotropy measurements are available for  $E < 500$  MeV.

4. Conclusion If we compare the pitch angle distribution and the energy spectrum of the GLE on February 16, 1984, with those of the GLE on May 7, 1978, we recognize that the two events had similar signatures. Therefore, the NM and spacecraft data for this event are again a key to study the acceleration of solar flare protons, their coronal propagation and their injection into the interplanetary medium.

5. Acknowledgements This research was supported by the Swiss NF (2.206-0.84) and the U.S./NSF (ATM-8324486 and INT-8118555). We thank all the principal investigators of neutron monitor stations who made data available to us. We are indebted to Drs. G. Trottet, K. L. Klein, and A. Magun for radio and microwave data and stimulating discussions. We gratefully acknowledge essential information on  $H\alpha$  observations by Dr. Prokakis and we thank H. Grädel for assistance in the data analysis.

#### 6. References

1. Debrunner, H., et al., 1984, J. Geophys. Res., 89, 769.
2. Lockwood, J.A., and H. Debrunner, 1985, to be pub. J. Geophys. Res.

3. Solar Geophys. Data, 1984, 476, Part 1.
4. Klein, K.L., and G. Trotter, 1985, private communication.
5. Debrunner, H., and J.A. Lockwood, 1980, J. Geophys. Res., 85, 6853.
6. Smart, D., et al., 1971, Proc. ICRC 12th, 2, 483.
7. Pomerantz, M.A., et al., 1985, Proc. IS/CRMH (Japan), 437.

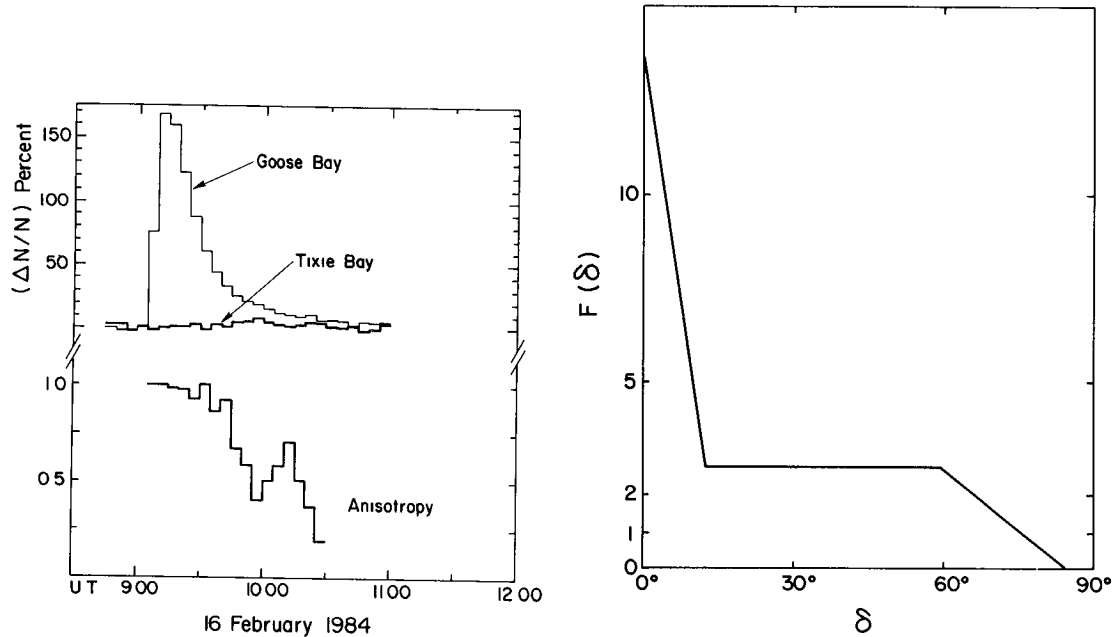


Fig. 1. Percent increase at Goose Bay and Tixie Bay NMs and anisotropy-time profile.

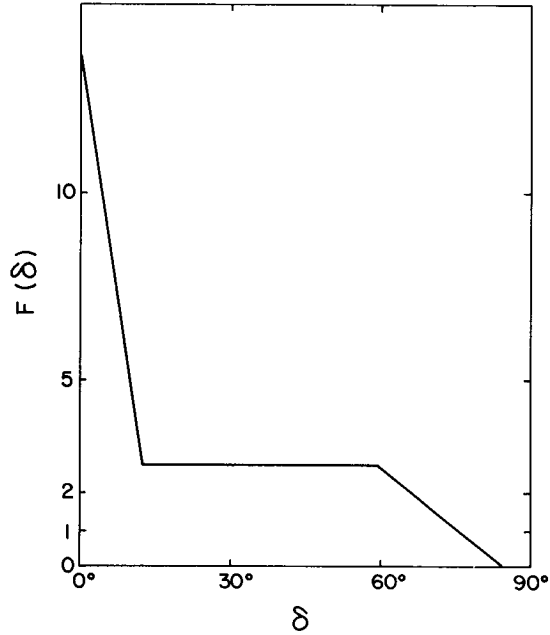


Fig. 3. Pitch angle distribution at time of maximum intensity.

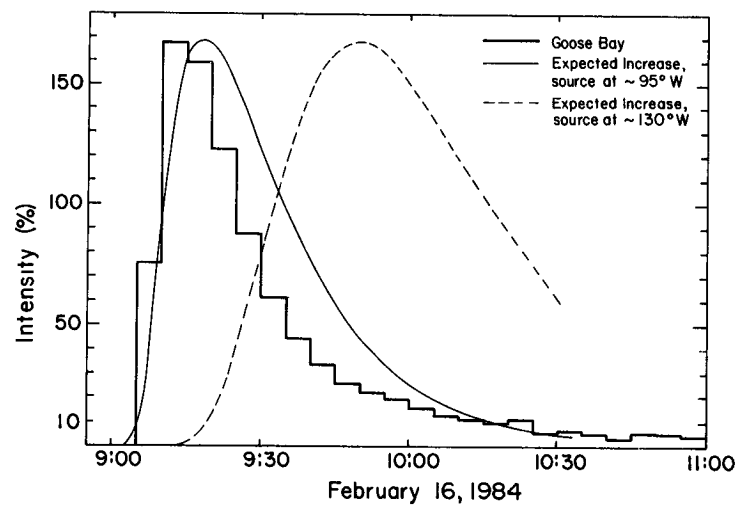


Fig. 2. Intensity-time profile at Goose Bay compared with expected increases for the solar flare locations at 95°W and 130°W.

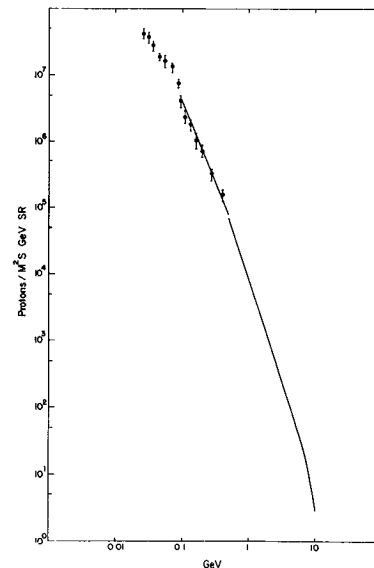


Fig. 4. Energy spectrum at the time of maximum intensity.



CONSTRAINTS ON SOLAR FLARE PARTICLE TRANSPORT  
MODELS FROM ANISOTROPY OBSERVATIONS AT VOYAGER 1

D.C. Hamilton, G.M. Mason and G. Gloeckler

Department of Physics & Astronomy  
University of Maryland, College Park, MD 20742 USA

ABSTRACT

In general a particle transport model for energetic solar flare particles contains a number of free parameters which are determined by fitting various features of observed particle events. Frequently the parameter values are not uniquely determined. In order to place tighter constraints on the models, we have examined the anisotropy of 1 and 25 MeV/nuc protons and helium nuclei during the 22 November 1977 solar particle event using data from the LECP experiment on Voyager 1 at 1.6 AU. We have combined these observations with the time-intensity profiles at Voyager 1 and at 1 AU from ISEE-1 and IMP-8 to determine the magnitude and radial dependence of the interplanetary diffusion coefficient and the required injection duration at the sun. The first order anisotropy amplitudes for both 1 MeV and 25 MeV protons are observed to decrease from maximum values ( $\sim 1$ ) during event onset at Voyager 1 to values consistent with convection in the solar wind at about 3 days into the event decay phase. The intensity and anisotropy profiles at 1.6 AU are consistent with predictions of diffusive transport with a modest mean free path ( $\lambda \sim 0.1$  AU). The radial dependence of  $K_r$  which was determined for low energy particles by Mason *et al.* (1) from the times-to-maximum intensity of 1 MeV/nuc helium at 1 AU and 1.6 AU ( $K_r = K_0 r^{1.3}$ ) predicts too rapid an intensity decay for the 25 MeV protons at 1.6 AU. We are required to abandon a simple power law radial dependence for  $K_r$  in order to fit all the ISEE and Voyager observations.

Acknowledgements. This work was supported by NASA under APL subcontract 601620 and contract NAS5-28704.

Reference

1. Mason, G.M. *et al.* 1985, 19th ICRC, La Jolla, paper SH3.2-5.

# LOW ENERGY PROTON BIDIRECTIONAL ANISOTROPIES AND THEIR RELATION TO TRANSIENT INTERPLANETARY MAGNETIC STRUCTURES : ISEE-3 OBSERVATIONS

R.G. Marsden, T.R. Sanderson, K.-P. Wenzel

Space Science Department of ESA  
ESTEC, Noordwijk, The Netherlands

E.J. Smith

Jet Propulsion Lab., California Institute of Technology,  
Pasadena, CA 91109, USA

**1. Introduction.** It is known that the interplanetary medium in the period approaching solar maximum is characterized by an enhancement in the occurrence of transient solar wind streams and shocks [1, 2] and that such systems are often associated with looplike magnetic structures or clouds [3, 4]. There is observational evidence that bidirectional, field-aligned flows of low-energy particles could be a signature of such looplike structures [5, 6, 11], although detailed models for the magnetic field configuration and injection mechanisms do not exist at the current time. In this paper we present preliminary results of a survey of low-energy proton bidirectional anisotropies measured on ISEE-3 in the interplanetary medium between August 1978 and May 1982, together with magnetic field data from the same spacecraft.

**2. Instrumentation and Analysis.** The particle measurements used in this analysis were obtained with the low-energy proton instrument on ISEE-3 [7], comprising three identical solid state detector telescopes oriented at 30°, 60° and 135° with respect to the spacecraft spin axis. Particles are counted in 8 logarithmically-spaced energy channels in the range 35 - 1600 keV, and with the exception of the highest energy channel (1000 - 1600 keV), data accumulated during each spacecraft revolution are sorted into 8 equal azimuthal sectors. Magnetic field measurements were obtained using the vector helium magnetometer [8] onboard ISEE-3.

In order to determine the anisotropy characteristics, the particle data in two channels (35-56 and 620-1000 keV) were first transformed into a frame of reference moving with the instantaneous solar wind velocity. These transformed data were then subjected to a spherical harmonic analysis in order to derive a series expansion of the 3-dimensional spatial distribution [9] from which the instantaneous particle intensity at 0°, 90°, and 180° relative to the positive B-field direction was calculated for each energy channel. The ratios of the harmonic components  $A_{10}/A_0$  and  $A_{20}/A_0$  where primed quantities refer to the solar wind frame, were used to define 1st and 2nd order anisotropies, respectively. A bidirectional flow (BDF) is seen as a reduction in the flux at 90° as compared to the fluxes at 0° and 180°, which remain approximately equal; in terms of the anisotropies, a BDF is characterised by a positive 2nd-order anisotropy, together with a 1st-order anisotropy which is close to zero. For the purpose of this study, since we are interested in relatively large scale phenomena, we have not considered BDFs of less than 3 hours duration.

We have examined plots of the magnetic field magnitude and direction for the same period for evidence of isolated, large-scale ( $\geq 0.1$  AU) structures convecting past the spacecraft, in particular for signatures of magnetic clouds as defined in [3]. For those candidate structures having a rotational signature

whereby the magnetic field vector rotates progressively in a plane, a minimum variance analysis has been performed to determine the degree of planarity.

**3. Results and Discussion.** From the 45-month data set used for this study, it was possible to identify 66 periods during which BDFs were present. In all cases, effects due to the bow shock have been excluded. By examining the magnetic field data corresponding to these periods, we have been able to group these BDF events into 5 classes as follows:

- I. 19 events associated with a transient magnetic structure having a rotational signature characteristic of a magnetic cloud, which are also related to the passage of an interplanetary shock.
- II. 12 events associated with a transient magnetic structure (non-rotational), which are also shock-related.
- III. 8 events associated with a transient magnetic structure having a rotational signature, but no shock-association.
- IV. 9 events associated with a transient magnetic structure having a non-rotational signature, but no shock-association.
- V. 18 events for which no clear transient magnetic structure could be identified.

From the above it is apparent that the majority of the observed BDFs are associated with transient features in the magnetic field, although not all events are related to classical, shock-associated magnetic clouds. In addition, it should be noted that we have identified a number of examples of classical magnetic clouds which have no related BDF signature in the energy range covered by our instrument.

It is beyond the scope of this paper to present examples of all the above event classes in detail; however, in Figs. 1 and 2 we show the combined particle and magnetic field data for two 3-day periods containing a class I and a class III event, respectively. In the upper panels we have plotted the intensity of the 620 - 1000 keV channel (Fig. 1) and the 35 - 56 keV channel (Fig. 2) at 0°, 90° and 180° with respect to the magnetic field direction; the second panel shows the ratio of the second harmonic components  $A_{20}/A_0$  in the solar wind frame. The three lower panels show the magnitude, elevation and azimuth (in GSE coordinates) of the magnetic field, respectively.

The period containing the class I event starts at 0000 UT on Sep. 28, 1978. At this time, the fluxes seen in all channels are still elevated as a result of the large solar particle event which started 5 days earlier. The intensity in the 620 - 1000 keV channel shows an increase starting at 0700 UT, probably associated with a 2B flare, located at N27, W19 [10] with  $H_\alpha$  maximum on Sep. 27, 1442 UT. An interplanetary shock was observed at the spacecraft at 2040 UT on Sep. 28; a second shock passed the earth at 0301 UT on Sep. 29, but was not seen at ISEE-3 due to a data gap. The particle intensity decreased sharply at 0830 UT, coincident with the arrival (presumably) of driver gas and an isolated magnetic structure possessing a clear rotational signature, which persisted until 0330 UT on Sep. 30. Throughout this period, bidirectional particle fluxes were observed, as evidenced by the large positive 2nd harmonic

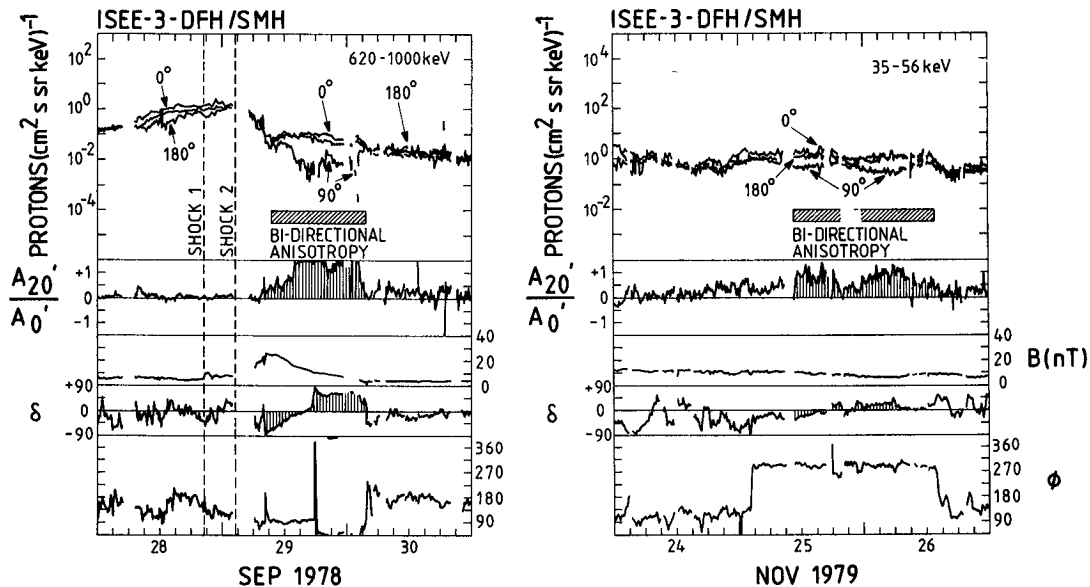


**Fig. 1.** (left) Proton intensity and anisotropy parameters, and magnetic data for the BDF event of 29 Sept. 1978.

**Fig. 2** (right) As for Fig. 1, for the BDF event of 25, 26 Nov. 1979.

which dominated the anisotropy signature, and the prominent decrease in the flux at  $90^\circ$  relative to the field-aligned component. The particle data at lower energies (not here) show evidence for two separate populations bounded by the discontinuity in the magnetic cloud signature occurring at 1720 UT on Sep. 29.

The 3-day period shown in Figure 2 starting at 0000 UT on Nov. 24, 1979 is characterised by the appearance of an isolated, stable magnetic structure at 0230 UT on Nov. 25, accompanied by bidirectional fluxes. In this example of a class III event, the magnetic signature is less rotational than in the class I event described above. As in the previous case, the bidirectional flow is not continuous at the same level throughout the event, but is interrupted, presumably by the passage of a flux tube separated from the cloud.

In addition to the classification described above, we have examined the statistical characteristics of the complete BDF event set, with the following results:

- a) 48 events are associated with isolated, transient magnetic structures, of which 27 show a rotational signature and 10 show a constant field orientation normal to the nominal spiral direction; the remaining 11, while clearly separated from the ambient medium, show no specific directional features. In general, the r.m.s. noise in the field seems to be smaller when bidirectional fluxes are present.
- b) The distribution of BDF event durations is presented in Fig. 3, the average duration being 15 hours. In 20% of the cases, the BDF persisted for more than 24 hours, and the longest event observed had a duration of 50 hours. In terms of the spatial extent of the structures supporting the flows, the above data imply an average scale size of  $\sim 0.15$  AU, with a maximum of 0.5 AU if we assume a nominal solar wind velocity of 400 km/s.

- c) 37 events followed the passage of an interplanetary shock, with a separation in time of, on average, 19 hours. This statistic should be treated with caution, however, since in several other events, the observed BDF may have been related to a shock which passed the spacecraft more than 40 hours previously.
- d) For 41 events, the amplitude of the 2nd harmonic at 35 keV is comparable to, or greater than, that at 620 keV.

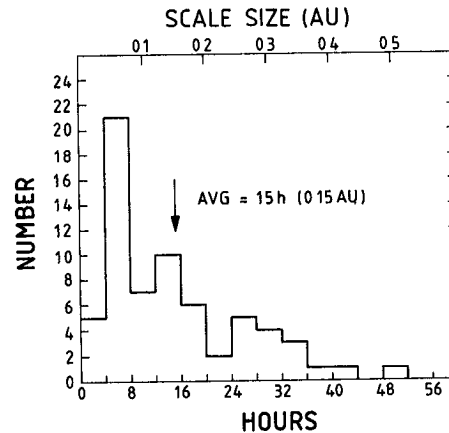


**Fig.3.** Distribution of BDF event durations. Scale size shown for solar wind vel. = 400 km/s.

Taking into account the relative propagation times for 35 and 620 keV particles together with point d) above, we suggest that, while undoubtedly fitting the data for a number of (in particular) class I events, the commonly proposed model (e.g. [11]) in which particles are confined in a simple, large-scale magnetic loop with mirroring occurring in the high-field regions close to the Sun cannot explain all our BDF observations. Given the uncertainty in the 3-dimensional field geometry within magnetic clouds which still exists, we cannot rule out effects of a more localised nature giving rise to the observed anisotropies, particularly for events having relatively short duration. The qualitative correlation between the degree of quietness of the magnetic field and the presence of bidirectional flows is clearly of importance, and will be addressed in a future paper.

**4. Acknowledgement.** Part of the research described in this paper was carried out by the Jet Propulsion Laboratory, under a contract with the National Aeronautics and Space Administration.

## REFERENCES

1. Burlaga, L.F. et al., *J.Geophys.Res.*, 89, 6579, 1984.
2. Smith, E.J., *Sp.Sci.Rev.*, 34, 101, 1983.
3. Klein, L.W. and Burlaga, L.F., *J.Geophys.Res.*, 87, 613, 1982.
4. Burlaga, L.F. et al., *Geophys.Res.Lett.*, 9, 1317, 1982.
5. Sanderson, T.R. et al., *Geophys.Res.Lett.*, 10, 916, 1983.
6. Palmer, I.D. et al., *J.Geophys.Res.*, 83, 75, 1978.
7. Sanderson, T.R. et al., *J.Geophys.Res.*, 86, 4425, 1981.
8. Frandsen, A.M.A. et al., *IEEE Trans.Geosci.Electron.*, GE-16, 195, 1978.
9. Sanderson, T.R. et al., *J.Geophys.Res.*, 90, 19, 1985.
10. *Solar-Geophys. Data*, 415-II, 29, 1979.
11. Kutchko, F.J. et al., *J.Geophys.Res.*, 87, 1419, 1982.

SECOND-ORDER COMPTON-GETTING EFFECT ON ARBITRARY INTENSITY DISTRIBUTION

C.K. Ng

Dept of Mathematics, University of Malaya  
Kuala Lumpur, Malaysia

**1 INTRODUCTION** Theoretical studies of energetic particles in space are often referred to a special frame of reference. To compare theory with experiment, one has to transform the particle distribution from the special frame to the observer's frame, or vice versa. Various methods have been derived to obtain the directional distribution in the comoving frame from the directional fluxes measured on a spacecraft (e.g., Erdos, 1981; Sanderson *et al.*, 1985, and references therein). These methods have become progressively complicated as increasingly detailed directional particle data become available.

We present here a set of 2nd order correct formulae for the transformation of an arbitrary differential intensity distribution, expressed as a series of spherical harmonics, between any two frames in constant relative motion. These formulae greatly simplify the complicated procedures currently in use for the determination of the differential intensity distribution in a comoving frame.

**2. THE DESIRED FORM OF THE TRANSFORMATION** In the observer's frame, let the particle differential intensity w.r.t. momentum (or rigidity) be expressed in terms of the spherical harmonics  $C_n^m$ ,  $S_n^m$  as :

$$j_p^S(p_s, \theta_s, \phi_s) = \sum_{n=0}^{\infty} \sum_{m=0}^n \{A_{nm}^S(p_s) C_n^m(\theta_s, \phi_s) + B_{nm}^S(p_s) S_n^m(\theta_s, \phi_s)\}. \quad (1)$$

We wish to transform this to the frame moving with velocity  $\underline{W}$  relative to the observer, also in terms of spherical harmonics :

$$j_p(p, \theta, \phi) = \sum_n \sum_m \{A_{nm}(p) C_n^m(\theta, \phi) + B_{nm}(p) S_n^m(\theta, \phi)\}. \quad (2)$$

Here  $C_n^m(\theta, \phi) = P_n^m(\cos \theta) \cos(m\phi)$ ,  $S_n^m(\theta, \phi) = P_n^m(\cos \theta) \sin(m\phi)$ ,  $(3)$

$P_n^m(\ )$  = associated Legendre function,  $p$  = particle momentum, and  $\theta, \phi$  are the polar and azimuthal angles of the particle arrival direction. The superscript or subscript  $S$  indicates that the quantity is referred to the frame of the observer/spacecraft.

In short, our purpose is to find the relation between the coefficients  $A_{nm}$ ,  $B_{nm}$  in the comoving frame and the coefficients  $A_{nm}^S$ ,  $B_{nm}^S$  and their  $p$ -derivatives in the observer's frame, and vice versa.

We denote below the components of  $\underline{W}$  along and normal to the magnetic field by  $\underline{W}_{\parallel}$  and  $\underline{W}_{\perp}$  respectively, and define  $\hat{W}_{\parallel} = \underline{W}_{\parallel}/W$ ,  $\hat{W}_{\perp} = \underline{W}_{\perp}/W$ , and  $\epsilon = W/v$ , with  $v$  the particle speed. We choose the polar coordinate axis to point along the magnetic field, and measure  $\theta$  from the direction of  $\underline{W}_{\perp}$ . Hence,  $\theta, \phi$  denote the particle pitch-angle and gyrophase respectively. We will refer to this coordinate system as the standard one.

**3. SOME CURRENT SOLUTIONS** Gleeson and Axford (1968) and Forman (1970) obtained 1st order transformations from (2) to (1), for  $j_p = A_{00}(p)$ . Forman's elegant approach uses the Lorentz invariance of the phase-space distribution function. Balogh *et al.* (1973) obtained a 2nd order result for the isotropic case and a 1st order result for the anisotropic case

that includes the  $n=1$  terms. Ng (1984) obtained a 2nd order transformation for gyrotropic distributions ( $j_p = \sum_n A_{no}(p) P_n(\cos\theta)$ ) valid for relativistic particles.

Another approach, taken by Sanderson *et al.* (1985), is based on a method by Ipavich (1974). This is outlined below. One may use eqn (12) of Ipavich (1974) to transform each term in the series (1), *provided one pays the price of using a non-standard coordinate system* in which the polar axis points along the velocity  $\underline{W}$ . Denote the non-standard polar and azimuthal angles by  $\theta^*$ ,  $\phi^*$ . This allows any term  $A_{nm}^S(p_s) C_n^m(\theta_s, \phi_s)$  for the phase-space density to be transformed to:

$$A_{nm}^S [p(1-2\epsilon \cos\theta^* + \epsilon^2)^{\frac{1}{2}}] C_n^m \{ \tan^{-1} [\sin\theta^* / (\cos\theta^* - \epsilon)], \phi^* \}, \quad (4)$$

and similarly for  $B_{nm}^S(p_s) C_n^m(\theta_s, \phi_s)$ . Following Ipavich and Sanderson *et al.*, one assumes a power-law spectrum ( $p_s d/dp_s \log A_{nm}^S(p_s) = -2r_n$ , and obtains from (4),

$$(1-2\epsilon \cos\theta^* + \epsilon^2)^{-r_n-1} A_{nm}^S(p) C_n^m \{ \tan^{-1} [\sin\theta^* / (\cos\theta^* - \epsilon)], \phi^* \}. \quad (5)$$

Eqn (5) may be compared to Sanderson *et al.*'s eqn (A11). There remains the task of converting (5) to the form (2), including a change from  $\theta^*, \phi^*$  back to the standard angular coordinates  $\theta, \phi$ .

Sanderson *et al.* accomplish the above by *numerically integrating* the transformed intensity obtained from (5) (their eqns (A11) and (A12)) over each sector, each energy interval and each telescope to produce an *equivalent set of counts in the comoving frame*, and then *fitting* (2) to the equivalent set of counts.

Although the assumption of a power-law spectrum may be avoided by using (4), the numerical integration and the second fitting are time-consuming and unnecessary for say,  $>10$  KeV protons, because we are able to obtain the transformation posed in Section 2, correct to  $O(W/v)^2$  and for arbitrary direction of  $\underline{W}$ .

#### 4. DERIVATION OF THE TRANSFORMATION FORMULAE We begin with

$$j_p(p, \theta, \phi) = \sum_{nm} \left\{ \frac{v p^2}{v_s p_s^2} A_{nm}^S(p_s) C_n^m(\theta_s, \phi_s) + \frac{v p^2}{v_s p_s^2} B_{nm}^S(p_s) S_n^m(\theta_s, \phi_s) \right\}, \quad (6)$$

and consider each term in the series. First we transform the spherical harmonics  $C_n^m(\theta_s, \phi_s)$ . Galilean transformation of momentum gives

$$\cos \theta_s = \cos \theta - \epsilon (\hat{W}_{||} - \zeta \cos \theta) + \frac{1}{2} \epsilon^2 [(3\zeta^2 - 1) \cos \theta - 2\hat{W}_{||} \zeta] + O(\epsilon^3), \quad (7)$$

$$\begin{aligned} \sin^m \theta_s \cos m \phi_s &= \sin^m \theta \cos m \phi + m \epsilon [\zeta \sin^m \theta \cos m \phi - \hat{W}_{||} \sin^{m-1} \theta \cos(m-1) \phi] + \\ &+ \frac{1}{2} \epsilon^2 \{ [m(m+2)\zeta^2 - m] \sin^m \theta \cos m \phi - 2m \hat{W}_{||} \zeta \sin^{m-1} \theta \cos(m-1) \phi + \\ &+ \hat{W}_{||}^2 (m-1)m \sin^{m-2} \theta \cos(m-2) \phi \} + O(\epsilon^3), \end{aligned} \quad (8)$$

$$\text{where } \zeta = -\frac{\underline{v} \cdot \underline{W}}{v W} = \hat{W}_{||} \cos \theta + \hat{W}_{\perp} \sin \theta \cos \phi, \quad (9)$$

$$\zeta \cos m \phi = \hat{W}_{||} \cos \theta \cos m \phi + \frac{1}{2} \hat{W}_{\perp} \sin \theta [\cos(m-1) \phi + \cos(m+1) \phi], \quad (10)$$

$$\zeta^2 \cos m \phi = (\hat{W}_{||}^2 \cos^2 \theta + \frac{1}{2} \hat{W}_{\perp}^2 \sin^2 \theta) \cos m \phi + \hat{W}_{||} \hat{W}_{\perp} \sin \theta \cos \theta \times$$

$$\times [\cos(m-1)\phi + \cos(m+1)\phi] + \frac{1}{4}\hat{W}_1^2 \sin^2\theta [\cos(m-2)\phi + \cos(m+2)\phi]. \quad (11)$$

Using (7) - (10), and various properties of  $P_n^m$ , we obtain

$$C_n^m(\theta_s, \phi_s) = C_n^m(\theta, \phi) + \epsilon(n+1)U_{n-1}^{mc}(\theta, \phi) + \epsilon n V_{n+1}^{mc}(\theta, \phi) + \epsilon^2(n-1)(n+1)X_{n-2}^{mc}(\theta, \phi) + \epsilon^2 n(n+1)Y_n^{mc}(\theta, \phi) + \epsilon^2 n(n+2)Z_{n+2}^{mc}(\theta, \phi) + O(\epsilon^3), \quad (12)$$

$$\text{where } (2n+1)U_{n-1}^{mc} = \frac{1}{2}\hat{W}_1(n+m-1)(n+m)C_{n-1}^{m-1} - \hat{W}_{||}(n+m)C_{n-1}^m - \frac{1}{2}\hat{W}_1 C_{n-1}^{m+1}, \quad (13)$$

$$(2n+1)V_{n+1}^{mc} = \frac{1}{2}\hat{W}_1(n-m+1)(n-m+2)C_{n+1}^{m-1} + \hat{W}_{||}(n-m+1)C_{n+1}^m - \frac{1}{2}\hat{W}_1 C_{n+1}^{m+1}, \quad (14)$$

$$(2n-1)(2n+1)X_{n-2}^{mc} = \frac{1}{8}\hat{W}_1^2 \frac{(n+m)!}{(n+m-4)!} C_{n-2}^{m-2} - \frac{1}{2}\hat{W}_{||} \hat{W}_1 \frac{(n+m)!}{(n+m-3)!} C_{n-2}^{m-1} + \frac{1}{4}(2\hat{W}_{||}^2 - \hat{W}_1^2) \frac{(n+m)!}{(n+m-2)!} C_{n-2}^m + \frac{1}{2}\hat{W}_{||} \hat{W}_1(n+m)C_{n-2}^{m+1} + \frac{1}{8}\hat{W}_1^2 C_{n-2}^{m+2}, \quad (15)$$

$$(2n-1)(2n+3)Y_n^{mc} = \frac{1}{4}\hat{W}_1^2 \frac{(n+m)!(n-m+2)!}{(n+m-2)!(n-m)!} C_n^{m-2} + \frac{1}{2}(2m-1)\hat{W}_{||} \hat{W}_1(n-m+1)(n+m)C_n^{m-1} + \frac{1}{2}[(2n^2+2n-2m^2-1)\hat{W}_{||}^2 + (n^2+n+m^2-1)\hat{W}_1^2]C_n^m + \frac{1}{2}(2m+1)\hat{W}_{||} \hat{W}_1 C_n^{m+1} + \frac{1}{4}\hat{W}_1^2 C_n^{m+2}, \quad (16)$$

$$(2n+1)(2n+3)Z_{n+2}^{mc} = \frac{1}{8}\hat{W}_1^2 \frac{(n-m+4)!}{(n-m)!} C_{n+2}^{m-2} + \frac{1}{2}\hat{W}_{||} \hat{W}_1 \frac{(n-m+3)!}{(n-m)!} C_{n+2}^{m-1} + \frac{1}{4}(2\hat{W}_{||}^2 - \hat{W}_1^2) \frac{(n-m+2)!}{(n-m)!} C_{n+2}^m - \frac{1}{2}\hat{W}_{||} \hat{W}_1(n-m+1)C_{n+2}^{m+1} + \frac{1}{8}\hat{W}_1^2 C_{n+2}^{m+2}. \quad (17)$$

Note that the functions  $U$ ,  $V$ ,  $X$ ,  $Y$ , and  $Z$  are all expressed in terms of the spherical harmonics  $C_n^m(\theta, \phi)$ , and that

$$P_n^{-m}(\theta, \phi) = (-1)^m P_n^m(\theta, \phi)(n-m)!/(n+m)!, \quad (18)$$

$$\zeta C_n^m = V_{n+1}^{mc} - U_{n-1}^{mc}, \quad (19)$$

$$\zeta[(n-2)U_{n-1}^{mc} + (n+3)V_{n+1}^{mc}] - \frac{1}{2}C_n^m = (4-2n)X_{n-2}^{mc} - 3Y_n^{mc} + (2n+6)Z_{n+2}^{mc}. \quad (20)$$

Secondly, we expand  $A_{nm}^S(p_s)$  about  $p = p_s$ :

$$A_{nm}^S(p_s) = A_{nm}^S(p) + \epsilon \zeta p A_{nm}^{S'}(p) + \frac{1}{2}\epsilon^2[(1-\zeta^2)p A_{nm}^{S''}(p) + \zeta^2 p^2 A_{nm}^{S'''}(p)] + O(\epsilon^3). \quad (21)$$

Then we multiply (21) and (12), and use (10), (11), (19) and (20) to express  $A_{nm}^S(p_s)C_n^m(\theta_s, \phi_s)$  in terms of a series of  $C_n^m(\theta, \phi)$  correct to  $O(\epsilon^3)$ . This expression actually applies to the transformation of phase-space distribution function, but will not be exhibited here.

Finally, multiplying

$$vp^2/(v_s p_s^2) = 1 + 3\epsilon\zeta - (3\epsilon^2/2)(1-5\zeta^2) + O(\epsilon^3) \quad (22)$$

into the above expression, and simplifying as before, we obtain

$$[vp^2/(v_s p_s^2)]A_{nm}^S(p_s)C_n^m(\theta_s, \phi_s) = A_{nm}^S C_n^m + \epsilon[(n-2)A_{nm}^S + p A_{nm}^{S'}]U_{n-1}^{mc} + \epsilon[(n+3)A_{nm}^S - p A_{nm}^{S'}]V_{n+1}^{mc} + \epsilon^2[(n-4)(n-2)A_{nm}^S + (2n-5)p A_{nm}^{S'} + p^2 A_{nm}^{S''}]X_{n-2}^{mc} + \epsilon^2[(n-2)(n+3)A_{nm}^S + 4p A_{nm}^{S'} + p^2 A_{nm}^{S''}]Y_n^{mc} + \epsilon^2[(n+3)(n+5)A_{nm}^S - (2n+7)p A_{nm}^{S'} + p^2 A_{nm}^{S''}]Z_{n+2}^{mc} + O(\epsilon^3), \quad (23)$$



the right hand side being evaluated at  $(p, \theta, 0)$ . Eqns (8), (10) - (17), (19) - (20) and (23) hold when we replace all the cosines dependent on  $\theta$  by sines,  $C_m^m$  by  $S_m^m$ ,  $U_m^m$  by  $U_m^m$ , etc. Substituting (23) into (6), we obtain the desired result in the form (2), as well as the relation between  $A_{nm}$  and  $A_{jk}^g$  and their derivatives. These, however, are not exhibited here for lack of space. For the inverse transformation, we merely need to interchange quantities labelled and unlabelled with S, and reverse the signs of  $\hat{W}_{||}$  and  $\hat{W}_{\perp}$  in the above.

**5. SOME IMPLICATIONS** For  $>10$  KeV protons, once  $A_{jk}^g$  and their 1st and 2nd derivatives are experimentally determined, one need only substitute these into the formulae to obtain the relevant  $A_{nm}$  in the comoving frame, bypassing the complicated procedures mentioned in Section 3.

The formulae are useful in other regards. For example, we have

$$A_{n0}^S = A_{n0} + \epsilon[(n+1)/(2n+3)][n-1+pd/dp][\frac{1}{2}\hat{W}_{\perp}(n+2)A_{n+1,1} - \hat{W}_{||}(n+1)A_{n+1,0}] + \epsilon[n/(2n-1)][n+2-pd/dp][\frac{1}{2}\hat{W}_{\perp}(n-1)A_{n-1,1} + \hat{W}_{||}nA_{n-1,0}] + O(\epsilon^2). \quad (24)$$

For highly anisotropic solar particles, the gyrotropic terms  $A_{k0} \gg$  the non-gyrotropic term  $A_{k1}$ . The former may be eliminated in (24) by choosing the  $\underline{ExB}$  drift frame ( $W_{||} = 0$ ). If in addition,  $A_{n-1,1}$  and  $A_{n+1,1}$  are negligible, then  $A_{n0} - A_{n0}^S = O(\epsilon^2)$ .

Next consider the 1st harmonic terms.

$$\begin{aligned} A_{10}^S &= A_{10} + \epsilon\hat{W}_{||}(3A_{00} - pA_{00}' - 2pA_{20}'/5) - \epsilon\hat{W}_{\perp}pA_{21}' + O(\epsilon^2), \\ -A_{11}^S &= -A_{11} + \epsilon\hat{W}_{\perp}(3A_{00} - pA_{00}' + pA_{20}'/5 - 6pA_{22}'/5) + 3\epsilon\hat{W}_{||}pA_{21}'/5 + O(\epsilon^2), \\ -B_{11}^S &= -B_{11} + 3\epsilon\hat{W}_{||}pB_{21}'/5 - 6\epsilon\hat{W}_{\perp}pB_{22}'/5 + O(\epsilon^2). \end{aligned} \quad (25)$$

Even if all the non-gyrotropic terms vanish, if  $pA_{20}' \neq 0$ , the 1st order 1st harmonic anisotropy vector is not aligned with  $\underline{W}'$ .

**6. REMARKS** The new formulae are useful in the study of transverse anisotropies. The derivation in Section 4 is being extended to cover relativistic particles (see also Ng, 1984). These and other considerations and a more complete account of the present work will be presented elsewhere.

**Acknowledgement.** This work was initiated whilst I enjoyed the hospitality of Professor E. C. Stone and his colleagues at Caltech. I thank B. L. Ng for her help in preparing the manuscript.

#### References

- Balogh, A., et al. (1973) *Planet. Space Sci.*, 21, 1802.
- Erdős, G. (1981) *17th ICRC, Paris*, Paper T5-14.
- Forman, M.A. (1970) *Planet. Space Sci.*, 18, 25.
- Gleeson, L.J. & Axford, I.A. (1968) *Astrophys. Space Sci.*, 2, 431.
- Ipavich, F.M. (1974) *Geophys. Res. Lett.*, 1, 149.
- Ng, C.K. (1984) *Res. Report #15/84*, Dept. of Maths., U of Malaya.
- Ng, C.K. (1985) This conference, Paper SH 3.1-11.
- Sanderson, T.R., et al. (1985) *J. Geophys. Res.*, 90, 19.

# DETERMINATION OF THE PITCH-ANGLE DISTRIBUTION AND TRANSVERSE ANISOTROPY OF INTERPLANETARY PARTICLES

C. K. Ng

Dept of Mathematics, University of Malaya  
Kuala Lumpur, Malaysia

**1. INTRODUCTION** We present a method to determine the directional differential intensity (d.d.i.), expressed in terms of spherical harmonics, from sectorized particle data, concurrent interplanetary magnetic field (IMF) and solar-wind velocity. In Section 2, we show the relation between the d.d.i. and the mean sector count rates  $X_1$ . In Section 3, we show how to estimate the d.d.i. from the measured  $X_1$  and the associated errors due to Poisson statistics. In Section 4, using the above method, we determine the pitch-angle distribution and the transverse anisotropy of the d.d.i. of low energy protons for the Day 118, 1978 solar particle event. In Section 5, we discuss an interesting correlation between the transverse anisotropy and the IMF direction.

## 2. RELATION BETWEEN DIRECTIONAL INTENSITY AND SECTOR RATES

We express the particle directional differential intensity as

$$J(p, \theta, \emptyset) = \sum_{n=0}^{\infty} \sum_{m=0}^n P_n^m(\cos \theta) \{ A_{nm}(p) \cos m\emptyset + B_{nm}(p) \sin m\emptyset \}, \quad (1)$$

where  $P_n^m$  = the associated Legendre functions,  $p$  = particle momentum,  $\theta$  = pitch-angle and  $\emptyset$  = gyrophase in the standard coordinate system (Ng, 1985). When the telescope points in the direction  $(\gamma, \eta)$ , it measures the differential count rates

$$C(p, \gamma, \eta) = \int_{\Omega} J(p, \theta, \emptyset) S[\theta'(\gamma, \eta, \theta, \emptyset)] \sin \theta d\theta d\emptyset, \quad (2)$$

where, following Sentman and Baker (unpublished manuscript), we express the angular response function of the particle telescope as

$$S(\theta') = \sum_{k=0}^{\infty} S_k P_k(\cos \theta') = \sum_{k=0}^{\infty} S_k \{ P_k(\cos \gamma) P_k(\cos \theta) + 2 \sum_{m=1}^k [(k-m)!/(k+m)!] P_k^m(\cos \gamma) P_k^m(\cos \theta) \cos m(\eta - \emptyset) \}. \quad (3)$$

It follows from the orthogonality of the spherical harmonics that

$$C(p, \gamma, \eta) = 4\pi \sum_{n=0}^{\infty} [S_n/(2n+1)] \sum_{m=0}^n \{ A_{nm}(p) \cos m\eta + B_{nm}(p) \sin m\eta \} P_n^m(\cos \gamma). \quad (4)$$

As the telescope sweeps over sector 1, we average (4) to obtain  $X_1(p)$  the mean differential count rate over sector 1,

$$X_1(p) = 4\pi \sum_{n=0}^{\infty} [S_n/(2n+1)] \sum_{m=0}^n \{ A_{nm}(p) \langle P_n^m(\cos \gamma) \cos m\eta \rangle_1 + B_{nm}(p) \langle P_n^m(\cos \gamma) \sin m\eta \rangle_1 \}, \quad (5)$$

where  $\langle \rangle_1 = (1/\Delta\psi) \int_{\psi_1}^{\psi_1+\Delta\psi} d\psi$ ,  $\psi$  = the spacecraft (s/c) spin-angle measured from the  $\psi_1$  projection of the IMF onto the spin plane, and  $(\psi_1, \psi_1+\Delta\psi)$  defines sector 1 (see the 2nd coordinate system in Fig. 1). For multiple-telescope systems (Sanderson & Hynds, 1977), eqn (5) should

be repeated for each telescope.

We now illustrate by specializing (1) and (5) to 8-sectored data for a telescope sweeping in the spacecraft's spin plane:

$$j(p, \theta, \varnothing) = \sum_{n=0}^4 A_{n0} P_n(\cos \theta) + \sum_{n=1}^3 A_{n1} P_n^1(\cos \theta) \cos \varnothing, \quad (6)$$

$$X_1 = 4\pi \sum_{n=0}^4 S_n A_{n0} Q_{n0}^1 / (2n+1) + 4\pi \sum_{n=1}^3 S_n A_{n1} Q_{n1}^1 / (2n+1), \quad (7)$$

$$\text{where } Q_{n0}^1 = \langle \sum_{j=0}^n a_j \sin^j \theta_B \cos^j \psi \rangle_1, \quad (8)$$

$$Q_{n1}^1 = \langle (\hat{W}_{11} \cos \psi + \hat{W}_{12} \sin \psi) \sum_{j=0}^n b_j \sin^j \theta_B \cos^j \psi \rangle_1, \quad (9)$$

$a_j$  = coefficient of  $x^j$  in  $P_n(x)$ ,  $b_j$  = coefficient of  $x^j$  in  $P_n^1(x)/(1-x^2)^{1/2}$ ,  $\theta_B$  = angle between IMF and s/c spin-axis, and  $(\hat{W}_{11}, \hat{W}_{12}, \hat{W}_{13})$  denotes a unit vector in the direction of  $\underline{E} \times \underline{B}$  in the 2nd coordinate system (Fig. 1). Note that the integrations in (8) and (9) may be performed readily in closed form.

**3. DETERMINATION OF  $j$  FROM MEASURED  $X_1$**  To simplify notation in the following, let

$$D_n = A_{n0} \quad (n=0,4), \quad D_n = A_{n-4,1} \quad (n=5,7), \quad (10)$$

$$R_n^1 = Q_{n0}^1 \quad (n=0,4), \quad R_n^1 = Q_{n-4,1}^1 \quad (n=5,7). \quad (11)$$

$$\text{We least-square fit } X_1 = \sum_{n=0}^7 C_n R_n^1, \quad (i=0,7), \quad (12)$$

to the 8 measured sector rates  $\bar{X}_1$ . This yields

$$\sum_{j=0}^7 H_{nj} C_j = \sum_{i=0}^7 R_n^1 \bar{X}_i, \quad (n=0,7), \quad (13)$$

$$\text{where } H_{nj} = \sum_i R_n^1 R_j^1, \quad (n=0,7; j=0,7). \quad (14)$$

Inverting (13), we have

$$C_n = \sum_k H_{nk}^{-1} \sum_i R_k^1 \bar{X}_i, \quad (n=0,7), \quad (15)$$

$$\text{and thence } D_n = \sum_i M_{ni} \bar{X}_i, \quad (n=0,7), \quad (16)$$

where  $M_{ni}$  is ultimately expressed in terms of  $Q_{n0}^1$ ,  $Q_{n1}^1$ , and  $S_n$ . Using (16), we may determine the coefficients  $A_{nm}$  in (6) by a matrix multiplication into the measured sector rates. When the IMF projection lies on a sector boundary, the symmetric matrix  $H_{nj}$  becomes singular. So we drop the  $A_{40}$  term in (6) whenever the IMF projection comes within  $2^\circ$  of a sector boundary.

Suppose that  $K_1$  counts are registered over the time interval  $t_c$  in sector 1. Assuming Poisson statistics, we estimate

$$X_1 = K_1/t_c, \quad \text{var}(X_1) = K_1/t_c^2, \quad \text{var}(D_n) = \sum_i M_{ni}^2 \text{var}(X_i). \quad (17)$$

If we define the anisotropy  $\xi_n = D_n/D_0$ , then, providing the counts are not too low,

$$\text{var}(\xi_n) \simeq (1/D_0^2) \sum_i (M_{ni} - \bar{\xi}_n M_{0i})^2 \text{var}(X_i). \quad (18)$$

Systematic errors are, of course, much harder to estimate.

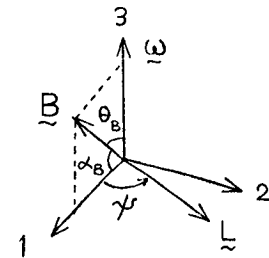


Fig. 1

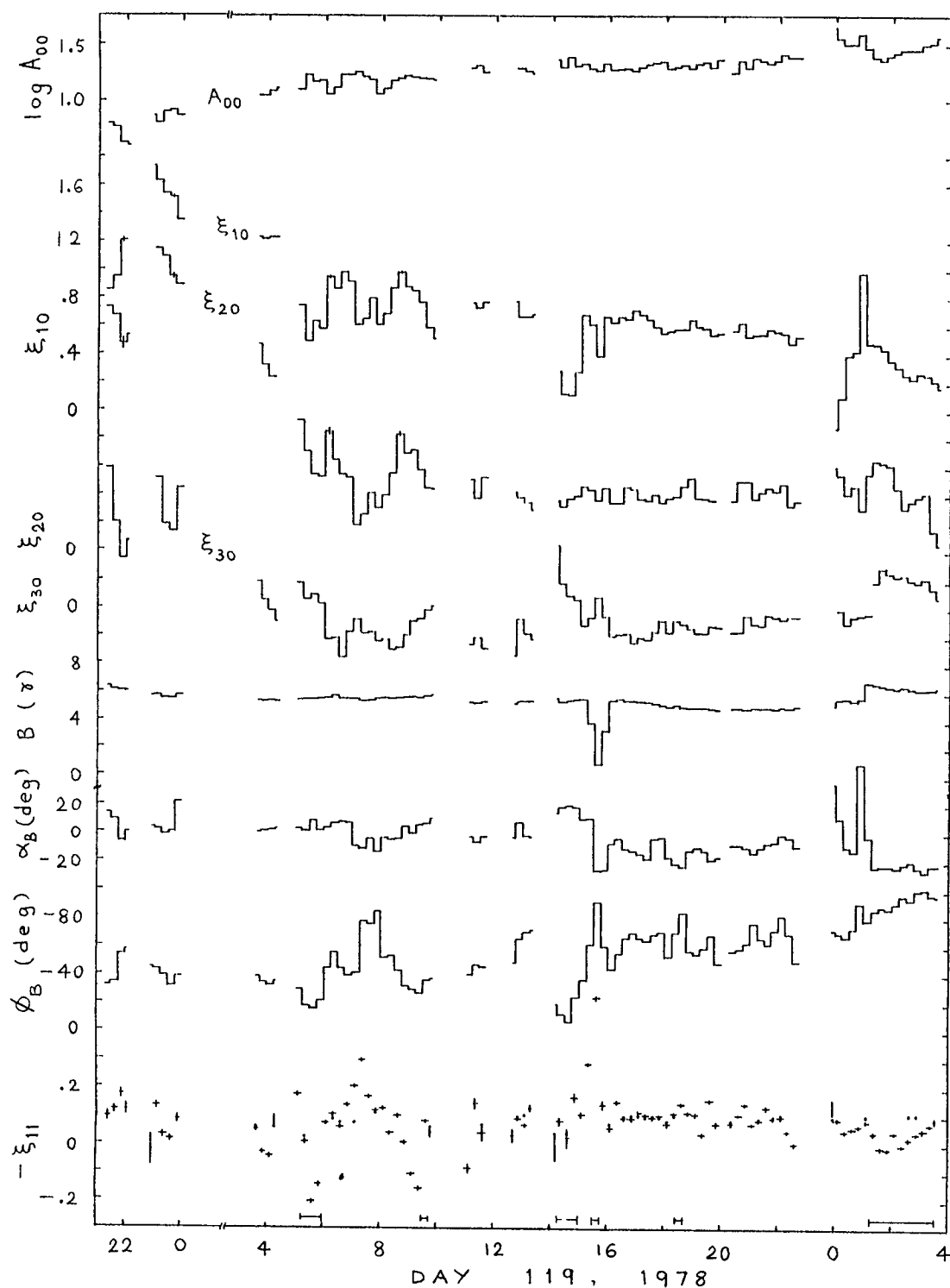


Fig. 2: 15-minute intensity and anisotropies of 1.4-2.5 MeV protons

4. APPLICATION As an example, we show in Fig. 2 the 15-min averages of  $A_{00}$ ,  $\xi_{10}$ ,  $\xi_{20}$ ,  $\xi_{30}$ , and  $-\xi_{11}$  for 1.4 - 2.5 MeV protons, determined

with the above method using 8-sectored particle data (P.I.: R.E. Vogt, CalTech), concurrent IMF (P.I.: N.F. Ness, GSFC), and hourly solar wind speed (P.I.: H. Bridge, MIT), measured aboard IMP-8 and accessed through NSSDC. Some typical standard errors due to Poisson statistics only are indicated by vertical bars.

Estimating the spectral slopes by using the corresponding results for 4-13 MeV protons, we have found the Compton-Getting corrections (Ng, 1985) for transformation to the  $\underline{ExB}$  drift frame to be small,  $<.002 A_{00}$ ,  $<.01$ ,  $<.01$ ,  $<.02$  for  $A_{00}$ ,  $\xi_{10}$ ,  $\xi_{20}$ , and  $\xi_{30}$  respectively. (For transformation to the solar wind frame, the corrections are of the order of  $0.04 A_{00}$ ,  $0.1$ ,  $0.3$ , and  $0.5$  respectively). Thus  $A_{00}$ ,  $\xi_{10}$ ,  $\xi_{20}$ ,  $\xi_{30}$  essentially characterise the pitch-angle distribution in the  $\underline{ExB}$  drift frame.

**5. DISCUSSION** The Compton-Getting correction,  $\varepsilon \hat{W}_1 (3 - pA_{20}/A_{00} + pA_{20}/5A_{00})$  to the transverse anisotropy  $-\xi_{11}$  is indicated by the dots in Fig. 2. The observed anisotropy varies in phase with this correction but is much larger in magnitude. The same feature, even more marked, is seen for 4-13 MeV protons. What is the cause of this large discrepancy?

For Fig. 2, IMP-8's GSE coordinates in  $R_E$  varies from (21.6, 21.5, 5.5) to (5.7, 29.5, 18.1). The times when the IMF is connected to the nominal bow shock (BS) are indicated by horizontal bars in Fig. 2 (Ng & Roelof, 1977). At ~1537 UT Day 119, some solar particles with guiding centres below the IMF through IMP-8 are probably shadowed by the nose of the BS, resulting in the observed peak value of  $-\xi_{11} = 0.53$ . However BS connection does not account for the general variation of  $-\xi_{11}$  in Fig. 2.

Close inspection reveals that the sector plot of  $X_1$  lags behind the IMF in directional changes. Hence a tentative explanation is that some observed 15-min averages contain a substantial fraction of non-gyrotropic distributions which reside a short distance ( $\sim 1$  gyroradius) beyond a 'kink' in the IMF. An alternative explanation is as follows. When  $\theta_B$  swings rapidly in an averaging interval such that its average value is close to one end of the range of values, then a field-aligned anisotropy  $\xi_{10}$  would "induce" a nonzero value of  $-\xi_{11}$ , i.e., the apparent value of  $-\xi_{11}$  is not real. Further studies with smaller averaging intervals would clarify this matter.

**6. CONCLUSION** We have shown how to obtain the directional differential intensity referred to the standard coordinate system (Ng, 1985) from sectored particle data and concurrent IMF and solar wind data. The corrections for transformation to the  $\underline{ExB}$  drift frame are explicitly calculated and found to be small for these  $\sim 1.5$  MeV protons. However, the new correction formulae would be important for  $\lesssim 500$  KeV protons. It is tentatively suggested that the 'observed' transverse anisotropy may in large part be induced by a rapidly changing IMF in the presence of a field-aligned anisotropy.

**Acknowledgement** Prof E.C. Stone's hospitality and the advice of Drs. R.A. Mewaldt and T.G. Garrad on CalTech EIS experiment are gratefully acknowledged. I thank B.L. Ng for helping to prepare the manuscript.

## References

- Ng, C.K. (1985) Paper SH 3.1-10, this conference.
- Sanderson, T.R. & Hynds, R.J. (1977) *Planet. Space Sci.*, 25, 799.
- Ng, C.K. & Roelof, E.C. (1977) *EOS Trans. A.G.U.*, 58, 1205.

PITCH ANGLE DISTRIBUTIONS OF SOLAR ENERGETIC PARTICLES AND  
THE LOCAL SCATTERING PROPERTIES OF THE INTERPLANETARY  
MAGNETIC FIELD

Beeck, J., and Wibberenz, G.

Institut für Reine und Angewandte Kernphysik, Universität Kiel  
Olshausenstr. 40, D-2300 Kiel, FR Germany

ABSTRACT

We discuss an approximate solution of the Fokker-Planck equation containing pitch angle scattering and adiabatic focusing. For modest focusing effects the omnidirectional density obeys an ordinary diffusion equation with a modified diffusion coefficient. The anisotropic part of the distribution function is properly normalized and split into an even and an odd part. The even part is determined by the ratio between the scattering mean free path and the focusing length and by the degree of polarisation of the magnetic field fluctuations. The odd part is determined by the deviation of the pitch angle scattering from isotropic scattering  $\alpha(\mu) \sim (1 - \mu^2)$ . The method supplies a powerful tool to obtain the local characteristics of pitch angle scattering. It is insensitive to long-lasting solar injections and to moderate radial variations of the mean free path. The method is applied to solar particle events observed on Helios-1 and -2. We find marked differences from one event to the other. Results are presented for the solar particle events of March 28, 1976; Nov 22, 1977; April 8, 1978; April 11, 1978. In general, the pitch angle coefficient has a pronounced minimum for pitch angles near  $90^\circ$ . The first three events are characterized by a small local degree of scattering, with the mean free path ranging from 0.5 to 1.0 AU, whereas the April 11, 1978, event is of a more diffusive nature with  $\lambda \approx 0.12$  AU.

## EXPONENTIAL ANISOTROPY OF SOLAR COSMIC RAYS

J. W. Bieber, P. A. Evenson, and M. A. Pomerantz  
 Bartol Research Foundation of The Franklin Institute  
 University of Delaware, Newark, Delaware 19716

## ABSTRACT

On 16 February 1984 a flare on the sun's invisible disk produced a large, highly anisotropic solar particle event. A novel technique, in which interplanetary scattering parameters are determined purely from the form of the particle anisotropy, is here applied to energetic particle data from neutron monitors and the ICE spacecraft.

1. Introduction. Recent theoretical investigations (Roelof, 1969; Kunstmann, 1979; Earl, 1981) indicate that the cosmic ray anisotropy may appropriately be expressed as an exponential function of pitch angle:

$$f = c_0 + c_1 B \exp \left\{ \frac{(4-q)\lambda}{3L} \mu |\mu|^{1-q} \right\}. \quad (1)$$

Here,  $f$  is the phase space density,  $c_0$  and  $c_1$  are constants,  $\mu$  is the cosine of pitch angle,  $B$  is the magnetic field magnitude,  $\lambda$  is the scattering mean free path,  $L$  is the magnetic field scale length, and  $q$  is a parameter which, according to quasilinear theory (Jokipii, 1971), is related to the slope of the power spectrum of magnetic field fluctuations. Provided that  $q$  and the ratio  $\lambda/L$  do not change with distance, (1) is an exact solution of the steady-state Boltzmann equation in arbitrary guiding field configurations, including the Parker field. Solar particle anisotropies are, of course, not precisely steady-state. Nonetheless, it might reasonably be expected that (1) constitutes a better approximation to actual anisotropies than the often utilized first-order anisotropy ( $f = c_0 + c_1 \mu$ ) which is a solution of neither the steady-state nor the time-dependent Boltzmann equation.

On 16 February 1984, a flare on the invisible disk of the sun produced an unusual solar particle event that was recorded by neutron monitors on Earth (Pomerantz et al., 1984) and by the MEH instrument aboard ICE, which at that time was located on nearly the same nominal Parker field line as Earth at a distance of 0.07 AU upstream. The best timing of the parent flare is given by the sudden onset of radio emission at 0858 UT (Earth-received time) from beyond the western limb of the sun. This highly anisotropic event provides an ideal observational basis for testing which of the alternate forms of pitch angle distribution -- first-order or exponential -- best describes energetic solar particle anisotropies.

2. Neutron Monitor Observations. To determine the form of solar particle anisotropy in this event, the fractional increases recorded by 8 polar neutron monitors during the interval 0900-1000 UT were corrected to sea level pressure. An effective value of  $\mu$  was calculated for each station. The data were then fitted to a first-order anisotropy and to the exponential anisotropy (1) with the parameter  $q$  set equal to unity. Separate determination of  $q$  from the available neutron monitor data was not feasible for this event.

Results of this analysis appear in Figure 1. It is immediately apparent that the exponential anisotropy provides a substantially better description of the data than the first-order anisotropy. The goodness-of-fit parameter,  $\chi^2$ , is nearly 10 times larger for the first-order fit than for the exponential fit. Even this poor fit for the first-order case is accomplished only by resort to the unphysical artifice of assuming negative densities for  $\mu$  less than -0.4. Changes in  $\mu$  appear between the two fits because the best-fit symmetry axis differs slightly for the two assumptions.

The value of  $\lambda/L$  corresponding to the exponential plotted in Figure 1 is 2.8. However, comparable agreement was obtained for  $\lambda/L$  in the range 2-10. The value of  $L$  at this time, as calculated for a Parker magnetic field corresponding to the ICE-observed solar wind speed of 280 km/s, was 1.4 AU. Hence, at neutron monitor energies ( $> 400$  MeV) the scattering mean free path in this event was 3 AU or larger.

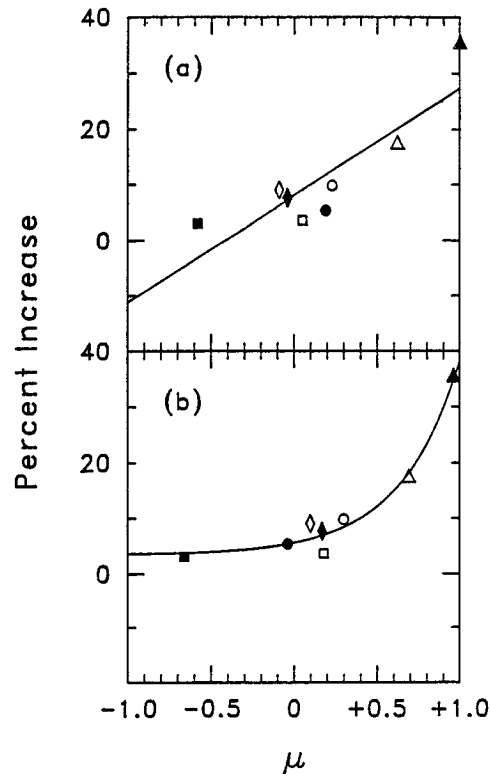


Fig. 1. Two alternate forms of pitch angle distribution are fitted to hourly-averaged neutron monitor data from Thule (○), McMurdo (●), Alert (□), Inuvik (■), Goose Bay (▲), Mawson (△), Apatity (◆), Oulu (◇).

3. Spacecraft Observations. Measurements of the flux of protons with energies 35-145 MeV from eight equally spaced arrival directions are made every 97 seconds by the MEH instrument on the ICE (formerly ISEE-3) spacecraft (Meyer and Evenson 1978). Since the magnetic field is also measured at the spacecraft (E. Smith, private communication via ISEE common datapool tape), a representative pitch angle for each viewing direction can be computed directly by averaging the magnetic field observations over the period of the particle flux measurement. This is in contrast to the neutron monitor analysis wherein the direction of the field was a free parameter. Figure 2 shows the 35-145 MeV ICE data (10 minute average) at approximately 0955 UT on 16 February 1984, near the maximum of the event at these energies. The



sectorized data obviously do not follow a straight line (first-order anisotropy) but the exponential (1), with a choice of  $q=1.2$  and  $\lambda/L=2.8$ , provides an excellent fit, as shown by the plotted curve.

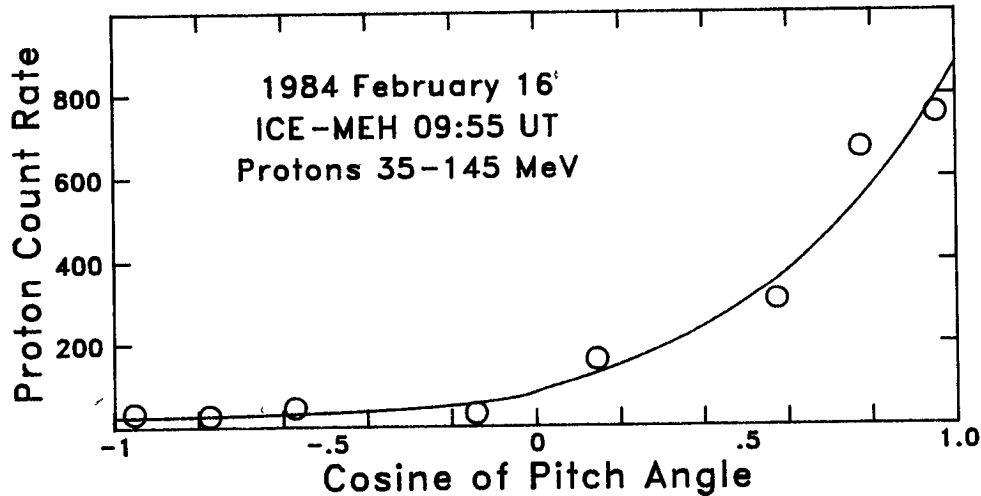


Fig. 2. Sectorized ICE particle data (circles) are compared to an exponential anisotropy (curve) with  $\lambda/L = 2.8$  and  $q = 1.2$ .

The persistent high anisotropy of the event and the long mean free path determined from the shape of the pitch angle distribution suggest that the entire time profile is a reflection of continued injection at or near the sun. We have modeled the time profile using coronal diffusion (Reid, 1964) and interplanetary focused diffusion (Bieber et al., 1980) and find excellent agreement. A key result of this analysis is that the flow at the position of the spacecraft is at all times approximately steady state. Changes with time are nearly all due to changes in the source strength at the sun.

Such a steady state flow may be used to look for changes in the scattering parameters which determine the shape of the pitch angle distribution. A related analysis conducted by Bieber and Pomerantz (1985) uses long term averages of neutron monitor data. The shape of the pitch angle distribution may be characterized many ways, one of which is to consider ratios of the amplitudes of harmonic components determined by Fourier analysis of the counting rate as a function of arrival direction. Figure 3 shows the average flux, ratio of second to first harmonic  $r_2/r_1$ , and ratio of third to first harmonic  $r_3/r_1$  as a function of time. Note the distinctly different values of the harmonic ratios before and after the data gap. This jump implies a reduction in the mean free path for scattering by almost a factor of two, while  $q$  remains nearly unchanged. It is likely that this change is related to the change in the properties of the solar wind which is indicated by the increase in the magnetic field magnitude also shown in Figure 3.

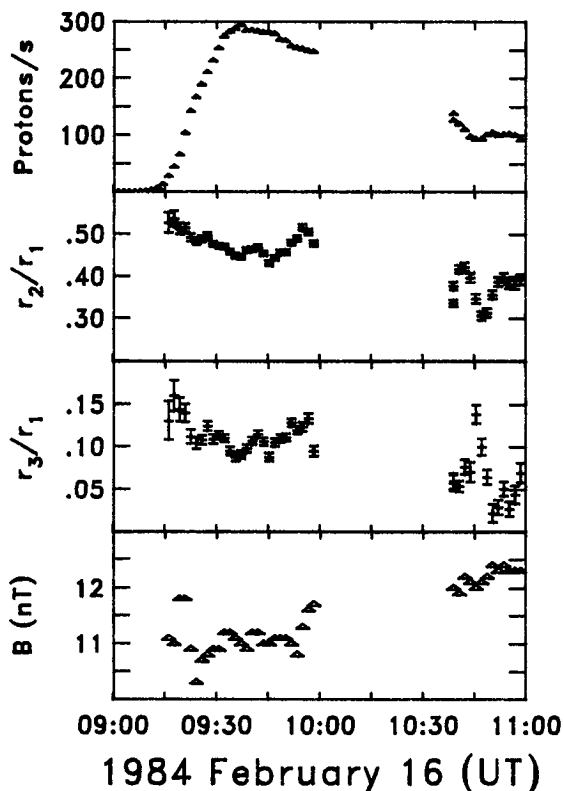


Fig. 3. Time profiles of average particle flux, harmonic ratios  $r_2/r_1$  and  $r_3/r_1$  (see text), and magnetic field  $B$  observed at ICE.

4. Conclusions. Local measurements of important parameters of interplanetary particle propagation can be made with high time resolution if particle anisotropies can be measured with sufficient statistical accuracy. Analysis of energetic particle data for the event of 16 February 1984 from neutron monitors and from ICE leads to the following conclusions: (1) Particle anisotropies are better described by an exponential function of pitch angle than by the commonly assumed first-order anisotropy. (2) Fitting to the exponential anisotropy allows both the scattering mean free path  $\lambda$  and the parameter  $q$ , which characterizes the dependence of the scattering rate upon pitch angle, to be determined. For this event, it is found that  $\lambda$  is greater than 3 AU and  $q$  is approximately 1.2. (3) An apparent change in the scattering mean free path occurred in connection with a small change in the magnitude of the interplanetary magnetic field.

5. Acknowledgments. This research was supported by the National Science Foundation under grants ATM-8303758 and DPP-8300544 and by NASA under grant NAG-5-374.

#### References

- Bieber, J. W., and M. A. Pomerantz, (1985), paper SH 4.5-21, this conference.  
 Bieber, J. W. et al., (1980), *J. Geophys. Res.*, **85**, 2313.  
 Earl, J. A., (1981), *Astrophys. J.*, **251**, 739-755.  
 Jokipii, J. R., (1971), *Rev. Geophys. Space Phys.*, **9**, 27-87.  
 Kunstmann, J. E., (1979), *Astrophys. J.*, **229**, 812-820.  
 Meyer, P. and P. Evenson, (1978), *IEEE Trans. Geosci. Electronics*, **GE-16**, 180.  
 Pomerantz, M. A. et al., (1984), *Proc. Intl. Symp. on C-R Modulation in the Heliosphere*, pp. 437-443, Morioka, Japan.  
 Reid, G. C., (1964), *J. Geophys. Res.*, **69**, 2659.  
 Roelof, E. C., (1969), *Lectures in High-Energy Astrophysics*, NASA Spec. Publ. 199, pp. 111-135, NASA, Washington, D. C.

## ENERGETIC SOLAR PARTICLE EVENTS

K.B.Fenton, A.G.Fenton and J.E.Humble  
 Physics Department, University of Tasmania  
 Box 252C, G.P.O., Hobart, Tasmania, Australia, 7001

1. Introduction. Studies of the arrival directions of energetic solar particles during ground level enhancements (GLE's) observed by neutron monitors have shown that, in general, in the first hour of the event most of the particles arrive with a distribution of pitch angles peaked about the garden-hose field direction in the vicinity of Earth (e.g., McCracken, 1962, Maurer et al., 1973, Duggal, 1979). During the first hour some of the particles arrive from the anti-solar direction, while in later stages of the event the intensity becomes more nearly isotropic as a result of scattering of particles in interplanetary space.

In this paper an attempt is made to determine the arrival directions of the particles during the early stages of the GLE of 16 February 1984 using the data currently available to us from high latitude neutron monitors near sea level where the cut-off is essentially atmospheric ( $\sim 1$ GV).

2. Data. In this event the first particles arrived at Earth during the interval 0905-0910 UT and the data we have used for this interval are listed in Table 1 together with the asymptotic viewing directions assumed for the neutron monitors for 2 GV particles (Shea and Smart, 1975). We also list the percentage increases observed in the next five minutes. These figures are expressed as the percentage above the level prevailing in the hour 0800-0900 UT.

TABLE 1 DATA FOR GLE OF 16 FEBRUARY 1984

STATION	ASYMPTOTIC DIRECTION AT 2GV		PERCENTAGE INCREASE	
	LATITUDE	LONGITUDE, $^{\circ}$ E	0905-0910	0910-0915
Goose Bay	-8	0	42.4	94.2
Deep River	-22	10	39.5	71.9
Mawson	-13	56	36.6	49.3
Kerguelen	26	152	5.5	11.0
Thule	68	324	0	8.4
Terre Adelie	-53	170	0	5.0
Inuvik	16	233	0	1.5
Alert	83	8	0	0
McMurdo	-67	275	0	0

3. Analysis. It was expected that during the first five minutes virtually all the particles would arrive from the garden-hose direction or from small angles relative to that direction, since the time would not be available for receiving scattered particles, except those scattered very close to Earth.

Following earlier authors, we use the symbol  $\delta$  to represent the angle between the asymptotic mean direction of arrival of the particles and the asymptotic viewing direction of a neutron monitor, calculated in most instances for 2 GV particles.

In spite of the apparent simplicity of this event, we have so far been unable fully to understand the pattern of arrival directions. At 0910 UT on 16 February 1984, the Sun was overhead at  $(-12^\circ, 42.5^\circ)$ , implying that if the solar wind speed were such that the garden-hose angle was  $45^\circ$ W of the Earth-Sun line, the mean arrival direction of the particles should have been  $(-12^\circ, 357.5^\circ)$ . However, the fact that the increases observed in the first five minutes at Goose Bay, Deep River and Mawson were so nearly the same would appear to require a near equality of the  $\delta$  values for these stations instead of the  $5^\circ$ ,  $16^\circ$  and  $57^\circ$  calculated for this case. By trial, we have found that if, instead, the mean arrival direction were  $(5^\circ, 25^\circ)$  the  $\delta$  values for Goose Bay, Deep River and Mawson would have been  $28^\circ$ ,  $31^\circ$  and  $36^\circ$  respectively, values consistent with the progression towards slightly smaller intensity increases for these stations. This arrival direction, however, implies a garden-hose angle of less than  $20^\circ$ W of the Earth-Sun line which would appear to be unacceptably small.

There is the further problem that for a mean arrival direction of  $(5^\circ, 25^\circ)$  Kerguelen has a  $\delta$  value for 2 GV particles of  $120^\circ$  and would not therefore be expected to receive prompt particles. However, a 5.5% increase occurred in the first five minutes, and the profile has the appearance characteristic of prompt particles. If it is assumed that, say, 4 GV particles were responsible for the increase at Kerguelen, the  $\delta$  value would be  $74^\circ$ . Although less than  $90^\circ$ , this value seems to be still too large for prompt particles. In any case Thule and Alert have  $\delta$  values of  $74^\circ$  and  $78^\circ$  respectively but registered no increase in the first five minutes. At this stage, we have not found a satisfactory solution to these problems.

A similar analysis of the next five minute interval, during which scattered particles were received at several monitors, has also failed so far to yield an orderly progression of percentage increase versus  $\delta$ . It is interesting to note that Pomerantz et al. (1984) found by analysing the hourly average data for this event that a smooth function of the percentage increase versus  $\cos \delta$  could be obtained. Whether this is due to the effect of smoothing fine structure is a matter to be investigated.

4. Comments. As with previous analyses which we have made of five minute data, e.g., the event of 7,8 December 1982 (Fenton et al., 1983), we believe that a more detailed treatment may be necessary in which the actual asymptotic directions at the time of the event are used and in which the over-simplification is eliminated of assuming that a single asymptotic direction can be used for each station. In a more detailed analysis, the responses of high altitude, as well as non-polar, monitors should also be taken into account. It should be possible to extend the analysis to one-minute data, at least for large GLE's for which accurately timed data are available, and thus obtain additional information on the scattering environment in the nearby interplanetary space.

5. Acknowledgements. We wish to thank the people responsible for the operation of the neutron monitors listed in Table 1 and their organizations for supplying us with their data. The project is supported in part by the Australian Research Grants Scheme.

References.

- Duggal, S.P., (1979), Rev. Geophys. and Space Phys., 17, 1021.  
Fenton, K.B., Fenton, A.G. and Humble, J.E., (1983), Proc. 18th ICRC, 4, 189.  
McCracken, K.G., (1962), J. Geophys. Res., 67, 435.  
Maurer, R.H., Duggal, S.P. and Pomerantz, M.A., (1973), J. Geophys. Res., 78, 29.  
Pomerantz, M.A., Bieber, J.W. and Evenson, P.A., (1984), Proc. Int. Symp. Cosmic Ray Modulation in the Heliosphere, Morioka, Japan, 437.  
Shea, M.A. and Smart, D.F., (1975), Air Force Cambridge Research Laboratories Environmental Research Papers, No. 502, AFCRL-TR-75-0177.

## CHANNELED PROPAGATION OF SOLAR PARTICLES

K A Anderson\* and W M Dougherty

Space Sciences Laboratory  
 University of California, Berkeley, CA 94720  
 U S A

1 Introduction *Bartley et al* (1966) and *McCracken and Ness* (1966) identified bundles of interplanetary magnetic field (IMF) lines that differed in direction from the interplanetary field lines in which they were imbedded. These bundles, called filaments by the authors, differed in direction by as much as several tens of degrees from the surrounding field. The filaments were first noticed due to the large and sudden change in flow direction of highly anisotropic solar flare protons in the energy range 1 to 13 MeV. Passage of the filaments over the spacecraft required a few hours, implying a diameter for the filaments of approximately  $3 \times 10^6$  km at a distance of 1 AU from the Sun. In 1968, *Jokipii and Parker* used *Leighton's* hypothesis of random walk of magnetic field lines associated with granules and supergranules (1964) to develop a picture of an interplanetary medium composed of a tangle of field lines frozen into the solar wind, but whose feet were carried about by the random motions at the solar surface. *Jokipii and Parker* noted that using a correlation length of 15,000 km — about the radius of a supergranule — the magnetic structure would be  $3 \times 10^6$  km in size at 1 AU. This is close to the size of the filaments as determined by *Bartley et al* and *McCracken and Ness*. These workers did not find changes in the solar particle intensity, anisotropy ratio or energy spectrum as the spacecraft entered the filament.

In this paper we analyze further the phenomenon of interplanetary filamentary structure. We have identified about 50 such well-defined structures in 1978 and 1979, mainly on the basis of intensity changes in fluxes of solar electrons of energy 2 to 10 keV. Ion intensity changes are often found to accompany the changes in electron intensity. We have made use of simultaneous observations of solar wind plasma and magnetic field on the ISEE-3 spacecraft in order to further characterize interplanetary filament structure.

2 Discussion Figure 1 shows a solar flare particle event as seen at 1 AU on the ISEE-3 spacecraft. After the impulsive phase, the electron intensity decays and the slower moving ions begin to appear at about 1800 UT. At 2000 UT the low energy electrons and the ions abruptly increase in intensity. About 6 hours later the particle intensity suddenly decreases. In this case, there are no well-defined changes in the solar wind or IMF parameters with which to associate the particle intensity changes. Of further interest is the small solar flare particle injection which begins at about 0100 UT on 21 May. From the observed velocity dispersion in the higher energy channels, we would expect the arrival of 2 keV electrons sometime after 0200 UT. The absence of a new injection of electrons at this time in the lowest energy channels could be simply due to the absence of low energy electrons in the flare. This seems unlikely to us since, in the many such flare events observed on ISEE-3, we almost always find a rising spectrum down to the lowest energies. We prefer to interpret the effect as being due to location of the small flare within the region of field lines which define the filament. After the filament passes over the spacecraft, electrons from the small flare can no longer reach the spacecraft. The presence of particles from the earlier flare for many hours before and after the passage of the filament implies that the particles from this flare were injected into a much larger spatial region than was the case for the smaller flare. Figure 2 shows that the angular distribution of the low energy electrons differs significantly from that in the surrounding IMF. Just before entry into the filament, the pitch angle distribution was nearly isotropic (I in Figure 2). Inside the filament, the percentage of the

\* Also Department of Physics

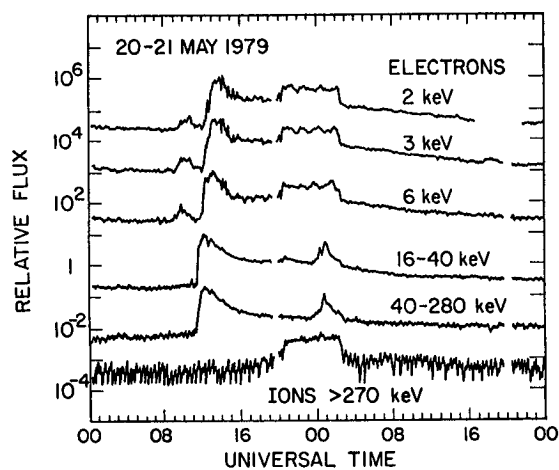


Figure 1 A broad filament interrupts the decay of a solar flare particle event for about 6 hours. The filament evidently connects the spacecraft to a place in the solar atmosphere where the emission of solar particles is greater than in the surrounding regions.

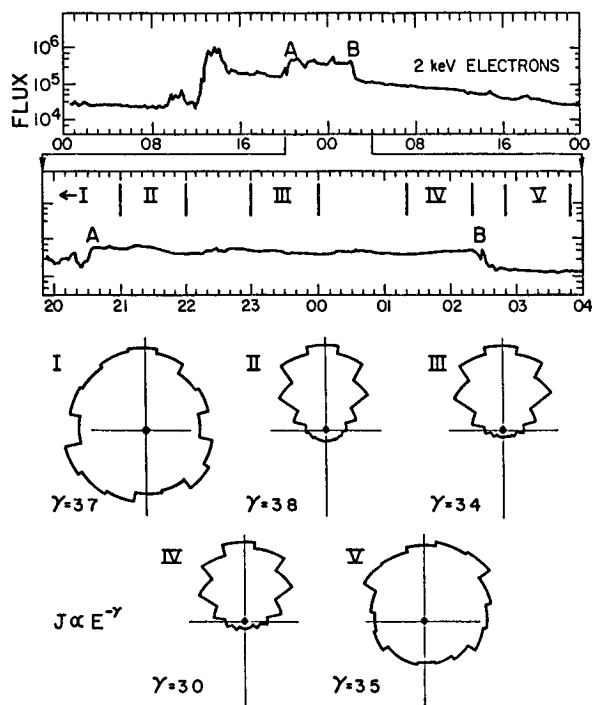


Figure 2 The pitch angle distribution of the low energy electrons in the filament shows a strong flow of particles away from the Sun. The energy spectrum of the electrons inside and outside the filament do not differ much, perhaps indicating the particles in the filament also come from the flare which began at 1107 UT.

electrons directed back toward the Sun is very small. After passage of the filament, the flow becomes much less anisotropic. The propagation conditions are very different for the low energy electrons inside the filament than for those in the surrounding interplanetary medium.

Figures 1 and 2 illustrate some of the features of filaments in the IMF as seen in low energy solar electrons. In this example, and in many others, there is little change in the solar wind and IMF parameters. Therefore, we will refer to particle effects such as those shown in Figures 1 and 2 as being due to particle propagation channels.

Figure 3 illustrates several features of these propagation channels. During the 24-hour interval shown, at least three of these can be identified. First, there are strong correlations with solar wind and IMF parameters. Perhaps the strongest of these is with solar wind number density.

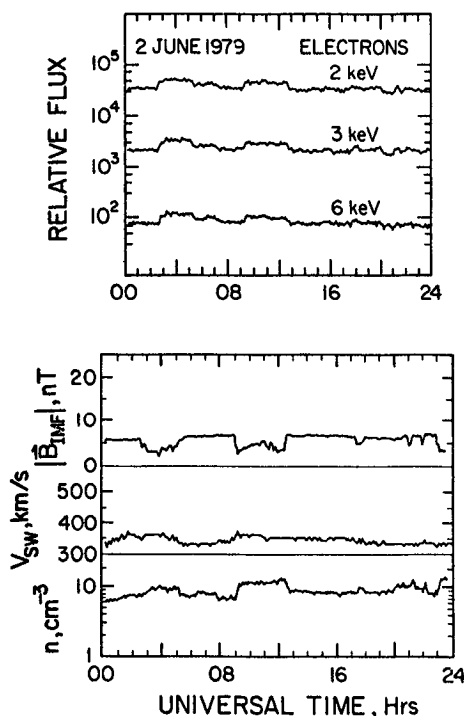


Figure 3 Particle propagation channels often occur in clusters. In this example at least three such channels can be identified. There are well-defined correlations with solar wind density and magnetic field changes.

Although not as clearly defined, solar wind speed changes appear to be spatially coincident with the particle channels. It is quite remarkable that the relative magnetic field decreases are so large. The sequence of particle channels shown in Figure 3 illustrates the tendency for them to come in clusters. Several may occur in one day, but then several days may go by without their appearance.

We have selected 37 of the most clearly defined examples of particle channels and, using solar wind velocity and IMF direction, calculated the spatial extent of each channel. The result is  $3.7 \pm 2.3 \times 10^6$  km, where we have given the average and the average deviation. We have not attempted to correct these numbers for geometrical effects based on assumed cross-section shapes for the channels. Our average value is somewhat higher than



that obtained by *Bartley et al* , but the agreement is nonetheless good

3. Conclusions Finally, we summarize a few of the results obtained to date

1) Particle propagation channels tend to come in clusters separated by a few hours. Intervals of days may elapse without the appearance of these features. There is a strong tendency for the particle channels to appear in populations of solar particles which are relatively young. Conversely, the channels are relatively rare near the end of long-lived streams of solar particles.

2) Particle propagation channels are defined by particle decreases as well as increases. The channels may contain ions as well as electrons. In some channels, the ions may show an increase while the electrons decrease, and *vice versa*.

3) The angular distribution of electrons inside the particle channels often differs greatly from the angular distributions outside the channel. This implies a considerable difference in the amount of magnetic turbulence in the frequency range 1 to 10 Hz, the frequencies most effective in scattering the pitch angles of low energy electrons.

4) We believe that particle channeling characterizes much of the interplanetary medium. While the average rate of occurrence of clearly defined ("square wave") particle channels may be on the order of only one per day, there appear to be many more channels which are less well-defined.

5) Correlation with solar wind and IMF parameters is highly variable. Sometimes the channel is distinctly defined by several of these parameters, at other times one parameter may mark the channel. In one case, a tangential discontinuity marks the edges of a particle channel (*Tsurutani, Personal Communication, April, 1985*).

6) The particle propagation channels consist of magnetic field lines which trace back to a distinctly different place in the solar particle source region, presumably in the solar atmosphere, than do field lines adjoined to the propagation channels.

4. Acknowledgements This work was supported by NASA grant NAG5-376

#### References

- Bartley, W. C., R. P. Bukata, K. G. McCracken and U. R. Rao, Anisotropic cosmic radiation fluxes of solar origin, *J Geophys Res* **71**, 3297, 1966
- Jokipii, J. R. and E. N. Parker, Random walk of magnetic lines of force in astrophysics, *Phys Rev Lett* **21**, 44, 1968
- Leighton, R. B., Transport of magnetic fields on the Sun, *Astrophys J* **140**, 1547, 1964
- McCracken, K. G. and N. F. Ness, The collimation of cosmic rays by the interplanetary magnetic field, *J Geophys Res* **71**, 3315, 1966

THE PROPAGATION OF SOLAR ENERGETIC PARTICLES  
IN MAGNETIC CHANNELS

\*F. B. McDonald  
NASA Headquarters

L. F. Burlaga  
NASA/Goddard Space Flight Center

The existence of interplanetary flow systems produced by the entrainment of interplanetary transients - consisting of flare-produced shocks, high-speed solar wind streams and coronal mass ejection - has been established by Burlaga and co-workers. This entrainment process produces enhanced regions of the interplanetary magnetic field that should be connected back to the solar corona. These compressed regions can provide a preferred magnetic channel for the propagation of solar cosmic rays. The characteristics of these events appear to be different from those previously reported by the NASA/University of New Hampshire team and the University of Chicago in their study of a large number of events in the region beyond 1 AU. These new events have a very flat energy spectra (with  $\gamma \approx 1.5$ ) that frequently extend to energies above 100 MeV and have a significant enhancement of MeV electrons. The combined data of Pioneer 11 and Voyagers 1 and 2 make it possible to separate temporal and spatial variations. The particle anisotropies are modest ( $<10\%$  at 12 MeV). Because of the field compression, adiabatic energy losses appear to be significantly reduced. This effect should be of general astrophysical significance since it provides a mechanism for injecting particles accelerated near a star into the interstellar region without large energy losses.

Frank B. McDonald  
NASA Headquarters/Code P  
Washington, DC 20546

\*Presented by

# RADIAL TRANSPORT OF $\sim 1$ MeV/nucleon IONS DURING THE 22 NOVEMBER 1977 SOLAR PARTICLE EVENT

G.M. Mason<sup>1</sup>, D.C. Hamilton<sup>1</sup>, G. Gloeckler<sup>1</sup> and B. Klecker<sup>2</sup>

<sup>1</sup>Dept. of Physics & Astronomy, Univ. of MD, College Park, MD 20742 USA

<sup>2</sup>Max-Planck-Institut für Extraterrestrische Physik, 8046 Garching, FRG

1. Introduction. Time-intensity profiles of solar flare energetic particle events carry information on the particle injection processes at the sun, as well as the transport of particles in interplanetary space. However, in order to help identify the individual processes of injection versus transport it is necessary to use observations taken at more than one radial location. We present here results of such a study concerning the 22 November 1977 solar particle event, observed with instruments at 1.0 and 1.55 AU. The observations are for particles of energies near 1 MeV/nucleon, considerably less than the  $\sim 10$ -20 MeV/nucleon energies typical of previous radial transport studies (e.g. 2,10). Thus, in the present work we are able to examine the validity of transport models to considerably lower energies than in previous work.

2. Observations. The 22 November 1977 event began at 0945 UT with a 2B flare at N24 W40. From this location it is reasonable to assume that particles had prompt access to the interplanetary magnetic field line connected to Earth. This solar particle event has been widely studied (e.g. references in 7). Figure 1 shows the time-intensity profiles for several species observed at 1 AU with the ISEE-1 ULEWAT sensor (5). Gaps in the profile are due to data removal around radiation belt passes. For He, the time of maximum (M) was about 36 hours after the flare (F), well before the passage of the flare-associated shock (S) late on November 25. Figure 2 shows time-intensity profiles for the same set of species observed at 1.55 AU (3) with the Voyager-2 LECF instrument (6). During this flare the Earth-Sun-Voyager angle was about  $5^\circ$ , and so this spacecraft was also well connected to the flare site. Although the Voyager profiles show some disturbance during the onset phase between 0000-1200 on November 23, it appears that the times to maximum can be identified, with a value of about 48 hours for He.

3. Model Fits. In modeling the time to maximum for low energy particles such as those in this study, it is essential to include the effects of convection and adiabatic deceleration (e.g. 9). Accordingly, we have used a model based on the spherically symmetric Fokker-Planck equation including diffusion, convection and adiabatic energy loss, numerically solved using the code of Hamilton (2). In the calculation we used a constant solar wind velocity typical for this period, an injection time at the  $H_\alpha$  onset, and an assumed particle number density in the form of a power law in energy/nucleon with spectral index derived from the observed spectra at 1 and 1.55 AU. The interplanetary diffusion coefficient had the functional form typical in radial propagation studies:  $\kappa = \kappa_0 r^b = v_{\text{particle}} \lambda_r / 3$ . Finite injection time profiles used the form  $I = I_0 \exp(-t/\sigma_t)$ . Following reference (7) it was assumed that  $\kappa_0$  scaled as  $(A/Q)^{b+55}$  for this particle event.

With the model so specified, the adjustable parameters are  $\lambda_r$ ,  $b$ ,

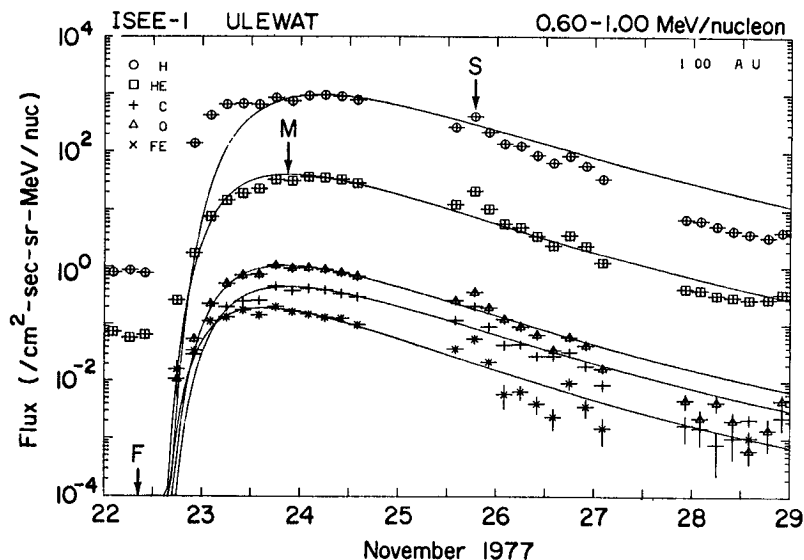


Figure 1

and  $\sigma_t$ ; note that  $\sigma_t$  is a source characteristic while  $\lambda_r$  and  $b$  are properties of the interplanetary transport. Fitting the Helium time to maximum at 1 and 1.55 AU does not uniquely determine the 3 parameters: an additional observation was needed. This was chosen to be the time to 1% of maximum intensity at 1 AU ( $\sim 10$  hours) for Helium, thus fitting the early rise portion of the event.

Figures 3 and 4 show families of curves in the  $\lambda_r - b$  plane which provide the required  $T_{\max}$  values at both sites: notice the wide range of values which are possible with an observation at 1 or 1.55 AU only. Overlaying Figures 3 and 4, an intersecting line is obtained, shown in Figure 5, which has the  $\lambda_r - b$  values which yield the observed  $T_{\max}$  values at both 1 and 1.55 AU. The intersection of this line with the locus of values for  $T_{1\% \text{ of max}} = 10$  hours (Figure 5) yields a unique set of values for  $\lambda_r$ ,  $b$  and  $\sigma_t$ , which are listed in Table 1. The uncertain-

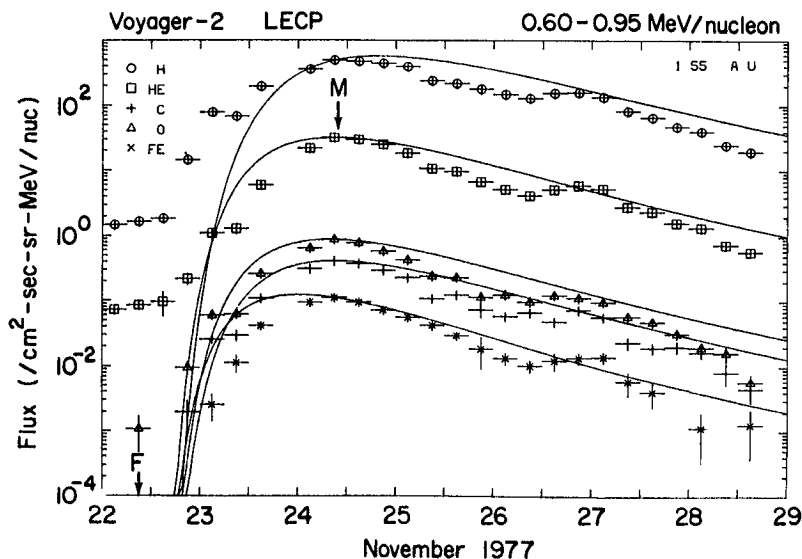


Figure 2

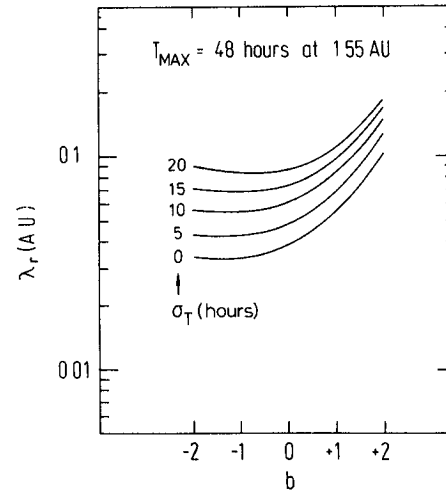
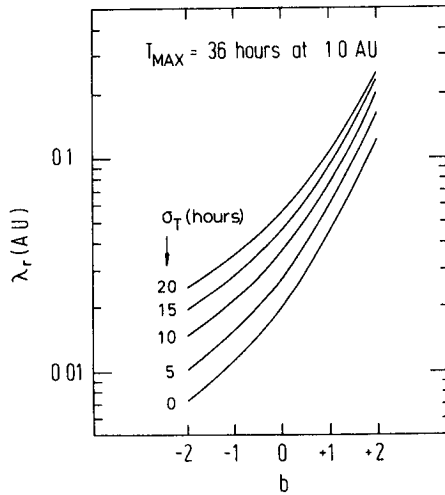
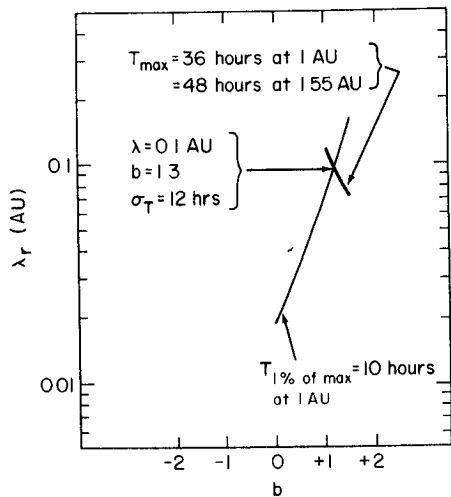


Figure 3  
ties in the values are based on an estimated uncertainty of  $\pm 20\%$  in  $\kappa$ .

Figure 4

Table 1  
Fit Parameters for 0.6-1.0 MeV/nuc Helium

$$\begin{aligned}\lambda_r &= 0.10 \pm 0.02 \text{ AU at 1 AU} \\ b &= 1.3 \pm 0.1 \\ \sigma_t &= 12 \pm 3 \text{ hours}\end{aligned}$$



95-16

Figure 5

Time intensity profiles for all species using the Table 1 values for He, and assuming scaling in  $\lambda_r$  as  $(A/Q)^{0.55}$ , are shown in Figures 1 and 2. Considering the 1 AU data in Figure 1, the fits are generally satisfactory for He, C, O and Fe up through the early decay phase, and they reproduce the temporal variations of the heavy ion ratios such as Fe/O seen in this event (7). Protons, however, have a fast rise time which is not fitted by the assumed scaling. This may be indicative of interplanetary acceleration for the protons, which, as the lowest rigidity particles in the set would be expected to be the most susceptible to such effects. The 1.55 AU fits are reasonable for the times to maximum and the decay phases, although

of course the model does not fit the previously noted distortions in the rise phase. As is the case at 1 AU, the protons observed at Voyager have a fast rise-time which does not follow the  $(A/Q)^{0.55}$  scaling used for the  $A/Z=2$  species.

4. Discussion. Although the value of  $\lambda_r$  found here is similar to previous studies (e.g. review in 8), the values found for  $b$  and  $\sigma_t$  are rather different from the higher energy studies (e.g. 1,2), which have generally yielded  $b \sim 0$  and  $\sigma_t = 0$  (delta function injection). If we were to force such a choice on the present observations at 1 AU, it is possible to find the required  $\lambda_r$  value from the curves in Figure 3-- however the resulting value ( $\lambda_r = 0.015$  AU) yields a  $T_{\max}$  of 66 hours at Voyager: 18 hours beyond the observed value, and well outside the experimental uncertainties. It is possible that this result represents a disagreement with the previous work. More likely, it is due to the fact that the particle energies are lower, and also that the two spacecrafts are relatively close to 1 AU and thus the observations are more sensitive to  $\sigma_t$  and the behavior of  $\lambda_r$  out to 1 AU than the previous studies at generally much larger radial distances. It should be possible to resolve these uncertainties by considering additional data such as anisotropies (4) and by analyzing additional particle events.

5. Acknowledgements. We are grateful to the MPE, UMD, Johns Hopkins/APL individuals responsible for the success of the ISEE and Voyager instruments. One of us (G.M.) wishes to thank the Max-Planck-Institut, Garching, for its hospitality during a visit when most of this study was carried out. This work was supported by NASA under contract NAS5-28704, grants NGR 21-002-224/316, and NAGW-101, by the NSF under grant ATM-84-07546, by NASA/APL subcontract 601620, and by the Bundesministerium fur Forschung und Technologie, contract RV 14-B8/74.

#### References

- (1) Goeman, R. and Webber, W.R. 1983, 18th ICRC, Bangalore, 10, 385.
- (2) Hamilton, D.C. 1977, J. Geophys. Res., 82, 2157.
- (3) Hamilton, D.C. and Gloeckler, G. 1981, 17th ICRC, Paris, 10, 49.
- (4) Hamilton, D.C. et al. 1985, 19th ICRC, LaJolla, paper SH 3.1-8.
- (5) Hovestadt, D. et al. 1978, IEEE Trans. Geo. El., GE-16, 166.
- (6) Krimigis, S.M. et al. 1977, Space Sci. Rev., 21, 329.
- (7) Mason, G.M. et al. 1983, Ap.J., 267, 844.
- (8) Palmer, I.D. 1982, Rev. Geophys. Space Phys., 20, 335.
- (9) Scholer, M. 1981, Adv. Sp. Res., 1, 121; 1976, Ap.J. (Letters), 209, L101.
- (10) Zwickl, R.D. and Webber, W.R. 1977, Solar Physics, 54, 457.

# ENERGETIC SOLAR PARTICLE FLUXES OUT TO 3 AU DURING THE MAY 7, 1978 FLARE EVENT

Lockwood, J.A.

Space Science Center, University of New Hampshire, Durham, NH 03824, USA

Debrunner, H.

Physikalisches Institut, University of Bern, 3012 Bern, Switzerland

Simultaneous solar proton flux measurements on IMP 7 and by the world-wide neutron monitor network during the May 7, 1978 flare event led us to conclude that in the energy range from 50 MeV to 10 GeV: 1) the propagation of the flare particles in the interplanetary magnetic field (IMF) between the sun and the earth was nearly scatter-free; and 2) therefore, the intensity-time (IT) profiles of the solar proton fluxes observed at earth for about one hour after onset represent the solar injection profiles even to energies as low as 50 MeV (Debrunner et al., 1984). Observations of the IMF at Helios A indicate that the IMF was undisturbed between the sun and Helios A at the time of the May 7, 1978 flare event; and, therefore, we infer that the solar particle propagation was also scatter-free from the sun to Helios A. We then made a detailed study of the acceleration and coronal transport of the flare particles and their injection into the IMF using the fine-time resolution data from IMP 7 and Helios A (Lockwood and Debrunner, 1983, 1985). The relative positions of IMP 7 and Helios A spacecraft along with the solar flare location are shown in Fig. 1. The IMF lines are drawn for a solar wind speed  $V_{sw} = 480$  km/s. As an example of the solar particle fluxes observed at IMP 7 and Helios A we show in Fig. 2 the responses of the energy channel with  $E_{median} \sim 90$  MeV. The coronal transport was then analysed by assuming a  $\delta$ -like acceleration of the protons at the flare site and by using the Reid (1964) and Axford (1965) model of two-dimensional diffusion with losses. Comparing the (IT) profiles from IMP 7 and Helios A, we found that the coronal diffusion coefficient  $D_s [cm^2/s] \sim 4.4 \cdot 10^{15} (E [MeV])^{-2}$  for  $20 \text{ MeV} < E < 500 \text{ MeV}$  and that the loss rate  $\beta \sim (2.9 \pm 0.5) \text{ hr}^{-1}$  for  $90 \text{ MeV} < E < 500 \text{ MeV}$ . To test the validity of the model used and the deduced parameters we then calculated the ratios of the maximum solar proton fluxes at IMP 7 and Helios A for the energy channels  $E_{median} \sim 90$  MeV and  $\sim 350$  MeV. The calculated ratios agree with the observed ones to within a factor of 2 which is good agreement. The constancy of the factor with energy further confirms the results of this analysis.

Here we apply the same model to interpret the solar proton fluxes observed on the Voyager (V) spacecraft, the locations of which are also given in Fig. 1. The solar particle fluxes for the two high energy telescopes (HET) from  $70 \text{ MeV} < E < 500 \text{ MeV}$  ( $E_{median} \sim 107 \text{ MeV}$ ) at V1 and V2 are combined and shown in Fig. 3. The combination of the data is valid because the counting rates of the four HETs agreed within statistical fluctuations. In Fig. 3 we also show the (IT) profile (shaded area) expected at V according to our model of only coronal transport without IMF diffusion. Comparing the onset time and (IT) profile of the theoretical response (no IMF diffusion) with the observed ones it is clear that the propagation of the solar protons was

diffusive beyond the orbit of the earth. In order to include the effects of the IMF diffusion we must determine the extent of the region over which the diffusion took place. We examined the plasma and magnetic field data on Helios A from April 25 to May 7, the Kp data at earth from April 29 to May 10, and magnetic field and solar wind data on V1 and V2 from May 7 to May 17. The shocks and/or disturbed regions found on May 7, 1978, at 0300 UT are indicated in Fig. 4. In this figure we have also shown the IMF lines to Voyager for  $V_{sw} = 420, 455,$  and  $490$  km/s. We infer that the propagation of the solar particles along the IMF lines to Voyager was scatter-free for  $r < 1.6$  AU and diffusive for  $r \geq 1.6$  AU.

To describe the diffusive propagation of the flare protons for  $r \geq 1.6$  AU we assume as explained in Fig. 5 one-dimensional diffusion along the IMF lines with a constant mean free path  $\lambda$ , an "absorbing" barrier at  $x = -2\lambda$ , and a  $\delta$ -like injection of  $N$  particles at  $x = 0, t = 0$ . The presence of an "absorbing" barrier at  $x = -2\lambda$  is the equivalent physical description of the transition of the flare protons from the undisturbed to the disturbed region. The density of solar particles is then:

$$n(x,t) = \frac{N}{2(\pi Dt)^{1/2}} \left\{ \exp\left(-\frac{x^2}{4Dt}\right) - \exp\left(-\frac{[x+4\lambda]^2}{4Dt}\right) \right\} \quad (1),$$

where  $D = \lambda v$ ,  $\lambda$  = mean free path for scattering and  $v$  is the particle velocity. If  $x \gg \lambda$ , then

$$n(x,t) = \frac{N}{(\pi Dt)^{1/2}} \cdot \frac{x}{vt} \cdot \exp\left(-\frac{x^2}{4Dt}\right) \quad (2),$$

which exhibits the same time dependence as 3-dimensional diffusion. The best fit of equation 2 to the Voyager data is found for  $\lambda = 0.04$  AU in the range  $1.6 \text{ AU} \leq r \leq 3.0 \text{ AU}$ . The theoretical data were normalized to the observations at the time of maximum and shown in Fig. 3. The agreement of the onset times and of the (IT) profiles over 3 days is excellent. From the solar transport model and the data from IMP 7 (Lockwood and Debrunner, 1985) we can estimate the value of  $N$  and predict the absolute maximum intensity at Voyager if we include the effect of the divergent IMF (Parker, 1963). The ratio of the observed to the predicted maximum fluxes at these large distances from the sun is strongly dependent upon the detailed structure of the IMF and  $V_{sw}$ . For example, we find that for  $V_{sw} = 420, 455$  and  $490$  km/s the ratios are 1.5, 5 and 15 respectively. If we include the effect of solar particles escaping from the diffusive region into the undisturbed region ( $r < 1.6$  AU), then being reflected in the undisturbed region, and later returning to the disturbed region, the ratios are reduced by about a factor of 3. The resulting ratios of 0.5, 1.7 and 3 respectively are in very good agreement using such a simple physical model.



We conclude that the coronal transport model developed in Lockwood and Debrunner (1985) and the description assumed here for the IMF diffusive propagation predict the observed solar proton fluxes at Helios A ( $r = 0.35$  AU), near earth, and at the Voyager spacecraft ( $r = 3$  AU) for the May 7, 1978 solar flare event.

### Acknowledgements

This research was supported by grants from the US NSF (ATM-8324486 and INT-81-18555) and from the Swiss NF (2.811-0.83). We gratefully acknowledge the assistance of Dr. R.E. McGuire and Dr. N. Lal to interpret the IMP 7 and Helios A solar proton data. We thank Dr. F. McDonald for making available the Voyager data and Mrs. G. Sebor and Mrs. G. Sturzenegger for computational assistance and preparing the manuscript.

### References

- Axford, W.F., Planet. Space Sci. **13**, 1301, 1965.  
 Debrunner, H., E. Fluckiger, J.A. Lockwood, and R.E. McGuire, J. Geophys. Res. **89**, 769, 1984.  
 Lockwood, J.A., and H. Debrunner, to be published in J. Geophys. Res. 1985.  
 Lockwood, J.A., and H. Debrunner, Proc. 18th Int. CRC 4, 185, 1983.  
 Parker, E.N., Interscience Pub. (J. Wiley & Sons), 1963.  
 Reid, G.C., J. Geophys. Res. **69**, 2659, 1964.

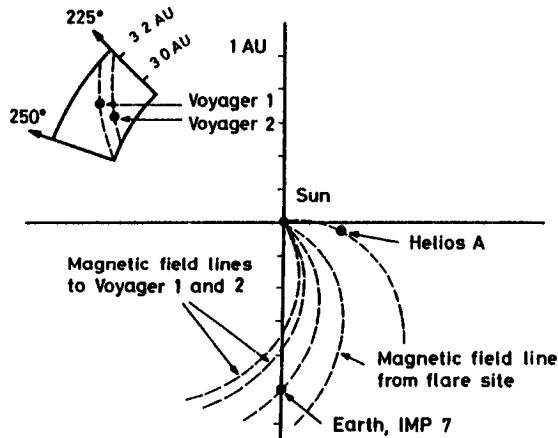


Fig 1 Location of Helios A, the earth, IMP 7, V 1 and V 2 on May 7, 1978.

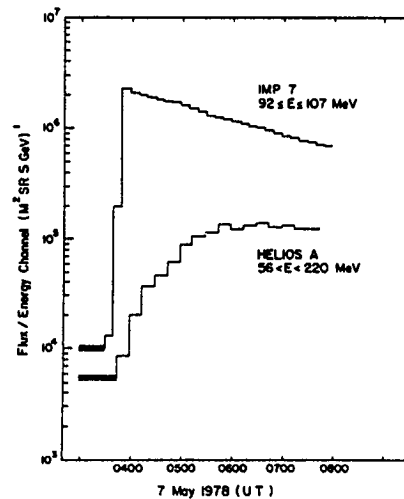


Fig. 2 Solar proton fluxes observed at Helios A and IMP 7 on May 7, 1978 for  $E_{\text{median}} \sim 90$  MeV

SH3.2-6

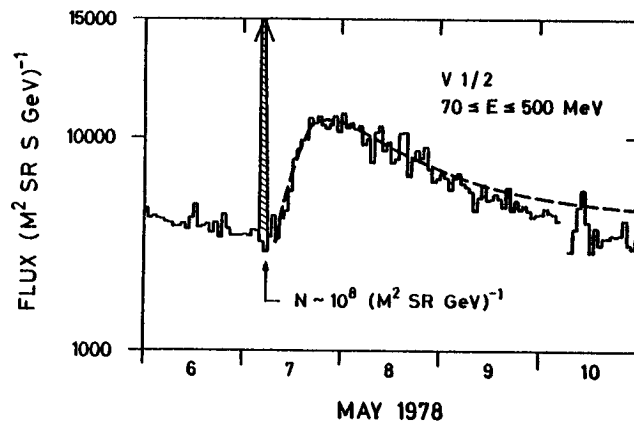


Fig. 3 Solar proton flux at V (—) compared with predicted flux (---) Shaded area is the expected solar proton flux with coronal transport only

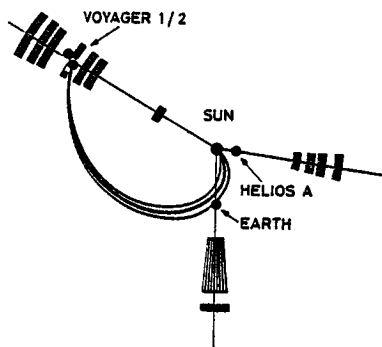


Fig 4 Locations of shocks and/or disturbed regions at 0300 UT on May 7, 1978

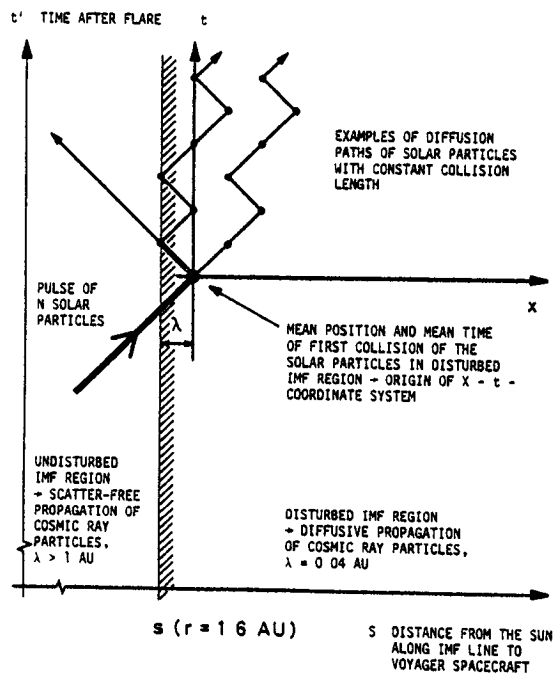


Fig 5 Schematic representation of the assumed model for the IMF diffusion

**THE LOCAL CHARACTERISTIC FUNCTION  
OF INTERPLANETARY PARTICLE PROPAGATION**

G. Green and W. Schlüter  
Institut für Reine und Angewandte Kernphysik  
Universität Kiel  
Olshausenstr. 40  
2300 Kiel, W-Germany

**ABSTRACT**

We define an easily measurable intensity function which characterizes the interplanetary propagation of charged solar flare particles. This function is nearly time invariant during a solar event despite the large variations of intensity and anisotropy, but varies from event to event. It characterizes the systematic and stochastic forces of the interplanetary magnetic field which focus and scatter the particles in pitch angle. The model of focused transport shows that this function is essentially determined by the local shape and amplitude of the pitch angle diffusion coefficient  $\kappa(\mu)$  and by the local value of the focusing length. The time profile of the solar particle injection is typically of negligible influence. The local characteristic function may be used as a powerful new tool for a systematic analysis of flare particle angular distributions. Examples are given.

# INVESTIGATION OF COSMIC RAY PROPAGATION IN INTERPLANETARY SPACE

Chebakova E.A., Kolomeets E.V., Sevast'yanov V.N.  
Kazakh State University, Timiryazeva St. 46,  
Alma-Ata 480121, USSR

It was established experimentally that propagation of solar cosmic rays (scr) in interplanetary space up to 1 A.U. in most cases was of diffusion character (Palmeira R.A.R., et al., 1971).

In present paper we describe solar cosmic ray events on the basis of equation given in the paper of Dolginov A.Z., Toptygin I.N., 1966):

$$\frac{\partial n}{\partial t} = \frac{1}{r^2} \cdot \frac{\partial}{\partial r} [r^2 \cdot (\alpha_r \cdot \frac{\partial n}{\partial r} - n \cdot V)] + \frac{\partial}{\partial \xi} \left\{ \frac{2}{3} \frac{V}{r} \cdot \alpha \cdot \xi \cdot n + D_\xi \left[ \frac{\partial n}{\partial \xi} - \frac{n(E^2 + P^2)}{E \cdot P^2} \right] \right\} \quad (1)$$

where  $n$  is density of particles in unit interval of kinetic energy  $\xi$ ,  $r$  - heliocentric distance,  $E$  and  $P$  - total energy and momentum of particle correspondingly,  $V$  - speed of solar wind,  $\alpha_r$  - coefficient of radial diffusion,  $D_\xi$  - coefficient of diffusion in space of energy,  $\alpha = (2m_0 c^2 + \xi) / (m_0 c^2 + \xi)$ , where  $m_0 c^2$  - energy at rest. Equation (1) describes process of diffusion propagation of charged component of solar cosmic rays including convection, adiabatic cooling and statistical acceleration. Numerical solution of equation (1) was based on the grid technique (Krylov V.I., et al., 1977).

Boundary conditions were taken in the form:  $n(r, \xi, t) = 0$ ;  $CnV - \alpha_r \frac{\partial n}{\partial r} = Q(\xi, t)$  at  $r = r_s$ , where  $Q$  is function of source,  $C$  - Compton-Getting factor,  $n(r_L, \xi, t) = 0$ ,  $r \in [r_s, r_L]$ ;  $n(r, \xi_1, t) = 0$ ,  $n(r, \xi_2, t) \sim \xi^{-\gamma_0}$ ,  $\xi \in [\xi_1, \xi_2]$ .

As a test problem we solved equation (1) by Monte Carlo technique using transit moments of the first and second orders of the equation (1) which is equation of Fokker-Planck type (Jokipii J.R., Levy B.H., 1977). Figure 1 shows calculated time-intensity profiles at 11 MeV at  $r = 1$  A.U.. Solid line represents the results of calculation by grid technique, histogram-Monte Carlo technique for the case of instantaneous injection of solar cosmic rays at point  $r = 0.01$  A.U. for  $\gamma_0 = 3.5$ ,  $r_L = 6$  A.U.,  $\xi_1 = 0.2$  MeV,  $\xi_2 = 50$  MeV,  $\alpha_r = \alpha_0 \xi^{0.5}$ ,  $\alpha_0 = \text{const}(r)$ ,  $\alpha_r(\xi = 11 \text{ MeV}) = 1.16 \times 10^{21} \text{ cm}^2/\text{s}$ ,  $V = 400 \text{ km/s}$ .

Figure 2 shows calculated energy spectra  $I_{tm}$  obtained on the basis of maximum intensity at  $r = 1$  A.U., when  $t = t_m$  and histogram represents the results of Monte Carlo technique, solid line - calculations by grid technique, dotted line shows the form of energy spectrum at source. The solid line at the bottom of figure 2 represents dependence of exponent  $\gamma$  on  $\xi$ , when  $I_{tm}$  is approximated with the function of the form  $\sim \xi^{-\gamma}$ , dotted line is value of  $\gamma_0$ . Hardening of scr energy spectrum at 1 A.U. is due to prevailing action of adiabatic cooling, when  $D_\xi = \alpha \frac{\xi \cdot P^2 \cdot \Delta U^2}{E^2 \cdot g^2}$  (Dolginov A.Z., Toptygin I.N., 1966), where  $\Delta U = 50 \text{ km/s}$  - speed of alfvén waves in solar

wind plasma at  $r=1$  A.U..

The dotted line in figure 1 is a result of solution of the equation (1) for all similar parameters and conditions except suggestion that  $\alpha_r(\xi) = \text{const} = 1,16 \times 10^{19}$  cm/s. This condition is equivalent to  $\gamma = \text{const}(t)$ . Good agreement in behaviour of  $I(t)$  was obtained for  $t > t_m$  when  $\gamma = \text{const}(t)$  for  $\alpha_r \neq \text{const}(\xi)$ .

Usually when propagation of cosmic rays is investigated it is suggested that  $\alpha_r(r, \xi) = f(r)\psi(\xi)$ . To study validity of this suggestion we described experimental solar cosmic ray time-intensity profile for 28.05.67 and 02.11.69 events. The data were taken from the paper of Lanzerotti L.J., 1975. Description was carried out by minimization the difference between experimental value of  $I(t)$  and theoretical ones. Minimization was carried out for scr at given energies in suggestion of instantaneous injection of particles and  $r_L = 20$  A.U., when  $\alpha_r = \alpha_0 r^b$  at ranges  $\alpha_r(r=1 \text{ A.U.}) \in [3,75 \times 10^{19} \text{ cm}^2/\text{s}; 3,75 \times 10^{21} \text{ cm}^2/\text{s}]$ ,  $b \in [-2, 2]$  with steps  $\Delta \alpha_0 = 0,1 \cdot \alpha_0^{\#}$ ,  $\Delta b = 0,5$ , where  $\alpha_0^{\#}$  - previous value of  $\alpha_0$ . Figure 3 shows obtained by minimization dependences  $\lambda_r(\xi)$ ,  $b(\xi)$  for 28.05.67 event and dependences  $\lambda_r(R)$ ,  $b(R)$  for 02.11.69 event, where  $\lambda_r$  - radial mean free path,  $R$  - rigidity of particle ( $\lambda_r = 3\alpha_r/U$ ,  $U$  - particle speed).

Figure 3a shows values of  $\lambda_r(\xi)$  and  $b(\xi)$  obtained by minimization of  $\chi^2$  (circles) and by least square method (rectangles) for  $\gamma_0 = 3$  for protons at energy  $\xi$ : 1.2-2,4 MeV, 2.5-4.3 MeV, 4.4-5.0 MeV; 5.0-9.4 MeV; 9.4-17.4 MeV; 16,5-19.7 MeV. Figure 3b shows  $\lambda_r(R)$  and  $b(R)$  for 02.11.69 obtained by minimization using least square technique for electrons at energies:  $>0,35$  MeV;  $>0,6$  MeV;  $>1,1$  MeV; for protons at energies: 1,1-2.5 MeV; 2.5-4.3 MeV; 5.0-8.8 MeV; 5.9-8.8 MeV, 8.8-16.7 MeV, 17.0-19,7 MeV; for alfa-particles at energies: 3.8-6.2 MeV; 6.2-8.5 MeV, 8.5-17.5 MeV, 17.5-24,5 MeV, 24.5-42.5 MeV, 42.5-83.5 MeV. Rhombs, circles and rectangles in the upper part of figure 3b are values of  $\lambda_r$  for electrons, protons and alfa-particles correspondingly.

Analysis of figure 3 reveals that  $\lambda_r \sim R^{\Delta}$ ,  $\Delta = 0,6$ ,  $\Delta = 0,27$  for events 28.05.67 and 02.11.69 correspondingly and  $\partial b / \partial R > 0$ . Solid smooth curves in figure 4 show the results of description of time-intensity profile of scr protons for 28.05.67 for  $\gamma_0 = 2,3$ ,  $\alpha_r = \alpha_0 r^b \xi^{\Delta}$ ,  $\Delta = 0,8$ ,  $b = 0,75 \cdot \lg \xi$ ,  $[\xi] = \text{MeV}$ . Coordinate axis for the given curve is shown with the help of arrow. Figures near curves are energy ranges of registration of solar cosmic rays. Solid line in figure 5 is description of energy spectrum of proton intensity  $I_{t_m}(\xi)$  for the given event.

Pronounced softening of  $I_{t_m}(\xi)$  at  $r=1$  A.U. ( $I_{t_m}(\xi) \sim \xi^{-2,6}$ ) with respect to scr spectrum at source where  $I(t=0; r=r_s) \sim \xi^{-1,6}$  should be noted.

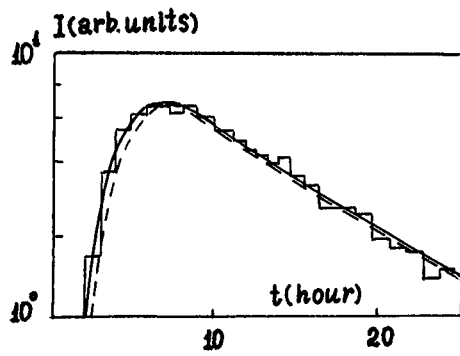


FIGURE 1.

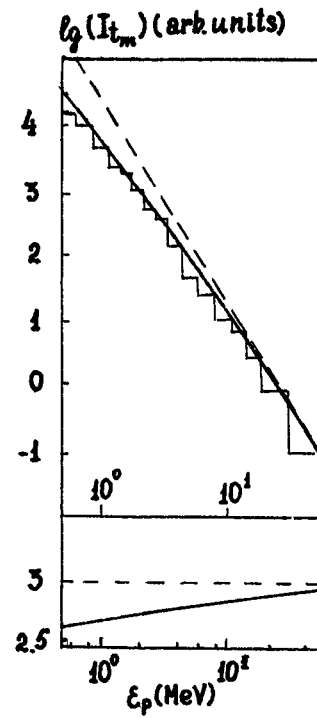


FIGURE 2.

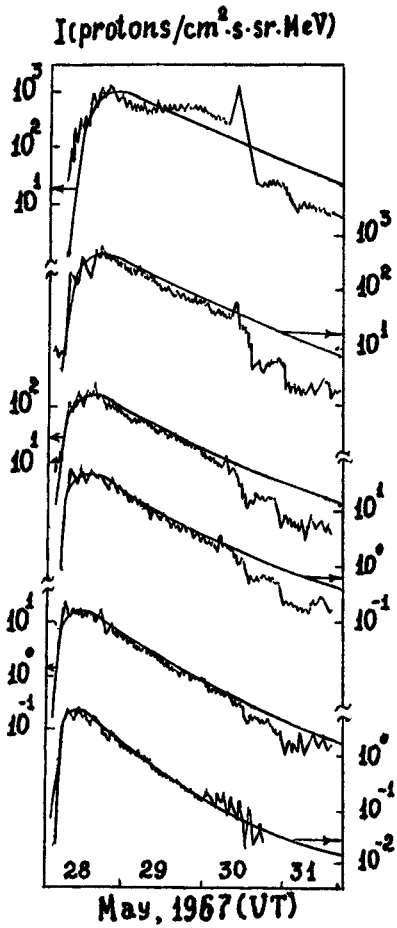


FIGURE 4.

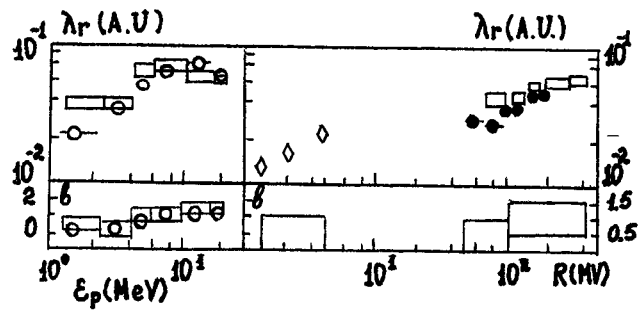


FIGURE 3.

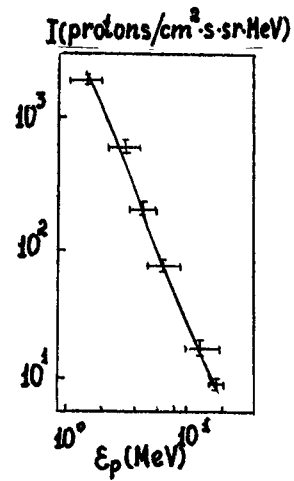


FIGURE 5.

Figure captions are given in the text.

Analysis of abovementioned results shows that suggestion of instantaneous injection allows to describe propagation of scr when function  $\mathfrak{A}_r(r,R)$  can not be factorized with respect to  $r$  and  $R$  and of  $\mathfrak{A}_r \sim r^b R^a$ , then  $\partial \mathfrak{A} / \partial R > 0$  and at  $r=1$  A.U.  $\mathcal{L}=0.3-0.6$  that is in good agreement with the data on frequency power spectrum of interplanetary magnetic field fluctuation.

#### R E F E R E N C E S

- Dolginov A.Z., Toptygin I.N., ZHETF, 1966, v.51, p.1771-1783.  
 Jokipii J.R., Levy E.H., Astrophys. J., 1977, v.213, p.L85-L88.  
 Kolomeets E.V., Sevost'yanov V.N., Stekol'nikov N.V., 17 ICRC, 1981, v.3, p.322-325.  
 Krylov V.I., Bobkov V.V., Monastyrsky P.I. Vychislitel'nye metody, M., 1977, v.2, p.155.  
 Lanzerotti L.J. VII Leninrgrad Mezhdun. Sem., L., p.161.  
 Palmeira R.A.R., et al., Leningrad Mezhdun. Sem., 1971, p.76-151.

## DIFFUSION-CONVECTION FUNCTION OF COSMIC RAYS

Gongliang Zhang and Guang Yang\*  
Institute of Space Physics, Academia Sinica  
Beijing, China

## ABSTRACT

This paper presents the fundamental properties and some numerical results of the solution of the diffusion equation of an impulsive cosmic-ray point source in an uniform, unbounded and spherically symmetrical moving medium.

**I. INTRODUCTION** The diffusion-convection(D-C) function is an elementary composite function of the solution of the D-C equation for the particles injected impulsively from a diffusive point source into a uniform, unbounded and spherically symmetrical medium. It is the analytic solution derived by the dimensional method for the propagation equation of solar cosmic rays in the heliosphere, i.e. the interplanetary space. Because of the introduction of convection effect of solar wind, a nonhomogeneous term appears in the propagation equation, it is difficult to express its solution in terms of the ordinary special functions. The research made so far has led to a solution containing only the first order approximation of the convection effect. Undoubtedly it is insufficient to study only the propagation of the particle with not too high energy. The solution we get with the dimensional method, up to date, is the most general solution of propagation equation in a uniform, unbounded and spherically symmetrical medium. It includes the higher orders of approximation for the convection effect, and has been used in discussing various kinds of propagation effects of solar cosmic ray, making propagation corrections and evaluating the equivalent diffusion coefficients.<sup>1,2</sup> The solution may also have its value for reference in the discussion of the diffusion in the ordinary moving medium.

It is necessary to point out that this solution is valid only in the case of a constant K. For the low energy particles, the energy of particles and also their diffusion coefficients change as a result of the adiabatic expansion loss and other processes. In this case, such limitations can be retrieved by the equivalent diffusion coefficient reflecting the average nature of propagation space.

The diffusion equation in a uniform, unbounded and spherically symmetrical medium is

$$r^2 \frac{\partial^2 U}{\partial r^2} + 2r \frac{\partial U}{\partial r} - \frac{r^2 \partial U}{K \partial t} = \frac{vr^2 \partial U}{K \partial r} + \frac{2Cvr}{K} U \quad (1.1)$$

where U is the number density of diffusing particle, C is a constant relating to the energy spectrum index. In the space far from the source, the solution satisfying condition

\* Presently at Department of Physics, University of New Hampshire, Durham, NH 03824, U.S.A.



$$U(r, t=0) = \frac{N}{4\pi r^2} \delta(r-r_0) \quad \text{and Eq. (1.1) is}^{(1)} \\ U(r, t) = \frac{N}{(4\pi r^2)^{1/2}} Z^{1/2} \exp\left[-\frac{(r-Vt)^2}{4Kt}\right] \phi(X, Z), \quad (1.2)$$

where  $\phi$  is 'diffusion-convection function' which the paper is going to discuss in detail. It can be expressed as a function of two dimensionless parameters as follows: Diffusion parameter  $Z = r^2/(4Kt)$ , Convection parameter for time

$X = (2C - 1)V(t/K)^{1/2}$ . Disregarding  $\phi$ , solution (1.2) is like a kind of the diffusion caused by a source moving outward with the convective velocity  $V$ . The equation of  $\phi$  is

$$r^2 \frac{\partial^2 \phi}{\partial r^2} + r \frac{\partial \phi}{\partial r} (2 - \frac{r^2}{Kt}) - \frac{r^2}{K} \frac{\partial \phi}{\partial t} = (2C - 1) \frac{Vr}{K} \phi \quad (1.3)$$

In case of no convection,  $V=0$  and  $\phi=1$ , solution (1.2) is a function of a single parameter  $Z$ . When convective effect is not too strong,  $\phi$  can be expanded into a power series of power series of parameter  $X$ :  $\phi(X, Z) = \sum_{l=0}^{\infty} X^l F(l, Z)$ , (1.4)

$F(l, Z)$  is called the  $l$ -th order influence function of convection, and its equation is

$$F''(l, Z) + [-1 + \frac{3}{2}Z] F'(l, Z) - \frac{1}{2}Z F(l, Z) = \frac{1}{2}Z^{1/2} F(l-1, Z) \quad (1.5)$$

Seeing that the solution must be finite at the origin,  $Z \sim 0$ , expression of  $F(l, Z)$  can be taken as

$$F(l, Z) = \sum_{m=0}^{\infty} Z^{m/2} \sum_{k=0}^{\infty} A(n, m, k) Z^k, \quad n = l - m. \quad (1.6)$$

**II. MAIN METHODS**  $A(n, m, k)$  is a multiple series relating to  $m$  and  $k$ , the lowest recurrence values for  $m$  and  $k$  are all zero. For the derivation of the general recurrence formula of  $A(n, m, k)$ , it is instructive to evaluate first from the lower-order coefficient  $A(n, m-1, k)$  the next one  $A(n, m, k)$  by recurring  $k$ . Then, the general formula of  $A(n, m, k)$  can be yielded as:

$$A(n, m, k) = A(n) a(n, m) \left[ \frac{n}{2}, \frac{m+1}{2} \right]_k s(n, m, k) \quad (2.1)$$

$$a(n, m) = \frac{(\frac{1}{2})_m}{(m+1)!}, \quad n \neq 0; \quad a(0, m) = \frac{2(m-1)!}{(m+1)!}, \quad m \neq 0; \quad a(0, 0) = 1 \quad (2.2)$$

$$s(n, m, k) = \sum_{k_1=0}^k \frac{s(n, m-1, k_1)}{(\frac{n}{2} + m - 1 + k_1)(\frac{m}{2} + k_1)} \quad (2.3)$$

$$s(n, m_0, k) = 1, \quad k = 0, 1, 2, \dots, \quad m_0 = 0, \quad n \neq 0, \quad m_0 = 1, \quad n = 0, \quad (2.4)$$

where coefficient  $A(n)$  is determined by the initial condition.

The multiple series  $s(n, m, k)$  can be transformed into a series composed of the higher-order  $\Gamma$  function (function  $\psi$  and  $G$ ).

From the initial condition at  $t = 0$  and the asymptotic value (2.7) of function as  $Z \rightarrow \infty$ , the recurrence formula of coefficient  $A(l)$  can be yielded:

$$\delta_l = \sum_{m=0}^{l-1} \frac{A(n)}{\Gamma(\frac{1}{2})} \left(\frac{1}{2}\right)^m s(n, m) + A(0) \left(\frac{1}{2}\right)^{l-1} S(0, l) = 0, \quad n = l - m, \quad A(0) = 1 \quad (2.5)$$

The higher order coefficient  $A$  is difficult to express in a simple form. However, it is quite convenient to calculate  $A(l)$  with the recurrence formulae (2.3) and (2.5) by computer. It can be shown that  $A(l)$  is an alternative sequence, and its absolute value decreases when  $l$  increases.

Formula (1.5) is a nonhomogeneous equation. Its nonhomogeneous terms are composed of the same functions of lower order. The formula of function  $F(l, Z)$  can be derived from formulae (1.6) and (2.1):

$$F(l, Z) = \sum_{m=0}^l Z^{m/2} a(n, m) A(n) f(n, m, Z) \quad (2.6)$$

The asymptotic value of  $f(n, m, Z)$  when  $t = 0$  or  $Z \rightarrow \infty$  is

$$f(n, m, Z)_{Z \rightarrow \infty} \sim \Gamma\left(\frac{1}{2}\right) Z^{-\frac{n-1}{2}} \exp(Z) \frac{(m+1)!}{\Gamma(n/2 + m)} \left(\frac{1}{2}\right)^m S(n, m) \quad (2.7)$$

Therefrom the recurrence formula (2.5) of coefficient  $A(l)$  can be formulated.

### III. DIFFUSION-CONVECTION FUNCTION $\phi(X, Z)$

For convenience of discussion, function  $\phi$  can be rewritten as

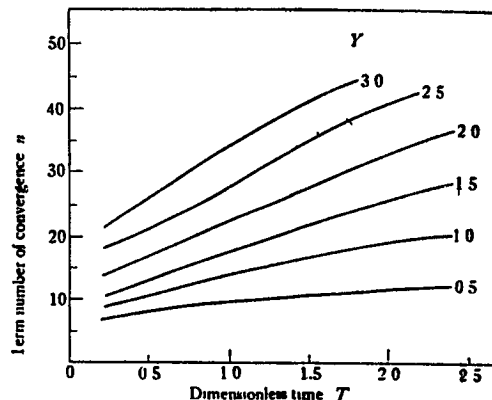
$$\phi = \sum_{n+m=0}^{\infty} A(n) a(n, m) X^n Y^m f(n, m, Z) \quad (3.1)$$

where  $Y$  is another dimensionless parameter, namely, the convection parameter for space:  $Y = (2C - 1) \frac{Vr}{2K} = XZ^{\frac{1}{2}} \quad (3.2)$

Fig. 1. illustrates the value of  $n$  for calculation of  $\phi$  as a function of  $Y$  and  $T$ , when the relative magnitude of the last term is less than 10. It can be seen that the term number of convergence increases with the value of  $Y$  and  $T$ . Function  $\phi$  is probably divergent as  $X > 3.00$ . So, we often restrict our discussion to propagation problem within the range  $X \leq 3.00$ .

Fig. 1.

Abscissa is the dimensionless time  $T$ , ordinate is the number of terms summing up the function  $\phi$  accurate to  $10^{-7}$ .



IV. VARIATION OF DENSITY  $U$  Variation of D-C function with the convection parameter for space  $Y$  and the dimensionless time  $T (= 4Kt/r^2)$  have already been shown in Fig. 1. of [2]. Plotted here is the variation of diffusing particles density  $U$  with  $T$  under the different conditions of solar wind convections (Fig. 2.). A set of curves on the left

side are the results calculated by Formula (1.2), taking  $2C - 1 = 4$ , or the differential-momentum-spectrum index of particles to be 5.5. Such case corresponds to that of the isotropic propagation. But in fact, propagation of cosmic rays particles in interplanetary space is anisotropic, the diffusion coefficient along the magnetic line  $K_{\parallel}$  is different from the transverse one  $K_{\perp}$ . In this case, propagation equation becomes

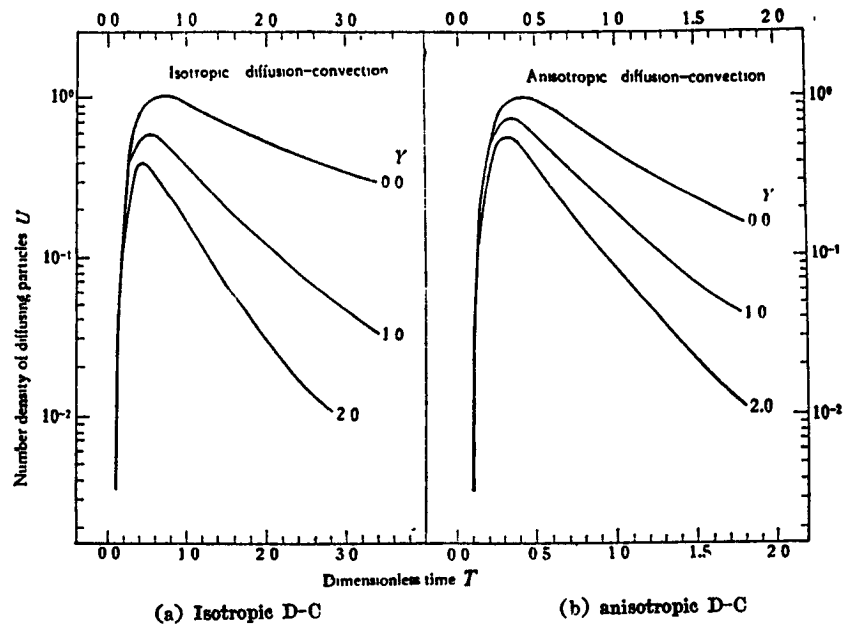
$$U = \frac{N}{(4\pi r^2)^{3/2}} z^{5/2} \frac{K_{\parallel}}{K_{\perp}} \left( \frac{\theta}{\sin \theta} \right)^{1/2} \exp \left[ -z \left( 1 + \frac{K_{\parallel}}{K_{\perp}} \theta^2 \right) \right] \cdot \exp \left[ H - \frac{H^2}{4z} \right] \phi(\chi z) \quad (4.1)$$

where  $\chi$  is the magnetic azimuth of observation point from the source, and  $H$  is the modulation parameter,  $H = \frac{Vr}{2K_{\parallel}}$  (4.2)

Substitute  $k_{\parallel}$  for  $K$  when  $Z$  is calculated.

Solution (4.1) of the anisotropic propagation equation is drawn by a set of curves of the right side of Fig2 when  $\theta = 0^\circ$ . It can be shown that the intensity of diffusing particles decreases and the maximum time moves up as the convection effect intensifies. Besides, the time scale of the isotropic D-C propagation is longer than that of the anisotropic one. Hence, it is possible to form an over estimation of equivalent diffusion coefficient if observational data is fitted merely by the former. However, better results can be got by using the model of anisotropic propagation.

Fig. 2



#### REFERENCES

- [1] Zhang, Gongliang, (1978), HIGH ENERGY PHYSICS AND NUCLEAR PHYSICS, 2, 200.
- [2] Zhang, Gongliang, SCIENTIA SINICA, 22(1979), 934.

# MONTE CARLO CALCULATIONS OF RELATIVISTIC SOLAR PROTON PROPAGATION IN INTERPLANETARY SPACE

M.Lumme, J.J.Torsti, E.Vainikka, J.Peltonen,  
M.Nieminen, E.Valtonen, and H.Arvela

Department of Physical Sciences, University of Turku, and  
Wihuri Physical Laboratory, University of Turku  
SF-20500 Turku, Finland

## ABSTRACT

Particle fluxes and pitch angle distributions of relativistic solar protons at 1 AU have been determined by Monte Carlo calculations. The analysis covers two hours after the release of the particles from the Sun and total of  $8 \cdot 10^6$  particle trajectories were simulated. The pitch angle scattering was assumed to be isotropic and the scattering mean free path was varied from 0.1 to 4 AU.

As an application, the solar injection time and interplanetary scattering mean free path of particles that gave rise to the GLE on May 7, 1978 were determined. Assuming exponential form, the injection decay time was found to be about 11 minutes. The m.f.p. of pitch angle scattering during the event was about 1 AU.

## 1. INTRODUCTION

When a relativistic charged particle is injected into the interplanetary space from the Sun it becomes under the influence of the interplanetary magnetic field (IMF). Due to the divergence of the IMF, the pitch angle,  $\alpha$ , of the particle decreases and the propagation becomes almost field-aligned. The nominal IMF is disturbed by small-scale irregularities, which act as scattering centers of the particles during their propagation. In these scattering processes the energy of the particle is conserved and the displacement of the guiding center is only of order of the gyroradius but the pitch angle of the particle changes.

When the scattering m.f.p.,  $\lambda$ , is very small compared with the scale length of the IMF, the propagation is dominantly stochastic and the particle flux density can be described by a diffusion equation. But when  $\lambda$  increases, the deterministic role of the focusing magnetic field becomes more important. During highly anisotropic events a general description of the interplanetary propagation of relativistic solar particles is possible only by using the Monte Carlo method.

Lockwood et al. (1982) have applied the particle distributions calculated by Monte Carlo method in an analysis of the GLE on May 7, 1978. They found an average scattering m.f.p. of 5 AU during this event.

## 2. PARTICLE PROPAGATION IN THE IMF

2.1. Magnetic Focusing. In this work we have approximated the interplanetary magnetic field by the classical Archimedean spiral field. The angular velocity of the Sun was  $2.865 \cdot 10^{-6}$  rad/s and the solar wind speed was 450 km/s, which is slightly above its average quiet time value.

The conservation of both the magnetic moment and the momentum of a particle during its propagation in a magnetic field of strength  $B$ , states that  $\sin^2\alpha/B$  remains constant.

2.2. Pitch Angle Scattering. The scattering of a particle from magnetic irregularities depends, in addition to the rigidity of the particle, also on the strength and structure of the scattering centers. If the distribution is forward with respect to the direction of motion before scattering, there is less back-scattering and consequently the total particle flux decreases faster, than if the scattering were isotropic. In this work we chose the pitch angle scattering to be isotropic.

2.3. The Monte Carlo Method. The particles were injected isotropically from the solar corona at a distance of 0.02 AU from the center of the Sun. The distance to the first scattering along the field line was taken to be  $\Delta s = -\lambda \ln x$ , where  $x$  is a random number evenly distributed between 0 and 1. After the scattering, a new pitch angle was given by  $\alpha = \arccos(1 - 2x)$ , where  $x$  is a new random number. Then the distance  $\Delta s$  to the next scattering center was determined as above. During two hours after the injection, the time elapsed and the pitch angle were recorded every time the particle passed 1 AU in either direction.

The number of trajectories calculated in this analysis varied from  $5 \cdot 10^5$  ( $\lambda = 0.1$  AU) to  $2 \cdot 10^6$  ( $\lambda = 4$  AU).

2.4. Anisotropy. Let us denote by  $F(\alpha)$  the pitch angle distribution and by  $I(\alpha_0)$  the average density of particles having the pitch angle  $\alpha \leq \alpha_0$ , and by  $I(\overline{\alpha}_0)$  the average density for  $\alpha > \alpha_0$ . The anisotropy of the solar particle flux is conventionally defined by either

$$A = \frac{F(0^\circ) - F(180^\circ)}{F(0^\circ) + F(180^\circ)} \quad \text{or} \quad A = \frac{I(90^\circ) - I(\overline{90^\circ})}{I(90^\circ) + I(\overline{90^\circ})}$$

During solar particle events, the detectors at Earth, having their asymptotic directions of approach near the IMF field line, receive the majority of solar particles from a very narrow but finite cone. Therefore, we defined the anisotropy between two stations as

$$A = \frac{I_1 - I_2}{I_1 + I_2}$$

where  $I_1$  and  $I_2$  are the average particle densities in the asymptotic cones to which the stations 1 and 2 mainly respond.

### 3. RESULTS AND DISCUSSION

3.1. Intensity at 1 AU. The intensity-time profiles of particles at 1 AU after a delta-like injection are shown in Figure 1. The particles arriving during the first minute are, in addition to the unscattered particles, also those which are scattered either near the Sun, where the focusing is very rapid, or near 1 AU, where the distance to be travelled at large pitch angles is short, and also those scattered almost in the forward direction. Thus, the relative number of particles arriving during the first minute is higher than  $\exp(-1.13/\lambda)$ , which represents the theoretical unscattered component.

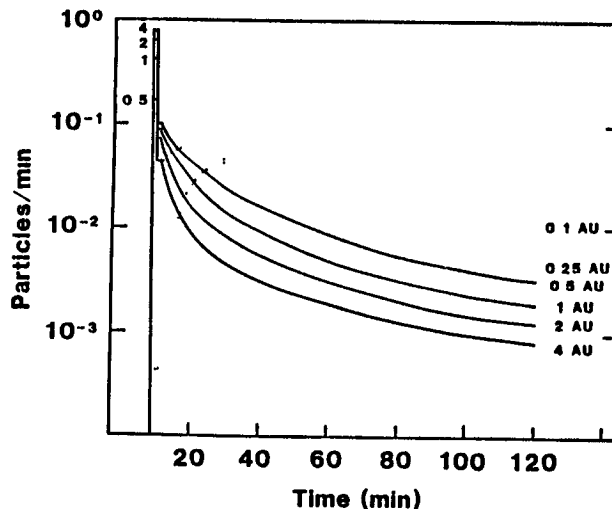


Fig. 1. Intensity-time profiles at 1 AU for various scattering mean free paths.

acceptance cone of Kerguelen was calculated by trajectory tracing method. The rigidities ranged from 3 to 10 GV, and also non-vertical directions were included.

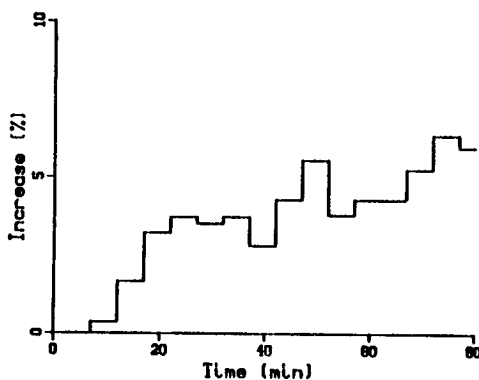


Fig. 2. Increase at "DRI".

has to be increased, since the particle flux decreases faster (see Fig. 1). In the following we illustrate a method, where both injection time and mean free path of pitch angle scattering are deduced simultaneously.

We first parametrize the injection profile as  $\exp(-t/\tau)$ . At each of the scattering mean free paths, 0.5, 1, 2, and 4 AU, we then calculate the theoretical intensity profiles at Kerguelen for various values of  $\tau$ . By comparing these profiles with the observed intensity profile we deduce the proper injection profile for each  $\lambda$ . In Figure 3 we show this comparison for  $\lambda = 1$  AU. The best fit of the  $(\lambda, \tau)$  pairs deduced in this way are (0.5 AU, 9 min), (1 AU, 11 min), (2 AU, 12 min), and (4 AU, 13 min).

Using these  $(\lambda, \tau)$  pairs we then calculate the anisotropy Kerguelen vs. DRI. In Figure 4 we show these anisotropy curves together with the observed anisotropy. The figure indicates that

3.2. The May 7, 1978 Solar Particle Event. On May 7, 1978, an increase in the counting rates of ground level neutron monitors was recorded starting in the time interval 0335-0340 UT. The increase exceeded 50 % at several stations. At Kerguelen, which had its asymptotic directions of approach ideally connected with the apparent source direction, the increase was more than 200 %.

The apparent source direction, which is the direction of the IMF line at Earth, was chosen to be 5 N, 90 E. This was estimated using data from the world-wide network of neutron monitors (Shea et al. 1979). The co-rotational

Due to the large fluctuations at stations receiving only back-scattered particles, we introduced a fictive station "DRI", where both the counting rate increase and the asymptotic directions are averages of the stations Deep River and Inuvik. The increase at this station is shown in Figure 2. The pitch angle interval it responds to was taken to range from  $120^\circ$  to  $160^\circ$  during the entire event.

An observed intensity profile can be related to several injection profiles depending on the scattering mean free path. By increasing  $\lambda$ , also the injection time

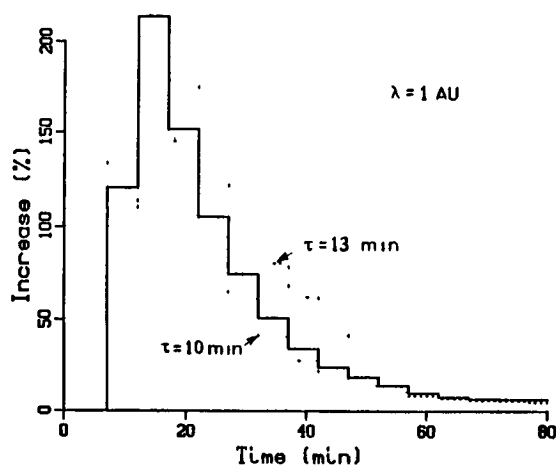


Fig. 3. Comparison between observed increase at Kerguelen (solid line) and increases deduced from Monte Carlo distributions at 1 AU (dotted, normalised at max increase).

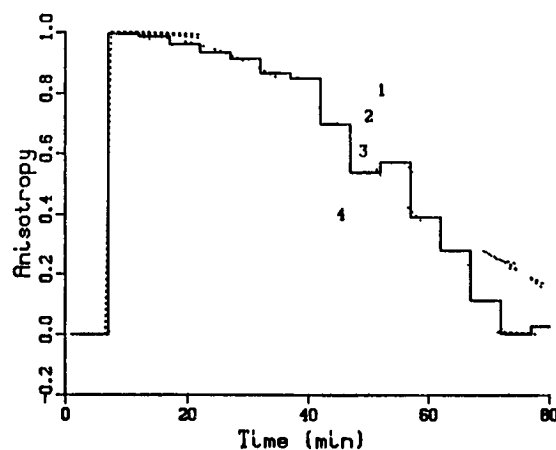


Fig. 4. Anisotropy Kerguelen vs. DRI during the GLE on May 7, 1978. Solid line: observed, dotted lines: theoretical curves: 1.  $\lambda = 4$  AU,  $\tau = 13$  min; 2. 2 AU, 12 min; 3. 1 AU, 11 min; 4. 0.5 AU, 9 min.

$\lambda = 1$  AU and that the decay time of exponential injection is 11 minutes. This scattering mean free path is significantly smaller than the previously published 3 - 5 AU (Debrunner and Lockwood, 1980; Lockwood et al., 1982).

#### 4. CONCLUSIONS

The intensity profiles of the particles after a delta-like injection from the Sun show that the interplanetary propagation is diffusive only at scattering mean free paths below 0.5 AU.

The scattering mean free path during the May, 7, 1978 solar particle event was about 1 AU and represented by exponential form, the injection had a decay time of about 11 minutes.

#### 5. ACKNOWLEDGEMENTS

We are grateful to D. Fouassier and to Margaret D. Wilson for providing us the data from Kerguelen and the Canadian stations.

#### REFERENCES

- Debrunner H and Lockwood J A, J. Geophys. Res. 85, 6853(1980)  
 Lockwood J A, Debrunner H, Fluckiger E, Neuenschwander H, and Schubnell M, J. Geophys. Res. 87, 4338(1982)  
 Shea M A et al., Proc. 18th Int. Cosmic Ray Conf. 5, 226(1979)

# ON REFLECTING BOUNDARY BEHIND THE EARTH'S ORBIT AT PROPAGATION OF FAST PARTICLES FROM SOLAR FLARES

A.S.Niskovskikh, A.T.Filippov

Institute of Cosmophysical Research & Aeronomy,  
Lenin Ave., 31, 677891 Yakutsk, USSR

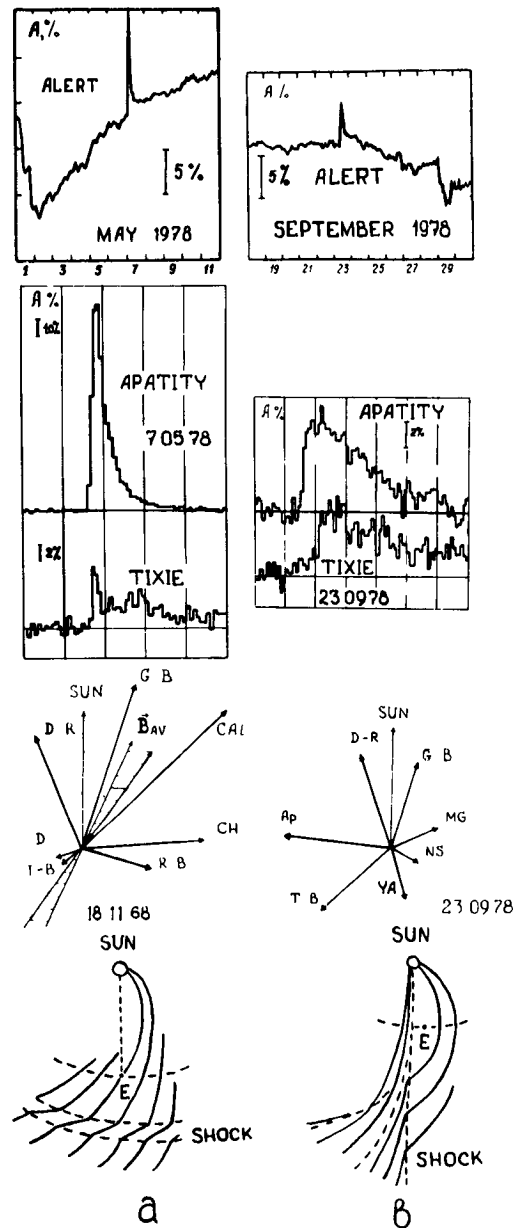
1. Introduction. The flares of solar cosmic rays (SCR) associated with the presence of shocks in interplanetary magnetic field and with their propagation at significant heliocentric distances were always of great interest 1,2 . Here we consider some events and problems concerning the peculiarities of propagation of flare CR in the interplanetary medium. The distinguishing feature of such events is the presence of shock front behind the Earth's orbit having formed either directly in the process of shock generation on the Sun or at large heliocentric distances as a result of the interaction of fast and slow quasistationary recurrent solar wind (SW) streams. Based on the experimental material we show here that the significant non-linear disturbances in IMF behind the Earth's orbit can yield the occurrence of the additional SCR flux from shock front region as a result of the interaction of flare flux with shock and a partial reflection from it.

2. Method and Results. For the analysis on the available data of superneutron monitor net from all the solar proton events (SPE) for 1968-1984 were selected two main groups: the events at Forbush-decrease recovery phase associated with the passage of shock from the Sun and the events at GCR decrease phase associated with the passage of the interacting recurrent SW streams. The first group: 18.11.68, 07.08.72, 07.05.78, 12.10.81, 26.11.82; the second one: 25.02.69, 24-25.01.71, 30.04.76, 23.09.78. The identification of recurrent streams with small-amplitude Forbush-decreases was carried out on [3]. Only the events with reliable observational data were considered. In Figure are shown the examples from each group. Here are given the hourly intensity values for Alert (top) and 5-minute values for two stations having the oppositely directed "receiving cones" . Also are shown the asymptotic directions of particle arrival [4] for the following stations: Ap-Apatity, MG-Magadan, NS-Novosibirsk, Ya-Yakutsk, CAL-Calgary, D-R - Deep River, G-B - Goose Bay, CH-Churchill, D-Dallas, T-B - Tixie Bay, R-B - Resolute Bay. The length of vector is proportional to SCR increase amplitude. At the bottom is shown the qualitative picture of the reflecting boundary of two types. For all the events were built the analogous graphs and "receiving cones". The examples in Figure are typical for each group. In the Table are presented the onset time of increase ( $t_{\text{ons}}$ ) for pairs of stations; the maximum ampli-



tude ( $A, \%$ ); the vertical cut-off rigidity ( $R_c$ ); the mean angle between asymptotic longitudes of energetic particles arrival for pairs of stations ( $\Delta \varphi$ ) and the mean  $\varphi_{me}$  angle between the direction of "Receiving cone" and the mean IMF direction in helioequator plane (OX-axis is sunward directed) for the station having the earlier time of increase onset. As is seen from the Table  $t_{ons}$  difference for the stations "looking" field-aligned sunward and in the opposite direction is significant and it reaches 30-40 min (for the event not under consideration here 16.02.84 it is  $\sim 60$  min). The differences in  $A, \%$  are also available.

**3. Discussion.** Similar delays for particles with  $E > 1$  GeV can hardly be explained by the diffusion process within the Earth's orbit. Therefore one can assume that shocks accompanying all these events are responsible for the time difference of SCR intensity increase onset. I.e. the delay was caused by the fact that after the passage of shock beyond 1 a.u. the IMF becomes a regular one [5] and flare SCR injected in such a medium being not inclined in the Earth's magnetosphere pass behind its orbit and be reflected from the shock reverse front (for recurrent streams a higher regularity degree of IMF was shown in [6]). In favour of the such argument is a positive correlation between the duration of delay of SCR increase onset and the time between Forbush-decrease onset and flare onset (i.e. the farther is shock behind the Earth's orbit, the longer is the delay time). The calculations [1] show that on the average the reflected particles change their pitch-angle by  $\sim 20^\circ$ . This value mainly is independent of the initial particle velocity or of shock parameters. We can conclude that the most SCR streams and shock interactions (reflections) are with no particle isotropization. If to try to recover the



Table

SPE	Station	$t_{\text{ons}}, \text{UT}$	A, %	$R_c, \text{GV}$	$\Delta \varphi$	$\varphi_{\text{ME}}$
18.11.68	Calgary	1045	17	1.07	~170°	~15°
	Tixie Bay	1105	2	0.45		
07.08.72	Sanae	1525	8	0.91	~170°	~15°
	Irkutsk	1555	1.5	3.56		
07.05.78	Apatity	0330	120	0.6	~180°	~15°
	McMurdo	0355	4	0.0		
12.10.81	Irkutsk	0610	4	3.56	~70°	-
	Magadan	0640	7.7	2.11		
26.11.82	Moscow	0250	4	2.39	~180°	-
	Magadan	0310	2	2.11		
25.02.69	Goose Bay	0920	16	0.6	~170°	~15°
	Tixie Bay	0950	2	0.45		
24.01.71	Inuvik	2330	14	0.16	~140°	~20°
	Alert	2340	15	0.0		
30.04.76	Kerguelen	2125	11	1.1	~110°	~45°
	Oulu	2140	4	0.77		
23.09.78	Apatity	1030	14	0.6	~150°	-
	Novosibirsk	1040	5	2.78		

picture of intensity increase change on SPE at the station "looking" anti-sunward direction taking into account the presence of shock behind the Earth's orbit, one can obtain the following result: the particles of direct SCR stream from the Sun trapped by the Earth's magnetosphere (if their number is sufficient) will produce the insignificant "diffusive" intensity increase during the delay of two oppositely "looking" stations, then will occur a sharp intensity increase caused by the arrival of SCR stream reflected from the shock. The above view point explains qualitatively both groups of events. For more convincing evidence of existence of the reflected SCR component the energy spectrum of reflected particles is of great interest. But its finding is impossible yet because of lack of data on stations "looking" strictly in the direction of the arrival of the reflected component.

At a detailed investigation in groups of each event were found the peculiarities which can be explained not only by the presence of shock behind the Earth's orbit, but also by the existence of "corks" near the Sun caused by thickening of IMF force lines in the direction towards photosphere. The similar peculiarities were manifested in "two-humped" change of SCR intensity increase. The first increase corresponds to the reflection from shock behind the Earth's orbit and has a delay ~ 20-25 min and the second one corresponds to the secondary reflection from the "cork" already with the

delay  $\sim$  50-60 min (such a phenomenon was observed for Tixie Bay on May 7, 1978).

4. Conclusion. From the above analysis one can conclude: it is most probable that for the peculiarities of SCR increase change in SPE on ground-based data (the delay of SCR increase onsets with  $E > 1$  GeV at various stations; the significant difference in amplitudes; "two-humped" structure of increase etc) are responsible strong non-linear IMF disturbances (shocks) playing a role of the reflecting boundary for energetic particles.

#### References

1. Pesses, M.E., (1982), Invited Paper Cospar Symposium on the Solar Maximum Year, Canada.
2. Scholer, M., (1982), Invited Talks 8-th European Cosmic Ray Symposium, Roma, 1.
3. King, J.H., (1977), Interplanetary Medium Data Book Appendix. Report WDC-A, Maryland, USA.
4. Cosmic Ray Tables, No.1, (1983), WDC-C2, Tokyo, Japan.
5. Samsonov, I.S. i dr., (1979), Kosmicheskiye Luchi Sverkh-vysokikh Energii, Yakutsk, 85.
6. Kozlov, V.I. i dr., (1974), Izv. AN SSSR, Ser.Fiz., No.9, 1908.

THE DISPERSIVE EVOLUTION OF CHARGED-PARTICLE BUNCHES  
IN RANDOM MAGNETIC FIELDS

J.A. Earl

Dept. of Physics & Astronomy, Univ. of MD, College Park, MD 20742

ABSTRACT

Shortly after a strongly anisotropic beam of charged particles is injected along a guiding magnetic field on which is superimposed a small random component, the particle density can be represented by a Gaussian profile whose center moves with the coherent velocity  $V_*$  and whose width increases with time at a rate controlled by the coefficient of dispersion  $D_*$ . Both parameters depend upon the mean free path  $\lambda$ , which characterizes scattering by the random fields, and the focusing length  $L$ , which characterizes spatial variations of the guiding field. These dependences are known explicitly for  $V_*$ . Formulae for  $D_*$  are available only in the limits of very weak and very strong focusing. This paper presents a new expression for  $D_*$ , which spans this gap.

1. Introduction. The equation which describes particle transport along a guiding field under the combined influences of scattering by magnetic turbulence and focusing by spatial inhomogeneities of the guiding field is

$$\frac{\partial f}{\partial t} + \mu V \frac{\partial f}{\partial z} = \frac{1}{2} e^G \frac{\partial}{\partial \mu} \phi e^{-G} \frac{\partial f}{\partial \mu}, \quad (1)$$

where  $f$  is particle density in phase space,  $z$  is distance along the guiding field,  $\mu$  is the pitch-angle cosine and  $V$  is particle velocity. If the coefficient of pitch-angle scattering is given by the standard form

$$\phi = \frac{3(V/\lambda)}{(2-q)(4-q)} (1-\mu^2) |\mu|^{q-1}, \quad (2)$$

where  $q$  is an index that measures the anisotropy of scattering, then the odd function  $G$  is given by

$$G\{z, \mu\} = -\frac{V}{B} \frac{\partial B}{\partial z} \int_0^{\mu} \frac{1-v^2}{\phi\{z, v\}} dv = \frac{(4-q)}{3} \frac{\lambda}{L} |\mu|^{1-q}, \quad (3)$$

where  $L$  is the focusing length and  $B$  is the guiding field. Throughout this paper both  $\lambda$  and  $L$  will be assumed to be constant.

Even with these assumptions, it is not possible to solve the transport equation in closed form. However, there are approximations that provide considerable insight into phenomena, such as those outlined in the abstract, that do not fit into the familiar picture of purely diffusive transport. A first-order analysis (Earl, 1981; Kunstmann, 1979) leads to simplified transport equations which describe coherent propagation in terms of infinitely narrow pulses, but which do not include the dispersive spreading of these disturbances. This paper presents a

second-order analysis which includes this effect.

In the context of new possibilities for numerical solutions opened up by advances in computer technology, the phenomenon of dispersion takes on special significance, for there is an artifact, which I call "numerical dispersion", and which can obscure the physical effect. (See Paper SH 4.1-4) Numerical dispersion is an artifact of the Boltzmann operator that appears on the left hand side of equation (1). Consequently, it is not affected by focusing. To avoid inaccuracies, it is necessary to specify sufficiently fine spatial resolution in the numerical implementation so that the numerical dispersion coefficient is much smaller than the physical one. This paper provides the quantitative knowledge of  $D_*$  needed to make this specification.

2. The Coefficient of Dispersion. The second approximation to the distribution function takes a form

$$f = F_{\#}\{z, t\} + \text{Be}^G H_{\#}\{z, t\} + W\{\mu\} \frac{\partial F_{\#}}{\partial z} - \text{Be}^G W\{-\mu\} \frac{\partial H_{\#}}{\partial z}, \quad (4)$$

in which the first two terms represent supercoherent and pseudodiffusive components that appeared in the first-order approximation and the second two are anisotropic components that are proportional to the spatial gradients of  $F_{\#}$  and  $H_{\#}$ . Both of these additions involve the same function  $W\{\mu\}$ , but the sign of its argument is different in the two new terms. This relationship reflects a fundamental symmetry of focused transport that I call the "principle of complementarity". When equation (4) is substituted in the transport equation, and when the first-order transport equations are satisfied, the following equation for  $W$  is obtained:

$$\frac{1}{2} \frac{\partial}{\partial \mu} e^{-G} \frac{\partial W\{\mu\}}{\partial \mu} - \frac{V_{\#} K}{L(K^2 - 1)} W\{-\mu\} = \left( \mu V + \frac{V_{\#}^2 K}{(K^2 - 1)} \right) e^{-G} - \frac{V_{\#} K}{(K^2 - 1)}, \quad (5)$$

where

$$K = \frac{1}{2} \int_{-1}^{+1} e^G d\mu, \quad (6)$$

is a normalization constant that goes from  $K = 1$  in the limit of weak focusing ( $\lambda/L \ll 1$ ) to  $K = \infty$  in the limit of strong focusing, and

$$V_{\#} = \frac{V}{2K} \int_{-1}^{+1} \mu e^G d\mu, \quad (7)$$

is a characteristic velocity that I call the pseudodiffusive velocity. Note that this is not the coherent velocity  $V_*$ , which is given by

$$V_* = \frac{V_{\#} K}{(K^2 - 1)^{1/2}}. \quad (8)$$

Although the presence of the term in  $W\{-\mu\}$  complicates equation (5), it can be solved for  $W$  with the aid of the method of

eigenfunctions. In fact, because this term is relatively small,  $W$  can be evaluated fairly accurately by a simple double integration.

When the additional terms in  $f$  are taken into account, the second-order transport equations take the forms

$$\frac{\partial F_{\#}}{\partial t} - V_{\#} \frac{\partial F_{\#}}{\partial z} + \frac{B}{K} \frac{\partial H_{\#}}{\partial t} = D_{*} \frac{\partial^2 F_{\#}}{\partial z^2}, \quad (9)$$

and

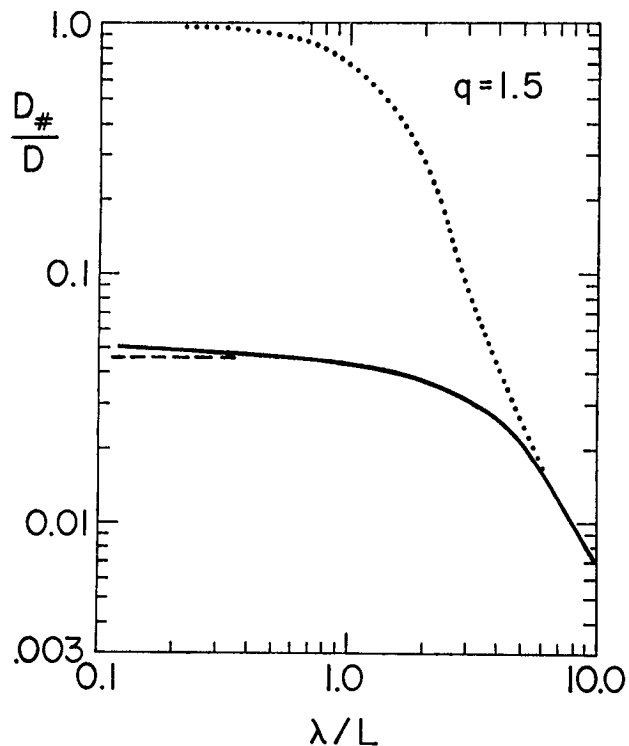
$$\frac{\partial H_{\#}}{\partial t} + V_{\#} \frac{\partial H_{\#}}{\partial z} + \frac{1}{BK} \frac{\partial F_{\#}}{\partial t} = D_{*} \frac{\partial^2 H_{\#}}{\partial z^2}, \quad (10)$$

in which the left hand sides reproduce the first-order transport equations and the right hand sides are second-order terms. Here, the coefficient of dispersion, given by

$$D_{*} = -\frac{1}{2K} \int_{-1}^{+1} d\mu \left( (\mu V + \frac{V_{\#} K^2}{K^2 - 1}) e^{-G} - \frac{V_{\#} K}{K^2 - 1} \right) W\{\mu\}, \quad (11)$$

determines the size of the new terms, which involve the second spatial derivatives of the supercoherent and pseudodiffusive components. They describe the dispersive aspect of coherent propagation, in which the delta function pulses of the first-order description are more accurately described as Gaussian disturbances whose centers move with the coherent velocity  $V_{*}$  while their widths increase with time at a rate controlled by the coefficient  $D_{*}$ .

In the figure, separate curves show how  $D_{*}$  depends upon  $(\lambda/L)$  when the function  $W\{\mu\}$  is evaluated in three different ways. The dashed curve gives the exact result, in which the term in  $W\{-\mu\}$  is retained in equation (5). The solid curve gives a much simpler result obtained from an approximate evaluation in which this term is ignored. For most applications, in which its ~20% deviation from the exact result is not important,



this approximation is adequate. In contrast, the dotted curve, which gives a result obtained by Kunstmann (1979) and by Bieber (1977)<sup>§</sup>, deviates by a factor of  $\sim 20$  at small values of  $(\lambda/L)$ . These results grew out of an analysis which describes correctly the strong focusing regime, but which does not take into account the coupling between components embodied in equations (9) and (10). Unless focusing is very strong, this neglect leads to a large overestimate of the dispersive effect.

3. Summary. The coefficient of dispersion given by equation (11) is a basic parameter needed to implement numerical solutions of the transport equation. In this context, where great accuracy is not required, the limitations of the present analysis to constant  $\lambda$  and  $L$  are not important.

4. Acknowledgements. This research was supported by the National Aeronautics and Space Administration through grant NGR-21-002-066.

#### References

- Bieber, J.W. 1977, Ph.D. thesis, University of Maryland.  
Earl, J.A. 1981, Ap.J., 251, 739.  
Kunstmann, J. 1979, Ap.J., 229, 812.

## NUMERICAL DESCRIPTIONS OF COSMIC-RAY TRANSPORT

J.A. Earl

Dept. of Physics &amp; Astronomy, Univ. of MD, College Park, MD 20742

J.R. Jokipii

Dept. of Planetary Sciences, Univ. of Arizona, Tucson, AZ 85721

## ABSTRACT

The behavior of energetic particles in the solar system is described by a well known Fokker-Planck equation. Although analytic methods yield insight into the nature of its solutions, especially in the diffusion regime, calculations that go beyond diffusion are very complicated. Under these circumstances, numerical computations offer the only feasible way to obtain concrete results. However, the reliability of these calculations is of concern, because numerical methods are notorious for their errors and artifacts. To address this concern, the well known Milne problem of classical transport theory has been analyzed with the aid of three different numerical methods. These are:

1. The method of eigenfunctions in which the distribution function is approximated by a sum of eigenfunctions of the scattering operator. Its complexity limits the practicality of this approach, but it is closely related to the analytic and classical approaches.
2. Numerical solutions of a finite-difference equation. This is the most practical approach, but it is subject to subtle errors.
3. Direct simulation of the scattering and streaming of individual particles with the aid of Monte Carlo methods. The accuracy of this approach is limited by statistical considerations, but it is closely related to the physics.

If proper precautions are taken to ensure its validity, the second method gives results that are in precise quantitative agreement with those of the first. Results of Monte Carlo calculations are not accurate enough to define non-diffusive effects, but in the diffusion regime, they are consistent with diffusion theory.

1. Introduction. According to Weinberg and Wigner (1958), the Milne problem is "the touchstone of classical transport theory". It is in this traditional role as a test for new developments that this famous problem is addressed here. More specifically, the steady-state diffusion of particles to a free escape boundary from a planar source deep within a one-dimensional medium, which is the configuration assumed in the Milne problem, is treated under the further assumptions that the diffusing medium is magnetic turbulence superimposed upon a uniform guiding field and that the particles are cosmic rays whose pitch-angles



relative to the guiding field undergo scattering that is described by the Fokker-Planck formalism. Within this framework, the algebra needed to obtain analytic solutions in terms of eigenfunctions becomes manageable, because temporal variations are absent. These solutions, which embody non-diffusive effects, provide a convenient and well understood standard for judging the accuracy with which numerical methods describe these effects.

Some basic aspects of this picture are outlined within these proceedings in Paper SH4.1-4, and this paper deals with the same transport equation, invokes the same definitions and notation, and insofar as possible, uses the same numbers.

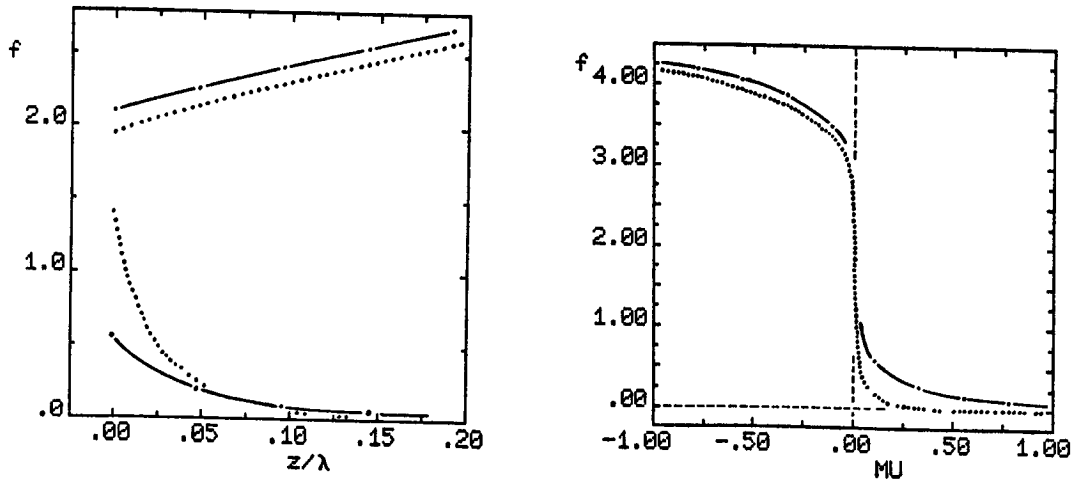
2. The Method of Eigenfunctions. This approach follows exactly the classical treatment in terms of spherical harmonics (Case and Zweifel, 1967, sec 8.4), except that the distribution function is expanded in terms of the scattering eigenfunctions tabulated by Bieber (1977) rather than in terms of Legendre polynomials. In the diffusion approximation, the distribution function  $f\{z, \mu\}$  is approximated essentially by the first two eigenfunctions. In this case, the isotropic density is finite at the surface, and if it is extrapolated beyond the boundary along the same uniform slope that applies to diffusion deep within the medium, it reaches zero at a distance of  $(2/3)\lambda$  outside the boundary. This result is exactly the one obtained from the classical  $P_1$  approximation. To obtain a better description, assume that solutions of the form

$$T\{\mu\} \exp\{-z/\Lambda\}$$

can be expanded as a finite sum of four or more scattering eigenfunctions. Then the matrix form of the transport equation can be solved only for certain specific values of  $\Lambda$  that correspond to a distinct set of transient eigenfunctions. (Note that the term "transient", which derives from classical transport theory, has nothing to do with temporal variations.) These are summed in such a way that the returning intensity at the surface is as near as possible to zero over the outward facing hemisphere. In practice, only the first transient is significant. For the examples computed with  $q = 1.8$ , which are discussed below, the first characteristic length is  $\Lambda = \lambda/40$ .

3. Numerical Solutions of a Finite-Difference Equation. These computations invoke the same formulation and scattering operator as in Paper SH4.1-4, except that steady injection was accomplished by specifying at a fixed value of  $z$  a constant angular distribution. Starting from the diffusion solution, computations were carried out for a time sufficient to allow a particle moving in a straight line to traverse ten times the distance between injection point and boundary. At this time, the flux was essentially independent of  $z$ , which means that the solution was very close to the steady state. (See Earl, 1974b, eq. 24.)

In the figures below, results are plotted for two different values of the spatial increment,  $\Delta z = \lambda/21$  (solid curves) and  $\Delta z = \lambda/210$  (dotted curves), which are, respectively, substantially larger and



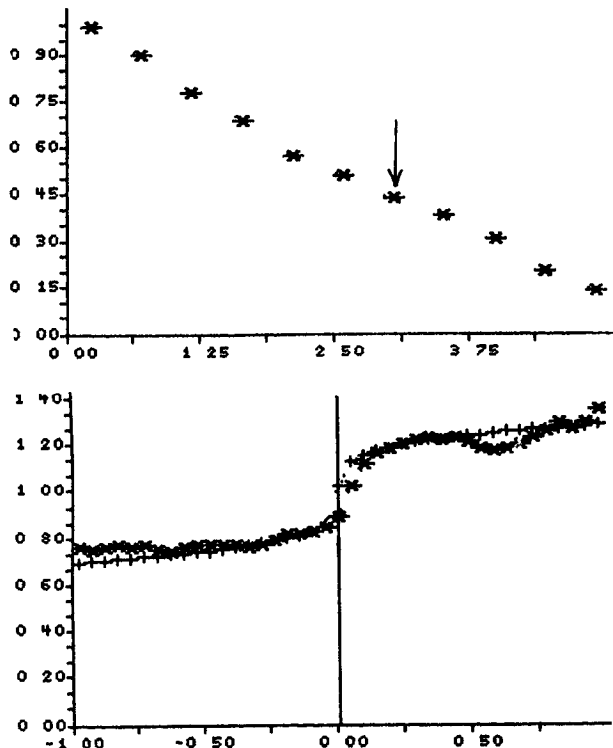
smaller than the characteristic length  $\lambda$ . Note that both increments are much less than the value  $(3/4)\lambda$  derived by Kota et al. (1982) as a condition for validity of the diffusive picture. The analytical solution described above was computed separately, but it cannot be plotted, because its deviations from the dotted curves are smaller than the dots. In the figure at the left, the curves at the top give the isotropic density and those below give ten times the coefficient  $f_2$  of the second scattering eigenfunction, which was obtained by expanding computed angular distributions as a series of four eigenfunctions. The surface density predicted at  $z = 0$  by the solid curve is  $\sim 8\%$  larger than expected. This discrepancy can be attributed to inaccuracies in the description of non-diffusive effects that can be seen in the curves below, which describe an even component that appears in the transient anisotropy, but not in the diffusion approximation. Here, the dotted curve follows exactly the expected exponential dependence characterized by  $\Lambda = \lambda/40$ , while the solid curve, whose spatial resolution is too coarse to describe this strong gradient, follows instead an exponential which has only 40% of the amplitude expected at the surface, and whose decay is characterized by  $\Delta z = \lambda/21$ .

In the figure to the right, the intensity at the surface is plotted as a function of pitch-angle cosine  $\mu$ . The eigenfunction solution is again indistinguishable from the dotted curve, whose rms deviation from expected values is 2.2%. Except for the point nearest to  $\mu = 0$ , the intensity predicted by the dotted curve within the hemisphere  $\mu > 0$  is essentially zero, while in contrast, the solid curve, which refers to an inappropriate choice of  $\Delta z$ , exhibits here a small but finite intensity. Because scattering cannot turn back escaping particles beyond the boundary, no returning intensity is expected, and its degree of absence can be taken as a figure of merit for comparison of different calculations.

4. The Monte Carlo Method. The Fokker-Planck formalism derives from a statistical model in which scattering results from many tiny deflections of particle trajectories by turbulent fields. With the aid of

computers, these random deflections can be simulated directly, and the history of individual particles can be traced through space and time. Two crucial points of this approach are to choose the amplitudes of the deflections to be consistent with the Fokker-Planck coefficient  $\psi$ , and to adjust time increments so that the systematic drift in pitch-angle is compatible with the random spreading.

Because of the limitations on accuracy imposed on this method by statistical considerations, it is very difficult to study the non-diffusive effects considered above. However, the figures to the right show results obtained in the diffusion regime from a Monte Carlo simulation of the Milne problem. Plotted above is the isotropic density as a function of distance, which shows the expected uniform slope downward to a finite density on the boundary at the right. The arrow here designates the point at which the angular distribution plotted below was obtained. This angular distribution is in good agreement with the one expected from diffusion theory, whose points are designated by + symbols.



5. Conclusions. The non-diffusive effects discussed above are miniscule, but the precision with which they are described numerically leaves little doubt that finite-difference calculations can give valid results, provided that their parameters are chosen appropriately. In the diffusion regime, Monte Carlo methods offer a useful alternative.

#### References

- Bieber, J.W. 1977, Ph.D. thesis, University of Maryland.  
 Case, K.M. and Zweifel, P.F. 1967, Linear Transport Theory (Reading: Addison-Wesley).  
 Earl, J.A. 1974a, Ap.J., 188, 379 (Paper II).  
 Earl, J.A. 1974b, Ap.J., 193, 231 (Paper III).  
 Earl, J.A. 1976, Ap.J., 205, 900 (Paper IV).  
 Kota, J., et al. 1982, Ap.J., 254, 398.  
 Weinberg, A.M. and Wigner, E.P. 1958, The Physical Theory of Neutron Chain Reactors (Chicago: University of Chicago Press).

## NUMERICAL AND ANALYTIC DESCRIPTIONS OF COSMIC-RAY TRANSPORT

J.A. Earl

Univ. of MD, Dept. of Physics &amp; Astronomy, College Park, MD 20742

## ABSTRACT

It is not trivial to solve the equations that describe charged particle transport with the aid of computers, for instabilities, inaccuracies, and subtle artifacts are well known afflictions of numerical analysis. Two specific points are:

1. To avoid gross inaccuracies, pitch-angle scattering must be treated with great care. In particular, slightly inappropriate numerical formulations give rise to mean free paths that are in error by large factors.

2. A previously unrecognized artifact, "numerical dispersion", is very similar to the physical phenomenon of dispersion. To avoid misinterpretations arising from this similarity, the spatial increment of the finite-difference grid must be a small fraction of the mean free path.

These points are illustrated by calculations based upon finite-difference approximations to the transport equation.

1. Introduction. The diffusive idealization, which has been almost universally invoked in discussions of cosmic-ray transport is easy to treat analytically. However, many observed phenomena give clear evidence for the presence of non-diffusive effects. One example is the so-called "scatter-free" propagation of kilovolt solar electrons which is inconsistent with diffusion, but which can readily be interpreted in terms of the coherent mode of propagation. Although the qualitative features of these effects have been outlined (Earl, 1974a, 1976), the theory is very complicated. Consequently, there is a need for reliable numerical computations which bypass these complexities and yield concrete results that are well suited for comparison with observations. This paper explores such methods within the limited context of rectilinear propagation of cosmic-ray along a uniform guiding field on which are superimposed random fields.

Under these circumstances, transport is described by

$$\frac{\partial f}{\partial s} + \mu \frac{\partial f}{\partial z} = \frac{\partial}{\partial \mu} \psi \frac{\partial f}{\partial \mu} \quad (1)$$

in which  $f$  is particle density in phase space,  $\mu$  is the pitch-angle cosine, and  $z$  is distance parallel to the guiding field. The parameter  $s = Vt$ , where  $V$  is particle velocity, plays the role of a temporal variable. The coefficient of pitch-angle scattering is given by

$$\psi = \frac{(3/2\lambda)}{(2-q)(4-q)} (1-\mu^2) |\mu|^{q-1}, \quad (2)$$

where  $\lambda$  is the mean free path, and  $q$  is an index that measures the anisotropy of scattering.

Diffusion refers to a configuration of slow temporal variations of the anisotropy and weak spatial inhomogeneities of the isotropic density  $F_0$  (Earl, 1974b), which act as the source of a diffusive anisotropy given by

$$F_1 = -V \frac{\partial F_0}{\partial z} g, \quad (3)$$

where

$$g\{\mu\} = [(4-q)\lambda/3] |\mu| |\mu|^{1-q} \quad (4)$$

is a solution of

$$\frac{\partial}{\partial \mu} \psi \frac{\partial g}{\partial \mu} = -\mu. \quad (5)$$

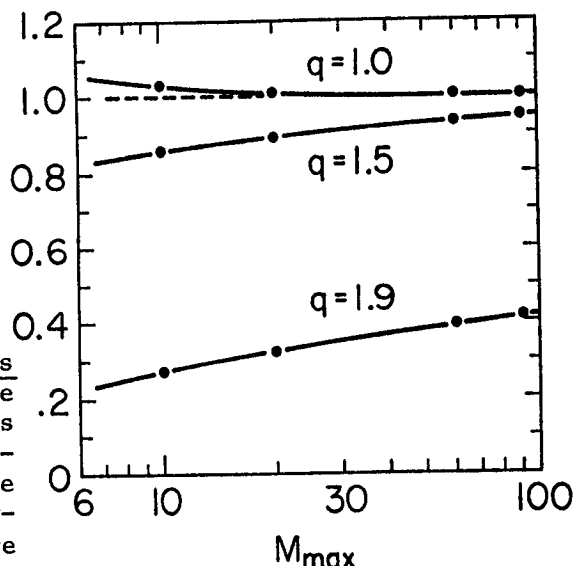
## 2. Finite-Difference Approximations to the Scattering Operator.

In the discrete formulation, the continuous variables are replaced by a three-dimensional grid whose spacings are  $\Delta z$ ,  $\Delta \mu$ , and  $\Delta s = V\Delta t$ , and the derivatives appearing in equation (1) are replaced by their finite-difference analogs. A test of the relationships implied by diffusion can be made without extensive calculations by replacing the differential operator in equation (5) by its finite version and solving numerically for the diffusive anisotropy. This procedure should give an answer consistent with equation (4), and if it does not, the effective mean free path is given by

$$\lambda = (3/2) \int_{-1}^{+1} \mu g \, d\mu. \quad (6)$$

Kota et al. (1982) gave an explicit finite-difference form for the scattering operator. Although this derivation seems eminently reasonable from the standpoint of both mathematics and physics, the resulting scattering operator does not pass this test near the threshold at  $q = 2$  for pure coherent propagation.

Mean free paths derived from this operator are given in the figure above, where the ratio of the actual value of  $\lambda$  obtained from equation (6) to the nominal value that appears in equation (2) is plotted against the number  $M = 2/\Delta \mu$  of increments in pitch-angle. The correspondence is close for  $q = 1$  and fairly close for  $q = 1.5$ , but for  $q = 1.9$ ,  $\lambda$  is a factor of  $\sim 2.5$  too small and shows little indication of converging to the nominal value as  $M$  increases. These inaccuracies are a consequence of the fact that weak scattering near  $\mu = 0$  gives rise to large deviations from the analytic behavior. To avoid these deviations, I use a finite operator constructed so that equation (5) is satisfied exactly when  $g$  is described by the analytic expression. Far from  $\mu = 0$ , this operator behaves the same as Kota's operator, but it also gives the correct diffusive anisotropy and makes the actual mean free path identical to the nominal one.



3. Numerical Dispersion. In a configuration of weak scattering, particle bunches propagate coherently in a moving Gaussian profile given by

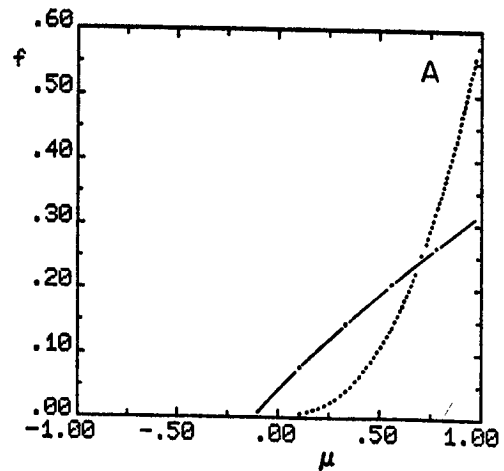
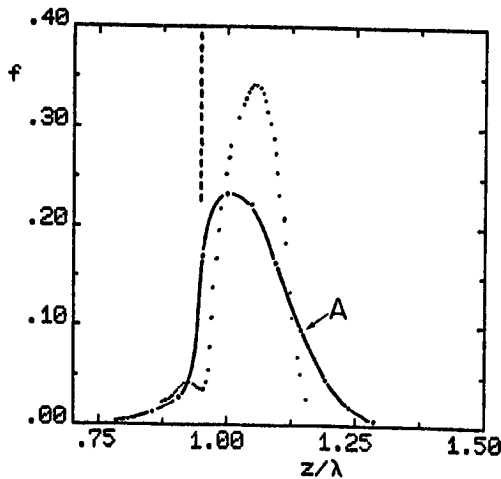
$$F_0 = 1/(4\pi D_* t)^{1/2} \exp\{-(z - V_* t)^2/4D_* t\} \quad (7)$$

where  $V_*$  is a characteristic velocity, which corresponds to an angular distribution that is nearly isotropic in one hemisphere and zero in the other, and  $D_*$  is the coefficient of dispersion, which describes the broadening of the Gaussian that arises from statistical fluctuations of individual velocities within this distribution. (Earl, 1974a).

The finite-difference implementation leads to a very similar effect which can be described by equation (7) with  $D_*$  replaced by

$$D_{\dagger} = \frac{1}{4} V (\Delta z - \frac{1}{2} \Delta s) \quad (8)$$

The total dispersion is a superposition of the physical effect described by  $D_*$  and the numerical effect described by  $D_{\dagger}$ . To ensure that physics dominates, the condition  $D_* \gg D_{\dagger}$  must be satisfied. In the examples presented below, where  $q = 1.8$ , this condition translates into a requirement that  $\Delta z < \lambda/40$ . This condition is similar in concept to the condition derived by Kota et al. for the validity of calculations of diffusion, which is  $\Delta z < 3\lambda/4$ . However, the required spatial resolution is much finer in the coherent regime than it is in the diffusion regime.



4. A Specific Example. To illustrate the points made above, two calculations were made which had identical values of  $\lambda$  and  $\Delta\mu = 0.22$ , but which had values  $\Delta z = \lambda/21$  (plotted as solid lines) and  $\Delta z = \lambda/210$  (plotted as dotted lines) that are, respectively, well below and well above the required spatial resolution. In the figure to the left, snapshots of the density profiles at the instant  $s = 0.19\lambda$ , display the familiar coherent pulses followed by small but perceptible wakes. At this time, the dotted peak has moved a distance of  $0.105\lambda$  to the right of the point indicated by a vertical dotted line at which a localized coherent angular distribution was injected at  $s = 0$ . This corresponds

to a coherent velocity  $V_* = 0.55V$  that is in good agreement with the corresponding velocity of  $0.53V$  tabulated by Bieber (1977). Similarly, the FWHM width of the pulse  $0.135\lambda$  is in good agreement with the width  $0.125\lambda$  expected from a combination of physical dispersion with  $D_* = 0.0064\lambda V$  and numerical dispersion with  $D_n = 0.001\lambda V$ .

The coherent velocity of the solid line peak is less than that of the dotted one and its dispersion, which is dominated by the numerical effect, is larger. To the right of point A, significant solid density appears in regions where the dotted density is zero. This discrepancy is relevant to descriptions of the early onset phase of solar particle events, for it means that the numerical dispersion can bring particles from the sun faster than the physics can, and this could lead to significant errors in the timing of flare events.

The angular distributions in the figure that appears at the right above add weight to this point. They refer to point A where the two profiles have equal densities and, consequently, can be directly compared without normalization. The dotted distribution is much more collimated in the forward direction near  $\mu = 1$  than the solid one is. It is clear that any attempts to interpret observed angular distributions of the first few particles arriving in a flare event should take rigorous measures to exclude the effect of numerical dispersion.

5. Conclusions. Before non-diffusive transport can even be considered, the scattering operator must be carefully tailored to give valid results in the diffusion regime. Once this has been done, calculations that take proper account of numerical dispersion give results in good agreement with those expected from the theory of coherent propagation, but not with those calculated with inadequate spatial resolution. This situation can lead to insidious errors, for the invalid results appear to be qualitatively reasonable, and can be detected only by quantitative tests.

6. Acknowledgements. This research was supported by NASA under Grant NGR 21-002-066.

#### References

- Bieber, J.W. 1977, Ph.D. thesis, University of Maryland.
- Earl, J.A. 1974a, Ap.J., 188, 379 (Paper II).
- Earl, J.A. 1974b, Ap.J., 193, 231 (Paper III).
- Earl, J.A. 1976, Ap.J., 205, 900 (Paper IV).
- Kota, J., et al. 1982, Ap.J., 254, 398.

## THE ROLE OF SHOCK WAVES IN MODULATION OF GALACTIC COSMIC RAYS SH 4.1-7

R.Gall<sup>1</sup>, B.T. Thomas<sup>2</sup> and H. Durand<sup>1</sup>

1. Instituto de Geofísica, Universidad Nacional Autónoma de México, MEXICO.
2. Computer Sciences Department, University of Bristol, Bristol, ENGLAND.

## INTRODUCTION

In the last decade our understanding of modulation of the galactic cosmic rays has considerably progressed by the exploration by space probes of major heliospheric structures, such as the Corotating Interaction Regions, the neutral sheet, and the compression regions of intense heliospheric magnetic fields. Also relevant in this context were the detections in the outer heliosphere of long lasting Forbush type decreases of cosmic ray intensity (1,2,3).

In this paper we shall present the results of our recent theoretical studies on the changes in intensity and energy, at different locations from the sun, induced by the passage of shocks across the heliosphere. In this short version of our research we shall deal mainly with the simplest cases of modulation of 1GV and 2GV particles by single or several shocks during periods of positive and negative solar field polarity.

We shall report here the results of the theoretical aspects of our research. The comparison of the theoretical predictions with space probe data (4,5) will allow us to draw conclusions on the role of shocks on the modulation on both the 11 and 22 year galactic cosmic ray cycles in the outer heliosphere and on the plausibility of the models and parameters used.

## METHOD AND MODELS

The modulation that the galactic relativistic cosmic rays undergo during their propagation across the heliosphere all the way to the observer, is studied by means of Liouville's theorem that states that the six dimensional phase space density  $f(\underline{r}, \underline{p})$  is conserved along the particle trajectories. In order to follow the past history of a particle of momentum  $\underline{p}$ , detected at  $\underline{r}$ , one must trace the trajectory of the particle all the way to the boundary.

The method which we used in our studies of shock induced Forbush Decreases (6,7), (the FdM method), consists of integration of full differential equation of motion  $d\underline{p}/dt = e(\underline{E} + \underline{v} \times \underline{B}/c)$  of a large number of particles moving in both Parkerian and magnetic field shock model, scattered also by small irregularities achieved by random angular deflection corresponding to a chosen diffusion coefficient. The trajectory of each individual particle is integrated back in time, all the way from the observer at  $\underline{r}$  to the chosen spherical boundary, keeping all along a detailed account, of the changing particle momentum. The intensity of the particle is inferred from the relation  $j = fp^2$ . We determine the associated intensity at the boundary by a power law in total particle energy of spectral index -2.6.

The FdM method allowed us to prove that the principal mechanism of Forbush decreases is simply the additional adiabatic cooling of the relativistic cosmic rays during their prolonged containment by magnetic field between the shock and the sun.

In the present research we use a method designed by B. Thomas (the BTM -



SH 4.1-7

method which saves much computer time. It differs from FdM in that instead of solving the full differential equation we now solve the Boltzmann equation and deal with the GC. We compute the focussing and all the drift velocities and evaluate the diffusion and the energy loss by the FdM method. Just as in FdM we impose a  $k_{||}$  and  $k_{\perp}$  and follow the trajectory integration of 50 particles, back in time, from the position of the observer all the way to the boundary; at every step size of the integration we compute the "average particle" position and pitch angle.

The momentum  $p_o$  at the boundary, averaged over all individual particles estimates is used to compute the intensity and particle energy loss at  $r$ . (For better understanding of FbM and TBM methods we refer the reader to reference 7)

We use the semispherical shock model of Dryer's type (8), a Parkerian-magnetic field model outside the shocks, and a magnetic field model inside the shock, given by  $B = B_o/r^2$ ;  $B\phi = (B_o/r)V_{\Omega} \sin\theta \{3 + 3\cos \pi(r-r_o)/d\}$ , where  $d$  is the width of the shock and  $r_o$  is the heliospheric distance of the shock interface.

In our elementary studies on the shocks influence of cosmic ray modulation we assume that all the shocks propagate with the same velocity of 400 klm/sec, its width changing with the position of the shock, given by  $d = 0.2x r_o$ . The shocks are placed at sufficiently large distance,  $\sim 20$  AU, from each other to avoid shock-shock interaction. Moreover the shock's loss of energy is not considered. A flat ecliptic neutral sheet-model is used; we place the observers at  $\lambda=0, \varphi=0$  and  $\lambda=5^\circ, \varphi=0^\circ$ , for positive and negative polarity periods, respectively.

#### RESULTS AND COMMENTS

Figure 1A exhibits the 22 years modulation of 1GV protons in the outer heliosphere induced by the diffusive propagation in a merely Parkerian magnetic field;  $k_{||} = .219 \times 10^{21} \text{ cm}^2/\text{sec}$  and  $7.68 \times 10^{21} \text{ cm}^2/\text{sec}$ , for 1 and 2GV respectively. As seen by observers located at different  $r$ , the intensities for negative polarity are not only higher than for positive polarity, but exhibit a relatively constant radial gradient. In the table below we list some of the modulation characteristics.

1	2	3	- 4 +	
1GV	80 UA: 42% 20 UA: 2.4%	0.7%/AU	25%	41.9%
2GV	80 UA: 30% 29 UA: 21%	.16%/AU	3.5%	9.1%

1. Proton rigidity.
2. The % ratio of negative to positive polarity intensities at 80 and 20 UA
3. Average intensity gradient of  $-20 < r < 80$  AU (negative polarity)
4. % of total energy ( $E_T$ ) loss by adiabatic cooling for 20 AU observer.

Obviously the theoretical data on propagation in Parkerian field is rather elementary as it does not include the effects induced by large magnetic heliospheric structures. Still it serves as a useful tool, as a first approximation, to which the effect of shocks, CIR or inclined neutral sheet can be separately added.

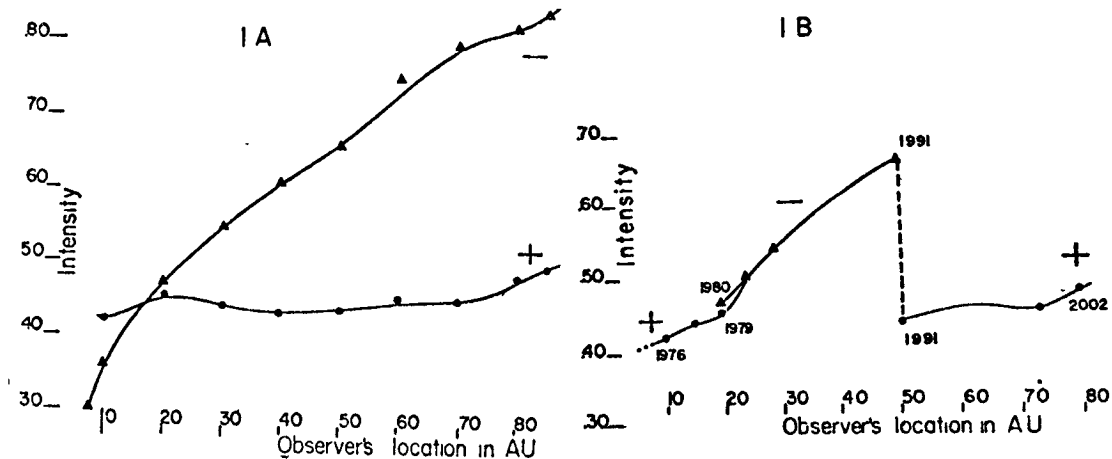


Fig.1A: Intensity of 1GV protons, detected by observers located along the ecliptic at different distances from the sun, for A- and A+ periods.

Fig.1B: The computed intensities of 1GV protons for 1976-2002 period. The sign of solar field polarity is marked.

Finally we shall discuss the modulation of cosmic rays induced by -- shocks. Using the BTM method and the shock and shock associated magnetic-field models, we have computed the intensities of 2 GV protons for the -- cases of 1, 2, and 4 shocks propagating across the outer heliosphere. -- Notice that it takes approximately 14 months for the shocks to propagate -- from the sun to the boundary. For the period of positive solar field polarity. An observer located at 17 AU will detect as illustrated in Fig.2A a similar pattern of intensity vs time, for the three cases mentioned. A typical Forbush type 15% intensity decrease, lasting approximately 100 days of equal decrease and recovery time, followed by a 40 days period of 5% -- intensity increase above the Parkerian propagation intensity level (which we shall call here PI). This increase is due to an acceleration, during -- the temporal trapping of particles between the shocks is followed by a recovery to practically PI level. Only in the case of 4 shocks one detects -- as slow intensity decrease of less than 4%.

This intensity vs time pattern, during A- period is very different from the one described above, which obviously implies an important 22 years -- cosmic rays intensity cycle.

As seen in figure 2B, the observer at 24 AU, sees a slight increase of intensity, lasting 40 and 80 days for 1 shock and 2 shocks, respectively; this is probably due to the typical PI increase during the A- periods.

This increase is followed by an abrupt 50% decrease that occurs at 30-AU for the case of 1 shock and at 50 AU for 2 shocks propagating across -- the outer heliosphere. Necessarily the intensity level will rise as the -- particles approach the vicinity of the boundary.

One must keep in mind that the pattern just used, corresponds to a -- rather simple model of shocks, described before. We plan to continue -- this research using a much more realistic shock models.

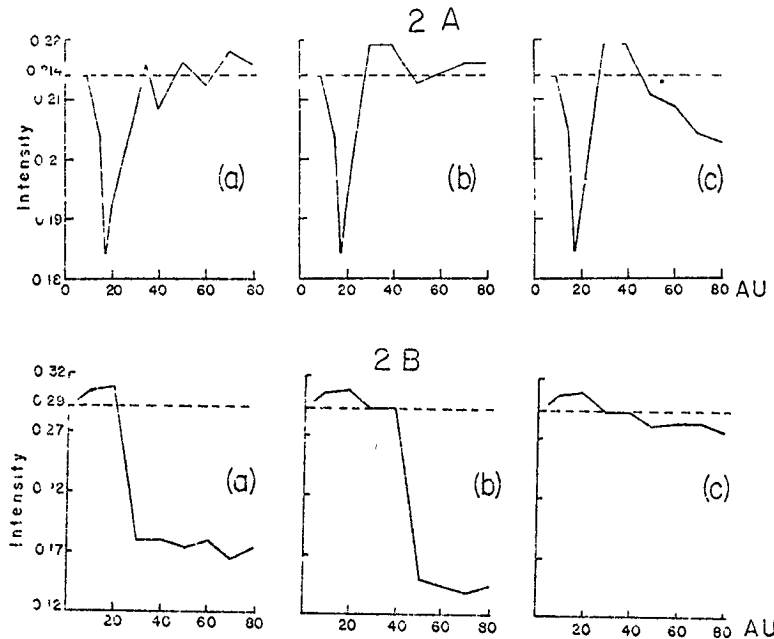


Fig.2A and 2B show the intensity variations during 340 days of observations by an observer located along the ecliptic at fixed distance from the sun. The variations are induced by one(a), two(b) or four(c) shocks. The abscissa marks the position  $x_0$  of the most advanced shock; it also provides the -- time:  $(t) \times 4.33$  days, measured from the day of emission of the mentioned-shock. (Fig.2A: observer at 17 AU, A-; Fig.2B observer at 24 AU, A+)

#### Aknowledgments

R.Gall is indebted to the UNAM Programa Universitario de Cómputo (PUC) where all the computation was carried out; thanks are especially due to Ing.Strassburger, PUC's research director, for his unconditional assistance. Thanks are also due to CONACYT for their economic cooperation.

H. Durand expresses his thanks to the local committee for their generosity that made possible his personal participation in the 19th. ICRC.

#### References

1. Pyle, K.R., et al, (1979), Large Scale Modulation of Galactic Cosmic Rays and Anomalous. He Observed at 16 AU with Pioneer 10, Proc. 16th. ICRC, 5, - 345-350, Kyoto, Japan, 1979.
2. Van Allen, J., (1979), Propagation of a Forbush Decrease in Cosmic Ray Intensity to 15.9 AU, Geophys. Res. Lett., 6(1), 566-568.
3. Fillius, W., et al, (1983), Cosmic Ray Gradients in the Outer Heliosphere - 18th. ICRC, 3, 55-58.
4. Fillius, W., and I. Axford, J. Geophys. Res. 90, (A1), 517-520, 1985.
5. Gall, R., and B.T. Thomas, (1981), A Theoretical Interpretation of - - Forbush Decreases, 17th. ICRC, 4, 1-4, 1981.
6. Thomas, B.T., and R. Gall, (1984), Solar Flare-Induced Forbush Decreases: - Dependence on shock Wave Geometry, J. Geophys. Res., 89 (A5), 2991-2996, 1984.
7. Kota, J. (1984), Time Reversed Method in Cosmic Ray Modulation Theory, - Proc. Int. Symp. Cosmic Ray Modulation in the Heliosphere, 153, Marioka, Japan, 1985.
8. Dwyer M., Interplanetary Shock Waves Generated by Solar Flares Space, - Sci. Rev. 13, 401, 1974.

THE INTENSITY RECOVERY OF FORBUSH-TYPE DECREASES AS A FUNCTION OF  
HELIOCENTRIC DISTANCE AND ITS RELATIONSHIP TO THE 11-YEAR VARIATION

Lockwood, J. A. and W. R. Webber  
Space Science Center, University of New Hampshire  
Durham, New Hampshire 03824 USA

Jokipii, J. R.  
Department of Planetary Sciences, University of Arizona  
Tucson, Arizona 95721 USA

1. Introduction. Recent observations of the cosmic-ray modulation, including particularly interplanetary radial gradient studies, have helped to identify two key questions which need to be answered in order to understand the cosmic-ray modulation process. One question is related to the importance of cosmic-ray particle drifts in both the short-term and 11-year modulation process. The other question is related to the degree to which the 11-year modulation process represents a superposition of transient (Forbush) decreases. Recent data indicating that the solar modulation effects are propagated outward in the heliospheric cavity [1,2,3,4] suggest that the 11-year cosmic-ray modulation can best be described by a dynamic time-dependent model.

In this context an understanding of the recovery characteristics of large transient Forbush-type decreases is important. This includes the typical recovery time at a fixed energy at 1 AU as well as at larger heliocentric radial distances, the energy dependence of the recovery time at 1 AU, and the dependence of the time for the intensity to decrease to the minimum in the transient decrease as a function of distance. We characterize these transient decreases by their asymmetrical decrease and recovery times, generally 1-2 days and 3-10 days respectively at  $\sim 1$  AU. Near earth these are referred to as Forbush decreases, associated with a shock or blast wave passage. At  $R \sim 10$  AU, these transient decreases may represent the combined effects of several shock waves that have merged together.

2. Observations. About thirty transient decreases from 1972-1984 observed at 1 AU (Fig. 1) for which data were available from the IMP spacecraft (P median  $\sim 1.7$  GV) and the Mt. Washington neutron monitor (P median  $\sim 5$  GV) were analyzed to determine the characteristic recovery time  $t_0$  at earth. Certain selection criteria were applied to these decreases: a) magnitude  $> 3\%$  as seen in daily average count rate of the Mt. Washington neutron monitor; and, b) effects of solar particles in the IMP cosmic-ray data should be small or negligible. The fractional decrease  $(\Delta N/N)$  was calculated from the logarithmic difference of the daily average counting rates recorded for three days before the decrease and at the minimum. For the recovery it is assumed that  $n = n_0 \exp(-t/t_0)$ , where  $n = \ln N - \ln N_m$  and  $n_0 = \ln N_0 - \ln N_m$ .  $N_0$  is the 3-day average intensity before the event,  $N$  is the intensity on day  $t$  and  $N_m$  is the minimum intensity (for details see [5]). In all cases the recovery could be fitted well by this form.

In Fig. 2 we have plotted the characteristic recovery time,  $t_0$ , derived in the manner described above for the IMP detector versus that for the neutron monitor at Mt. Washington. Clearly the data are fitted by  $t_0(MW) = t_0(IMP)$  with an average  $\approx 5$  days which implies that the decay time in these events is on the average the same for the two

instruments differing by a factor of 3 in the rigidity of their mean responses. We also observe that: 1) there is no significant difference in recovery times for events classed as Co-rotating Interaction Regions (CIR), having a more symmetrical decrease and recovery time, and the classical Forbush-type transients; 2)  $t_o$  does not depend upon the magnitude of the decrease; 3)  $t_o$  does not change significantly before and after the solar magnetic field reversal in 1980; and 4)  $t_o$  is the same in the decreasing phase of the solar cycle (before 1981-1982) and in the recovery part of the cycle.

We have investigated the heliocentric radial dependence of  $t_o$  for 19 transient decreases, of which 16 were included in the analysis of the energy dependence of  $t_o$  above, utilizing additional data from cosmic-ray telescopes ( $E > 60$  MeV) on Voyagers 1 and 2, and Pioneer 10. An additional criterion imposed for this latter study is that  $(\Delta N/N)$  of the transient must be  $\sim 10\%$  as seen in the daily average count rate of the IMP detector at 1 AU. This latter criterion enables the transient events to be more clearly identified as they move outward and possibly coalesce with other decreases at  $R \sim 10$  AU [6]. For 13 of the 19 events examined we believe that there is little doubt about the association at various radial distances. For only one transient decrease is  $t_o$  less at larger  $R$ . In Fig. 3 we show an example of a transient decrease which has been traced from 1 AU to 21 AU. The dependence of  $t_o$  upon heliocentric radial distance for the ensemble of all 16 events is shown in Fig. 4. It is evident that on the average the magnitude of  $t_o$  becomes much longer as  $R$  increases [see 7]. The data shown in Fig. 4 can be fitted by  $t_o(R)/t_o(1) = 1.26 \exp(0.090R)$ , where  $R$  is the radial distance in AU.

From a comparison of the magnitude of the "same" event  $(\Delta N/N)$  at different  $R$  we find no strong dependence of  $(\Delta N/N)$  upon  $R$ . A possible reason for this behavior as opposed to a more rapid decrease in magnitude expected for a single shock is that, as suggested by [6], the transients seen at  $R \sim 10$  AU probably represent the coalescence of several smaller transients seen at 1 AU.

For 10 out of 19 transient decreases we also determined the time  $T$  from onset to the minimum intensity as a function of  $R$ . We find  $T(R)/T(1) = 1.10 \exp(0.055R)$  where  $T(R)$  is the value at  $R$  and  $T(1)$  at earth. This means that at  $R \sim 10$  AU it takes about twice as long to reach minimum. We find that from 1 to 30 AU the ratio  $(t_o/T)$  increases slowly, due to the longer recovery time at larger  $R$ . The fact that this ratio is  $\gg 1$  clearly indicates that we are observing asymmetrical transient decreases at large  $R$ , however.

3. Physical Model for the Observed Energy and Spatial Dependence of the Recovery Time. A physical model based upon a time-dependent, two-dimensional numerical solution to the cosmic-ray transport with a single shock weakening with distance has been developed by one of us (JRJ) to study these transient events [8]. The transient is represented by a disturbance propagated into the steady-state cosmic-ray distribution. The intensities at several radii and energies are studied. This model predicts that there should be only a small dependence of  $t_o$  upon energy at a given  $R$  as is observed. The variation of intensity with  $R$  depends mainly on the decay of the disturbance as it propagates through the heliosphere. For an e-folding distance of 5-7 AU for the weakening of the shock, the variation of the recovery time with energy and heliocentric radius is given in Table 1.

Table 1: Variation of Recovery Time  $t_o$  With Energy and Heliocentric Radius.

Energy [GeV]	Distance [AU]	1.7	3.3	5.0
1.3		5.3	7.5	9.7
3.6		5.0	7.0	8.6
9.1		4.5	5.9	7.6

These properties are in excellent qualitative agreement with the observations reported here. Precise quantitative agreement is not expected at this stage given that the model is only two-dimensional and the evolution of the disturbance is quite simple.

We conclude that for the transient decreases observed here:

- 1) the average recovery time  $t_o$  from transient decreases at 1 AU is energy independent and  $t_o \sim 5$  days;
- 2)  $t_o$  is essentially the same before as after the solar magnetic field reversed in 1980;
- 3)  $t_o$  is constant throughout the solar modulation cycle;
- 4) the ratio of recovery times  $t_o(R)/t_o(1)$  increases with  $R$  and is about 5 times longer at 20 AU than at 1 AU;
- 5) the time for the decrease to reach minimum,  $T$ , increases about 10%/AU out to 20 AU; so that at 20 AU it is  $\sim 2$  times longer than at 1 AU;
- 6) these results are well described by a two-dimensional numerical solution to the cosmic-ray transport equation which incorporates an outward moving weakening shock.

#### 6. Acknowledgments.

The authors want to thank F.B. McDonald and T. von Rosenvinge for making data available from Pioneer and Voyager spacecraft and IMP satellite respectively. The studies by JAL, WRW and JRJ were supported, in part, by grants from NSF (ATM-8304486), NASA/GSFC (NAS5-24354) and NSF (ATM-8317701) and NASA (NSG-7101) respectively.

#### References

1. McDonald, F.B., et al., (1981), Ap. J., 249, L71.
2. Webber, W.R. and J.A. Lockwood, (1981), J. Geophys. Res. 86, 11458.
3. McKibben, R.B., et al., (1982), Ap. J., 254, L23.
4. Lockwood, J.A. and W.R. Webber, (1984), J. Geophys. Res., 89, 17.
5. Lockwood, J.A. and W.R. Webber, (1985), to be pub. J. Geophys. Res.
6. Burlaga, L., et al., (1984), J. Geophys. Res., 89, 6579.
7. Van Allen, J.A., (1979), Geophys. Res. Lett., 6, 566.
8. Jokipii, J.R., and J. Kota, (1983), Ap. J., 265, 573.

#### Figure Captions

- Fig. 1 Mt. Washington neutron monitor monthly average count rate. Upper panel indicates transient decreases  $> 3\%$  observed at Mt. Washington.
- Fig. 2  $t_o$  for IMP vs.  $t_o$  for Mt. Washington neutron monitor.
- Fig. 3 Count rate of IMP8, V1, V2, and P10 for transient decrease on July 12, 1982.
- Fig. 4 Ratio  $t_o(R)/t_o(R=1)$  vs. radial distance  $R$ .

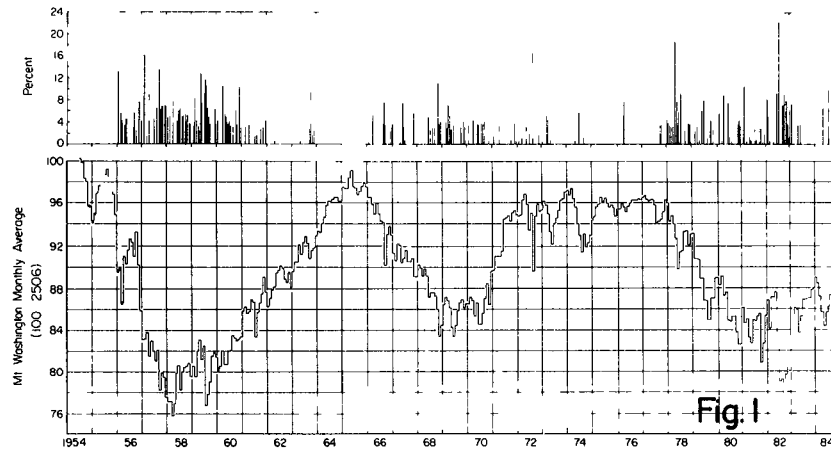


Fig. 1

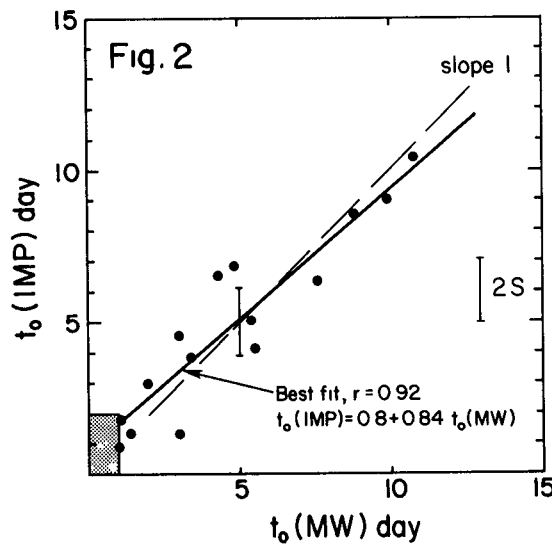


Fig. 2

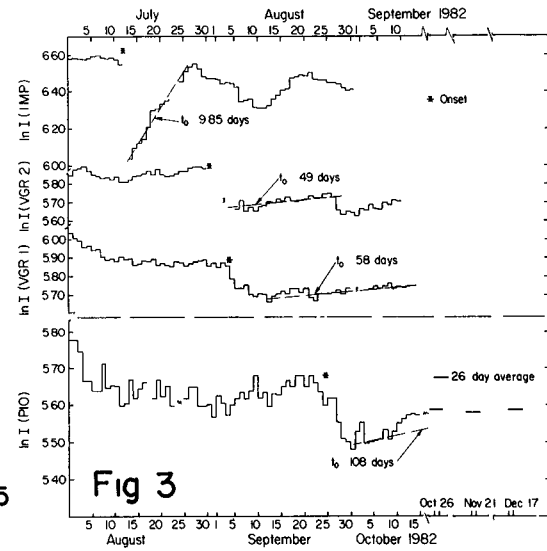


Fig 3

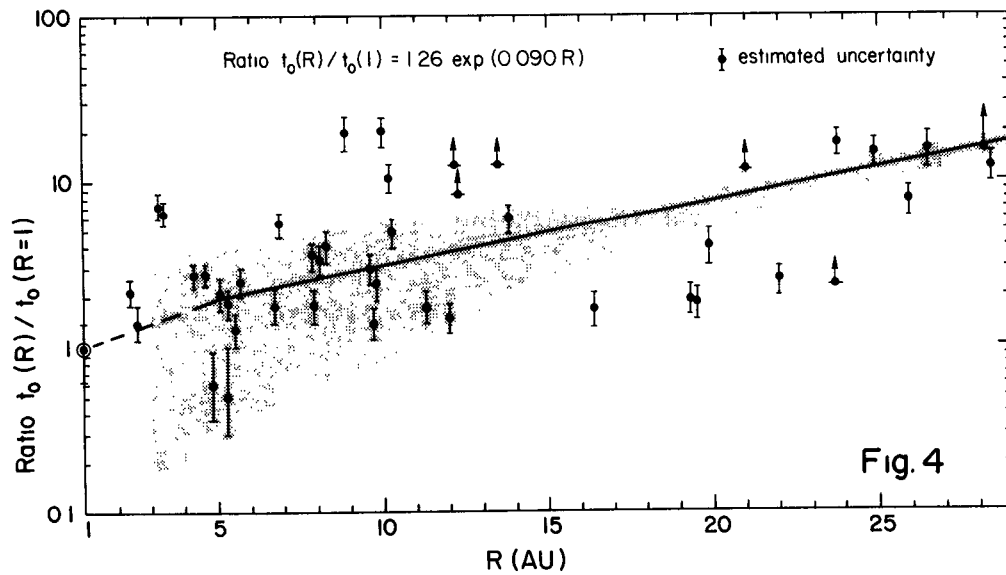


Fig. 4

# **CUMULATIVE EFFECT OF FORBUSH DECREASES IN THE HELIO-SPHERIC MODULATION DURING THE PRESENT SOLAR CYCLE**

S. P. Agrawal<sup>1</sup>, B. L. Mishra<sup>1</sup>, A. K. Jain<sup>1,2</sup>

<sup>1</sup>Physics Department (Vikram Space Physics Centre)  
A.P.S. University, Rewa (M.P.) 486003, India

<sup>2</sup>Government Engineering College  
Rewa (M.P.) 486002, India

## **ABSTRACT**

We generate a monthly Forbush decrease index (Fd-I) and compare it with the observed long-term changes in the cosmic ray intensity near earth at energies  $> 1$  Gev over 1976-83. Significant correlation is observed between the two except for 1978. Such an effect is also seen in the correlation plot between the solar flare index (SFI) and Fd-I.

**1. Introduction.** Characteristics of the long term variation of cosmic ray intensity have been obtained in the past using neutron monitor data (e.g. Lockwood and Webber, 1984). Recent studies from spacecraft have determined the radial gradient of cosmic ray intensity to a distance of up to 30 AU (e.g. Venkatesan et al., 1984; Van Allen and Randall, 1985). Furthermore specific cosmic ray intensity changes such as Forbush decreases have also been studied to large heliospheric radial distances (Van Allen, 1979; and references therein). The purpose of this paper is to explore the role of the short-term cosmic ray intensity decreases in generating the profile of the cosmic ray long-term variation.

**2. Analysis and Results.** The percent deviation has been calculated for each month for the interval 1976-83, using the cosmic ray intensity maximum for the months of Sept.-Nov. 1976 as 100%. The Forbush decrease index (Fd-I) is computed from the hourly data of Deep River neutron monitor after examining the plots of a number of stations as well. The magnitude of each Fd is added to form a cumulative total of all the Fd's observed in a month; such a total is the index, Fd-I. Similarly, the solar flare index (SFI) has been computed by using all solar flares (importance  $> 1$ ) and by assigning a weight according to the numerical importance of the flare and the relative brightness of each solar flare. Such objective criteria give proper weight to the energetic flares, which generally produce much larger decreases in cosmic ray intensity (Shukla et al., 1978).

The long-term modulation has been reported to be a direct consequence of large number of solar flares (e.g. Hatton, 1980; Agrawal, 1983; and references therein). Similarly, the Fd effects are also the consequence of energetic solar flares (Shukla et al., 1978). We therefore suggest that the long term modulation is the cumulative effect of large number of small and big Fd's, the validity for which is examined in Figure 1. Note that the cosmic ray intensity reaches a maximum in 1976, and a minimum in 1982. However, the Fd-I changes very



abruptly, with a very large peak in 1978, and with a conspicuous minimum in 1980. The anomalous behaviour of low Fd activity during 1980 is being investigated separately in a paper (SH 5.1-15). Moreover, the peak value of Fd-I in 1978, is of considerable interest, and will be discussed further.

Note from Fig. 1 that both  $R_z$  and SFI are still increasing during 1978, while Fd-I shows a very large peak in 1978. Geomagnetic disturbance index Ap also shows moderately low values till 1981, after which it increases, (probably associated with the dominating effect of coronal holes).

The correlation between the long term cosmic ray variations and the Forbush decrease index, is investigated by a cross-plot (Fig. 2) using monthly values for the two quantities during 1976-83. Note that in spite of significant correlation, many points lie close to X-axis. Opposite is true for the year 1978, when most of the points lie close to y-axis, indicating large Fd-I without any associated cosmic ray decreases. Nevertheless, correlated changes observed during other periods show that the long term modulation of cosmic ray intensity can be understood in terms of the cumulative effect of Fd's. We believe that the exception during 1978 of Fd-I on %-deviation of cosmic rays is perhaps attributable to the faster recovery of cosmic rays during 1978. This needs further investigation as also why during certain months of high solar activity no Forbush decreases are seen.

The correlation between Fd-I and percent cosmic ray deviations, with SFI during 1976-83, is shown in Figure 3(a) and (b). Note again that large Fd-I's are associated with small SFI during 1978. Reverse is true for certain months in 1980. The correlation is poor in 1980 and during the recovery of cosmic ray intensity in 1983, when large cosmic ray intensity deviations are observed for low values of SFI. Nevertheless, Figure 3(a) indicates a correlated variation in the cosmic ray intensity with the observed changes in SFI. Thus, from Fig. 3(a) and 3(b), we observe the effect of SFI on both Fd-I and cosmic ray intensity (except for certain specific periods mentioned earlier), which also in turn justify the correlation shown in Fig. 2. It is therefore, reasonable to presume that the long term cosmic ray variation is generated by the cumulative effect of Forbush decreases, and the departure is quite significant during 1978 and 1980, in the present sunspot cycle.

#### 4. References.

- Agrawal, S. P., (1983), Space Sci. Rev., 34, 127.  
 Hatton, C. J., (1980), Solar Phys. 66, 159.  
 Lockwood, J. A., and W. R. Webber, (1984), J. Geophys. Res., 89, 17.  
 Shukla, A. K., J. P. Shukla, S. M. Sharma, R. L. Singh, and S. P. Agrawal (1978), Ind. J. Radio & Space Phys. 7, 179.  
 Van Allen, J. A., (1979), Geophys. Res. Lett., 6, 566.  
 Van Allen, J. A. and B. A. Randall, (1985), J. Geophys. Res. 90, 1399.  
 Venkatesan, D., R. B. Decker and S. M. Krimigis, (1984), J. Geophys. Res. 89, 3735.

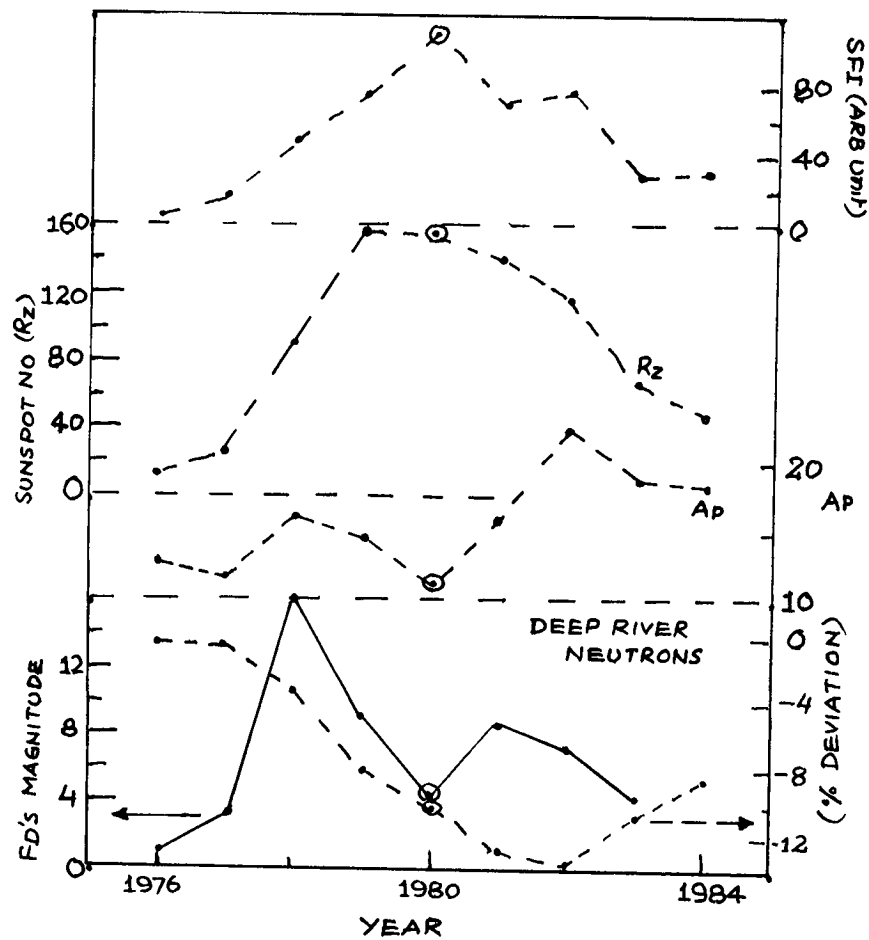


Figure 1 Yearly means of the solar flare index, sunspot number, Ap index, Forbush decrease index (Fd-I) and the cosmic ray intensity deviations from its maximum value, for 1976-84. The annual average values for 1984 are derived from limited number of monthly values. A large peak in Fd-I in 1978 is clearly evident.

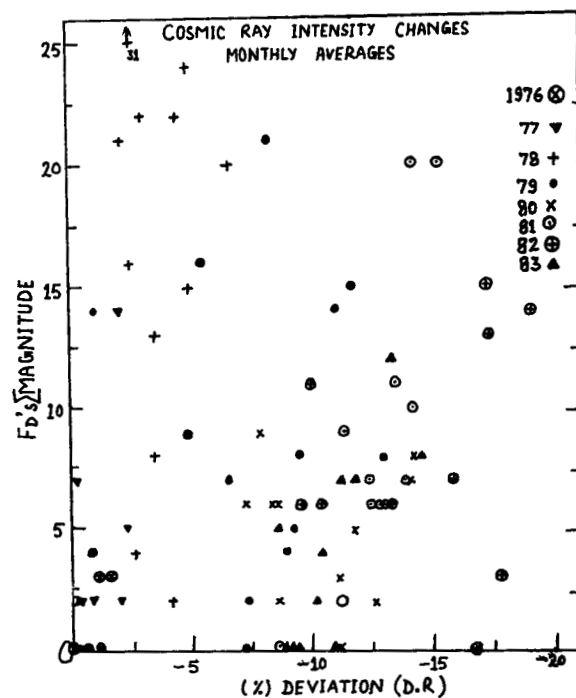


Figure 2 Cross-plot of monthly values of % deviation of cosmic ray intensity and Fd-I during 1976-83 with various symbols for different years.

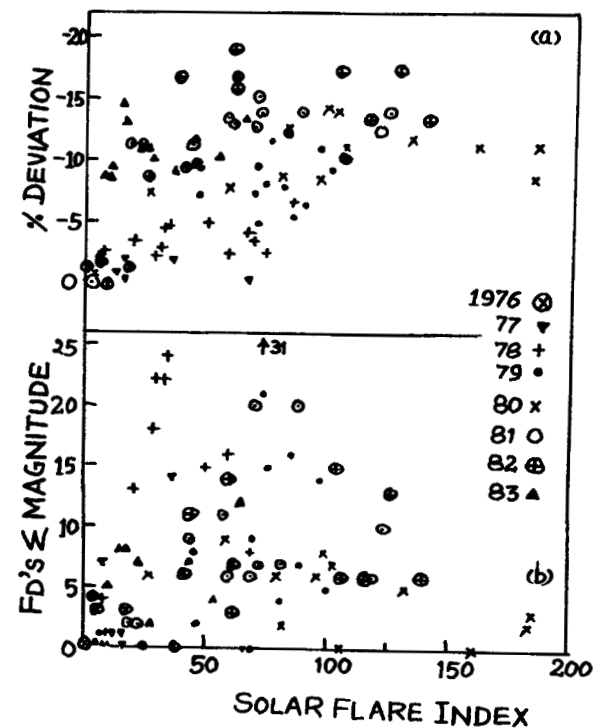


Figure 3 (a,b) Crossplot of monthly values of SFI and (Fd-I)/percent deviation of cosmic rays during 1976-83. Symbols are the same as used in Figure 2.

## COSMIC RAY MODULATION AND MERGED INTERACTION REGIONS

L. F. Burlaga, and M. L. Goldstein  
NASA/Goddard Space Flight Center  
Laboratory for Extraterrestrial Physics  
Greenbelt, MD 20771

F. B. McDonald  
NASA Headquarters, Washington, DC 20546

## ABSTRACT

Beyond several AU, interactions among shocks and streams give rise to "merged interaction regions" in which the magnetic field is turbulent. The integral intensity of  $> 75$  MeV/Nuc cosmic rays at Voyager is generally observed to decrease when a "merged interaction region" moves past the spacecraft and to increase during the passage of a rarefaction region. When the separation between interaction regions is relatively large, the cosmic ray intensity tends to increase on a scale of a few months. This was the case at Voyager 1 from July 1, 1983 to May 1, 1984, when the spacecraft moved from 16.7 to 19.6 AU. Changes in cosmic ray intensity were related to the magnetic field strength in a simple way. It is estimated that the diffusion coefficient in merged interaction regions at this distance is  $\sim 0.6 \times 10^{22} \text{ cm}^2/\text{s}$ .

1. Introduction. Variations in the intensity of galactic cosmic rays  $> 75$  MeV/nucleon near 11 AU on scales ranging from approximately a day to a year were found to be related to the interplanetary magnetic field in observations from Voyagers 1 and 2 from June, 1982 to August, 1983 (Burlaga et al., 1985a). The long-term variation of cosmic ray intensity was related to the strength and separation of interaction regions. It decreased or remained relatively low when interaction regions were strong and closely spaced, and it increased when the interaction regions were weaker and widely spaced. These results are consistent with the idea that modulation is caused by diffusion in turbulent magnetic fields (Morrison, 1956) and the observation that modulation effects propagate outward from the sun at the solar wind speed (McDonald et al., 1981). A non-steady model of the 11-year variation which incorporates diffusion and propagation of shells of disturbances has been constructed by Perko and Fisk (1983).

The purpose of this paper is to extend the analysis of Burlaga et al. (1985a) to examine the relation between cosmic ray intensity and the interplanetary magnetic field from July 1, 1983 to May 1, 1984, using Voyager 1 data. During this interval the spacecraft moved from a heliocentric distance of 16.7 AU to 19.6 AU and from a heliographic latitude of  $20^\circ$  to  $23^\circ$ .

2. Observations. The intensity of cosmic rays  $> 75$  MeV/nucleon, measured by the CalTech/University of New Hampshire/Goddard Space Flight Center experiment is shown in Figure 1, together with the strength of the interplanetary magnetic field measured by the GSFC magnetometer (N. Ness, Principal Investigator). The magnetic field strength was normalized by the spiral magnetic field strength,  $B_p = 4.75 \times (1 + r^2)^{1/2} / r^2$ . Thus, the magnetic field fluctuations in Figure 1 are perturbations on the large-scale average magnetic field, which are produced by dynamical interplanetary processes.

Figure 1 shows a correlation between  $B/B_p$  and the cosmic ray intensity  $C$ :  $C$  generally decreases during the passage of an interaction region or merged interaction region ( $B/B_p > 1$ ) and it increases during the passage of a rarefaction region ( $B/B_p < 1$ ). A similar correlation was observed near 11 AU by Burlaga et al. The net effect in the period shown in Figure 1 is an overall increase in cosmic ray intensity. The cosmic ray intensity profile is the result of a competition between the effects of

interaction regions and those of rarefaction regions. In this interval, the interaction regions were relatively weak ( $(B/B_p)_{\max} < 2.5$ ) and the corresponding decreases in  $C$  were relatively small, while the rarefaction regions were large in extent, allowing more than enough time to recover from the individual decreases.

3. Model. Burlaga et al. (1985a) modeled the variation of cosmic ray intensity observed near 11 AU from July, 1982 to August, 1983 with the following set of equations:

$$\frac{dC}{dt} = -D (B/B_p - 1) \quad \text{when } B/B_p > 1 \quad (1)$$

$$\frac{dC}{dt} = R \quad \text{when } B/B_p \leq 1 \quad (2)$$

where  $D$  and  $R$  are constants and  $B/B_p$  is the measured magnetic field strength as a function of time. Using the 24-hour averages of  $B/B_p(t)$  shown in Figure 1, choosing  $D = 0.004$  (counts/sec/day) and  $R = 0.002$  (counts/sec/day) and taking the initial value of  $C$  at July 1, 1983, these

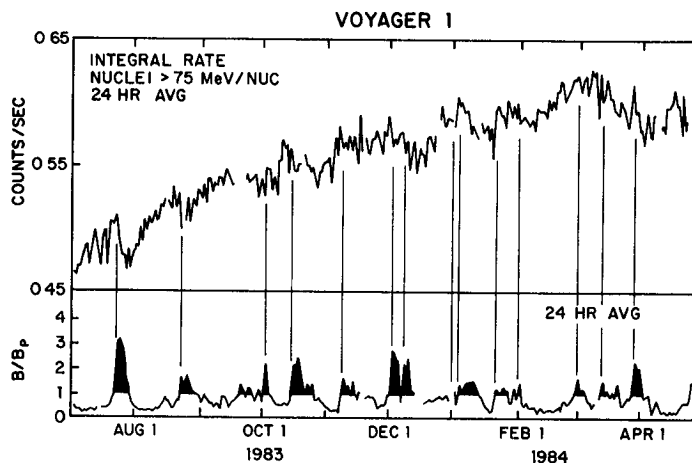


Fig. 1 Intensity of cosmic rays  $> 75$  MeV/nuclei versus time (top) and magnetic field strength relative to the spiral field strength versus time (bottom).

equations were integrated to obtain the model cosmic ray intensity profile shown in Figure 2. The observed 24-hour averages of  $C(t)$  for  $> 75$  MeV/nucleon cosmic rays are also plotted in Figure 2, for comparison. Note that the model curve has been plotted with a constant offset of 0.03 (counts/sec/day) for the sake of clarity, but its initial value can be chosen to be identical to the observed value for the integration of (1) and (2). Between March 10 and March 20 there was a decrease in cosmic ray intensity which is not predicted, because there was no large increase in  $B/B_0$  at this time (see Figure 1). Except for this anomaly, the model provides a very good approximation to the cosmic ray observations throughout the 10-month interval.

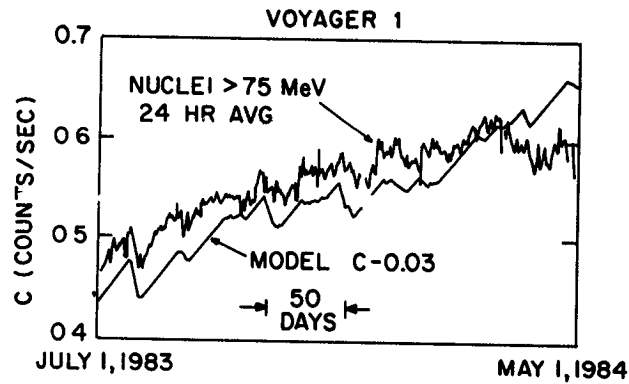


Fig. 2 The result of a model (see text) together with a plot of the observed counting rates.

A theoretical basis for the model given by (1) and (2) has recently been given by Chih and Lee (1985). They found that under certain assumptions

$$\frac{dC}{dt} = -\frac{V}{L} (C - C_0) - \frac{V}{K} C_0 \frac{\delta B}{B_0}, \quad (3)$$

where  $K$  is the diffusion coefficient,  $V$  is the solar wind speed,  $L$  is a characteristic length and  $\delta B$  is a measure of the fluctuations of  $B$ . It has been observed that  $\delta B/B \approx 0.3$  between 1 AU and 5 AU, varying slowly with distance as  $r^{-1/3}$  (Burlaga et al., 1982), so it is reasonable to take  $\delta B/B_0 = 0.3 B/B_0$  in (3). In this case the second term on the RHS of (3) has the same form as (1), and one can use our value of  $D$  to estimate the diffusion coefficient  $K$ . With  $D = 0.004$  (counts/sec/day),  $V = 400$  km/s,  $C_0 = 0.55$  counts/sec and  $\delta B/B = 0.3$  one finds  $K = 0.6 \times 10^{22} \text{ cm}^2 \text{ s}^{-1}$ . This is somewhat smaller than the value chosen by Chih and Lee (because we used  $\delta B/B = 0.3$ ), but it is close to the value for the diffusion coefficient used by Perko and Fisk (1983) to describe the 11-year variation. Identifying the first term on the RHS of (3) with  $R$  in (2), and taking  $C - C_0 \approx 0.03$  counts/sec, one finds that  $R = 0.002$  (counts/sec/day) implies  $L \approx 4$  AU.

In Figure 3 we show spectra of the components of  $B$  (upper curve), the magnitude of  $B$  (lower curve) and the magnetic helicity times frequency ( $fH_m$ ) computed from one hour average Voyager 1 data from July 1, 1983 to May 1, 1984, using the fast Fourier transform method with 26 degrees of freedom, without detrending or filtering the data (Matthaeus and

Goldstein, 1982). Positive values of magnetic helicity are denoted as circles, negative values as triangles. Assuming that plasma is convected past the spacecraft at the mean solar wind speed in the interval,  $\bar{V}$ , the frequency  $f_c$  corresponding to the correlation length  $L$ , is  $f_c = \bar{V}/L$ , and this is shown by the arrow in Figure 3.

The spectrum of power in the components of  $B$  has the form  $f^{-5/3}$ , expected for homogeneous turbulence in the range  $4 \times 10^{-6}$  Hz to  $2 \times 10^{-5}$  Hz, corresponding to periods from 14 hours to 3 days. This is consistent with earlier results showing that the fluctuations in interaction regions are turbulent. At periods between 4 days and 15 days, the spectrum of power in the components of  $B$  was  $\propto f^{-1}$ , which is probably either a remnant of the spec-

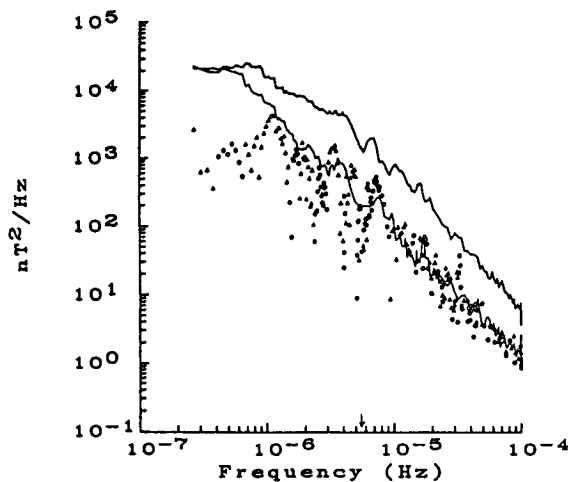


Fig. 3 Power spectra of the magnetic field (see text).

trum of fluctuations introduced at the source (Goldstein et al., 1984; Burlaga et al., 1985b) or evidence of an inverse cascade of magnetic helicity expected in fully developed MHD turbulence (Frisch et al., 1975; Montgomery and Matthaeus, 1981). If the former interpretation is correct, its presence is another indication that turbulence did not develop sufficiently to modify the initial spectrum in this quasi-stationary flow system, despite the long time available for evolution, viz.  $\sim 18$  AU/400 km/s  $\rightarrow$  78 days.

#### References

- Burlaga, L., (1984), Space Sci. Rev., **39**, 255.  
 Burlaga, L. F. and J. King, (1979), J. Geophys. Res., **84**, 6633.  
 Burlaga, L. F. et al., (1982), J. Geophys. Res., **87**, 4345.  
 Burlaga, L. F. et al., (1984), J. Geophys. Res., **89**, 6579.  
 Burlaga, L. F. et al., (1985a), NASA/GSFC TM 86193.  
 Burlaga, L. F. et al., (1985b), NASA TM 86213.  
 Chih, P. P. and M. A. Lee, preprint, (1985), submitted to J. Geophys. Res.  
 Frisch et al., (1975), J. Fluid Mech., **68**, 769.  
 Goldstein, M. L. et al., (1982), J. Geophys. Res., **87**, 6011.  
 Matthaeus, W. H. and M. L. Goldstein, (1984), J. Geophys. Res., **89**, 3747.  
 Matthaeus, W. H. and D. Montgomery, (1981) J. Plasma Phys., **25**, 11.  
 McDonald, F. B. et al., (1981), Ap. J. (Letters), **249**, L71.  
 Morrison, P., (1956), Phys. Rev., **101**, 1397.  
 Perko, J. S. and L. A. Fisk, (1983), J. Geophys. Res., **88**, 9033.

## PROPAGATION OF THE PHASE OF SOLAR MODULATION

Miriam A. Forman  
State University of New York  
Stony Brook, NY 11794-2100 USA

Frank C. Jones  
John S. Perko<sup>1</sup>  
Goddard Space Flight Center  
Greenbelt, MD 20771-0665

## ABSTRACT

The phase of the 11-year galactic cosmic-ray variation, due to a varying rate of emission of long-lived, propagating regions of enhanced scattering, travels faster than the scattering regions themselves. The radial speed of the 11-year phase in the quasi-steady, force-field approximation is exactly twice the speed of the individual, episodic decreases. A time-dependent, numerical solution for 1-GeV protons at 1 and 30 AU gives a phase speed which is 1.85 times the propagation speed of the individual decreases.

1. Introduction. Sudden decreases in cosmic-ray intensity have been observed to propagate outward in the ecliptic plane at about 400-500 km/s, the solar wind speed [McDonald et. al., 1981; McKibben et. al., 1982; Van Allen, 1979; Venkatesan et. al., 1984; see review by Burlaga, 1983]. These decreases are related to regions of enhanced magnetic field strength and turbulence, which strongly suggests enhanced reflection and scattering of cosmic rays. Although these regions are very prominent near the ecliptic plane, it is not clear that all modulation can be ascribed to them. We do not know how their effects extend out of the ecliptic, nor how they may modify the expected modulation due to large-scale drift and the neutral sheet [Jokipii & Davila, 1981; Kota & Jokipii, 1982].

If the 11-year modulation cycle is due to an 11-year cycle in the emission of such propagating regions, as suggested in the references above and by Perko & Fisk [1983], then how would the phase of the 11-year modulation propagate? Venkatesan et. al. [1984] have remarked that "an unexpected result of [our] study is the apparent simultaneity (to within one solar rotation) of the occurrence of solar minimum at [1 and] 10 AU." This implies a phase speed of >700 km/s, which is distinctly faster than the 500 km/s of the observed episodic decreases. We show in this paper that the simplest episodic model of modulation predicts that the phase speed of the 11-year modulation moves outward at up to twice the speed of the

<sup>1</sup>NAS/NRC Resident Research Associate



individual intensity decreases.

2. Heuristic Model. We consider propagating, episodic modulation in a quasi-steady, "Force-field" model [Gleeson & Axford, 1968]. The modulation parameter is defined as

$$\phi(r,t) = \int_r^R V dr' / K(r',t)$$

where "V" is the solar wind speed and "K(r',t)" is the radial diffusion coefficient for the cosmic rays. Since 1/K is proportional to the amount of turbulence, and regions of turbulence propagate at speed V,

$$\phi(r,t) = \int_r^R V dr' / K(0,t-r'/V)$$

$\phi$  then varies with the solar cycle because of the changing rate of emission from the Sun of scattering regions which propagate outward at speed V to a boundary at R, where their effect ceases.

A scattering region emitted from the Sun at time  $t_0$  causes a cosmic-ray decrease to begin at radius  $r_1$  when the region passes at time  $t_1 = t_0 + r_1/V$ . At  $r_2 > r_1$ , it begins at  $t_2 = t_0 + r_2/V$ . The end of the effect at both  $r_1$  and  $r_2$  occurs near the time  $t_E = t_0 + R/V$  when the region leaves the modulating sphere at radius R. For various reasons, the end is not clearly seen in observations. Still, the middle of the lasting effect on modulation at  $r_1$  occurs at time  $t_{m1} = (t_1 + t_E)/2 = t_0 + (r_1 + R)/2V$ , and likewise at  $r_2$ ,  $t_{m2} = t_0 + (r_2 + R)/2V$ . Thus, because the beginning of the effect travels at speed V, but the end of it occurs at the same time everywhere, the overall lasting effect of each scattering region propagates at speed 2V.

Alternatively, the solar cycle can be modelled by varying the averaged level of turbulence in the solar wind and propagating it outward. Then the modulation parameter  $\phi(r,t)$  is the integral from r to R of V/K at the Sun at time  $(t-r'/V)$ . If V/K varies as  $\cos(\omega t)$  at the Sun, then  $\phi$  varies with time as  $\cos[\omega(t-(R+r)/2V)]$ . Again, this shows that the phase velocity of the variation in modulation is 2V.

3. Numerical Results. Perko & Fisk [1983] modelled an 11-year cycle in modulation based on episodic events. They assumed the Sun emits spherically-symmetric regions in which scattering is enhanced by a maximum factor of 10 over a band 2 AU wide. The regions travel outward at a speed of 400 km/s until they reach a boundary at 100 AU, where they disappear. The rate of emission was made to vary from one every 4 months at solar minimum to one every 2 weeks at solar maximum. The recovery phase of the cycle was modelled by reversing that behavior. The diffusion coefficient in the undisturbed solar wind (outside the discrete scattering regions) was set at

$$K = 4.3\beta(2 + p^2) 10^{21} \text{ cm}^2/\text{s}$$

where " $\beta$ " is the ratio of particle speed to the speed of light and " $p$ " is particle rigidity. For boundary conditions and other details of the calculation, see Perko & Fisk [1983]. The result (Fig. 1) of their numerical integration of the time-dependent transport equations reproduces many of the features of the 11-year modulation. In particular, the episodic decreases propagate at the same speed as the scattering regions (see solid bar at the base of Fig. 1, which shows the propagation time of a scattering region and its accompanying intensity decrease going from 1 to 30 AU). The general level of modulation increases as the rate of emission of these regions increases; but as the rate decreases, the total number of regions in the heliosphere goes down, and there is a cosmic-ray minimum and recovery.

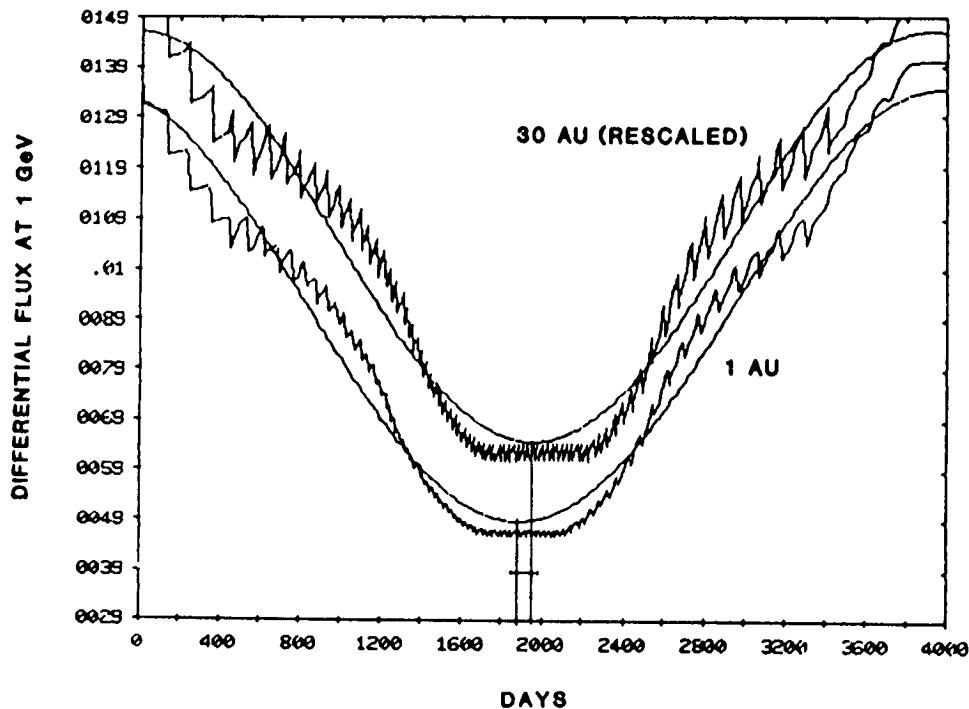


Fig. 1. Numerical calculation of flux (arbitrary units) of 1-GeV protons over the solar cycle, from one sunspot minimum to the next, at 1 and 30 AU. Individual decreases in intensity propagate from 1 to 30 AU in 125 days, shown by the bar at the base of the figure, but the time delay between cosmic-ray minima is only 68 days, shown by the vertical lines.

The smooth curves superposed on the numerical results are sine functions fitted to the results by a least-squares algorithm. The fitted parameters of the sine curves yielded the times of cosmic-ray minimum at 1 and 30 AU. These are indicated by the vertical lines connecting the curves with the abscissa.

It is a remarkable new result that the cosmic-ray minimum at 30 AU shown in Figure 1 occurred only 68 days after the minimum at 1 AU, which implies a propagation speed of 740 km/s, 1.85 times faster than the 400 km/s speed of individual decreases.

4. Conclusions. This simple model demonstrates that the phase of the 11-year cosmic-ray cycle, including recovery, propagates outward even under the simplified assumption of spherical symmetry. This outward propagation may not, therefore, be considered as a signature of models that allow preferential access to the solar cavity via the polar regions. Furthermore, this modulation phase moves at approximately twice the solar wind speed because the flux at a given radius depends on the average state of the heliosphere in the region between this radius and the outer boundary.

5. Acknowledgements. This work was supported by the Solar-Terrestrial Theory Program of the National Aeronautics and Space Administration.

#### References

- Burlaga, L. F., 1983, Proc. 18 ICRC, Bangalore, 12, 21.  
 Gleeson, L. J., and W. I. Axford, 1968, Astrophys. J., 154, 1011.  
 Jokipii, J. R., and J. M. Davila, 1981, Astrophys. J., 248, 1156.  
 Kota, J., and J. R. Jokipii, 1982, Geophys. Res. Lett., 9, 656.  
 McDonald, F. B., N. Lal, J. H. Trainor, M. A. I. Van Hollebeke, and W. R. Webber, 1981, Astrophys. J., 249, L71.  
 McKibben, R. B., K. R. Pyle, and J. A. Simpson, 1982, Astrophys. J., 254, L23.  
 Perko, J. S., and L. A. Fisk, 1983, J. Geophys. Res., 88, 9033.  
 Van Allen, J. A., 1979, Geophys. Res. Lett., 6, 656.  
 Venkatesan, D., R. B. Decker, and S. M. Krimigis, 1984, J. Geophys. Res., 89, 3735.  
 Webber, W. R., and J. A. Lockwood, 1981, J. Geophys. Res., 86, 11458.

# LATITUDE VARIATION OF RECURRENT FLUXES IN THE OUTER SOLAR SYSTEM

*S P Christon and E C Stone*  
*California Institute of Technology, USA*

(Confirming Abstract)

Recurrent low-energy ( $\gtrsim 0.5$  MeV) proton flux enhancements, reliable indicators of corotating plasma interaction regions, were observed on the Voyager 1 and 2 and Pioneer 11 spacecraft in the heliographic latitude range  $2^{\circ}\text{S}$  to  $23^{\circ}\text{N}$  and the heliocentric radial range 11 to 20 AU [Christon and Stone, 1985]. After a period of rather high correlation between fluxes at different latitudes in early 1983, distinct differences developed in the fluxes during an overall flux decrease. The flux intensities returned to higher levels in early 1984 and differences in both the recurrence frequency and flux intensity persisted into 1985, as Voyager 1 traveled to 23 AU and  $25^{\circ}\text{N}$  latitude. Intercomparison of data from the three spacecraft indicates that the flux differences are most likely due to latitudinal, rather than radial or temporal, variations.

## References

Christon, S P and E C Stone [1985], *Geophys Res Lett*, 12, 109.

## LONGITUDINAL DISTRIBUTION OF COSMIC RAYS IN THE HELIOSPHERE

R. E. Gold<sup>1</sup> and D. Venkatesan<sup>1,2</sup>

<sup>1</sup>The Johns Hopkins University, Applied Physics Laboratory  
Laurel, MD 20707  
USA

<sup>2</sup>University of Calgary  
Calgary, Alberta, T2N 1N4  
Canada

## ABSTRACT

The longitudinal distribution of cosmic ray intensity has been examined during the years 1974-1976 when the persistent high speed solar wind stream structures produced a well-ordered inner heliosphere. Solar wind velocity is mapped back to the sun and compared with cosmic ray intensity which is represented relative to the solar rotation average. Low solar wind velocity is observed to be a necessary, but not sufficient, condition for the occurrence of higher cosmic ray intensities at 1 AU. These relative enhancements cover a restricted range of heliographic longitudes and persist for several solar rotations. The observed solar wind and cosmic ray intensity relationships are consistent with a simple model suggested here in which cosmic ray modulation is very weak in the inner heliosphere, sunward of the first shock crossing on each field line and more intense in the outer heliosphere.

1. Introduction. The extremely well-ordered and persistent high speed solar wind stream structure during the years 1974 through 1976 provide us with a unique opportunity to compare cosmic ray intensity with solar wind velocity. Earlier studies [1, 2, 3, 4] have shown that no simple relationship exists at 1 AU; but, direct correlations between velocity and intensity may hold only over restricted time periods. The very persistent streams in the ecliptic plane that resulted from extensions of the solar polar coronal holes in the years 1974-76 provide us with a new perspective in which the relative cosmic ray intensity changes over restricted longitude ranges may be compared because the average cosmic ray intensity was only changing slowly over the time scale of many solar rotations. This quasi-equilibrium in the cosmic ray intensity is disturbed during the rest of the solar cycle by transient phenomena related to solar activity; hence the choice of this period for study.

2. Observations. The solar wind data used in this study were from the near-earth observations in the Omni Tape of J. King (NSSDC) supplemented with the isolated data points available from Pioneers 6 through 9. The solar wind observations were mapped back to the sun using the approximation of radial propagation at constant velocity as described in [5, 6]. Each solar wind observation is assumed to have originated at the subsolar point and propagated to the spacecraft with the observed speed. The emission longitude from the sun is therefore  $\phi_E = \phi_0 - \Omega_\odot R/V$

SH 4.1-14

where  $\phi_0$  is the subsolar longitude at the time of observation,  $\Omega_0$  is the solar sidereal rotation rate,  $R$  is the heliocentric radial distance of the observing spacecraft and  $V$  is the solar wind velocity. Each of the observed velocities was assigned to the mapped longitude, which is also the foot point of its field line, and plotted in Figure 1 at the emission time ( $t_E$ ) resulting from the constant velocity approximation  $t_E = t_{OBS} - R/V$ , where  $t_{OBS}$  is the observation time. The near-earth cosmic ray intensity was determined from the CPME experiment on IMP-8. The M scintillator channel responds to all ions  $\gtrsim 35$  MeV/nuc. Details of the CPME experiment are contained in [7]. Each M scintillator observation was associated with the mapped heliographic longitude of the solar wind observed at the same time. These cosmic ray intensities were then plotted in Figure 2 as a function of  $\phi_E$  and  $t_E$ . The intensities are represented as the ratio to the average intensity at all longitudes with the same emission day (i.e., each vertical cut through Figure 2 averages to a value of 1.0).

**3. Discussion and Conclusions.** The cosmic ray intensity in Figure 2 shows relative enhancements over restricted ranges of heliographic longitude that extend over several months in 1975. The largest increases are seen between  $150-240^\circ$  in April through June and  $270-330^\circ$  in September through December. These correspond to the regions between the high speed streams seen in Figure 1. Similar periods are found in the 1974 and 1976 data as well. The 1975 data are shown here because they are free of large solar flare effects and Forbush decreases which disturb some of the solar rotation averages during high activity periods in 1974 and 1976. However, there are well defined cosmic ray enhancement periods during each of the years in the study period. During each of the cosmic ray enhancements, the observed solar wind velocity is low. These enhancements tend to fall in the gaps between the high speed streams and near the edges of the stream seen at 1 AU. However, low solar wind velocity is not always associated with enhanced cosmic ray intensity on the corresponding field lines within the study period. Thus, low solar wind velocity appears to be a necessary, but not sufficient, condition for relative cosmic ray enhancements of restricted azimuthal size that persist for several solar rotations.

The relationship between solar wind velocity and cosmic ray intensity during the interval 1974-76 can be clarified by referring to the solar wind mapping in Figure 3. This is an  $R-\phi$  plot with radial distance increasing downward and heliographic longitude increasing to the right, modulo  $360^\circ$ . The line at the top shows the approximate solar wind velocity profile at the high corona that would produce a stream configuration like that observed between April and July 1974. The mapping was constructed using the observed velocities in May 1974. The CIR boundaries in the figure were determined by connecting the appropriate points in the mapped solar wind data from near-earth and Pioneer 11. The field lines were drawn by extrapolating the near-earth velocity outward until it encountered a CIR boundary. The CIR's are shaded and note that beyond  $\sim 10$  AU all field lines from the inner heliosphere have intersected at least one shock. The region of enhanced cosmic ray intensity in May 1974 is shown as the heavy bar at 1 AU centered near  $180^\circ$ . The enhanced cosmic rays are seen on field lines that extend to

SH 4.1-14

large radial distances before they intersect a shock. This suggests a very simple model for relative variation of cosmic ray intensities in the inner heliosphere.

In the outer heliosphere, from the heliopause all the way inward to the innermost shock boundary, all of the plasma has been through a shock. Now imagine that this "shocked" plasma defines a uniformly modulating region for cosmic rays. This is the shaded region in Figure 3 and it determines the long term intensity variations throughout the heliosphere. Let the inner heliosphere (where the field lines are visible in Figure 3) modulate the cosmic rays only very weakly. Then we would expect a general pattern in which the relative intensity within a solar rotation at 1 AU would be enhanced on field lines that extend far out into the heliosphere before they encounter a CIR shock boundary. This condition is generally found in the trailing edge of large solar wind streams where the velocity is relatively low. The theoretical implications of this model are discussed by Roelof [8] in this conference.

4. Acknowledgements. This work has been supported in part by NASA under Task I of Contract N00024-85-C-5301 between The Johns Hopkins University and the Department of the Navy and in part by NSF under Grant ATM 83-05537.

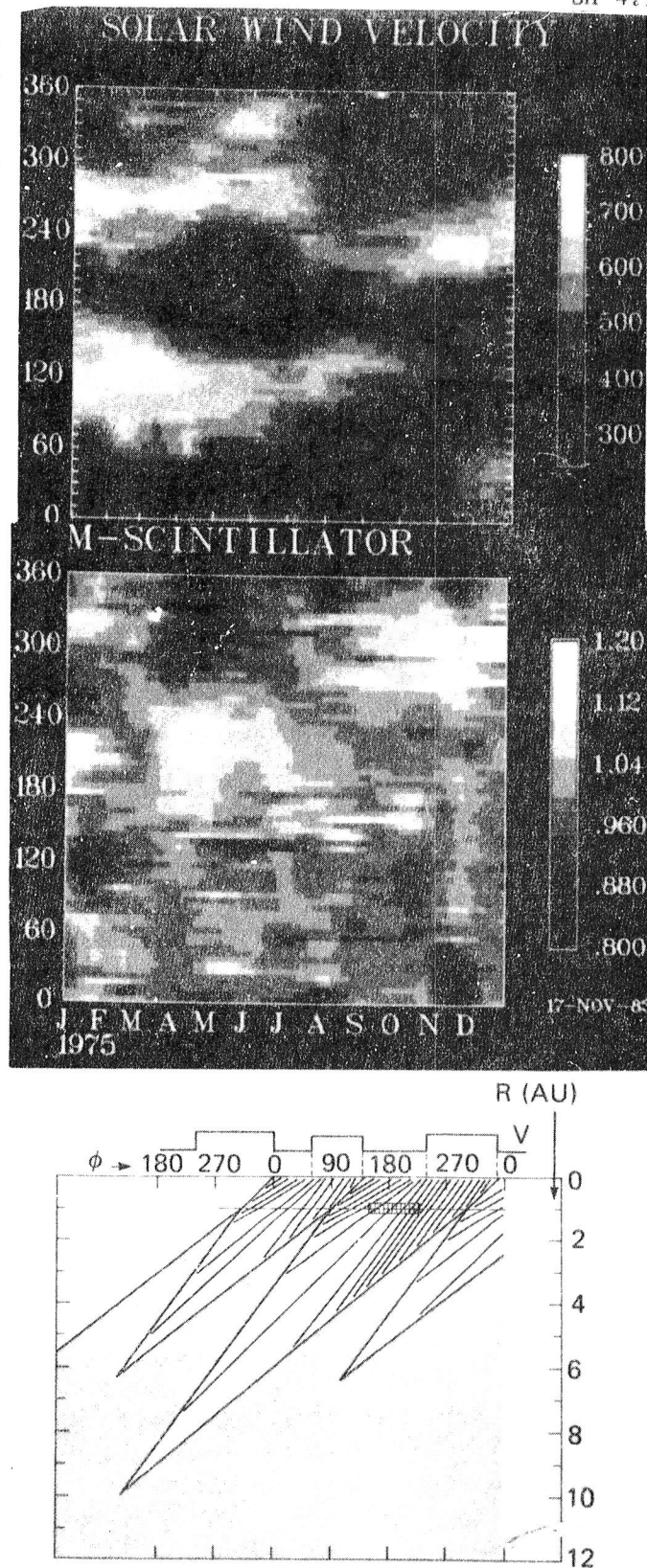
#### References

1. Mathews, T., J. J. Quenby and J. Sear, (1971), Nature, 229, 246.
2. Hedgecock, P. C., J. J. Quenby and S. Webb, (1972), Nature Physical Science, 240, 173.
3. Intrilligator, D. S., (1975), Proc. of the 14th International Cosmic Ray Conference, Munich, 3, 1033.
4. Barichello, J. C., (1978), M. Sc. Thesis, University of Calgary.
5. Synder, C. W. and M. Neugebauer, (1966), Solar Wind, Pergamon, New York.
6. Nolte, J. T. and E. C. Roelof, (1973), Solar Phys., 33, 241.
7. Krimigis, S. M., T. P. Armstrong and J. W. Kohl, (1973), Proc. Int. Conf. Cosmic Rays, 13th, 2, 1656.
8. Roelof, E. C., (1985), Proc. Int. Conf. Cosmic Rays, 19th, Paper SH 4.1-21.

Fig. 1. Solar wind velocity during 1975 expressed as a grey shade from 250-800 km/sec. The data are plotted at the heliographic longitude of the foot point of the field line on which they were observed and at their emission time from the sun.

Fig. 2. Cosmic ray intensity ( $> 35$  MeV) from the M scintillator channel of the CPME experiment on IMP-8. The data are plotted at the same coordinates as the solar wind velocity observed at the same time. Intensity is expressed as a ratio to the average over all longitudes for the corresponding emission time. Thus any vertical stripe in the figure will average to unity.

Fig. 3. A radius-longitude plot of the solar wind streams during May 1974. The line at the top is the approximate velocity profile at the sun that would produce the observed speeds at 1 AU. The field lines are extrapolated from the observed solar wind speeds at 1 AU. The shaded area is CIR. The CIR boundaries are reconstructed from Pioneer 11 and near-earth data. The cross-hatched area at 1 AU near  $180^\circ$  shows the region of enhanced cosmic ray intensity.





## THE 1973-1984 SOLAR MODULATION OF COSMIC RAY NUCLEI

M. Garcia-Munoz, K.R. Pyle and J.A. Simpson<sup>\*</sup>  
 Enrico Fermi Institute, University of Chicago  
 Chicago, IL, USA

**ABSTRACT.** As a continuation of our program of solar modulation studies we have carried out new measurements, with the University of Chicago cosmic ray telescope on the Earth satellite IMP-8, of the intensity time variations and the energy spectra of galactic cosmic ray protons, helium, carbon and oxygen from 1980 through 1984 including the recent solar maximum. In order to test the applicability of a steady state model of solar modulation during a period which includes times of rapidly changing modulation, we have compared these fluxes with the predictions of a conventional model of solar modulation which assumes equilibrium between modulation mechanisms. It is found that for a reasonable range of variations of the diffusion coefficient the model predictions can be made to agree with the measurements at essentially all times during the studied period. The model can account also for the observed hysteresis effects between cosmic rays of different rigidities.

1. Introduction. It has been observed that during the recent solar maximum the decreases and increases in cosmic ray intensity due to modulation level variations propagate outward from the Sun at approximately the solar wind velocity. (McDonald et al., 1981; McKibben, Pyle, and Simpson, 1982, 1985; Fillius and Axford, 1985). This fact together with the evidence that the radius of the modulation region is certainly greater than 30 A.U. and possibly as large as 50 to 150 A.U. implies that it takes to the disturbances responsible for these variations a time of the order of one year or more for propagation to the outer limits of the heliosphere. Therefore, at times of rapidly changing modulation, the modulation mechanisms may not be in equilibrium.

This work is a study of the modulation of cosmic ray nuclei in a time interval from 1973 through 1984, including the recent solar maximum. Measurements of the intensity time variations and differential energy spectra during this period are interpreted in the frame of a conventional model of solar modulation which assumes steady state (i.e. equilibrium) and absence of drifts. By using empirical diffusion coefficients and their time variations it is found that the model can reproduce at 1 A.U. the main features of time intensity variations and differential energy spectra of cosmic ray nuclei through the entire solar modulation cycle.

2. The Modulation Model. The model is described in Evenson et al. (1983). In it the solar wind velocity,  $V$ , is constant, and equal to 400 km/sec, and the diffusion coefficient is given by

$$k = \beta p^\alpha k(r); \quad k(r) = k_0 \exp [(r-1)/29] \quad (1)$$

---

<sup>\*</sup>and Department of Physics

where  $P$  is particle magnetic rigidity,  $r$  distance from the Sun in A.U.,  $\beta$  particle velocity in units of velocity of light and  $k$  and  $\alpha$  are functions of rigidity and time. It is assumed that the local interstellar electron differential spectrum is as deduced from

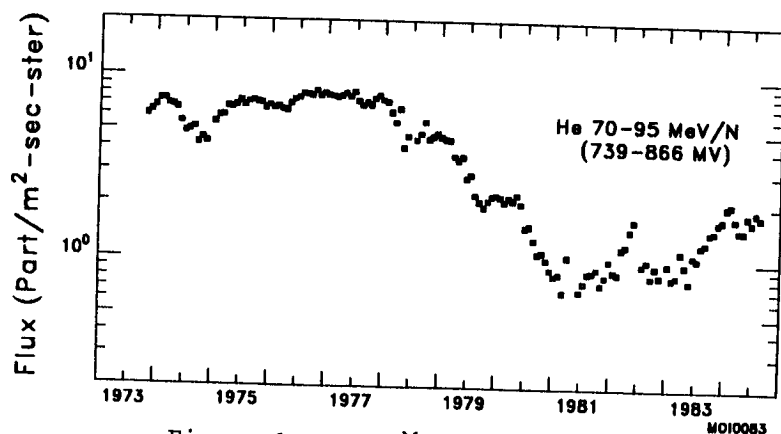


Figure 1

synchrotron radiation by Cummings *et al.* (1973). Comparison with measured differential nuclear and electron spectra at 1 A.U. during solar minimum leads to the local interstellar nuclear spectra. In this model the depth of modulation at a point  $r$  is given, for a heliosphere of radius  $R$ , by the force-field parameter, or modulation parameter

$$\phi(r) = \frac{1}{3} \int_r^R \frac{v}{k(r)} dr \quad (2)$$

and thus it is independent of the specific functional form of  $k(r)$ . Therefore, other  $k(r)$  functions different from the one selected in (1) could lead also to the same modulation depth.

Perko and Fisk (1983) have developed a time-dependent model of solar modulation in which the parameter varying with time is the frequency of outward propagating depressions in  $k(r)$  which simulate zones of increased scattering associated with solar flare shocks. In our calculations of cosmic ray intensities at 1 AU,  $k(r)$  appears only in integral form in the determination of the modulation depth  $\phi$ .

**3. Measurements and Calculations.** Figure 1 shows the time dependence from 1973 through 1984 of the 70-95 MeV/n  $^4\text{He}$  flux measured at 1 A.U., averaged in solar rotation intervals. The data are from the University of Chicago instrument onboard the IMP 8 spacecraft. Note that the 70-95 MeV/n  $^4\text{He}$  flux does not contain anomalous helium, even at times of solar minimum. The anomalous helium, when present, extends below about 60

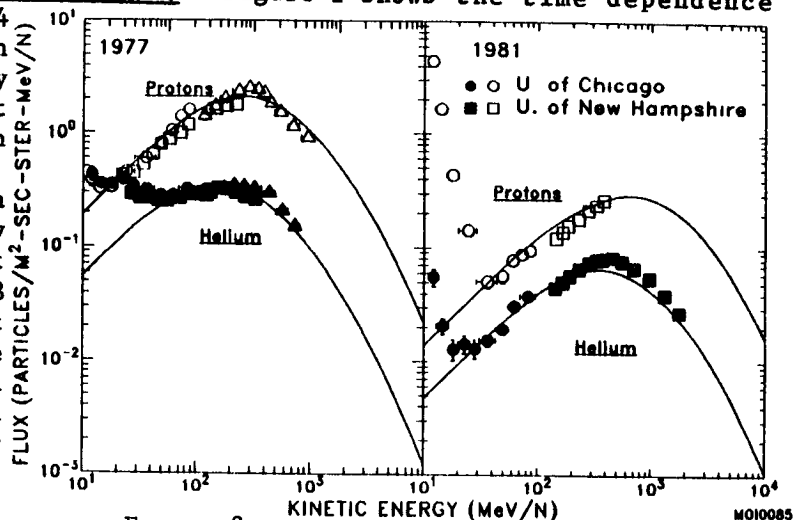


Figure 2

MeV/n. We have continued measuring the differential energy spectra of 10-95 MeV/n protons and helium from 1980 through 1984, adding to our previous measurements which extended up to 1979 (Evenson *et al.*, 1983). Figure 2 shows the 1977 differential energy spectra at solar minimum, as reported by Evenson *et al.* (1983), and the 1981 spectra at solar maximum, where we have added the University of New Hampshire data (Webber *et al.*, 1983). The curves in the figure are the fluxes predicted by the modulation model. Spectral measurements and theoretical fits have been obtained in this way from 1977 through 1984. The corresponding diffusion coefficients from solar minimum 1977 through solar maximum 1981, as the adjustable parameters, are shown in Figure 3. Each of these diffusion coefficients corresponds to a modulation depth  $\phi$  and gives a modulated helium spectrum with a value for the 70-95 MeV/n helium flux. Therefore, there is a one-to-one relationship between  $\phi$  and the 70-95 MeV/n helium flux.

The next step is to use this relationship and use as input the 70-95 MeV/n He flux, from 1973 through 1984, in order to deduce the model predictions of the fluxes of protons, carbon, and oxygen cosmic rays in other energy (rigidity) intervals through the same period and compare these predictions with the IMP 8 measurements. Figure 4 shows, for the 1973-1984 time interval, the comparison of model predictions (histograms) and measurements (data points) for 63-95 MeV/n protons, 45-178 MeV/n carbon and 53-211 MeV/n oxygen. It can be seen that in general there is good agreement between model and measurements. The larger disagreements can be immediately traced to the very well known phenomenon of hysteresis (Cooper and Simpson, 1979) by which higher rigidities

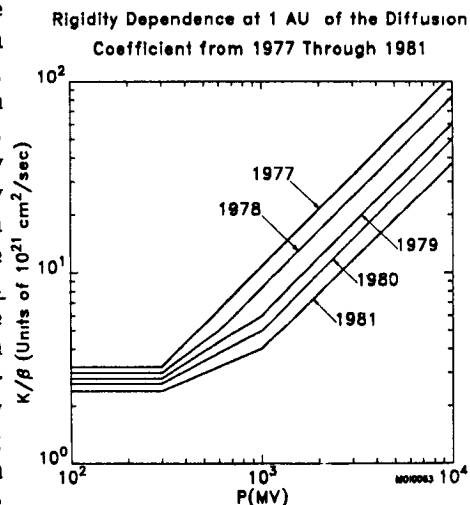


Figure 3

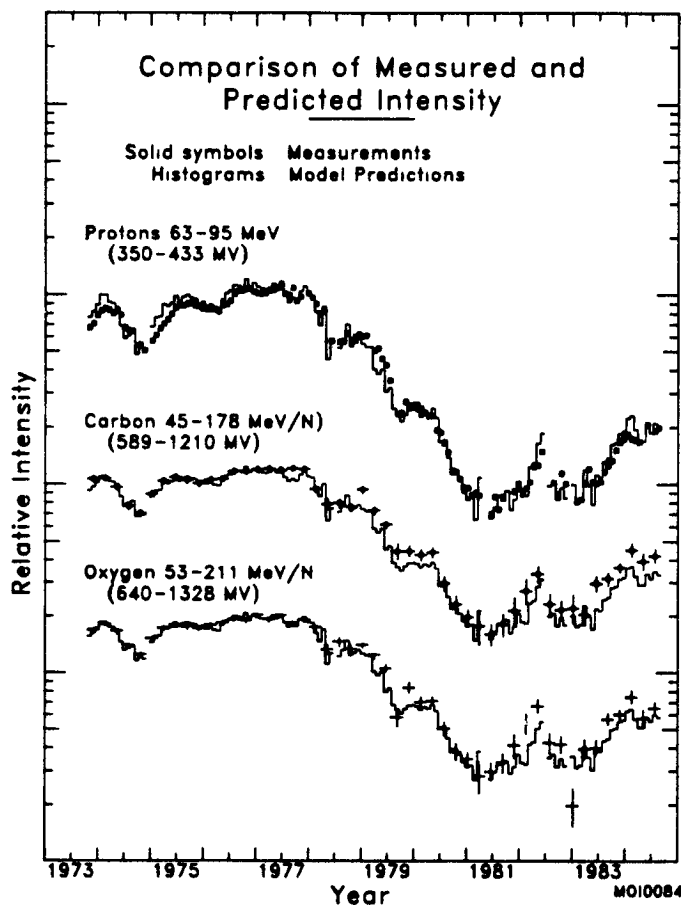


Figure 4

recover faster than lower rigidities as can be seen clearly in Figure 4 during the recoveries of the years 1982 and 1984. However, hysteresis can be easily incorporated in our simplified model by raising the high rigidity part of the diffusion coefficient relative to the low rigidities during the recovery phase. In this way a good fit to the 1983 and 1984 spectra is obtained, as is shown, for the particular case of protons and helium, in Figure 5.

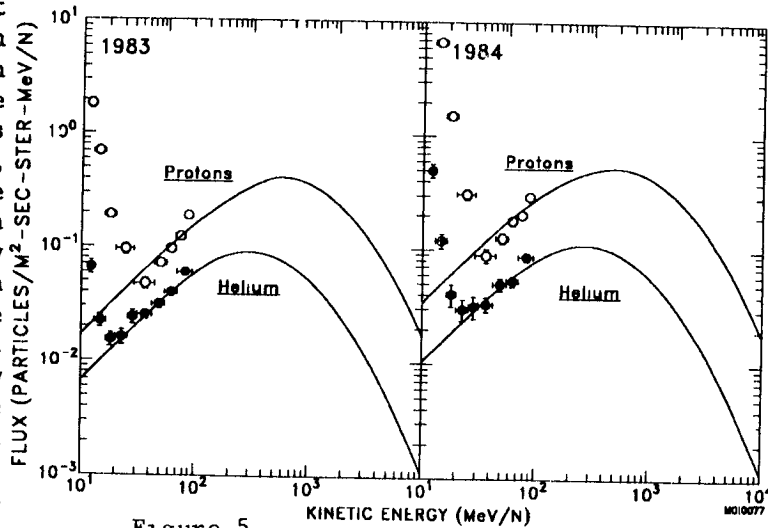


Figure 5

4. **Conclusions.** Empirical diffusion coefficients can be obtained by assuming at all times steady state in the heliosphere and fitting simultaneously the differential energy spectra of protons and helium at 1 AU in successive years from solar minimum 1977 through solar maximum 1981. These diffusion coefficients define a simple relationship between 70-95 MeV/n helium flux and depth of modulation. This relationship can be used to predict the main features at 1 AU of the intensity time dependence of other cosmic ray nucleons in different rigidity intervals from 1973 through 1984. The hysteresis effects can be accounted for by modification of the diffusion coefficients in selected rigidity intervals.

5. **Acknowledgements.** We thank James Beatty for data analysis and Scott Marusak for assisting in the preparation of the data. This research was supported in part by NASA Grant NGL 14-001-006 and NASA Contract NAS 5-28442.

#### References

- Cummings, A.C., Stone, E.C., and Vogt, R.E. 1973., Proc. 13th Int. Cosmic Ray Conf. (Denver), 1, 335.
- Cooper, J.F. and Simpson, J.A. 1979, Proc. 16th Intl. Cosmic Ray Conf. (Kyoto) 12, 176.
- Evenson, P., Garcia-Munoz, M., Meyer, P., Pyle, K.R. and Simpson, J.A., 1983, Ap. J. Letters, 275, L15
- Fillius, W. and Axford, I. 1985, J. Geophys. Res., 90, 517
- McDonald, F.B., Lal, N., Trainor, J.H., Van Hollebeke, M.A.I, and Webber, W.R., 1981, Ap. J. Letters, 249, L71
- McKibben, R.B., Pyle, K.R., and Simpson, J.A., 1982, Ap. J. Letters, L23, 1985, This conference, Paper SH 4.7-7.
- Perko, J.S. and Fisk, L.A. 1983, J. Geophys. Res., 88, 9033
- Webber, W.R., Kish, J.C. and Schrier, D.A. 1983, Proc. 18th Int. Cosmic Ray Conf. (Bangalore), 3, 35

# COSMIC RAY MODULATION IN A RANDOM ANISOTROPIC MAGNETIC FIELD

L.I.Dorman

Institute of Terrestrial Magnetism, Ionosphere and Radio Wave Propagation of the USSR Academy of Sciences, 142092 Troitsk, Moscow Region, USSR

Yu.I.Fedorov, M.I.Katz, S.F.Nosov, B.A.Shakhov

The Astronomical Observatory of the Ukrainian Academy of Sciences, 252127, Kiev, Goloseevo

Inhomogeneities of the interplanetary magnetic field can be divided into small-scale and large-scale ones<sup>1,2</sup>, as may be required by the character of the problem of cosmic ray (CR) propagation. CR propagation in stochastic magnetic fields is of diffusion character. The main contribution into the scattering of CR particles is made by their interaction with inhomogeneities of the magnetic field  $H(r,t)$  which have characteristic dimensions  $l$  of the order of Larmor radius  $R = cp/eH$  of particle ( $p$  is the absolute value of particle momentum,  $e$  is particle charge,  $c$  is velocity of light). Scattering of particles on such inhomogeneities leads to their diffusion mostly along a magnetic field with characteristic dimensions of variation in space exceeding the mean free path  $\lambda$  of particles before their scattering. In view of this fact the inhomogeneities of the interplanetary field can be divided into small-scale ( $l < \lambda$ ) and large-scale ( $l > \lambda$ ) ones, and the random magnetic field can be represented as a sum of the small-scale  $\mathcal{H}_1(r,t)$  and the large-scale  $\mathcal{H}_2(r,t)$  fields. The boundary value  $l_0$  of the inhomogeneities can be determined by several lengths  $\lambda$  of the mean free path of particles and  $l_0$  can be taken as the principal scale of the small-scale turbulence. The choice of the scale  $L_0$  of the large-scale turbulence depends on a concrete formulation of the problem.

It is necessary to divide a random field into small-scale and large-scale parts because one cannot describe the whole of the magnetic field turbulence spectrum on a single basis in terms of the local isotropy. As the scale of fluctuations increases, the statistic distribution of these fluctuations becomes, apparently, nonisotropic in space.

The diffusion coefficient along the large-scale field  $H$  for  $R \ll l_0$  can be written in the form<sup>2</sup>

$$D_{||} = \frac{v \lambda_{||}}{3}, \quad \lambda_{||} = \frac{v(v+2) \Gamma(\frac{v-1}{2})}{3 \sqrt{\pi} (v+1) \Gamma(v/2)} (cp/e)^{2-v} l_0^{v-1} \frac{\tilde{H}^v}{\langle \mathcal{H}_1^2 \rangle}; \quad v > 1 \quad (1)$$

where  $\tilde{H} = |\tilde{H}| = |\vec{H}_0 + \vec{\mathcal{H}}|$ ,  $H_0$  is a regular magnetic field,  $\nu$  is the index of the frequency spectrum of the small-scale turbulence,  $\Gamma(x)$  is gamma-function,  $V$  is particle velocity,  $\lambda_{||}$  is the mean free path of a particle along the field  $H$  before scattering.

The transport equation in the case of the field  $\tilde{H}$  has the form [2,3/

$$\frac{\partial N}{\partial t} = \nabla_{\alpha} \partial_{\alpha\lambda} \nabla_{\lambda} N - (\vec{u} \vec{\nabla}) N + (\vec{\nabla} \vec{u}) \frac{p}{3} \frac{\partial N}{\partial p} \quad (2)$$

where  $N(r, p, t)$  is CR particle concentration,  $u$  is solar wind velocity,  $\nabla_{\alpha} \equiv \partial / \partial r_{\alpha}$ ,  $\partial_{\alpha\lambda}$  is tensor diffusion coefficient which for a strong field  $\tilde{H}^2 \gg \langle \mathcal{H}_i^2 \rangle$ ,  $R \ll \lambda_{||}$ , can be written as

$$\partial_{\alpha\lambda} = \partial_{||} h_{\alpha} h_{\lambda} \quad (3)$$

where  $\vec{h} = \vec{\tilde{H}} / \tilde{H}$ . If the field  $\tilde{H}$  is represented by a sum of the random  $\vec{\mathcal{H}}$  and the regular  $\vec{H}_0$  fields, the expression (3) for  $\langle \mathcal{H}_i^2 \rangle \ll H_0^2$  can be rewritten as

$$\partial_{\alpha\lambda} = \partial_{||}^0 (n_{\alpha} n_{\lambda} + n_{\alpha} \mathcal{H}_{\lambda} H_0^{-1} + n_{\lambda} \mathcal{H}_{\alpha} H_0^{-1} + (\nu-2) n_{\alpha} n_{\lambda} \mathcal{H}_{\alpha} \mathcal{H}_{\lambda} H_0^{-2}) \quad (4)$$

where  $\vec{n} = \vec{H}_0 / H_0$ ,  $\partial_{||}^0 = \partial_{||} \tilde{H}^{\nu} / H_0^{\nu}$ .

The coefficient  $\partial_{\alpha\lambda}$  in (2) depends on the random field  $\vec{\mathcal{H}}(r, t)$  and, hence, the function  $N[\vec{\mathcal{H}}(r, t); (r, p, t)]$  itself is a functional of the random field, and if eq. (2) is averaged over a large-scale random field, we can use the standard averaging procedure [4/]. As a result, we are led to the following equation for the mean CR concentration  $\langle N \rangle$

$$\frac{\partial \langle N \rangle}{\partial t} = \nabla_{\alpha} \bar{\partial}_{\alpha\lambda} \nabla_{\lambda} \langle N \rangle - (\vec{u} \vec{\nabla}) \langle N \rangle + \frac{p}{3} \vec{\nabla} \vec{u} \frac{\partial \langle N \rangle}{\partial p}, \quad (5)$$

where

$$\begin{aligned} \bar{\partial}_{\alpha\lambda} &= \partial_{||} n_{\alpha} n_{\lambda} + \bar{\partial}_{\alpha\lambda}^{\perp} + \partial_{\alpha\lambda}^{\prime\prime\perp}, \\ \bar{\partial}_{||} &= \partial_{||}^0 \left\{ 1 + H_0^{-2} (\nu-1)^2 n_{\beta} n_{\gamma} \int d\vec{k} \mathcal{B}_{\beta\gamma}(\vec{k}) \right\}, \\ \bar{\partial}_{\alpha\lambda}^{\perp} &= \partial_{||}^0 H_0^{-2} \Delta_{\alpha\beta} \Delta_{\lambda\gamma} \int d\vec{k} \mathcal{B}_{\beta\gamma}(\vec{k}); \Delta_{\alpha\beta} = \delta_{\alpha\beta} - n_{\alpha} n_{\beta}, \end{aligned} \quad (6)$$

$$\bar{\partial}_{\alpha\lambda}^{\prime\prime\perp} = \partial_{||}^0 H_0^{-2} \Delta_{\alpha\beta} \Delta_{\lambda\gamma} \int d\vec{k} \mathcal{B}_{\beta\gamma}(\vec{k}); \Delta_{\alpha\beta} = \delta_{\alpha\beta} - n_{\alpha} n_{\beta}, \quad (7)$$

$$\overline{\mathcal{D}}_{\alpha\lambda}^{\prime\prime} = \mathcal{D}_{\parallel}^0 (\Delta_{\alpha\beta} n_{\beta} n_{\lambda} + \Delta_{\lambda\beta} n_{\beta} n_{\alpha}) \int d\vec{k} B_{\beta\gamma}(\vec{k}) \quad (8)$$

Here  $B_{\alpha\lambda}(\vec{k})$  is a Fourier-transform of the correlation tensor of a random magnetic field. When deriving (5), we used the hypothesis of frozen turbulence.

For an isotropic probability distribution of fluctuations of the field  $\mathcal{H}(\mathbf{r}, t)$  we have

$$\overline{\mathcal{D}}_{\parallel} = \mathcal{D}_{\parallel}^0 \left( 1 + \frac{(\nu-1)^2}{3} \frac{\langle \mathcal{H}^2 \rangle}{H_0^2} \right), \quad (9)$$

$$\overline{\mathcal{D}}_{\alpha\lambda}^{\perp} = \frac{1}{3} \mathcal{D}_{\parallel}^0 \frac{\langle \mathcal{H}^2 \rangle}{H_0^2} \Delta_{\alpha\lambda}, \quad \mathcal{D}_{\alpha\lambda}^{\prime\prime, \perp} = 0, \quad (10)$$

$$\langle \mathcal{H}^2 \rangle = 8\pi \int_{L_0} d\vec{k} k^2 B(k). \quad (11)$$

Here  $L_0$  is the maximum dimension of large-scale inhomogeneities.

The coefficient  $\mathcal{D}_{\alpha\lambda}^{\perp}$  describes particle transport across a regular magnetic field under the action of a large-scale random field. Its expression for the isotropic case agrees with the analogous expression obtained in the papers by Toptygin /2/ in the averaging of the kinetic equation for  $\mathcal{D}_{\parallel}^0 = \mathcal{D}_{\parallel}$ . In our case, however  $\mathcal{D}_{\parallel}$  depends on the random field  $\mathcal{H}$ , and to compare it with the value of  $\mathcal{D}_{\parallel}^0$  one should average  $\mathcal{D}_{\parallel}$  over an ensemble of a large-scale random field. As a result we have  $\langle \mathcal{D}_{\parallel} \rangle = \mathcal{D}_{\parallel}^0 (1 + \nu \langle \mathcal{H}^2 \rangle / H_0^2)$  ( $\nu = 1$ ). Such a renormalization of the diffusion coefficient will not affect noticeably the values of  $\mathcal{D}_{\alpha\lambda}^{\perp}$  and  $\mathcal{D}_{\alpha\lambda}^{\prime\prime, \perp}$  in which  $\mathcal{D}_{\parallel}^0$  is replaced by  $\langle \mathcal{D}_{\parallel} \rangle$  without an essential change in their values, but the coefficient of longitudinal diffusion changes the form. So, for the expression (9) we have

$$\overline{\mathcal{D}}_{\parallel} = \langle \mathcal{D}_{\parallel} \rangle \left\{ 1 - \frac{1}{3} \frac{\langle \mathcal{H}^2 \rangle}{H_0^2} (3\nu - (\nu-1)^2) \right\}, \quad (12)$$

from which one can conclude that an isotropic large-scale turbulence changes particle diffusion along the regular field if the spectrum of small-scale turbulence does not fall very rapidly, namely, if the index of the spectrum  $\nu$  is not larger than  $\nu \approx 4.8$ . Usually  $\nu = 1 - 2/2$ .

Large-scale turbulence of a magnetic field in interplanetary space is apparently anisotropic, i.e. spatial probability distribution of a random magnetic field has a distinguished direction  $\mathbf{e}$ . As working models of anisotropic tur-

bulence we take its two limiting cases: two-dimensional and one-dimensional fluctuation distribution. In the case of two-dimensional turbulence, the correlation tensor  $B_{\alpha\beta}$  will be written in the form

$$B_{\alpha\beta}^{\perp}(\vec{k}) = B^{\perp}(k_{\perp}^2) \left( \delta_{\alpha\beta} - \frac{k_{\alpha}^{\perp} k_{\beta}^{\perp}}{k_{\perp}^2} \right) \delta(k_{\parallel}); \quad (13)$$

and for the one-dimensional model we have

$$B_{\alpha\beta}^{\parallel}(\vec{k}) = B^{\parallel}(k_{\parallel}^2) \delta(k_{\perp}^2) (\delta_{\alpha\beta} - e_{\alpha} e_{\beta}); \quad k_{\parallel} = k \vec{e}, \quad k_{\perp} = |\vec{k} - k_{\parallel} \vec{e}| \quad (14)$$

where  $B^{\perp}$  and  $B^{\parallel}$  are corresponding spectral functions.

For two-dimensional turbulence with a distinguished direction  $\vec{e} \parallel \vec{n}$  the values of the diffusion coefficient are

$$\overline{D}_{\parallel} = \langle D_{\parallel} \rangle \left\{ 1 - \nu \frac{\langle \mathcal{H}_{\perp}^2 \rangle}{H_0^2} \right\}; \quad \overline{D}_{\alpha\beta}^{\perp} = \langle D_{\parallel} \rangle \frac{\langle \mathcal{H}_{\parallel}^2 \rangle}{H_0^2} \Delta_{\alpha\beta} \quad (15)$$

$$\overline{D}_{\alpha\beta}^{\parallel} = 0; \quad \langle \mathcal{H}_{\parallel}^2 \rangle = 2\pi \int_{L_0}^{\infty} dk_{\perp} k_{\perp} B^{\perp}(k_{\perp}^2)$$

$L_0$  is the principal scale of inhomogeneities in the direction transverse to  $H_0$ .

In the model of one-dimensional turbulence with a distinguished direction along the solar wind velocity,  $\vec{e} \parallel \vec{u}$ , we have

$$\overline{D}^{\parallel} = \langle D_{\parallel} \rangle \left\{ 1 - (\nu - 1) \frac{u_{\perp}^2}{u^2} \frac{\langle \mathcal{H}_{\perp}^2 \rangle}{H_0^2} \right\}; \quad \overline{D}_{\alpha\beta}^{\perp} = \langle D_{\parallel} \rangle \frac{\langle \mathcal{H}_{\perp}^2 \rangle}{H_0^2} \left\{ \frac{1}{3} \Delta_{\alpha\beta} - \frac{u_{\alpha}^{\perp} u_{\beta}^{\perp}}{u^2} \right\},$$

$$\overline{D}_{\alpha\beta}^{\parallel} = \langle D_{\parallel} \rangle \frac{\langle \mathcal{H}_{\perp}^2 \rangle}{H_0^2} (\nu - 1) \frac{u_{\parallel}}{u^2} (u_{\alpha}^{\perp} u_{\beta}^{\perp} + u_{\alpha} u_{\beta}^{\perp}); \quad \langle \mathcal{H}_{\perp}^2 \rangle = 2\pi \int_{(L_0^u)^{-1}}^{\infty} dk_{\parallel} B^{\parallel}(k_{\parallel}^2);$$

$$k_{\parallel} = (\vec{k} \vec{u}) / u,$$

where  $u_{\parallel}$  and  $u_{\perp}$  are a parallel and a perpendicular components of the solar wind velocity vector relative to the regular magnetic field direction,  $L_0^u$  is the principal scale of inhomogeneities along  $u$ . In this case the cross diffusion coefficient  $\overline{D}_{\alpha\beta}^{\perp}$  is nonzero, whereas in all the rest of the considered cases it is equal to zero. The latter model of large-scale turbulence is apparently a most realistic reflection of the situation in interplanetary space with fluctuations going radially from the Sun, with systems of discontinuities and waves following one another in the far regions of solar wind.

## REFERENCES

1. Toptygin I.N. Fast particles interaction with a magnetohydrodynamic turbulence. *Astrophys. Space Sci.*, vol.20, 1973, p. 329-350.
2. Toptygin I.N. Cosmic rays in interplanetary fields. M.: Nauka, 1983.
3. Dorman L.I. *Exper. and Theoret. bases of CR astroph.* M.: Nauka, 1971.
4. Rytov S.M., Kravtsov Yu.A., Tatarsky V.I. *Introduction to statistical radiophysics. P.2. Random Fields.* M.: Nauka, 1971.



EVIDENCE FOR REGIONS OF NEGLIGIBLE COSMIC-RAY MODULATION  
IN THE INNER HELIOSPHERE ( $< 10$  AU)

E. C. Roelof

The Johns Hopkins University, Applied Physics Laboratory  
Laurel, Maryland, 20707, U.S.A.

ABSTRACT

Gold and Venkatesan [1] report observations of periods during 1974-1976 when extended regions of heliolongitude that emitted lower-than-average solar wind velocities at 1 AU also exhibited higher-than-average cosmic-ray intensities as measured by the  $E > 35$  MeV CPME anti-coincidence scintillator ( $28 \text{ cm}^2$  omnidirectional geometric factor) on IMP-8. Their observations can be reproduced by a simple model, based on the observed steady solar wind structure, wherein there is little modulation of cosmic rays in the inner heliosphere until they reach the shocked plasma beyond the stream interactions in the outer heliosphere ( $\sim 5$ -10 AU). Beyond the interaction boundary, the intensity exhibits a constant radial gradient ( $\sim 2\%/ \text{AU}$ ). The model also offers an explanation for the irregular behavior of the rotation-averaged radial gradients observed by inside 10 AU, as well as the significant, but often ephemeral, latitude gradients observed by Voyagers 1 and 2 and IMP-8 [2].

1. Introduction. Gold and Venkatesan [1] present correlated IMP-8 observations of integral cosmic ray intensity ( $> 35$  MeV) and solar wind velocity during the previous minimum in solar activity (1974-6). The use of the anti-coincidence scintillator of the JHU/APL Charged Particle Measurements Experiment (CPME) as a cosmic ray detector was described in detail by Roelof, Decker and Krimigis [2]. They note that long-lived recurrent regions of enhanced cosmic ray intensity fall within recurrent regions of low speed solar wind (although they state that the converse is not necessarily so). They offer a qualitative explanation based on a sketch (reproduced here in Panel (b) of the Figure) of the quasi-stable solar wind structure deduced by extrapolating solar wind velocities outward with constant speed from IMP-8 and Pioneer-11, a technique observationally validated for this period in the study of Mitchell, Roelof and Wolfe [3]. The cosmic ray intensity enhancement of May 1974 occurred on extrapolated stream lines that intersected the furthest reaches of the "cavity" formed by the reverse shock of the preceding co-rotating interaction region (CIR) and the forward shock of the succeeding CIR. Gold and Venkatesan therefore suggest that the modulation is weaker in the "cavity" than in the shocked plasma beyond its boundary.

2. Analysis. Suppose the cosmic ray modulation beyond the cavities formed by the CIR's is described by a uniform radial gradient  $g$  ( $\%/ \text{AU}$ ) so that the intensity  $j$  may be written  $j = j_0 \exp (gr)$ . Here  $j_0$  would be the intensity at the sun if the modulation region extended uniformly inward to  $r = 0$ . However, we shall assume that  $g = 0$  inside the

SH 4.1-21

cavities; we could chose a small, but non-zero value of  $g$  inside the shocks, but the simplicity of the suggested model calls for a simple treatment. We assume that the cosmic ray populations are ordered along field lines in the inner heliosphere, as was demonstrated by the Voyager/IMP comparisons in 1977-8 [2]. In a steady solar wind structure, the large-scale interplanetary magnetic field lines follow the solar wind stream-lines, as viewed in a frame co-rotating with the sun. Then the intensity at the Earth when its heliolongitude is  $\phi$  should be the intensity at the cavity boundary where the solar wind stream, extrapolated outward from 1 AU, intersects the forward or reverse shock bounding a CIR. Call the helioradial distance of this intersection  $r_s(\phi)$ . Then the cosmic ray intensity at Earth at heliolongitude  $\phi$  is simply  $j(\phi) = j_0 \exp [r_s(\phi)]$ .

The calculation of  $r_s(\phi)$  is not difficult; the values could actually just be scaled off Panel (b) of the Figure. An extrapolated idealized field line has the equation  $r(\phi') = a + V(\phi) (\phi - \phi')/\Omega$ , where  $\phi$  is the heliolongitude of the line at 1 AU ( $r = a$ ),  $V(\phi)$  is the velocity there, and  $\Omega$  is the solar sidereal rotation rate. The CIR boundaries can be parametrized by a pseudo-field line with the velocities of the forward ( $V_F$ ) or reverse ( $V_R$ ) shock and the extrapolated crossings of those lines at 1 AU ( $\phi_F$  and  $\phi_R$ ). The lines in the rarefaction between high ( $V_H$ ) and low ( $V_L$ ) speed regions can be idealized as a "dwell" in which the lines appear to emanate from a single coronal longitude ( $\phi_0$ ):  $r(\phi') = a (\phi_0 - \phi')/(\phi_0 - \phi)$ . We compute  $r_s(\phi)$  for the four regions of the idealized stream structure shown in Panel (c) of the Figure: I,  $V(\phi) = V_H$ , intersection of high speed solar wind with reverse shock  $V = V_R$ ; II and III, rarefaction, as shown in Panel (b); and IV,  $V(\phi) = V_L$ , intersection of low speed solar wind with forward shock  $V = V_F$ . The resulting formulas are:

$$r_s(\phi) = a + (V_H V_R / \Omega) \frac{\phi_R - \phi}{V_H - V_R} \quad \text{Region I}$$

$$r_s(\phi) = a \frac{1 + (V_R / \Omega a)(\phi_R - \phi_0)}{1 - (V_R / \Omega a)(\phi_0 - \phi)} \quad \text{Region II}$$

The corresponding formulas for Regions III and IV are obtained by replacing  $V_R$  with  $V_F$ ,  $V_H$  with  $V_L$  and  $\phi_R$  with  $\phi_F$ . The result of the calculation is plotted in Panel (a) of the Figure with dashed lines indicating the regions where the over-simplification of the model is most extreme.

3. Comments. As could have been seen directly from Panel (b), the cosmic ray enhancement falls in the longitudes of high values of  $r_s(\phi)$  shown in Panel (a); not so evident in Panel (a) is the sharpness of the peak within the rarefaction region. Since  $d\phi/dt = -\Omega'$ , the synodic rotation rate, the  $r_s(\phi)$  plot is just a time plot running backwards (see lower scale). The intensity history, if treated as a fractional change, is  $\ln(j/j_1) = g(r_s - a)$  where  $j_1$  would be the minimum intensity predicted by the model. A peak radial distance of 9

SH 4.1-21

AU beyond the Earth with a radial gradient of 2%/AU would give a fractional enhancement of  $j/j_1 = 1.20$ . This is within the range of maximum/minimum intensities presented in Figure 2 of [1]; note that Figure 2 and Figure 3 of that paper are from different years. Also, the longitude used in Figure 2 of [1] is not the Earth heliolongitude used here, but rather the estimated source longitude of the observed solar wind stream. The latter longitude is inappropriate for galactic cosmic ray studies - for example, it would compress the entire rarefaction region of Panel (a), with its attendant intensity enhancements, into a single longitude on their plot. A more appropriate longitude for labelling field lines in the outer heliosphere is the heliolongitude of the innermost spacecraft being used, as was done here and was discussed in [2].

The exercise of this paper is intended mainly to illustrate the very plausible circumstance that cosmic ray modulation in the inner heliosphere ( $r \lesssim 10$  AU) may be quite variable (depending on stream structure evolution) with radial gradients much smaller than in the very different plasma/field regimes of the outer heliosphere. An extremely significant result from the VGR/IMP high time resolution (1 h) intensity comparisons [2] was that there were entire solar rotations devoid of significant gradients between 1 and 3-5 AU! Equally important were the ephemeral latitudinal gradients  $\sim 1\%/deg$  lasting  $\lesssim 1$  rotation (which would go essentially undetected if gradients are computed from 25-day averages as in other measurements done with less sensitive instruments). Our present study suggests an intriguing explanation for latitude gradients in the inner heliosphere. Suppose we compare intensities on two field lines passing through the same longitude ( $\phi$ ) at 1 AU, but at different latitudes ( $\theta$ ); this was the technique by which field-aligned latitudinal gradients were found in [2]. If the boundaries of the "cavity" were inclined to the solar equatorial plane owing to latitudinal shears described by terms like  $(\partial V/\partial \theta)$  or  $(\partial \phi_o/\partial \theta)$  in solar wind velocity structure, then we would have a latitudinal intensity gradient  $\partial(\ln j)/\partial \theta = g[(\partial r_s/\partial V_1)(\partial V_1/\partial \theta) + (\partial r_s/\partial \phi_k)(\partial \phi_k/\partial \theta)]$  where, for example,  $V_1 = V_H$ ,  $V_R$  and  $\phi_k = \phi_R$ ,  $\phi_o$ . A shear of  $\partial V/\partial \theta \approx (100 \text{ km/s})/(10 \text{ deg})$  is not unreasonable [3], and from Panel (a), we see that  $\partial r_s/\partial V \approx (5 \text{ AU})/(100 \text{ km/s})$  in the peak. Consequently, a latitudinal gradient  $\partial(\ln j)/\partial \theta \approx (2\%/AU)[(5 \text{ AU})/(100 \text{ km/s})][(100 \text{ km/s})/(10 \text{ deg})] = 1\%/deg$ , as observed [2], could be produced by shears in the stream/shock structure.

4. Acknowledgements. This work was encouraged by my valued colleagues R. E. Gold and D. Venkatesan, and supported in part by the Air Force Geophysics Laboratory under Task ZF10 of Contract N00024-85-C-5301 between The Johns Hopkins University and the Department of the Navy.

#### 5. References.

1. Gold, R. E., and D. Venkatesan, (1985), Proc. Int. Conf. Cosmic Rays, 19th, Paper SH 4.1-14.
2. Roelof, E. C., Decker, R. B. and S. M. Krimigis, (1983), J. Geophys. Res., **88**, 9889.

3. Mitchell, D. G., E. C. Roelof and J. H. Wolfe, (1981), J. Geophys. Res., 86, 165.

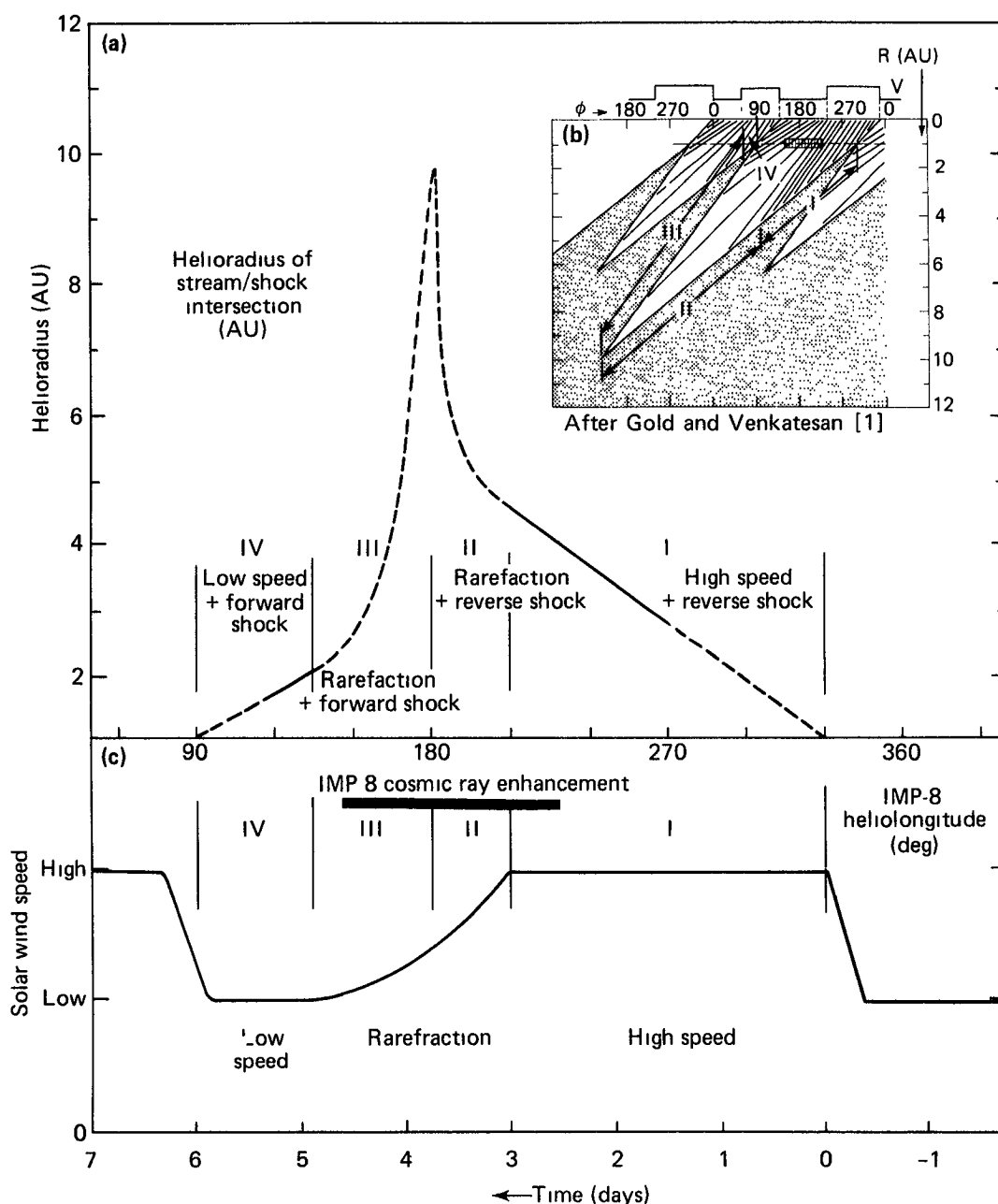


Figure: (a) Outer helioradius  $r_s(\phi)$  of intersection of interplanetary field lines from IMP-8 heliolongitude ( $\phi$ ) with "cavity" boundary formed by interacting CIR's sketched in (b), as proposed in [1], for the steady solar wind speed profile shown in (c). If there is no cosmic-ray radial gradient within the "cavity" and a constant radial gradient ( $g$ ) beyond it, the intensity profile at  $r = a = 1$  AU is  $j = j_1 \exp [gr_s(\phi) - a]$ .

## NOTES ON DRIFT THEORY

R.A. Burger, H. Moraal PU-CSIR Cosmic Ray Research Unit, Dept. of Physics,  
Potchefstroom University, Potchefstroom, 2520  
South Africa

G.M. Webb: Dept. of Planetary Sciences, Univ. of Arizona, AZ 85721, U.S.A.

## ABSTRACT

It is shown that there is a simpler way to derive the average guiding centre drift of a distribution of particles than via the so-called "single particle" analysis. Based on this derivation it is shown that the entire drift formalism can be considerably simplified, and that results for low order anisotropies are more generally valid than is usually appreciated. This drift analysis leads to a natural alternative derivation of the drift velocity along a neutral sheet. Full derivations are given in Burger, Moraal and Webb (1985; referred to as BMW), of which copies will be available at the Conference.

1. Alternative Derivation of Drift Velocity. A particle at position  $\underline{x}$ , with momentum  $\underline{p}$ , velocity  $\underline{v}$ , in a magnetic field  $\underline{B}$  has a gyroradius  $\underline{R} = \underline{b} \times \underline{p}/q$ , where  $\underline{b} = \underline{B}/B^2$ . Its guiding centre is at  $\underline{x}_g \equiv \underline{x} - \underline{R}$ . Differentiation of  $\underline{x}_g$  w.r.t. time in the steady state ( $\partial/\partial t = 0$ ), with employment of the Lorentz force  $\underline{\dot{p}} = q(\underline{E} + \underline{v} \times \underline{B})$  then gives

$$\langle \underline{v}_g \rangle = \langle \underline{v}_{||} \rangle + \underline{E} \times \underline{b} + \langle \underline{p} \times (\underline{v} \cdot \underline{\nabla}) \underline{b} \rangle / q, \quad (1)$$

for the instantaneous, average drift velocity of particles inside a volume element  $d^3x$  around  $\underline{x}$ . For a particle distribution function  $F(\underline{x}, \underline{p}, t)$  with density  $N$ , this average is defined as

$$\langle \dots \rangle = (1/N) \int \dots F d^3p = (1/N) \int dpp^2 \int \dots F d\Omega, \quad (2a)$$

where  $d\Omega = \sin\theta d\theta d\phi$ . We shall also use differential (omnidirectional) averages in momentum space in the interval  $(p, p + dp)$  denoted by

$$\langle \dots \rangle_\Omega = \int \dots F d\Omega / \int F d\Omega \quad (2b)$$

In terms of directions in momentum space,  $\underline{p}$  may be written as

$$\underline{p} = p(\cos\theta \underline{e}_1 + \sin\theta \cos\phi \underline{e}_2 + \sin\theta \sin\phi \underline{e}_3), \quad (3)$$

with  $\theta$  the pitch and  $\phi$  the phase angle relative to  $\underline{B}$ . In index notation the last term of (1) is  $\epsilon_{ijk} \langle p_j v_k \rangle b_{k,\ell} / q$  and determination of  $\langle \underline{v}_g \rangle$  or  $\langle \underline{v}_g \rangle_\Omega$  only requires finding the components  $\langle p_j v_k \rangle$  of the  $\langle \underline{p} \underline{v} \rangle$  tensor, given a particular  $F$ . In BMW it is shown that the most complicated  $F$  which gives a tractable expression for  $\underline{v}_g$  is

$$F(\underline{x}, \underline{p}, t) = F_{00} + \{F_{10} \cos\theta + F_{11} \sin\theta \cos\phi + F_{1,-1} \sin\theta \sin\phi\} + \sum_{\ell=2}^{\infty} F_{\ell 0} P_\ell(\cos\theta), \quad (4)$$

where  $P_\ell$  are the Legendre polynomials. The  $\langle \underline{p} \underline{v} \rangle$  tensor is of the form:

$$\langle \underline{p} \underline{v} \rangle = \begin{bmatrix} \langle p_{||} v_{||} \rangle & 0 & 0 \\ 0 & \frac{1}{2} \langle p_{\perp} v_{\perp} \rangle & 0 \\ 0 & 0 & \frac{1}{2} \langle p_{\perp} v_{\perp} \rangle \end{bmatrix}, \quad \langle p_{||} v_{||} \rangle = \frac{1}{3} \langle p v (1 + \frac{2}{5} \frac{F_{20}}{F_{00}}) \rangle$$

$$\frac{1}{2} \langle p_{\perp} v_{\perp} \rangle = \langle p_2 v_2 \rangle = \langle p_3 v_3 \rangle$$

$$= \frac{1}{3} \langle p v (1 - \frac{1}{5} \frac{F_{20}}{F_{00}}) \rangle \quad (5)$$

For this form of  $F$ , the average drift velocity (1) becomes

$$\langle \underline{v}_g \rangle = \langle \underline{v}_{||} \rangle + \underline{E} \times \underline{b} + \frac{1}{q} \left[ \frac{1}{2} \langle p_{\perp} v_{\perp} \rangle \nabla \times \underline{b} + (\langle p_{||} v_{||} \rangle - \frac{1}{2} \langle p_{\perp} v_{\perp} \rangle) \frac{1}{B} (\nabla \times \frac{\underline{B}}{B})_{\perp} \right] \quad (6)$$

There are six noteworthy points about this seemingly familiar result: (i) It is the *instantaneous* average guiding centre velocity of particles in the volume element  $d^3x$  in terms of the fields  $\underline{E}$  and  $\underline{B}$  *inside*  $d^3x$ . The usual "single particle" derivations (e.g. Rossi and Olbert, 1970) give a similar result, but for the *time* (gyroperiod) averaged drift velocity in terms of the fields  $\underline{E}_g$  and  $\underline{B}_g$  *at the guiding centres*. (ii) Our analysis does not need the usual "single particle" condition that  $R \ll L$  (where  $L$  is the smallest scale length of variation of  $\underline{E}$  and  $\underline{B}$ ). But, this does not mean that (6) is valid for any ratio  $R/L$ , as is discussed in Section 3. (iii) The result (6) is usually interpreted to hold only for gyrotropic distributions, in which  $F_{||} = F_{||,1} = 0$  in (4), (e.g. Rossi and Olbert, 1970, Lee and Fisk, 1981). This too strict condition on  $F$  stems from imprudent mixing of the  $\langle \underline{p} \underline{v} \rangle$  tensor with the pressure tensor  $P = N(\langle p \underline{v} \rangle - \langle p \rangle \langle \underline{v} \rangle)$ . (iv) If  $F$  is of the simple form  $F = (1 + \cos \theta)^{\gamma}$ , the underlined term in (6) exceeds the first one in  $[\ ]$  only if  $\gamma \geq 3.56$ . This represents a much higher anisotropy than usually found in Astrophysical applications, because then fully 95% of the particles have pitch angles in the forward range  $0 < \theta < \pi/2$ . (v) For first order anisotropies,  $F_{\ell j}(\ell \geq 2) = 0$ , the exact guiding centre velocity is form (5):

$$\langle \underline{v}_g \rangle = \langle \underline{v}_{||} \rangle + \underline{E} \times \underline{b} + (P/qN) \nabla \times \underline{b} \quad (7a)$$

$$\text{or } \langle \underline{v}_g \rangle_{\Omega} = \langle \underline{v}_{||} \rangle_{\Omega} + \underline{E} \times \underline{b} + (pv/3q) \nabla \times \underline{b} \quad (7b)$$

where  $P = (N/3) \langle pv \rangle$  is the scalar pressure. Because of the error mentioned in (iii), this is usually quoted as an approximate result, strictly valid for isotropic distributions only. (vi) Since

$$\nabla \times \underline{b} = \frac{1}{B} \left[ \frac{\underline{B} \times \nabla B}{B^2} + \nabla \times \frac{\underline{B}}{B} \right], \quad (8)$$

the last term in (7) is the sum of the usual gradient and curvature drift.

2. Average Particle Velocity  $\langle \underline{v} \rangle$  and Nomenclature. From the first moment of the Vlasov Equation  $\partial F / \partial t + \underline{v} \cdot \nabla F + \underline{p} \cdot \nabla_p F = 0$ , it is readily shown that in the steady state the average particle velocity for a distribution of the form (4) is

$$\langle \underline{v} \rangle = \langle \underline{v}_{||} \rangle + \underline{E} \times \underline{b} + \frac{1}{q} \left[ \frac{b}{N} \nabla (N \langle \frac{1}{2} p_{\perp} v_{\perp} \rangle) + (\langle p_{||} v_{||} \rangle - \frac{1}{2} \langle p_{\perp} v_{\perp} \rangle) \frac{1}{B} (\nabla \times \frac{\underline{B}}{B})_{\perp} \right] \quad (9)$$

The underlined term is identical to the one in (6). For first order anisotropies this reduces to the well-known form

$$\langle \underline{v} \rangle = \langle \underline{v}_{||} \rangle + \underline{E} \times \underline{b} + 1/(qN) \underline{b} \times \nabla P, \quad (10a)$$

or in the differential case

$$\langle \underline{v} \rangle_{\Omega} = \langle \underline{v}_{||} \rangle_{\Omega} + C \underline{E} \times \underline{b} + pv/(3qU) \underline{b} \times \nabla U \quad (10b)$$

where  $U = p^2(1/4\pi)/Fd\Omega$  is the differential number density in  $(p, p+dp)$ , and  $C = 1 - (1/3U) \partial / \partial p (pU)$  the Compton-Getting factor. The results (10) are standard in cosmic ray literature.

From the definition  $\underline{x}_g = \underline{x} - \underline{R}$  it follows that  $\langle \underline{v}_g \rangle = \langle \underline{v} \rangle - \langle d\underline{R}/dt \rangle$ . The average circulation velocity  $\langle d\underline{R}/dt \rangle$  is usually called the diamagnetic drift, and together with  $\langle \underline{v} \rangle$ , these two velocities are frequently referred to as *collective plasma drifts*. This is in opposition to the guiding centre drift which is called a "single particle drift". The average guiding centre drift seems equally collective to us. We also argue that the guiding centre drift is the *only* drift, because it is designed to tell you where the distribution goes after the troublesome, typically dominant circular motion of each particle has been subtracted.

In BMW these arguments are extended to the non-steady state ( $\partial/\partial t \neq 0$ ). After multiplication of all velocities with  $qN$  it is easily shown that for first order anisotropies

$$\underline{J} = \underline{J}_g + \underline{J}_b + \underline{J}_p = \underline{J}_g + \nabla \times \underline{M} + \partial \underline{\Pi} / \partial t, \quad (11)$$

where  $\underline{M} = -N \langle \underline{p} \cdot \underline{v} \rangle \underline{b}$  is the diamagnetic moment per unit volume and  $\underline{\Pi} = \underline{b} \times N \langle \underline{p} \rangle$  the polarisation vector of the plasma. The total plasma current density is therefore the sum of the guiding centre (or free) current density, the diamagnetic (or bound) current density and the polarisation current density. When standard "single particle" drift analyses are used, the equivalent result for (11) can only be written down readily for the perpendicular components (e.g. Parker, 1957). Northrop (1961, 1963) also included the parallel components but he needed the introduction of a distribution function  $F_g$  for guiding centres in addition to  $F$ , and elaborate algebra to do it. By contrast our result is essentially true per definition.

3. Neutral Sheet Drift. Standard drift theory breaks down at neutral sheets ( $B=0$ ) because the condition  $R/L \ll 1$  is violated. Our derivations are independent of this ratio but they still break down. The reason follows from Figure 1 which shows a field  $\underline{B} = B(x) \underline{e}_z$ , with  $B(x)$  homogeneous in  $x$ , and  $dB/dx$  any arbitrary large positive value. The drift of particles such as (a) and (b) is perfectly well described by the last term of (7), independent of the magnitude of  $dB/dx$ . However (8) shows that at  $x=0$ ,  $\underline{v} \times \underline{b} \rightarrow \infty$ , while Figure 1 suggests that individuals drift with finite velocity. Consequently  $\langle \underline{v}_g \rangle$  cannot be infinite (as it was used by Jokipii and Thomas (1981, and references therein)). The obvious reason for this breakdown is that the drift velocity at  $x=0$  depends on the phase angle at the point of crossing.

The drift in and around a neutral sheet is readily calculated if  $\underline{B}$  is given by  $B(x) = [2H(x) - 1] B_0 \underline{e}_z$ , where  $B_0$  is a constant and  $H$  the unit step function at  $x=0$ . Figure 2 shows the orbit of a particle with velocity  $\underline{v} = (v, \theta, \phi)$ , projected onto the plane  $\theta = \pi/2$ . It last crossed the sheet at point a under phase angle  $\phi_c$ , and will again do so at point b after having completed a projected arc length  $s = 2R_0(\pi - \phi_c) \sin \theta$ , where  $R_0 = p/(qB_0)$ . At that time the guiding centre abruptly jumps a distance  $\ell = 2R_0 \sin \theta \sin \phi_c$  in the direction of  $-\underline{e}_y$ . Therefore the component of the (time averaged) guiding centre velocity in the direction  $-\underline{e}_y$  may be taken as

$$v_{gy} = \ell / \Delta t = (\ell/s) v \sin \theta = [v / (\pi - \phi_c)] \sin \theta \sin \phi_c \quad (12)$$

From the relation  $\cos \phi_c = \cos \phi + x / (R_0 \sin \theta)$  it follows that of all the particles momentarily inside  $d^3x$ , at a distance  $x$  from the sheet, only those with

$$\theta_1 < \theta < \pi - \theta_1 \text{ and } \phi_1 < \phi < 2\pi - \phi_1, \text{ where } \sin \theta_1 = x / (2R_0) \text{ and } \cos \phi_1 = 1 - x / (R_0 \sin \theta) \quad (13)$$

can cross the sheet before completing a full orbit. Therefore the directionally averaged drift velocity over an isotropic particle distribution inside  $d^3x$  is

$$\langle \underline{v}_g \rangle_\Omega = -\underline{e}_y (v/4\pi) \int_{\theta_1}^{R-\theta_1} d\theta \sin^2 \theta \int_{\phi_1}^{2\pi-\phi_1} d\phi \sin \phi_c(\theta, \phi) / [\pi - \phi_c(\theta, \phi)] \quad (14)$$

The  $x$ -component of the drift velocity oscillates and does not contribute to the average, while the  $z$ -component of the average is zero for an isotropic distribution. The integral (14) can be evaluated as a series at  $x=0$  to give  $\langle \underline{v}_g \rangle = -0.463 \underline{e}_y$ , while its numerically calculated value in the range  $-2R_0 \leq x \leq 2R_0$  is shown in Figure 2.

This interpretation of guiding centre drift at a neutral sheet differs considerably from previous ones. Firstly, there is no sheet current density of the form  $\underline{J}(x) = J_0 \delta(x) \underline{e}_y$  as is sometimes suggested. In fact the assumed isotropy implies  $\underline{J} = 0$  everywhere, even in a volume element  $d^3x$  at  $x=0$ . Secondly, the distribution in the entire range  $-2R_0 < x < 2R_0$  progresses (drifts) in the direction  $-\underline{e}_y$ , instead of the infinite sheet drift current  $\underline{J}_g = J_{g0} \delta(x) \underline{e}_y$  derived by Jokipii *et al.* (1977) from the  $\nabla \times B/B^2$  term in (F).

As an example we consider the motion of cosmic rays in the interplanetary magnetic field.

$$\underline{B} = B_0(r_0/r)^2 [\underline{e}_r - (\Omega r \sin \theta / V) \underline{e}_\phi] [1 - 2H(\theta - \pi/2)], \quad (15)$$

where  $\Omega$  is the angular velocity of the Sun,  $V$  is the radial solar wind velocity and the function  $(1-2H)$  models a flat neutral plane at  $\theta = \pi/2$ . The neutral sheet drift (14) will be experienced by cosmic ray particles within an angle  $\Delta\theta = 2R_0/r$  from the plane. If  $V = 400 \text{ kms}^{-1}$ ,  $\Omega = (2\pi/27) \text{ day}^{-1}$ ,  $r = 1 \text{ A.U.}$ , and  $B_0 = 5/\sqrt{2} \text{ nT}$  ( $|B| = 5 \text{ nT}$  at Earth), it is readily shown that

$$\Delta\theta \approx 0.72 (P/P_0) r (r^2 + r_0^2)^{-1/2} \text{ degrees}, \quad (16)$$

where  $P$  is particle rigidity with  $P_0 = 1 \text{ GV}$ . Typical cosmic ray protons with kinetic energy  $T = 250 \text{ MeV}$ ,  $P = 0.75 \text{ GV}$  are therefore convected along the neutral plane in a region with thickness  $2\Delta\theta \approx 1$  degree. This neutral plane drift effect is not included in existing drift models of cosmic ray modulation. Jokipii and Thomas (1981, and references therein) used the  $\delta$ -function type drift velocity at the neutral plane, derived from the  $\nabla \times \underline{B}/B^2$  term. Potgieter and Moraal (1985) used a finite neutral plane drift velocity pattern, similar to that of Figure 2, but not based on the fundamental arguments used here. In their model the angular region  $\Delta\theta$  in (16) could i.a. be varied in an empirical and unjustified way, and it is significant that cosmic ray observations were better explained with finite neutral plane drift in a region  $\Delta\theta \geq 1^\circ$ , than with a  $\delta$ -function type drift at  $\theta = \pi/2$  only.

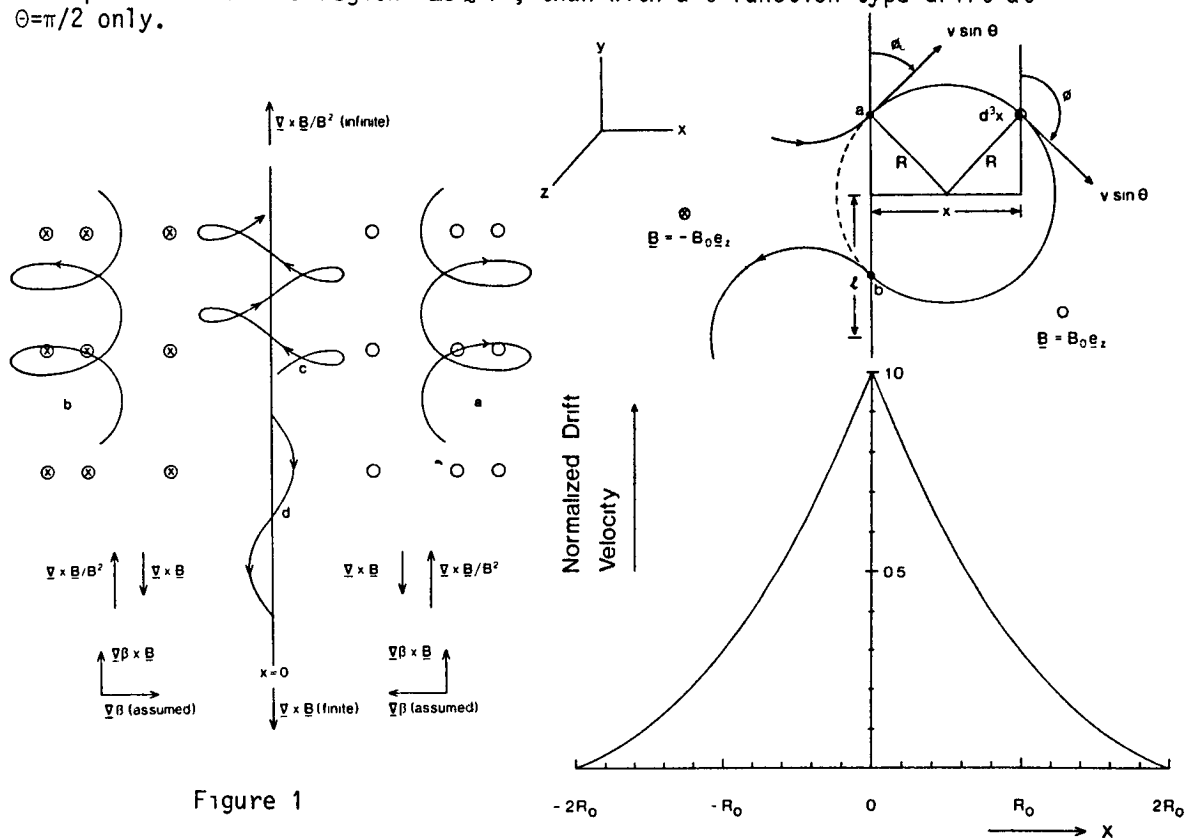


Figure 1

Figure 2

#### References

- Burger, R.A., Moraal, H., & Webb, G.M.: 1985, Preprint available at Conference.  
 Jokipii, J.R., Levy, E.H., & Hubbard, W.B.: 1977, *Ap. J.*, **213**, 861.  
 Jokipii, J.R., & Thomas, B.: 1981, *Ap. J.*, **243**, 1115.  
 Lee, M.A., & Fisk, L.: 1981, *Ap. J.*, **248**, 836.  
 Northrop, T.G.: 1961, *Ann. Phys.*, **15**, 79.  
 Northrop, T.G.: 1963, *Adiabatic Motion of Charged Particles*, Interscience, N.Y.  
 Parker, E.N.: 1957, *Phys. Rev.*, **107**, 924.  
 Potgieter, M.S., & Moraal, H.: 1985, *Ap. J.*, **294**, (July 15 issue).  
 Rossi, B., & Olbert, S.: 1970, *Intr. to the Phys. of Space*, Mc Graw-Hill, N.Y.



## DRIFT AND OBSERVATIONS IN COSMIC-RAY MODULATION. I.

M. S. Potgieter<sup>1</sup>Space Science Center, University of New Hampshire,  
Durham, NH 03824, USA1. Introduction

Gradient and curvature drift, which are explicitly contained in standard cosmic-ray transport theories, were neglected until the mid-1970's. It was then realized that the sector structure of the interplanetary magnetic field (IMF) observed in the ecliptic plane does not pervade the whole heliosphere (e.g., Smith et al., 1978), but has a topology corresponding closely to that of a dipole at the Sun. Since then, several drift models based on the numerical solution of the cosmic-ray transport equation were published (Jokipii and Kopriva, 1979; Kota and Jokipii, 1983, and references therein). These models, mostly concerned with proton modulation, illustrate the general features of drift and show that drift has a rather dominant effect on solutions over a wide range of parameters.

The independently developed drift model of Potgieter and Moraal (1983, 1985) in general confirms these results, according to which the four basic effects - convection, diffusion, drift and energy change - each contribute to the modulation of cosmic rays in the heliosphere. The relative importance of drift has, however, not yet been established. In order to do so, observational evidence of effects primarily dependent on drift are required.

The change in polarity of the large-scale IMF is of fundamental importance in drift models. A major implication of this reversal in polarity is that protons and electrons should, due to drift, exhibit different behavior during consecutive solar activity cycles. A charge-sign dependent effect should therefore be observable, the magnitude of which may indicate the relative contribution of drift to the modulation of cosmic rays.

In this paper we report on our investigation of this effect using observed solar minimum spectra (Webber et al., 1983) and on the change in phase and amplitude of the diurnal anisotropy observed after the IMF polarity reversals in 1969-71 and 1980 (Potgieter and Moraal, 1983).

2. Model Calculations

We solved the steady-state transport equation numerically assuming azimuthal symmetry. The solar wind is assumed to increase rapidly as a function of radial distance  $r$  to  $400 \text{ km s}^{-1}$  in a spherical heliosphere with an outer boundary at  $r_b = 50 \text{ AU}$ . The interstellar input spectra, boundary conditions, the spatial and energy dependence of the diffusion coefficients are given and motivated by Potgieter and Moraal (1985).

The IMF is assumed an Archimedean spiral with reversal of polarity across a flat neutral sheet. The reversal can be made either abrupt or smooth using a transition parameter  $\theta_{\perp} = 90^\circ$  and  $85^\circ < \theta_{\perp} < 90^\circ$  respectively. The drift velocity field calculated with  $\theta_{\perp} = 86^\circ$  is schematically presented for protons in Fig. 1.

<sup>1</sup> Also: Dept. of Physics, Potchefstroom University, South Africa

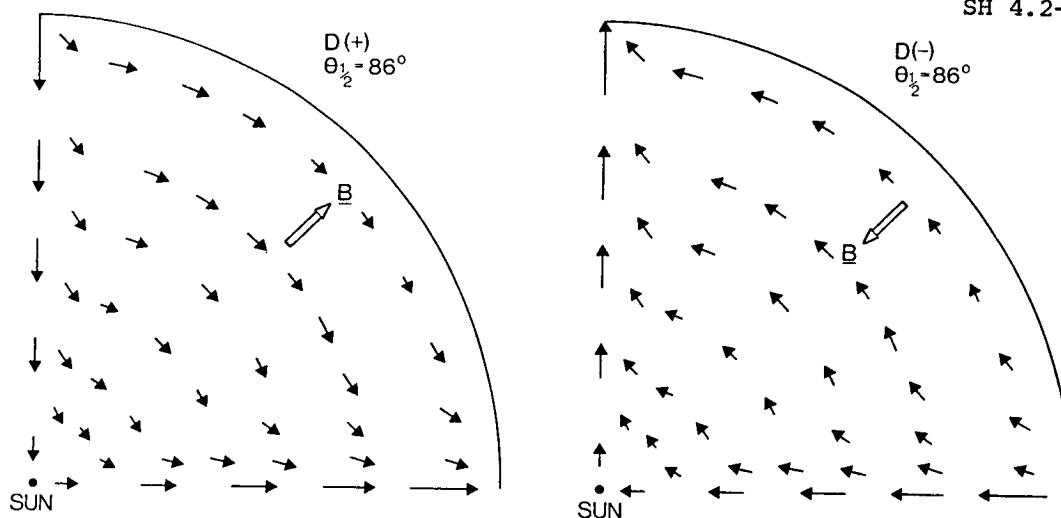


Fig. 1: Drift velocities for protons in the meridional plane with the transition parameter  $\theta_1 = 86^\circ$ . D(+):  $\sim 1970-1980$ . D(-):  $\sim 1959-1970$ ; 1980-1991. The drift velocities reverse direction for electrons.

According to Fig. 1 positively charged particles are transported from the polar regions to the inner heliosphere during the D(+) epoch (including 1976-77) but from the outer equatorial regions to the inner heliosphere during the D(-) epoch (including 1965). This effect is quantitatively illustrated in Fig. 2 of Part 2 (Paper SH4.2-5). In contrast with the no-drift case, protons and electrons reaching Earth should traverse different regions of the heliosphere during consecutive solar minimum periods, causing a charge-sign dependent effect.

### 3. Results and Discussion

No-drift models have become less successful to simultaneously fit proton and electron spectra observed before and after IMF polarity reversals, e.g., the 1965 and 1977 spectra (Evenson et al., 1983). This indicates that the detailed behavior of low energy electrons and protons cannot be fully understood within the framework of numerical solutions to the spherically symmetric transport equation (see e.g., Rockstroh, 1977).

Recently, Evenson and Meyer (1984) reported that although protons and electrons responded to the onset of less modulation in much the same way in 1981-82, there is a systematic difference between the two sets of data. The electrons recovered more rapidly than the protons and were not as strongly modulated with increased activity in late 1982. Moreover, this effect is totally different from that observed by Burger and Swanenburg (1973) in 1968-72 when the electron recovery lagged behind that of protons. Perko (1984) used a time-dependent spherically symmetric model, doing calculations for an entire solar cycle, to establish to what extent the difference in rigidity between the data sets of Evenson and Meyer could produce the observed hysteresis. He found that the hysteresis went in the sense of the Burger-Swanenburg data. No-drift models can therefore neither explain the observed effect nor the higher electron intensities, but lower proton intensities observed in 1965 compared to that observed in 1976-77.

Our model, based on the assumption of steady-state and a flat neutral sheet, is applicable only to periods of minimum solar activity. This is, however, also the time for the best ordered, large-scale IMF and the most likely period for drifts to occur. We therefore concentrated on a simultaneous fit to the observed 1965 and 1977 proton and electron spectra compiled by Evenson et al. (1983).

In contrast with the no-drift models, we could fit the mentioned spectra using one single set of modulation parameters, except for a change in the polarity of the IMF. Our result is best illustrated when compared to the ratio of the 1977 and 1965-66 data for protons and electrons respectively (Webber, et al., 1983). This is shown in Fig. 2.

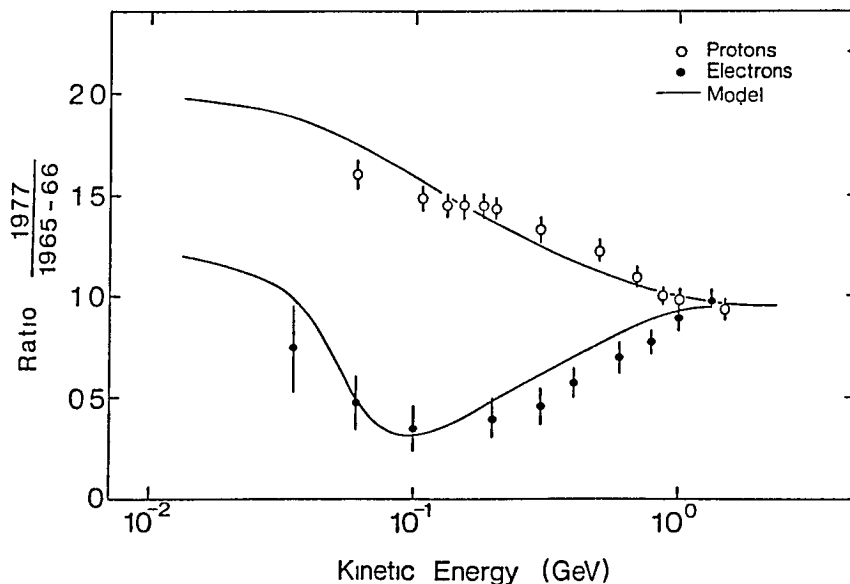


Fig. 2: Drift model calculations compared to proton and electron ratios for 1977 relative to 1965-66 (Webber, et al., 1983). The parameters used are given by Potgieter and Moraal (1985).

We want to emphasize that, other than perhaps less sophisticated equipment, there is no reason to doubt the validity of the 1965-66 electron data (Webber, private communication). We therefore interpret the result of Fig. 2 as a charge dependent effect due to drift, causing a factor of  $\sim 2$  difference at 500 MeV between consecutive solar minimum electron spectra.

An observation which is also unambiguously related to the reversal of the IMF polarity, is the shift in phase and amplitude of the diurnal anisotropy observed in 1969-71 and again in 1980-81 (Swinson, 1983). Fig. 3 shows, on a harmonic dial, the observed geomagnetically corrected anisotropy vector, calculated from the diurnal variation in the Hermanus neutron monitor (4.55 GV) counting rate. The vectors are averaged for 1964-66 and 1975-77; also for the entire period between polarity reversals, i.e., 1959-70 and 1971-79 respectively. These are compared to the calculated anisotropies at 1 GeV, using the same single set of modulation parameters used in Fig. 2. Our model is at least consistent with the observed shift in both phase and amplitude of the diurnal anisotropy following the 1969-71 polarity reversal, an effect which cannot be simulated by conventional spherically symmetric models.

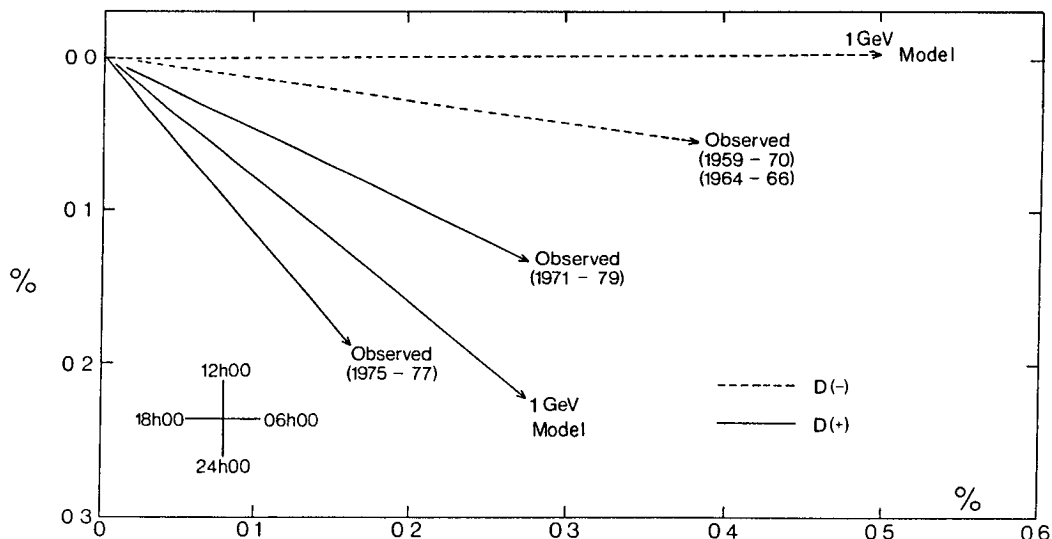


Fig. 3: The observed diurnal anisotropy (Hermanus, 4.55 GV), compared to the computed anisotropy vectors at 1 GeV. The observed values are averaged for the time periods indicated.

#### 4. Summary and Conclusions

We have illustrated that a relative simple drift model can, in contrast with no-drift models, simultaneously fit proton and electron spectra observed in 1965-66 and 1977, using a single set of modulation parameters except for a change in the IMF polarity. We interpret this result, together with the observation of Evenson and Meyer (1984) that electrons are recovering more rapidly than protons after 1980, in contrast with what Burger and Swanenburg (1973) observed in 1968-72, as a charge-sign dependent effect due to the occurrence of drift in cosmic-ray modulation. The same set of parameters produces a shift in the phase and amplitude of the diurnal anisotropy vector, consistent with observations in 1969-71 and 1980-81.

#### 5. Acknowledgements

This work was supported, in part, by the Space Science Center, University of New Hampshire and by the South African CSIR.

#### References

- Burger, J.J. and Swanenburg, B.N., 1973, *J. Geophys. Res.*, **78**, 292.  
 Evenson, P., et al., 1983, *Ap. J.*, **275**, L15.  
 Evenson, P., and Meyer, P., 1984, *J. Geophys. Res.*, **89**, 1647.  
 Jokipii, J.R., and Kopriva, D.A., 1979, *Ap. J.*, **234**, 384.  
 Kota, J., and Jokipii, J.R., 1983, *Ap. J.*, **265**, 573.  
 Perko, J.S., 1984, Ph.D. Thesis, Univ. of New Hampshire, Durham, NH.  
 Potgieter, M.S., and Moraal, H., 1983, 18th ICRC (Bangalore), **10**, 5.  
 Potgieter, M.S., and Moraal, H., 1985, *Ap. J.*, in press.  
 Rockstroh, J.M., 1977, Ph.D. Thesis, Univ. of New Hampshire, Durham, NH.  
 Smith, E.J., et al., 1978, *J. Geophys. Res.*, **83**, 717.  
 Swinson, D.B., 1983, Proc. 18th ICRC (Bangalore), **10**, 55.  
 Webber, W.R., et al., 1983, Proc. 18th ICRC (Bangalore), **3**, 35.

## DRIFT AND OBSERVATIONS IN COSMIC-RAY MODULATION. II.

M.S. Potgieter  
 Space Science Center, University of New Hampshire,  
 Durham, NH 03824 USA

1. Introduction

In Part 1 (SH4.2-4) we have quantitatively shown that our drift model can simultaneously fit the observed 1965-66 and 1977 electron and proton spectra, in contrast with spherically symmetric models. We interpret this result as evidence of a charge-sign dependent effect due to particle drift. Using the same set of parameters, we could also simulate a shift in the phase and amplitude of the diurnal variation in the cosmic-ray (CR) intensity by reversing the polarity of the interplanetary magnetic field (IMF).

In this paper, again using the same set of parameters, we show that drift can cause significant differences in the radial and latitudinal dependence of cosmic rays for consecutive solar minimum periods. We also searched the literature for additional modulation features related to the IMF polarity reversal and therefore relevant to determining the role of particle drift in the modulation of cosmic rays.

2. Model Calculations

Using the parameters of Part 1, we calculated the radial and latitudinal dependence of the 100 MeV proton intensity for two consecutive solar minimum periods. The radial dependence, with the radial gradient  $G_r$  in %/AU, is shown in Fig. 1a. The latitudinal dependence, with the latitudinal gradient  $G_\theta$  in %/degree, is shown for 1 AU and 20 AU in Fig. 1b and Fig. 1c respectively. For the D(+) period (1976),  $G_r$  remains almost constant for most of the heliosphere with a rapid increase near the boundary, and  $G_\theta$  almost identical at 1 AU and 20 AU. For the D(-) period (1965),  $G_r$  is overall larger and decreases toward the boundary, while  $G_\theta$  differs significantly for the two drift cases at 1 AU, and at 20 AU. (Note the difference in the intensity for the two drift solutions at 1 AU and 20 AU). The general behavior of the density gradients displayed in Fig. 1a-c is a feature of all drift models.

One of the best manifestations of the effect of drift becomes apparent when the transport equation is solved using  $\theta$ -(polar angle) dependent Gaussian spectra at the outer boundary instead of the full  $\theta$ -independent interstellar spectrum. By shifting these spectra (half-width of  $10^\circ$ ) consecutively in  $10^\circ$  intervals from the heliospheric poles to the equator, the results shown in Fig. 2 were obtained. Protons reaching Earth from a particular region on the outer boundary are expressed as percentage of those that would have reached Earth if a full interstellar spectrum was used. The calculations were repeated for increasing values of the parallel diffusion coefficient  $K_{||}$  with other parameters unchanged. Solution (b) in Fig. 2 corresponds to the solutions in Fig. 1a-c. (Note that  $(K_{||})_0$  is a constant in the expression for  $K_{||}$  given by Potgieter and Moraal, 1985). These results show, in contrast with the no-drift case, that drift causes positively charged particles reaching Earth to predominantly come from the outer

equatorial regions during a D(-) period (1965), but from the outer polar regions when the IMF changes polarity. A factor 3 increase in  $K_{II}$  extends this region to include mid-latitudes, while the situation remains virtually unchanged for the D(-) period. In general these calculations show that oppositely charged particles should traverse different regions of the heliosphere (Part 1). Another implication is that the (anti) correlation between variations in the CR intensity and solar activity parameters should exhibit a 22-year cycle.

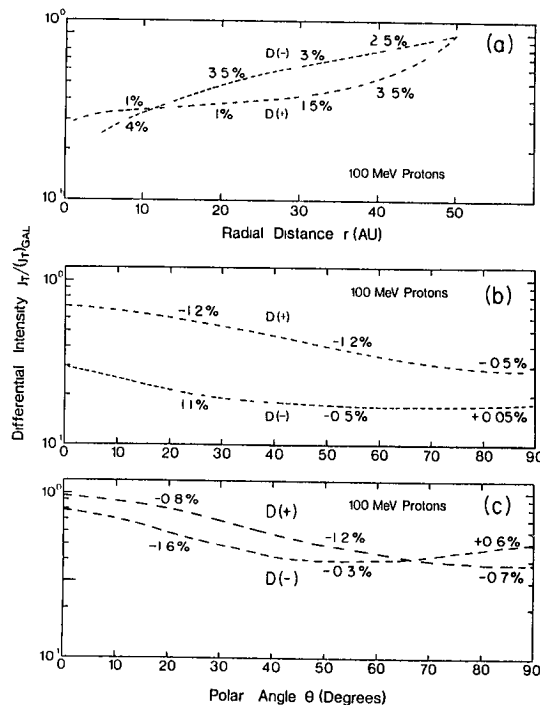


Fig. 1: (a) The radial dependence in the equatorial plane ( $\theta = 90^\circ$ ), (b) the latitudinal dependence at 1 AU and (c) at 20 AU, of the 100 MeV proton intensity. (The differential gradients are in %/AU; -latitudinal gradients are in %/degree).

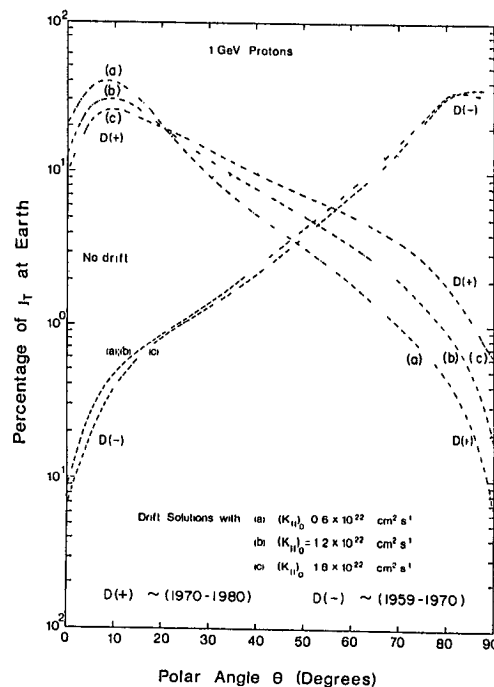


Fig. 2: The calculated percentage of 1 GeV protons reaching Earth from a particular region at the outer boundary for the two drift cases compared to the no-drift situation. The equatorial plane is at  $\theta = 90^\circ$ .

### 3. Discussion of Results and Observations

Fig. 1a-c show that drift can cause significant differences in the radial and latitude dependence of cosmic rays during consecutive solar minimum periods. Compared to our results, the observed integral latitudinal gradient (Decker et al., 1984) is as yet inconclusive about the role of drift. Jokipii (1984), however, by carefully simulating the exact observational conditions near the neutral sheet using a three-dimension drift model, found excellent agreement with the results of Newkirk and Fisk (1985), who studied the statistical dependence of CR intensity on the distance from the neutral sheet.

Less encouraging are observed integral radial gradients recently reported by Webber and Lockwood (1985) and McKibben et al. (1985). The radial gradient seems to decrease since 1981, which is not expected

from a drift point of view. It also appears that our model predicts the radial gradient too small for the 1976 solar minimum period. Since both the radial and latitudinal gradients are rather insensitive to parameter variations in drift models, these observations may become an interesting challenge to these models. It is also a complicating factor in explaining the role of drift concerning the anomalous components. However, the near constancy of the integral radial gradient observed before 1980, despite large changes in solar activity (Webber and Lockwood, 1985), is consistent with our model, but not with time-independent spherically symmetric models. In these models a direct relation exists for variations in  $K_p$  and the radial gradient.

Potgieter et al. (1980) calculated neutron monitor differential response functions from latitude survey data for 1954, 1965 and 1976, and found that the 1965 response function deviates significantly from those for 1954 and 1976. Using the parameters of Part 1, which fit the low-energy 1965-66 and 1977 proton and electron data, we could not simulate the observed large difference between the corresponding response functions, although we obtained a split in the right direction. The complicating factor here is that the low-energy proton fluxes were higher in 1976-77 than in 1965, while the neutron monitor counting rates were lower in 1976-77 compared to 1965.

Another relevant observation is the change in direction of the annual wave vector, derived from the yearly variations in CR intensity, in 1958-59 and again in 1968-69 (e.g., Antonucci et al., 1978; Nosaka, et al., 1984). Whether drift effects are the predominant cause of this observation, is not yet clear and has to await more detailed studies.

From 1972-77 the CR intensity was an extended, rather flat plateau preceded by a fast recovery over 2 years in 1970-72. (See the correlation study of Akasofu et al., 1985 regarding this period). During the 1965 solar minimum the intensity was peaked, preceded by an extended recovery period of  $\sim 7$  years. This behavior is consistent with the feature of drift models that the proton intensity is less sensitive to variation in modulation parameters during a D(+) cycle (1970-80) compared to the 11-years before and after this period (Jokipii and Thomas, 1981; Kota and Jokipii, 1983; Potgieter and Moraal, 1985).

Shea and Smart (1981) found a correlation coefficient of -0.86 between the geomagnetic aa-index - a measure of disturbance in the ecliptic plane - and the CR intensity for the years around 1965. For this period Aldagarova et al. (1979) found that the CR intensity correlates best to coronal green line (CGL) intensity in the  $-20^\circ$  to  $+20^\circ$  heliolatitude range. However, for the years around 1976, Shea and Smart found a correlation coefficient of +0.28 and Aldagarova et al. the best correlation for  $+30^\circ$  to  $+50^\circ$ , and to a lesser extent for  $-20^\circ$  to  $-30^\circ$  heliolatitude. In combination these observations indicate that during a D(+) cycle (1976), variations in the CR intensity correlate better with solar activity parameters in a much wider heliolatitude range compared to a D(-) period (1965) when cosmic rays are predominantly transported to the inner heliosphere via the equatorial regions. (See also Jokipii, 1981). The same conclusion can be reached from the observations of Nagashima and Morishita (1980), Pandey et al. (1983) and Vernov et al. (1983), despite different data and techniques used by them. These observations are consistent with our calculations shown in Fig. 2 and the drift velocities shown in Part 1.

#### 4. Summary and Conclusion

In Part 1 we discussed two key observations relevant to determining the relative importance of drift in cosmic-ray modulation. In the present paper, using the same set of parameters, we have illustrated the significant effect of drift on the radial and latitudinal dependence of cosmic rays for consecutive solar minimum periods. Compared with the integral radial gradient observed in 1976 (Webber and Lockwood, 1985), the calculated value seems too small. A detailed comparison will however have to await the forthcoming solar minimum. The same applies to the latitudinal gradient which is as yet inconclusive about drift effects.

Searching the literature for observations related to the IMF polarity reversal (in addition to Part 1), we found distinct difference in neutron monitor response functions for consecutive solar minimum periods, and also in the annual variations of cosmic rays observed before and after polarity reversals. Whether drift is the predominant effect is however not yet clear. We also found several reports which indicate better correlation between variations in the cosmic-ray intensity and solar activity parameters (e.g., the corona green line intensity) over a much wider range of heliolatitude during 1970-80 compared to before this period. These observations are consistent with drift models according to which cosmic ray protons primarily come via the polar regions during a D(+) period (1970-80), but primarily via the equatorial regions during D(-) periods. The observed peak vs. plateau in cosmic-ray intensity for the years around 1965 and 1976 respectively is also consistent with the general feature of drift models according to which the proton intensity is more sensitive to changes in modulation conditions during 1970-80 compared to before 1970.

#### 5. Acknowledgements

This work was supported in part by the South African CSIR and the Space Science Center, University of New Hampshire.

#### References

- Akasofu, S.I., et al., 1985, J. Geophys. Res., 90, 4439.
- Aldagarova, Kh.Z., et al., 1979, Proc. 16th ICRC (Kyoto), 3, 343.
- Antonucci, E., et al., 1978, Ap. J., 220, 712.
- Decker, R.B., et al., 1984, Ap. J., 278, L119.
- Jokipii, J.R., 1981, Geophys. Res. Lett., 8, 837.
- Jokipii, J.R., 1984, Proc. Int. Symp. C.R., Morioka, Japan.
- Jokipii, J.R., and Thomas, B., 1981, Ap. J., 243, 1115.
- Kota, J., and Jokipii, J.R., 1983, Ap. J., 265, 573.
- McKibben, R.B., et al., 1985, Ap. J., 289, L35.
- Nagashima, K., and Morishita, I., 1980, Planet. Space Sci., 28, 195.
- Newkirk, G., and Fisk, L.A., 1985, J. Geophys. Res., 90, 2391.
- Nosaka, T., et al., 1984, J. Geomagn. Geoelectr., 36, 73.
- Pandey, P.K., et al., 1983, Proc. 18th ICRC (Bangalore), 3, 91.
- Potgieter, M.S., et al., 1980, South Afr. J. Phys., 3, 90.
- Potgieter, M.S., and Moraal, H., 1985, Ap. J., in press.
- Shea, M.A., and Smart, D.F., 1981, Adv. Space Res., 1, 47.
- Vernov, S.N., et al., 1983, Proc. 18th ICRC (Bangalore), 3, 187.
- Webber, W.R., and Lockwood, J.A., 1985, Paper SH4.3-1, this conference.



## COSMIC RAY NORTH-SOUTH ANISOTROPY 1961-1983

J. W. Bieber and M. A. Pomerantz  
Bartol Research Foundation of The Franklin Institute  
University of Delaware, Newark, DE 19716  
USA

## ABSTRACT

Measurements from neutron monitors in Thule (Greenland) and McMurdo (Antarctica) have been used to determine yearly values of the cosmic ray north-south anisotropy over the period 1961-1983. The results strongly suggest that superposed upon the mean anisotropy of 0.05% is a solar cycle variation of amplitude 0.03%. No evidence for a dependence of the anisotropy upon polarity of the solar poloidal magnetic field is found.

1. Introduction. Detailed information on the spatial distribution of cosmic rays in the heliosphere is essential for testing theories of the solar cycle modulation of galactic cosmic rays. An invaluable tool for probing the spatial distribution is the steady-state north-south anisotropy of cosmic rays, which has been found to be intimately related to the cosmic ray radial gradient (Swinson, 1969; Bercovitch, 1970; Iucci and Storini, 1972; Yasue, 1980; Pomerantz et al., 1982). Most investigations of this effect, however, have been limited to intervals of a few years, or else have combined data from many years, such that yearly variations were not evident. As a result, possible solar cycle or solar polarity dependences of the north-south anisotropy, and hence of the radial gradient at  $> 1$  GV rigidities, are not well determined.

With the availability of neutron monitor data from north and south polar stations from 1961 to the present, an interval of more than 2 solar cycles, a comprehensive analysis of long-term changes in the north-south anisotropy is now feasible. The information gained through this analysis will provide important observational constraints that models of cosmic ray modulation must satisfy.

2. Results. Previous investigations of the steady-state north-south anisotropy have typically reported magnitudes  $\sim 0.1\%$  or less. In order to extract this exceedingly small signal from the neutron monitor data, the method of analysis was designed with these goals in mind: (1) to reduce the effect of unrelated cosmic ray variations of much larger amplitude, (2) to take into account possible systematic variations in the relative efficiencies of the north and south polar detectors, and (3) to obtain reliable error estimates, which are essential for proper interpretation of the results. In essence, the method involved calculating, separately for toward and away polarity of the interplanetary magnetic field, the ratio of counts recorded at Thule to counts

recorded at McMurdo. The anisotropy was calculated for each solar rotation period from these ratios and from the relative efficiency of the two detectors, which was also determined separately for each solar rotation period. Finally, a yearly average of the anisotropy and an error estimate were calculated from this set of solar rotation values.

Results of the analysis appear in Figure 1, where yearly averages of the north-south anisotropy  $\xi_{NS}$  are plotted with  $\pm 1\sigma$  error bars. By convention,  $\xi_{NS}$  is taken to be the value determined for toward sector polarity, with a positive value indicating that the observed cosmic ray intensity was larger at the north polar station than at the south polar station. With this convention, a positive value of  $\xi_{NS}$  is expected if the anisotropy arises from a positive radial gradient.

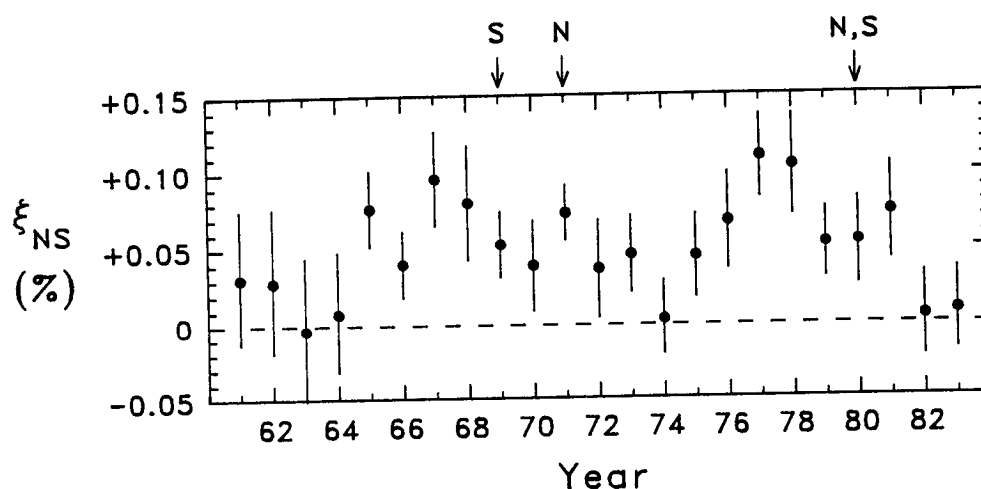


Fig. 1. Cosmic ray north-south anisotropy over a period of two solar cycles, as determined from neutron monitor observations at Thule and McMurdo. Arrows indicate years in which the sun's north (N) and/or south (S) pole changed magnetic polarity.

Note that there is no a priori reason that the method of analysis would preferentially yield positive values of anisotropy over negative ones. Thus, Figure 1 provides strong support for the interpretation that the steady-state north-south anisotropy results from a positive radial gradient via the  $\vec{B} \times \vec{v} \cdot \vec{n}$  drift, with most points indicating positive values of anisotropy that differ significantly from zero.

### 3. Discussion.

#### Solar Cycle Variation of $\xi_{NS}$ :

The value of the steady-state north-south anisotropy averaged over the 23-year period of this study is  $\xi_{NS} = 0.052\%$ . However, a possible solar cycle variation with period  $\sim 10$  years is strongly

suggested by Figure 1. To test this possibility quantitatively, the data of Figure 1 were assumed to be described by a constant plus a 10-year sinusoidal variation, with the phase and amplitude of the 10-year wave and the constant to be determined according to goodness-of-fit. The resulting constant term and wave amplitude were 0.053% and 0.028%, respectively, with the wave peaking in 1968 and 1978. Statistical tests indicate that there is only a 0.6% probability that a wave of this amplitude would occur by chance. Thus, a solar cycle variation of the cosmic ray north-south anisotropy is established with a high degree of confidence.

#### Effect of Drifts in Cosmic Ray Transport:

As illustrated in Figure 2, modulation models in which drifts play a predominant role predict that the radial profile of cosmic ray density will differ substantially between epochs of positive and negative polarity of the solar poloidal magnetic field (Jokipii and Kopriva, 1979). At a radial distance of 1 AU, the radial gradient -- i.e., the slope of the curves in Figure 2 -- is predicted to be substantially larger during epochs of negative solar polarity ( $A < 0$ ) than during epochs of positive solar polarity ( $A > 0$ ). This, in turn, would imply that the north-south anisotropy should show a corresponding dependence upon solar polarity.

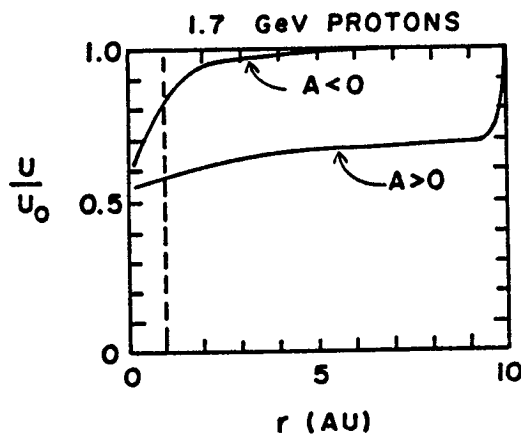


Fig. 2. Predicted relative intensity of cosmic rays as a function of radial distance ( $r$ ) from the sun. Adapted from Figures 8 and 9 of Jokipii and Kopriva (1979).

The data of Figure 1 are inconsistent with this theoretical expectation. The average value of  $\xi_{NS}$  for the period 1961-1968, an epoch of negative solar polarity, was found to be 0.053%. Similarly, the value for the period 1972-1979, an epoch of positive solar polarity, was found to be 0.055%. A solar polarity dependence of the north-south anisotropy is not evident.

## Cosmic Ray Radial Gradient:

The equations of cosmic ray transport permit information on the cosmic ray radial gradient to be inferred from a measurement of the north-south anisotropy. Since the relevant technique has been discussed by other investigators (e.g., Yasue, 1980), only results will be presented here. The average value of north-south anisotropy (0.053%) determined above corresponds to a radial gradient of 1.7%/AU at a rigidity of 10 GV, while the 10-year variation of the anisotropy suggests that the gradient actually oscillates between values  $\sim 0.8\%/AU$  and  $\sim 2.6\%/AU$ , the peaks occurring in 1968 and 1978. These inferred values of radial gradient appear to be generally consistent with recent spacecraft determinations of the integral radial gradient and its variation at lower energies (e.g., McKibben et al., 1985; Van Allen and Randall, 1985).

4. Acknowledgments. C. H. Tsao contributed significantly to the extensive computer analysis involved in this work. This research was supported by the National Science Foundation under grants ATM-8303758 and DPP-8300544.

References

- Bercovitch, M., (1970), Determination of the heliocentric cosmic ray density gradient using neutron monitor data, Acta Physica Academiae Scientiarum Hungaricae, 29, Suppl. 2, 169.
- Iucci, N., and M. Storini, (1972), The north-south anisotropy and the cosmic-ray radial gradient in the vicinity of the earth, Il Nuovo Cim., 10B, 325-333.
- Jokipii, J. R., and D. A. Kopriva, (1979), Effects of particle drift on the transport of cosmic rays. III. Numerical models of galactic cosmic-ray modulation, Astrophys. J., 234, 384-392.
- McKibben, R. B., K. R. Pyle, and J. A. Simpson, (1985), Changes in radial gradients of low-energy cosmic rays between solar minimum and maximum: Observations from 1 to 31 AU, Astrophys. J., 289, L35-L39.
- Pomerantz, M. A., S. P. Duggal, A. J. Owens, M. F. Tolba, and C. H. Tsao, (1982), Cosmic ray north-south anisotropy: The role of the interplanetary magnetic field, J. Geophys. Res., 87, 10325-10330.
- Swinson, D. B., (1969), 'Sidereal' cosmic-ray diurnal variations, J. Geophys. Res., 74, 5591-5598.
- Van Allen, J. A., and B. A. Randall, (1985), Interplanetary cosmic ray intensity: 1972-1984 and out to 32 AU, J. Geophys. Res., 90, 1399-1412.
- Yasue, S., (1980), North-south anisotropy and radial density gradient of galactic cosmic rays, J. Geomag. Geoelectr., 32, 617-635.

# NORTH-SOUTH ASYMMETRY IN ACTIVITY ON THE SUN AND COSMIC RAY DENSITY GRADIENTS

D.B. Swinson<sup>1</sup>, M.A. Shea<sup>2</sup>, and J.E. Humble<sup>3</sup>

<sup>1</sup> Department of Physics and Astronomy, The University of New Mexico, 800 Yale N.E., Albuquerque, New Mexico 87131.

<sup>2</sup> Air Force Geophysics Lab., Hanscom AFB, Bedford, MA 01731.

<sup>3</sup> Department of Physics, University of Tasmania, Hobart, Tasmania, Australia 7001.

**INTRODUCTION.** One method of detecting a perpendicular cosmic ray density gradient ( $\nabla N_p$ ) is to make use of the contribution of the drift term  $\vec{B} \times \nabla N_p$  to the solar cosmic ray diurnal variation. This method has been described by Swinson [1970, 1976] and by Hashim and Bercovitch [1972]. The  $\vec{B} \times \nabla N_p$  term produces a flow in the ecliptic plane perpendicular to the IMF  $\vec{B}$ , with the sense of the flow depending upon the sense of  $\vec{B}$ ; this field-dependent flow adds vectorially to the usual azimuthal streaming which produces a cosmic ray intensity maximum at 18 hours solar time (after correction for geomagnetic bending). In the case of a southward perpendicular gradient, when the IMF is away from the sun, the resultant diurnal variation should have a larger amplitude, and the time of maximum should occur a little earlier, whereas if the IMF is toward the sun, the resultant diurnal variation should have a smaller amplitude with a later time of maximum. Swinson and Kananen [1982] have used this method to analyze neutron monitor and underground muon data, separated according to IMF sense, from 1965 to 1975, to show that there is a perpendicular cosmic ray gradient that pointed southward prior to 1969, and a suggested northward pointing gradient after the reversal of the sun's polar magnetic field in 1969-71.

**DATA.** In this paper we will consider data from four underground cosmic ray telescopes, two in the northern and two in the southern hemisphere. The telescopes are Embudo Cave (35.20°N, threshold rigidity 19 GV, median rigidity 132 GV), Socorro (34.04°N, threshold rigidity 45 GV, median rigidity 305 GV), Bolivia (16.31°S, threshold rigidity 16 GV, median rigidity 125 GV) and Hobart, (42.85°S, threshold rigidity 30 GV, median rigidity 162 GV). The data presented are for the periods 1965-83, 1968-83, 1965-76 and 1965-83, respectively. The yearly average solar diurnal variation for each telescope has been determined for days when the IMF was toward (T) and away from (A) the sun. The amplitude data are presented (the A amplitude should exceed the T amplitude for a southward gradient).

In Figure 1 the annual A and T amplitudes for each station, for all available data, are plotted for 1965 to

1983. The A amplitude points are joined by solid lines and the T amplitude points by dashed lines; shading occurs when A amplitudes are greater than T amplitudes, indicating a southward perpendicular gradient. The vertical lines on the diagram indicate the end of the solar polar field reversals of 1969-71 and 1980-81. Prior to 1971 there is a consistent predominance of A amplitudes over T amplitudes in both hemispheres, which is consistent with a southward perpendicular gradient during this period. After 1971, the northern hemisphere telescopes (Embudo and Socorro) show some dominance of T-amplitudes, while the southern hemisphere telescopes (Bolivia and Hobart) show little change from the pre-reversal situation. The average annual errors for the amplitudes plotted in Figure 1 are  $\pm 0.14\%$  for Embudo,  $\pm 0.165\%$  for Socorro,  $\pm 0.16\%$  for Bolivia and  $\pm 0.125\%$  for Hobart.

In order to look for a possible cause for a perpendicular cosmic ray gradient we have examined data on the N-S asymmetry in activity on the sun. One might expect that when activity is greater on the sun's northern hemisphere, that activity might be more effective in sweeping cosmic rays out of the heliosphere above the ecliptic plane or in preventing galactic cosmic rays from entering, leading to a S-pointing perpendicular gradient. Here, we extend a study by Roy [1977], which used the "major" flares as defined by the comprehensive flare index, CFI, [Dodson and Hedeman, 1971] to show that between 1959 and 1970 there was a greater frequency of flares in the northern hemisphere of the sun than in the southern hemisphere; this northern hemisphere asymmetry was not evident from 1971 to 1974. This paper extends the results of Roy through 1980.

The number of flares in each hemisphere was counted as a function of month and year, using observations from the worldwide network of solar optical and radio patrol stations. From these data, an annual average for the per-

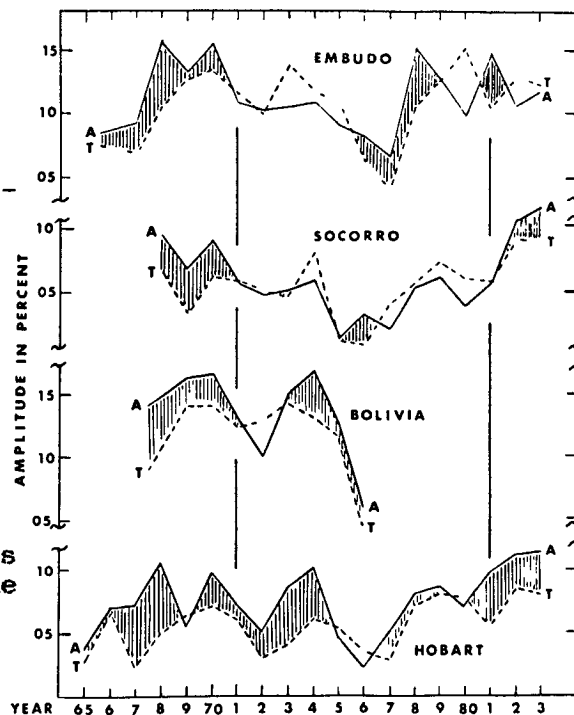


Figure 1. Yearly average amplitudes of away polarity days (solid line) and toward polarity days (dashed line) for underground muon telescopes in Embudo, Socorro, Bolivia, and Hobart, 1965-1983.

The shaded areas occur when the amplitude for the away polarity exceeds that for the toward polarity.

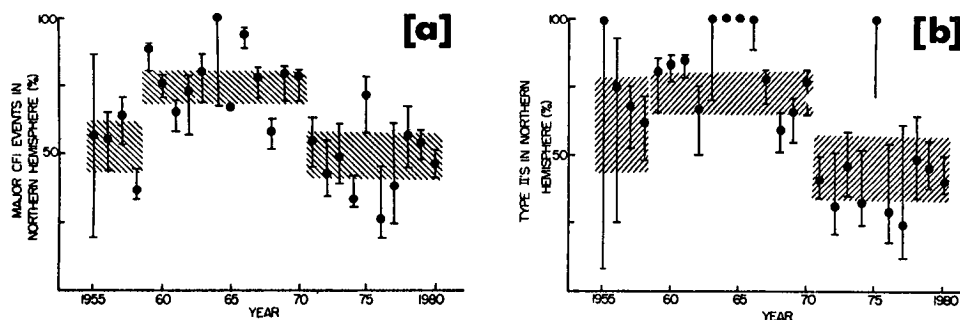


Figure 2(a) The percentage of "major" flares, as defined by the comprehensive flare index, that occurred in the northern hemisphere of the sun from 1955 through 1980, and (b) the percentage of flares with Type II radio emission that occurred in the northern hemisphere of the sun from 1955 through 1980. See text for further explanation.

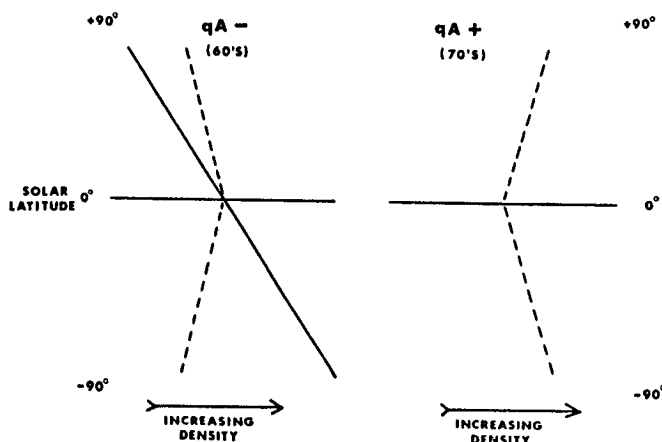
centage of major events in the northern solar hemisphere was determined, and these annual averages are displayed as solid dots in Figure 2(a). The data have also been arranged into groups of years, and the average for each group of years falls within the shaded regions in Figure 2(a). It is clear that there is a strong, statistically significant dominance of solar northern hemisphere activity from 1959 to 1970, with an essentially even distribution of activity between the two solar hemispheres before and after that period.

This same method was applied to a sub-set of these "major" events -- the events for which metric Type II solar radio emission has been associated. These events were selected primarily because a Type II radio burst is indicative of a shock passing through the corona between 1.5 and 2 solar radii, which could subsequently effect the cosmic ray intensity in the inner heliosphere, particularly at that latitude. This sub-set of Type II events is displayed in Figure 2(b), where the results are comparable to those in Figure 2(a). Data in Figure 2 are preliminary; a complete analysis will be published later.

**DISCUSSION AND CONCLUSION:** The marked N-S asymmetry in solar activity (with predominant activity in the sun's northern hemisphere) during the 1960's could certainly account for a S-pointing cosmic ray gradient. It is also clear from the data in Figure 1 that the response to this change in solar activity asymmetry, and the related change in the perpendicular cosmic ray density gradient, is different for cosmic ray telescopes in the earth's northern and southern hemispheres. Northern hemisphere detectors see a S-pointing gradient in the 60's and a N-pointing gradient after 1971, while southern hemisphere telescopes see a S-pointing gradient both before and after the reversal.

These results can be accounted for by a combination of a

Figure 3. Schematic representation of perpendicular cosmic ray density gradients. North-South symmetrical (dashed lines) and North-South asymmetrical (solid lines) are shown for the two IMF configuration  $qA-$  and  $qA+$ .



N-S symmetrical gradient, and a significantly larger N-S asymmetrical gradient that is present only during the 1960's (dashed lines and solid lines, respectively, in Figure 3). The N-S symmetrical gradient arises naturally as the result of cosmic ray trajectories in the heliosphere [Erdos and Kota, 1981; Kota and Jokipii, 1983]; for these symmetric gradients, the cosmic ray intensity decreases with increasing heliolatitude before the 1969-71 reversal, and increases with increasing heliolatitude after the reversal as shown schematically in Figure 3. The N-S asymmetrical gradient is greater in magnitude than the symmetrical gradients, and is S-pointing above and below the equator before the reversal, as shown schematically by the solid line in Figure 3; the asymmetrical gradient is attributed to the N-S asymmetry in solar activity demonstrated in Figure 2. After the reversal there is no N-S solar activity asymmetry and therefore no N-S asymmetrical cosmic ray density gradient. Cosmic ray telescopes in the northern hemisphere therefore see a density gradient above the ecliptic plane that is S-pointing before the reversal and N-pointing after it, while telescopes in the southern hemisphere see a gradient below the ecliptic plane whose resultant effect is S-pointing before and after the reversal, leading to the cosmic ray effects seen in Figure 1.

**ACKNOWLEDGEMENTS.** The work of one of the authors (DBS) was supported by the Atmospheric Sciences Section, National Science Foundation, under grant ATM-8305098.

#### REFERENCES.

- Dodson, H.W. & E.R. Hedeman, UAG-14, World Data Center A, 1971.  
 Erdos, G. & J. Kota, Proc. 17th ICRC (Paris), 10, 105, 1981.  
 Hashim, A & M. Bercovitch, Planet. Space Sci., 20, 791, 1972.  
 Kota, J. & J.R. Jokipii, Astrophys. J., 256, 573, 1983.  
 Roy, J.-R., Solar Physics, 52, 53, 1977.  
 Swinson, D.B., J. Geophys. Res., 75, 7303, 1970.  
 Swinson, D.B., J. Geophys. Res., 81, 2075, 1976.  
 Swinson, D.B. & H. Kananen, J. Geophys. Res., 87, 1685, 1982.



## COSMIC RAY INTENSITY AND THE TILT OF THE NEUTRAL SHEET

T. Saito<sup>1</sup> and D. B. Swinson<sup>2</sup><sup>1</sup> Onagawa Magnetic Observatory and Geophysical Institute,  
Tohoku University, Sendai 980, JAPAN<sup>2</sup> Department of Physics and Astronomy, The University of  
New Mexico, 800 Yale N.E., Albuquerque, NM 87131ABSTRACT

Recent publications have related long-term variations in cosmic ray intensity at the earth with long term variations in the tilt of the neutral sheet in the inner heliosphere. In this paper we compare the tilt of the neutral sheet from 1971 to 1974 with the cosmic ray intensity at earth, recorded by the Mt. Washington neutron monitor. The remarkable large decreases in cosmic ray intensity which occurred in 1973 and 1974 correlate well with excursions in the tilt of the neutral sheet which occurred earlier during these same two years.

INTRODUCTION: Recently Hoeksema et al. [1982, 1983] have determined the structure of the heliospheric current sheet, computed on a source surface at 2.35 solar radii, using solar magnetograph data from the Stanford Solar Observatory. They note that the extent in latitude of the neutral sheet slowly increased from  $\sim 15^\circ$  near sunspot minimum in 1976, to  $\sim 50^\circ$  by 1978, and extending nearly to the poles by solar maximum. Similar behavior has been noted earlier by Saito [1975, 1984]; in Figure 1 examples of the neutral sheet configuration near solar minimum (1954) and close to solar maximum (1968-69) are shown. The sheet is obtained by drawing the Parker spirals from the interplanetary neutral line on the solar source surface (the central sphere), where the source surface sphere with real radius of 2.6 solar radii is exaggerated in the figure to a radius of 30 solar radii for clarity. The outer sphere, which has a radius of one astronomical unit, shows the neutral sheet configuration near the earth.

The neutral sheet, as displayed in Figure 1, will of course extend well beyond the earth, presumably to the limits of the heliosphere, and will therefore influence the trajectories of incoming galactic cosmic rays which will eventually be detected at the earth. It would seem probable that a greater inclination of the current sheet (from its position at solar minimum), with its accompanying enhanced warping, would present a potentially longer path for galactic cosmic rays between the heliopause and the earth, and would lead to a reduction in cosmic ray intensity at the earth. Kota and Jokipii [1983] have calculated particle trajectories in a 3-dimensional IMF, incorporating a wavy neutral sheet,

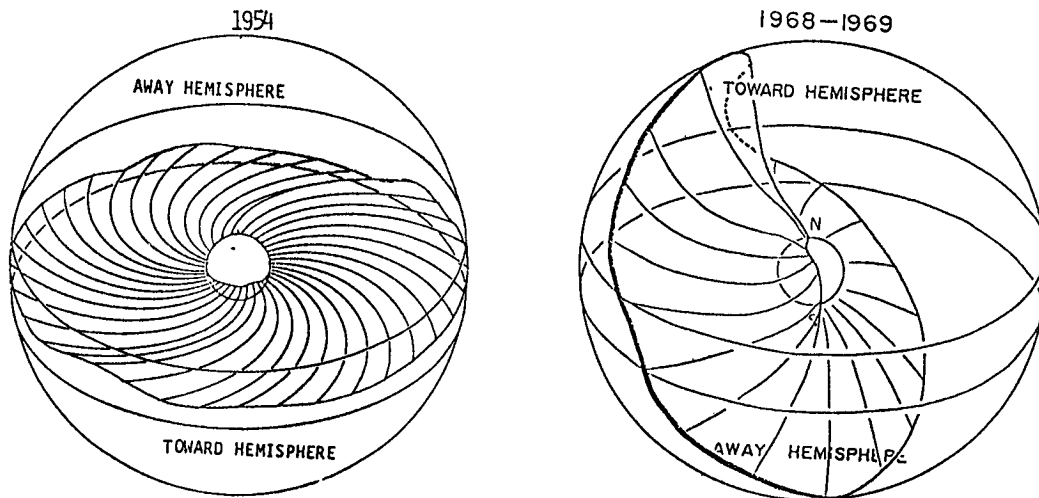


FIG. 1. Neutral sheet configuration between the sun and the earth near solar minimum (1954) and near solar maximum (1968-69).

for both polarities of the sun's polar magnetic field. They find that, when the field is away from the sun in the sun's northern hemisphere ( $qA+$ ), cosmic rays enter the heliosphere preferentially by way of the poles, while for the opposite magnetic configuration ( $qA-$ ) cosmic rays enter preferentially via the neutral sheet. By incorporating a tilt angle for the neutral sheet that is small near solar minimum and larger at solar maximum, they are able to account for the variation in cosmic ray intensity at the earth during the two solar cycles from 1958 to 1980.

Smith and Thomas [1985] have used the data of Hoeksema et al. [1982, 1983] to determine the inclination of the neutral sheet from 1976 to 1982, and they have compared the inclination with cosmic ray intensity at earth measured by the Deep River neutron monitor, and with cosmic ray intensity measurements in space made by Pioneer 10 as it proceeded from 10 to 30 AU. They note, as was predicted by Kota and Jokipii [1983], that the sensitivity of the cosmic ray intensity to changes in the tilt of the neutral sheet was significantly different before and after the reversal of the heliospheric magnetic field. They observed a good correlation between increasing tilt angle and decreasing cosmic ray intensity, with the sensitivity being enhanced when the field was inward in the northern solar hemisphere ( $qA-$ ).

In this paper we examine the correlation between the inclination of the neutral sheet between 1971 and 1974 and the cosmic ray intensity at the earth as measured by the Mt. Washington neutron monitor during that period.

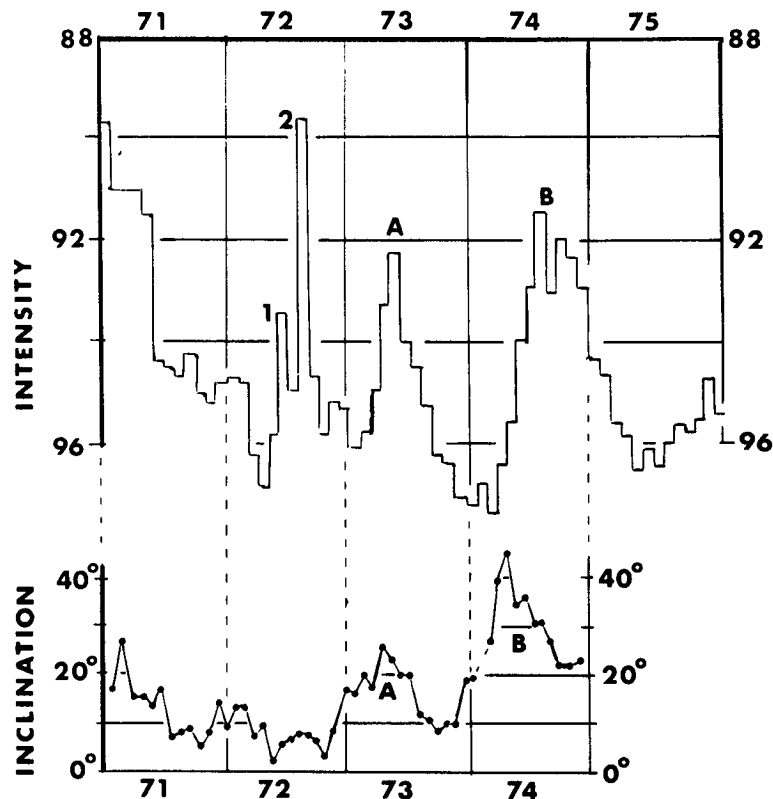


FIG. 2. (Top) Mt. Washington Neutron Monitor monthly average counting rate for 1971-1975, with intensity scale inverted, and (bottom) the average inclination of the neutral sheet for each solar rotation for 1971-1974.

**DATA:** K-Corona data have been used to determine the configuration of the heliomagnetospheric neutral sheet, and the inclination has been obtained for every Carrington rotation from 1971 to 1974. The basic data are the synoptic charts of K-corona intensity from 1971 to 1974. The latitude of the neutral line  $\Lambda_0(\Phi)$  for a certain longitude  $\Phi$  is obtained as  $\Lambda_0(\Phi) = 1/2 \{ \Lambda_N(\Phi) + \Lambda_S(\Phi) \}$ , where  $\Lambda_N$  and  $\Lambda_S$  indicate the latitudes of the northern and southern borders of the bright K-coronal belt at longitude  $\Phi$ . We define the tilt of the neutral sheet as the angle between the plane fitted to the various values of  $\Lambda_0(\Phi)$ , for one rotation, and the heliographic equator. The average inclination angles for each rotation are displayed at the bottom of Figure 2. At the top of the Figure the monthly average Mt. Washington neutron monitor counting rate is displayed [Lockwood and Webber, 1984], with the scale inverted i.e., intensity increases in the downward direction. The rate is normalized to 100 = 2506. In addition to the general correlation between the cosmic ray intensity and the inclination angle over the entire period, we note two very marked decreases in cosmic ray intensity in 1972; these are labeled 1 and 2 in Figure 2.

These decreases are due to events on the sun, and are not related to any changes in the neutral sheet. The most marked of these decreases (#2) occurred in August 1972 and was so energetic that it was observed even by underground muon telescopes at Embudo and Socorro (with threshold rigidities 19 GV and 45 GV), as well as by neutron monitors [Swinson, 1973].

The other two notable cosmic ray intensity decreases occurred in 1973 and 1974 and they have not thus far been accounted for. They are labeled A and B in Figure 2. These two large intensity decreases were preceded by two large excursions in the inclination of the neutral sheet, also labeled A and B in Figure 2. In light of this, as well as the previous observations, it seems reasonable to ascribe the intensity decreases to the excursions in the inclination of the neutral sheet. The delay between the maximum inclination of the neutral sheet and the subsequent minimum in cosmic ray intensity can be accounted for by noting that the inclinations noted in Figure 2 are observed at the solar source surface, and this pattern has to be carried out to the outer heliosphere at the solar wind speed before incoming galactic cosmic rays realize its full effect.

These correlations between cosmic ray intensity and the inclination of the neutral sheet provide further support for the gradient drift model of cosmic ray modulation.

**ACKNOWLEDGMENTS:** The authors express their thanks to J. R. Jokipii and E. J. Smith for valuable discussions, and to E. J. Smith for communicating the Smith and Thomas [1985] results prior to their publication. The work of one of the authors (DBS) was supported by the Atmospheric Sciences Section, National Science Foundation, under grant ATM-8305098.

#### REFERENCES

- Hoeksema, J. T., J. M. Wilcox, and P. H. Sherrer, J. Geophys. Res., 87, 10, 331, 1982.
- Hoeksema, J. T., J. M. Wilcox, and P. H. Sherrer, J. Geophys. Res., 88, 9910, 1983.
- Kota, J. and J. R. Jokipii, Astrophys. J., 265, 573, 1983.
- Lockwood, J. A. and W. R. Webber, J. Geophys. Res., 89, 17, 1984.
- Saito, T., Sci. Rept. Tohoku Univ., Ser. 5, Geophys., 23, 37, 1975.
- Saito, T., Extended Abstracts of Joint U.S.-Japan Seminar on the Heliosphere, 35, Kyoto, 1984.
- Smith, E. J. and B. T. Thomas, Preprint, submitted to J. Geophys. Res., 1985.
- Swinson, D. B., J. Geophys. Res., 78, 1707, 1973.

# DIFFERENTIAL MEASUREMENT OF COSMIC-RAY GRADIENT WITH RESPECT TO INTERPLANETARY CURRENT SHEET

*S P Christon, A C Cummings, and E C Stone  
California Institute of Technology*

*K. W. Behannon, and L F Burlaga  
Goddard Space Flight Center*

## ABSTRACT

Simultaneous magnetic field and charged particle measurements from the Voyager spacecraft at heliographic latitude separations from  $10^\circ$  to  $21^\circ$  are used to determine the latitude gradient of the galactic cosmic ray flux with respect to the interplanetary current sheet. By comparing the ratio of cosmic ray flux at Voyager 1 to that at Voyager 2 during periods when both spacecraft are first north and then south of the interplanetary current sheet, we find an estimate of the latitudinal gradient with respect to the current sheet of approximately  $-0.15 \pm 0.05\%$ /deg under restricted interplanetary conditions.

**1. Introduction.** Organization of cosmic ray flux about the heliographic equator should result from symmetries in the interplanetary magnetic field produced by the sun's rotation. However, if particle drifts are important in cosmic ray transport, the cosmic ray flux should be organized with respect to the interplanetary current sheet. This symmetrizing property of the current sheet has been demonstrated in a three-dimensional model of cosmic ray transport including particle drifts [Kota and Jokipii, 1983]. At 1 AU, gradients with respect to the current sheet  $G_\theta$  of up to  $\sim -0.33\%$ /deg have been identified for cosmic ray protons with energies  $>100$  MeV in various integral energy ranges [Newkirk et al., 1984, Newkirk and Fisk, 1985].

The interplanetary current sheet is a surface separating regions of magnetic field pointing generally toward or away from the sun. In its least complicated configuration, the near-sun current sheet is essentially a circle tilted with respect to the heliographic equator. As the rotating sun's magnetic field is drawn out by the solar wind, warping of the current sheet ensues, thus allowing two spacecraft separated in latitude to sample fluxes on either side of it (Figure 1). The near-sun current sheet extends up to  $\sim 60^\circ$  north N and south S of the equator and produces an interplanetary sector pattern that varies between two and four sectors during the period of this study [Hoeksema, 1984].

We determine  $G_\theta$  using spacecraft trajectory information, the ratio of cosmic ray flux, and observations of the current sheet (magnetic field sector boundaries) at Voyager 1 (V1) and Voyager 2 (V2), separated in latitude by  $10^\circ$  to  $21^\circ$ . Such a differential measurement has significantly smaller non-latitudinal intensity variations than a single-point measurement such as the type employed by Newkirk et al. and Newkirk and Fisk. The cosmic ray flux at an observation point in the heliosphere is  $j = j_0 \exp(G_r(r-R_0)) \exp(G_\theta(\theta-\theta_{cs}))$ , where  $G_r$  is the radial gradient,  $G_\theta$  is the colatitude gradient with respect to the current sheet,  $R_0$  is the radius of the boundary of the heliosphere,  $j_0$  is the cosmic ray flux at  $R_0$ , assumed constant,  $\theta_{cs}$  is the colatitude of the current sheet, and  $r$  and  $\theta$  are the radius and colatitude of the observation point. Heliographic colatitudes  $\theta$  from  $0^\circ$  to  $180^\circ$  correspond to

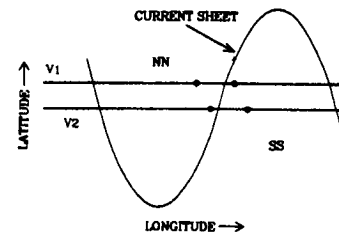


Fig. 1 Schematic representation of NN and SS configuration

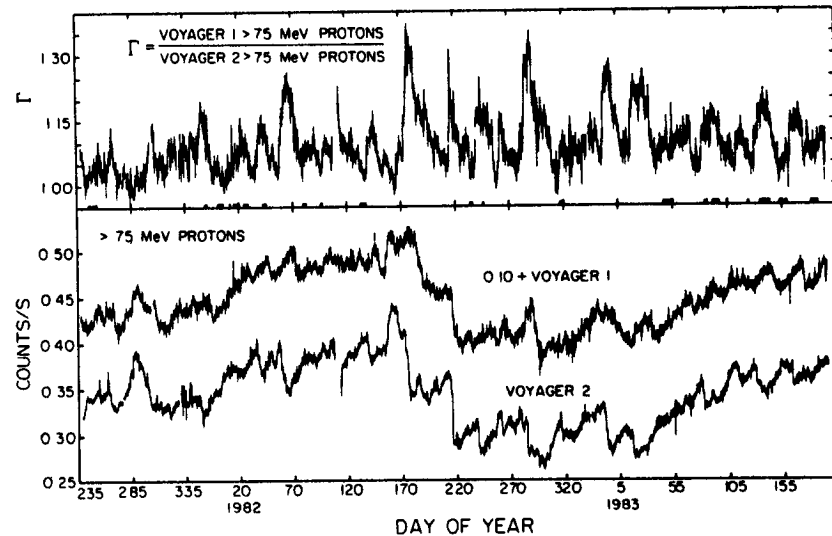
heliographic latitudes from 90°N to 90°S. Time series of simultaneous observations at two points in interplanetary space well separated in latitude allow estimates of  $G_\theta$  to be obtained for each interval in the series. These individual estimates of  $G_\theta = (\ln \Gamma - G_r (\tau_1 - \tau_2)) / (\theta_1 - \theta_2)$ , where the subscripts 1 and 2 refer to V1 and V2, respectively, and  $\Gamma$  is the ratio of the flux at V1 to that at V2, are independent of variations in the separation of the observation points. Statistically weighted averages of

$\langle G_\theta \rangle_{NN(SS)} = \sum_{i(j)} w_{\theta i(j)} G_{\theta i(j)} / \sum_{i(j)} w_{\theta i(j)}$  and  $\langle G_r \rangle = [\sum_i w_{\theta i} G_{\theta i} - \sum_j w_{\theta j} G_{\theta j}] / (\sum_i w_{\theta i} + \sum_j w_{\theta j})$ , where  $i(j)$  runs from 1 to  $n_{NN}(n_{SS})$ , the number of observations when both spacecraft are north (NN) or both south (SS) of the current sheet. The first character of the two character identifier represents the magnetic field region for V1, the second for V2. Data for NS and SN configurations are also collected and are used independently, and in combination with the NN and SS data, to estimate  $G_r$ .

## 2. Data Selection.

This study covers the period from day 240, 1981 until day 190, 1983, while the V1-V2 separation increased from 1.9 to 4.7 AU in radial distance from the sun and from 10° to 21° in latitude. V1 traveled from 11 to 17 AU and from 6°N to 20°N. V1-V2 longitude separation was  $\leq 16^\circ$ . Daily samples of counting rates of protons with energies  $>75$  MeV and a median energy  $\sim 1.1$  GeV measured by the nearly identical High Energy Telescopes of the Voyager Cosmic Ray Subsystem [Stone et al., 1977], and  $\Gamma$  the ratio of V1 to V2 counting rate samples are plotted in Figure 2. Calendar days for the NN and SS data sets are highlighted in the upper panel by underscoring. We have compared measurements taken at both spacecraft on the same day under the assumptions that convective effects are unimportant on the average, consistent with long-interval average observations [Venkatesan et al., 1983], and that local variations in the cosmic ray intensity, after eliminating solar flare transient effects, are due to variations in the distance to the current sheet [Newkirk and Fisk, 1985].

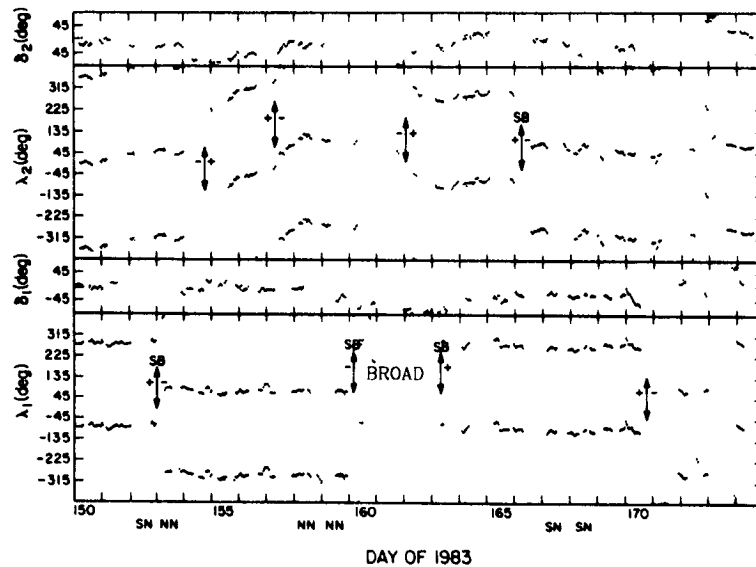
Fig 2 Daily samples of the counting rates of  $>75$  MeV protons from V1 and V2 (V1 is offset for clarity) and  $\Gamma$  the ratio of V1 to V2 counting rate samples. Uncertainties are due to counting statistics.



The counting rates of  $>75$  MeV and  $\sim 1$  MeV protons were used to eliminate periods possibly contaminated by solar flare particles and Forbush decreases. Proton energy spectra and elemental abundance measurements at lower energies were also used for this purpose. Hourly averages of the interplanetary magnetic field azimuth and elevation angles (Figure 3) measured by the Voyager Magnetic Field Experiment were used to determine the less active magnetic field periods, sector

polarities, and transition regions between sectors. Time blocks of data were identified when V1 and V2 were in regions of magnetic field pointing generally toward or away from the sun along the expected field direction, which is generally perpendicular to the radial direction in the outer solar system and parallel to the equatorial plane near the equator. The minimum sector length used herein is 4-5 days, so that V1 and V2 were most likely in field regions associated with plasma flows from the sun's polar coronal holes. This produced Data Set (DS) I. Then days with a poorly defined transition region at either end of the magnetic sector and days with azimuthal turbulence were eliminated in order to produce DS II. Finally, days with elevation angles pointing away from the equatorial region and days with elevation angle turbulence were collected into subset DS IIb. When the elevation angle changes by a large amount in less than a day or two as in DS IIb, it is likely to represent a dynamical effect such as the passage of transient material or perhaps reconnection at a sector boundary, either of which could alter the cosmic ray gradient. Those quietest days remaining are subset DS IIa.

Fig 3 Magnetic field azimuth and elevation angles from V1 and V2. The azimuth,  $\lambda$ , is  $0^\circ$  when the field is directed away from the sun and the elevation,  $\delta$ , is  $0^\circ$  when the field is along the spacecraft-sun line. Two cycles of  $\lambda$  are plotted. Arrows highlight transition regions interpreted as current sheet crossings. Those labeled "SB" are similar to sector boundaries at 1 AU.



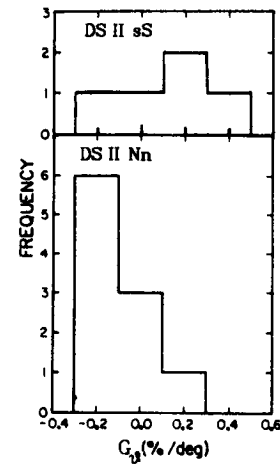
**3. Observations and Discussion.** Determination of  $\langle G_\theta \rangle$  requires knowledge of the value of  $G_r$ , which can be estimated from NS and SN data sets, since the latitude gradients, which have opposite signs in the two hemispheres should average to zero. Averaged over NS and SN,  $\langle G_r \rangle_{NSSN} = 2.21 \pm 0.11 \text{ \%}/\text{AU}$ , consistent with radial gradients reported by [Venkatesan et al., 1983].  $G_r$  can also be determined by averaging the NN and SS data sets, assuming that  $G_\theta$  is negligible. This results in  $\langle G_r \rangle_{NNSS} = 2.29 \pm 0.13 \text{ \%}/\text{AU}$ , consistent with  $\langle G_r \rangle_{NS,SN}$ , and suggesting that the best estimate is the average over all 152 days of data which yields  $\langle G_r \rangle = 2.25 \pm 0.08 \text{ \%}/\text{AU}$ . Note that an uncertainty of  $0.1 \text{ \%}/\text{AU}$  in the assumed  $G_r$  introduces an error of only  $0.01 \text{ \%}/\text{deg}$  in the derived  $\langle G_\theta \rangle$ .

$\langle G_\theta \rangle$  and  $\langle G_\phi \rangle$  have been calculated both without restrictions on spacecraft position (unrestricted average), and with restrictions on spacecraft position with respect to the current sheet based upon time to or from the closest sector boundary crossing (restricted average). Requiring V2 to be closer to the current sheet than V1 for NN data and V1 closer than V2 for SS data (see e.g., Figure 1), should enhance the measured  $\langle G_\theta \rangle$ .

Table 1  $\langle G_\theta \rangle$  and  $\langle G_\phi \rangle$  (# days of observation)

unrestricted average			
DS	$\langle G_\theta \rangle_{NN}$ (%/deg)	$\langle G_\theta \rangle_{ss}$ (%/deg)	$\langle G_\phi \rangle$ (%/deg)
I	$0.02 \pm 0.03$ (52) <sup>#</sup>	$-0.02 \pm 0.04$ (22)	$0.02 \pm 0.03$ (74)
II	$0.03 \pm 0.04$ (29)	$-0.01 \pm 0.04$ (19)	$0.02 \pm 0.03$ (48)
Ila	$-0.02 \pm 0.05$ (21)	$-0.06 \pm 0.03$ (6)	$-0.01 \pm 0.04$ (27)
Ilb	$0.14 \pm 0.09$ (8)	$0.01 \pm 0.05$ (13)	$0.06 \pm 0.05$ (21)
restricted average			
DS	$\langle G_\theta \rangle_{Nn}$ (%/deg)	$\langle G_\theta \rangle_{sS}$ (%/deg)	$\langle G_\phi \rangle$ (%/deg)
I	$-0.12 \pm 0.04$ (21)	$0.09 \pm 0.07$ (7)	$-0.11 \pm 0.03$ (28)
II	$-0.18 \pm 0.05$ (10)	$0.12 \pm 0.09$ (5)	$-0.16 \pm 0.04$ (15)
Ila	$-0.18 \pm 0.05$ (10)	$-0.06 \pm 0.08$ (1)	$-0.15 \pm 0.05$ (11)
Ilb	----- (0)	$0.20 \pm 0.09$ (4)	$-0.20 \pm 0.09$ (4)

Table 1 lists values of  $\langle G_\theta \rangle$  and  $\langle G_\phi \rangle$  for both positional criteria (the lower case subscript is for the spacecraft closer to the current sheet) using  $G_r = 2.25$  %/AU for the radial gradient correction. Note that the unrestricted  $\langle G_\phi \rangle$  displays no observable gradient, while the restricted  $\langle G_\phi \rangle$  is statistically significant and is approximately  $-0.15 \pm 0.05$  %/deg. Since differences between DS Ila and DS Ilb are statistically insignificant, we have no evidence that field elevation turbulence affected our measurements. Figure 4 shows the separation of the Nn and sS subsets for DS II with the restricted average. Note that, even with such a small data set, a separation of means and modes of the Nn and sS distributions, attributable to a small, negative latitude gradient, is evident. Further studies are required to determine whether such gradients are typical of other time periods.

Fig 4  $\langle G_\phi \rangle$  for DS II, restricted average

**4. Acknowledgements** We are grateful for the contributions of R E Vogt, other Voyager Cosmic Ray Subsystem team members, and N F Ness. Work at Caltech was supported in part by the National Aeronautics and Space Administration under contract JPL 49-556-63120-0-2600 and grant NGR 05-002-160.

#### References

- Decker, R B, S M Krimigis, and D Venkatesan [1984], *Astrophys J Lett*, 278, L119  
 Hoeksema, J T [1984], *Ph D Thesis*, Stanford University, Stanford CA  
 Kota, J and J R Jokipii [1983], *Astrophys J*, 265, 573  
 Newkirk, G, J Lockwood, M Garcia-Munoz, and J A Simpson [1984], *EOS, Trans, Am Geophys U*, 65, 1034  
 Newkirk, G and L A Fisk [1985], *J Geophys Res*, 90, 3391  
 Venkatesan, D, Decker, R B, and S M Krimigis [1984], *J Geophys Res*, 89, 3735



## SPATIAL VARIATION OF COSMIC RAYS NEAR THE HELIOSPHERIC CURRENT SHEET

J. R. Jokipii

University of Arizona, Tucson, Az.

and

J. Kota

Central Research Institute for Physics, Budapest

**ABSTRACT.** We report a quantitative comparison between theoretical predictions and observations of the intensity of galactic cosmic rays near the interplanetary current sheet. Comparison of our model calculations is made with a statistical analysis of observations of galactic cosmic rays at Earth and the simultaneous position of the current sheet. We use an ensemble of different current sheet inclinations, in order to make the analysis of the computations approximate the method used to analyse the data.

**1. INTRODUCTION.** The transport of cosmic rays in the interplanetary magnetic field is the consequence of four basic effects - diffusion, convection, cooling and gradient and curvature drifts. The resulting transport equation for the distribution function  $f$  may be written:

$$\frac{\partial f}{\partial t} = \nabla \cdot (\underline{\kappa} \cdot \nabla f) - \underline{V} \cdot \nabla f + \frac{1}{3} \nabla \cdot \underline{V} \frac{\partial f}{\partial p} \quad (1)$$

where  $P$  is momentum,  $\underline{V}$  is wind velocity and  $\underline{\kappa}$  is the diffusion tensor.

A variety of solutions of this equation has appeared in the literature. A straightforward application of the equation leads to a situation in which the particle drifts play a very important and perhaps dominant role in the modulation of galactic cosmic rays (see, e.g. Jokipii and Kopriva, 1979, Jokipii and Davila, 1981, and Kota and Jokipii, 1982). The problem of the intensity near the interplanetary current sheet was first addressed observationally by Newkirk and Lockwood (1981). Subsequently, Kota and Jokipii (1982) showed that the Newkirk and Lockwood results were consistent with their three-dimensional code.

More-sophisticated analyses of the observations were reported by Newkirk and Fisk (1985) and Newkirk, Asbridge and Lockwood (1985). Here we determine the agreement of these observations with our model.

**2. The Model Calculations.** We have developed a 3-dimensional code to solve the full transport equation. We use a straightforward extrapolation of observations taken near the ecliptic plane. The model is static in a coordinate frame corotating with the Sun. The numerical technique and details of the model are described elsewhere (Kota and Jokipii 1982). The interplanetary magnetic field is the same as that used by Jokipii and Thomas (1981). The field at the solar surface is assumed to be uniform and radial, with opposite signs on either side of a magnetic equator. This magnetic equator is a tilted plane at the sun, which is a wavy neutral sheet at larger heliocentric radii in interplanetary space (see Figure 2 of Jokipii and Thomas 1981). The degree of waviness increases from a minimum near solar minimum to a large value near 90° near sunspot maximum. The field on either side of the current sheet is an Archimedean spiral. The case in which the northern hemisphere field is outward corresponds to the field parameter  $A$  being positive. The solar wind speed was taken radial and constant in magnitude at  $400 \text{ km s}^{-1}$ . We are not yet able to use a spatially-varying solar wind speed.

The parallel diffusion coefficient,  $K_{||}$ , was assumed to be inversely proportional to the magnetic field strength,  $B$ ,

$$K_{||} = K_0 P^{\frac{1}{2}} \beta (B_{\text{earth}}/B) \quad (2)$$

with  $P$  being the particle rigidity in GV,  $\beta$  is the particle velocity in units of velocity of light, and  $K_0$  is a normalization constant in the

range  $10^{21} - 10^{23}$  if  $\kappa$  is expressed in  $\text{cm}^2/\text{sec}$  (see, eg., Jokipii and Davila, 1981). The ratio of perpendicular and parallel diffusion coefficients was kept constant at  $\kappa_{\perp}/\kappa_{\parallel} = 0.05-0.10$ . To reduce computing requirements the outer boundary was set at  $r = 15$  AU, with some runs carried out for a 30 A.U. boundary. The general features of the solutions have been discussed in detail elsewhere (Kota and Jokipii, 1982), and their discussion will not be repeated here, except to reiterate that the solutions are clearly affected by the particle drifts. Of most interest here is the dependence of the intensity on the structure of the interplanetary current sheet illustrated in the contour plot in figure (1). It is clear that the magnetic field organizes the cosmic-ray intensity in a characteristic manner relative to the current sheet, and that this organization is different for the two signs of the interplanetary magnetic field. Note also, for future reference, that the intensity is not simply dependent on the distance from the current sheet.

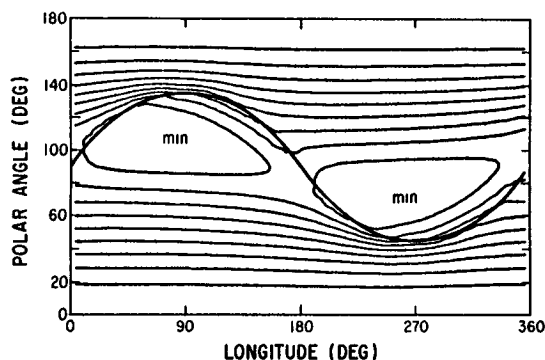


Fig. 1 Computed contours of equal intensity at a radius of 1 A.U., for protons of energy 2.36 GeV. Inclination of current sheet =  $45^\circ$ .  $\kappa_0 = 1.0 \times 10^{22} \text{ cm}^2/\text{sec}$ , and the outer boundary was at 15 A.U. All other parameters as in Jokipii and Kota, 1982.

### 3. Comparison With Observations

#### a. The Data.

Given the above, it is of interest to study observationally the relationship between the current sheet and cosmic rays. The analyses carried out by Newkirk and Lockwood (1981) and Newkirk and Fisk (1985a) and Newkirk, Asbridge and Lockwood (1985) attacked this problem statistically, in order to minimize the problem of transient, time-dependent effects. They studied the dependence of the intensity of the Mt. Washington neutron monitor (to protons of about 5.3 GeV energy) on the distance from the current sheet, for data obtained in the years 1973-1978. Data from the years around sunspot maximum were not included. They determined the position of the current sheet from coronal white light data, which has been determined to be quite accurate. Their figure (9) shows a scatter plot of the daily intensity vs. the heliomagnetic latitude at the point of observation (defined as the angular distance in degrees along a meridian to the current sheet, which defines the heliomagnetic equator). The data show considerable scatter, which is to be expected since effects of transient disturbances, etc. may be expected to disrupt the pattern. Nonetheless, there is a clear trend in the data, and the solid line gives the best fit of the function

$$I = a_0 + a_1 \sin^2(\lambda_{ms}) \quad (3)$$

to the data, where  $\lambda_{ms}$  is heliomagnetic latitude. The fit to the data, with  $a_0 = 2407$  and  $a_1 = -117$  is quite well-determined. In a subsequent paper, Newkirk, Asbridge and Lockwood examined the energy dependence of the ratio  $a_1/a_0$  by analysing data from a variety of other sources. These data show that the effect depends inversely on energy, scaling approximately as  $T^{-0.8}$ . It should be noted, however, that this observational result is still consistent with there being no instantaneous latitudinal gradient. For, since all of the observations are taken near the solar equatorial plane, the large values of  $\lambda_{ms}$  occurred when the current sheet was far from the equatorial plane, and the inclination of

the current sheet was large. Hence, if the intensity of cosmic rays globally were small when the current-sheet inclination was large, then a scatter plot of  $\lambda_{mg}$  vs intensity would tend to be lower at large  $\lambda_{mg}$ , as is observed. We will not discuss this possibility any further here, as it does not affect the analysis.

b. The Model Calculations.

In order to compare these data with the model, it is important to simulate the methods used to analyse the data very accurately.

First, we note that the inclination of the current sheet varied considerably over the time period spanned by the data set, so it would not be appropriate to use only one simulation, with one current sheet inclination. Second, the orbit of the Earth carries the point of observation sinusoidally seven degrees above and below the heliographic equator. Since the maximum value of  $\lambda_{mg}$  in the data set shown in figure (9) of Newkirk and Fisk is approximately  $55^\circ$ , a maximum current sheet inclination of  $45^\circ$  would give a maximum  $\lambda_{mg}$  of  $52^\circ$ . The work of Jokipii and Thomas (1981) suggests a minimum inclination of the order of  $15^\circ$ . Hence, three different inclinations, 15, 30, and 45 degrees were computed for each parameter set. A fourth inclination of 0 degrees was also used in some of the runs, with little change in the results. Then, to simulate the motion of the Earth in its orbit, the intensity was determined at a number of points, which were spaced in heliographic latitude and longitude just as the Earth is in its orbit. For each such point, in addition to the computed intensity,  $j$ , the heliomagnetic latitude  $\lambda_{mg}$  as defined by Newkirk and Fisk was calculated.

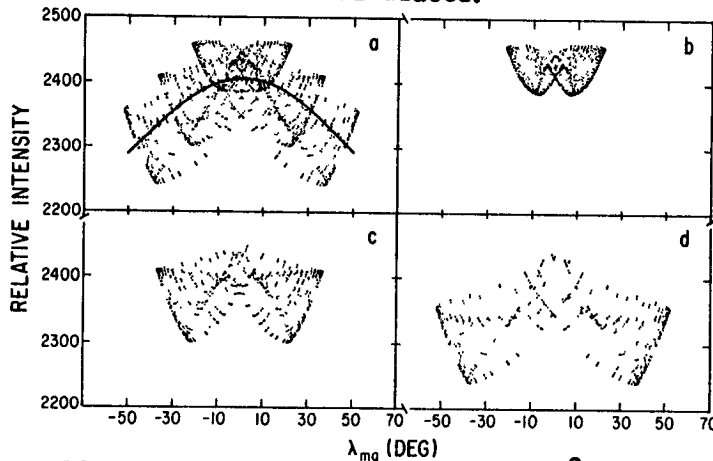


Fig. 2 a. Scatter plot of intensity vs  $\lambda_{mg}$  summed over three inclinations 15, 30 and 45 degrees, for the parameters of fig 1. b,c,d give the individual contributions for the three inclinations.

The resulting set of points ( $j, \lambda_{mg}$ ), for three inclinations and along the Earth's orbit is illustrated in figure (2a) for one set of parameters. Note that there is considerable scatter in the points, reflecting the fact that the computed intensity depends on other parameters as well as  $\lambda_{mg}$ . Nonetheless, the calculated values show a trend toward decreasing intensity as  $\lambda_{mg}$  increases, similar to that found in the data by Newkirk and Fisk. Figures (2 b,c,d) show the scatter plot obtained for the individual inclinations.

Finally, a least squares fit of equation (3) to the synthesized scatter plot was made to obtain the "theoretical value" of the coefficients  $a_0$  and  $a_1$  for each given set of parameters. This procedure was repeated for each set of parameters (diffusion coefficient normalization, energy, etc). As mentioned above, the absolute values are irrelevant, so the ratio  $a_1/a_0$  is used in what follows. Illustrated in figure (3) gives the variation of this ratio for a range of diffusion-coefficient normalizations for particles of energy 2.36 GeV, together with the value for this energy given by Newkirk, Asbridge and Lockwood (1985). Clearly, there is a broad range of plausible diffusion coefficients for which the computed value is close to that observed.

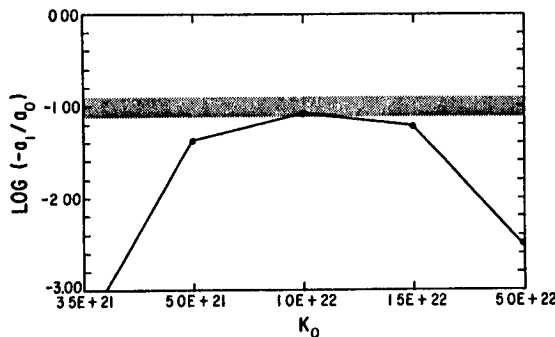


Fig. 3 Dependence of computed  $a_1/a_2$  on  $K_0$  for the parameters in figures 1 and 2. Horizontal band is observed value.

We also studied the energy dependence of the ratio  $a_1/a_0$ . We found that although the calculated value does indeed decrease with increasing particle energy, and agrees well with the data at a few GeV energy, the functional dependence is not the simple power law seen in the data. We expect that changing the energy dependence of the diffusion tensor could improve agreement here, but have not been able to verify this.

**4. Summary and Interpretation** The analysis presented above demonstrates that a model of modulation, in which the dominant physical effect is the large-scale structure of the interplanetary magnetic field, is quantitatively consistent with the analysis of the data reported by Newkirk and Lockwood (1981) and Newkirk and Fisk (1985a,b). At present the only significant discrepancy appears to be in the somewhat different energy dependences obtained from the data and from the model, and it appears likely that modifying the diffusion coefficient may improve this. Taken together with other comparisons of the theory with data, including the prediction of 22-year solar magnetic cycle effects (Jokipii and Thomas, 1981, and Kota and Jokipii, 1982), and detailed comparison with the inclination of the current sheet (Smith and Thomas, 1985), this suggests that many features of the solar-cycle modulation of galactic cosmic rays are a consequence of the model, and that drifts may well be a dominant process in solar modulation.

**Acknowledgements.** This work owes much to the participants in the Workshop on Cosmic Ray Modulation, where it was conceived. We thank G. Newkirk for providing data prior to publication. This work was supported, in part, by the National Science Foundation under Grant ATM-220-18, and by the National Aeronautics and Space Administration under Grant NsG-7101.

#### REFERENCES

- Jokipii, J. R., *Geophys. Res. Lett.*, **8**, 837, 1981.  
 Jokipii, J. R., Levy, E. H., and Hubbard, W. B., *Astrophys. J.*, **213**, 861, 1977.  
 Jokipii, J. R., and Kopriva, David A., *Astrophys. J.*, **234**, 384, 1979.  
 Jokipii, J. R., and Davila, J. M., *Astrophys. J.*, **248**, 1156, 1981.  
 Jokipii, J. R., and Thomas, B., *Astrophys. J.*, **243**, 1115, 1981.  
 Kota, J., and Jokipii, J. R., *Astrophys. J.*, **265**, 573, 1982.  
 Newkirk, G., and Lockwood, J. A., *Geophys. Res. Lett.*, **8**, 619, 1981.  
 Newkirk, G. and Fisk, Lennard A., *J. Geophys. Res.*, in press, 1985.  
 Newkirk, G., Asbridge, John, and Lockwood, John A., *J. Geophys. Res.*, in press, 1985.  
 Shea, M. A., and Smart, D. F., *Advances in Space Research*, Vol. 1, #3, 147, 1981.  
 Thomas, Barry T., and Smith, Edward J., *J. Geophys. Res.*, **86**, 11105, 1981.

## EFFECTS OF A WAVY NEUTRAL SHEET ON COSMIC RAY ANISOTROPIES

J. Kóta (1,2) and J.R. Jokipii (1)

(1) The University of Arizona, Tucson, Arizona, USA

(2) Central Research Institute for Physics, Budapest, Hungary

**Abstract.** We present the first results of our 3-D numerical code calculating cosmic ray anisotropies. The code includes diffusion, convection, adiabatic cooling, and drift in an interplanetary magnetic field model containing a wavy neutral sheet. We find that the 3-D model can reproduce all the principal observations for a reasonable set of parameters.

**Introduction.** In the last decade, the effects of curvature and gradient drifts became a central issue in the theory of cosmic ray transport. It has been suggested that drift may play an important, and perhaps dominant, role in cosmic ray propagation in the heliosphere, and it may be responsible for the asymmetries appearing in consecutive 11-year cycles (Jokipii, Levy and Hubbard 1977; Jokipii and Kopriva 1980; Kóta 1979; Jokipii and Thomas 1981; Kóta and Jokipii 1983). The first success of drift models in explaining galactic cosmic-ray phenomena was the explanation of the phase shift of the solar daily variation (Levy 1976) observed in the years of the seventies, following the polarity reversal of the solar magnetic field. The first quantitative 2-dimensional (2-D) calculation was carried out by Jokipii and Kopriva (1980). In this work, however, the too small value of the diffusion coefficient,  $\kappa$ , led to unreasonable anisotropies in some cases. Kóta (1981) derived an approximate force-field solution with a virtually perfect isotropy. This model, however, relied upon the too simple picture of 'hard-sphere' scattering.

The well known phase shift of the solar daily variation (Duggal and Pomerantz, 1975) is naturally explained by 2-D models (Levy 1976, Kadokura and Nishida 1984). The magnetic configuration of the seventies ( $A > 0$ ) yields a smaller radial density gradient which cannot balance the convection by the solar wind and thus results in a net outward streaming. Another well established observation is the presence of the polarity dependent N-S anisotropy associated with the  $\mathbf{B} \times \nabla n$  streaming (Bercovitch 1970, Pomerantz and Bieber 1984). In the seventies ( $A > 0$ ), this streaming is directed away from the neutral sheet. In a 2-D model, this pattern of streaming is hard to reconcile with the  $\text{div } \mathbf{S} < 0$  requirement, thus 2-D models are bound to encounter difficulties in explaining both observations.

The basic difficulty, in principle at least, may be removed if, violating the axial and N-S symmetries, a wavy neutral sheet is included. It is the purpose of this work to demonstrate that a 3-D model is indeed able to reproduce all components of the observed anisotropies. We present the first anisotropy results of our 3-D code incorporating a wavy neutral sheet.

**The Model.** We used a 3-D numerical code to solve the modulation equation including diffusion, convection, adiabatic deceleration and drift. The model and the scheme of calculation were described in detail elsewhere (Kóta and Jokipii 1983, see also the preceding paper SH-4.2-10 in this issue). Briefly, a usual spiral field is adopted, the magnetic equator is a tilted plane at the sun, which then evolves into a wavy sheet (Jokipii and Thomas 1981). The case of  $A > 0$  corresponds to outward polarity above

the sheet and inward polarity below the sheet while  $A < 0$  corresponds to the opposite configuration (sixties and eighties). Steady state is assumed in the frame corotating with the sun. The most serious limitation of the code is that it assumes constant solar wind speed thus many phenomena, like shocks, are precluded.

Calculations were carried out for protons in the 1 - 10 GV range. The parallel diffusion coefficient,  $\kappa_{\parallel}$ , was assumed to be inversely proportional to the magnetic field strength,  $B$ ,

$$\kappa_{\parallel} = K_0 P^{1/2} \beta (B_{\text{earth}}/B)$$

with  $P$  being the particle rigidity in GV,  $\beta$  is the particle velocity in units of velocity of light, and  $K_0$  is a normalization constant in the range of  $10^{21} - 10^{23}$  cm<sup>2</sup>/sec. The ratio of the perpendicular and parallel diffusion coefficients was kept constant at  $\kappa_{\perp}/\kappa_{\parallel} = 0.05-0.20$ .

Results and Discussion. Anisotropies were calculated at three heliocentric distances (0.5, 1, and 5 AU) over the full range of heliographic latitudes and longitudes. Here, we present the results near the earth. The anisotropies to be reported are obtained at the helioequator, at 1 AU, and averaged over longitudes in a magnetic sector.

The ecliptic components of the anisotropy responsible for the solar daily variation are given in Figures 1 and 2 ( $P=2.3$  GV;  $\kappa_{\perp}/\kappa_{\parallel} = 0.05$ ). It should be noted that the anisotropies obtained for a flat sheet (dashed lines) show sharp changes at the neutral sheet. The actual values (dots) may considerably differ from the averages over a ( $-5^\circ, 5^\circ$ ) latitude band (open circles). In most cases,  $A > 0$  gives an earlier phase and a smaller amplitude which is in general agreement with observations. Similar results were obtained for other rigidities, too. At large values of  $K_0$ , understandably, drift effects diminish and a near perfect corotation applies. The breaks in the lines in the  $K_0 = 1.5-5 \cdot 10^{22}$  cm<sup>2</sup>/sec range indicate that corotation should be reached somewhere in this interval.

Figure 3 shows  $\xi_{\odot}$ , the zenith angle component of the average near earth anisotropy above the neutral sheet for  $P = 2.3$  GV. Consider first the case  $A > 0$ , when the 'observed' value of  $\xi_{\odot}$  is negative in accordance with the sense of the  $\mathbf{B} \times \nabla n$  streaming. Curve (a) corresponding to  $\kappa_{\perp}/\kappa_{\parallel} = 0.05$  and  $\alpha = 15^\circ$  yields the correct sign for  $\xi_{\odot}$ . Larger tilt angle ( $\alpha = 30^\circ$ , curve (b)), however, may already give positive values, too. If we take, on the other hand, a larger perpendicular diffusion (curve (c):  $\kappa_{\perp}/\kappa_{\parallel} = 0.20, \alpha = 30^\circ$ )  $\xi_{\odot}$  will again point in the proper direction for all values of  $K_0$ . The underlying physical picture is that, in the case of large tilt angles and small perpendicular diffusion, most particles reach the earth without having interacted with the neutral sheet. Being too far from the earth, the neutral sheet becomes irrelevant for  $A > 0$ . As for  $A < 0$ , particles intersect the sheet several times before reaching the earth. As a result, the calculated  $\xi_{\odot}$  always shows the proper sense and is fairly independent of the tilt angle,  $\alpha$ .

Figure 4 indicates that the magnitude of  $\xi_{\odot}$  increases and its sign becomes more distinctive with increasing rigidities. This finding can also be anticipated since drift effects are expected to be more pronounced at higher rigidities.

The typical azimuthal dependence of the N-S anisotropy is presented in Figure 5. In most cases, we cannot find a one-to-one correspondence between the sign of  $\xi_{\odot}$  and the polarity of the field. In general, smaller tilt angle, and larger  $\kappa_{\perp}$  results in a better correlation; the

correlation also improves at higher rigidities. At 5 AU heliocentric distance, virtually all our runs gave a 100 percent correlation. To interpret this, we note that the waves in the neutral sheet become relatively tighter at larger distances from the sun. Thus we expect the effects of waviness to be more direct there.

**Conclusion.** Our numerical results demonstrate that the inclusion of a wavy neutral sheet may explain all components of the observed anisotropies. We find a general agreement between 'theoretical' and 'observed' anisotropies for a wide range of parameters. At high latitudes, well above or below the sheet, however, we predict the anisotropy to point toward the equator in the case of  $A > 0$ . This is in contrast to the poleward direction expected from the  $\underline{B} \times \underline{\nabla}n$  term only.

**Acknowledgement.** This work was supported by the National Science Foundation under Grants ATM-220-18 and INT-8400591.

### References.

- Bercovitch, M. 1970: Acta Phys. Hung., 29, Suppl 2, 169  
 Duggal, S. P. and Pomerantz, M. A. 1975: Proc. 14th ICRC, Munich, 4, 1209  
 Jokipii, J. R. and Kopriva, D. A. 1980: Ap. J., 234, 384  
 Jokipii, J. R. and Thomas, B. T. 1981: Ap. J., 243, 1115  
 Jokipii, J. R., Levy, E. H. and Hubbard, W. B. 1977: Ap. J., 213, 861  
 Kota, J. 1979: Proc. 16th ICRC, Kyoto, 3, 13  
 Kota, J. 1981: Adv. Space Res., 1, no. 3, 135  
 Kota, J. and Jokipii, J. R. 1983: Ap. J., 265, 573  
 Levy, E. H. 1976: J. Geophys. Res., 81, 2082  
 Kadokura, A. and Nishida, A. 1984: Proc. Int. Symp. on CR Modulation, Morioka, Japan 1984, p177  
 Pomerantz, M. A. and Bieber, I. W. 1984: Proc. Int. Symp. on CR Modulation, Morioka, Japan 1984, p39

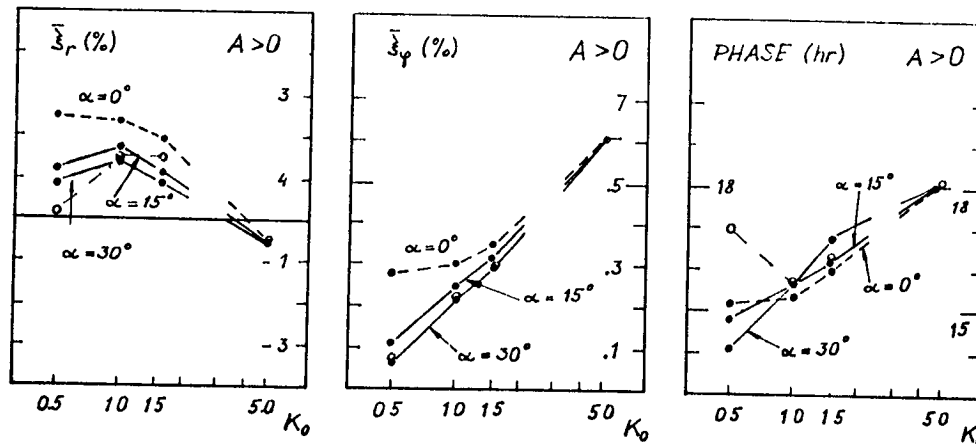


Figure 1. Radial and azimuthal components of the average near earth anisotropy calculated for  $A > 0$ ,  $P = 2.3 \text{ GV}$ ,  $\kappa_\perp/\kappa_\parallel = .05$ . Dashed and solid lines refer to flat (see text) and wavy sheets, respectively.  $K_0$  is in units of  $10^{22} \text{ cm}^2/\text{sec}$ . The phases of the resulting daily waves are also shown.

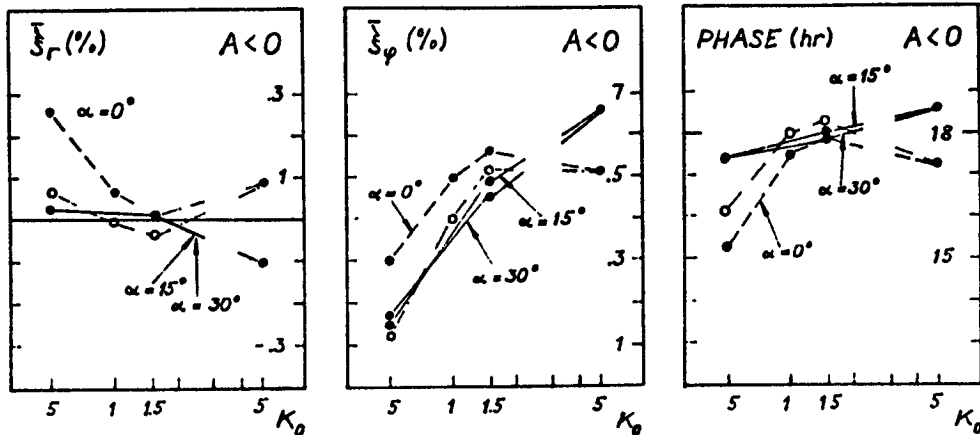


Figure 2. Same as Fig. 1., for  $A < 0$ .

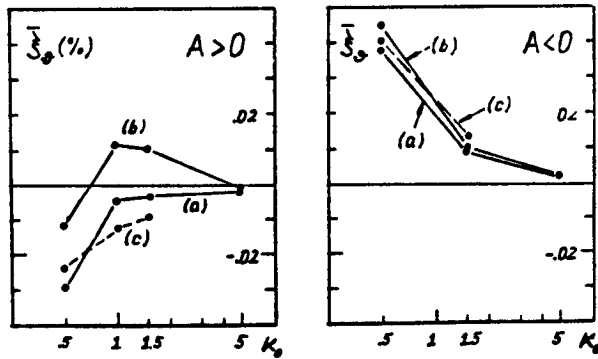


Figure 3. The average value of  $\bar{\xi}_\varphi$  for the earth being above the neutral sheet.  $P=2.3$  GV,  $K_0$  is in units of  $10^{22}$  cm<sup>2</sup>/sec.

(a)  $\kappa_1/\kappa_2 = .05$ ,  $\alpha = 15^\circ$ ;  
 (b)  $\kappa_1/\kappa_2 = .05$ ,  $\alpha = 30^\circ$ ;  
 (c)  $\kappa_1/\kappa_2 = .20$ ,  $\alpha = 30^\circ$ .

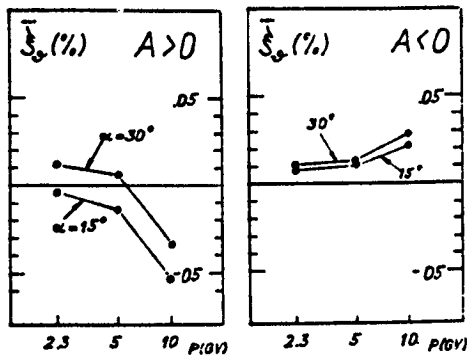


Figure 4.  $\bar{\xi}_\varphi$  vs rigidity calculated for  $K_0 = 10^{22}$  cm<sup>2</sup>/sec,  $\kappa_1/\kappa_2 = 0.05$ .

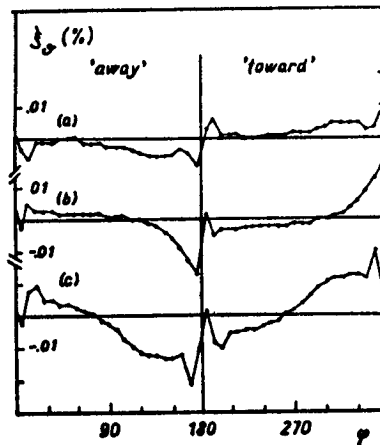


Figure 5. Azimuthal dependence of  $\bar{\xi}_\varphi$  calculated for  $P=2.3$  GV,  $\kappa_1/\kappa_2 = .05$ .  
 (a)  $A > 0$ ,  $\alpha = 15^\circ$ ; (b)  $A > 0$ ,  $\alpha = 30^\circ$ ;  
 (c)  $A < 0$ ,  $\alpha = 15^\circ$ .



## EFFECTS OF SOLAR MAGNETIC FIELD ON COSMIC RAYS

Gonchar G.A., Kolomeets E.V.,  
Lyakhova A.Kh., Slyunyaeva N.V., Stekol'nikov N.V.  
Kazakh State University, Timiryazeva St. 46,  
Alma-Ata 480121, USSR

The paper is devoted to some aspects of problem of galactic cosmic ray (gcr) propagation including inversion of solar total magnetic field (stmf) and to analysis of experimental facts related to heliomagnetic cycle.

It is known (Jokipii I.R., et al., 1977, Krainev M.V., 1979, Erkhov V.I., et al., 1983) that the global structure of solar total magnetic field (Parker's field) results in additional flux of gcr generated by curvature and gradient drifts. Velocity of charged particles drift is

$$\mathcal{D}_i = \frac{\partial \mathcal{X}_{ij}^{(A)}}{\partial x_j} \quad (1)$$

where  $\mathcal{X}_{ij}^{(A)}$  - antisymmetric part of diffusion tensor. It can be written for stmf in the form

$$\vec{\mathcal{D}} = \vec{\mathcal{D}}_1 + \delta(\theta - \pi/2) \vec{\mathcal{D}}_2 \quad (2)$$

where  $\vec{\mathcal{D}}_1$  is regular part and  $\vec{\mathcal{D}}_2$  - singular part of velocity. Delta function is connected with the fact of existence of boundary between inward and outward lines of force of magnetic field of the Sun that is neutral current sheet.

The main equation including diffusion, convection, energy changes and drifts in heliocentric system of coordinate is of the form:

$$\frac{1}{r^2} \frac{\partial}{\partial r} \left[ r^2 \left( \mathcal{X}_{22} \frac{\partial n}{\partial r} - nu - n \mathcal{D}_2 \right) \right] + \frac{1}{r \sin \theta} \frac{\partial}{\partial \theta} \left[ \sin \theta \left( \mathcal{X}_{\theta\theta} \frac{\partial n}{\partial \theta} - n \mathcal{D}_\theta \right) \right] + \frac{2u}{3} \frac{\partial}{\partial \mathcal{E}} (d\mathcal{E}n) = 0 \quad (3)$$

where  $d = \frac{\mathcal{E} + 2m_0}{\mathcal{E} + m_0}$ ,  $n$  is density of galactic cosmic rays,  $\mathcal{E}$  - kinetic energy. To analyse effects related to redistribution of galactic cosmic rays due to drift motion let's consider the equation including only convection, diffusion along lines of force of magnetic field and drift. We obtain

$$\frac{1}{r^2} \frac{\partial}{\partial r} \left[ r^2 \left( \mathcal{X}_{\theta\theta} \frac{\partial n}{\partial r} - nu - n \mathcal{D}_2 \right) \right] - \frac{1}{r \sin \theta} \frac{\partial}{\partial \theta} \left[ \sin \theta n \mathcal{D}_\theta \right] = 0 \quad (4)$$

Integration of equation (4) over  $\theta$  within the limits of  $\pi/2 - \mathcal{E}$  and  $\pi/2 + \mathcal{E}$  and approaching  $\mathcal{E}$  to zero gives following condition:

$$n(r, \mathcal{E}, \theta = \pi/2) = n_0(\mathcal{E}) \quad (5)$$

where  $n_0(\mathcal{E})$  - density of galactic cosmic rays out of modulation region that is for  $r > r_0$ .

It should be noted that on the basis of general

mathematical considerations (Mors F.M., Feshbach G., 1958) condition (5) has sense only for odd cycles of solar activity. In order to solve parabolic equation (4) we used traditional boundary conditions for this kind of the problems (Ashirov R.R. et al., 1979, Krylov V.I., et al., 1977)

$$n(z=z_0, \varepsilon, \theta) = n_0(\varepsilon); \left[ \sigma n + (1-\sigma) \frac{\partial n}{\partial z} \right] \Big|_{z=0} = 0 \quad (6)$$

where  $\sigma$  - parameter.

The set of boundary conditions (5) and (6) allows to solve equation (4) correctly. Grid technique and Crank Nicholson schemes (Krylov V.I., Bobkov V.V., Monastyrsky V.I., 1977) were employed for solution. Equation (4) was solved for the energy range  $\varepsilon > 1 \text{ GeV}$ . Figure 1 shows radial variation of  $n/n_0$  at the heliolatitude  $-7$  for energies 1 and 10 GeV. Figure 2 illustrates latitudinal variations of  $n/n_0$  for the energies. Following values of latitudinal gradient of gcr were obtained at the orbit of the Earth:

$$\frac{1}{n} \frac{\partial n}{\partial \theta} (\varepsilon = 1 \text{ GeV}) = 1.9\% / \text{a.u.} \quad \frac{1}{n} \frac{\partial n}{\partial \theta} (\varepsilon = 10 \text{ GeV}) = 0.16\% / \text{a.u.}$$

Hence including in the equation of gcr propagation the term describing drift of particles results in redistribution of density, appearance of latitudinal gradient and reduction of modulation depth.

Let's consider and analyse experimental data connected with heliomagnetic cycle. As follows from abovementioned facts latitudinal gradient results in N-S asymmetry (Kolomeets E.V., et al., 1977). Let's consider asymmetry of cosmic rays and solar activity. Figure 3 shows amplitude of north-south asymmetry in the stratosphere data of Mirny and Murmansk at the depths of  $20 \text{ g/cm}^2$  (a) and  $480 \text{ g/cm}^2$  (b). One can see that amplitude of the effect grows with the depth in the atmosphere, this fact demonstrates rigid energy spectrum of the effect.

The investigation of solar activity during the last magnetic cycle reveals pronounced N-S asymmetry at all heliolatitudes. Figure 4 shows north-south asymmetry for the ranges of heliolatitudes (20-30) (a); (30-40) (b); (40-50) (c). One can see 22-year wave in N-S asymmetry. The change of the sign of north-south asymmetry occurs during the periods of inversion of solar total magnetic field. Periods of inversion are shaded.

In order to study nature of 22-year variation of neutron component of cosmic rays we analysed continuous set of the data of neutron monitors of the worldwide network for the last magnetic cycle. The wave averaged over two eleven-year cycles was substracted from original data to exclude 11-year variation. Figure 5(a) shows obtained 22-year variation for Deep River station.

Taking into account 22-year wave in solar activity we

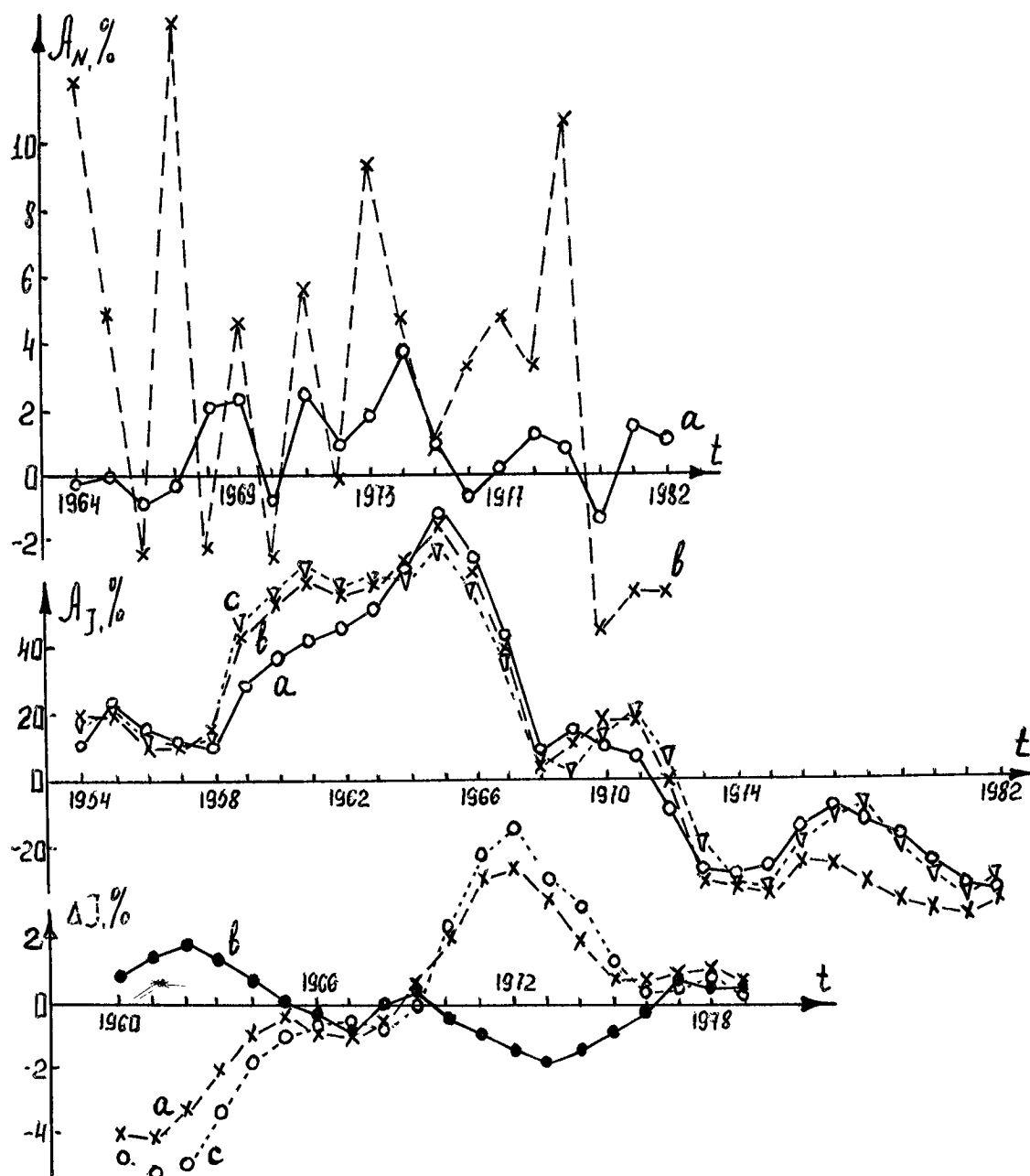


Fig.3. Temporal variation of amplitude of N-S asymmetry stratosphere data of Mirny and Murmansk).

Fig.4. Temporal variation of N-S asymmetry of solar activity at various heliolatitude regions.

Fig 5. 22-year variation of cosmic ray intensity, observed at Deep River. (a) -22-year wave in cosmic rays expected due to corresponding variation of solar activity. (b)- variation of cosmic ray intensity due to drift effects.

determined contribution of the wave to cosmic ray intensity. 22-year wave in cosmic rays expected due to 22-year variation of solar activity was found on the basis of empirical relation between solar activity and cosmic ray intensity. The result is given in figure 5 (b). One can see that obtained change in cosmic rays due to solar activity is in opposite phase with the observed variation of cosmic rays. Subtracting from obtained 22-year wave wave expected due to corresponding variation of solar activity we obtained variation of cosmic ray intensity produced by other mechanisms and among them drift of particles in solar total magnetic field. So corresponding variation of solar activity, inversion of solar total magnetic field, drift effects and other space distributions contribute to the observed 22-year variation.

### REFERENCES

- Ashirov R.R., Kolomeets E.V., Stekol'nikov N.V. Modeli izotropnoi, anizotropnoi diffuzii i parametry, opredelyayushie modulyaziyu galacticheskikh kosmicheskikh luchej, Alma-Ata, Kitap, 1979.  
 Bazilevskaya G.A., Krainev M.B., et al., Izv. AN SSSR, ser. fiz., 1983, v.47, p.1669.  
 Erkhov V.I., Kolomeets E.V., et al., Izv. AN SSSR, ser. fiz., 1983, v.9, p.1822.  
 Jokipii I.R., Levy E.N., Astrophys. J., 1977, v.213, L85.  
 Kolomeets E.V., Lyakhova A.Kh., Stekol'nikov N.V., 18 ICRC, 1983, v.11, p.1.  
 Kolomeets E.V., Bychkovskaya A.Kh., Zysmanovich A.G. 15 ICRC, 1977, v.3, p.170.  
 Krainev M.B. 16 ICRC, 1979, v.3, p.230.  
 Krylov V.I., Bobkov V.V., Monastyrskii V.I. Vychislitel'nye metody, Nauka, Moskva, 1977, v.2, p.146.  
 Mors F.M., Feshbach G., Metody teoreticheskoi fiziki, IL, Moskva, 1958, v.1, p.657.

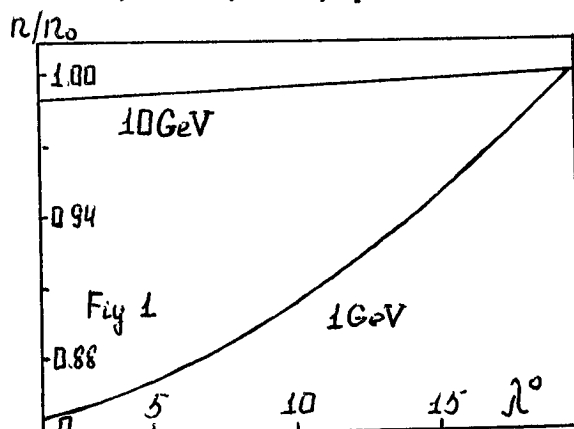


Fig.1. Radial dependence of gcr density at heliolatitude at energy 1 and 10 GeV.

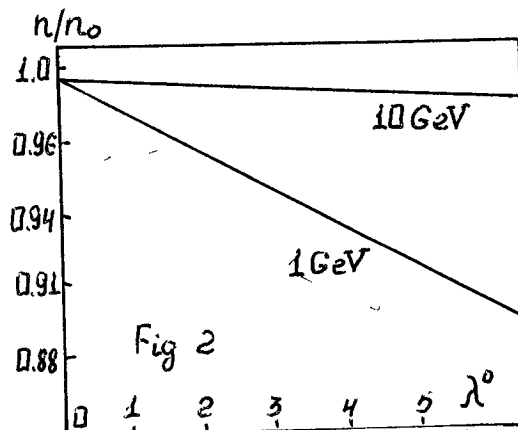


Fig.2. Latitudinal dependence of gcr density at energies 1 and 10 GeV.

# DETERMINATION OF GALACTIC COSMIC RAY LATITUDINAL GRADIENT USING EARTH BASED DETECTORS

Badruddin and R.S.Yadav

Space Science Group, Dept. of Phys., A.M.U., Aligarh (India)

## ABSTRACT

Using cosmic ray intensity data of Deep River Neutron monitor and relation between solar wind velocity and heliomagnetic latitude, an attempt has been made to evaluate quantitatively the latitudinal gradient of cosmic ray intensity during the periods dominated by a two sector pattern. Assuming a constant orientation of the heliospheric current sheet on a time scale of the order of a year, a relationship is determined between the cosmic ray intensity and the heliomagnetic latitude.

1. Introduction. Galactic cosmic ray intensity gradients play an important role in guiding theoretical models of cosmic ray transport in the heliosphere. The behaviour of radial and latitudinal intensity gradients with time and heliocentric radial distance is of interest for the overall understanding of the cosmic ray modulation. Most of the earlier studies of latitudinal gradients were made with respect to heliographic equator or the ecliptic plane. However, with the realization of the importance of heliospheric current sheet, two recent studies (Badruddin et al., 1985; Newkirk & Fisk, 1985) have addressed this problem by assuming the heliospheric current sheet to be the heliomagnetic equator.

In this extension, of our earlier analysis, we shall give a quantitative relationship for determining the heliomagnetic latitudinal gradient at IAU during a period (1974) dominated by two sector pattern.

2. Method. We have calculated the heliomagnetic latitude ( $\theta$ ) using the relationship, given by Zhao and Hundhausen (1981), between the solar wind velocity and heliomagnetic latitude both before and after the earth's crossing of the heliospheric current sheet (sector crossing), assuming the minimum velocity near the current sheet. Thus knowing the heliomagnetic latitude on days before and after the sector crossing, the latitudinal gradient of cosmic ray intensity with respect to zero latitude is calculated. Since the heliospheric current sheet (sector boundary) is thought to constitute a basic 'plane' of symmetry (Smith and Barnes, 1983), the distance of the observations above or below the current sheet was considered more appropriate to a search for latitude dependence than the distance from the solar equator.

3. Results and Discussion. In Fig. I we have shown the average latitude gradient in 1974 with respect to heliomagnetic equator, which we have assumed to be the heliospheric current sheet. We have not considered the solar rotations in which there was any sharp increase or decrease of cosmic ray intensity. It can be seen from Fig. I that the cosmic ray

intensity decreases as the heliomagnetic latitude of the earth from the heliospheric current sheet increases. The relation between the gradient and the latitude for 1974 can be expressed as:

$$G_{\theta} (\%) = -0.036 |\theta| \quad \text{for } 0^{\circ} \leq |\theta| \leq 30^{\circ}$$

Further, the maximum gradient from -1% to -3% has been found in different solar rotations.

The heliomagnetic latitude determined on different days using the relation between the solar wind velocity and heliomagnetic latitude (Zhao & Hundhansen, 1981) before and after the sector crossing and the corresponding gradient in cosmic ray intensity and solar wind velocity variations are shown in Fig. 2. It is seen that during this period the cosmic ray gradient closely follows the solar wind velocity which increases away from the current sheet. The presence of such a latitudinal gradient of cosmic ray intensity indicate that some of the time variations observed at the earth are caused by the spacial variation of solar wind velocity with respect to heliomagnetic latitude (current sheet). Hakamada and Munakata (1984) suggested that solar wind speed depend on the angular distance from the magnetic neutral line (current sheet) and does not depend on the heliographic latitude of the Earth.

Roelof et al. (1983) using the data from IMP-8 and the closely spaced Voyager-I and 2 spacecrafts found heliolatitudinal gradient in  $\geq 35$  Mev protons of  $\sim 2\%$  -  $5\%$  per degree in short lived (10-30 days) structures, and  $1\%$  -  $2\%$  per degree in structures recurring over a few solar rotations. From an analysis of IMP-8 and Voyager-1 and 2 data from 1972 through early 1982, Venkatesan et al. (1984) concluded that, when corrected for radial gradients of  $3\%$  per AU, the intensity difference between either Voyager-I or Voyager-2 and IMP-8 was consistent with a heliolatitudinal gradient  $0.00\%$  per degree for  $\geq 70$  Mev protons. In another study, Decker et al. (1984) examined the integral cosmic ray intensities (proton energy  $\geq 70$  Mev) between Voyager-I and Voyager-2 in the 8-13 AU helioradial range and over  $3^{\circ}$  -  $16^{\circ}$  heliolatitude separation during the first 17 months of the cosmic ray recovery in 1981-82. These data are also consistent with the heliolatitude gradient  $\sim 0$  to  $-0.4\%$  per degree. They admit that this null result is apparently still at least consistent with either model of Fisk (1976) or Kota and Jokipii (1983), however, due to non availability of the location of Voyager-I & 2 relative to the heliospheric current sheet a detailed comparison with either the Fisk or Kota & Jokipii model is not possible. A preliminary analysis by Lockwood and Webber (1984) using the 26 days average Voyager-I and 2 counting rate gives less than  $-0.1\%$  per degree heliolatitudinal gradient during 1981-82 period for more than 60 Mev particles.

From neutron monitor observations in 1975, Newkirk and Lockwood (1981) found a value of about  $-0.04\%$  per degree at 5 Gev for latitudinal gradient. The theoretical prediction, including a warped current sheet yield about  $-0.06\%$  per degree (Kota and Jokipii, 1982). For 1970-79 period the symmetric

SH 4.2 -I3

latitudinal gradient away from the current sheet is estimated to be  $-.06\%$  per degree (Newkirk and Fisk, 1985) which is not much different from our estimate of  $\approx -.04\%$  per degree for the year 1974.

4. Conclusion: It has been found that the cosmic ray intensity decreases as the angular distance of the earth from the heliospheric current sheet (heliomagnetic equator) increases. During 1974 (for solar rotations in which there is no transient decrease of large amplitude) the maximum (negative) gradient from  $-1\%$  to  $-3\%$  has been found in different solar rotations assuming the heliospheric current sheet to be the heliomagnetic equator. The relation between the cosmic ray gradient and the heliomagnetic latitude can be expressed as:

$$G_{\theta} (\%) = -0.36 |\theta| \quad \text{for} \quad 0^{\circ} \leq |\theta| \leq 30^{\circ}$$

The presence of such a latitudinal gradient indicates that some of the time variations of cosmic rays observed at the earth are caused by the spacial variation of the solar wind velocity with respect to current sheet. It may be possible that it is the heliospheric current sheet and not the helio-equatorial plane that is of physical significance when one is calculating the heliolatitudinal gradients of galactic cosmic ray (Venkatesan et al., 1984). Since the relation between cosmic ray intensity and the heliomagnetic latitude may vary during the course of a solar cycles, a clear picture of heliomagnetic latitudinal gradient will emerge when the precise knowledge of heliospheric current sheet position during different epoch of solar activity cycle is available.

5. Acknowledgement. One of the authors (Badrudain) acknowledges the financial support from C.S.I.R., New Delhi.

#### References

- Badrudain, R.S. Yadav, and K.R. Yadav, Planet. Space Sci., 33, 191, (1985).  
 Decker, R.B., Krimigis, S.M. and Venkatesan, D., Astrophys. J., 278, L119, (1984).  
 Fisk, L.A., J. Geophys. Res., 81, 4646, (1976).  
 Hakamada, K. and Munakata, Y., J. Geophys. Res., 89, 357, (1974).  
 Kota, J. and Jokipii, J.R., Geophys. Res. Lett., 9, 656, (1982).  
 Kota, J. and Jokipii, J.R., Astrophys. J., 265, 573, (1983).  
 Newkirk, G. Jr. and Lockwood, J.A., Geophys. Res. Lett., 8, 619, (1981).  
 Newkirk, G. Jr. and Fisk, L.A., J. Geophys. Res., 90, 3391, (1985).  
 Roelof, E.C., Decker, R.B. and Krimigis, S.M., J. Geophys. Res., 88, 9889, (1983).  
 Smith, F.J. and Barnes, A., Solar Wind Five (Ed. H. Neugebauer) NASA Publ. 2280, 521, (1983).  
 Venkatesan, D., Decker, R.B. and Krimigis, S.M., J. Geophys. Res., 89, 3735, (1984).  
 Zhao, X.-P. and Hundhausen, A.J., J. Geophys. Res., 86, 5423, (1981).

SH 4.2-13

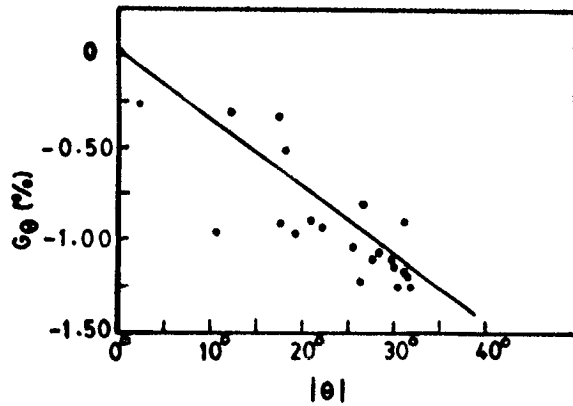


Fig.1

Fig.1 shows the average heliomagnetic latitude gradient calculated from Deep River neutron intensity for 1974.

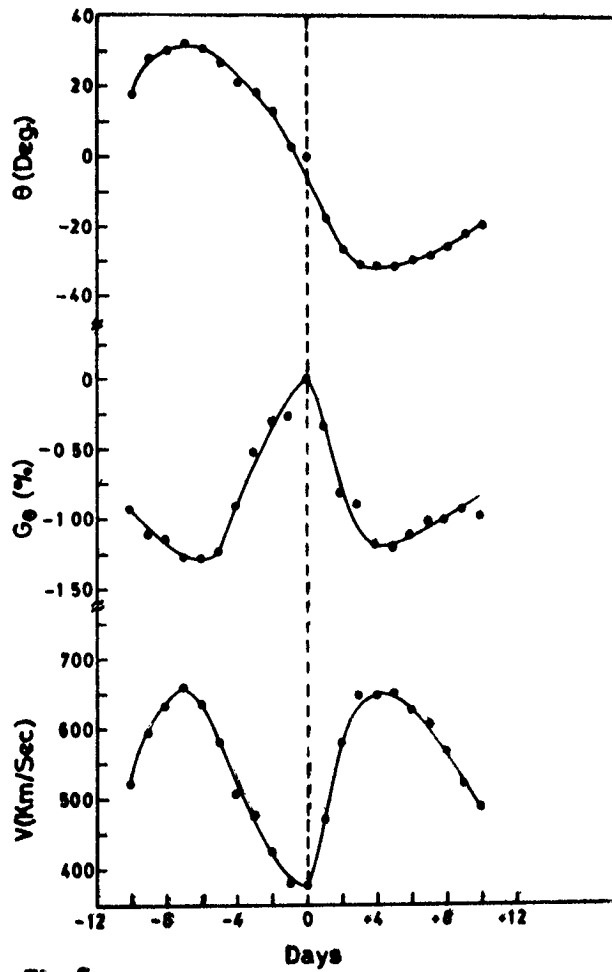


Fig.2

Fig.2 shows the variation of heliomagnetic latitude, the cosmic ray gradient and the solar wind velocity on the days before and after sector crossing for 1974.



THE EXPECTED COSMIC RAY DENSITY AND STREAM DISTRIBUTIONS  
AT THE HELIOLATITUDINAL ASYMMETRY OF SOLAR WIND

Alania M.V., Aslamazashvili R.G., Dorman L.I., Iskra K.  
Institute of Geophysics, Georgian Academy of Sciences USSR,  
IZMIRAN, Moscow Region, USSR, Agriculture - Teacher  
University, Physics and Biophysics Dep., Siedlce POLAND

ABSTRACT

The results of the spatial distribution of cosmic ray density, gradients and anisotropy obtained on the basis of the numerical solution of the anisotropic diffusion equation with an account of solar wind velocity change depending on the latitudinal angle  $\Theta$  of the form  $U = U_0 e^{\alpha \Theta}$  and the diffusion coefficient depending on the spatial coordinates and the particle rigidity are presented. It is shown that the increase of the solar wind velocity and the diffusion coefficient with the heliolatitude leads to the gradient distributions that are in accord with the experimental data observation in cosmic space. In the paper the results of the energetic spectrum of 11 and 22-year cosmic ray variations obtained with an account of direction of the general magnetic field of the Sun are presented.

1. Introduction. The measurements by radio-astronomic methods show that solar wind velocity remains almost stable at medium heliolatitudes and increases in high areas. /1/ In all probability this is connected with coronal holes in the sun, which occur predominantly at medium and high heliolatitude. /2/ The open structures of the magnetic field in coronal holes contributes to the free exit of solar wind plasma from these areas and is thus a cause of high speed streams. Furthermore the strength of the magnetic inhomogeneities in these streams decreases and because of this the cosmic ray diffusion coefficient increases.

2. The theoretical model. Cosmic ray diffusion in interplanetary space is described by the equation. /3/

$$\frac{\partial n}{\partial t} = \nabla_i (\chi_{ik} \nabla_k n) - \nabla_i (n \cdot U_i) + \frac{1}{3R^2} \frac{\partial}{\partial R} (R^3 n) \cdot \nabla_i U_i \quad (1)$$

We assumed that solar wind velocity  $U$  changes depending on heliolatitudes as follows:

$$U = U_0 (2 - e^{\alpha(\Theta - \frac{\pi}{2})})$$

where  $\alpha = 0.44$  and is independent of radial distance within the modulation boundaries. The diffusion coefficient  $\chi$  depends on particle rigidity  $R$  and spatial coordinates as follows:

$$\chi = \chi_0 (1 + r) \cdot e^{R_1/R} (R_2 + R)^2 \cdot (1 + \beta(1 - \sin \Theta))$$

where  $R_1 = 0.05$  GV,  $R_2 = 3$  GV,  $r$  is distance from the sun,  $\beta = 19$ . Equation (1) is solved with spherical coordinates  $r, \Theta, \varphi$  for a steady state situation  $(\frac{\partial n}{\partial t} = 0, \frac{\partial n}{\partial \varphi} = \frac{\partial^2 n}{\partial \varphi^2} = 0)$

The defined assumptions are valid for long-period variations when the galactic cosmic ray diffusion time is considerably less than the time needed for a change in the surrounding conditions. Equation (1) is solved by a network method for boundary conditions where  $\rho = \frac{r}{r_0}$  and  $r$  is the distance from the sun,  $r_0$  the radius of the extent of modulation.  $B = \frac{n}{n_0}$ , where  $n$  and  $n_0$  are the cosmic ray particle density in interplanetary space and in the galaxy.

3. Results. Equation (1) is solved with regard to the anti symmetrical part of tensor diffusion, that is to say with regard to the particle drift in a regular interplanetary field of the sun under two conditions: a/ When the lines of force of the magnetic field go from the northern hemisphere of the sun to the southern hemisphere  $/H^+ /$  and b/ when the opposite is true  $/H^- /$ .

Fig.1 shows the distribution of radial gradients of cosmic rays on depending to the distance for 10 Gev energy particles.

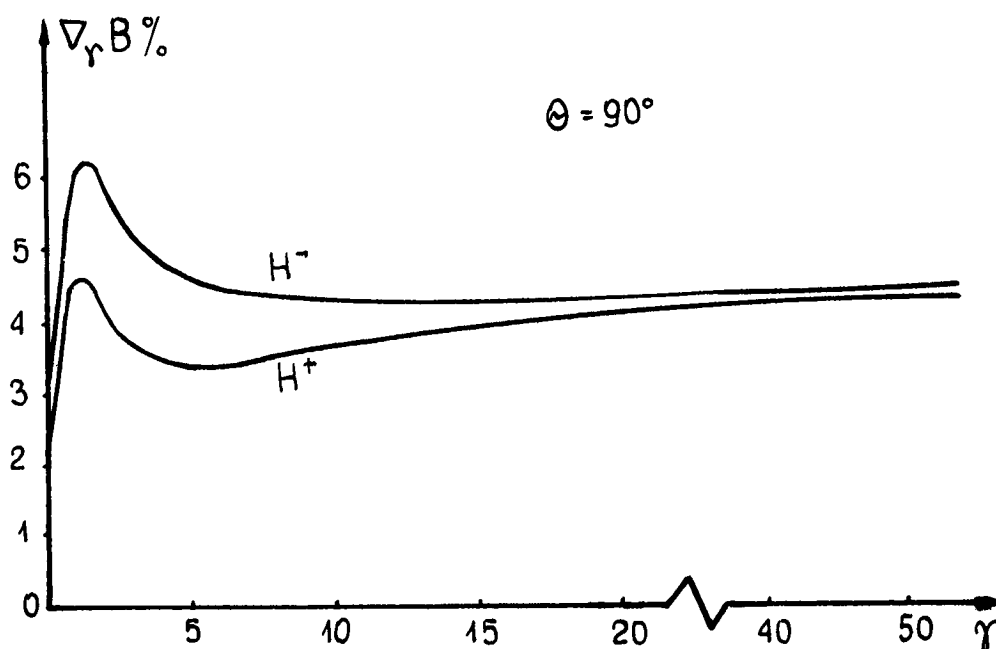


Fig. 1

Fig.2 shows the expected energy spectra for the 11-year variation in the event of  $/H^+ /$  and  $/H^- /$  and also the 22-year variation caused by cosmic ray particle drift.  $/H^+ - H^- /$

4. Discussion and conclusion. For all other conditions being equal the cosmic ray density is greater for an 11-year cycle solar activity when the lines of force go from the northern hemisphere of the sun to the south  $/H^+ /$ . In this event the hemisphere sucks in cosmic-ray particles inwards from its external surroundings. It is interesting to compare the expected radial gradient distribution with the experimental

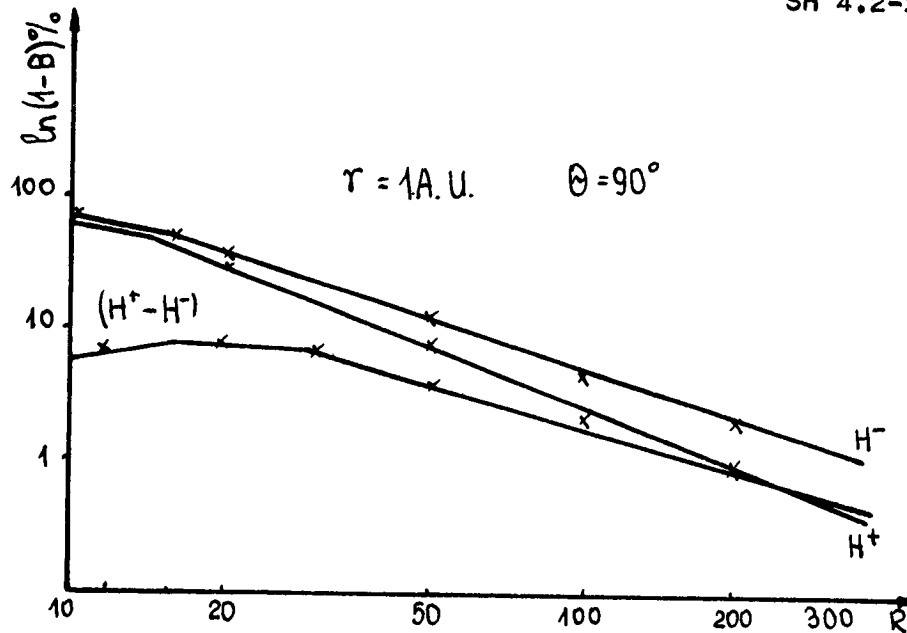


Fig. 2

data obtained from the American space station. /4/ At a distance of 1-5 AU sufficiently good coincidence can be observed. It is especially worth noticing the existence of the maximum radial gradient in the region of 2-5 AU which coincides with the observed experimental data. In the data of Pioneer 10 and 11 no maximum was observed in the radial gradient distribution in the region of 2-5 AU /5/ and in relation to this, a divergence from the expected distribution can be noticed, obtained on the basis of a solution of the anizotropic diffusion equation type (1) with the boundary conditions  $\frac{\partial B}{\partial \varphi}|_{\varphi=0} = 0$  /6/ A solution of equation (1) with boundary conditions of the type  $\frac{\partial B}{\partial \varphi}|_{\varphi=0} \neq 0$  shows a small maximum. /7/

In this way it appears that the expected radial gradient distribution with distance depends on the choice of boundary conditions near the sun, that is to say on the physical conditions around the sun. The boundary condition  $\frac{\partial B}{\partial \varphi}|_{\varphi=0} = 0$  actually corresponds with the symmetrical distribution of density B, when for  $\varphi = 0$ , B = minimum.

The boundary condition  $\frac{\partial B}{\partial \varphi}|_{\varphi=0} \neq 0$  does not impose any demands on the distribution B, it results from the fact that all cosmic ray particle streams are at an equal zero for  $\varphi = 0$ . Accordingly, it is seen that the anizotropic diffusion equation type (1) describes the behaviour of cosmic ray particles  $\gg 2-3$  GV in interplanetary space, however in solving it the physical conditions around the sun must be taken into consideration as these are effected considerably by the boundary conditions for  $\varphi = 0$ . It is especially worth noticing the fact the energy spectrum for an 11-year variation in the case of  $H^+$  is softer than for  $H^-$ . Apart from this it would be an unusually important experimental confirmation of 22-year variation spectrum caused by par-

title drift during a period of 2 consecutive 11-year cycles of solar activity.

#### REFERENCES

1. Vlasov V.I. Geomagnetism and Aeronomy, Vol. XIX, No 3, p. 401, 1979
2. Timothy A.F. et al, Solar Phys. Vol. 42, NL, p. 135, 1975
3. Dorman L.I. "Cosmic Rays", North - Holland Publishing Company - Amsterdam, Oxford, American Elsevier Publishing Company, INC - New York, 1974
4. Venkatesan D. et al, Journal of Geophysical Res. Vol.89, No 6A, p. 3735, June 1, 1984
5. Mc Kibben R.B., et al, 1982 Ap. J. 254, L 23
6. Alania H.V., et al, Izv. AN SSSR, Ser. fiz., Vol. 48, No 11, p. 2103.
7. Alania H.V., et al, Geomagnetism and Aeronomy, Vol. 17, No 2, p. 131, 1977

# LATITUDINAL GRADIENTS OF COSMIC RAYS AND THE POLARITY REVERSAL OF THE HELIOSPHERIC MAGNETIC FIELD A PRELIMINARY EVALUATION

G Newkirk, Jr  
National Center for Atmospheric Research, Boulder, Colorado

J A Lockwood  
University of New Hampshire, Durham, New Hampshire

M Garcia-Muñoz  
and  
J A Simpson  
University of Chicago, Chicago, Illinois

*1 Introduction* A central uncertainty in understanding the propagation and modulation of galactic cosmic rays is whether or not the cross-field drift of particles in the large-scale heliospheric magnetic field plays an important role (Burlaga, 1983, Jones, 1983). Studies of measured differences in various cosmic ray properties between epochs having positive and negative polarity of the heliospheric field have led to inconclusive results. A major uncertainty is the interpretation to be placed on differences in behavior between successive solar cycles separated by approximately 11 years, accidental differences from cycle to cycle may be confused with differences which are truly dependent upon the polarity of the field.

Since theoretical models of cosmic ray propagation including drifts predict the presence of an unambiguous latitudinal gradient of particle flux with respect to the heliospheric current sheet, one might expect that observation of this parameter could provide a means of resolving the question. However, neither analyses of the latitudinal gradient at one rigidity (Newkirk and Fisk, 1985) nor of the rigidity dependence of this parameter during the last solar minimum (Newkirk *et al.*, 1985) have done so. The reason for this failure is that models both with and without large-scale drifts can be adjusted within reasonable limits to provide agreement with the observations.

However, if drift effects are significant, the gradient of cosmic rays with respect to the current sheet should exhibit a *strong* sensitivity to the polarity of the large-scale magnetic field in the heliosphere (Jokipii and Kopriva, 1979, Kota and Jokipii, 1982). For example, at 2 GV and an inclination of the current sheet to the solar equator of  $30^\circ$ , the latitudinal gradient should increase from  $-3\% AU^{-1}$  in the 1969-80 cycle to  $-13\% AU^{-1}$  in the 1980-90 cycle. Even though the current sheet is usually more complex than a plane inclined to the solar equator and the observations represent the average of a variety of inclinations, this four-fold increase in the magnitude should provide unambiguous evidence for the importance of drifts. Naturally, models without drifts are insensitive to the polarity of the large-scale field.

This investigation provides preliminary answers to the questions (1) Does the latitudinal gradient change as predicted by the drift-dominated models? and (2) Does the rigidity dependence of the latitudinal gradient display any sensitivity to the polarity of the field?

*2 Data Analysis* Our approach is to examine the gradient of cosmic ray flux in ecliptic latitude with respect to the current sheet at 1 AU for equivalent epochs before and after the reversal of the large-scale solar magnetic field in late 1980. We use synoptic K-coronameter observations to locate the position of the coronal current sheet, which we assume projects radially out to 1 AU according to the locally observed solar wind speed. The methodology is described in detail in Newkirk and Fisk (1985) and Newkirk *et al.* (1985). Cosmic ray fluxes between 0.9 GV and 35 GV (see Table) provide the basic data. The epochs chosen for the comparison are DOY 1 1971 to DOY 250 1972 and DOY 1 1983 to DOY 140 1984. Both periods include the early recovery stage of cosmic ray modulation and occur when the configurations of polar coronal holes and the current sheet were roughly similar (Figure 1). Daily mean fluxes were used throughout the study and, since we are concerned with the steady-state distribution of cosmic rays, days when the

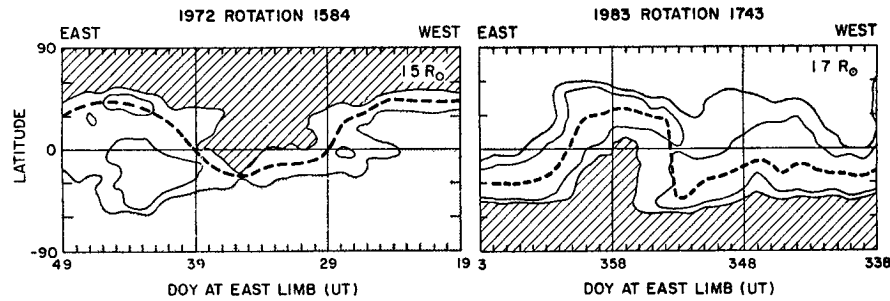


Fig 1 Synoptic contour maps of the polarization-brightness product of the K-corona allow the "band of coronal streamers" and the assumed location of the coronal current sheet (heavy dashed) to be located for typical rotations in 1972 and 1983. For clarity only two contour levels are shown. Cross hatched and stippled areas indicate positive and negative magnetic polarities of the dominant magnetic field in the polar coronal holes as inferred from either a potential extrapolation of the photospheric fields or the polarity of the interplanetary field. During both epochs, the current sheet extends up to  $35^\circ$  from the equator.

interplanetary medium was disturbed or when solar energetic particles contaminated the record were excluded from the analysis. For the purposes of this study we have defined as disturbed any day influenced by a classical Forbush decrease in the Mt. Washington neutron monitor data. Days contaminated by solar energetic particles were identified in the IMP ( $> 106$  MeV) channel and, to insure homogeneity, the same days were eliminated from all three records.

**3 Results** Figure 2 contains an example of the profile of cosmic ray flux with respect to the heliospheric current sheet. The scatter of the individual daily values indicates that considerable variation unrelated to the separation of the earth from the current sheet is present. However, a least-means-square fit of the form

$$U = a_0 + a_1 \sin^2 \lambda_{mg},$$

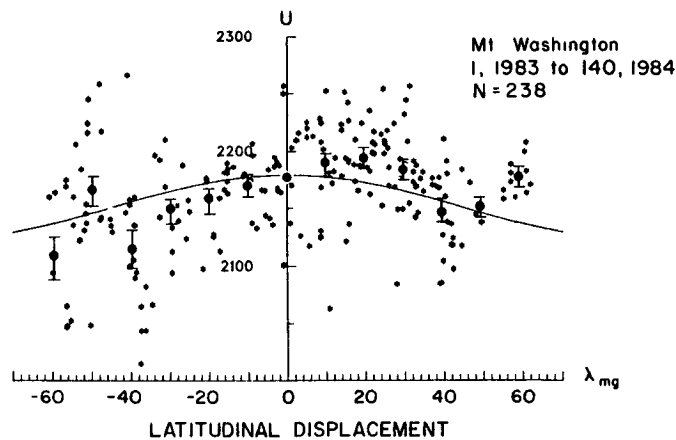


Fig 2 An example of the latitudinal variation detected in the individual daily values of cosmic ray flux (\*) and in the means of each  $10^\circ$  interval (●). Range lines give the standard deviations of the means. The smooth curve is the least-mean-square fit of the equation to the daily values. For this example  $a_0 = 2179 \pm 3$ ,  $a_1 = -56 \pm 13$ .

where  $\lambda_{mg}$  is the inferred separation in ecliptic latitude between the Earth and the current sheet, is able to define the parameter  $a_1$  with a precision of 20 to 30% for most cases. Of course, longer data intervals containing more points would produce a more precise result, however, the additional data are not yet available for the post-1980 interval and the pre-1980 interval has been limited deliberately to include approximately the same number of data points in both sets. The rela-

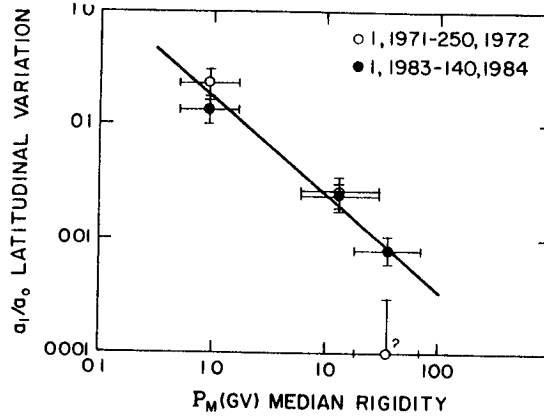


Fig 3 The rigidity dependence of the relative latitudinal gradient  $-a_1/a_0$  shows no significant difference between the 1971-72 and the 1983-84 intervals

latitudinal gradients  $a_1/a_0$  appear in the Table along with  $P_F$ , the probability that the coefficient  $a_1$  is zero according to Fisher's F-test of the deviations of the daily points from the curve (Bevington, 1969). Although the data are noisy, all except the Huancayo value for 1971-72 are reasonably well established. The rigidity dependence of the latitudinal variation is displayed graphically in Figure 3. Vertical range lines indicate the standard error of estimate of the quantity  $a_1/a_0$  while horizontal range lines delineate the limits within which 50% of the cosmic ray counting ray is generated. The straight line indicates the variation  $P^{-0.72}$  estimated from a larger rigidity range for the four year period 1974-77 (Newkirk, *et al* 1985).

Table  
Parameters of the Cosmic Ray Monitors  
and  
Relative Latitudinal Gradients

Detector System	Reference	$P_M (GV)$	1971-72		1983-84	
			$-a_1/a_0$	$P_F$	$-a_1/a_0$	$P_F$
Huancayo	Simpson and Wang, 1970	35 (18-70)	$0.001 \pm 0.002$	$6 \times 10^{-1}$	$0.008 \pm 0.002$	$8 \times 10^{-3}$
Mt Washington	Lockwood and Webber, 1967, 1979	13 (6-30)	$0.026 \pm 0.008$	$1 \times 10^{-3}$	$0.024 \pm 0.006$	$10^{-5}$
IMP-8(106 MeV)	Garcia-Muñoz <i>et al</i> , 1975	0.9 (0.5-1.7)	$0.23 \pm 0.07$	$5 \times 10^{-4}$	$0.14 \pm 0.03$	$2 \times 10^{-5}$

$P_M$  = median rigidity (Newkirk, *et al*, 1985), ( ) = 50% range

4 *Conclusions and Discussion* Within the statistical limits imposed by the currently available data and the noise inherent in the determination of the latitudinal gradient, no evidence for the expected change in the latitudinal gradient from pre-1980 to post-1980 epochs can be found. In addition, the rigidity dependence of the gradient appears to be the same in the two epochs. Thus, we can find no evidence for a sensitivity of the latitudinal gradient to the polarity of the large-scale heliospheric magnetic field such as has been predicted by models incorporating particle drifts.

5 *Acknowledgements* The National Center for Atmospheric Research is sponsored by the National Science Foundation. The research of J. A. Lockwood was supported in part by the National Science Foundation under Grant ATM-8304486 while that of M. Garcia-Munoz and J. Simpson was supported by NASA contract NAS-5-25731 and NSF Grant ATM-82-06418. The authors thank D. G. Sime for reading and criticizing the manuscript before submission.

#### 6 References

- Bevington, P. R., *Data Reduction and Error Analysis for the Physical Sciences*, McGraw-Hill, New York, 1969, p. 200.
- Burlaga, L. F., Understanding the heliosphere and its energetic particles, *Proc. 18th International Cosmic Ray Conf., Invited Reviews*, Bangalore, 12, 21, 1983.
- Garcia-Munoz, M., G. M. Mason, J. A. Simpson, The cosmic-ray age deduced from the  $^{10}\text{Be}$  abundance, *Astrophys. J. Lett.*, **201**, 145, 1975.
- Jokipii, J. R., and D. A. Kopriva, Effects of particle drift on the transport of cosmic rays. III. Numerical models of galactic cosmic-ray modulation, *Astrophys. J.*, **234**, 384, 1979.
- Jones, F. C., Cosmic ray modulation and anomalous component, *Rev. Geophys. and Space Physics*, **21**, 318, 1983.
- Kota, J., and J. R. Jokipii, Cosmic rays near the heliospheric current sheet, *Geophys. Res. Lett.*, **9**, 656, 1982.
- Lockwood, J. A., and W. R. Webber, Differential response and specific yield functions of cosmic ray neutron monitors, *J. Geophys. Res.*, **72**, 3395, 1967.
- Lockwood, J. A., and W. R. Webber, Cosmic ray modulation during solar activity cycle 20, *J. Geophys. Res.*, **84**, 120, 1979.
- Newkirk, G., Jr., and L. A. Fisk, Variation of cosmic rays and solar wind properties with respect to the heliospheric current sheet, I. 5 GeV protons and solar wind speed, *J. Geophys. Res.*, **90**, 3391, 1985.
- Newkirk, G., Jr., J. Asbridge, J. A. Lockwood, M. Garcia-Munoz and J. A. Simpson, Variations of cosmic rays and solar wind properties with respect to the heliospheric current sheet, II. Rigidity dependence of the latitudinal gradient of cosmic rays at 1 AU, *J. Geophys. Res.*, submitted April 1985.
- Simpson, J. A. and J. R. Wang, The eleven-year and residual solar modulation of cosmic rays (1952-1969) *Astrophys. J.*, **161**, 265, 1970.



THE INFLUENCE OF NONSTATIONARITY OF THE SOLAR  
ACTIVITY AND GENERAL SOLAR FIELD ON MODULATION  
OF COSMIC RAYS

Zusmanovich A.G., Kryakunova O.N., Churunova L.F.,  
Shvartsman Ya.E.

Institute of Ionosphere of AN KazSSR, 480068,  
Alma-Ata, USSR.

ABSTRACT. It was conducted numerical model of the propagation of galactic cosmic rays in the interplanetary space for the case when the modulation depth determined by the level of the solar activity changed in time. Also the contribution of the particles drift in the regular field was calculated and it was shown the agreement with experimental data about the ratio of protons and electrons in two solar activity minima.

The stationary spherical-symmetric approach of weak modulation was applied for the investigation of galactic cosmic ray modulation /1-3/. For the cosmic rays intensity at the Earth's orbite we write

$$n(r, t) = n_0 \exp \left[ - \int_r^{r_0} \frac{U(r)}{\alpha(r)} dr \right], \quad (1)$$

where  $U$  is the solar wind velocity,  $\alpha$  is the diffusion coefficient,  $r_0$  is the dimension of modulation region. We'll consider the simple modelling problem. Let us break the integral in (1) for  $N$  equal parts assuming  $U_i / \alpha_i$  is constant for each interval  $\Delta r$ . Then we have for  $K$ -moment in case, when  $\alpha = \text{const}(r)$

$$\frac{n_K}{n_0} = \exp \left[ - \sum_{i=0}^N y_{iK} \right], \quad y_{iK} = \frac{U_{iK}}{\alpha_{iK}} \Delta r \quad (2)$$

and for gradient  $g_{iK}$

$$g_{iK} = \left\{ \exp \left[ - \sum_{i=1}^N y_{iK} \right] - \exp \left[ - \sum_{i=1}^N y_{iK} \right] \right\} / 2 \exp \left[ - \sum_{i=1}^N y_{iK} \right] \Delta r, \quad i \geq 1 \quad (3)$$

In case when  $\alpha \sim r$

$$\frac{n_K}{n_0} = \prod_{i=0}^N \left[ \frac{1+6i}{1+6(i+1)} \right]^{y_{iK}}, \quad y_{iK} = \frac{U_{iK}}{\alpha_{iK}} r_i, \quad r_i = 1 a u, \quad (4)$$

$$g_{iK} = \left\{ \prod_{i=1}^N \left[ \frac{1+6i}{1+6(i+1)} \right]^{y_{iK}} - \prod_{i=1}^N \left[ \frac{1+6i}{1+6(i+1)} \right]^{y_{iK}} \right\} \times \left\{ 2 \prod_{i=1}^N \left[ \frac{1+6i}{1+6(i+1)} \right]^{y_{iK}} \Delta r \right\}^{-1} \quad (5)$$

The interval  $\Delta r$  was chosen equal to 6 a.u. The values  $y_{ik}$  were generated as follows: for  $t=0$  (i.e.  $k=0$ ) the sum of all terms of  $y_{ik}$  sub i was filled up by numbers  $a_0$  which were chosen so as their sum is equal to 1.8 (that correspond to modulation coefficient at solar activity maximum). Hence it follows  $a_0=0.164$ . For the first column  $y_{0k} = a_0 - kb$  to  $k=15$  then  $y_{0k} = y_{15} + kb$  ( $15 < k \leq 30$ ) and again  $y_{0k} = y_{30} - kb$  ( $k > 30$ ). The value  $b$  was chosen equal to 0.01. Thus the values  $y_{0k}$  (in Fig. 1a) represent the solar activity cycle. The results obtained from (2) and (4) have been shown in Fig. 1a. One can see that the lag of cosmic rays intensity increase is bigger in case when the diffusion coefficient is independent on the distance from the Sun. The results of

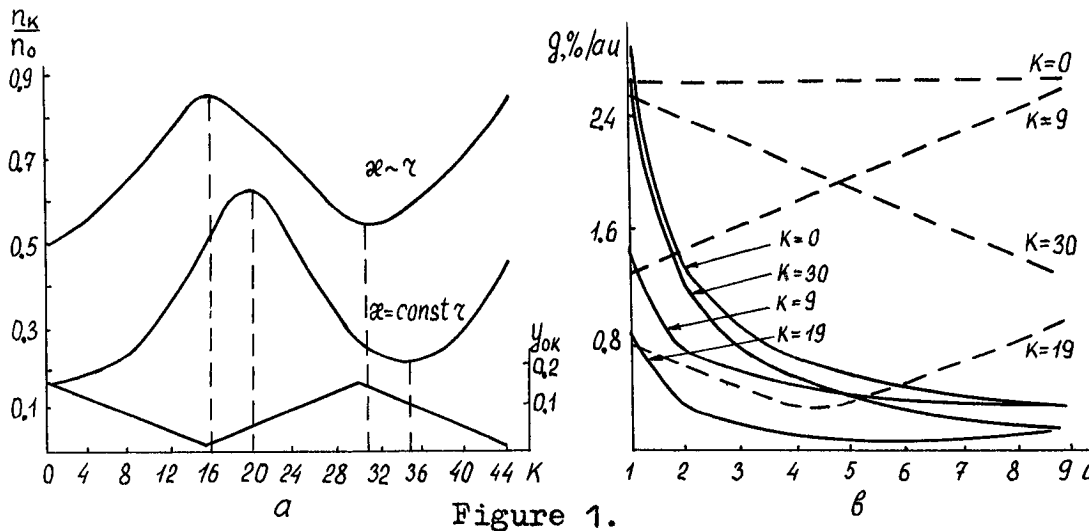


Figure 1.

the calculations of radial gradient for  $\alpha = \text{const}$  ( $r$ ) (dotted line) and  $\alpha \sim r$  (solid line) have been shown in Fig. 1b. We have constant gradient for uniform filling of modulation region ( $k=0$ ). Then gradient increases with distance at decreased "solar activity" branch and it decreases at the increased branch ( $k=30$ ). The change of gradient with distance has complicated form at transition period ( $k=19$ ). Introducing the dependence  $n_k/n_0$  on the particle rigidity  $R$  through the dependence  $\alpha(R)$  in the form [4/

$$\alpha(R) = \alpha_0 f(R), \text{ where } f(R) = \frac{R^{1.5} (R + R_0)^{1.5}}{(1 + R_0)^{1.5} (R^2 + 0.88)^{0.5}}, \quad (6)$$

we have for  $\alpha = \text{const}(r)$

$$\frac{n_k}{n_0} = \exp \left[ -\frac{1}{f(R)} \sum_{i=0}^N y_{ik} \right] \quad (7)$$

and for  $\alpha \sim r$

$$\frac{n_k}{n_0} = \prod_{i=0}^N \left( \frac{1 + 6i}{1 + 6(i+1)} \right)^{\frac{y_{ik}}{f(R)}} \quad (8)$$

Energy spectra of the cosmic rays intensity normalized at the solar activity minimum have been shown in Fig.2. The solid lines correspond to the case  $\alpha = \text{const}(r)$ , dotted lines -  $\alpha \sim r$ , symbols are values  $k$ -different moments of "solar activity" cycle. The curves with  $k=0$  and  $k=30$  correspond to the same "solar activity" level, however the curves differ greatly in appearance. Analogously the curves with  $k=7, 37$  and  $k=23$  correspond to the same "solar activity" level.

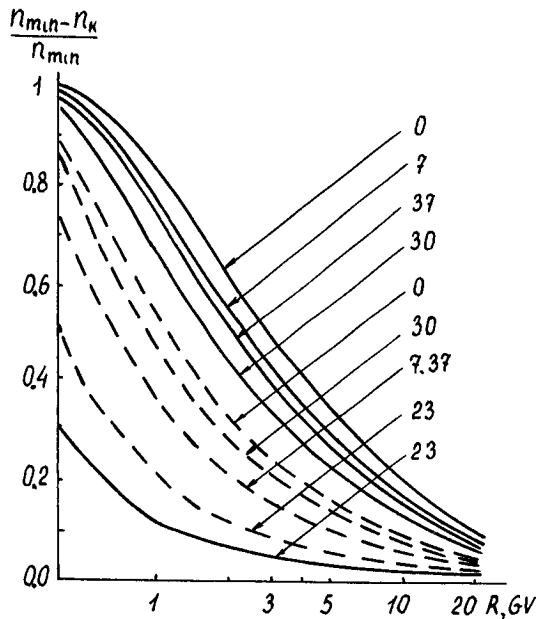


Figure 2.

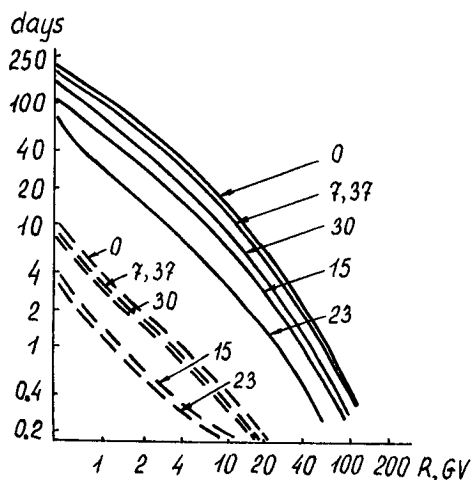


Figure 3.

In /9/ the values of the absolute coefficients of "usual" convective-diffusion modulation (determined by the solar activity level)  $K_1$  and effect of the influence of general solar fields  $K_2$  were determined by investigation the con-

The influence this factor on the lag time modulation effects relatively to changes of the solar activity level is shown in Fig.3 (solid lines for case  $\alpha = \text{const}(r)$ , dotted lines for the case  $\alpha \sim r$ , symbols are values  $k$ ). The values of the lag time  $\tau_i$  were calculated with method described in /5/, then total lag time determined by  $\tau = \sum_{i=1}^n \tau_i$

Thus one can see that the nonstationarity of modulation properties of the solar wind and its distribution with distance from the Sun essentially influences on the energy spectra of particles, gradients of cosmic rays intensity in the interplanetary space and the lag time of modulation effects relatively to changes of the solar activity level observed near the Earth when the dimension of the cosmic ray modulation region is greater than 50 a.u.

Moreover the particles drift in the regular magnetic field connected with general solar field /6-8/ gives certain contribution to the break of the relation between cosmic ray intensity and the observed solar activity level.

nection between the cosmic ray intensity and HL-index of solar activity. On the whole the observed intensity is determined in this model by

$$J(\varepsilon, \kappa_1, \kappa_2) = J_0(\varepsilon) \exp \left[ -\frac{\kappa_1}{f(R)} + \frac{\kappa_2}{f_2(R)} \right], \quad (9)$$

where  $f(R)$  is the same that in (6),  $f_2(R) = \lambda \rho / (\lambda^2 + \rho^2)$ ,  $\rho$  is Larmor radius,  $\lambda$  is determined from (6), ( $\alpha = \lambda v / 3$ ).

$\frac{n_{1977}}{n_{1965-66}}$

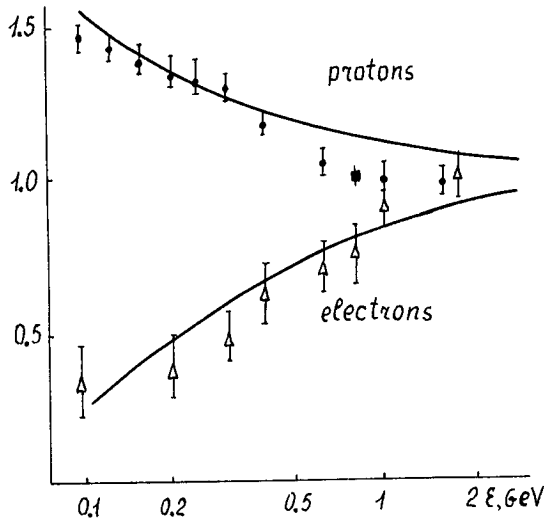


Figure 4.

for these ratios in the energy interval 0.1 - 2 GeV. It seems a good agreement between our calculations and the experimental ratios.

We have shown that the effects connected with nonstationarity of the modulation properties of the solar wind and the particles drift in the regular ray field exerts essential influence on galactic cosmic ray modulation.

#### REFERENCES.

1. Webber W.R. Proc. 16th ICRC, Kyoto, 1979, 14, 253.
2. Owens A.J. Rev. Geophys. Space Phys., 1979, 17, 560.
3. Antonova V.P., et al. Izv. AN SSSR. Ser. fiz., 1981, 45, 1287.
4. Zusmanovich A.G. Proc. 16th ICRC, Kyoto, 1979, 3, 366.
5. Zusmanovich A.G., Kryakunova O.N. Proc. 18th ICRC, Bangalore, 1983, 3, 19.
6. Krainev M.B., Stozhkov Yu.I. Izv. AN SSSR. Ser. fiz., 1979, 43, N 12, 2603.
7. Alania M.V., Dorman L.I. Proc. 16th ICRC, Kyoto, 1979, 3, 57.
8. Zusmanovich A.G. Proc. 18th ICRC, Bangalore, 1983, 3, 118.
9. Zusmanovich A.G. et al. Proc. 18th ICRC, Bangalore, 1983, 3, 102.
10. Webber W.R. et al. Proc. 18th ICRC, Bangalore, 1983, 3, 35.

The sign before  $\kappa_2$  is positive for 1954 and 1976, and negative for 1965. In [9] it was found that  $\kappa_1 = 0.21 \pm 0.08$ ;  $0.32 \pm 0.10$  and  $0.35 \pm 0.10$  for 1954, 1965 and 1976 respectively, the values  $\kappa_2$  are equal  $+0.14 \pm 0.03$ ;  $-0.09 \pm 0.04$  and  $+0.11 \pm 0.03$  for the same periods. Hence we have:

$$\frac{J_{1977}}{J_{1965}} = \exp \left[ -\frac{0.03}{f(R)} + \frac{0.2}{f_2(R)} \right] \quad (10)$$

The results of the calculations using (10) for  $R_0 = 15$  GV have been shown by curves in Fig. 4 for protons and electrons. In this figure we have presented the direct experimental data from [10].

THE EFFECT OF THE NEUTRAL SHEET STRUCTURE OF THE  
INTERPLANETARY MAGNETIC FIELD ON COSMIC RAY  
DISTRIBUTION IN SPACE

Alania M.V., Aslamazashvili R.G., Bochorishvili T.B.,  
Djapiashvili T.V., Tkemaladze V.S.

The Institute of Geophysics, Georgian Academy of  
Science, Z.Rukhadze str.1, 380093, Tbilisi

ABSTRACT

1. The results of the numerical solution of the anisotropic diffusion equation are presented in the paper. It is shown that the modulation depth of galactic cosmic rays is defined by degree of curvature of the neutral current sheet in Heliosphere. 2. The effect of the regular interplanetary magnetic field (IMF) on cosmic ray anisotropy in the epoch of solar activity minimum (in 1976) is analysed by the data of the neutron super-monitors of the world network and the heliolatitudinal gradient and cosmic ray diffusion coefficient are defined.

The theoretical model. The recent investigations/1,2/ show that the neutral current sheet changes its range significantly for 11-year period of the Sun's cycle and can be one of the reasons of cosmic ray modulation. Really, the curvatures of the interplanetary magnetic field lines of forces (IMF) correspond to the waved structure of the neutral sheet that is identical with the appearance of high-value zenithal component of IMF. Hz. The experimental observations in space show that Hz component of IMF is, in the mean, a high value  $\sim 2 \cdot 10^{-9} \text{ nT} / 3/$  and therefore, its account in solution of cosmic ray anisotropic diffusion equation is of necessity.

The anisotropic diffusion equation /4/ for the stationary case is used:

$$\nabla_i (\mathcal{D}_{ik} \nabla_k n) - \nabla_i (n u_i) + \frac{1}{3R^2} \frac{\partial}{\partial R} (R^3 n) \nabla_i u_i = 0 \quad (1)$$

where  $\mathcal{D}_{ik}$  - the tensor coefficients of diffusion,  $n$  and  $R$  - the density and the rigidity of the particle, and  $u_i$  - solar wind velocity. It is suggested in equation solution (1) that the radius of the modulation volume is 50 a.u.,  $u = 4.10 \text{ cm/s}$ , the diffusion coefficient along the magnetic field has the form

$$\mathcal{D}_{||} = \mathcal{D}_0 \text{EXP}(R_1/R) \cdot (R_2 + R)^2 \varphi(\theta) \cdot \phi(r) \quad (2)$$

where  $\mathcal{D}_0 = 10^{22} \text{ cm}^2/\text{sec}$ ,  $R_1 = 0.05 \text{ GV}$ ,  $R_2 = 3 \text{ GV}$ ,  $\varphi(\theta)$  is changed in the range 1-5 from the helioequator to the near-polar region, and  $\phi(r) = 1 + \alpha(r/r_0)$ , where  $\alpha = 0, 1$ ,  $r_0$  - modulation region radius.

The range of the waved structure of the neutral current sheet is given in the form

$$\gamma = A \gamma_0 (\tau/\tau_0) \cos(16 \pi \tau/\tau_0) \quad (3)$$

$A$  and  $\gamma_0$  are chosen so that the neutral current sheet on the Earth's orbit ( $\tau = 1.5 \cdot 10^{13}$  cm) is at the heliolatitude  $10^\circ$ . In this case  $A = 5$  and  $\gamma = 10^\circ$ .

The equation (1) is solved by the net method for the two dimensional case ( $\tau, \theta$ )  $\frac{\partial \eta}{\partial \phi} = \frac{\partial^2 \eta}{\partial \phi^2} = 0$  and the results are presented in Fig. 1a, b. The curve (a) shows the change of the relative density of 10 Gev energy cosmic rays, when the curvature (3) is defined by the parameter  $A = 0.5$ , i.e. the maximum removal of the neutral sheet from the equator of the Sun on the Earth's orbit is  $L = 2.5 \cdot 10^{12}$  cm. The curve (b) shows the case, when  $A = 0$  and  $L = 0$ . It is seen that, really, with the increase of neutral current sheet range, the significant cosmic ray modulation is expected, which by its value is compared with the amplitude of 11-year variation in the energy region 10-20 Gev.

The experimental data on cosmic ray anisotropy.

It has been shown in our previous paper /5/ that the particle drift effect at the expense of the gradient and the curvature of the interplanetary magnetic field (IMF) is revealed singlevaluedly, especially in the epoch of solar activity minimum. It is known that the particle drift effect in distribution of cosmic ray density and anisotropy can be calculated with the antisymmetric part of the anisotropic diffusion tensor /6/, but, in our opinion, this problem is not always clear, and therefore, sometimes the incorrect interpretation is made. E.g. as it has been done in the report /7/ while reviewing paper /5/, where the epoch of solar activity minimum 1965- has been considered.

Four neutron super-monitor stations: Kiel, Norikura, Lomnitsky Stif and Khafelakar have been chosen for revealing the effect of the particle drift in cosmic ray anisotropy (1976). The data of these stations were free from the trends with the periods more than 24 hours and the harmonic coefficients  $A_1$  and  $B_1$  for every day were defined. Then they were averaged depending on the Earth's location in "+" and "-" sectors of IMF. ("+" corresponds to the direction of the magnetic lines of forces from the Sun, and "-" toward the Sun). Then, the values  $A_\tau$  and  $A_\phi$  have been defined in cosmic space taking into account the drift into the Earth's magnetic field and the coupling coefficients /8/ and the means by all four stations were found. The results are presented in Fig. 2, where the solid vectors correspond to the theoretical results, and the dashed ones- the experimental data of observation.

It can be seen that a good accord is existed there.

Having the values  $A_\tau$  and  $A_\phi$  for "+" and "-" sectors of IMF the algebraic equations have been constituted of the form:

$$A_r^{\pm} = \mathcal{D}_{rr} \frac{\partial n}{\partial r} \pm \mathcal{D}_{r\theta} \frac{\partial n}{\partial \theta} - 1.5 u \cdot B ; \quad A_{\varphi}^{\pm} = \mathcal{D}_{\varphi r} \frac{\partial n}{\partial r} \pm \mathcal{D}_{\varphi \theta} \frac{\partial n}{\partial \theta} \quad (4)$$

Solving the system of equations (4) the mean solar wind velocity is found, and the ratios  $\alpha = \mathcal{D}_{\perp} / \mathcal{D}_{\parallel}$  and  $\alpha_1 = \mathcal{D}_{\perp} / \mathcal{D}_{\parallel}$  are estimated. ( $\mathcal{D}_{\perp}$ ,  $\mathcal{D}_{\parallel}$  and  $\mathcal{D}_{\varphi}$  - the transversal, Hall and parallel diffusion coefficients) and the heliolatitudinal gradient and the diffusion coefficient are estimated.

#### Discussion and conclusion

1. The degree of curvature of the IMF neutral layer influences appreciably cosmic ray modulation. The modulation depth is large during the extend of the waved neutron layer and can be compared with the amplitude of 11-year variation in the energy region 10-20 GeV.

2. The particle drift effect at the expense of the gradient and the curvature of IMF is revealed singlevaluedly in Cosmic ray anisotropy in the epoch of solar activity minimum in 1976.

3. The inverse problem is solved by the equation (4). The solar wind velocity  $u = 455 \text{ km/s}$  (the direct observations by /9/ give  $u = 450$ ) and ratio  $\alpha$  of the transverse diffusion coefficient  $\mathcal{D}_{\perp}$  to the parallel one  $\mathcal{D}_{\parallel}$  ( $\alpha = 0.3$ ) are defined.

It is of interest to note that the same value has been obtained for 1965 too.

4. The heliolatitudinal gradient and the diffusion coefficient have been estimated from (4) with the given radial gradient of cosmic rays constituting

$\nabla_r n = (1-2) \% / \text{a.u.}$   
 $\nabla_{\theta} n = (0.2-0.4) \% / \text{a.u.}$ ,  $\mathcal{D}_{\parallel} = (0.6-1.3) 10^{23} \text{ cm}^2/\text{s}$  respectively.

#### REFERENCES

1. Hoeksema J.T., Wilcox S.M. and Scherrer P.H., SUIPR, Report №924, Stanford, California, 1982.
2. Thomas B.T. and Goldstein B.E., Solar Wind Five, NASA, p.44, 1982.
3. Slavin J.A. and Smith E.L., Solar Wind Five, NASA, p.323, 1982.
4. Dorman L.T. "Astrophizicheskie aspekty kosmicheskikh luchej". "Nauka", M. 1975.
5. Alania M.V. et al., 18th ICRC, Bangalore, India, L.P., Vol. 10, pp. 91, 1983.
6. Jokipii J.R., Levy E.H. and Hubbard W.B., Astr.J., 213, 864-868, 1977.
7. Jones F.G., 18th ICRC, Bangalore, India. Invited and Rapporteur Papers, Vol. 12., p.379, 1983.
8. Nagashima K. et al., Coup. Coef. of Cosmic Rays, Nagoya, Japan, 1982.

9. King J.H. Interplanetary Medium Data Book, NSSDC/WDC-A, 1977.  
 10. Webber W.R. and Lockwood J.A., 18th ICRC, Bangalore, India, L.p., Vol.10, p.22, 1983.

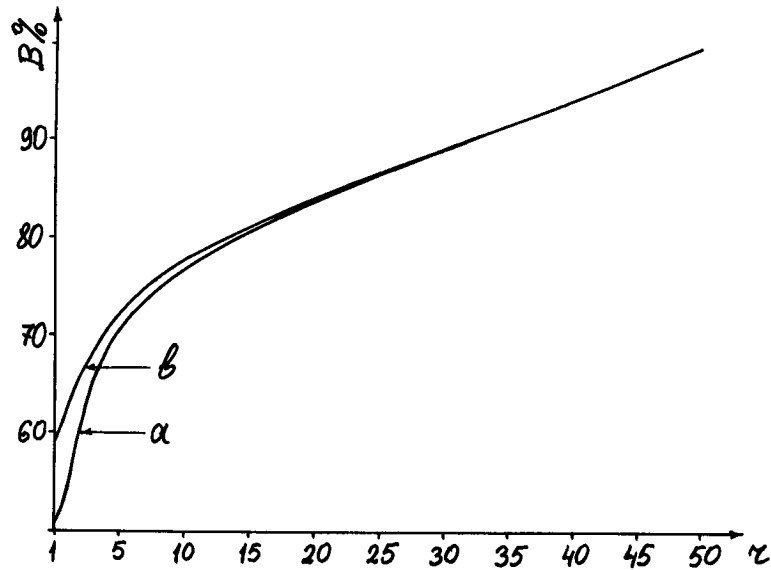


Fig. 1.

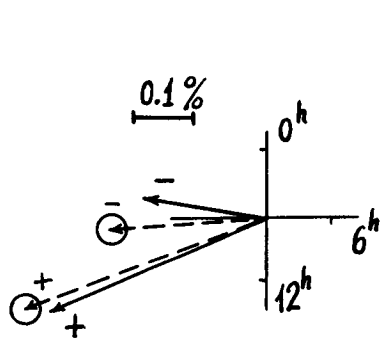


Fig. 2.

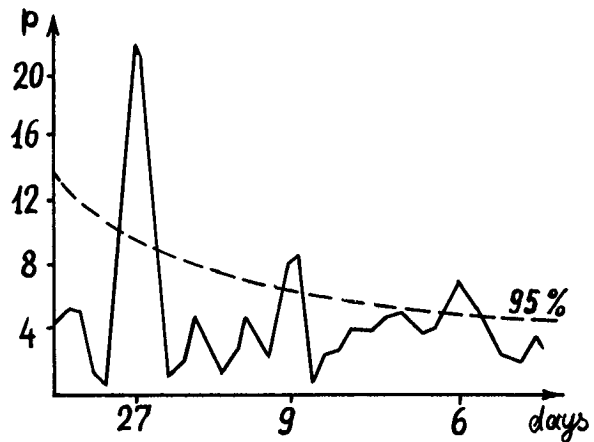


Fig. 3.



SH-4.2-19

ON THE INFLUENCE OF THE HELIOMAGNETOSPHERIC  
PERIPHERY ON THE GALACTIC COSMIC RAYS

Krainev M.B., Stozhkov Yu.I.,

P.N. Lebedev Physical Institute of the Academy  
of Sciences of the USSR, Leninsky Prospect, 53,  
117924, Moscow, USSR

Charakhchyan T.N.

Institute of Nuclear Physics, Moscow State  
University, 119899, Moscow, USSR

ABSTRACT

The suggestion is substantiated that the periphery of the heliomagnetosphere - the region which properties depend on both solar wind and interstellar space parameters - play much more important role in the solar modulation of the galactic cosmic rays than usually believed.

1. INTRODUCTION.

As a rule the electromagnetic fields in the galactic cosmic ray modulation region are specified by the extrapolation of those known at  $r \leq 30$  AU. Clearly the restriction imposed on the possible modulation region characteristics in this scheme also limits the range of the explicable by means of it galactic cosmic ray phenomena. Let us call the galactic cosmic ray modulation accomplished in conformity with the above scheme the "internal" modulation.

The mentioned extrapolation is valid only in the case when the whole modulation region is inside the supersonic and superalfvenic solar wind which properties are controlled entirely by the Sun. In this work the suggestion is substantiated that the galactic cosmic rays should (and probably do) undergo considerable transformation in the transition region between the supersonic solar wind and the undisturbed by the Sun galactic space.

2. THE THEORETICAL REASONS.

First of all note the discrepancy of the "internal" modulation scheme during the periods when the large-scale magnetic field distribution in the quiet (i.e. undisturbed from the outside) solar wind is a dipole-like one. In this case because of the space charge the potential of the inside of the modulation region boundary surface considerably depends on the heliolatitude while the exterior of the same surface conforming to the undisturbed galactic space is equipoten-

tial. To settle this contradiction the transition region should be included in the galactic cosmic ray modulation region<sup>/1,2/</sup>.

In /3-5/ the processes in this transition region are considered for the explanation of some galactic cosmic ray effects. It is important that for these explanations the fundamental difference of the modulation parameters from those of the Quiet solar wind is necessary: the nonradial flow of plasma /4,5/ and the large latitude component of the interplanetary magnetic field /3-5/.

At the same time the qualitative character of /3-5/ should be noted as well as the obvious insufficiency of the method suggested in /1,2/ to allow for the transition region influence on the galactic cosmic rays. This method using the Liouville theorem and the potential difference between the inside points of the quiet solar wind and the infinity (so called the "external" modulation of the galactic cosmic rays) takes into account only the charge distribution in the quiet solar wind and completely disregard the galactic space characteristics: the presence of the galactic magnetic and electric fields, the movement of the solar system through the interstellar matter and so on.

### 3. THE EXPERIMENTAL REASONS.

A. The most dramatic feature of the galactic cosmic rays which is evidently beyond the scope of the "internal" modulation is their behaviour in the low energy range ( $E \leq 80$  MeV/n) during 1971-1978 - the "anomalous component" (AC), /6/. The characteristics of these particles - their elemental and isotopic compositions, energy spectra - so differ from the expected ones that there are many advocates of the hypothesis /7/, according to which the source of the anomalous component is the interstellar neutral gas, i.e. AC does not have any bearing to the galactic cosmic rays. Yet some features in cosmic ray behaviour force us to regard the "anomalous component" as the natural part of the complex galactic cosmic ray phenomenon taking place during this period:

- 1) The time behaviour of the anomalous component fluxes is very similar to that of the protons and helium nuclei of higher energy;
- 2) The very important fact, connecting anomalous component with the protons, is the similar (and anomalous) behaviour of their radial gradients. With the growth of the solar activity in 1979-1980 the gradients of both anomalous component and protons of  $E=29-67$  MeV sharply drop off /8/.

SH-4.2-19

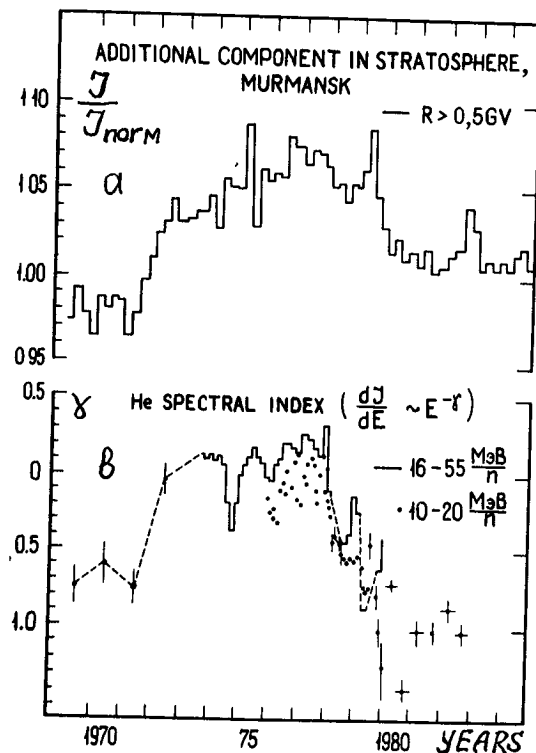


FIGURE 1

In Fig.1 the behaviour of the anomalous component (He spectral index:  $dJ/dE \sim E^{-\gamma}$ , /8,9/,8) is correlated with that of so called "the additional component in stratosphere", (a), which, as shown in /10/, is due to the primary H and He nuclei in the energy range 100-500 MeV/n.

The likeness of the behaviour of the anomalous component and of protons is rather difficult to understand from the viewpoint of the current hypotheses on their origin /6/. In /2/ we suggested the scheme of AC formation by the acceleration of low energy galactic cosmic rays in the process of their "external" modulation. The same process results in the considerable increase of higher energy particles.

B. The unusual from the viewpoint of the "internal" modulation the galactic cosmic ray phenomena take place during the periods of the inversion of the general magnetic field of the Sun (GMFS).

In /11-13/ we subdivided the galactic cosmic ray behaviour during GMFS inversion into two phenomena:

I - Due to the supposed attenuation of the interplanetary magnetic field strength the decrease of the galactic cosmic ray modulation so much the greater (and the more prolonged) the greater the particle energy is. This explanation of the "energetic hysteresis" is entirely in the scope of the "internal" modulation scheme.

II - The phenomenon depending on the type of GMFS inversion (characterized by the sign of the  $dM_z/dt$ , where  $M_z$  is the projection of the general magnetic field of the Sun magnetic dipole moment on the Sun rotation axis) delaying with respect to the first phenomenon by 1-2 years. We relate this delay to the location of the process responsible for the second phenomenon on the periphery of the helio-magnetosphere.

Fig.2 shows the galactic cosmic ray behaviour according to the stratospheric data (Murmansk,  $R=0.56V$ ) during the periods of GMFS inversions in 1969-71 ( $dM_z/dt > 0$ , a)

SH-4.2-19

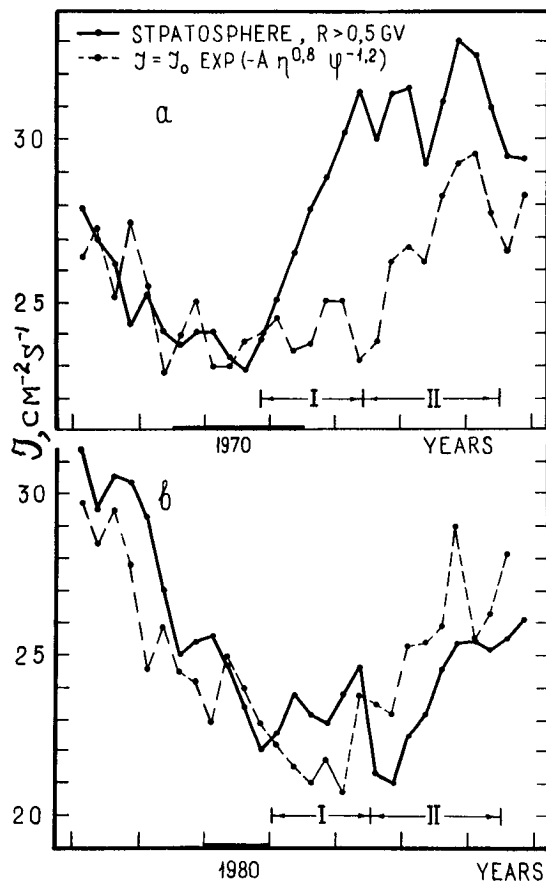


FIGURE 2.

and 1980 ( $dM_z/dt < 0$ , b) marked by the thick section on t-axes. The periods of I and II phenomena are shown as well. A dashed lines indicate the galactic cosmic ray intensity according to the expression

$$J = J_0 \exp(-A \cdot \eta^{0.8} \cdot \varphi^{-1.2}),$$

where  $\eta$  and  $\varphi$  are the number of sunspot groups and their mean heliolatitude, respectively. This expression is thought of as describing due to the Sun alone (i.e. "internal") and normal (i.e. in the absence of the "energetic hysteresis") galactic cosmic ray modulation. It is seen from Fig.2 that in the initial stage of the inversion anomaly (the first phenomenon) intensity quickly increases for both types of the inversion, this increase persisting during the second phenomenon in ( $dM_z/dt > 0$ )-inversion, but changing into decrease in ( $dM_z/dt < 0$ )-inversion.

**4. THE CONCLUSION.** To understand the galactic cosmic ray behaviour it is necessary to develop much more real model of the heliomagnetosphere than used now.

## REFERENCES

1. Krainev M.B. (1981), Proc.17 ICRC, Paris, 3, 357
2. Krainev M.B. (1981), Proc.17 ICRC, Paris, 3, 361
3. Ahluwalia H.S., (1979), Proc.16 ICRC, Kyoto, 12, 216
4. Krivoshepin P.A. et al, (1981), Proc.17 ICRC, Paris, 4, 33
5. Kravtsov N.G. et al, (1984), Izv.Akad.nauk SSSR, ser.fiz., 43, 2129
6. Simpson J.A., (1983), in "Compos. and Origin of Cosmic Rays"
7. Fisk L.A. et al, (1974), Astrophys.Journ., 190, L35
8. McKibben R.B. et al, (1983), Proc.18 ICRC, Bangalore, 3, 63
9. Garcia-Munoz M. et al, (1981), Proc.17 ICRC, Paris, 3, 270
10. Svirzhevskaya A.K. et al, (1985), Proc.this conf., SH 4.4-18
11. Krainev M.B. et al, (1983), Proc.18 ICRC, Bangalore, 3, 23
12. Krainev M.B. et al, (1983), Proc.18 ICRC, Bangalore, 3, 95
13. Krainev M.B. et al, (1984), Izv.Akad.nauk, ser.fiz., 43, 2100 (in russ.)

# SPATIAL DISTRIBUTION OF COSMIC RAYS IN MAGNETIC CYCLES OF THE SUN

M.V. Alaniya

Institute of Geophysics of the Academy of Sciences of Georgian SSR, Tbilisi, USSR

R.T. Gushchina, L.I. Dorman

Institute of Terrestrial Magnetism, Ionosphere and Radio Wave Propagation, USSR Academy of Sciences, 142092 Troitsk, Moscow Region, USSR

Space-time distribution of CR density  $B$  is determined from the solution of anisotropic diffusion equation (Dorman, 1965). The boundary problem is solved in a quasistationary (the delay of CR relative to cyclic variations of solar activity is taken into account) axisymmetric case under the following boundary conditions

$$\left. \frac{\partial B}{\partial r} \right|_{r=0} = 0; \quad B|_{r_0=1} = 1, \quad B|_{r=350GV} = 1,$$

where  $r$  is the distance from the Sun,  $r_0$  is the dimension of the modulation region,  $R$  is particle rigidity. The specificity of our modulation model is the use (in line with the works by Alaniya et al., 1981, 1983) of the empirical dependence of the free path of particles for scattering on the observed latitudinal distribution of solar activity. Another specific feature of the model is an account of an additional effect due to the drift of charged particles towards the helio-equator plane or backward, depending on the direction of the total magnetic field of the Sun.

The intensity of coronal radiation ( $\lambda = 5303\text{\AA}$ ) and the area of solar spots were chosen as indices of helio-activity. Out of many observed manifestations of solar activity these characteristics have been chosen in the assumption that their cyclic variations are a reflection of a corresponding manifestation of poloidal and toroidal components of the magnetic field of the Sun. Such interdependence was also pointed out by Parker (1982). To confirm this assumption, the behaviour of the north-south asymmetry of the chosen indices of solar activity was studied in detail in 18-21 cycles in the periods of inversion of the total magnetic field of the Sun. It has been shown (Alaniya et al., 1983) that inversion of magnetic fields in high-latitudinal regions of the Sun starts in the hemisphere where the activity is maximal, and the most convincing proof of it is given by the intensity variation of the green coronal line. Thus, deter-

aining the variation of the free path for particle scattering by means of the dependence which takes into account simultaneously the change in the solar spot areas and in the coronal radiation intensity ( $\lambda = 5303 \text{ \AA}$ ) and the delay of CR, one can associate the observed cyclically varying solar activity on the entire sphere and the spatial distribution of the diffusion tensor.

Under the above boundary conditions and under the assumptions concerning the dependence of the free path on the distance and rigidity (see Alaniya et al., 1981) the numerical solution of the CR transport equation makes it possible to estimate an additional effect induced by particle drift from poles to the equator and backwards depending on the direction of the large-scale magnetic field of the Sun. Figure I presents the latitudinal distribution of the expected modulation depth  $B$  for two different configurations of the total magnetic field of the Sun, as well as the modulation depth calculated for the case where the drift effect is disregarded.

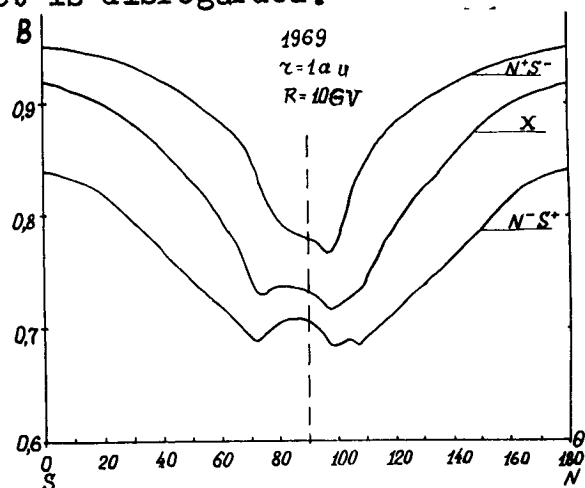


Fig. I The expected relative density of CR with a rigidity of 10 GV in 1969 at a distance  $r = 1 \text{ a.u.}$  versus the heliolatitude with an account of drift fluxes ( $N-S^-$  - towards the ecliptic plane,  $N-S^+$  - backward and without an account of the drift  $x$ ).

The calculations show that an account taken of this effect may increase or decrease (depending on the direction of the background magnetic field of the Sun) the modulation depth about by  $1/3$ .

According to our calculations for some periods in 19-21 cycles of solar activity, the expected amplitudes of long-term variations of CR with a rigidity of 10 GV (in the determination of which the drift of charged particles is taken into account) are in a good agreement with the ones

observed on neutron monitors (which register particles with the effective rigidity of 10 GV).

From the obtained space-time distribution of the relative CR density we have determined the expected transverse gradients, which are the measure of nonsphericity of the modulation process. Increasing in the activity maxima, the latitudinal gradients whose value depends on the epoch of the solar activity cycle must show up the features of spatial distribution connected with the specificities of the CR modulation model under consideration (Fig.2).

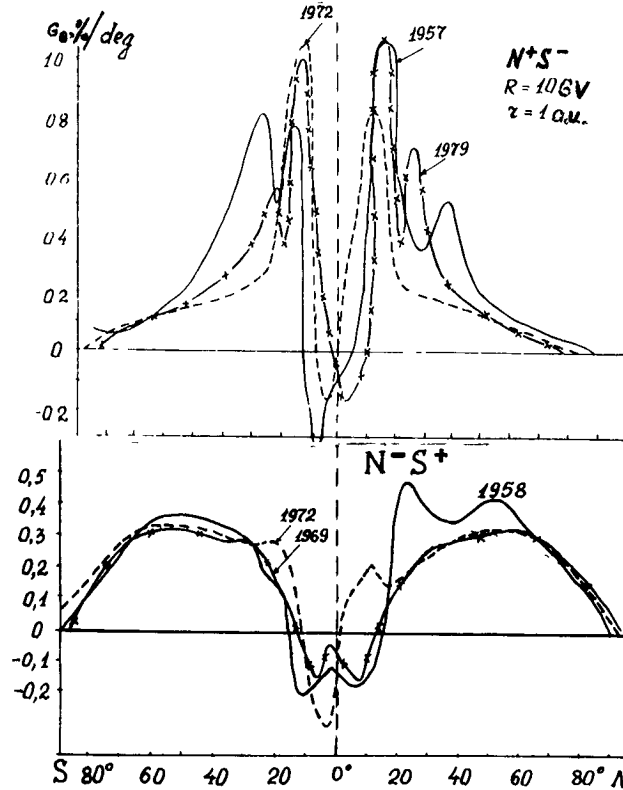


Fig. 2. The expected transverse gradient in the maxima of 19-21 cycles of solar activity for different configurations of the total magnetic field.

For the configuration of the total magnetic field of the Sun, where the magnetic field lines leave the North pole and enter the South pole ( $N-S^-$ ), the maximum of the transverse gradient must be observed at helio-latitudes  $\pm(10^\circ - 15^\circ)$ , and for the inverse configuration it shifts towards higher helio-latitudes ( $\pm(40^\circ - 50^\circ)$ ). Besides, for both field configurations on the Sun, at low helio-latitudes the transverse gradient is sign-variable, which confirms the results of meteorite studies (Lavrukhina, Ustinova, 1981).

Note that the agreement between the expected transverse gradients and those observed on cosmic apparatuses (according to Lockwood and Webber, 1984) is only of a qualitative character because one should bear in mind the difficulties in the interpretation of space measurements, which are connected with the fact that the angle of cosmic apparatus declination from the helio-equator plane is at the present time not large, and the problem of separation of radical and transverse gradients has not yet been clearly solved.

#### REFERENCES

1. Dorman L.I.. 9-th Intern.Cosmic Ray Conf., London, 1965, v.I, p. 292.
2. Alaniya M.V., Dorman L.I., Gushchina R.T.. 17-th Intern. Cosmic Ray Conf., Paris, 1981, v. 3, p. 349.
3. Alaniya M.V., Gushchina R.T., Dorman L.I., 18-th Intern. Cosmic Ray Conf., Bangalore, 1983, v. 10, p. 99.
4. Parker E.N.. Cosmic Magnetic Fields, M., Mir, 1982, v. 2, p. 479.
5. Lavrukhina A.K., Ustinova G.K., 17-th Intern. Cosmic Ray Conf., Paris, 1981, v. 3, p. 238.
6. Lockwood J.A., Webber W.R.. Astrophys. J., 1984, v. 279, N I, pt. I, p. 151.



# 11- AND 22-YEAR VARIATIONS OF THE COSMIC RAY DENSITY AND OF THE SOLAR WIND SPEED

N.P.Chirkov

Institute of Cosmophysical Research & Aeronomy  
Lenin Ave., 31, 677891 Yakutsk, USSR

## ABSTRACT

Cosmic ray density variations for 17-21 solar activity cycles and the solar wind speed for 20-21 ones are investigated. The 22-year solar wind speed recurrence was found in even and odd cycles which allows to forecast it. The 22-year variations of cosmic ray density opposite to the solar wind speed and solar activity were found. The account of solar wind speed in 11-year variations significantly decreases the modulation region of cosmic rays with  $E = 10-20$  GeV.

1. Introduction. Many authors [1-4] to investigate the nature of 11-year variations of cosmic ray density use solar activity and obtain the large sizes of modulation region. But according to the equation of transfer the agent modulating cosmic rays should be proportional to the solar wind speed. If the latter is not proportional to the solar activity then the conclusions on large sizes of cosmic ray modulation region will be incorrect.

2. Results. To study the regularities of the solar wind speed the geomagnetic activity (aa-index) was used taking into account their close relationship [5,6]. The averaged picture of geomagnetic and solar activities is presented in Fig.1 [7] where data for 1868-1977 were used. In the left the odd solar cycles, in the right the even ones are shown. From Fig.1 it is seen that on the average in odd cycles a close correlation with solar activity is observed and in even cycles - a bad one. Both in even and odd cycles the two maxima of geomagnetic activity are observed. The first maximum coincides with the solar activity maximum, the second one delays by 1 year in odd cycles and by 4 years in even ones. The solar wind speed should have the similar regularity which in 20 and 21 solar cycles was observed [8,9]. The second maximum of geomagnetic activity has 22-year recurrence either in even or odd cycles which allows to forecast it [6,7]. The next second maxima of geomagnetic activity and solar wind speed should be observed in 1996 and 2004. Presented in Fig.1 picture of behaviour of geomagnetic activity and solar wind speed should significantly complicate the 11-year variation of cosmic ray density as it is was observed [10].

Here we continue the investigation of [10] for more

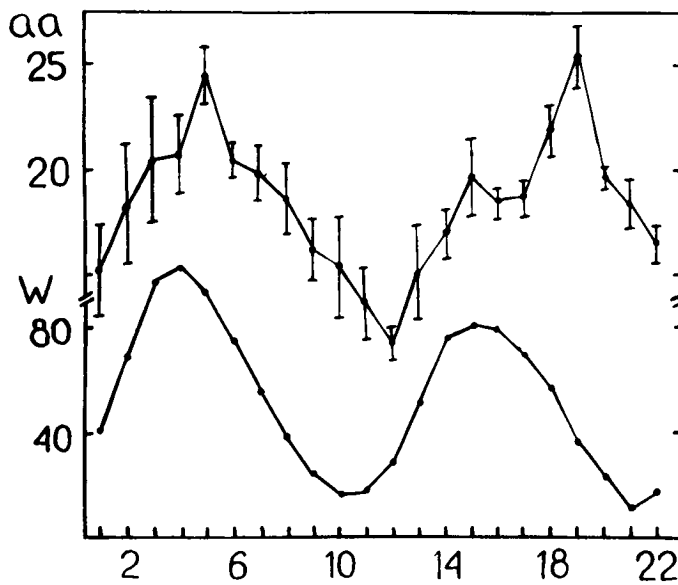


Fig.1. 22-year averaged data of aa-index and of Wolf numbers for 1868-1977

extend energy range of the observed cosmic ray variations. The ionization chamber data for 17-21 solar cycles and the neutron and balloon data for 19-21 ones were used. Correlation and regression coefficients  $a, b$  in the equations of type

$$\Delta I = a \Delta W + b \Delta aa,$$

where  $\Delta I, \Delta W, \Delta aa$  are deviations from mean values and are presented in the Table. The values of a total correlation coefficient  $R$  and values of

$$\sigma = \sqrt{\sum (\Delta I_{obs} - \Delta I_{cal})^2 / n}$$

are also presented. From the Table it is clear that the account of the solar wind speed significantly improves the relationship.

The correlation coefficient is 0.89 - 0.96. The calculated and observed values of  $I$  are shown in Fig.2 from which their good agreement is evident. As it is seen from the Table  $\sigma$  for ionization chamber is 0.2 - 0.4%, for neutron monitors  $\sigma = 1.3 - 2.7\%$ , for balloons  $\sigma = 3.7 - 5.9\%$  which is better by several times than obtained by other methods.

Table

Cycle	$r_{I,W}$	$r_{I,aa}$	$r_{W,aa}$	$R$	$a$	$b$	$\sigma$
Ionization chamber, $\Delta I^k$							
17	$-0.88 \pm 0.08$	$-0.34 \pm 0.32$	$-0.03$	0.95	$-0.014$	$-0.083$	0.2
18	$-0.84 \pm 0.09$	$-0.66 \pm 0.17$	$0.39 \pm 0.26$	0.92	$-0.014$	$-0.098$	0.4
19	$-0.91 \pm 0.05$	$-0.93 \pm 0.04$	$0.85 \pm 0.08$	0.96	$-0.006$	$-0.107$	0.3
20	$-0.82 \pm 0.09$	$-0.35 \pm 0.25$	$-0.15 \pm 0.28$	0.95	$-0.012$	$-0.056$	0.2
21	$-0.79 \pm 0.14$	$-0.54 \pm 0.24$	$0.09$	0.92	$-0.010$	$-0.073$	0.3
Neutron monitor, $\Delta I^m$							
19	$-0.84 \pm 0.09$	$-0.91 \pm 0.05$	-	0.92	$-0.024$	$-0.865$	2.7
20	$-0.92 \pm 0.04$	$0.05$	-	0.93	$-0.090$	$-0.081$	1.3
21	$-0.70 \pm 0.14$	$-0.56 \pm 0.28$	-	0.89	$-0.066$	$-0.607$	2.4
Balloons, $\Delta I^c$							
19	$-0.95 \pm 0.04$	$-0.92 \pm 0.05$	-	0.97	$-0.096$	$-0.051$	5.1
20	$-0.91 \pm 0.05$	$0.06$	-	0.92	$-0.254$	$-0.249$	3.7
21	$-0.78 \pm 0.14$	$-0.45 \pm 0.28$	-	0.89	$-0.182$	$-1.222$	5.9

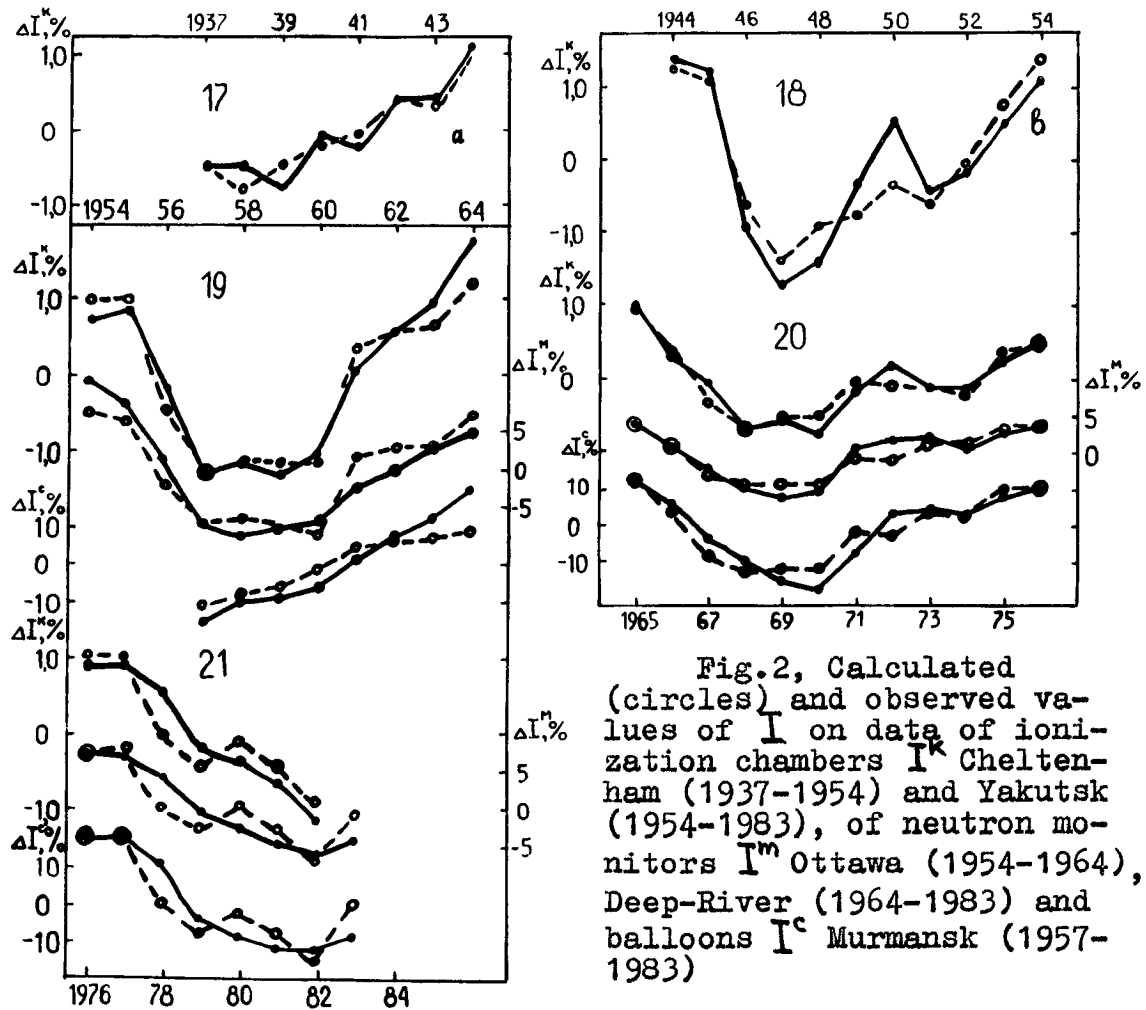


Fig.2, Calculated (circles) and observed values of  $I$  on data of ionization chambers  $I^k$  Cheltenham (1937-1954) and Yakutsk (1954-1983), of neutron monitors  $I^m$  Ottawa (1954-1964), Deep-River (1964-1983) and balloons  $I^c$  Murmansk (1957-1983)

The solar wind enhancement at solar activity decrease caused the delay of recovery of cosmic ray intensity by 1-2 years in 19 cycle and by 3 years in 21 cycle caused also the repeated decreases of  $I$  in 18 and 20 cycles in 4-5 years after the solar activity maximum.

A good agreement (within 6 months) of calculated and observed values  $\Delta I$  allows to estimate the sizes of cosmic ray modulation region  $\sim 30$  AU. The use of monthly values of smoothed for a year  $I$ ,  $w$  and  $aa$ -index allows to decrease the sizes of modulation region up to  $\leq 10$  AU.

In [11] the 22-year variations of solar and geomagnetic activities were found. The even and odd cycles being closely related than odd and even ones. The similar dependence was found in [12] for cosmic ray density and it is expected in solar wind speed. The 22-year variations of cosmic ray density are opposite to 22-year variations of solar activity and of solar wind speed.

References

1. Chirkov, N.P. i dr., 1962, Variatsii intensivnosti kosmicheskikh luchei. Trudy YAF SO AN SSSR, ser.fiz., 4, 122.
2. Simpson, J.A., 1963, Preprint No.25. Poniticiae acad.scient.scripta varia.
3. Krymsky, G.F., 1969, Modulatsiya kosmicheskikh luchei v mezhplanetnom prostranstve, Moskva, Nauka.
4. Dorman, I.V., Dorman L.I., 1967, Kosmicheskiye luchy, 8, 100.
5. Snyder, C.W. et al., 1963, J.Geophys.Res., 68, 6361.
6. Chirkov, N.P., 1980, Variatsii kosmicheskikh luchei i solnechnyi i solnechnyi veter, Yakutsk, 18.
7. Chirkov, N.P., Samsonov, I.S., 1984, Geomagnetism i aeronomiya, 24, 2, 300.
8. Crooker, N.U. et al., 1977, J.Geophys.Res., 82, 1933.
9. Solar Wind, 5, Woodstock, Program and Abstracts, 1982.
10. Chirkov, N.P., Kuzmin, A.I., 1979, Proc.16-th ICRC, 3, 360.
11. Chirkov, N.P., 1985, Geomagnetism i aeronomiya, 3.
12. Chirkov, N.P., 1983, Geomagnetism i aeronomiya, 23, 6, 1015.

# DIFFERENCE BETWEEN EVEN AND ODD 11-YEAR CYCLES IN COSMIC RAY INTENSITY

J.A. Otaola, R. Pérez-Enríquez and J.F. Valdés-Galicia  
Instituto de Geofísica, UNAM, México 04510, D.F.

## ABSTRACT

Cosmic ray data for the period 1946-1984 are used to determine the run of the cosmic ray intensity over three complete solar cycles. The analysis shows a tendency towards a regular alternation of cosmic ray intensity cycles with double and single maxima. Whereas a saddle-like shape is characteristic of even cycles, odd cycles are characterized by a peak-like shape. The importance of this behaviour is discussed in terms of different processes influencing cosmic ray transport in the heliosphere.

1. Introduction. The anomalous behaviour of the cosmic ray intensity after the 1968 solar maximum in the 20th solar cycle has been described by several authors. This was characterized by the softening of the spectra (Evenson et al., 1983), the sudden recovery of the intensity (Kuzmin et al., 1977), a poor correlation of the cosmic ray intensity with solar activity (Akopian et al., (1981) and the sudden appearance of anomalous components in the cosmic rays (García Muñoz et al., 1981; McDonald et al., 1981).

The purpose of this study is to show that the 1946-1957 11-year cycle in cosmic ray intensity also presents this characteristic behaviour and that this seems to be the result of a similar behaviour in solar activity during even sunspot cycles. A possible physical interpretation to this phenomenon is given in terms of different contributions of drift, convection and diffusion to the whole modulation process.

2. Data. The basic data used in the present study are the monthly values of the cosmic ray intensity and the smoothed sunspot numbers over the period 1946-1984, thus covering three complete 11-yr cosmic ray intensity cycles. As the cosmic ray data are derived from the ion chamber at Huancayo (1946-1957) and the neutron monitor at Deep River (1958- 1984), and they represent two different kinds of data, we integrated them following the method described by Nagashima and Morishita (1980) which, from the point of view of long term modulation, is permissible as a first approximation.

In Figs. 1a. and 1b. the smoothed sunspot number and the integrated cosmic ray intensity over the period 1946-1984 are shown. The cosmic ray intensity is expressed in percent decrease with respect to the maximum intensity level

established in May, 1965. The cosmic ray intensity, on the other hand, was smoothed using an ultra lowpass filter which essentially gives the trend of the input function and effectively removes the rapid fluctuations (Behannon and Ness, 1966). The smoothed intensity is shown as the dashed curve in Fig. 1b.

In these curves the hatched regions represent the times of reserval of the solar magnetic field and the notation  $\vec{M} \uparrow \uparrow \vec{\Omega}$  and  $\vec{M} \uparrow \downarrow \vec{\Omega}$  indicates the magnetic moment parallel and anti-parallel to the angular velocity axis of rotation of the Sun, respectively.

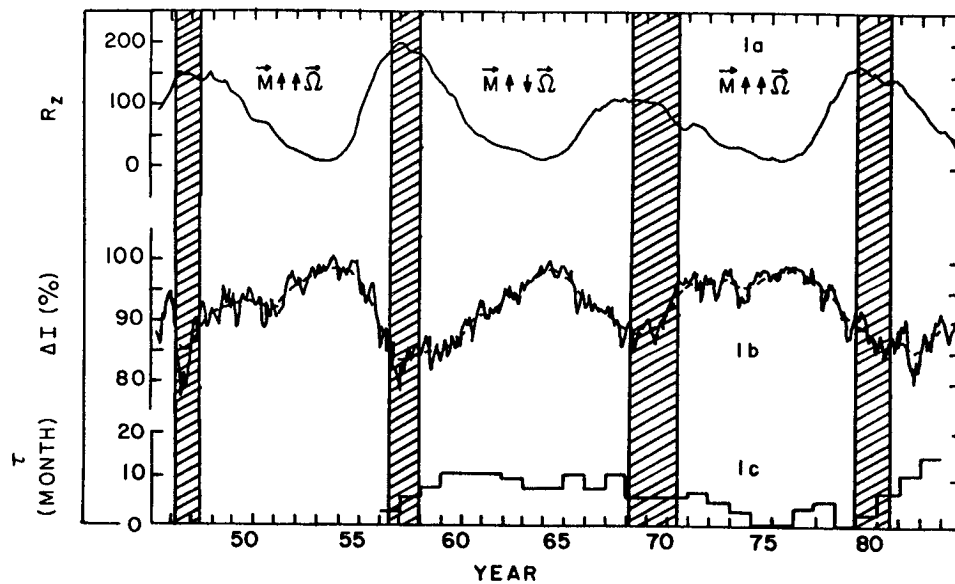


Fig. 1. a) Zurich sunspot number. b) Integrated cosmic ray intensity (solid line) and smoothed curve (dashed line). c) Time lag of intensity behind sunspot number for 11 years from  $t-10$  years to  $t$ .

3. Results and Discussion. From the smoothed curve of cosmic ray intensity shown in Fig. 1b, one can see that the shape of the  $\vec{M} \uparrow \uparrow \vec{\Omega}$  cycles differs systematically and markedly from the shape of the  $\vec{M} \uparrow \downarrow \vec{\Omega}$  cycle. Whereas the shape of the  $\vec{M} \uparrow \downarrow \vec{\Omega}$  cycle is characterized by a simple and relatively smooth increase to the maximum ( $\sim 7.5$  yr), the  $\vec{M} \uparrow \uparrow \vec{\Omega}$  cycles, on the average, are characterized by a two maxima structure in which the first maxima is reached relatively rapid after the previous minimum in the cosmic ray intensity ( $\sim 3-4$  yr) and the second, the main and also more developed, tends to occur

at the same time in the cycle that the maximum of the  $\vec{M}\uparrow\downarrow\vec{Q}$  cycle.

This different behaviour between  $\vec{M}\uparrow\uparrow\vec{Q}$  and  $\vec{M}\uparrow\downarrow\vec{Q}$  cycles is also shown in the time lag  $\tau$  of cosmic ray intensity behind solar activity, as measured by the smoothed sunspot number. This 22-yr variation in the time lag, already found by Nagashima and Morishita (1980), in which  $\tau$  is greater in  $\vec{M}\uparrow\downarrow\vec{Q}$  cycles than in  $\vec{M}\uparrow\uparrow\vec{Q}$  cycles, as can be seen in Fig. 1c, clearly shows that particles reach the Earth more easily when their access route is by the heliospheric polar regions than when they gain access along the current sheet (Kota and Jokipii, 1982). In this case as the route of access becomes longer due to the waviness of the neutral sheet the time lag  $\tau$  is also longer as one would expect from theoretical considerations.

However, what this model does not explain is the two maxima structure during the  $\vec{M}\uparrow\uparrow\vec{Q}$  cycles. This behaviour is, in fact, also present in solar (Dodson and Hedeman, 1975) and in geomagnetic activity as measured by the aa-index (Halenka, 1983). According to the Dodson and Hedeman's results the solar activity during even sunspot cycles are characterized by two well defined "stillstands" in the level of activity during the declining phases of such cycles. On the other hand, Halenka shows that the aa-index during even solar cycles also presents this characteristic while the odd cycles do not.

Therefore, the results shown here clearly establish a marked distinction between even and odd solar activity cycles which in turn are reflected both in geomagnetic activity and cosmic ray intensity.

4. Conclusions. The results presented above point out towards a modulation mechanism, during even cycles, where convection plays a more important role than during odd cycles, where diffusion dominates, while the effect of drifts only determines how the particles gain access to the observation point. That is, charge dependent effects are not the dominant processes in cosmic ray modulation.

#### References

1. Akopian, S. K. et al. (1981), 17th ICRC, Paris, 3, 227.
2. Behannon, K. W. and N. F. Ness (1966). Nasa T N D-3341.
3. Dodson, H. W. and E. R. Hedeman (1975). Solar Phys., 42, 121.
4. Evenson, P. et al. (1983). 18th ICRC. Bangalore, 3, 27.

5. García Muñoz, M. et al. (1981). 17th ICRC, París, 3, 270.
6. Halenka, J. (1983). Studia geoph. et geod., 27, 46.
7. Kota, J. and J. Jokipii (1982). Astrophys. J., 265, 573.
8. Kuzmin, A. I. et al. (1977). 15th ICRC, Plovdiv, 3, 150.
9. McDonald, F. B. et al. (1981). 17th ICRC, París, 3, 263.
10. Nagashima, K. and I. Morishita (1980), Planet. Space Sci., 28, 195.



# THE DEPENDENCE OF SOLAR MODULATION ON THE SIGN OF THE COSMIC RAY PARTICLE CHARGE

M. Garcia-Munoz, P. Meyer\*, K.R. Pyle and J.A. Simpson\*  
Enrico Fermi Institute, University of Chicago, Chicago, Illinois

and

P. Evenson  
Bartol Research Foundation, University of Delaware, Newark, Delaware

## ABSTRACT

We compare the solar modulation of galactic cosmic ray helium and electrons at 1 AU, within the 600-1000 MV magnetic rigidity interval, from 1965 through 1984. The time-intensity variations during the two solar maxima around 1970 and 1981 show that after 1970 the helium intensity recovers earlier than that of the electrons, whereas after 1981 the electron intensity recovers earlier than that of helium. The flux ratio of helium to electrons (He/e) undergoes a major increase during the 1969-1971 period and a major decrease during 1979-83. These experimental results can be interpreted as due to a dependence of the solar modulation of galactic cosmic rays on the sign of the particle charge, possibly as a consequence of drifts due to gradients and curvatures in the interplanetary magnetic field. However, the comparison of the shapes of the intensity-time curves of helium and electrons in the period 1970-1981 does not support a major specific prediction of the drift model.

1. Introduction. The perception that the interplanetary magnetic field is a distorted dipole, coherent in large scale, suggests that drifts due to field gradients and curvatures may play a significant role in solar modulation (Jokipii *et al.*, 1977).

Because the drifts of particles of opposite charge move in opposite directions, the modulation effects on nuclei at a given point in the interplanetary space will be different from those on electrons.

This paper addresses the problem of the importance of drifts - trying to detect differences in the modulation of nuclear and electron cosmic rays that could be in principle attributed to the presence of drifts. We study the modulation of 70-95 MeV/n (739-866 MV) cosmic ray helium-4 and 600-1000 MeV cosmic ray electrons from 1965 through 1984 with special emphasis on the intervals around the two consecutive solar maxima in 1970 and 1981 in which the interplanetary magnetic field changed polarity.

2. The Experimental Data. Most of the experimental data used in this work have been obtained with the University of Chicago cosmic ray telescopes flown on balloons or aboard satellites.

Figure 1 shows the time dependence, within the 1960-1984 period of: (A) 27-day averages of the Climax neutron monitor counting rate, and; (B) 2-day averages of the 70-95 MeV/n helium-4 flux measured mostly by the U. of Chicago telescopes on IMP-3, 4, 5, 6 and 8. The open circles

---

\*and Department of Physics.

are derived from the differential energy spectra and the near-continuous curve is derived from helium count rates identified by pulse height analysis.

Figure 2 shows the time dependence of the 600-1000 MeV cosmic ray electron flux. The open circles have been derived from differential energy spectra measured with experiments flown on balloons. The 1968-1971 solid curve represents

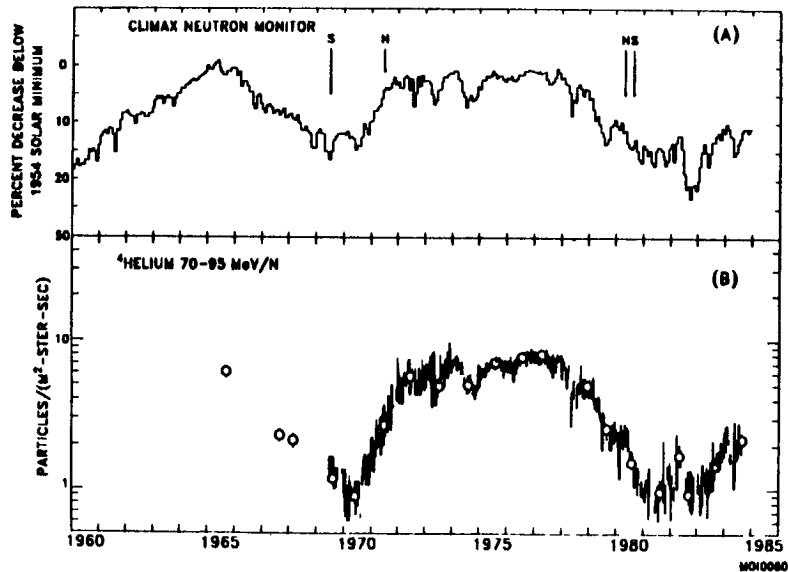


Figure 1

continuous measurements of 700-1000 MeV electrons measured on the satellite OGO-5 (Burger and Swanenburg, 1973), normalized to the 1968-71 balloon measurements. The curve of small points from 1978 through 1984 are daily rates of  $\sim 600$ -1000 MeV electrons measured by the Chicago ISEE-3 telescope (Evenson and Meyer, 1984). This curve can be normalized either to the 1982 or to the 1984 balloon measurements (the 1979 balloon point, measured during a Forbush decrease, cannot be used for normalization). Because the 1982 balloon flight data was taken not long after a sharp cosmic ray decrease we have normalized to the 1984 point. However, the conclusions reached in this paper are independent of which point, 1982 or 1984, is used for normalization. The arrows in Figures 1 and 2 point at the times when the solar polar magnetic fields reversed polarity (Howard, 1981).

**3. The Relative Modulation of Nuclei and Electrons.** An overview of the relative modulation of 70-95 MeV/n helium-4 and 600-1000 MeV electrons is given in Figure 3, where the ratio He/e has been plotted as a function of time. Some of the ratios have been calculated using differential energy spectra of both helium and electrons (filled circles), while others have been calculated using differential energy spectra of helium and continuous satellite measurements of

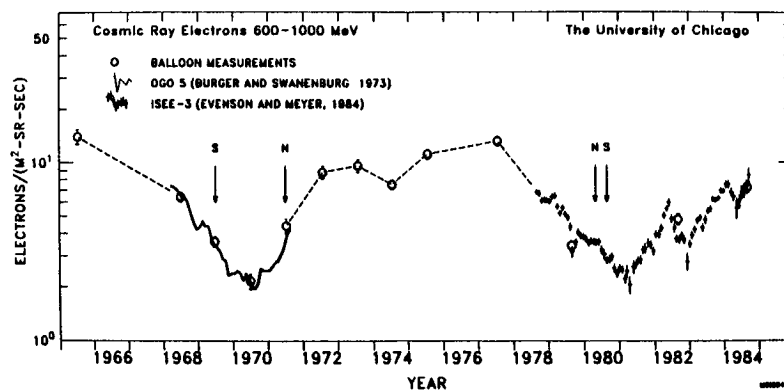


Figure 2

electrons (semifilled circles) and, finally, others using continuous satellite measurements of both helium and electrons (open circles).

The dashed vertical lines mark the times at which the individual fluxes of 70-95 MeV/n helium and 600-1000 MeV electrons reached their minimum values during the two consecutive solar maxima. Again the arrows mark the times of polarity reversal of the solar polar magnetic fields.

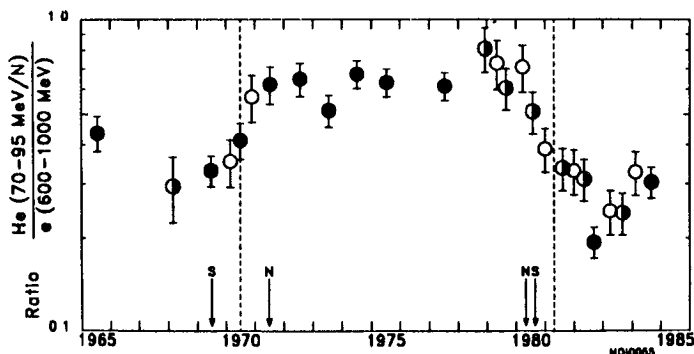


Figure 3

Figure 3 clearly shows a difference in the modulation of cosmic ray particles of opposite charge during the two solar maxima. The ratio He/e increases from 1968-69 to 1971-72, while it decreases from 1979 to 1982-83. As can be seen in Figure 2, normalizing the ISEE-3 fluxes to the 1982 balloon point would further decrease the He/e ratio after 1977, except, of course, the ratio associated with the 1984 balloon point. Thus the opposite character of the time dependence of the ratios around the two solar maxima persists, regardless of the balloon point used to normalize the ISEE-3 data.

**4. Discussion and Conclusions.** As can be seen in Figures 1 and 2, the periods 1971-73 and 1982-84 are similar time intervals in which the cosmic rays recover from the preceding minimum intensity and increase towards the maximum associated with solar minimum activity. During these periods, in which the interplanetary magnetic field has opposite polarities, the ratio between the fluxes of cosmic ray helium and electrons, of nearly the same rigidity but opposite particle charge, differ by more than a factor 2. The fact that the electrons have higher velocity than the helium nuclei cannot alone explain the difference in the ratios, because any effect exclusively dependent on velocity is expected to be equally present in both compared periods.

The above facts suggest that a modulation process sensitive to the particle charge is operating in the interplanetary medium and an obvious candidate is drifts due to gradient and curvature in the interplanetary magnetic field as proposed by Jokipii *et al.* (1977).

However, although the results of the present work would be consistent with a significant role of drifts in solar modulation, they do not support one of the predictions of the recent drift model of solar modulation by Kota and Jokipii (1983). Their model predicts that, as a consequence of the predominant role played by drifts and the simultaneous presence of a wavy current sheet, the intensity of cosmic ray nuclei during the two halves of the 22-year magnetic cycle must have a very different time dependence, being relatively sharply peaked during the semicycle in which drifts bring positive particles from the equator to the heliospheric poles (e.g., around the 1965 solar minimum) and having a rather broad plateau during the semi-cycle in which drifts run in opposite direction (e.g., around the 1976 solar minimum). This is what is actually observed in the Climax neutron monitor counting rate for the solar minima of 1965

and 1976 (Figure 1A). Since drifts run in opposite direction for negative particles, it is predicted that for cosmic ray electrons the shapes of the two semi-cycles should appear interchanged during the period 1959-1981. The data assembled in this work allow a check of this specific prediction for the 1970-1981 semicycle. Figure 4 shows a superposition of the time dependence of 70-95 MeV/n helium and 600-1000 MeV electron fluxes both normalized to the years 1970 and 1977. Note that from 1970 to 1980 the time dependence of the helium and electron fluxes have very closely the same shape, in disagreement with the model prediction.

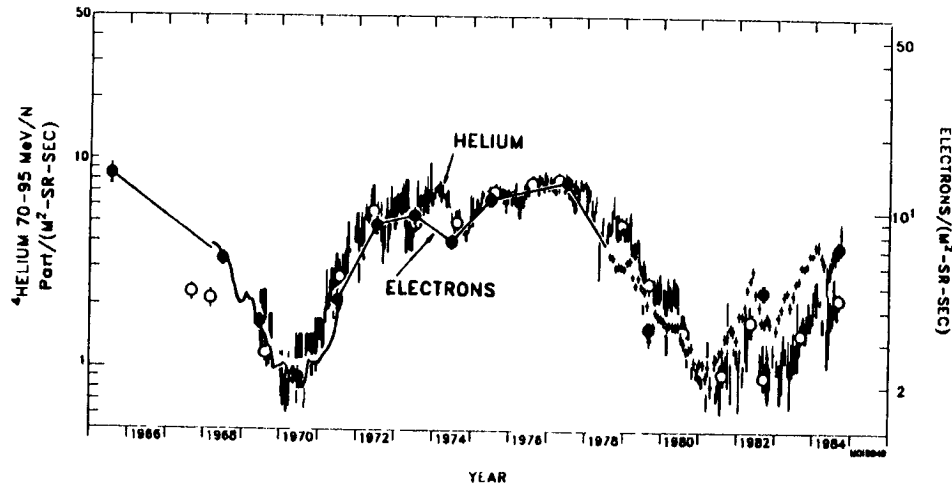


Figure 4

5. **Acknowledgements.** We thank Scott Marusak and Leo Krawczyk for their assistance in the preparation of the data, and Leonard Shulman and Evelyn Tuska for their assistance in the 1984 balloon flight. This research was supported in part by NASA grants NGL 14-001-005, NGL 14-001-006 and NAG 5-374, NASA Contracts NAS 5-28442 and NAS 5-28500 and NSF Grants ATM 84-12382, ATM 84-03718 and ATM 84-01427.

## 6. References

- Burger, J.J. and Swanenburg, B.N., (1973), *J. Geophys. Res.*, **78**, 292.  
 Evenson, P., and Meyer, P., (1984), *Phys. Rev. Letters*, **17**, 329.  
 Howard, R., (1981), Smithsonian Ap. Obs. Spec. Rep. No. 393, 155.  
 Jokipii, J.R., Levy, E.H. and Hubbard, W.B., (1977), *Ap.J.*, **213**, 861.  
 Kota, J., and Jokipii, J.R., (1983), *Ap.J.*, **265**, 573.

AN UPDATE ON THE CORRELATION BETWEEN THE COSMIC RADIATION INTENSITY  
AND THE GEOMAGNETIC AA INDEX

M. A. Shea and D. F. Smart  
Air Force Geophysics Laboratory  
Hanscom AFB, Bedford, MA, 01731, U.S.A.

ABSTRACT

A statistical study between the cosmic ray intensity, as observed by a neutron monitor, and of the geomagnetic aa index, as representative of perturbations in the plasma and interplanetary magnetic field in the heliosphere, has been updated to specifically exclude time periods around the reversal of the solar magnetic field. The results of this study show a strong negative correlation for the period 1960 through 1968 with a correlation coefficient of approximately -0.86. However, there is essentially no correlation between the cosmic ray intensity and the aa index for the period 1972-1979 (i.e. correlation coefficient less than 0.16). These results would appear to support the theory of preferential particle propagation into the heliosphere via the ecliptic during the period 1960-1968 and via the solar polar regions during 1972-1979.

1. Introduction. The work of Jokipii et al. (1977) and subsequent publications has created considerable interest and discussion with their suggestion that the modulation of the galactic cosmic ray intensity should have a component controlled by the state of the interplanetary magnetic field as transported out from the sun, and hence there should be a solar cycle effect on the drift of cosmic rays in the heliosphere. In this paper we report the results of a study correlating the cosmic ray intensity at the earth with a solar and a geomagnetic parameter for periods between successive solar maxima.

2. Data Utilized. For this study the following data were utilized:  
Neutron monitor data. The monthly averages of the cosmic ray intensity as measured by the Mt. Washington neutron monitor were selected primarily because of the long data base (June 1954 to the present time), the stability of the station over this long time period, and the fact that this station, located at a geomagnetic cutoff of  $\sim 1.3$  GV, monitors the full galactic cosmic ray intensity. In addition the monthly averages of the cosmic ray intensity as measured by the Chicago neutron monitor were also utilized for the period January 1953 until the monitor closed in December 1971. These data were used primarily to allow inclusion of data as far back as 1953. The correlations reported herein were repeated using both the Mt. Washington data and the Chicago data for periods of time where the data were both available; the results were essentially the same for those time periods.

Geomagnetic data. The monthly averages of the geomagnetic aa index were selected as the parameter describing the status of the geomagnetic field and hence is a measure of turbulent plasma in the ecliptic plane. This index is computed from the K index of two antipodal observatories (invariant magnetic latitude  $50^\circ$ ) providing a quantitative characterization

of the magnetic activity which is homogenous throughout the long data base (1868 to the present). A full description of this index is given by Mayaud (1973). We have utilized the aa index as being representative of the geomagnetic activity at the earth; we consider this activity to be the product of the interaction between the earth's magnetic field and the interplanetary magnetic field carried past the earth by the solar wind. Cosmic ray transport in the heliosphere would be affected by turbulence in the plasma and the interplanetary magnetic field. In contrast to the sunspot number, which may have some relationship to the three dimensional structure of the heliosphere, the geomagnetic aa index should represent disturbances only in the ecliptic plane at the position of the earth.

Solar data. The monthly averages of the Zurich relative sunspot number,  $R_z$ , were selected as a solar parameter. Although the Zurich relative sunspot number does not directly control the galactic cosmic ray intensity observed at the earth, it is an indicator of activity on the sun and is inversely correlated with the cosmic ray intensity throughout a solar cycle. This is probably because the sunspot number reflects activity over a range of heliocentric latitudes from about  $45^\circ\text{N}$  to about  $45^\circ\text{S}$ , and hence has some relationship to the three dimensional structure of the heliosphere.

3. Method. Using the method of least squares, linear correlations between the monthly averages of the cosmic ray intensity and the (a) sunspot number and (b) aa index were calculated for selected time intervals. In contrast to an earlier study (Shea and Smart, 1981), the results reported here are restricted to the following intervals:

January 1953 (Chicago data) through August 1956 (44 months);

June 1959 through December 1968 (115 months);

March 1972 through December 1979 (94 months).

The polarity at the north and south solar pole does not change at the same time. For example, the south pole changed polarity in July-August 1969; the north pole in August 1971. Since we wanted to restrict this analysis to periods when the solar polar magnetic fields were well defined, we excluded the months from September 1956 through May 1959 and January 1969 through February 1972 from this analysis.

Galactic cosmic ray particles observed at the earth have propagated through the heliosphere and are affected by the magnetic inhomogeneities encountered on their transit. Since recent results indicate that the heliosphere extends well beyond 30 AU and this distance corresponds to a solar wind transit time of four months, correlations were made between the monthly average cosmic ray intensity and averages of the aa index and the sunspot number for successively longer time periods preceding the monthly cosmic ray intensity. For each specific interval being studied the monthly average cosmic ray intensity (as recorded by neutron monitors) for month  $N$ , was first correlated against the Zurich relative sunspot number (or the aa index) for the same month. Next the same monthly average cosmic ray intensity for month  $N$ , was correlated against the two-month average sunspot number (or the aa index) for months  $N$  and  $N-1$  and similarly for the three-month average sunspot number (or the aa index) for months  $N$ ,  $N-1$ , and  $N-2$ , etc., to a maximum of 30 months.

Variations of the cosmic ray intensity, the sunspot number and the aa index for the period 1954-1979 are illustrated in Figure 1. For simplicity 3-month averages are plotted in this figure although monthly averages were utilized in this analysis.

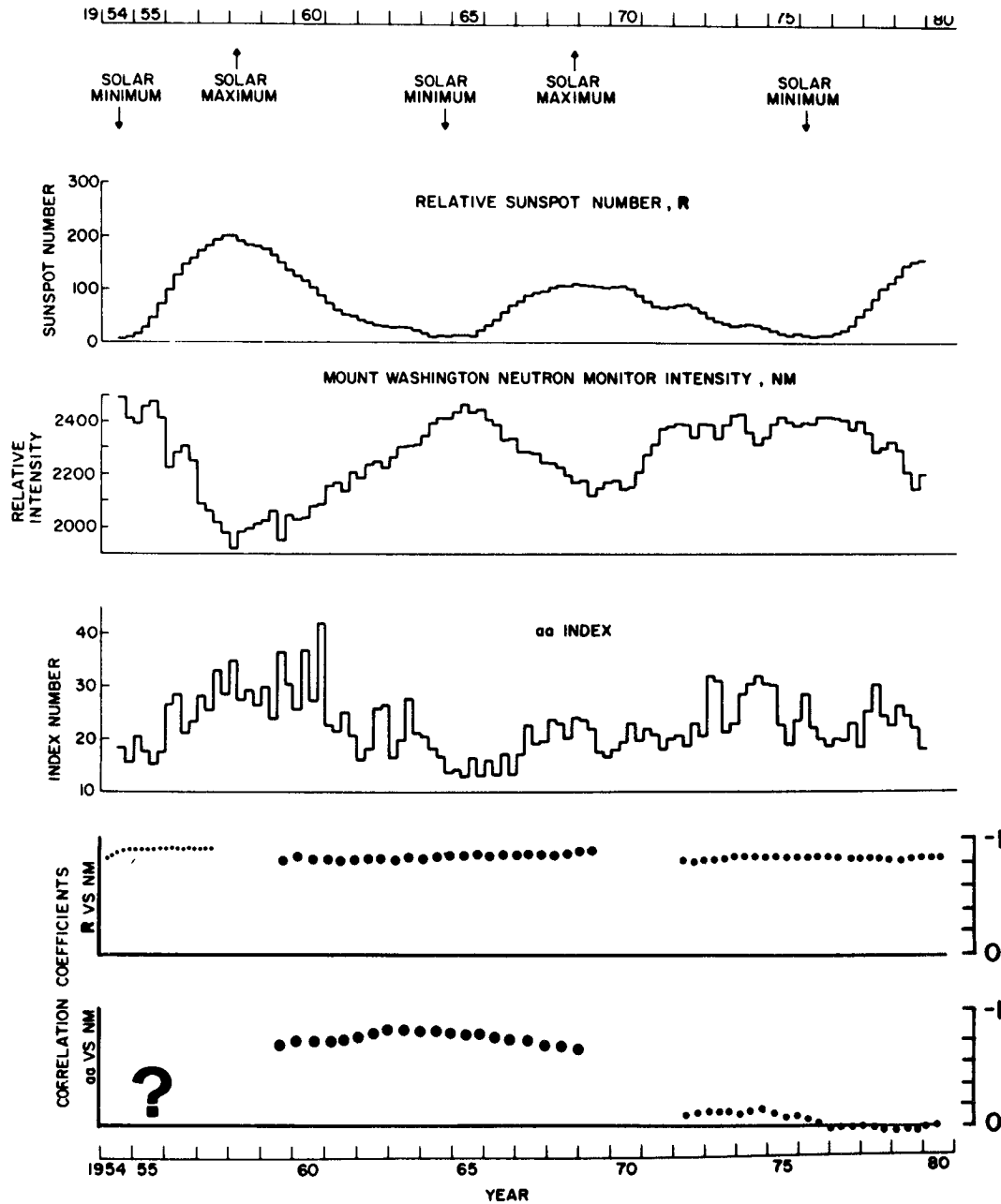


Fig. 1. The Zurich relative sunspot number, the cosmic ray intensity as measured by the Mt. Washington neutron monitor, and the aa index from 1954 through 1979. Solar minima and solar maxima are indicated at the top of the figure. The correlation coefficients are illustrated at the bottom of the figure where the individual dots represent the correlation coefficient for successively longer time lags. The question mark in the lower left indicates that it was not possible to reach any conclusion for the time period January 1953 to December 1957 because of the small time period. See text for additional description.

4. Results and Discussion. The values of the correlation coefficients for the various data sets studied are shown in the bottom section of Figure 1 where the individual dots represent the correlation coefficient for successively longer time lags. The relative position of each dot represents the time lag used for each correlation for the time period shown. For example, the first dot in each sequence represents the correlation coefficient when correlating the cosmic ray intensity for month N with the sunspot number (or aa index) for month N; the second dot represents the correlation of the cosmic ray intensity for month N with the sunspot number (or aa index) for months N and N-1 (i.e. 1-month lag), the third dot represents the correlation of the cosmic ray intensity for month N with the sunspot number (or aa index) for months N, N-1, and N-2 (i.e., two-month lag), etc. These results show that the cosmic ray intensity is inversely correlated with both the sunspot number and the geomagnetic aa index for the time interval essentially centered around the solar minimum between the 19th and 20th solar cycles. For the time period centered around the solar minimum between the 20th and 21st solar cycles, the correlation between the cosmic ray intensity and the sunspot number is approximately the same as for the earlier period; however, the value of the correlation coefficient between the cosmic ray intensity and the geomagnetic aa index reduces considerably to essentially zero.

These results are consistent with the suggestion that the sense of the drift of cosmic rays in the heliosphere is a component of the cosmic ray propagation as hypothesized by Jokipii et al. (1977), Jokipii and Kopriva (1979), and Jokipii (1981). Briefly they suggest that the drift component of cosmic rays (i.e., positively charged atomic nuclei) may have preferential entry into the heliosphere via the helio equatorial plane if the northern solar polar magnetic field is negative (i.e., direction of the field into the northern solar pole as was the case from 1959 to 1968) and that this drift component may have preferential entry into the heliosphere via the solar poles if the northern solar polar magnetic field is positive (i.e., directed out of the northern solar pole as was the case from 1972 to 1980). Thus if the cosmic ray flux has a significant drift component via the helio-equatorial plane an inverse correlation with the aa index would be expected, and if the cosmic rays have preferential entry via the solar poles, this correlation should be considerably smaller. This would be consistent with our correlation coefficients between the cosmic ray intensity and the aa index of -0.86 for June 1959-December 1968 and essentially 0 for March 1972-December 1979.

5. Acknowledgments. We would like to acknowledge helpful discussions with M. Forman, J. Feynman, C. Hatton, R. Jokipii, and M. Lee.

#### References

- Jokipii, J.R., E.H. Levy, and W.B. Hubbard, *Astrophys. J.* **213**, 861, 1977.  
 Jokipii, J.R. and D. A. Kopriva, 16th International Cosmic Ray Conference, *Conference Papers* **3**, 7, 1979.  
 Jokipii, J.R., *Geophys. Res. Lett.*, **8**, 837, 1981.  
 Mayaud, P.N., *A Hundred Year Series of Geomagnetic Data 1868-1967*, IAGA Bulletin No. 33, IUGG Publications Office, Paris, 1973.  
 Shea, M.A., and D.F. Smart, *Adv. Space Res.*, **1**, 147, 1981.



505  
AUTHOR INDEX

AGRAWAL, SP	BURLAGA, LF
392	346,445
ALANIA, MV	396
465,477	CANE, HV
ALANIYA, MV	94,66,14
485	CANFIELD, RC
ALEKSEEV, NV	86
205	CHANG, CR
ALVAREZ, M	86
18,22,26	CHARAKHCHYAN, TN
30,34,110	481
ANDERSON, KA	CHEBAKOVA, EA
342	356
ARMSTRONG, TP	CHIRKOV, NP
174,192	489
ARVELA, H	CHRISTON, SP
364	445,404
ASLAMAZASHVILI, RG	200
465,477	CHUPP, EL
BABAYAN, VK	126,146
372	CHURONOVA, LF
BADRUDDIN,	473
461	CLIVER, EW
BAGDASARIAN, MB	94,14
372	COOPER, JF
BALOGH, A	126,146
178	CUMMINGS, AC
BANDLE, J	445,200
174	DAIBOG, EI
BEECK, J	62
334	DEBRUNNER, H
BEHANNON, KW	351,317
445	126
BELOV, AV	DECKER, RB
118	10,166
BIEBER, JW	DENEHY, BV
335,433	142
BISWAS, S	DENNIS, BR
221	38
BLOKH, YAL	DIETRICH, WF
118	277
BOBROVSKAYA, VV	DJAPIASHVILI, TV
205	477
BOCHORISHVILI, TB	DORMAN, LI
477	413,485
BRAVO, S	465
257	DOUGHERTY, WM
BRENEMAN, HH	342
217,213	DROGE, W
BRIGGS, PR	2
192	DURAND, H
BURGER, RA	384
421	DURGAPRASAD, N
BURLAGA, LF	221

506  
AUTHOR INDEX

DVORYANCHIKOV, YAV	GLOECKLER, G
289	182,321
EARL, JA	241
380,376	GOLD, RE
ECKES, S	186,405
192	GOLDSTEIN, ML
EFIMOV, YUE	396
154	GONCHAR, GA
ELLISON, DC	457
6	GREEN, G
ERDOS, G	355
178	GRIGOROV, NL
EROSHENKO, EA	205
118	GUSHCHINA, RT
EVENSON, P	485
130,309	HAMILTON, DC
497,74,201	321
EVENSON, PA	HOVESTADT, D
335	281,182
FAN, CY	241,245
241	285,74
FEDOROV, YUI	HUDSON, HS
413	50,58
FENTON, AG	HUMBLE, JE
339	339,437
FENTON, KB	INOUE, A
339	138
FILIPPOV, AT	IPAVICH, FM
368	182,241
FISK, LA	ISHKOV, VN
241	118
FLUCKIGER, E	ISKRA, K
317,126	465
FORMAN, MA	ITO, K
400	297
FORREST, DJ	IUCCI, N
126,146	134
249	IWERS, B
FRYE, GM	102
142	JAIN, AK
GALINDO TREJO, J	392
78	JOKIPII, JR
GALLEGOS, A	449,388
18,22,26	453,376
30,34	JONES, FC
GALL, R	400
384	KAHLER, SW
GALVIN, AB	94,269,14
241	KANBACH, G
GARCIA-MUNOZ, M	126
469,409	KATZ, MI
497	413
GARCIAMUNOZ, M	KEPPLER, E
409	158

507  
AUTHOR INDEX

KESSEL, RL	LOCKWOOD, JA
174	351,469
KIRSCH, E	317,388
158	LOGACHEV, YI
KLECKER, B	62
182,241	LUHN, A
285	241,245
KLEIN, KL	285
46	LUMME, M
KLIMENKO, VV	364
313	LYAKHOVA, AKH
KOCHAROV, GE	457
154,150	MACE, O
KOCHAROV, LG	142
293,289	MACKINNON, AL
KOGA, R	42
142	MACLENNAN, CG
KOHNO, T	186
297,301	MANDZHAVIDZE, NZ
KOLOMEETS, EV	150
457,356	MARSDEN, RG
KONDRATYEVA, MMA	322
205	MARTINIC, NJ
KOTA, J	138
449,453	MASON, GM
KOVALTSOV, GA	281,321
106	MCDONALD, FB
KOZLOV, SA	346,209,98
122	396
KOZLOVSKY, B	MCGUIRE, RE
249,253	94,66,14
KRAINEV, MMB	317,225
481	190
KRIMIGIS, SM	MEYER, JP
186,170	233
KROEGER, R	MEYER, P
130	130,497,74
KRYAKUNOVA, ON	201
473	MIKRYUKOVA, NA
KUNOW, H	313
305	MISHRA, BL
KURT, VG	392
62	MOBIUS, E
KUZHEVSKY, BM	285
229	MORAAL, H
LANZEROTTI, LJ	421,421
186	MOROZOVA, EI
LAVILLE, A	313
18,34	MOSES, D
LIGGETT, M	74,201
269	MOUSSAS, X
LIN, RP	162
269,273	MULLAN, DJ
LOCKWOOD, JA	237

508  
AUTHOR INDEX

MURPHY, RJ	PISARENKO, NF
249,253	313
NECHAEV, OYU	POMERANTZ, MA
229	335,433
NEUBAUER, FM	POTGIETER, MS
162	429,425
NEUSTOCK, HH	PYLE, KR
102	409,497
NEWKIRK, G	RAMATY, R
469	6,249,253
NG, CK	REAMES, DV
326,330	281,269
NIEMINEN, M	225,265
364	273,273
NIKOLAEV, VS	REGUERIN, A
196	138
NISKOVSKIKH, AS	REPPIN, C
368	126
NITTA, N	RICHTER, K
301,54	158
NOSOV, SF	RIEGER, E
413	146
NUBER, R	RIVERO, F
174	110
NYMMIK, RA	ROELOF, EC
205	417
OHI, Y	RYAN, JM
297	1,82
OHKI, KI	SAITO, T
50	441
ORISHCHENKO, AV	SAKURAI, K
293	297
OTAOLA, JA	SANDERSON, TR
493	322
OUENBY, JJ	SARRIS, ET
162	170
OWENS, A	SAVENKO, IA
142	229
PAKHOMOV, NI	SCHELLERT, G
122	305
PALENQUE, E	SCHLICKEISER, R
138	2
PARISI, M	SCHLUTER, W
134	355
PELTONEN, J	SCHOLER, M
364	182,241
PEREZ-ENRIQUEZ, R	SCHWENN, R
257,493	162
PEREZ-PERAZA, J	SECHINOV, VP
18,22,26	205
30,34,110	SEMUKHIN, PE
PETUKHOV, SI	106
196	SEVAST'YANOV, VN
PISARENKO, NF	356

509  
AUTHOR INDEX

SHAFFER, YUG	TAQUICHIRI, MA
313	138
SHAKHOV, BA	THOMAS, J
413	142
SHAPOVALOVA, LA	TIMOFEEV, VE
122	313
SHARE, GH	TKEMALADZE, VS
126,146	477
SHEA, MA	TORSTI, JJ
437,501	364
SHEELEY, NR	TRAINOR, JH
94	209,98
SHIELDS, JC	TRETYAKOVA, CHA
192	205
SHVARTSMAN, YAE	TROTTER, G
473	42,46
SIGNORINI, C	TSUNETA, S
134	50
SIMNETT, GM	TURPANOV, AA
70,38,82	196
SIMPSON, JA	VAHIA, MN
469,277	221
409,497	VAINIKKA, E
SLYUNYAEVA, NV	364
457	VAKULOV, PV
SMART, DF	205,205
501	VALDES-GALICIA, JF
SMITH, EJ	162,493
322	VALTONEN, E
STEKOL'NIKOV, NV	364
457	VAN HOLLEBEKE, MAI
STOKER, PH	209,98
114	VAUCLAIR, S
STOLPOVSKY, VG	233
62	VENKATESAN, D
STONE, EC	392,405
445,217	VESTRAND, WT
213,404	126,146
200	VILLORESI, G
STONE, RG	134
94,269,14	VILMER, N
265	42
STORINI, M	VLAHOS, L
134	10,166
STOZHKOVA, YUI	VOLODICHEV, NN
481	229
SUDA, T	VON ROSENVINGE, TT
301	281,66,14
SWINSON, DB	225,190
437,441	WADA, M
TAKAHASHI, K	138,301
138	WATANABE, H
TAKENAKA, T	54,90
297	WEBBER, WR

510  
AUTHOR INDEX

WEBBER, WR  
388,200  
WEBB, GM  
421  
WENZEL, KP  
322  
WIBBERENZ, G  
102,305  
334  
YADAV, RS  
461  
YANAGIMACHI, T  
297  
YANCHUKOVSKY, AL  
122  
YANG, GL  
360  
YANKE, VG  
118  
YOSHIMORI, M  
54,90  
YU, C  
261  
ZHANG, GL  
360  
ZHAN, S  
261  
ZHOU, R  
261  
ZHURAVLEV, DA  
205  
ZUSMANOVICH, AG  
473



## BIBLIOGRAPHIC DATA SHEET

1 Report No NASA CP-2376 Volume 4	2 Government Accession No	3. Recipient's Catalog No	
4 Title and Subtitle 19th International Cosmic Ray Conference Conference Papers		5 Report Date August 1985	
		6. Performing Organization Code 665	
7. Author(s) Frank C. Jones, compiler		8. Performing Organization Report No.	
9. Performing Organization Name and Address Laboratory for High Energy Astrophysics Goddard Space Flight Center Greenbelt, MD 20771		10 Work Unit No	
		11. Contract or Grant No	
12 Sponsoring Agency Name and Address National Aeronautics and Space Administration Washington, D. C. 20546		13. Type of Report and Period Covered  Conference Publication	
		14. Sponsoring Agency Code	
15 Supplementary Notes			
16 Abstract These volumes contain papers submitted for presentation at the 19th International Cosmic Ray Conference, held on the campus of the University of California, San Diego in La Jolla, CA., August 11-23, 1985. The conference is held every other year. The present volume contains papers with Paper Codes SH 1.1 through SH 4.2 and deals with x-rays, electrons, protons, and neutrons from solar flares, the propagation of solar particles in the solar corona and interplanetary space, and episodic and lo.			
17 Key Words (Selected by Author(s)) solar flares, solar protons, solar neutrons, propagation, solar modulation		18 Distribution Statement  Unclassified - Unlimited  Subject Category - 93	
19 Security Classif (of this report) Unclassified	20 Security Classif (of this page) Unclassified	21 No. of Pages	22 Price*







National Aeronautics and  
Space Administration

**Goddard Space Flight Center**  
Greenbelt, Maryland 20771